Optical feedback frequency-stabilized cavity ring-down spectroscopy - Highly coherent near-infrared laser sources and metrological applications in molecular absorption spectroscopy

Johannes Burkart

UNIVERSITÉ DE GRENOBLE

THÈSE

Pour obtenir le grade de

DOCTEUR DE L'UNIVERSITÉ DE GRENOBLE

Spécialité : **Physique de la matière condensée et du rayonnement**

Arrêté ministériel : 7 août 2006

Présentée par

Johannes BURKART

Thèse dirigée par **Samir KASSI**

préparée au sein **du Laboratoire Interdisciplinaire de Physique (LIPhy)** et de **l'Ecole Doctorale de Physique**

Optical feedback frequency-stabilized cavity ring-down spectroscopy

Highly coherent near-infrared laser sources and metrological applications in molecular absorption spectroscopy

Thèse soutenue publiquement le **25/09/2015**,
devant le jury composé de :

M. Eric LACOT
Université de Grenoble, Professeur de l'Université, Président
M. Daniel LISAK
Université Nicolas Copernic de Toruń, Professeur associé, Rapporteur
M. Marco MARANGONI
École polytechnique de Milan, Professeur associé, Rapporteur
Mme Anne AMY-KLEIN
Université Paris 13, Professeur de l'Université, Examinatrice
M. Samir KASSI
Université de Grenoble, Ingénieur de Recherche CNRS, Directeur de thèse

Für meine Eltern

Acknowledgements

First and foremost, I would like to express my deep gratitude to my PhD supervisor Samir Kassi for the fascinating scientific journey he took me on. Thank you for opening so many possibilities for my scientific and personal development and for being available day and night with your advice and guidance, always ready to share your tremendous scientific and technological knowledge, while nonetheless granting me a lot of freedom and responsibility in our common research.

Then, I would like to sincerely thank the whole group LAME. It has always been an honor and a pleasure for me to work in this great team, and I will keep a very precious memory of your inspiring kindness, generosity and open-mindedness. Thank you for all your help and for the many good times together - whether at work or outside of the lab.

In particular, I am very grateful to Alain Campargue for sharing his office with me, for his warmth and for his invaluable advice in any situation. I will keep a very fond memory of our beautiful view on squirells, rabbits and liquid-nitrogen-induced haze and many other memorable moments together. I would like to thank Erik Kerstel for his continued support over all these years, and Daniele Romanini for the many stimulating and fascinating discussions making me benefit from his deep insight into subtle mechanisms and phenomena of cavity enhanced absorption spectroscopy. Furthermore, I would like to thank him and Thibault Desbois, Jean-Luc Martin and Guillaume Méjean for technical support and counsel, as well as for helping us out with components, devices and instruments whenever necessary. I gratefully acknowledge Serge Béguier for providing me with his line fitting procedures, and for many interesting discussions on advanced absorption line profiles and fitting algorithms. Finally, special thanks go to my fellow ground-floor PhD students Chadi, Ekaterina, Janek, Marine, Mathieu, Semeon and Tim.

I am thankful to the directors of LIPhy for having constantly supported our research, first to Jacques Derouard who played a vital part in making my PhD project possible in the first place, and later to Jean-Louis Barrat and Eric Lacot who also provided persistent support for the eventually successful acquisition of a self-referenced optical frequency comb by our group. I would also like to mention the precious initial funding for our project by Pôle SMINGUE of Université Joseph Fourier, which allowed us to set up the first OFFS-CRDS prototype. Furthermore, I gratefully acknowledge the three-year PhD fellowship at Université Joseph Fourier granted to me by the French Ministry of Higher Education and Research for carrying out the work presented here.

Many thanks go to all LIPhy staff for the pleasant, friendly atmosphere in our lab, and to all fellow PhD students for the legendary cakes after the PhD seminars and for all the great times spent together, especially at our amazing PhD weekends.

Furthermore, I am very grateful to André, Bernard, Christophe, Damien, David, Ralph and Robert from the LIPhy workshop for precision machining, for sharing their huge know-how, and for the many interesting discussions. It was a great feeling to know I could always count on your help. My special thanks go to David for having realized so many crucial and challenging parts for the OFFS-CRDS setup, going through all highs and lows of

successive phases of prototyping and optimization. This contribution by our workshop was vital for the research reported in this thesis.

My sincere thanks also go to Annick, Chantal, Jessie, Nadine, Sabine and Sandrine Ferrari for their kind support when facing any type of administrative challenge. They were always available and very helpful, and eventually never left any problem unsolved.

I am happy and grateful to have had the opportunity of collaborating with Marco Marangoni and his PhD student Tommaso Sala during my thesis. Tommaso's time in Grenoble was among the most stimulating during my PhD thesis, and together we made significant advances along several lines in an incredibly productive but pleasant atmosphere. Thank you for your kindness and for making my PhD thesis so much richer.

It was a pleasure and a very valuable experience to be part of the ANR project "LITOS" from the very beginning, and I am grateful to Mathieu Daëron for giving me this opportunity. I would also like to thank him and Erik Kerstel for their precious assistance in analyzing the first proof-of-principle carbon dioxide isotopic ratio measurements by OFFS-CRDS, and, more generally, for sharing their deep insight into stable isotope science and atmospheric physics. Furthermore, I gratefully acknowledge Amaëlle Landais for making the development of an OFFS-CRDS instrument dedicated to water vapor isotopic ratios possible in the framework of the ERC project "COMBINISO".

I would like to express my sincere thanks to Daniel Lisak and Marco Marangoni for accepting the task of reviewing my PhD thesis. I would like to thank them as well as the further jury members Anne Amy-Klein and Eric Lacot for participating in my PhD defense, and for the constructive remarks they provided on my thesis manuscript.

Many thanks also go to Alain, Daniele, Erik, Mathieu, Tim and Zsófia for proofreading parts of this thesis manuscript and for providing many valuable comments and suggestions. I am especially grateful to Samir and to my parents for their tireless efforts in reading the entire manuscript in meticulous detail. With the hours and hours they spent reading this thesis they greatly improved its quality and readability.

Audrey, Caroline, Emiko, Guillaume, Hugo, Jaka, Jens, Jia-Ying, Katharina, Lauriane, Maike, Mathieu, Mathilde, Matthias, Melanie, Nicolas, Orso and Vilius, your friendship made our years in Grenoble so precious and unforgettable. Thank you for everything.

I would like to express my great gratitude to Brigitte, Györgyi, Gábor, István and Jürgen for the sacrifices they have made to support Zsófia, Ferenc and me in the months of thesis writing. Without your help up close and from afar I would not have been able to realize the thesis manuscript in its present form. Furthermore, I would like to thank my grandparents for their genuine interest in my work and for their constant encouragement. Finally, I am deeply indebted to my parents, who have given me infinitely much and have always supported me in any way imaginable.

Above all, I cannot thank my wife Zsófia enough for her loving support and her precious advice, and my son Ferenc for giving me so much happiness and strength. You two mean the world to me. You are the light of my life.

Contents

Chapter 1

Introduction

After over 100 years of breakthroughs, discoveries and accomplishments, molecular spectroscopy is facing new frontiers in the 21st century.

The numerous fascinating avenues of current research include several tests of fundamental physical laws. Laboratory experiments have set stringent upper bounds for potential violations of the symmetrization postulate of quantum mechanics by searching for molecular transitions to states which cannot exist if symmetrization prevails [1, 2]. Potential variations of the proton-to-electron-mass ratio are being sought for in laboratory experiments [3] and on a cosmological scale, using H_2 lines in the absorption spectra of quasars [4]. Similar experimental techniques are used for probing a potential cosmological variation of the electromagnetic fine structure constant [5].

The revolution in frequency metrology brought about by the emergence of optical frequency combs [6] has also boosted molecular spectroscopy experiments for absolute transition frequency measurements down to the 100-Hz-level [7–9]. A strong synergy exists between such studies providing experimental frequency data with unprecedented accuracy on the one hand, and parallel enormous progress in *ab initio* calculations based on first principles [10–12] on the other hand. Providing stringent tests of quantum electrodynamics, this has opened the door to searches for a potential fifth force beyond the Standard Model of particle physics in basic molecular systems [13].

Furthermore, there is an exciting quest for the first experimental observation of shifted energy levels in chiral molecules which is expected on the grounds of parity violation by the weak interaction [14, 15]. Resolving the resulting minute transition frequency differences between enantiomers by precision laser spectroscopy is a continued experimental challenge [16, 17]. An elucidation of parity violation effects in molecular systems could contribute to a better understanding of the origin of homochirality of biomolecules, which is intimately linked to the origin of life.

Closing in on the applications targeted by the developments in this thesis, let us mention that molecular spectroscopy can also contribute to the redefinition of the Kelvin in terms of an exactly defined value for the fundamental Boltzmann constant k_B [18]. This update of the international unit system SI (Système International), which also concerns the kilogram, the ampere and the mole, is expected to be adopted by the General Conference on Weights and Measures (CGPM) in 2018 [19]. Up to then, further precise measurements of k_B with distinctly different experimental techniques have been recommended by the Committee on Data for Science and Technology (CODATA) [20], in order to provide an independent verification of the accepted value for k_B, thus laying a solid foundation for the redefinition of the Kelvin. One such technique is the spectroscopic measurement of k_B through the Doppler broadening of a molecular absorption line in a sample in thermal equilibrium [18], which is illustrated in Fig. 1.1a. First experimental determinations of

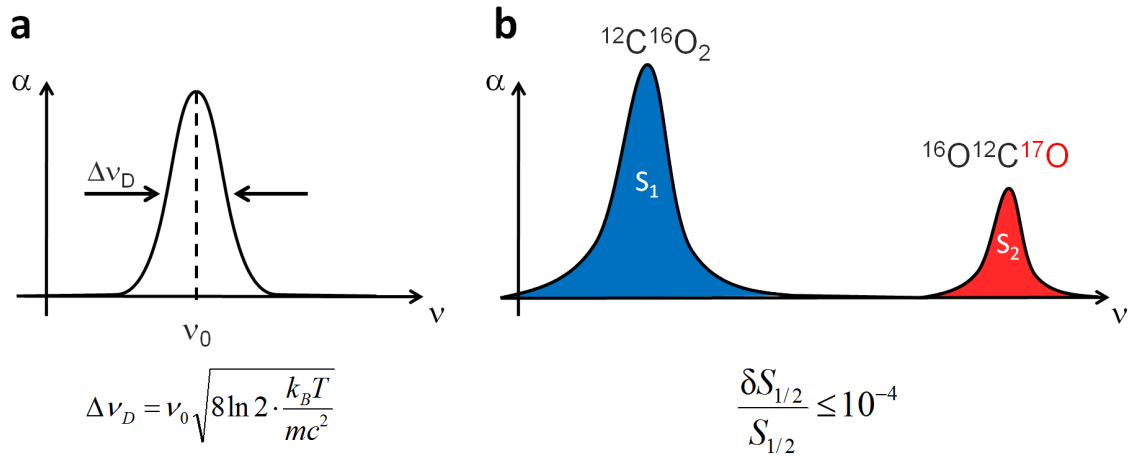

Figure 1.1 Two promising metrological applications of molecular absorption spectroscopy: absolute temperature or Boltzmann constant measurements by the Doppler width $\Delta\nu_D$ of an absorption line (a), and isotopic ratio measurements by the integrated absorptions S_1 and S_2 of two absorption lines belonging to two isotopologues of one molecular species, here in the case of CO_2, with a relative error below 10^{-4} (b). The two illustrations both depict absorption spectra with an absorption coefficient α as a function of optical frequency ν. k_B: Boltzmann constant, T: temperature, m: molecular mass, c: speed of light, ν_0: absorption line center frequency.

k_B with this method [21–23] were in agreement with the accepted value and showed a promising potential for reaching a competitive precision of a few parts per million (ppm) [24–26] in the near future.

This ppm-precision goal sets the same strict requirements on the frequency resolution and stability of any spectrometer used for such a measurement. Furthermore, it challenges the most advanced theoretical models used for describing the shape of a molecular absorption line [27, 28]. Providing insights into intermolecular interaction processes, molecular line shape studies are another domain of molecular spectroscopy where fast progress is currently made through the close cooperation of experimentalists and theoreticians.

Physically sound absorption line profile models are also vital for the rapidly developing application field of isotopic ratio measurements by laser spectroscopy [29]. As illustrated in Fig. 1.1b, the integrated absorption due to a line corresponding to a certain isotopologue of a molecular species is proportional to the number density of that isotopologue. Tiny changes in the isotopic composition of different natural or artificial samples are due to fractionation processes, in particular by the different kinetics and equilibrium thermodynamics of isotopologues with different mass, but also independently of mass, by a differing isotopologue photochemistry, for instance. These subtle isotopic signatures carry a wealth of information on the processes which occurred during the formation or the lifetime of a substance. Consequently, their precise and reliable measurement is highly relevant to environmental sciences and paleoclimatology [30–33]. Optical measurements by laser spectroscopy have been demonstrated for atmospherically relevant species such as water [34, 35], carbon dioxide [36, 37] or methane [38], for instance. Such compact laser instruments, including commercial [39] and field-deployable [40] devices, can complement or eventually replace conventional dual-inlet mass spectrometers, which are both bulky and expensive. Another crucial advantage of spectroscopic approaches is their high intrinsic isotopologue selectivity, which is due to the fact that different isotopologues have distinct and resolved infrared spectra. Consequently, even isotopologues of nearly equal mass can be clearly distinguished by laser spectroscopy.

At Laboratoire Interdisciplinaire de Physique (LIPhy) in Grenoble, which was formerly known as Laboratoire de Spectrométrie Physique (LSP), we build on a long-lasting tradition of fundamental and applied research in molecular spectroscopy. In particular, LIPhy researchers have been pioneering development of state-of-the art laser techniques and instruments for molecular absorption spectroscopy, such as continuous-wave cavity ring-down spectroscopy (CW-CRDS) [41], optical-feedback cavity-enhanced absorption spectroscopy (OFCEAS) [42] and mode-locked cavity-enhanced absorption spectroscopy (ML-CEAS) [43], which have been invented or realized for the first time at LIPhy. The common ground of all these techniques is the use of optical resonators with highly reflective mirrors, which guarantee high resolution and sensitivity by providing a sharp frequency grid and a strong interaction enhancement between light and molecular samples.

To cite just a few examples of the manifold research directions in molecular spectroscopy at LIPhy, let us mention CRDS with record-breaking absorption sensitivity for detecting previously inaccessible absorption features [44], fundamental physics studies [12, 45], and broadband rovibrational spectroscopy [46, 47] for providing comprehensive coverage in spectroscopic databases, which are beneficial for a wide range of applications, such as planetology [48, 49], for instance. Further efforts are directed at the development of compact laser instruments for the measurement of isotopic ratios [35, 50] and the detection of trace gases for environmental sciences [51, 52], pollution monitoring [53, 54], real-time breath analysis [55], and the in situ detection of elusive atmospheric radicals [56, 57], which play a key role in ozone photochemistry.

While traditionally reaching record sensitivities in terms of absorption, the frequency precision of spectrometers at LIPhy was first limited by a frequency axis calibration based on grating spectrograph or reference etalon readings and reference lines, and lately by the measurement precision of optical wavemeters, which reach a frequency resolution at the MHz level at best.

To go beyond this limitation, we set out on the development of an ultrastable V-shaped optical cavity as a dedicated reference resonator for frequency-stabilization and linewidth-narrowing of a conventional near-infrared diode laser by optical-feedback locking [58]. Combined with radio-frequency fine-tuning using an integrated electro-optic single-sideband modulator, we thus realized a highly stable, yet tunable laser source with sub-kHz linewidth, outperforming our best wavemeter by three orders of magnitude in terms of resolution and short-term stability. Importantly, the narrow linewidth of this VCOF (for V-Cavity Optical Feedback) laser allows its efficient injection into an optical cavity with highly reflective mirrors. Clearly, the work in [58] prepared the ground for the developments reported here.

A first objective of this thesis was to fully characterize the frequency noise and stability properties of the VCOF laser. This was a non-trivial task due to the fact that no other light source at LIPhy came close to being sufficiently coherent for qualifying as a reference oscillator for the sub-kHz-linewidth laser.

The heart of our project was to use this stable VCOF laser for realizing a novel cavity ring-down spectrometer with unprecedented frequency stability and resolution and further increased absorption sensitivity. This Optical Feedback Frequency-Stabilized Cavity Ring-Down Spectrometer (OFFS-CRDS) was designed for tackling challenging metrological applications of molecular absorption spectroscopy, such as Doppler thermometry or isotopic ratio measurements (cf. Fig. 1.1). Metrology, as the science of measurements, dictates rules for rigorous measurement procedures and requires an experimental setup which allows traceable measurements of physical quantities. Such measurements are linked to primary standards, which put the definition of the SI units into practice, by an unbroken

chain of calibration measurements with a complete uncertainty analysis and error budget.

Once OFFS-CRDS was operational, our objective was threefold. We aimed at fully characterizing the performance of the new spectrometer, at understanding and alleviating its limitations, and at carrying out first spectroscopic applications exploiting its characteristic qualities.

In line with the discussion above, this thesis consists of three parts. The first part focuses on the realization and characterization of highly coherent near-infrared laser sources for precision spectroscopy. The second part details design aspects and characteristics of the new OFFS-CRD spectrometer and provides a general analyis of limitations of CRDS. The third part reports metrological applications of OFFS-CRDS to the rovibrational spectroscopy of CO_2 with a particular focus on saturated absorption.

Throughout its three parts, the present treatise is based on six peer-reviewed articles and one theoretical supplementary material, which are concise, yet detailed accounts of the major scientific results obtained in the framework of this thesis. For the specialist reader, it may be opportune to start off by reading these articles to gain a broad overview of the results which have been obtained. Afterwards, the reader may turn to the additional technical and experimental details as well as further theoretical and experimental results reported here. As far as possible, the chapters were designed to be self-sufficient, and references to previous or following sections are made wherever it was opportune. Consequently, the reader interested in one particular aspect of the present work may focus on the corresponding chapter to begin with.

Naturally, this thesis can be read equally well in a linear fashion. Chapters on basic concepts, intended to provide a physical and methodological background and an overview of the relevant literature, are alternated with chapters dedicated to the presentation and discussion of our scientific results. This linear structure is meant to provide a consistent global picture and is recommended to the novice reader.

In Chapter 2, we provide an introduction to basic concepts of laser frequency stability and phase noise, as well as measurement and stabilization schemes. In a similar manner, optical single-sideband modulation, self-referenced optical frequency combs, as well as the basic physics and recent developments of ultrastable optical cavities for laser stabilization will be introduced.

In Chapter 3, the original publication reporting the VCOF laser is followed by an experimental section detailing its frequency-noise characterization with a massive reference etalon, as well as long-term frequency drift measurements using either narrow saturated absorption features or an optical frequency comb. Eventually, ongoing developments on improved V-shaped reference cavities are presented.

In Chapter 4, we explore straightforward methods for transferring the coherence of our VCOF laser to other, noisier near-infrared lasers well outside the VCOF laser bandwidth. These techniques are based on ultra-fast frequency and phase corrections to the noisy laser light field by single-sideband modulation in a feed-forward configuration. Beside a methodological and theoretical analysis, we present two articles reporting experimental results on sub-radian phase coherence transfer and frequency-offset locking on the one hand, and a generalization of this scheme for coherence transfer over a broad spectral interval by an optical frequency comb on the other hand. The studies in this chapter were carried out in collaboration with the group of Prof. Marco Marangoni from Politecnico di Milano.

In Chapter 5, we provide a brief introduction to historical and methodological aspects of CRDS and discuss two different theoretical approaches. Then, ultra-sensitive and frequency-stabilized CRDS techniques from the literature, which are relevant to OFFS-

CRDS, are reviewed. Eventually, some exciting recent trends and developments in CRDS are discussed.

In Chapter 6, we render a detailed account on the new OFFS-CRD spectrometer. The original publication of the method is followed by an in-depth discussion of all relevant experimental and technical details including data processing and automation routines. At the end of the chapter, an experimental study characterizing the dependence of the absorption detection limit on spectrum averaging is presented, reaching a record low on a narrow spectral zone.

In Chapter 7, systematic error sources and limitations of CRDS are analyzed from a general point of view. Covering a broad range of adverse effects, the discussion combines findings from the literature with our own experimental studies and theoretical developments. The comprehensive overview of errors and biases provided in this chapter are meant to promote a considered use of CRDS for metrological applications.

In Chapter 8, an introduction to some basic concepts of rovibrational absorption spectroscopy is given, with a particular focus on line profile models. The second half of the chapter is dedicated to an article reporting further performance characterizations and improvements in OFFS-CRDS as well as proof-of-principle applications to broadband spectroscopy and precision line shape measurements.

In Chapter 9, a literature review on saturated absorption studies by CRDS is followed by a detailed theoretical analysis of weak saturation effects in CRDS. In particular, we derive an analytic formula for the non-exponential ring-down signal in this regime and apply it to saturated-absorption experiments by OFFS-CRDS. Then, a frequency-comb-assisted OFFS-CRDS setup is presented, which was used for measuring twelve $^{12}C^{16}O_2$ transition frequencies near 1.6 µm with an accuracy of a few kHz, again in collaboration with the Marangoni group of Politecnico di Milano. After the original article reporting these results, the data processing and error analysis are discussed in more detail, as well as the impact of these new CO_2 reference frequencies for spectroscopic databases.

In Chapter 10, a conclusion of the work carried out in the framework of this thesis is drawn. Providing an outlook to research activities in the near future, we show preliminary results on the first application of OFFS-CRDS towards optical isotopic ratio measurements of ^{17}O in CO_2. Eventually, a general perspective on future developments and applications of OFFS-CRDS is given.

Part I

Highly coherent and tunable laser sources for precision spectroscopy

Chapter 2

Methodological foundations and state of the art

Almost 100 years ago, Albert Einstein predicted the existence of a stimulated emission process of radiation [59] theoretically. This pioneering contribution and many ensuing studies ([60], for instance) paved the way to a radiation source of unprecedented spectral purity, the ammonium maser (**m**icrowave **a**mplification by **s**timulated **e**mission of **r**adiation) realized by James Gordon, Herbert Zeiger and Charles Townes [61] 60 years ago. Five years later, it was followed by Theodore Maiman's ruby laser (**l** for light) in the visible domain of the electro-magnetic spectrum [62].

After these breakthroughs, it took another 45 years until the Nobel prize in Physics was awarded to Theodor Hänsch and John Hall in 2005, in particular for their contribution to the development of self-referenced optical frequency combs. Such frequency combs have revolutionized optical frequency metrology by mapping an optical frequency to two radio frequencies (RF) and one integer [6, 63], as will be discussed in detail in a later section of this chapter. The radio frequencies can be readily measured using a frequency counter, or locked using analog electronics, thus yielding a straightforward optical frequency measurement at an accuracy ultimately limited by the primary caesium clock used for realizing the current definition of the SI-second as $9,192,631,770$ oscillation periods of a hyperfine transition in ground-state ^{133}Cs (SI=**S**ystème **I**nternational d'Unités) [64]. A symbolic depiction of such an electron-nucleus spin flip transition for the case of the hydrogen atom is shown in Fig. 2.1. This phenomenon was judged so fundamental and universal by NASA (National Aeronautics and Space Administration) scientists that the pictogram was engraved on the unmanned Pioneer-10 and Pioneer-11 space probes as a message to potential intelligent extraterrestrial lifeforms who might retrieve the spacecraft. Today, hydrogen masers based on this hyperfine transition are still very powerful

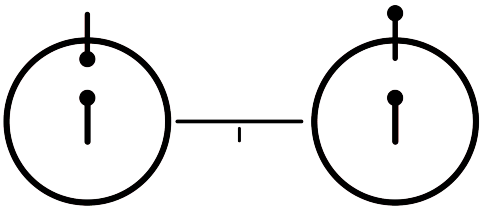

Figure 2.1 Symbolic depiction of the 21-cm-wavelength hyperfine transition of the hydrogen atom by NASA scientists Carl Sagan and Frank Drake.

tools for precision spectroscopy [65], by virtue of their outstanding frequency stability, which typically outperforms rubidium-referenced crystal-oscillator clocks by three orders of magnitude.

The coherence length of a light source can provide an intuitive grasp of the extreme stability properties of maser and laser oscillators. It can be defined as the maximum optical path length difference between two light fields originating from that same source at which temporally and spatially stable interference fringe patterns can still be observed. A rough mathematical formulation for this condition can be obtained by considering the width $\Delta\nu$ of the frequency spectrum of a light source. Assuming a dephasing of less than 2π for components from both ends of the spectrum leads to the following simple expression for the coherence length L_c:

$$L_c \approx \frac{c}{\Delta\nu}, \tag{2.1}$$

where c is the vacuum speed of light. Its exact 9-digit value is fixed to $c = 299,792,458\,\mathrm{m/s}$, thereby defining the meter as the base unit of length in the SI [66]. The fundamental dispersion relation

$$c = \lambda\nu \tag{2.2}$$

links the frequency ν of an electro-magnetic wave to its vacuum wavelength λ. The wavenumber $\tilde{\nu} = 1/\lambda$, typically expressed in units of cm^{-1}, is a derived frequency unit commonly used in molecular spectroscopy. With the dispersion relation (2.2), the coherence length (2.1) of a light source can be rewritten in terms of its spectral width $\Delta\lambda$ around a central wavelength λ:

$$L_c \approx \frac{\lambda^2}{\Delta\lambda} \tag{2.3}$$

Visible white light from a black-body source, such as the sun, for instance, is characterized by a continuous spectrum centered around 550 nm and spanning approximately 300 nm . In this case, Eq. (2.3) yields a coherence length of only 1 µm, implying that white-light interferometers need to work at optical path differences below this value. Except for the case of bidirectional Sagnac loop interferometers [67], where both beams travel an identical optical path in opposite directions, meeting this criterion often constitutes a considerable experimental challenge. With an emission frequency on the order of 24 GHz, stable to a few parts in 10^{12} at the timescale of one second, the first ammonium laser [61] featured an unprecedented spectral purity corresponding to a coherence length of over 7000 km. Today, laser oscillators locked to ultrastable optical resonators, which will be discussed in greater detail in Section 2.4 below, exhibit second-scale linewidths down to 40 mHz at optical frequencies on the order of 200 THz [68]. This corresponds to a coherence length of $7 \cdot 10^6$ km, 18 times the distance between earth and moon.

The ground-breaking scientific advances discussed above are only the tip of the iceberg of the enormous progress which was made in the physics of stable oscillators, ultramonochromatic light sources and frequency metrology over the past century. The benefits of ultrastable lasers for fundamental physics in general, and for precision spectroscopy and time and frequency metrology in particular, are numerous.

The objective of this chapter is to provide a general introduction to the study of highly coherent optical oscillators, in order to lay a solid foundation for the discussion of methods and results on laser frequency stabilization and coherence transfer in this thesis, while embedding it in a broader context. An exhaustive, complete and profound treatment of this vast field, however, is beyond the scope of this Thesis and not attempted here.

2.1 Frequency stability and phase noise

An ideally monochromatic oscillator at angular frequency ω_0 is characterized by the time-dependent field amplitude

$$E(t) = E_0 \cos(\omega_0 t + \varphi_0) \tag{2.4}$$

where E_0 is the maximum field amplitude and φ_0 the initial phase of the oscillation.

By contrast, in a real oscillator, there are random phase fluctuations due to noise processes, such as the spontaneous emission of a photon with random phase in the laser medium. This is only one particular example, as there are myriads of atoms in the laser medium, charge carriers in the driving electronics and photons in the pump field and in the laser resonator, which, in turn, is subject to mechanical perturbation, while all are affected by thermal motion and the statistics related to thermal excitation. Due to the complex interactions between all these system constituents, many other stochastic mechanisms may affect the oscillation of the laser field, giving rise to a random noise process in laser phase. Consequently, $\varphi(t)$ becomes a time-dependent quantity $\varphi(t)$, and $E(t)$ then reads

$$E(t) = E_0 \cos(\omega_0 t + \varphi(t)) \tag{2.5}$$

The explicit time-dependency of the phase noise $\varphi(t)$ alters the instantaneous frequency $\omega(t) = \mathrm{d}(\arg[E(t)])/\mathrm{d}t$ of the oscillator:

$$\omega(t) = \frac{\mathrm{d}(\omega_0 t + \varphi(t))}{\mathrm{d}t} = \omega_0 + \frac{\mathrm{d}\varphi(t)}{\mathrm{d}t} \tag{2.6}$$

This fundamental relationship therefore inseparably links phase and frequency noise processes, which are two representations of the same physical reality. For comparing characteristics of oscillators from different domains of the electro-magnetic spectrum, the instantaneous frequency is often expressed as a normalized relative frequency $y(t)$ with respect to the reference frequency ω_0 defined as

$$y(t) = \frac{\omega(t) - \omega_0}{\omega_0} \tag{2.7}$$

The phase noise processes in φ, ω and y can be decomposed into contributions from many spectral frequencies f, which are also called Fourier frequencies in honor of the father of spectral analysis [69]. To examine their respective impact on the total noise process, let us first consider the autocorrelation function $R_y(\tau)$ of the quantity $y(t)$, which is given by

$$R_y(\tau) = \lim_{T\to\infty} \frac{1}{2T} \int_{-T}^{T} y(t+\tau) y^*(t) \mathrm{d}t \tag{2.8}$$

where the asterisk denotes the complex conjugate. The power spectral density (PSD) of $y(t)$ then reads

$$S_y(f) = 2 \int_{-\infty}^{\infty} R_y(\tau) \mathrm{e}^{-i2\pi f\tau} \mathrm{d}\tau \tag{2.9}$$

and gives the spectral contribution to $y(t)$ from the Fourier frequency interval $[f, f + \mathrm{d}f]$. This important result is the Wiener-Khintchine theorem [70, 71]. The power spectral density in Eq. (2.9) is implicitly one-sided, in that its domain of definition is the positive real axis $f \geq 0$. The factor of two in (2.9) originates from the conversion of a symmetric, two-sided PSD into a one-sided PSD of the same integrated area, which is most commonly

used in practice. According to Eqs. (2.8) and (2.9), the total variance σ_y^2 in $y(t)$ is given by

$$\sigma_y^2 = \int_0^\infty S_y(f)\mathrm{d}f \tag{2.10}$$

Relations analogous to Eq. (2.9) also hold for all other time-domain signals. Corresponding to $\varphi(t)$, for instance, $S_\varphi(f)$ is the phase noise PSD, which reveals the spectral composition of the underlying phase noise processes. Moving from angular frequencies to frequencies, one may define the instantaneous detuning $\Delta(t)$ of the laser field in Eq. (2.5) with respect to its nominal frequency $\omega/(2\pi)$ as

$$\Delta(t) = \frac{\omega(t) - \omega_0}{2\pi} \tag{2.11}$$

With (2.11), the equivalence relation (2.6) between phase and frequency noise combined with the Δ- and φ-variants of Eq. (2.9) yields the following important relationship between the phase- and frequency-noise power spectral densities:

$$S_\Delta(f) = f^2 S_\varphi(f) \tag{2.12}$$

Common noise processes exhibit power-law-scaling with Fourier frequency in $S_\Delta(f)$, and consequently in $S_\varphi(f)$. For instance, a random walk of laser phase leads to $S_\Delta(f) = \text{const.}$, called white frequency noise. Another very common noise process often dominating at low Fourier frequencies is so-called $1/f$ or flicker noise of technical origin, which is characterized by $S_\Delta(f) \sim 1/f$. For a more detailed discussion on physical phase noise processes and an overview on their different power-law scalings in $S_\Delta(f)$ and $S_\varphi(f)$, see [72] and Table 2.1 therein, for instance.

Another important quantity is the power spectral density $S_E(f)$ of the light field $E(t)$ itself, derived via the autocorrelation function $R_E(\tau)$:

$$S_E(\omega) = 2\int_{-\infty}^{\infty} R_E(\tau)\mathrm{e}^{-i\omega\tau}\mathrm{d}\tau \tag{2.13}$$

This quantity, which is not to be confounded with $S_\Delta(f)$ or $S_\varphi(f)$, is proportional to the power spectrum of the electro-magnetic field. When measured, it directly provides the laser linewidth in terms of the width of the peak at ω_0. It is also useful for retrieving the autocorrelation function of the light field by inverting the Fourier transformation in Eq. (2.9). A very interesting property of $S_E(\omega)$, which is useful for characterizing the phase coherence of narrow-linewidth lasers, is the relationship between phase variance σ_φ^2 and the power P_c in the coherent delta-peak carrier at ω_0, as compared to the total signal power $P_{tot} \sim \int_0^\infty S_E(\omega)\mathrm{d}\omega$ [73]:

$$\frac{P_c}{P_{tot}} = \mathrm{e}^{-\sigma_\varphi^2} \tag{2.14}$$

This equation will be used in Article 2 on page 51 for characterizing the sub-radian phase-coherence transfer by single-sideband modulation in a feed-forward configuration.

An analytic relationship between $S_\varphi(f)$ and $S_E(\omega)$ can be developed [74, 75] by writing the autocorrelation for the field $E(t)$ as

$$R_E(\tau) = E_0^2 \mathrm{e}^{i\omega_0\tau}\mathrm{e}^{-2\int_0^\infty S_\Delta(f)\frac{\sin^2(\pi f\tau)}{f^2}\mathrm{d}f} \tag{2.15}$$

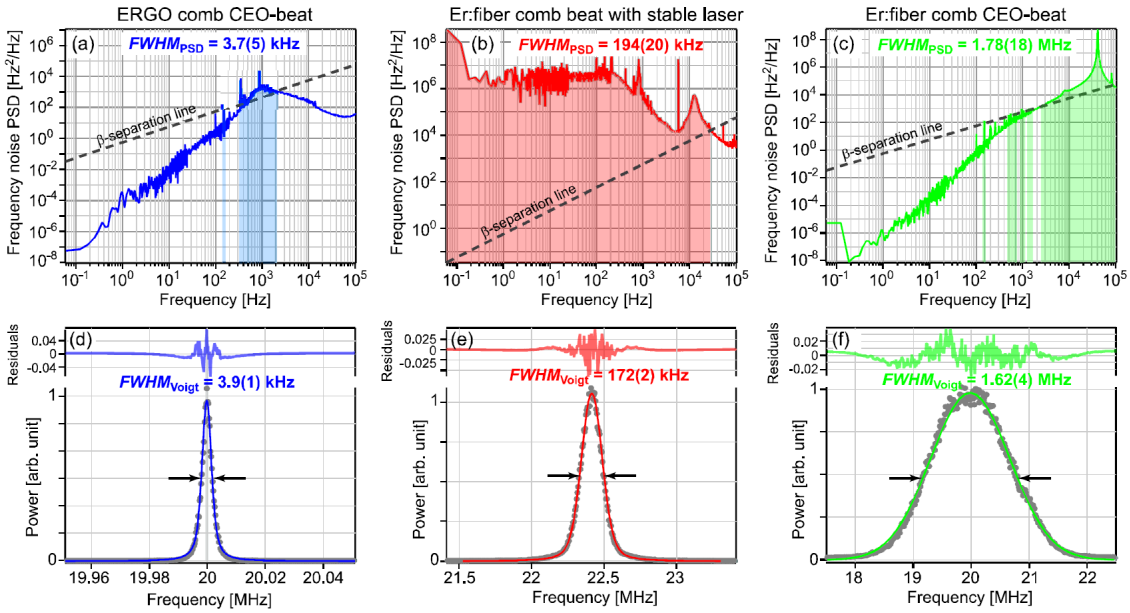

Figure 2.2 Experimental study on the combined frequency noise power spectral densities (upper panels) and optical power spectra (lower panels) of three laser pairs by Bucalovic *et al.* [76]. The areas under each frequency noise PSD to be used in Eq. (2.18) for estimating the laser linewidth with the β-separation-line technique are indicated by darker shades. Adapted from [76] (Figure 2).

Then, $S_E(\omega)$ follows from Eq. (2.13). Unfortunately, this expression can only be evaluated analytically in a few simple cases [75], for instance for pure white frequency noise:

$$S_\Delta(f) = h_0 \Leftrightarrow S_E(\nu) = E_0^2 \frac{h_0}{(\nu - \nu_0)^2 + \frac{\pi^2 h_0^2}{4}} \tag{2.16}$$

where frequency units $\nu = \omega/(2\pi)$ and $\nu_0 = \omega_0/(2\pi)$ have been used. Consequently, the power spectrum of an oscillator exhibiting pure white frequency noise is a Lorentzian with full width at half maximum (FWHM) πh_0 centered at ν_0. The dashed line for the free-running DFB laser in Article 1 on page 32 was evaluated on this basis, and corresponds to a Lorentzian laser lineshape with 2 MHz FWHM. When an explicit analytic form for $S_E(\omega)$ does not exist, or in the case of an experimentally measured frequency noise PSD, one must resort to a numerical integration of Eqs. (2.15) and (2.13) while ensuring that numerical pitfalls due to the rapidly oscillating integrand or due to the integration bounds are avoided, which is a challenging endeavor in practice [76].

To address this issue in the case where only the laser linewidth is of interest, Di Domenico and co-workers have proposed a simple geometrical approach to deduce an approximate value for laser linewidth directly from the frequency-noise PSD of an oscillator [75]. To this end, they showed that the sections of the PSD lying below the so-called β-separation line

$$\beta(f) = \frac{8 \ln 2}{\pi^2} f \tag{2.17}$$

do not contribute appreciably to the FWHM of the optical lineshape. Physically, in a modulation-sideband picture of frequency noise, this is due to the fact that contributions at small modulation depths affect mainly the Lorentzian wings of the optical lineshape, whereas high modulation depth processes contribute to the central Gaussian portion, which determines the FWHM. Let A equal the sum of all areas under the curve $S_\Delta(f)$ on intervals where $S_\Delta(f) > \beta(f)$. Then, the β-separation-line estimate for the laser FWHM $\Delta\nu_{FWHM}$

reads

$$\Delta\nu_{FWHM} \approx \sqrt{8\ln 2 \cdot A} \tag{2.18}$$

This simple and elegant procedure for obtaining the laser linewidth is illustrated on the experimental examples shown in Fig. 2.2. One can see that, in spite of significantly different noise structures and orders of magnitude, the combined linewidths estimated with the β-separation-line technique are in good agreement with the values determined directly from the power spectra of the respective two-laser beat notes.

Another very important concept in frequency metrology concerns a time-domain characterization of oscillator frequency stability. In order to mark out random noise from divergent drift processes, Allan suggested a two-sample variance [77] closely related to the one originally proposed by Neumann *et al.* [78]. Taking adjacent dead-time free normalized frequency averages $\overline{y_j} = 1/\tau \int_0^\tau y\,(j\tau + t')\,\mathrm{d}t'$ over a time interval τ, the so-called Allan variance $\sigma_y^2(\tau)$ reads

$$\sigma_y^2(\tau) = \frac{1}{2}\left\langle (\overline{y_{j+1}} - \overline{y_j})^2 \right\rangle, \tag{2.19}$$

where the angle brackets denote a time average over all squared normalized frequency differences. As an example, the Allan deviation $\sigma_y(\tau)$ for the laser oscillator of a state-of-the-art optical clock based on strontium atoms inside an optical lattice [79] is shown on the left of Fig. 2.3.

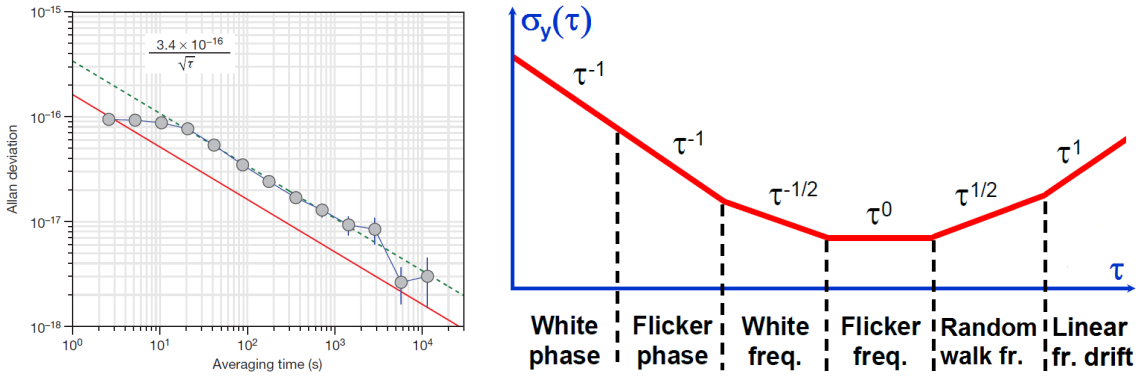

Figure 2.3 Left: Allan deviation $\sigma_y(\tau)$ for a state-of-the-art strontium lattice clock by Bloom *et al.* [79]. The dashed line indicates the averaging behavior expected for random white frequency noise. Adapted from [79] (Figure 1a). The solid red line is a fundamental quantum noise limit. Right: Power-law behavior of the Allan deviation with averaging time τ in double-logarithmic scaling for different phase and frequency noise mechanisms as well as linear frequency drifts.

On the right of Fig. 2.3, the power-law scaling of the Allan variance for different noise processes is sketched schematically. Conveniently measured, typically on the heterodyne beat note of two optical fields, using a dead-time free counter in the radio-frequency domain, the Allan variance thus provides a wealth of information about the noise characteristics of an oscillator, the presence of drifts, as well as the precision level which can be ultimately attained by averaging. The Allan variance follows from the frequency noise PSD by the following relationship [72]:

$$\sigma_y^2(\tau) = 2\int_0^\infty S_y(f)\frac{\sin^4(\pi\tau f)}{(\pi\tau f)^4}\mathrm{d}f \tag{2.20}$$

Consequently, the Allan variance of an oscillator can be determined from its frequency noise PSD, while the inverse is not true in general. Consequently, the characterization in terms of a PSD should be preferred whenever possible, as it provides complete information about the noise properties of the oscillator.

As a concluding remark, let us note that Werle and co-workers have applied the concept of Allan variance to the measurement stability and averaging behavior analysis of molecular absorption spectrometers [80, 81]. In this thesis, the technique was used to characterize the OFFS-CRDS spectrometer in Articles 4 on page 90 and Article 5 on page 160.

2.2 Frequency noise measurement and laser stabilization techniques

The frequencies of optical oscillators on the order of hundreds of THz lie well outside the realm of electronics, turning a measurement of their phase and frequency noise characteristics into an experimental challenge. Nevertheless, many powerful techniques based on different physical mechanisms exist.

A very common approach is based on the heterodyne beat-note between two optical oscillators. Consider the superposition of two fields $E_1(t)$ and $E_2(t)$ as in Eq. (2.5) on a photodetector, yielding the signal $S(t)$:

$$S(t) \sim (E_1(t) + E_2(t))^2 = E_1^2 + E_2^2 + E_1 E_2 \cos\left((\omega_2 - \omega_1)\, t + \varphi_2(t) - \varphi_1(t)\right) \qquad (2.21)$$

where terms oscillating at optical frequencies $\omega_{1/2}$ or higher were omitted, as they are orders of magnitude beyond the bandwidth of any photodiode. The signal in Eq. (2.21) oscillates at the difference frequency of both fields. Consequently, for sufficiently similar optical frequencies, the problem of relative phase noise measurement has been transferred to the radio-frequency domain.

There, a measurement of the combined linewidth can be readily carried out by examining the beat note power spectrum $S_E(\omega)$ with a radio frequency spectrum analyzer. In this process, the shape of the optical spectrum is preserved in the radio frequency domain on the condition that the width of the spectrum is small compared to the beat note frequency $\omega_2 - \omega_1$ [74].

The heterodyne beat note can also be used for characterizing the long-term stability of both oscillators as well as their underlying noise processes. To this end, a dead-time free radio-frequency counter may be employed, which counts the number of cycles N of the beat note signal in a gate time interval t_g yielding the instantaneous frequency of the beat note $f = N/t_g$. The accuracy of this frequency can be ensured by referencing the counter to a 10 MHz timebase signal based on a GPS-disciplined hydrogen-maser or rubidium-clock (GPS: global positioning system). The dead-time free instantaneous frequency measurements can then be used for determining the Allan variance of the system by inserting them into Eq. (2.19), making oscillator stability characterization at hundreds of THz possible, as in the case of the optical atomic clock in Fig. 2.3. There, the Allan variance from the beat note of two independent clock lasers was divided by $\sqrt{2}$ to reflect the performance of the single system, by assuming statistically independent, but equivalent noise processes for the two systems. If, on the contrary, one reference oscillator with supreme frequency stability is available, it can be used for a direct characterization of a noisier oscillator with negligible own noise contribution. This was the case for the characterization of free-running laser noise by a sub-kHz reference laser in Fig. 2a of Article 2 on page 51, for instance.

Finally, the beat note signal (2.21) can also be processed using a radio-frequency discriminator, or frequency-to-voltage converter [82]. Such a device provides a voltage signal proportional to the instantaneous frequency of the beat note and allows a direct determination of its frequency and phase noise PSDs $S_y(f)$, $S_\Delta(f)$ and $S_\varphi(f)$by means of Eqs. (2.8-2.12).

A sensitive phase discriminator for the beat note signal (2.21) can be realized by multiplying it with a local oscillator signal $E_{LO}\cos(\omega_{LO}+\varphi_{LO})$ with negligible phase noise using a radio-frequency mixer. The RF mixer output signal $U(t)$ then reads

$$U(t) \sim E_{LO}E_1E_2\cos(\omega_{LO}+\varphi_{LO})\cos((\omega_2-\omega_1)t+\varphi_2(t)-\varphi_1(t)) \tag{2.22}$$

$$\sim E_{LO}E_1E_2\cos((\omega_2-\omega_1-\omega_{LO}+\varphi_2(t)-\varphi_1(t)-\varphi_{LO})) \tag{2.23}$$

after having cut all signals at frequencies $\omega_2-\omega_1$ or higher by a low-pass filter. In the special case of two highly coherent sources with $\varphi_2(t)-\varphi_1(t) \ll 1$, the choices $\omega_{LO}=\omega_2-\omega_1$ and $\varphi_{LO}=-\pi/2$ lead to

$$U(t) \sim E_{LO}E_1E_2\sin(\varphi_2(t)-\varphi_1(t)) \sim (\varphi_2(t)-\varphi_1(t)) \tag{2.24}$$

Consequently, $U(t)$ acts as a phase discriminator yielding a voltage proportional to the relative phase of the two fields in this regime.

This mixer operation at quadrature as in Eq. (2.24) is particularly useful when using $U(t)$ as an error signal for an active servo control phase phase-locking the two optical oscillators to $\Delta\varphi \approx 0$ at an angular frequency offset ω_{LO}. The basic structure of such a phase-locked loop (PLL), whether electronic or optical (OPLL), is shown in Fig. 2.4. The

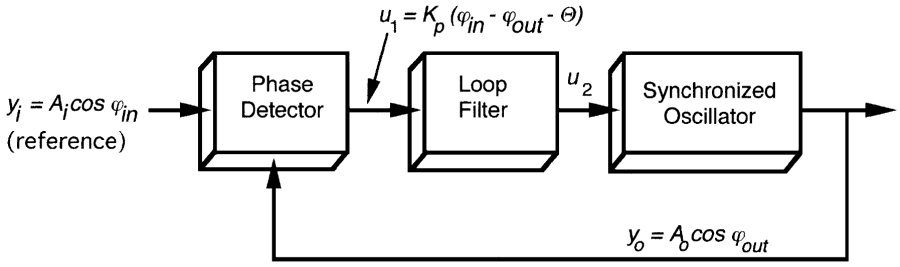

Figure 2.4 Block diagram of a basic phase-locked loop (PLL). Adapted from [83] (Figure 1.1).

control signal u_2 in Fig. 2.4 can be the pump current of a diode laser, for instance. Their particularly fast modulation response has allowed the realization of analog OPLLs with servo bandwidths as high as 180 MHz [84, 85] in the field of microwave telecommunication, yielding a phase lock with a root-mean-square (rms) phase error down to 0.2 rad between lasers with free-running linewidths of several MHz dominated by fast white frequency noise. Commercial modules for realizing an optical phase-locked loop based on the mixing signal from a heterodyne beat note and a local oscillator also exist and feature bandwidths of several tens of MHz. As an example, let us mention the Toptica mFALC 110 module, without endorsing it in any way. For a noisier relative phase rapidly varying by several radians, a digital phase discriminator can relax servo bandwidth requirements and provide a reliable lock with wide locking range at the price of slightly increased residual phase error. A prominent example for such a system is the broad-range digital phase-frequency detector by Prevedelli, Freegarde and Hänsch [86].

For measuring the frequency noise PSD of a laser without down-conversion into the radio-frequency domain, optical frequency discriminator schemes exist. They are based

on physical processes which exhibit a narrow response as a function of optical frequency conveying them high discrimination sensitivity. As discussed in detail in Section 3.2.1, we have used the transmission of a high-finesse Fabry-Pérot cavity with a mode width of 9 kHz for measuring the frequency noise PSD of the sub-kHz VCOF laser. A similar approach consists in using a Doppler-broadened absorption line [87] as an optical frequency discriminator. For obtaining higher frequency sensitivity, using a saturated-absorption feature (cf. Chapter 9) may be an interesting alternative.

Another approach to measuring the phase and frequency stability of an optical oscillator without an independent reference consists in the time-delayed interference of two light fields from the same source. Intuitively, the introduction of a time delay τ approaches an experimental realization of the autocorrelation function (2.8) of the light field. The interference can be carried out by splitting the signal into two parts, inserting a fiber-optic delay line τ in one of the two arms, and recombining the delayed and undelayed beams. This setup constitutes a Mach-Zehnder type interferometer which converts phase fluctuations of the light fields into intensity variations which can be detected using a photodiode. If an additional frequency shift is introduced in one interferometer arm, for example by means of an acousto-optic modulator (AOM), the interference signal can be studied in the radiofrequency domain by means of an RF spectrum analyzer. An example for such an experiment can be seen in Fig. 2.5, showing the delay-line-measured power spectrum of a distributed-feedback (DFB) laser at 1.55 µm shifted to 200 MHz by an AOM.

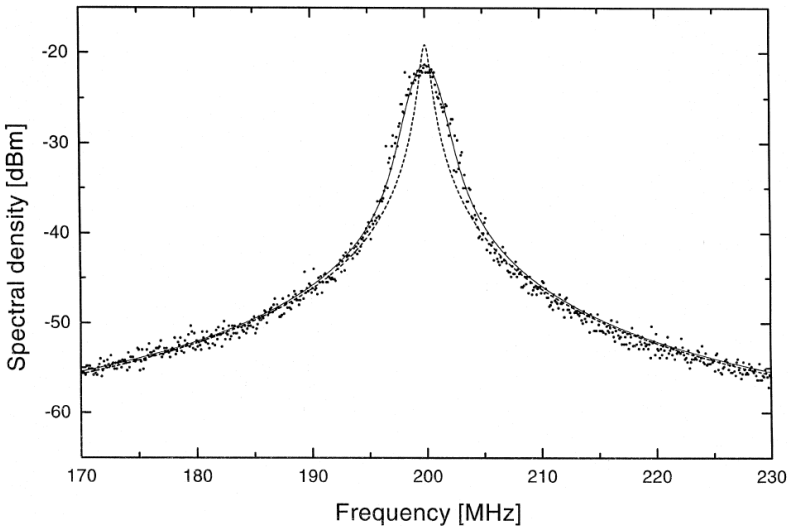

Figure 2.5 Radio-frequency power spectrum from a self-heterodyne measurement of a DFB laser with a 6-km-long delay line by Ludvigsen *et al.* [88]. The solid line corresponds to an optical lineshape with flicker and white noise contributions. The white-noise contribution corresponds to a Lorentzian with a linewidth of 440 kHz (dashed line). Adapted from [88] (Figure 2).

The phase noise PSD S'_φ of the interferometer output signal may be measured using a radio-frequency phase discriminator. Then, the phase noise PSD S_φ of the optical oscillator can be retrieved using the relation [72]

$$S'_\varphi(f) = 4\sin^2\left((\pi f\tau)^2\right) \cdot S_\varphi(f) \tag{2.25}$$

Consequently, the observable noise signature in the interferometer output signal vanishes quadratically as $f\tau \to 0$. In view of this property of Eq. (2.25), the elegant delay-line technique is unfortunately impractical for characterizing sub-kHz-linewidth lasers with important frequency noise contributions at Fourier frequencies below $f_c = 100\,\mathrm{Hz}$ (cf. Fig.

5 of Article 1). To resolve such slow fluctuations in the time domain, a delay line with a length of $c/f \approx 3000\,\mathrm{km}$ would be necessary. In such situations, partial information on the high-frequency noise properties of the laser can nevertheless be extracted even with a short delay line [88].

For further details on phase and frequency noise measurement techniques, see [72], for instance. Let us note that amplitude noise, which is present in real systems and was set aside here and in the preceding section for the sake of simplicity, can not be distinguished from frequency noise in all of the above measurement schemes. Consequently, it is important to evaluate its impact by means of an independent measurement. In practice, amplitude noise is often negligible in sensitive phase or frequency noise measurements [73].

While electronic solutions to laser stabilization are most common, diode laser frequency stabilization and linewidth narrowing by resonant optical feedback from a high-finesse resonator is a physically appealing and powerful technique. Physically, the high sensitivity of such lasers to optical feedback is due to the coupling between electric field amplitude and phase in the semiconductor laser medium via charge-carrier density variations [89]. Dahmani, Hollberg and Drullinger first demonstrated how the reinjection of light transmitted by an optical cavity into the laser medium leads to a linewidth-narrowing by three orders of magnitude and self-locking of laser frequency to cavity resonance [90].

This optical feedback self-locking phenomenon can be seen as an optical form of injection locking, where a resonant circuit starts oscillating at the frequency of another oscillator which is used for exciting the first one, provided that there is a sufficiently strong coupling between the two [72]. A mechanical analogon to this behavior is the anti-phase synchronization of two pendulum clocks mounted on a common support discovered by Huygens in 1665 [91].

An in-depth theoretical treatment of the Maxwell-Bloch equations in a laser medium with an optical feedback term was given by Laurent and co-workers [92]. The main results of their analysis have been summarized and discussed in [58]. Another detailed introduction to optical feedback self-locking in view of optical feedback cavity-enhanced absorption spectroscopy (OFCEAS) is provided in [42]. Finally, a concise discussion on essential features and relations of the phenomenon can be found in the introductory part of Article 1 on page 32. As discussed in the article, we have demonstrated that optical feedback self-locking allows sub-kHz laser frequency stabilization with a simple lock-in-based servo loop at a bandwidth of a few 100 Hz, six orders of magnitude lower than the servo bandwidths of most sophisticated analog OPLLs.

2.3 Optical single-sideband modulation

An optical frequency shifter is an important ingredient for a broad range of experiments in laser physics, frequency metrology and spectroscopy. It allows fine tuning of the frequency of a light field with the accuracy and precision of a radio-frequency signal without perturbing the laser oscillation it originates from. Most often, an acousto-optic modulator (AOM) is used for this purpose. It increases or decreases the photon energy by absorption or emission of a phonon in a travelling sound wave in the modulator medium, leading equally to a slight deflection of the light beam corresponding to momentum conservation. Typical AOM shift frequencies range from several tens to several hundreds of MHz. The AOM bandwidth is limited by the propagation time of the sound wave inside the modulator, which is typically on the order of several $100\,\mu\mathrm{s}$, corresponding to a bandwidth in the few-MHz range [93]. An important advantage of AOMs is the high conversion efficiency of the frequency shifting process, which can reach up to 90%.

A distinctly different physical approach to optical frequency shifting is electro-optic single-sideband modulation with an integrated dual-parallel Mach-Zehnder modulator (MZM). Such a modulator typically features an electro-optic bandwidth from virtually DC to 20 GHz or higher [94, 95] and can shift the frequency of a light wave on that same interval on both sides of the carrier frequency. Operated as a differential quadrature phase-shift keying (DQPSK) transmitter for high-speed fiber-optic telecommunication [94–96], the integrated modulator can encode two bits of digital information in one phase jump of the light field, yielding a data rate up to 100 Gbit/s when exploiting a 50 GHz electro-optic bandwidth [95].

Here, we will give a brief introduction to the basic principles and characteristics of continuous-wave operation of an MZM as a single-sideband modulator. The nested Mach-Zehnder-interferometer waveguide structure of the MZM originally proposed and realized by Izutsu and co-workers [97] is shown in Fig. 2.6. A lithium niobate waveguide is split

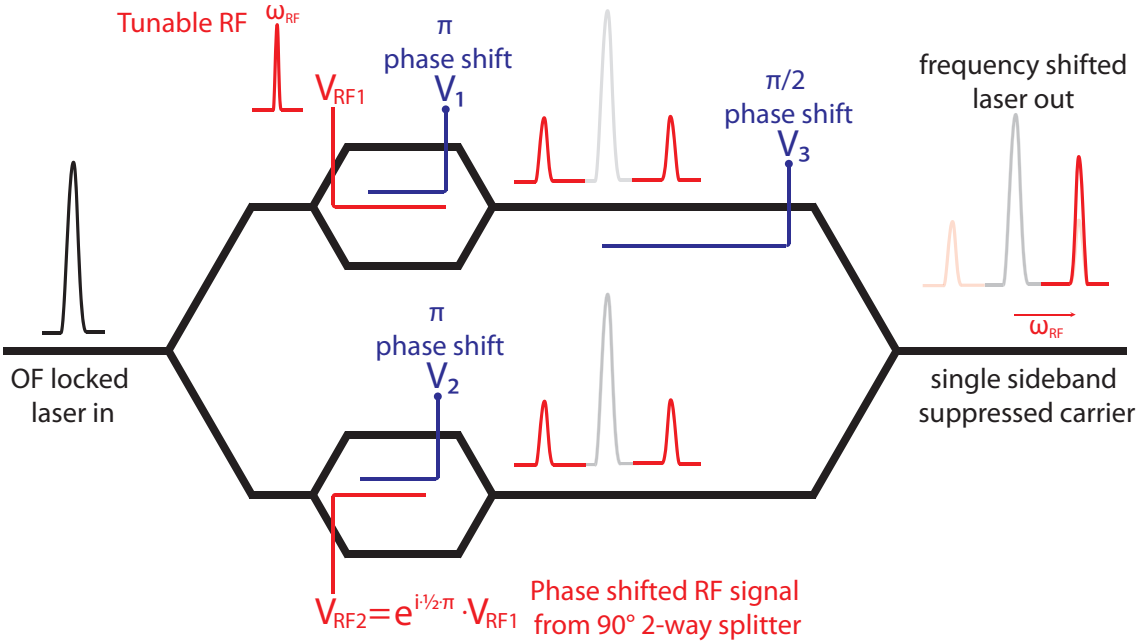

Figure 2.6 Schematic sketch of the lithium niobate waveguide structure (thick black lines) of a dual-parallel Mach-Zehnder modulator with DC electrodes (blue) and RF electrodes (red). The corresponding RF and optical signals are represented by qualitative sketches of their power spectra.

into two symmetric arms, each bifurcating into another parallel waveguide pair, which subsequently recombines and eventually merges with the second arm, providing a single-waveguide output. This waveguide configuration constitutes a triple integrated Mach-Zehnder interferometer (MZI), with two small child MZIs nested in the big parent MZI. The static phase shifts in the three MZIs, the interferometric working points, are controlled by applying static electric fields across the waveguides in both arms of each MZI. By the electro-optic Pockels effect, these fields lead to refractive index changes in lithium niobate, which are equal in magnitude but opposite in sign for the two arms of each interferometer. Both contributions thus produce a static dephasing of the light waves in each MZI, which is controllable by the voltage applied to the respective DC electrode (blue lines in Fig. 2.6). A detailed experimental study of the interferometric transfer functions of the three MZIs is given in [58].

In a similar fashion, travelling-wave radio-frequency electrodes are used for applying

rapidly varying electric fields across the waveguides in both arms of the child MZIs, giving rise to phase modulation sidebands on the respective optical carrier wave. As illustrated in Fig. 2.6, the 90° phase shift between the RF signals applied to the two child MZI is of key importance for single-sideband operation. As a static dephasing of π is applied to the two child MZIs, they become opaque for the optical carrier and transmit only the phase modulation sidebands. A third static dephasing of $\pm\pi/2$ is applied between the two arms of the parent MZI. Thanks to the different intrinsic phase structure of the two-sideband signals in each arm of the parent MZI related to the 90° RF dephasing discussed above, this interferometric working point enables destructive interference on one sideband and constructive interference on the other, yielding a single-sideband suppressed carrier (SSB-SC) output signal.

Beyond this qualitative discussion of single-sideband modulation, a detailed theoretical analysis of the multiple interferences inside the MZM is provided in Section 4.3. In reality, small optical and RF amplitude unbalance effects, imperfections of the interferometric working points and the 90° RF phase shift, as well as higher-order sidebands due to deep phase modulation lead to the presence of residual unwanted spectral components in the MZM output signal. The spectral purity of the MZM output signal in terms of the suppression ratios of these unwanted signal, which are typically on the order of 30 dB, is characterized in Fig. 4 of Article 1 on page 32. As a rough rule of thumb, the single-sideband output power of a fibered MZM can reach up to -12 dB of its input. An experimental study on MZM output power as a function of driving RF power is reported in [58].

2.4 Ultrastable optical cavities

Narrow lasers locked to ultrastable cavities have numerous applications in fundamental physics and frequency metrology [63]. Most importantly, they fulfilled a necessary condition for the advent of a new generation of optical atomic clocks [98–100], by providing a clock laser with adequate short-term stability and linewidth for probing ultra-narrow clock transitions with sufficient resolution. An extreme example is an octupole transition in the $^{171}Yb^{+}$-ion with a natural lifetime on the order of several years [101]. As a matter of fact, till very recently, the characteristics of ultrastable cavities were one of the key limitations of optical clock stability [102, 103]. At present, a state-of-the-art relative stability and accuracy approaching fundamental noise limits at a few 10^{-18} has been achieved with a strontium lattice clock [79].

Another natural application of ultra-narrow lasers lies in the field of precision spectroscopy. As a prime example, let us mention the spectroscopy of narrow 1S-2S two-photon transitions in atomic hydrogen and deuterium with a natural linewidth of 1.3 Hz [65, 104]. The resulting hyperfine splittings and isotope shifts provided fundamental test for quantum electrodynamics (QED). Turning to molecular spectroscopy, we proposed [58] using a dedicated highly stable V-shaped cavity for a new type of optical feedback frequency-stabilized cavity ring-down spectrometer, whose realization is discussed in the second part of this thesis.

Before discussing design and performance aspects of state-of-the-art optical cavities, let us first recall the underlying physics as well as some of their elementary properties.

2.4.1 Fabry-Pérot resonator basics

In its simplest realization, an optical cavity consists of two partially transparent mirrors aligned along an optical axis, as shown on the left of Fig. 2.7. This setup is also called

Fabry-Pérot cavity or resonator in honor of Charles Fabry and Alfred Pérot who first described the interference fringes arising from the multiple reflections of a light field between two partially reflective glass interfaces and used such a system as an interferometer [105].

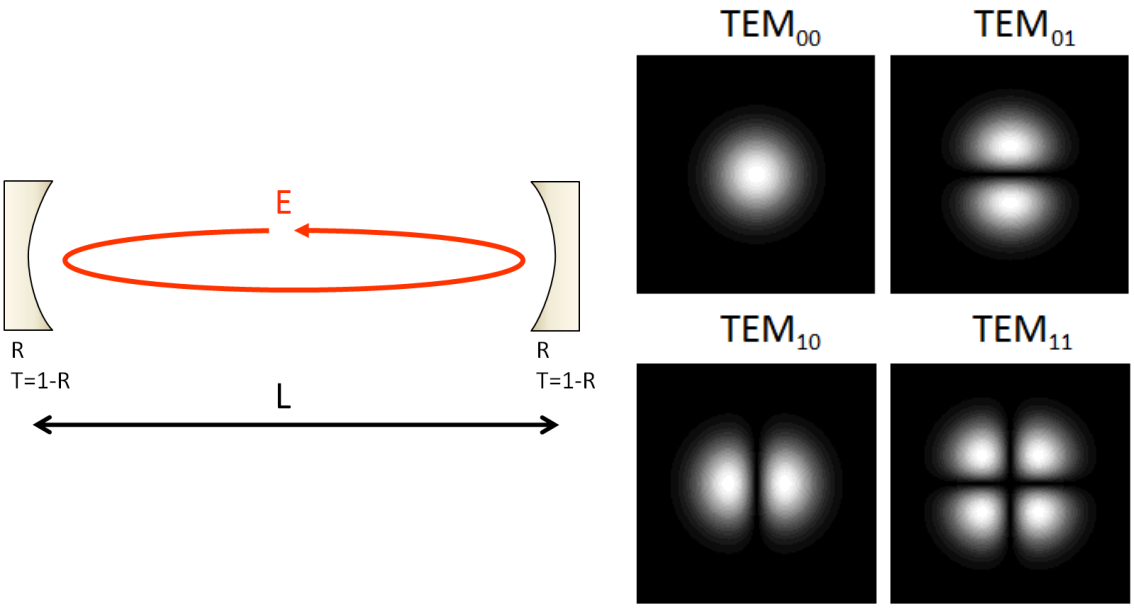

Figure 2.7 Left: Schematic sketch of a linear optical cavity of length L, for the idealized case of two mirrors with reflectivity R and loss-free transmission $T = 1-R$. The intracavity electric field is denoted E. Right: Intensity distribution of the lowest-order Hermite-Gauss transverse modes TEM_{mn} of an optical cavity with cartesian symmetry.

Light fields inside the resonator must fulfill the electromagnetic wave equation with the boundary conditions imposed by the cavity mirrors. In the paraxial approximation of beams propagating at small angles with respect to the optical axis, the spatial part of each solution can be written as a linear combination of the so-called Gauss-Hermite modes [106]. These modes are most commonly labeled TEM_{mn} (for transverse electro-magnetic) and can be observed in virtually all laser resonators and Fabry-Pérot cavities due to breaking of cylindrical symmetry, for instance by a slight astigmatism of cavity mirrors, with different radii of curvature along two principal axes. The spatial distribution of light intensity in the four lowest-order TEM_{mn} modes in the plane orthogonal to the optical axis is illustrated on the right of Fig. 2.7. The corresponding electric field amplitude E_{mn} is given by the expression [107, 108]

$$E_{mn} = E_0 \frac{w_0}{w(z)} \mathrm{H}_m\left(\frac{\sqrt{2}x}{w(z)}\right) \mathrm{H}_n\left(\frac{\sqrt{2}y}{w(z)}\right) \mathrm{e}^{-\frac{r^2}{w(z)^2} + i\frac{kr^2}{2R(z)} - i(m+n+1)\arctan\frac{z}{z_R} + i(kz-\omega t)} \tag{2.26}$$

where z is the optical axis, x and y are the transversal coordinates with $r^2 = x^2 + y^2$, and H_i denotes the i-th Hermite polynomial [109]. The curvature radius of the wavefront $R(z) = z \cdot \left(1 + \left(\frac{z_R}{z}\right)^2\right)$ and the beam radius $w(z) = w_0\sqrt{1 + \left(\frac{z}{z_R}\right)^2}$. Therein, the so-called Rayleigh range z_R is determined by the resonator condition that the wavefront curvature at the mirror surface must equal the mirror radius of curvature r. For a symmetric resonator with two identical mirrors at a geometric distance L, it reads

$$R\left(\frac{L}{2}\right) = \frac{L}{2}\left(1 + \frac{4z_R^2}{L^2}\right) = r \tag{2.27}$$

yielding

$$z_R = \frac{L}{2}\sqrt{\frac{2r}{L} - 1}. \tag{2.28}$$

Finally, the beam waist w_0 is determined by z_R through

$$w_0 = \sqrt{\frac{\lambda z_R}{\pi}} \tag{2.29}$$

Let us note that (2.28) only has a real solution if $L \leq 2r$. A more rigorous analysis using the $ABCD$ matrix formalism (see e.g. [110]) confirms that this is indeed the geometric condition for stable light propagation in the resonator. This stability criterion is often formulated in terms of the resonator parameter g:

$$-1 < g = \left(1 - \frac{L}{r}\right) < 1 \tag{2.30}$$

In the steady state, the light field in a Fabry-Pérot cavity is the superposition of an infinite number of light fields having travelled a growing number of round-trips inside the cavity. For constructive interference of all these field contributions, the round-trip phase of light in the cavity must be a multiple of 2π. Taking both the plane wave phase ikz and the Gouy phase $-i(m+n+1)\arctan\frac{z}{z_R}$ [111, 112] in Eq. (2.26) into account, this leads to the following expression for the resonance frequencies ν_{lmn} of the optical cavity:

$$\nu_{lmn} = \frac{c}{2n_0 L} \cdot \left(l + \frac{m+n+1}{\pi} \cdot \arccos g\right) \tag{2.31}$$

where n_0 denotes the refractive of the intracavity medium to distinguish it from the Hermite-Gauss mode index n. According to Eq. (2.31), the frequency spacing f_{FSR} between two equivalent TEM_{mn} modes of adjacent longitudinal mode number l and $l+1$ simply reads

$$f_{FSR} = \frac{c}{2n_0 L} \tag{2.32}$$

This so-called free spectral range (FSR) is the periodicity of the cavity transverse mode frequency spectrum. Although the discussion in this section is limited to linear cavities, the FSR of a V-shaped cavity with three mirrors and two arms of length L shall be quoted here for the sake of completeness:

$$f_{FSR_V} = \frac{c}{4n_0 L} \tag{2.33}$$

For a detailed treatment of the properties of V-shaped cavities, see [58], for instance. Let us note that the transverse mode resonance frequencies according to Eq. 2.31 are based on several idealizations, such as the paraxial approximation or the assumption of isotropic mirror curvature. Consequently, as discussed in Section 3.2.1 and 7.7, several frequency splittings due to the lifting of degeneracy in Eq. (2.31) lead to a much more complex transverse mode spectrum for a real Fabry-Pérot cavity [113–115].

The frequency-dependent normalized transmission of the cavity T_{cav} follows from a quantitative analysis of the steady-state superposition of field contributions with a growing number of intracavity round trips (see [116], for instance). This treatment yields the well-known Airy function

$$T_{cav} = \frac{(1-R)^2}{(1-R)^2 + 4R\sin^2\left(\frac{\Phi}{2}\right)} \tag{2.34}$$

as a function of mirror reflectivity R and round-trip phase Φ. For $R \to 1$, the resonances of (2.34) become very narrow. Consequently, around resonance $\Phi \equiv 0 \mod 2\pi$ a first-order expansion in Φ can be made:

$$T_{cav} \approx \frac{\frac{(1-R)^2}{R}}{\Phi^2 + \frac{(1-R)^2}{R}} \tag{2.35}$$

This is a Lorentzian function with full width at half maximum $\Delta\Phi = 2(1-R)/\sqrt{R}$. Comparing this to the full phase span 2π yields the finesse F of the cavity, which is defined as the ratio of free spectral range to cavity modewidth $\Delta\nu$:

$$F = \frac{f_{FSR}}{\Delta\nu} = \frac{2\pi}{\Delta\Phi} = \pi\frac{\sqrt{R}}{1-R} \tag{2.36}$$

In the high-finesse limit $R \to 1$, the formula for the finesse can be further simplified to $F = \pi/(1-R)$ in good approximation. The cavity transmission formulae (2.34) and (2.35) can be reconverted to a frequency description by replacing $(\Phi \mod 2\pi) = 2\pi\Delta/f_{FSR}$ with the detuning Δ from cavity resonance. Consequently, a high-finesse optical cavity is a sharp band-pass frequency filter and a sensitive frequency discriminator. For a more detailed in-depth analysis of Fabry-Pérot resonator physics, let us refer the reader to [107, 108, 110].

By inspection of Eq. (2.31) with the explicit expression $g = (1 - L/r)$, one sees that the resonance mode shift $\mathrm{d}\nu_{lmn}$ of the TEM_{mn} mode with longitudinal mode number l is linked to a cavity length change $\mathrm{d}L$ by

$$\frac{\mathrm{d}\nu_{lmn}}{\mathrm{d}L} = -\frac{\nu}{L}\left(1 - \frac{1}{l}\cdot\frac{m+n+1}{\pi\sqrt{2\frac{r}{L}-1}}\cdot\left(1 + \frac{(m+n+1)\arccos\left(1-\frac{L}{r}\right)}{\pi l}\right)^{-1}\right) \tag{2.37}$$

With $1/l \ll 1$ for macroscopic cavities, this reduces to

$$\frac{\mathrm{d}\nu}{\nu} \approx -\frac{\mathrm{d}L}{L}, \tag{2.38}$$

independently of transverse mode number, so that the indices have been dropped. Let us note that the correction term to (2.38) in Eq. (2.37) is not necessarily negligible for microscopic cavities with small l, or in the case of exotic macroscopic cavities very close to the stability limit $L \to 2r$. For such near-concentric cavities, the $1/\sqrt{2(r/L)-1}$-term diverges, thus compensating for the smallness of $1/l$. Finally, in the case of our ultrastable cavity with $r = 1\,\mathrm{m}$ and $L = 15\,\mathrm{cm}$ discussed in Chapter 3, $\nu \approx 186\,\mathrm{THz}$ implies $l \approx 380000$, and the relative error due to the correction term in (2.37) is only $2.4 \cdot 10^{-7}$, confirming that Eq. (2.38) indeed holds in very good approximation.

2.4.2 Ultrastable cavity design and performance characteristics

The fundamental significance of relation (2.38) for laser stabilization was first explicitly discussed by Salomon, Hils and Hall in their seminal contribution [117] aiming at the realization of lasers with mHz-level linewidth for applications in fundamental physics. The authors demonstrated experimentally that two lasers tightly locked to adjacent modes of one Fabry-Pérot cavity by means of a sufficiently high-bandwidth analog servo loop exhibited a relative linewidth on the order of 50 mHz and Hz-level long-term stability. Consequently, it became clear that the problem of achieving sub-Hz laser frequency stability could be reduced to the mere technical challenge of designing an ultrastable Fabry-Pérot resonator. Over the last decades, enormous progress has been made in the development

of such ultrastable optical cavities, and the discussion here can inevitably only provide a selective review of some milestones of this process in order to elucidate essential principles of ultrastable cavity design.

In general, the dominant drift mechanism of a cavity is due to temperature-induced length changes, which lead to a resonance frequency shift

$$\frac{\mathrm{d}\nu}{\nu} = -\frac{\mathrm{d}L}{L} = -\alpha \mathrm{d}T \tag{2.39}$$

according to Eq. (2.38). This experimental issue could be solved by virtue of commercial glass ceramic materials with specified coefficient of thermal expansion (CTE) below $10^{-8}\,1/\mathrm{K}$, notably ultra-low expansion (ULE) glass [118] and Zerodur [119]. To form an optical cavity from these materials, two ultra-polished dielectric mirrors are optically bonded to the two ends of an ULE or Zerodur cavity spacer using intermolecular adhesion forces. An experimental characterization of the zero-crossing of the cavity CTE as a function of temperature can be used to stabilize the reference cavity at a temperature of virtually zero CTE. In this regime, the total cavity expansion becomes dominated by the dielectric mirror coatings, as their microscopic µm-level thickness is partially compensated for by an extremely small thermal inertia [120]. Optically contacted ultra-low expansion material cavities thus reduced temperature expansion effects by several orders of magnitude as compared to Invar cavities. An overview of the physical properties of typical ultrastable cavity materials is given in Table 5.2 of [58] and Table 3.3 of [72], for instance. In order to make temperature-related drift mechanisms negligible, a considerable effort in temperature stabilization is nevertheless necessary. Typically, this encompasses passive isolating layers and an actively temperature-stabilized low-gradient enclosure. Furthermore, the cavity must be installed on low-conduction posts in a high-vacuum chamber featuring one or several heat shields with low emissivity to protect the cavity from thermal heat transfer [58, 68, 120].

As the cavity resonance frequencies scale with the inverse of the refractive index n_0 of the residual intracavity gas according to Eq. (2.31), a pressure increase $\mathrm{d}P$ inside the cavity leads to a frequency variation

$$\frac{\mathrm{d}\nu}{\nu} \sim -\mathrm{d}P \tag{2.40}$$

This relationship, which will be discussed again in Section 3.2.2 (cf. Eqs. (3.12) and (3.13)), implies that the reference cavity and its surroundings must be pumped down to a vacuum with a residual-pressure stability better than $10^{-7}\,\mathrm{mbar}$ for Hz-level laser frequency stabilization [58]. To avoid vibration-induced perturbations of cavity length, the high vacuum from an initial pump-down is generally maintained using an ion pump without any moving parts.

Vibrations from seismic and acoustic origin are another important technical challenge in achieving Hertz-linewidth lasers. An established design principle is vertical mid-plane mounting of the cavity spacer in order to achieve a rough first-order compensation of cavity length changes due to vibration-related accelerations acting on the cavity [121, 122]. In practice, a useful technique to further minimize cavity acceleration sensitivity is based on a mounting scheme which allows for fine-tuning of the cavity support contact points. This allows an experimental determination of the mount position for first-order vibration insensitivity by observing the cavity response to excitation by a vibrating platform [123]. Alternatively, finite-element modeling of the cavity can be used for determining the optimal configuration before constructing the setup, providing a nearly vibration-insensitive cavity without any iterative mounting adjustments. This approach is illustrated on the right of Fig. 2.8. In analogy to the efforts for thermal isolation and stabilization, a damping enclosure for isolating the cavity from acoustic perturbations and an active vibration-cancellation platform for absorbing accelerations of seismic origin are generally used for

reducing the expected vibration-induced frequency noise to a negligible level.

With all these technical measures taken, the reference cavity performance approaches the fundamental physical limit of the definition of cavity length at temperatures $T > 0$. Due to thermal motion, the length of the cavity is not an exact constant, but subject to statistical fluctuations. This thermal noise limit [72, 121, 124] can be analyzed using the fluctuation-dissipation theorem of statistical physics, which relates random fluctuations of a system to its losses. An important result, which might seem counter-intuitive at first sight, is that the thermal noise of the spacer is negligible with respect to the contribution from the mirror substrate and its dielectric coating in general. Physically, this is due to the sub-mm size of the laser beam sampling only a small portion of the mirror surface, leading to less efficient statistical averaging of fluctuations as compared to the cm-scale spacer [124]. The power spectral density of thermal noise is proportional to both temperature and the mechanical loss rate of the sample. Therefore, working at low temperatures with materials exhibiting a high mechanical quality factor Q constitutes an optimal choice for reducing the fundamental stability limit set by thermal noise. Consequently, fused silica mirror substrates ($Q_{FS} \approx 10^6$) should be preferred to their ULE ($Q_{ULE} \approx 6 \cdot 10^4$) and Zerodur ($Q_{ZD} \approx 3 \cdot 10^3$) counterparts [124], as illustrated by the thermal noise budget on the left of Fig. 2.8.

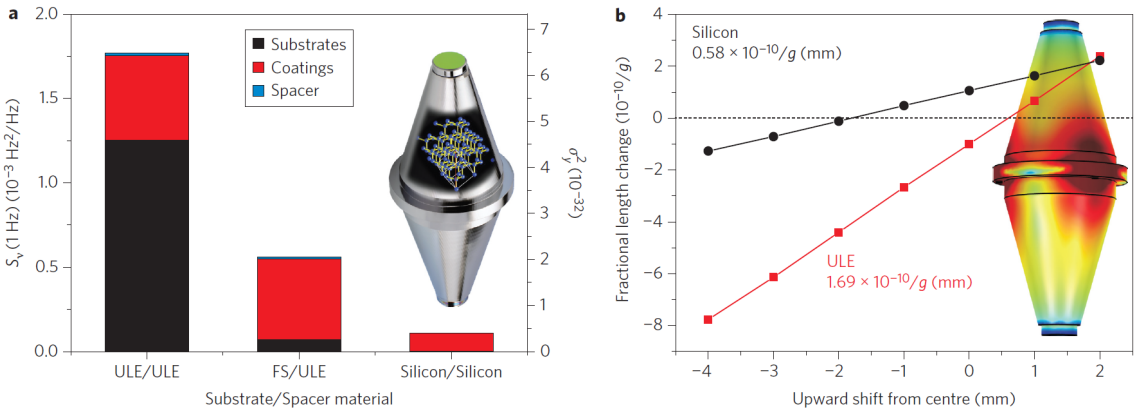

Figure 2.8 Left: Comparison of thermal noise PSDs and Allan variance thermal noise floors for different cavity spacer and mirror substrate materials for the ultrastable cavity geometry shown in the inset. Right: Acceleration sensitivity of the near-mid-plan-mounted cavity in the inset determined by finite-element simulation. The optimal mounting position for first-order vibration insensitivity depends on the spacer material. Colors in the inset depict the distribution of strain energy in the cavity spacer. Adapted from [68] (Figure 1).

Monocrystalline silicon has an even higher quality factor ($Q_{Si} > 10^7$) and a zero-crossing of its CTE at 124 K [68]. Kessler and co-workers have exploited these highly advantageous properties for engineering the ultra-stable cavity illustrated in Fig. 2.8, consisting of a single-crystal silicon spacer with two equally monocrystalline, optically bonded mirrors with aligned crystal axes [68]. The authors demonstrated that a laser locked to this vibration- and temperature-insensitive silicon reference cavity features a fractional frequency stability of 10^{-16} at a second-timescale, a linewidth of 50 mHz and long-term frequency excursions below 19 Hz over one day.

2.4.3 Pound-Drever-Hall locking

Beyond optical feedback self-locking as discussed in Section 2.2, many techniques for locking a laser to the resonance of an optical cavity or vice-versa exist. For retrieving the necessary frequency-discriminator error signal measuring the detuning of laser and cavity resonance, they use different physical approaches, for instance based on geometric [125] or polarization [126, 127] effects. The Pound-Drever-Hall (PDH) technique is particularly frequently used in various experimental contexts and owes its success to its high performance in terms of gain, bandwidth, locking range and robustness. Based on a microwave-oscillator stabilization scheme by Pound [128], it has been adapted to the optical domain by Drever, Hall and co-workers [129].

Here, instead of focussing on the original realization, let us discuss the basic principles and properties of PDH locking on the modified, Mach-Zehnder-modulator-based and all-fibered PDH locking scheme shown on the left of Fig. 2.9. The experimental realization of this scheme for tightly locking a high-finesse cavity to a stable laser, which was proposed in [58], is discussed in detail in Section 6.2.2, as well as in Article 4 on page 90 and Article 5 on page 160.

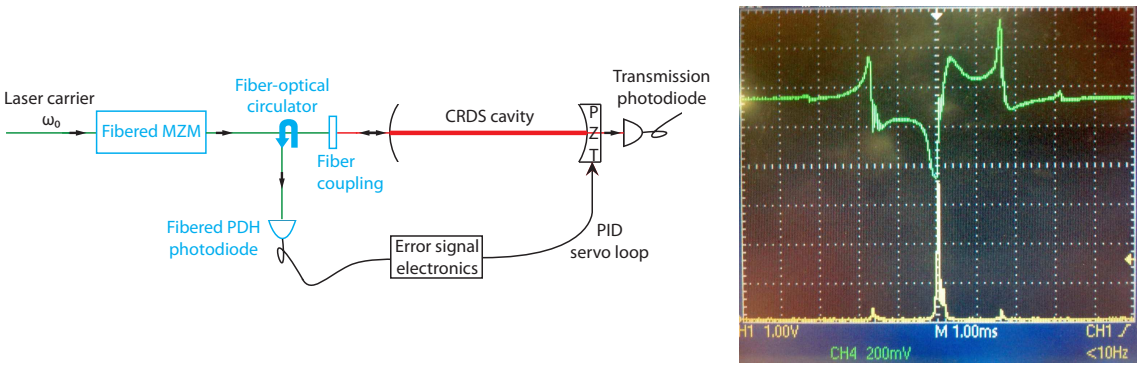

Figure 2.9 Left: Schematic sketch of a modified Pound-Drever-Hall locking scheme using a fibered Mach-Zehnder modulator as a phase modulator and a fiber-optic circulator in order to retrieve the cavity reflection signal on a fibered photodiode. Right: Oscilloscope traces of an experimental PDH error signal (upper green curve) versus cavity transmission (lower yellow curve) during a length scan of the cavity. Note the presence of transient ringing effects [130] on the error signal in the present rapid-scanning regime. A contribution from the weak second-order modulation sidebands can be clearly discerned on the error signal trace.

Physically, the PDH mechanism is based on the presence of phase modulation sidebands serving as an optical frequency and phase reference for the optical carrier and vice-versa. The cavity reflection signal contains both the incoming laser directly reflected off the cavity and the backwards transmission from inside the cavity. The heterodyne interference of these light fields on a photodiode leads to a signal oscillating at the modulation frequency Ω of the sidebands. Demodulation with a radio-frequency mixer and subsequent low-pass filtering yields the PDH error signal, which is sensitive to the relative phase of the incoming and the intracavity field. Consequently, it can detect fast phase fluctuations as well as detuning-dependent phase shift of cavity backward transmission, and thus acts as a combined frequency and phase discriminator [129]. An experimental PDH error signal obtained through a length sweep of an OFFS-CRDS ring-down cavity (cf. Part II) against a sub-kHz-linewidth laser (cf. Chapter 3) is shown on the right of Fig. 2.9.

When the carrier is close to resonance, a complete non-resonant reflection of the phase modulation sidebands can be assumed in good approximation as long as $\Omega \neq f_{FSR}$. Under this condition, the PDH error signal S_{PDH} close to resonance can be written as [72]

$$S_{PDH} \sim J_0(\delta\varphi)J_1(\delta\varphi){E_0}^2 \cdot \frac{\Delta}{\delta\nu} \tag{2.41}$$

where $\delta\nu$ and Δ denote the cavity modewidth and the detuning from resonance, respectively. $J_0(\delta\varphi)E_0$ and $J_1(\delta\varphi)E_1$ are the electric field amplitudes of the optical carrier and the phase-modulation sidebands, respectively. Therein, $J_0(\delta\varphi)$ and $J_1(\delta\varphi)$ are first-kind Bessel functions of phase modulation depth $\delta\varphi$, which can be approximated as $J_0 \approx 1$ and $J_1 \approx \delta\varphi/2$ for small modulation depths $\delta\varphi \ll 1$. Due to the heterodyne amplitude multiplication in (2.41), small $\delta\varphi$ are sufficient for obtaining a usable PDH error signal. Equation (2.41), which holds for $\Delta/\delta\nu \ll 1$, corresponds to the central steep slope of the experimental PDH error signal shown on the right of Fig. 2.9. The full shape of the signal is obtained when the complete expressions for amplitude and phase of the reflected carrier and sidebands are taken into account, as in [72], for instance.

In the PDH-scheme illustrated on the left of Fig. 2.9, phase modulation sidebands are generated by applying phase-modulated radio frequency signals to the driving electrodes of a Mach-Zehnder modulator. In this way, a single-sideband signal with phase-modulation satellites is provided at MZM output. This technique is further illustrated in Fig. 1 of Article 5 on page 160. An important feature of this approach is that the residual carrier does not have phase-modulation sidebands and that those of the suppressed other sideband have opposite polarity. Therefore, even the hypothetical danger of accidental locking on one of these small residual spectral components is not given in this locking scheme. The fiber-optic circulator of the present setup is a robust and cost-effective alternative to the free-space polarizing beam splitter and quarter-wave plate of the original PDH setup. Importantly, it allows injecting the cavity with an arbitrary, typically linear, polarization state (cf. Section 7.7). Furthermore, it is a helpful tool for finding the beam alignment for optimal mode-matching and guarantees an intrinsic alignment of cavity backward transmission and fibered PDH photodiode.

2.5 Self-referenced optical frequency combs

The last decades have seen a burst of new science and technological progress related to femtosecond pulse lasers in general, and in optical frequency combs in particular. Reviewing this rapidly developing field from a general point of view of ultrafast laser physics [131, 132] or direct frequency comb spectroscopy [133, 134] is beyond the scope of this thesis. For a broader overview, the reader is referred to [72], for instance. Here, we will focus on a concise discussion of self-referenced optical frequency comb synthesizers for the direct and absolute measurement of optical frequencies [135, 136], which have triggered a golden age of optical frequency metrology [6] and optical atomic clocks [98], distinguished by the Nobel prize in Physics co-awarded to Theodor Hänsch and John Hall [63, 137].

The term frequency comb originates from a frequency domain representation of femtosecond laser pulses. Such pulses arise when a huge number of longitudinal modes ν_m of a laser are locked to in-phase oscillation by a physical process such as self-focussing by the nonlinear optical Kerr effect, for instance. According to elementary Fourier analysis, the free spectral range $f_{FSR} = c/(2n_0L)$ between longitudinal laser cavity modes (cf. Eq. (2.32)) equals the repetition rate $f_{rep} = f_{FSR}$ of the resulting pulse train. Consequently, the following relationship holds for the teeth ν_m of this equidistant comb in frequency

space:

$$\nu_m = m \cdot f_{rep} + f_{CEO}, \tag{2.42}$$

with a zero-offset frequency f_{CEO} whose physical origin will be discussed in the following. This frequency-space representation of an optical frequency comb is illustrated in Fig. 2.10b.

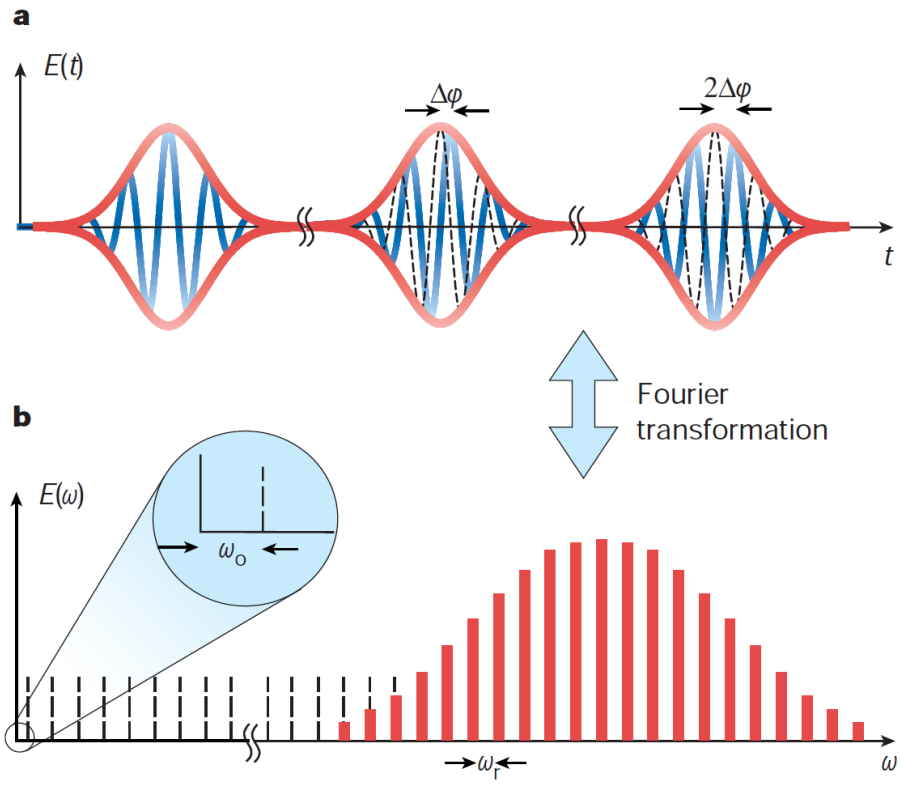

Figure 2.10 A mode-locked femtosecond pulse laser in the time (a) and frequency domain (b). ω_r and ω_0 denote pulse repetition rate and carrier-envelope offset, respectively, which are both expressed as angular frequencies here. Adapted from [6] (Figure 1).

In the time domain, depicted in Fig. 2.10a, the pulse train originates from a giant pulse circulating inside the laser cavity. A fraction of its power is transmitted by the cavity whenever the pulse arrives at the output mirror. This happens at a period of $2n_0L/c$, corresponding to the repetition rate f_{rep} found above. Due to dispersion notably from the wideband mirrors and the active medium, the group and phase velocities in the cavity, $v_g = \mathrm{d}\omega/\mathrm{d}k$ and $v_p = \omega/k$, respectively, are not exactly equal. This leads to a phase slip φ_{CEO} between the pulse envelope and its carrier field oscillation at each subsequent round trip,

$$\varphi_{CEO} = 4\pi\nu_c L \left(\frac{1}{v_g} - \frac{1}{v_p} \right), \tag{2.43}$$

with the pulse carrier frequency ν_c. As illustrated in Fig. 2.10, this time-domain phase-slip leads to the frequency domain zero-offset f_{CEO}

$$f_{CEO} = \frac{\varphi_{CEO}}{2\pi} \cdot f_{rep} = 2\nu_c L \left(\frac{1}{v_g} - \frac{1}{v_p} \right) \cdot f_{rep} \tag{2.44}$$

introduced in Eq. (2.42) above. If f_{CEO} should exceed f_{rep}, it can be replaced by an equivalent frequency *modulo* f_{rep}, so that Eq. (2.42) is still fulfilled after an adequate

renumbering of modes.

In view of Eq. (2.42) it is clear that if f_{rep} and f_{CEO} can be measured or stabilized precisely, the optical frequency comb constitutes a frequency ruler with hundreds of thousands of markings ν_m whose absolute values are known to an accuracy corresponding to the error propagation of f_{FSR} and f_{CEO} in (2.42). Referenced to a rubidium-disciplined crystal oscillator or a hydrogen maser, their short-term stability is typically on the order of 10^{-12} or 10^{-15}, respectively. At optical frequencies on the order of 10^{15} Hz, this corresponds to an absolute frequency measurement with accuracies down to the Hz-level. The ultimate limitation at present is the accuracy of the respective primary standard caesium clock realizing the SI second.

The stabilization of f_{FSR} is rather straightforward, in that it can be easily measured by counting the comb repetition rate f_{FSR} on a fast photodiode. This provides the error signal for an active servo control of cavity length L, for example using a piezo-electric actuator or a fast electro-optic phase modulator, in order to keep f_{FSR} locked to an adequate local oscillator radio frequency.

The measurement and stabilization of f_{CEO} is a much more challenging experimental task and has been the bottleneck for the realization of an optical frequency comb synthesizer for long. An experimental solution came within reach with the realization that spectral self-broadening processes in nonlinear materials with a strong third-order susceptibility $\chi^{(3)}$ preserve the phase-coherence of the original femtosecond pulse [138]. Consequently, as soon as highly nonlinear nano-structured photonic crystal fibers became available, an octave-spanning frequency comb was realized [139]. Such a comb allows a direct measurement of f_{CEO} by superposing a frequency-doubled portion of the broadened comb with a portion of the original broadened comb on a photodiode, giving rise to a beat note signal between the teeth $2\nu_m$ from the first and ν_{2m} from the second field, respectively. According to Eq. (2.42), the corresponding beat frequency amounts to

$$2\nu_m - \nu_{2m} = 2mf_{rep} + 2f_{CEO} - (2mf_{rep} + f_{CEO}) = f_{CEO} \tag{2.45}$$

Illustrated in Fig. 2.11, this strikingly simple and elegant principle underlying self-referenced optical frequency combs is commonly called $f-2f$ interferometry. Once measured, f_{CEO} can be stabilized to a reference radio frequency, typically by means of a servo loop on pump laser power. Such a system is called optical frequency comb synthesizer (OFCS), as full control of f_{rep} and f_{CEO} implies that any optical frequency within the spectral bandwidth of the comb can be realized on demand as one of the comb teeth ν_m.

With an OFCS, measuring the absolute frequency ν_0 of any continuous-wave laser within the spectral bandwidth becomes straightforward. After spectral pre-filtering using a grating or a narrowband interferometric filter, the relevant fraction of the OFC can be superposed with the laser field in order to generate a beat note at the frequency difference f_{BN} between the laser and the closest tooth ν_{m_0} of the OFCS according to Eq. (2.21). Such measurements are discussed in Article 6 on page 192, with the experimental setup reported in Fig. 1 therein. According to Equation (1) of that article, the absolute frequency ν_0 of the laser can be deduced from the beat note frequency f_{BN} as

$$\nu_0 = \text{Round}\left(\frac{\tilde{\nu}_0 - f_{CEO} - sf_{BN}}{f_{rep}}\right) f_{rep} + f_{CEO} + sf_{BN}, \tag{2.46}$$

provided that an approximate value $\tilde{\nu}_0$ for the frequency to be measured is known to an accuracy better than $f_{rep}/2$. Furthermore, Eq. (2.46) necessitates a knowledge of the beat note sign s, which is 1 for $\nu_0 > \nu_{m_0}$ and -1 otherwise, and implies $f_{CEO} > 0$, which must be ensured experimentally. An easy way of determining s consists in slightly varying

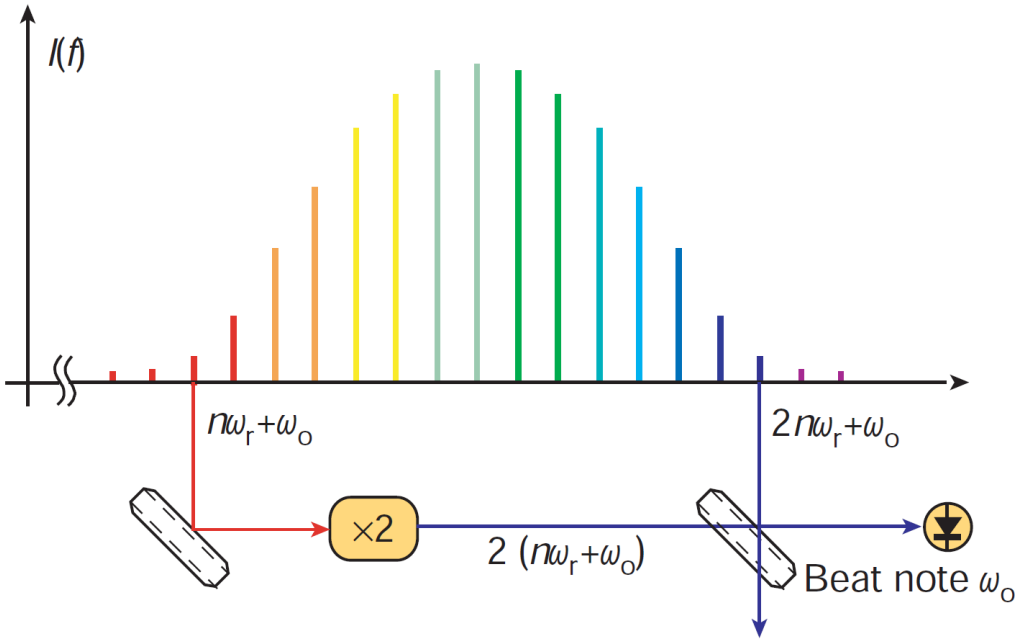

Figure 2.11 Schematic depiction of $f - 2f$ interferometry for determining the carrier-envelope offset frequency f_{CEO} in an octave-spanning frequency comb by comparing the frequency-doubled red end of the comb spectrum to its blue end. Adapted from [6] (Figure 3).

the OFC repetition rate: $s = 1$ if f_{BN} decreases for increasing f_{rep}, and $s = -1$ if f_{BN} increases for increasing f_{rep}.

Chapter 3

Sub-kHz laser stabilization by optical feedback from a highly stable V-shaped cavity

Soon after the beginning of our project of developing a ring-down spectrometer based on an optical feedback frequency-controlled laser, we were faced with the realization that mere linewidth-narrowing of a distributed-feedback (DFB) diode laser from several MHz down to a yet unknown value well below the MHz-level was not sufficient for metrological applications in molecular spectroscopy [58]. As a matter of fact, locked-laser frequency drifts of several tens of kHz per second were observed, and unambiguously attributed to the dimensional instability of the V-shaped feedback cavity used at that time. When applied to point-by-point absorption spectroscopy, laser frequency drifts of this extent would lead to a severely distorted frequency axis, impeding the very applications the new spectroscopic setup was being developed for.

One potential solution would have been the use of a frequency-stabilized Helium-Neon (HeNe) laser for stabilizing the spectrometer frequency axis at the MHz-level. Introduced to CRDS by Hodges and co-workers in 2004 [140], this approach will be reviewed in Section 5.3. Typical high-end commercial stable HeNe lasers, such as the Melles-Griot model 05-STP-901 used in these CRDS experiments [141], feature a specified short-term stability on the order of ±500 kHz at 1 min observation time. Although very competitive, this performance is still insufficient for most challenging metrological applications, such as the optical measurement of the Boltzmann constant discussed in the introduction. In spite of its considerable experimental complexity, even a HeNe laser stabilized to an iodine transition [142–144] would not have been a perfect solution for stabilizing the ring-down spectrometer frequency axis, as its short-term linewidth of several kHz is much larger than the sub-Hz linewidth level theoretically attainable by optical feedback locking [58, 92].

In the light of these considerations and the recent ground-breaking developments in ultrastable Fabry-Pérot resonators from the field of frequency metrology discussed in Section 2.4, we chose to stand by our original experimental approach. We proposed to harness the advantages of such ultrastable resonators for metrological molecular absorption spectroscopy and developed a highly stable V-shaped reference cavity for optical feedback laser frequency stabilization [58].

This approach implies tackling the considerable technical challenges of thermal and vibrational insensitivity, isolation and stabilization of the cavity. For over a decade, significant progress has been made in this field in leading standards and metrology labs. Consequently, for the conception of our stable reference cavity, we followed the basic de-

sign principles of classical ultrastable cavity designs [120, 122] detailed in Section 2.4, based on a vertically mid-plane-mounted ultra-low expansion glass spacer. These cavities feature two ultrapolished mirrors optically contacted to the two spacer end facets by molecular adhesion. For realizing a cavity with three mirrors, we were constrained to abandon this method. Our original approach for realizing a V-shaped cavity consists in tightly contacting two precision-machined low-expansion mirror holders to the spacer. This first highly stable V-shaped cavity is shown in Fig. 2 of Article 1 on page 32.

When locking a standard DFB diode laser to this reference cavity, its linewidth narrows to the sub-kHz level and the laser inherits the long-term frequency stability of the cavity. However, for high-resolution spectroscopy, fine tunability is no less important than stability. Therefore, we proposed to use an integrated electro-optic Mach-Zehnder modulator (MZM) as an optical single-sideband frequency shifter for spectroscopy [58]. Combining these elements thus provides us with a fine-tunable V-Cavity Optical-Feedback-stabilized laser source (VCOF).

The first Section of this Chapter contains the original article demonstrating the experimental principles, the realization and the performances of this VCOF source. Subsequently, further details on the frequency noise measurement reported in the Article are given, *en passant* revealing the polarization mode splitting of the etalon used for this purpose. Then, further characterizing long-term drifts of the V-cavity experimentally, we present a saturation spectroscopy measurement of the cavity resonance frequency drift with astonishingly high resolution using a molecular transition as a physical frequency reference. Finally, an absolute measurement of the V-cavity-locked laser frequency by means of an optical frequency comb is reported. At the end of this Chapter, we provide an overview of ongoing developments on the realization of a new generation of quasi-monolithic ultrastable V-shaped cavities based on optical contacting.

3.1 Article 1 - Optical feedback stabilized laser tuned by single-sideband modulation

In the following article [145], the methodological foundation as well as the experimental setup for a VCOF laser source are introduced and presented, focussing on the two key ingredients optical feedback frequency stabilization and MZM-based single-sideband frequency tuning. Then, important aspects and details of the highly stable V-shaped reference cavity design as well as its temperature stabilization and vacuum systems are discussed. In the experimental part, measurements of the cavity free spectral range, finesse and thermal expansion coefficient are reported, allowing the estimation of an upper bound for V-cavity mode frequency drifts. Another important measurement concerns the spectral purity of the MZM single-sideband output in terms of the extinction ratio of unwanted frequency components. Finally, a measurement of the frequency noise power spectral density of the MZM-tuned optical-feedback-stabilized laser light is shown and interpreted.

Let us note that the free spectral range measurements discussed in Section 3.2.2 based on saturated absorption and in Article 5 on page 160 with an optical frequency comb provide a much more precise value for the V-cavity free spectral range than the measurement reported in Article 1 with a wavemeter. Further details on the VCOF laser frequency noise measurement shown in Fig. 5 of Article 1 will be discussed in Section 3.2.1 following the article.

Optical feedback stabilized laser tuned by single-sideband modulation

Johannes Burkart, Daniele Romanini, and Samir Kassi*

Laboratoire Interdisciplinaire de Physique (LIPhy), CNRS—Université Joseph Fourier Grenoble (UMR 5588), 140 Rue de la Physique, BP 87, Saint Martin d'Hères 38402, France

**Corresponding author: samir.kassi@ujf-grenoble.fr*

Received March 28, 2013; revised May 14, 2013; accepted May 14, 2013; posted May 14, 2013 (Doc. ID 187904); published June 7, 2013

We report a subkilohertz-linewidth distributed-feedback diode laser that is optical-feedback locked to a highly stable V-shaped cavity with drift rates below 20 Hz/s. This source is continuously tunable over 1 THz around 1590 nm by selecting a cavity mode and using an innovative single-sideband modulation scheme, which allows for frequency shifting over up to 40 GHz with millihertz accuracy. This robust setup achieves high performance without advanced vibration isolation and will be a powerful tool for metrological applications, in particular a redetermination of the Boltzmann constant by molecular spectroscopy. © 2013 Optical Society of America

OCIS codes: (140.3425) Laser stabilization; (120.3930) Metrological instrumentation; (140.3490) Lasers, distributed-feedback; (140.4780) Optical resonators; (130.4110) Modulators.

http://dx.doi.org/10.1364/OL.38.002062

Semiconductor laser self-locking due to optical feedback [1] is an intriguing phenomenon, which has been theoretically understood [2] and widely used in various fields [3,4]. Feedback photons coming from inside a high-finesse cavity counteract the random walk of laser phase due to spontaneous emission, leading to drastic linewidth narrowing and to robust laser frequency stabilization. Despite the efficient high-frequency noise rejection [5] and relative experimental simplicity offered by this technique, its ultimate potential has never been fully exploited due to insufficient reference cavity stability. Here, we present a novel highly stable cavity used for distributed feedback (DFB) diode laser frequency stabilization by optical feedback. By injecting the stabilized laser light into a fibered Mach–Zehnder modulator (MZM) [6], we obtain a finely tunable light source with excellent spectral purity. An optical determination of the Boltzmann constant [7], the generation of accurately tunable terahertz radiation, and optical isotopic ratio measurements are only a few examples of its potential applications.

A reference cavity inside a temperature-stabilized vacuum chamber is the heart of our setup, shown in Fig. 1. Its V-shaped geometry ensures that only light from a cavity resonance is reinjected into the DFB laser diode, producing optical feedback locking [4]. It follows from theory [2] that as long as the free-running laser detuning $\delta\nu$ from reference cavity resonance remains within a locking range Δ, there exists a feedback phase φ that forces locked laser emission to this resonance frequency:

$$\varphi = \arcsin(2\delta\nu/\Delta). \tag{1}$$

The locking range Δ grows with the square root of feedback rate [2] and is set to one free spectral range (FSR) of the reference cavity for continuous locking by means of a polarizing Glan–Taylor beam splitter. The feedback phase φ is actively kept at its optimal value by a piezoelectric transducer (PZT) governing the distance between laser and reference cavity. A first-derivative error signal is retrieved at cavity transmission by modulating the laser diode injection current at a few kilohertz. As only a small fraction of the laser power is needed for optical feedback locking, the rest is injected into a polarization-maintaining fiber. It is then coupled into the MZM (Covega Mach-10-060), an integrated lithium niobate electro-optic modulator with nested Mach–Zehnder interferometer waveguide structure. Applying two orthogonal radio frequency (RF) signals in the gigahertz range to the MZM, multiple voltage-controlled interferences in the Mach–Zehnder waveguide [6] generate a single-sideband modulation signal with suppressed carrier. This allows for frequency fine tuning covering more than one FSR of the reference cavity. Therefore, any frequency within the laser gain bandwidth becomes accessible with a precision given by the accuracy of the RF, the residual noise on the feedback phase [cf. Eq. (1)], and the stability of the reference cavity resonance frequency ν. Its fluctuations $\Delta\nu$ are caused by changes ΔL of the cavity's optical armlength L: $\Delta\nu/\nu = -\Delta L/L$. Therefore, our design aims at minimizing the cavity's susceptibility to thermal expansion, vibrational perturbations, and pressure fluctuations.

As in standard ultrastable cavity designs [8,9], we use an ultralow expansion glass (ULE) spacer to minimize thermal expansion effects. We achieve the mirror tilt

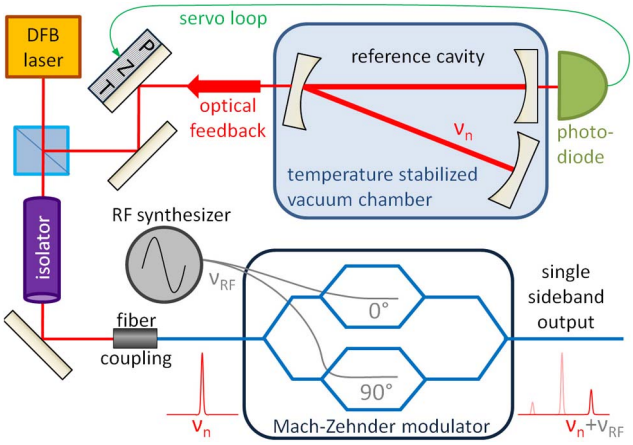

Fig. 1. Schematic sketch of the experimental setup. PZT, piezoelectric transducer; ν_n, reference cavity resonance frequency; ν_{RF}, driving RF.

needed for a V-shaped cavity configuration (Fig. 1) with two mechanically prealigned cavity flanges machined from the low-expansion alloy Super Invar. Being held in tight contact with the 15 cm long ULE glass spacer by six stiff stainless steel springs, this glue-free configuration guarantees automatic and permanent optical alignment. Figure 2 shows this highly stable reference cavity, held by a stainless steel clamp ring that is supported by three Macor glass ceramic legs limiting heat conduction and mounted onto the vacuum chamber bottom flange. Following established design concepts [8–10], our reference cavity features a high degree of symmetry and vertical mid-plane mounting. This reduces its sensitivity to vibration-induced length changes. It is installed inside a vacuum chamber pumped down to 2×10^{-7} mbar, thereby reducing refractive index related fluctuations of its resonance frequencies to the order of 1 Hz. The vacuum chamber contains an aluminum radiation shield and is placed inside an acoustic noise-reducing thermally insulated wood enclosure fixed to a commercial optical breadboard. We actively stabilize the average value of two temperature probes at opposite ends of the vacuum chamber to 23°C, with in-loop root mean square (RMS) temperature fluctuations of 250 μK and temperature differences between the probes always smaller than 8 mK.

We have verified the easy and wide tunability of the locked laser frequency ν_0 by performing laser diode temperature sweeps. As long as the laser's free-running frequency remains within the locking range of a reference cavity mode, its emission frequency remains unaffected. When the locking range of one mode is left, the laser automatically locks to the adjacent cavity resonance, changing its emission frequency by one FSR. For a scan from −10°C to 60°C, the DFB laser locked to 2059 consecutive modes of the reference cavity, thereby covering a spectral interval of more than 1 THz between 1587 and 1596 nm. Measuring the locked laser frequencies during the scan with a high-resolution wavemeter yields a measurement for the V-shaped cavity mean FSR $c/(4L) = (491.381 \pm 0.001)$ MHz, where c is the speed of light. The cavity modewidth of (2205.2 ± 0.1) Hz at

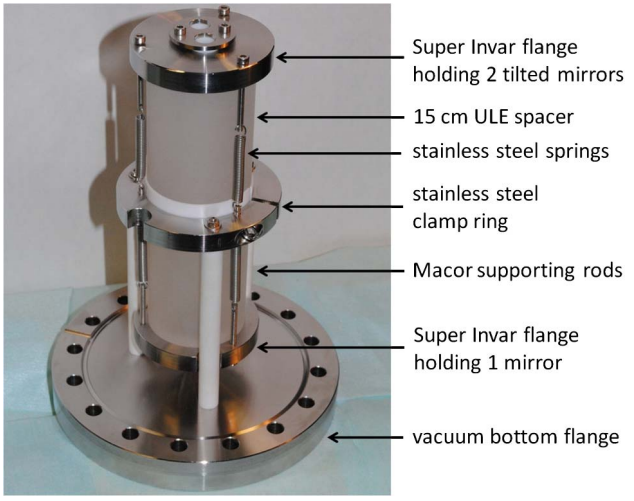

Fig. 2. Highly stable V-shaped cavity.

$\nu_0 = 188.4818$ THz determined by cavity ring-down measurements [11] therefore implies a finesse $F = 222830 \pm 10$. To obtain an experimental upper bound for the maximum reference cavity drift rate $\dot{\nu}$, we relate it to thermal expansion due to heat transfer processes via

$$\dot{\nu} = -\nu\alpha\Delta T/\tau, \tag{2}$$

where ΔT is the difference between the vacuum chamber wall and cavity temperatures, α is the effective (linear) coefficient of thermal expansion of the composite cavity, and τ is the time constant of heat transfer between vacuum chamber and reference cavity. As shown in Fig. 3, we have determined α and τ experimentally by measuring the frequency drift of the locked laser after a sudden vacuum chamber temperature change of −3 K. The rapid active stabilization of the in-loop outer surface temperature (∼2 h) is followed by the thermalization of the whole vacuum chamber (∼12 h), which afterwards acts as an ideal thermal reservoir. This leads to the exponential decay of the locked laser frequency with time constant $\tau = (12 \pm 1)$ h, which is visible in Fig. 3. The total frequency drift observed for the −3 K temperature change implies an effective coefficient of thermal expansion $\alpha = -(6.0 \pm 0.2) \times 10^{-7}$ K^{-1}. Using the conservative experimental assessment $|\Delta T| < 8$ mK, Eq. (2) yields $|\dot{\nu}| < 20$ Hz/s. Other potential drift mechanisms such as material aging, fluctuating laser power dissipation by cavity mirrors, and varying spring tension were evaluated and found to be negligible. As only about 1 mW of the 30 mW total laser power is needed for continuous optical feedback locking, roughly 15 mW is available at the MZM input after fiber coupling. Driving the MZM with a RF synthesizer referenced to a rubidium timebase, we obtain 1 mW of single-sideband power and achieve frequency shifting with millihertz accuracy over more than 1 GHz, limited by the bandwidth of our 90° two-way splitter. Although this is more than sufficient for bridging the gap between the V-shaped reference cavity modes here, it could be extended to up to 40 GHz with the appropriate commercially available RF equipment. In order to characterize the spectral purity of the MZM output, we have injected it into a scanning Fabry–Pérot cavity serving as an optical spectrum analyzer. The result in Fig. 4 shows that the extinction ratios of the optical carrier and the other sideband with respect to the single sideband were better than 28 dB. The observed transmission peak shape is due to the buildup and ring-down dynamics of intracavity intensity. To measure the frequency noise of our light

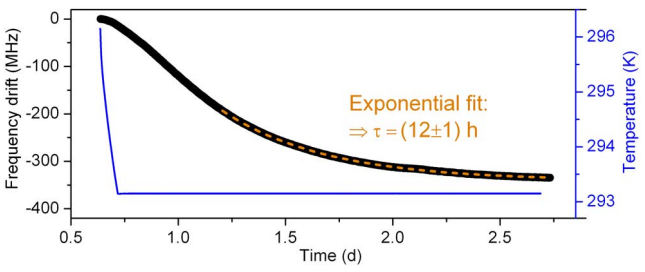

Fig. 3. Locked laser frequency response to vacuum chamber temperature change (thin curve).

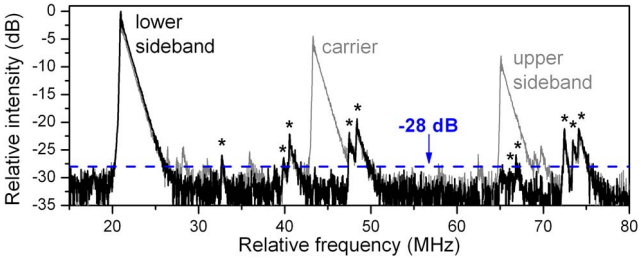

Fig. 4. MZM output power spectrum analyzed with a scanning cavity (*, transverse modes) for bad (light gray curve) and optimal (dark curve) control voltages.

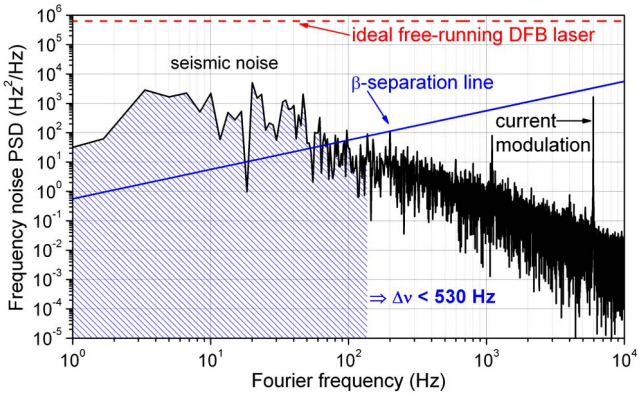

Fig. 5. Frequency noise PSD of the single-sideband light measured by means of the Super Invar etalon. The shaded area A corresponds to a laser linewidth $\Delta\nu = \sqrt{8\ln(2)A}$ [12].

source, we used a Super Invar Fabry–Pérot etalon with a finesse of $(5.5 \pm 0.1) \times 10^5$ and a FSR of (4.8 ± 0.1) GHz as a frequency discriminator. We tuned the single sideband to the side of a transmission mode and extracted the combined frequency noise power spectral density (PSD) of laser and etalon shown in Fig. 5 from the transmission signal. The measurement exhibits a dominant contribution from low-frequency seismic perturbations. The frequency modulation sideband due to diode current modulation at about 5.9 kHz is clearly visible, and a sharp mechanical resonance of the setup around 1.1 kHz is also observable. However, these two contributions to the locked laser linewidth are negligible at present. In general, the laser frequency noise is certainly lower than the measured curve (Fig. 5), as the latter contains the frequency noise contribution of the etalon, which is most probably non-negligible. In any event, the observed frequency noise PSD implies an upper bound of $\Delta\nu <$ 530 Hz for final laser full width at half-maximum (FWHM) by the graphical β-separation line technique [12] (Fig. 5). This constitutes a narrowing by almost 4 orders of magnitude starting from a free-running DFB laser with a linewidth of 2 MHz and nearly ideal white frequency noise [13].

In conclusion, we have stabilized a DFB diode laser to a novel highly stable V-shaped reference cavity by optical feedback. Single-sideband modulation with a MZM provides us with a source that is continuously tunable over more than 1 THz with frequency drifts below 20 Hz/s. Its linewidth below 530 Hz corresponds to a narrowing by almost 4 orders of magnitude. It is expected to be further reduced to the theoretically predicted ultrastable regime of 300 mHz by active vibration isolation and operation at the zero- coefficient-of-thermal-expansion temperature. Already, at present, the stable, tunable and narrow source presented here has the potential for an optical measurement of the Boltzmann constant at a 10^{-6} uncertainty level and could become a widespread tool for other demanding spectroscopic and metrological applications necessitating a highly linear frequency axis.

This work was supported by Pôle SMINGUE (Université Joseph Fourier).

References

1. B. Dahmani, L. Hollberg, and R. Drullinger, Opt. Lett. **12**, 876 (1987).
2. P. Laurent, A. Clairon, and C. Breant, IEEE J. Quantum Electron. **25**, 1131 (1989).
3. A. Hemmerich, D. H. McIntyre, C. Zimmermann, and T. W. Hänsch, Opt. Lett. **15**, 372 (1990).
4. J. Morville, S. Kassi, M. Chenevier, and D. Romanini, Appl. Phys. B **80**, 1027 (2005).
5. Y. Zhao, Q. Wang, F. Meng, Y. Lin, S. Wang, Y. Li, B. Lin, S. Cao, J. Cao, Z. Fang, T. Li, and E. Zang, Opt. Lett. **37**, 4729 (2012).
6. M. Izutsu, S. Shikama, and T. Sueta, IEEE J. Quantum Electron. **17**, 2225 (1981).
7. C. Daussy, M. Guinet, A. Amy-Klein, K. Djerroud, Y. Hermier, S. Briaudeau, C. J. Bordé, and C. Chardonnet, Phys. Rev. Lett. **98**, 250801 (2007).
8. B. C. Young, F. C. Cruz, W. M. Itano, and J. C. Bergquist, Phys. Rev. Lett. **82**, 3799 (1999).
9. A. D. Ludlow, X. Huang, M. Notcutt, T. Zanon-Willette, S. M. Foreman, M. M. Boyd, S. Blatt, and J. Ye, Opt. Lett. **32**, 641 (2007).
10. T. Kessler, C. Hagemann, C. Grebing, T. Legero, U. Sterr, F. Riehle, M. Martin, L. Chen, and J. Ye, Nat. Photonics **6**, 687 (2012).
11. D. Z. Anderson, J. C. Frisch, and C. S. Masser, Appl. Opt. **23**, 1238 (1984).
12. G. di Domenico, S. Schilt, and P. Thomann, Appl. Opt. **49**, 4801 (2010).
13. R. Engelbrecht, B. Lins, P. Zinn, R. Buchtal, and B. Schmauss, Appl. Phys. B **109**, 441 (2012).

3.2 Frequency noise and long-term drift

Beyond the mere realization of the highly stable VCOF setup, evidence was provided in [58] for its exceptional coherence properties and long-term stability. However, a fully quantitative characterization proved to be challenging, as this new laser was by far the narrowest and stablest light source available at LIPhy. In this Section, the different steps undertaken to fully characterize the properties of the VCOF laser source are reported. First, further details on experimental and evaluation aspects of the frequency noise measurement reported in Article 1 above are given. Then, new data is presented on a measurement revealing long-term VCOF drifts with kHz-level resolution through spectroscopy of ultra-narrow saturated absorption signatures. Finally, a brief account on absolute VCOF frequency measurements and drift characterization with a self-referenced optical frequency comb is rendered. These latter measurements were carried out in the framework of a collaboration project with the group of Professor Marco Marangoni from Politecnico di Milano.

3.2.1 Frequency noise measurement using a high-finesse etalon

The sharp TEM_{00} resonances of a high-finesse Fabry-Pérot cavity convert optical frequency variations into transmission changes according to the Airy formula Eq. (2.34). With its kHz-level mode width, such a linear etalon with highly reflective dielectric mirrors is a very sensitive interferometric frequency-to-amplitude converter and a powerful tool for frequency noise characterization. It constitutes a pragmatic and practical experimental solution, as it does not require a spectrally narrower reference laser as in heterodyne beat-note-based approaches or a complex experimental setup as in sub-Doppler saturated absorption discriminator schemes [146].

Therefore, we chose to construct the monolithic, compact and massive Super Invar [147] etalon shown in Fig. 3.1. Two quarter-inch dielectric mirrors with peak reflectivity at 1580 nm were inserted into the etalon and tightly contacted to the metal surface by tightening viton O-rings to their rear sides using stainless steel disks and M3 screws. With a bulk length of $(45.0 \pm 0.1)\,\mathrm{mm}$, the etalon features a mirror spacing of $(31 \pm 0.1)\,\mathrm{mm}$. According to Eq. (2.32), the FSR between two of its TEM_{00} modes therefore equals $f_{FSR} = (4.84 \pm 0.02)\,\mathrm{GHz}$. We mode-matched the VCOF laser to the TEM_{00} mode of the etalon by means of an aspheric lens and two metallic steering mirrors. To reach a resonance of the etalon, we took advantage of the broad and ultra-fine tunability of the single-sideband-modulated VCOF laser and used a home-made automated LabVIEW tracking program. The measurement principle for this frequency discriminator based on single-sideband-tuning and a high-finesse resonator is sketched in Fig. 3.2.

With the laser centered on the etalon TEM_{00} resonance, we rapidly scanned the single-sideband (SSB) frequency by an amount $\Delta\nu$ by means of a synthesizer-generated RF sweep. This led to the etalon transmission curve $T(\Delta\nu)$ reported in Fig. 3.3. The intensity of any one of the two peaks in the transmission curve in Fig. 3.3 can be maximized by appropriately bending the single-mode fiber, thereby changing the polarization of the light incident on the etalon. When the transmission through one mode has been optimized in this manner, the signal from the other peak vanishes. We therefore interpret the transmission curve in Fig. 3.3 as a direct observation of the splitting of the etalon TEM_{00} resonance into a doublet of two eigenmodes with nearly orthogonal polarization. This splitting cannot be accounted for by the commonly used scalar, polarization-independent TEM_{mn} Gauss-Hermite resonator modes, which are solutions to Maxwell's equations in the paraxial approximation. The paraxial treatment predicts a frequency splitting of higher-order TEM_{mn} modes due to mirror astigmatism, that is a slight ellipticity of the mirror surface. However, it results in degenerate polarization eigenmodes and, consequently, cannot ac-

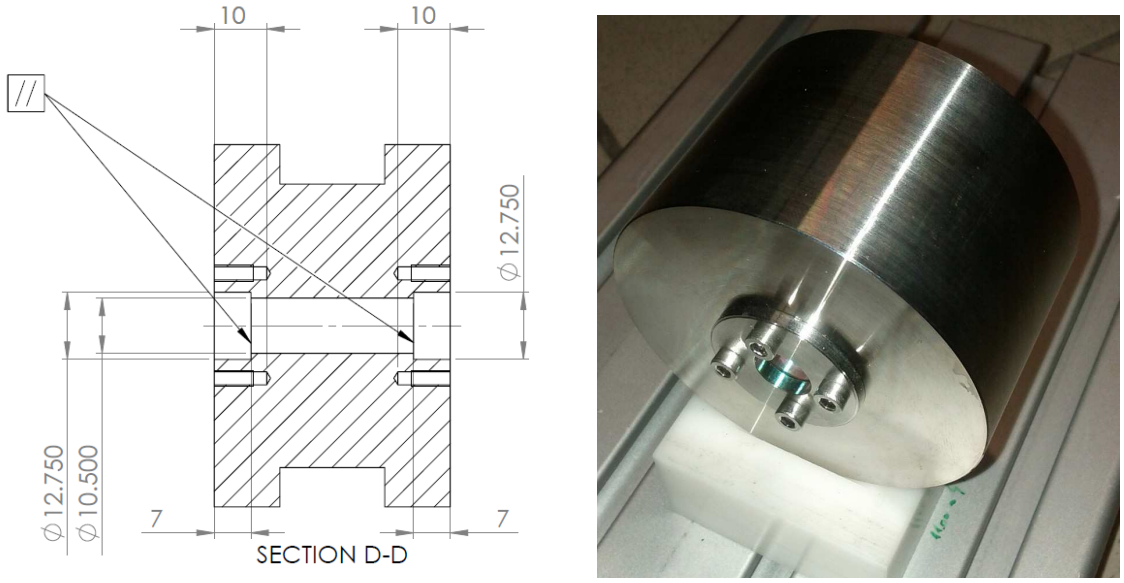

Figure 3.1 Super Invar etalon acting as an optical frequency discriminator for measuring the frequency noise of the optical feedback frequency-stabilized, single-sideband-tuned laser.

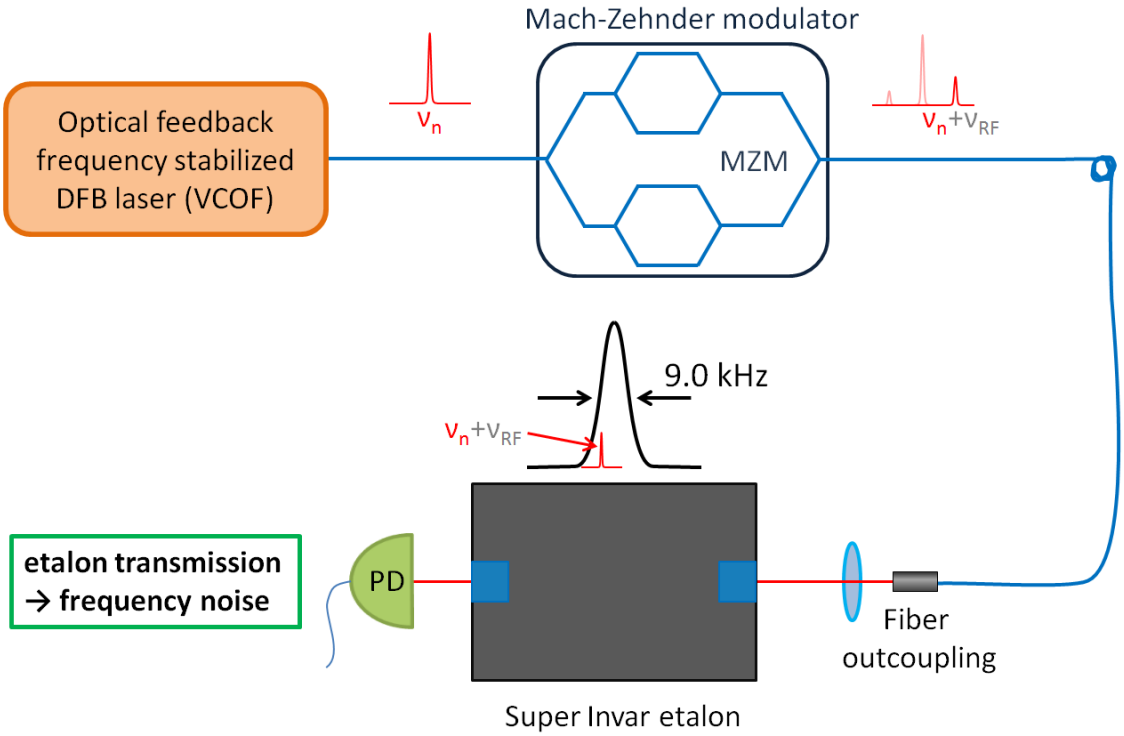

Figure 3.2 Principle and schematic sketch of the single-sideband-tuned VCOF frequency noise measurement with a Super Invar etalon. Blue curved lines: Optical fibers, red straight lines: free-space laser beam, PD: photodiode.

count for the observed transmission doublet shown in Fig. 3.3. A theoretical treatment of Fabry-Pérot resonators beyond the paraxial approximation, in spheroidal coordinates, shows that the degeneracy of higher-order TEM_{mn} modes with $m + n > 0$ is lifted by a mechanism which can be interpreted as a form of spin-orbit coupling for the resonant

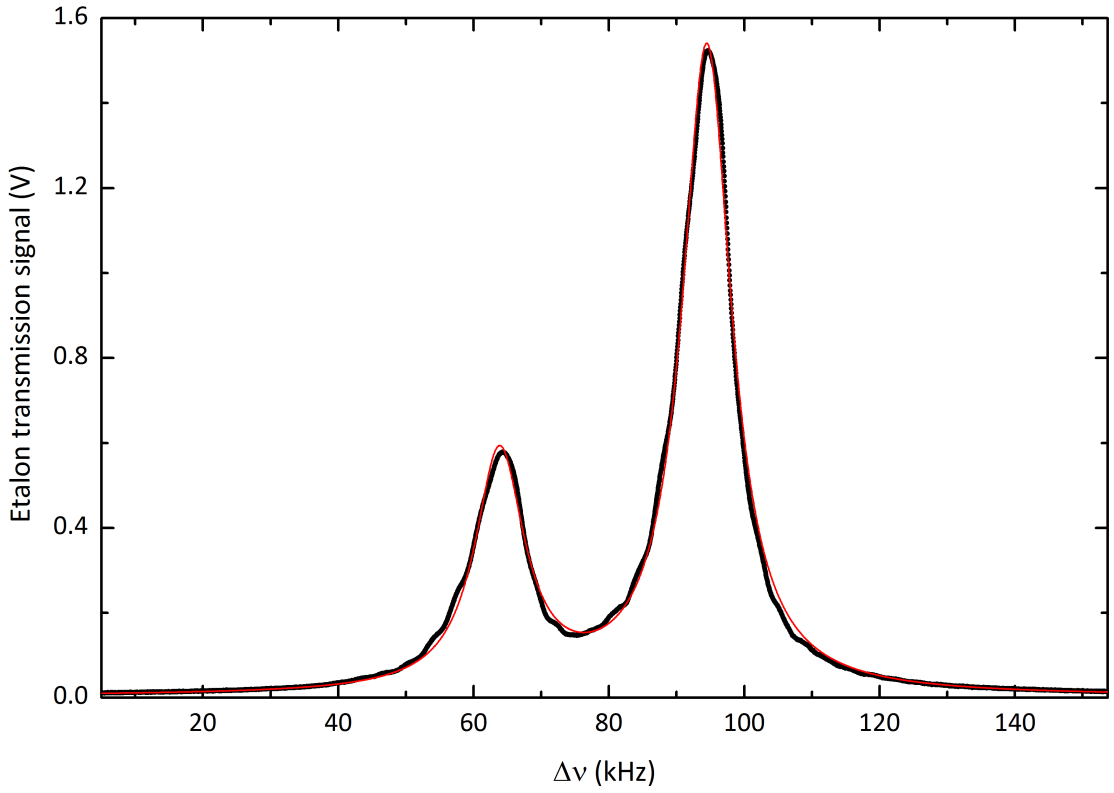

Figure 3.3 Polarization splitting of the Super Invar etalon TEM_{00} mode observed through single-sideband transmission during a frequency sweep over 100 kHz in 20 ms recorded at a sampling rate of 500 kHz.

intracavity field [114]. However, this theory predicts a degeneracy of the two polarization TEM_{00} modes in the case of spherical mirrors. By considering the polarization-dependent phase shift due to the reflection of light from an elliptic paraboloidal surface beyond the paraxial approximation, Uphoff *et al.* have shown that the degeneracy of the two polarization TEM_{00} modes is lifted by mirror astigmatism [115]. They demonstrated that this geometric polarization splitting mechanism is dominant for mirror curvature radii comparable to the wavelength of the intracavity field. In the present case of a macroscopic etalon, however, we have checked that this effect must be smaller than 20 Hz and thus cannot account for the 31-kHz-splitting of the TEM_{00} mode observed here.

Consequently, we attribute the TEM_{00} polarization doublet of the Super Invar etalon to residual and stress-induced birefringence of the highly reflective dielectric mirror coating [148]. Indeed, significant stress-induced birefringence is expected in our screw-fastened setup due to the strong forces applied to both mirrors. This birefringence should be accompanied by a slight polarization dependence of mirror losses [148]. This dichroism is small and one may assume equal losses for both polarization modes in a very good approximation, implying equal ring-down times and mode widths for both TEM_{00} modes. Therefore, we fitted 90 measured transmission curves $T(\Delta\nu)$ like the one shown in Fig. 3.3 with two Lorentzians of equal full width Γ and an offset B:

$$T(\Delta\nu) = \frac{A_1\Gamma}{(\Delta\nu - \Delta\nu_1)^2 + \Gamma^2/4} + \frac{A_2\Gamma}{(\Delta\nu - \Delta\nu_2)^2 + \Gamma^2/4} + B \tag{3.1}$$

As expected, fluctuations of the experimental data around the fit curve are the strongest on the slopes of both TEM_{00} modes, corresponding to the frequency-to-amplitude noise conversion by the etalon. The fit yielded a Lorentzian full mode width $\Gamma = (8991 \pm 1)$ Hz

and a polarization splitting of $\Delta = (31.04 \pm 0.03)\,\mathrm{kHz}$, that is $\Delta/\Gamma = 3.453 \pm 0.004$ in units of the cavity mode width. Together with the FSR value determined above, this measurement yields a precise value for the etalon finesse at 1590 nm, which amounts to $F = f_{FSR}/\Gamma = 538000 \pm 2000$. The mode splitting Δ corresponds to a birefringence-induced round-trip phase shift of $\Delta\varphi = 2\pi\Delta/f_{FSR} = 12$ µrad in the etalon. A detailed discussion of the impact of birefringence, dichroism and the polarization mode splitting on cavity ring-down-spectroscopy will be given in Section 7.7.

Here, for measuring the combined frequency noise of the VCOF laser and the Super Invar etalon, we simply bent the single-mode fiber to achieve a reasonably good match between the fiber output polarization and one of the polarization modes of the etalon, resulting in a single-Lorentzian transmission function as in Eq. (2.35). Inverting this equation, the offset-cleaned transmission time series $T(t)$ with peak amplitude A yields a direct measurement of the instantaneous relative frequency $\Delta(t)$ of the single-sideband VCOF source:

$$\Delta(t) = \frac{\Gamma}{2}\sqrt{\frac{A}{T(t)} - 1} \tag{3.2}$$

The optimal working point of this etalon frequency discriminator is the steepest point of the transmission slope where the conversion is nearly linear. Consequently, the neighborhood of this point was chosen for the experimental frequency noise measurement. Keeping the VCOF single-sideband near this point as long as possible is important for maximizing the measuring time interval. Therefore, the etalon was installed in a thermally isolating polystyrene box limiting its resonance frequency drift. The measured etalon transmission trace $T(t)$ shown in Fig. 3.4 corresponds to the combined VCOF-etalon frequency noise power spectral density shown in Fig. 5 of Article 1. By Eq. (3.2), $T(t)$ yields a measure-

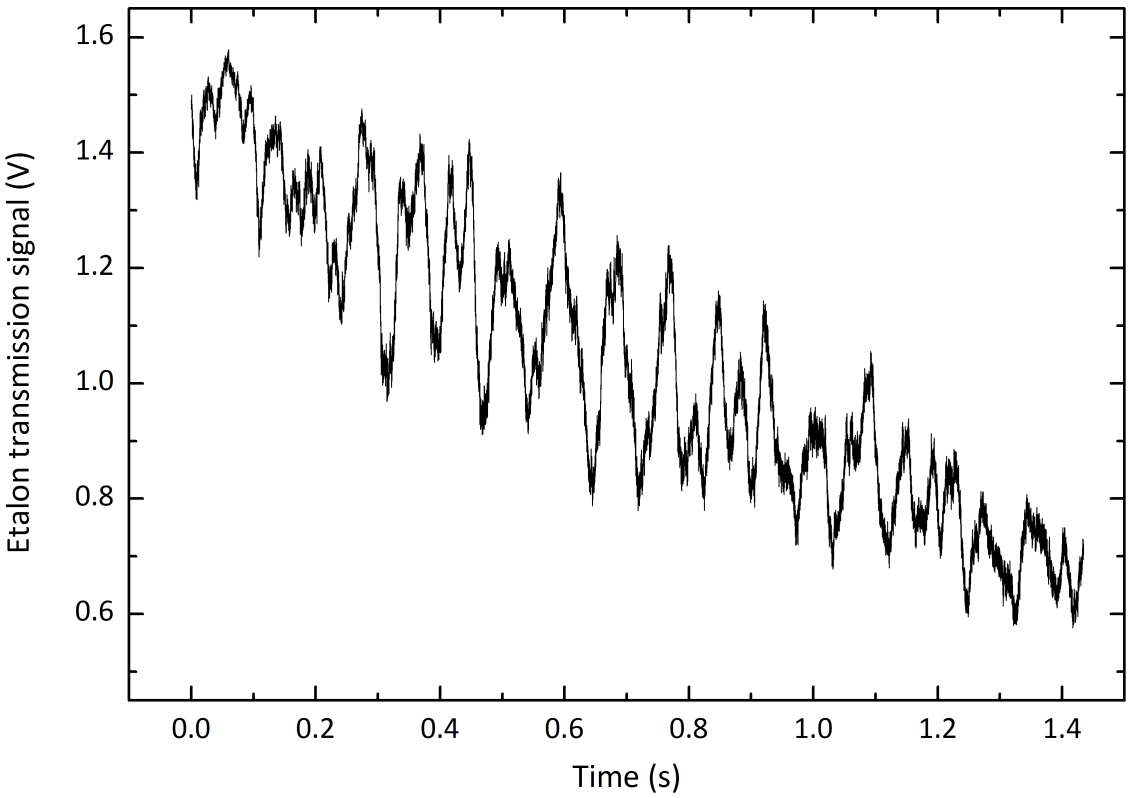

Figure 3.4 Super Invar etalon TEM_{00} mode transmission for a VCOF single-sideband at fixed radio frequency, recorded at a sampling rate of 500 kHz.

ment of the relative frequency $\Delta(t)$ between VCOF single sideband and etalon resonance.

As the Super Invar etalon was not temperature stabilized, a linear 2.6 kHz/s drift had to be substracted in $\Delta(t)$ prior to obtaining the frequency noise PSD as the Fourier transform of $\Delta(t)$. After the linear drift correction, $\Delta(t)$ exhibits a root-mean-square noise of 450 Hz, in good agreement with the upper bound of 530 Hz obtained from the PSD in Fig. 5 of Article 1 using the β-separation line technique.

3.2.2 Drift monitoring by saturated molecular absorption

In this section we present results on a VCOF frequency drift measurement by optical feedback frequency-stabilized cavity ring-down spectroscopy (OFFS-CRDS) of saturated molecular absorption. Here, we will focus on the basic principle of the measurement and an analyis and discussion of the results. The theoretical and methodological background for the spectroscopic technique will be discussed later in this thesis, especially in Chapters 6 and 9.

The measurement principle here is conceptually similar to the way an optical atomic clock works. It consists in tuning a narrow laser into resonance with a molecular transition. Setting aside bias sources discussed below, the molecular transition frequency is a physical property of nature, and constant over time to the best of current knowledge. Here, the aforementioned resonance is a very narrow absorption feature, commonly called Lamb dip, which is examined with an intense light field at low pressures. Under typical experimental conditions, its width is of a few hundred kHz, making it three orders of magnitude narrower than a conventional low-pressure absorption line at room temperature. Consequently, for a spectroscopic scan across the Lamb dip lasting a few minutes, a frequency measurement with a precision ranging from 1 to 15 kHz is obtained.

The measurement was carried out on three absorption lines of CO_2 near 1.6 µm, at a partial pressure of 0.28 Pa. They are identified in Table 3.1 and shall be called A, B, and C hereafter for the sake of simplicity. Their absolute transition frequencies are known with an accuracy at the few kHz level from a frequency-comb assisted saturation spectroscopy study carried out in the framework of this thesis. A detailed discussion of these results can be found in Section 9.4 and in Article 6 therein. The lines A, B and C were automatically measured over and over again by sequentially cycling them in a loop, recording the saturated absorption spectra on a span of 6 MHz around the center of each line in frequency steps of 50 kHz. After an appropriate fit, as in Section 9.4.2, each measurement yields a dip center frequency with kHz precision. Over one day, 305 such Lamb dip measurements were carried out. The observed line center frequencies relative to their initial value are shown in Fig. 3.5. The spectrometer frequency axis is taken as static, as if the VCOF laser were perfectly stable. Consequently, any VCOF drift translates into a change in the observed center position. Nevertheless, a necessary condition for interpreting an apparent line center change as a VCOF frequency drift is that the observed changes must be identical for all measured absorption lines, as their cause then lies outside the realm of

Table 3.1 CO_2 absorption lines from the 30013←00001 band (cf. Section 8.1.1) used for measuring VCOF frequency drifts by saturation spectroscopy. See Section 9.4 and Table 9.1 therein for details on the transition frequencies and their uncertainties (in parantheses).

Symbol	Transition	Frequency (kHz)	Wavenumber (cm^{-1})
A	P20	186200304287.5 (6.4)	6210.97360253
B	P18	186254902896.0 (4.1)	6212.79481607
C	P16	186308650583.8 (3.6)	6214.58764596

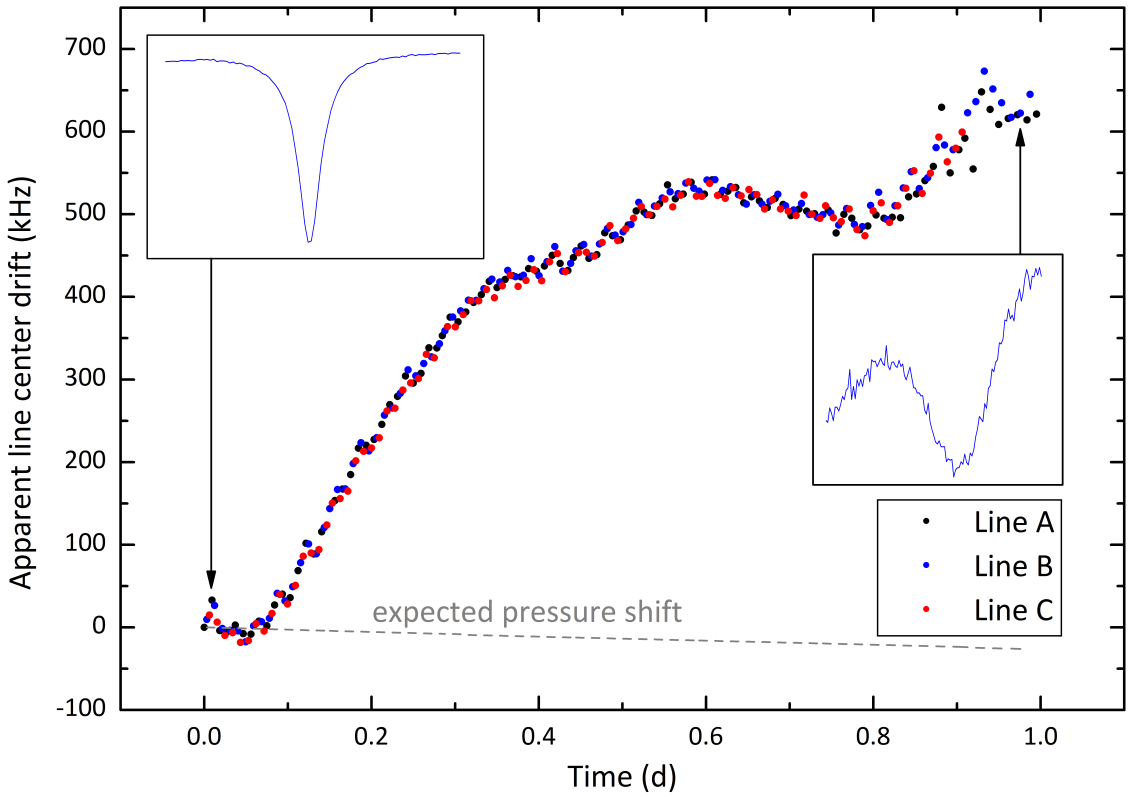

Figure 3.5 Change in apparent line center frequency over time for three CO_2 lines measured by OFFS-CRDS, revealing the drift of the V-shaped reference cavity. The insets show experimental Lamb-dip spectra from beginning and end of the measurement period, respectively, with absorption (y axis) as a function of optical frequency (x axis).

spectroscopy. Fig. 3.5 clearly confirms that this important consistency-check condition is met, showing a perfect alignment of the black, blue and red curves, corresponding to the lines A, B, and C, respectively.

The observed dip frequencies exhibit a global long-term trend towards higher Lamb dip frequencies, corresponding to a linear −7 Hz/s drift rate of VCOF frequencies on average. The most probable origin of this drift follows from the consideration on the V-cavity free spectral range below. The highest instantaneous drift rate evidenced by the data in Fig. 3.5 is 22 Hz/s. This result is consistent with the findings of Article 1, where the temperature stabilization and thermal isolation was significantly better than during the present experiment. Under those temperature stabilization conditions, a maximum drift of 20 Hz/s was predicted based on the experimental results.

Now let us turn to the inherent frequency noise level of this spectroscopic laser frequency drift monitoring technique. The frequency measurement noise level at the beginning of the recording period is on the order of 1 kHz per dip. This degree of precision and accuracy is way better than what could be achieved with state-of-the-art optical wavemeters, which feature a short-term stability of a few hundred kHz at best. This performance is due to the high signal-to-noise ratio of the first measurements. It amounts to up to 140, as shown in the upper left inset of Fig. 3.5. Over time, the Lamb dip signal-to-noise ratio decreases as saturation fades out due to a rise in intracavity pressure over time. This pressure increase originates from outgassing of molecules previously adsorbed on the cavity walls and will be discussed in detail in Section 6.2.4. At the end of the scan, the dip is broad and shallow, as shown in the inset on the right of Fig. 3.5, and the frequency

measurement noise approaches 15 kHz, still very competitive with Doppler-broadened techniques. Not only does the increase in intracavity pressure impair saturation, but it also shifts the transitions linearly to lower frequencies due to the inter-molecular collisions perturbing the molecular energy levels. Taking coefficient values from the literature [149] to convert the intracavity pressure reading to an expected pressure shift curve, we obtained the dashed line in Fig. 3.5. Compared to the observed dip-frequency drift, the pressure shift has opposite sign and negligible magnitude.

In Fig. 3.5, the traces were superposed using three offsets Δ_A, Δ_B and Δ_C added to the respective data set, so that the mean difference between the three curves equals zero. The noise around this zero determines the uncertainty of the relative frequency measurement. In this way, the frequency spacings $\Delta_{BA} = \Delta_B - \Delta_A$ and $\Delta_{CA} = \Delta_C - \Delta_A$ were determined to be

$$\Delta_{BA} = (54598724.7 \pm 1.7)\,\text{kHz} \tag{3.3}$$
$$\Delta_{CA} = (108346535.4 \pm 1.4)\,\text{kHz} \tag{3.4}$$

These values are to be compared to the literature values from Table 3.1, which are

$$\Delta_{BA_{lit}} = (54598608.5 \pm 7.6)\,\text{kHz} \tag{3.5}$$
$$\Delta_{CA_{lit}} = (108346296.3 \pm 7.3)\,\text{kHz} \tag{3.6}$$

The uncertainties of the literature values are worst-case estimates based on the results in Chapter 9. Comparing the experimental and literature spacings, one finds the offsets

$$\xi_{BA} = \Delta_{BA} - \Delta_{BA_{lit}} = (116.2 \pm 7.8)\,\text{kHz} \tag{3.7}$$
$$\xi_{CA} = \Delta_{CA} - \Delta_{CA_{lit}} = (239.1 \pm 7.4)\,\text{kHz} \tag{3.8}$$

We shall see in the following that these discrepancies are due to the fact that the V-shaped cavity free spectral range value $\tilde{\nu}_{FSR} = 491395463\,\text{Hz}$ from Article 5 on page 160, which was implicitly used for determining Δ_{BA} and Δ_{CA} does not reflect the real FSR ν_{FSR} of the V-cavity at the time of this measurement. In accordance with Equation (2) of Article 5, ξ_{CA} is proportional to the FSR error $\xi_{FSR} = \tilde{\nu}_{FSR} - \tilde{\nu}_{FSR}$:

$$\xi_{CA} = -(k_C - k_A)\xi_{FSR} \tag{3.9}$$

Naturally, the same equation holds for ξ_{BA} with k_B. The V-shaped cavity mode numbers k_A, k_B and k_C with respect to an arbitrary mode zero, which were used for stabilizing the VCOF laser, were counted with an optical wavemeter whose precision allows their unambiguous identification. Here, the number of VCOF modes separating the three measurements were $k_B - k_A = 111$ and $k_C - k_A = 225$. Inserting this result in Eq. (3.9) together with (3.8) yields a precise value for the current V-cavity FSR:

$$\xi_{FSR} = -(1063 \pm 33)\,\text{Hz} \tag{3.10}$$
$$\Rightarrow \nu_{FSR} = \tilde{\nu}_{FSR} + \xi_{FSR} = (491394400 \pm 33)\,\text{Hz} \tag{3.11}$$

The current FSR thus significantly disagrees with the previously used value $\tilde{\nu}_{FSR}$, which had been determined with outstanding Hz-level precision in Fig. 2 of Article 5 on page 160.

This FSR change is attributed to a continuous pressure increase in the V-shaped cavity enclosure during the one year period between the two measurements. As a matter of fact, the vacuum chamber was evacuated to well below the 10^{-6} mbar-level during the previous precise FSR measurement. Then, it needed to be isolated from a defective turbomolecular pump using a high-vacuum gate valve and has not been repumped since. Consequently, a

substantial quantity of molecules, essentially water, is expected to have desorbed from the walls of the vacuum cell, which had never been baked out. The residual gas at pressure P resulting from this outgassing leads to an increased refractive index n inside the V-shaped cavity shifting its modes to lower frequencies.

Quantitatively, the inverse proportionality of the V-cavity FSR to n is given in Eq. (2.33). It implies that a small refractive index change δn leads to an FSR change

$$\Delta\nu_{FSR} = -\frac{\delta n}{n}\nu_{FSR} \approx -\delta n \cdot \nu_{FSR} \tag{3.12}$$

For a dilute gas, $n \approx 1$ was inserted in the last step in very good approximation. δn is related to the pressure increase δP in a closed volume at constant temperature by

$$\delta n = m\delta P \tag{3.13}$$

with a proportionality constant m depending on the polarizability of the gas molecules, as discussed in [58], for instance. For water vapor, an approximate value $m_{vapor} = 2.2 \cdot 10^{-7}\,\mathrm{mbar}^{-1}$ can be calculated from the findings in [150]. It is not very different from the value $m_{air} = 2.7 \cdot 10^{-7}\,\mathrm{mbar}^{-1}$ for dry air from the same reference, indicating that the exact intracavity gas composition is not a critical parameter here. Inserting $\delta\nu_{FSR} = \xi_{FSR}$ in Eq. (3.12), one obtains $\delta n = 2.16 \cdot 10^{-6}$. Using Eq. (3.13), this corresponds to a partial pressure of water vapor inside the vacuum cell of $P = 10\,\mathrm{mbar}$. As no pressure gauge was installed on the vacuum line before the gate valve isolating the vacuum cell from the defective turbo pump, this result cannot be independently confirmed. However, it appears perfectly realistic in view of the long outgassing period and the vapor pressure of water, which amounts to 29 mbar at 23.5 deg, the temperature of the V-shaped cavity and its enclosure. Translating the total refractive index change δn over one year into a frequency drift, one realizes that the modes of the V-shaped cavity must have drifted by $\delta n\nu$, equalling about 400 MHz at $\nu \approx 186\,\mathrm{THz}$. Per unit of time, this corresponds to a 12.7 Hz/s drift on average. This is in good agreement with the 7 Hz/s trend observed during the one-day scan presented here, noting that the outgassing rate is expected to reduce over time when approaching the vapor pressure.

With the new FSR value ν_{FSR}, let us determine the predicted line position of B relative to A expected from Eqs. (3.9) and (3.10):

$$\xi_{BA_{expected}} = -(k_B - k_A)\xi_{FSR} = (118.0 \pm 3.7)\,\mathrm{kHz} \tag{3.14}$$

Therefore, the difference in the spacing between lines B and A from the present study and from Chapter 9 amounts to

$$\xi_{BA} - \xi_{BA_{expected}} = -(1.8 \pm 8.6)\,\mathrm{kHz} \tag{3.15}$$

This result is completely consistent with zero, thereby indicating a perfect agreement between the two independent Lamb-dip frequency measurements on the same lines, providing further evidence for the validity of both studies.

In conclusion, monitoring three saturated absorption Lamb-dips by OFFS-CRDS over one day has served a threefold purpose: First, it confirmed the outstanding linearity of the spectrometer frequency axis due to the stability of the VCOF laser and related findings in Article 1. Second, it yielded a very precise updated value for the V-cavity FSR, evidencing that it had slightly changed over one year, most probably due to water outgassing from the V-cavity vacuum cell walls. Finally, it provided a successful verification of a frequency spacing between CO_2 lines which had been measured with kHz-level accuracy during the frequency-comb-assisted OFFS-CRDS experiments reported in Article 6 and Section 9.4.

To make a closing remark let us point out that the measurement principle described here can be modified to yield a laser frequency stabilization approach somewhat complementary to the stable-reference-cavity approach chosen in this thesis. By adding a frequency dithering of the laser around the center of the dip, a first-derivative lock-in detection approach can be used for detecting the dip center. Using the corresponding error signal, the laser frequency can thus be locked to the saturated absorption resonance, guaranteeing its long-term stabilization to the molecular reference. Such approaches have already been implemented and used for setting up molecular spectroscopy experiments targeting metrological applications [151].

3.2.3 Absolute frequency measurement with an optical frequency comb

At present, the most accurate technique for measuring the optical frequency of a laser consists in superposing its light with that of a self-referenced optical frequency comb (OFC) on a photodetector. As discussed in 2.5, this gives rise to a beat note signal as in Eq. (2.21). It can be measured in order to determine the absolute optical frequency of the laser according to Eq. (2.46), provided that its approximate frequency is already known to better than half the OFC repetition rate f_{rep}.

We had the opportunity to carry out such an OFC-VCOF beat note measurement in the framework of a collaboration project with the group of Prof. Marco Marangoni from Politecnico di Milano. Using their self-referenced Toptica FFS model frequency comb with a repetition rate locked at $f_{rep} = 100\,\mathrm{MHz}$, a carrier-envelope-offset frequency stabilized to $f_{CEO} = 20\,\mathrm{MHz}$ and an intrinsic linewidth on the order of 200 kHz, we could measure the absolute frequencies of several V-cavity modes the VCOF laser was locked to. The measurement procedure and the results obtained are discussed in greater detail in Article 5 on page 160 and in Article 6 on page 192. Beyond the enormous benefits these measurements have for frequency-calibrated molecular spectroscopy (cf. Section 9.4), they were also exploited to determine the V-cavity FSR with Hz-level precision, as reported in Article 5.

Finally, monitoring the absolute frequency of the VCOF laser locked to one mode over a longer period of time also reveals the slow drifts of the V-shaped reference cavity. The results obtained in this respect are reported in terms of the Allan deviation plot in Fig. 2 of Article 6. They are in very good agreement with the findings of the previous Section and shall be rapidly reviewed here for the sake of completeness. From a single-shot precision of 200 kHz, the Allan deviation averages down as white noise until it reaches a minimum at 1.4 kHz after 30 s averaging time. Beyond this point, it increases again due to a 28 Hz/s drift. The precision of this OFC-VCOF beat note frequency measurement is ultimately limited by two mechanisms: At short averaging times, the OFC short-term noise does not allow resolving the narrow VCOF laser linewidth, and at long averaging times the V-shaped reference cavity drift dominates.

3.3 Development of a new generation of V-shaped ultrastable cavities

Based on the highly stable V-shaped cavity prototype from [58], we have realized a second cavity with several design improvements. Trying to reduce the first cavity's abnormally high coefficient of thermal expansion of $-6 \cdot 10^{-7}\,\mathrm{K}^{-1}$ discussed in Article 1 and in [58], the second cavity uses an ULE spacer with ultra-polished end facets and threaded M3 $\times$ 0.5 rods and nuts as well as Belleville washers instead of stainless steel springs for providing a more uniform and rigid contact between the mirror holders and the spacer. In order to prevent vibrations from impairing locked-laser linewidth, the vacuum system was redesigned

to operate as a closed system with a small ion pump (GammaVacuum 3S-CV-1V-5K). To further reduce the passive thermal isolation of the cavity, the aluminium foil heat shield of the first setup was replaced by a massive copper cylinder between cavity and vacuum cell. This improved composite V-cavity is shown on the left of Fig. 3.6.

Figure 3.6 Improved first-generation composite ULE-glass and SuperInvar V-cavity with half-inch mirrors (left) and second-generation quasi-monolithic Zerodur cavity with optically contacted one-inch mirrors (right), mounted on the bottom flanges of their respective vacuum cells. Note the difference in scaling between the two photos, which show a CF100 flange with an outer diameter of 152 mm on the left, and a CF160 flange with an outer diameter of 199 mm on the right.

On the right of this same figure, an entirely new, second-generation V-shaped ultrastable cavity is shown which was developed in parallel. In terms of cost, a huge difference between roughly 1 k€ for the composite cavity and 20 k€ for the second-generation cavity is to be acknowledged. However, the high price is outweighed by the expected reduction in vibration sensitivity and two-orders-of-magnitude improvement in locked-laser long-term stability.

This second-generation V-cavity design is based on a 18-cm-long rectangular Zerodur spacer with a slightly beveled, roof-shaped top and ultrapolished end facets. Optical contacting of a one-inch mirrors to each facet then yields a quasi-monolithic, intrinsically aligned V-shaped cavity. Zerodur is a near-zero thermal expansion glass ceramics with a specified coefficient of thermal expansion below $\pm 7 \cdot 10^{-9}\,\mathrm{K}^{-1}$ in the highest quality grade,

which was used here. Carried by three long, thermally isolating Macor rods, the cavity is installed in a full-coverage, massive copper heat shield isolated from the vacuum cell by three Macor spacers. The only five small openings of this heat shield are inevitably necessary for laser beam transmission and pumping. Fig. 3.7 shows a section view of this setup.

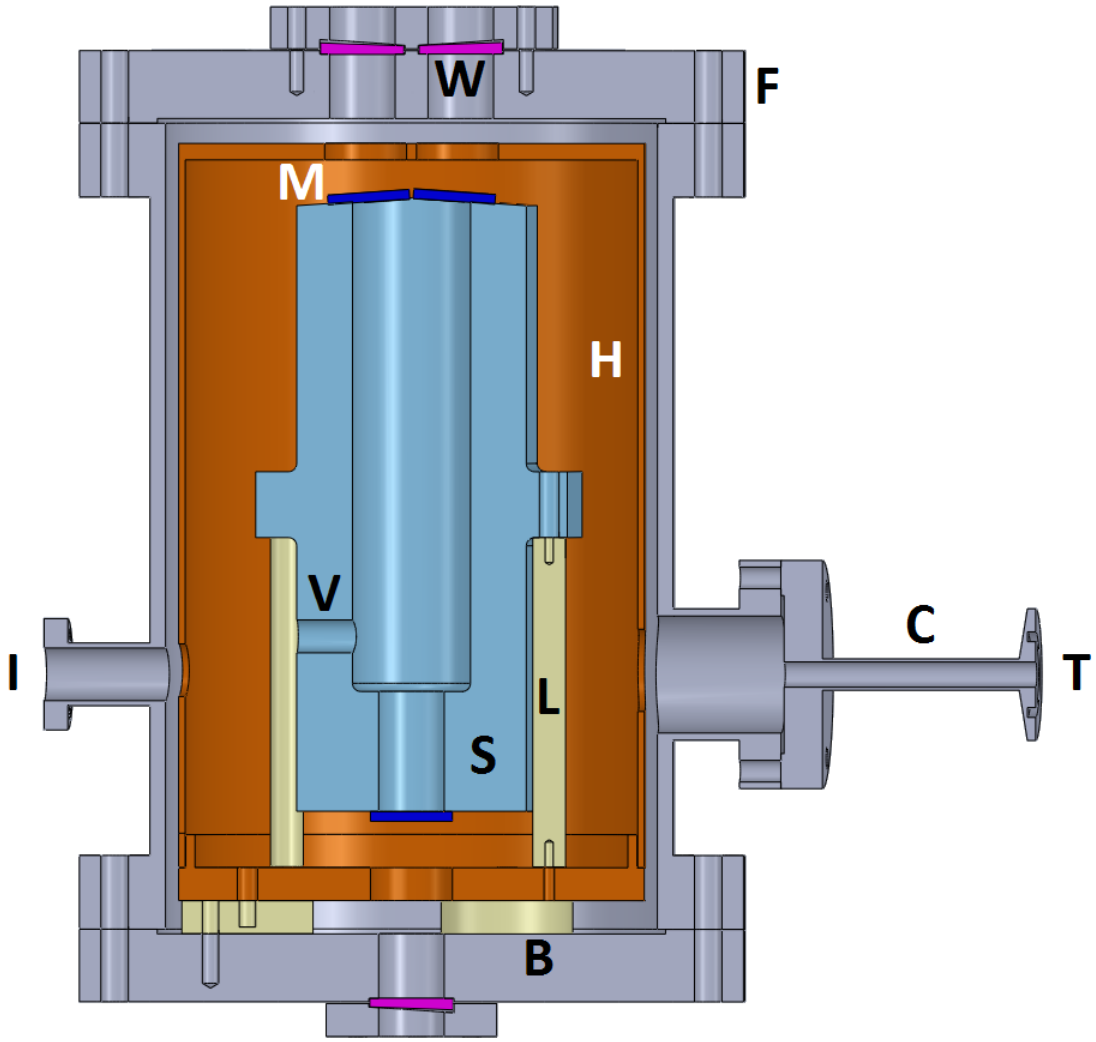

Figure 3.7 Section view of the computer-aided-design assembly of the second-generation ultrastable cavity setup. F: CF160 ultra-vacuum flanges. M: Three one-inch dielectric mirrors (blue) optically contacted to the Zerodur spacer S, which has a lateral venting hole V. L: Three leg-type Macor rods carrying the spacer S. H: Massive copper heat shield with three circular openings for laser beam transmission and two lateral openings for pumping. B: Three Macor sockets carrying the heat-shield-cavity assembly. I: CF16 flange for connecting the ion pump. T: KF25 flange for connecting a turbomolecular pump for initial pumping. C: copper tube which can be irreversibly sealed by deformation. W: three wedged, anti-reflection-coated windows for laser beam transmission (magenta). A length scale is given by the CF160 flanges, whose diameter is 199 mm.

As in all previous V-cavity setups, virtual leaks due to air trapped in inaccessible small volumes inside the vacuum system were systematically avoided. Using the same ion pump as above (GammaVacuum 3S-CV-1V-5K), the vacuum system was definitively isolated from the turbo-molecular pump (Pfeiffer Vacuum HiPace 80) used for the initial pump-down

by means of a copper tube, which was irreversibly deformed until it was completely leak-tight. First tests for both cavities showed that their respective vacuum systems operate well below the 10^{-6} mbar-level under exclusive ion pumping. To resist extreme temperature gradients in rough field-campaign environments, the second-generation vacuum cell is housed in a copper enclosure inside a passively isolating wood box. The six sides of the copper box are actively stabilized to equal temperature individually, by means of inter-calibrated temperature probes, resistive rubber heating pads tailored to the size of the copper faces and a home-made dedicated ARDUINO micro-computer-based temperature stabilization scheme.

The realization of the experimental setups described here, which are close to operational, was carried out by two fellow PhD students, Mathieu Casado and Tim Stoltmann, in the framework of their joint PhD projects between LIPhy and Laboratoire des Sciences du Climat et de l'Environnement (LSCE) in Gif-sur-Yvette, France, as discussed in more detail in Chapter 10.

Chapter 4

Feed-forward coherence transfer between lasers by optical single-sideband modulation

Transferring the stability and narrow linewidth of the VCOF laser source discussed in the last chapter to lasers in other spectral regions is an extremely attractive vision for phase-coherent and metrological applications in general, and for broadband high-resolution molecular spectroscopy in particular. At Laboratoire Interdisciplinaire de Physique, for example, in the near-infrared only, we have almost 90 butterfly distributed feedback (DFB) laser diodes with MHz-level linewidth at our disposal, covering the spectral interval between 1265 and 1705 nm without any spectral gap. Conveying the stability characteristics of the VCOF laser to any of these commercial lasers would provide a significant added value to all spectroscopic studies, with the benefits of a stable and linear spectrometer frequency axis and an efficient injection of high-finesse cavities discussed in detail in Part II.

The main experimental challenge to this endeavor is the high phase noise of typical DFB lasers with a linewidth of several MHz, due to white frequency noise extending up to very high Fourier frequencies [152]. While this could be accomplished using ultra-fast optical phase-locked loops with tedious high-bandwidth electronics (cf. Section 2.2), feed-forward locking is a powerful and conceptually strikingly simple alternative. In simple terms, this technique consists in measuring the frequency and phase error of the noisy slave laser with respect to the stable reference laser for subsequently applying it as an *a posteriori* correction to the noisy light field using a fast phase and frequency actuator. As we will demonstrate in the following, this feed-forward approach can provide phase-locking at an arbitrary frequency offset without the loss of lock typically occuring in feedback schemes under very big and abrupt phase and frequency perturbations of the slave laser.

Here, we will first consider the basic principles of feed-forward coherence transfer by revisiting some crucial previous works from the literature. Then, we present results from a collaboration project with the group of Prof. Marco Marangoni from Politecnico di Milano, who have made pioneering contributions to the field [93, 153]. The guiding idea was to unite our know-how on feed-forward frequency stabilization and on Mach-Zehnder-modulator-based optical single-sideband modulation (cf. Section 2.3) in order to realize feed-forward frequency and phase locking schemes with unprecedented correction bandwidth and spectral coverage. Our first study demonstrates what we call optical phase cloning, that is a coherence transfer at a 100-mrad phase error level, using an integrated electro-optic Mach-Zehnder modulator as a feed-forward frequency shifter. Subsequently,

we provide a detailed theoretical analysis of this coherence transfer technique, characterizing its limitations and exploring the different pathways for frequency-offset-locking. Finally, in another proof-of-principle study, we demonstrate that the MZM-based feed-forward scheme can be generalized using an optical frequency comb as a transfer oscillator, by transferring the coherence of our sub-kHz source to a DFB laser over 10 THz away, independently of the common-mode noise of the teeth of the comb.

4.1 Principles of feed-forward frequency stabilization

Before turning to a rigorous theoretical analysis of feed-forward phase and frequency locking with a Mach-Zehnder single-sideband modulator in Section 4.3, let us first discuss the basic principles of feed-forward stabilization schemes in terms of frequency offsets and corrections. Later, it will become evident that the same relationships hold for optical phase correction, provided that the correction bandwidth of the feed-forward system is sufficient.

The general setting of feed-forward schemes comprises a master laser at frequency ν_0, which is typically, but not necessarily, highly coherent, as well as a noisy slave laser at a detuned frequency ν_{CW}. The feed-forward correction of slave laser frequency consists in a two-step process.

First, the frequency error of the slave laser is measured in terms of a heterodyne beat note between the two lasers (cf. Eq. (2.21), which has a frequency $f_{BN} = \nu_{CW} - \nu_0$. Second, an *a posteriori* frequency correction corresponding to the measured error is applied to the slave laser field using a frequency actuator such as an acousto-optic modulator (AOM) or an optical single-sideband modulator. This yields a feed-forward-corrected optical output frequency $\nu_{FF} = \nu_{CW} - f_{BN} = \nu_{CW} - (\nu_{CW} - \nu_0) = \nu_0$, thus restoring the reference of the master laser on the slave laser. This is coincidence locking.

The beat note f_{BN} can also be mixed with a radio frequency (RF) local oscillator (LO) at frequency f_{LO} before carrying out the correction. Assuming $f_{LO} > f_{BN}$ without loss of generality, this provides a frequency-shifted beat note $f'_{BN} = f_{LO} - f_{BN} = f_{LO} - (\nu_{CW} - \nu_0)$. Then, the feed-forward correction is obtained by the frequency actuator adding f'_{BN} to slave laser frequency. This yields an output frequency $\nu'_{FF} = \nu_{CW} + f'_{BN} = \nu_{CW} + f_{LO} - \nu_{CW} + \nu_0 = \nu_0 + f_{LO}$, that is the master frequency with an arbitrary RF shift. This is the offset-locking configuration illustrated in Fig. 4.1.

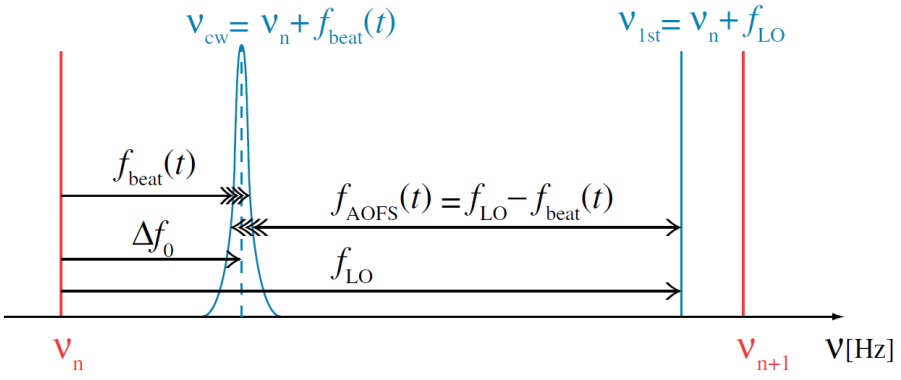

Figure 4.1 Schematic sketch of the frequencies involved in the feed-forward offset-locking of a slave laser at frequency $\nu_{cw}(t)$ to a tooth ν_n of an optical frequency comb. $f_{beat}(t)$ is the beat note frequency providing the physical error signal and f_{LO} is a radio-frequency local oscillator frequency for offset locking. $f_{AOFS}(t)$ is the feed-forward correction applied to the slave laser light by the acousto-optic frequency shifter, yielding an output stabilized at an offset f_{LO} from the comb mode ν_n. Adapted from [93] (Figure 1).

The term ν_n in the figure refers to a tooth of the frequency comb which was used by Sala and co-workers for feed-forward offset-locking of an external cavity diode laser (ECDL) [93]. The authors demonstrated a narrowing of the ECDL linewidth from the MHz-level to the comb linewidth of 10 kHz and a relative linewidth of comb and ECDL of 3.1 kHz, limited by the response bandwidth of the AOM used as the feed-forward frequency actuator.

The bandwidth of the correction is a main limitation of feed-forward frequency and phase control in practice. In the discussion here, an immediate feed-forward response was implicitly assumed, corresponding to an infinite correction bandwidth, which is an obvious idealization. Finite lags and response times in the feed-forward correction lead to an imcomplete or erroneous compensation of phase errors of the slave laser field. The impact of a correction delay τ was studied theoretically and experimentally by Gatti and co-workers [153]. In particular, they showed that the correction bandwidth f_{BW} of the feed-forward control system depends on τ according to

$$f_{BW} \approx \frac{1}{2\pi\tau}. \tag{4.1}$$

By reducing their AOM frequency shifter delay time to a 200-ns level by an optimized beam alignment, the authors achieved a correction bandwidth on the order of 1 MHz yielding a sub-radian phase lock of a DFB laser to a frequency comb. The impact of a finite delay in the feed-forward correction on residual phase noise will also be treated theoretically in Section 4.3.

In prior literature, a feed-forward scheme was used for a shot-noise-limited stabilization of the carrier-envelope offset of an optical frequency comb [154], which is a signal with a low intrinsic noise level. Griffin and Kitayama have realized a single-sideband-modulation approach [155] similar to the scheme discussed in the next section, however targeting the domain of optical millimeter-wave generation. As broadband spectral purity of the feed-forward controlled light field is of no concern in that field, the optical output in their study consisted of several spectral components, including noisy and broadened ones. Consequently, this technique is not suited to applications such as high-resolution spectroscopy and coherent manipulation of atoms or molecules.

4.2 Article 2 - Optical phase cloning by an integrated dual-parallel Mach-Zehnder modulator

In the following article [156], feed-forward phase coherence transfer from the sub-kHz-linewidth VCOF laser to a DFB laser with 2.6-MHz linewidth at 1 ms observation time and white frequency noise is demonstrated. Using an electro-optic MZM single-sideband modulator as a fast phase and frequency actuator, both offset and coincidence locking regimes were explored and characterized.

First, the experimental principle and general aspects of the feed-forward approach to phase locking are discussed. A detailed description of the electronic and optical setup for error signal detection, phase and frequency correction and coherence transfer characterization is provided. Then, experimental power spectra of beat notes of the VCOF reference laser with the free-running DFB laser and the feed-forward-corrected MZM output are examined, both at coincidence with the VCOF laser and under offset-frequency tuning, indicating phase coherence well below the radian level in both cases. This was confirmed by a measurement of the VCOF-MZM-output beat note phase noise power spectral density in both regimes. The direct homodyne interference signal between reference laser and

MZM output on a balanced photodetector was used for measuring a time series of their relative optical phase, again indicating a root-mean-square phase error at the 100-mrad level. Finally, the narrow and stable feed-forward-corrected slave laser light was injected into a ring-down cavity in order to illustrate the robustness of the scheme under slave laser frequency variations and its applicability to high-finesse cavity-enhanced spectroscopy.

Optical phase cloning by an integrated dual-parallel Mach–Zehnder modulator

Johannes Burkart,[1,2] Tommaso Sala,[3] Samir Kassi,[1,2] Daniele Romanini,[1,2] and Marco Marangoni[3,*]

[1]*Univ. Grenoble Alpes, LIPhy, F-38000 Grenoble, France*

[2]*CNRS, LIPhy, F-38000 Grenoble, France*

[3]*Physics Department of Politecnico di Milano and IFN-CNR, Piazza Leonardo da Vinci 32, 20133 Milano, Italy*

**Corresponding author: marco.marangoni@polimi.it*

Received November 13, 2014; revised January 13, 2015; accepted January 16, 2015;
posted January 21, 2015 (Doc. ID 222450); published February 26, 2015

The use of a dual-parallel Mach–Zehnder modulator in a feed-forward configuration is shown to serve the purpose of cloning the optical phase of a master oscillator on a distributed-feed-back (DFB) slave laser exhibiting a multi-MHz-wide frequency noise spectrum. A residual phase error of 113 mrad is obtained together with an extremely high control bandwidth of hundreds of megahertz and a gigahertz-level capture and tuning range. Besides offering a dramatic improvement over feedback loops, this approach is susceptible of hybrid integration in a cost-effective compact device benefiting from the wide tunability of DFB lasers.

OCIS codes: (140.3425) Laser stabilization; (120.3930) Metrological instrumentation; (250.7360) Waveguide modulators.

http://dx.doi.org/10.1364/OL.40.000816

Recent progress in various fields, such as frequency metrology [1], high-resolution spectroscopy [2], optical atomic clock developments [3,4], gravitational wave detection [5], frequency transfer and timing synchronization across fiber networks [6,7], is relying more and more on ultra-stable narrow-linewidth laser oscillators. These are typically obtained by locking diode or fiber lasers to the resonances of high-finesse ultra-stable optical cavities, with linewidths ranging from a quite typical Hz-level down to 40 mHz [8]. Cloning the optical phase of such an oscillator on a second noisier and less-expensive laser is highly desirable: it may allow matching the absorption features of predetermined spectroscopic targets, reaching the telecom range needed for frequency transfer or remote clock delivery across long-haul fiber links, or simply adding frequency tunability to an inherently rigid laser system. Optical frequency combs have been shown to serve the purpose of phase-coherent transfer across octave-spanning frequency gaps [9], but the extent to which phase coherence is transferred remains mainly limited by the control bandwidth of feedback systems typically used for optical phase correction.

Physical factors such as the frequency modulation response of the slave laser and the propagation delay within the servo loop typically provide an upper limit to the control bandwidth of a few MHz. This is not enough to compensate for the high-frequency pedestal in the noise spectrum of most common lasers, such as fiber or semiconductor distributed feedback lasers. Similar bandwidth limitations come into play with feed-forward control schemes relying on the acousto-optic control of the slave laser frequency [10]. With this approach, root-mean-square (rms) phase errors of few tens of milliradians have been demonstrated, but starting with relatively quiet signals, such as those for carrier-envelope-phase control of mode-locked lasers [11]. Ultra-fast optical phase-locked loops with bandwidths as high as 300 MHz have been demonstrated so far exclusively in the telecom field [12], searching for solutions to coherent optical detection in long-haul transmission systems, but require a monolithic integration of laser source and control electronics that limits the domain of application [13,14]. In the telecommunication field, extremely fast feed-forward schemes based on electro-optic Mach–Zehnder modulators (MZMs) have been also demonstrated, yet restricted to the target of optical millimeter-wave generation [15]. In such case, usage of a simple MZM did not allow generation of a clean single-frequency optical output, accurately cloning the master laser field, whereas, as we show in the following, a dual-parallel MZM configuration may efficiently serve the purpose.

In this Letter, we present a powerful approach for cloning the optical phase of a laser oscillator with minimal residual phase error. It relies on a dual-parallel MZM operated as a single-side-band generator [16] in a feed-forward control scheme. We show that such a device, primarily developed for quadrature phase-shift keying transmission [17], can provide plug-and-play phase corrections with an electro-optic bandwidth as large as 20 GHz. It also enables precise and straightforward multi-GHz frequency tunability of the slave laser with respect to the master, thus mimicking the behavior of offset-frequency locking servos without any fast phase detector or lock-relock procedure.

Figure 1(a) illustrates the operation principle of the optical phase cloner. A fast optical detector records the beat note of a slave laser with noisy frequency output ν_s mixed with a much narrower master laser with frequency ν_m. The beat signal between the two lasers, $f_{\mathrm{beat}} = \nu_s - \nu_m$, drives an MZM whose interferometric working points allow for the generation of a single-sideband suppressed-carrier output with frequency $\nu_{\mathrm{out}} = \nu_s - f_{\mathrm{beat}} = \nu_s - \nu_s + \nu_m = \nu_m$, thus in an ideal frequency coincidence with the master laser. If the beat signal is additionally mixed with a tunable radio-frequency (RF) local oscillator (LO), the MZM output can be arbitrarily offset with respect to the master, up to its 20 GHz bandwidth limit. The experimental setup used for optical phase cloning and the characterization

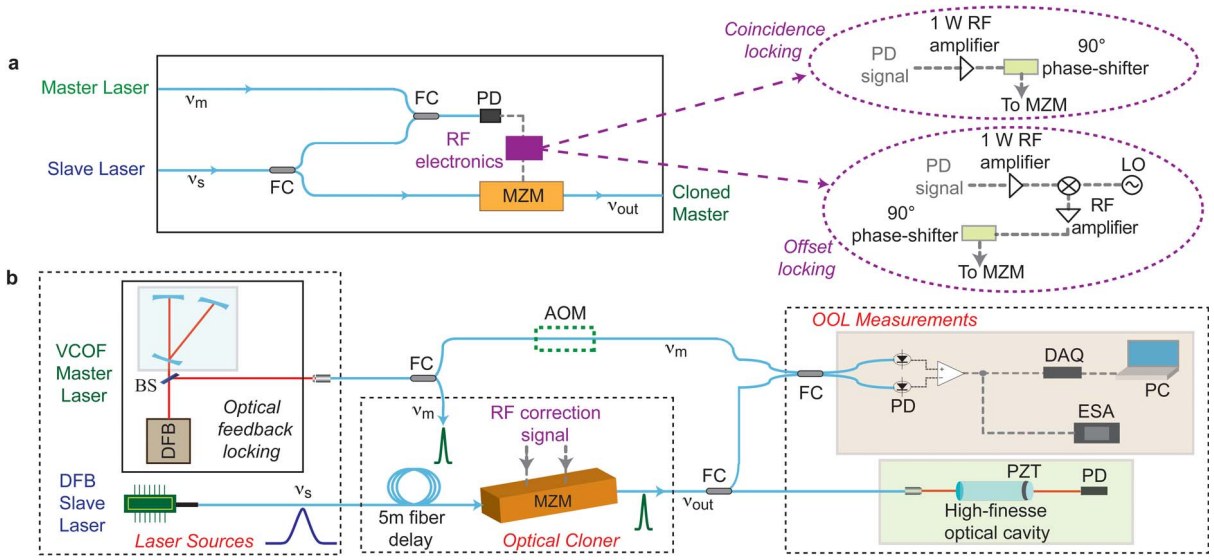

Fig. 1. Experimental layout. (a) Schematic of the optical phase cloner. (b) Overview of the experimental setup. Blue: optical fiber link; red: free-space laser beam; dashed: electrical signal. OOL, out-of-loop phase noise characterization. PD, photodiodes; MZM, dual-parallel Mach–Zehnder modulator. FC, 2×2 fiber couplers; LO, RF local oscillator driving a double-balanced mixer. AOM, acousto-optic modulator (optional); PC, computer; ESA, electrical spectrum analyzer; DAQ, data acquisition card; PZT, piezoelectric actuator.

of the device is schematically illustrated in Fig. 1(b). The highly stable master laser was a V-cavity optical-feedback (VCOF) source based on optical self-locking of a DFB diode laser to a high-finesse ultra-stable V-shaped cavity housed in a temperature-stabilized vacuum chamber [18]. It features a linewidth below 500 Hz over 1 s and linear drift rates below 20 Hz/s. The slave laser was a butterfly-packaged DFB laser coarsely tuned by temperature control and pumped at constant current. Both lasers were fiber coupled and operated around 1614 nm. Using fibers in all propagation parts, master and slave laser were made to beat on a 10-GHz-bandwidth InGaAs photodiode (Nortel PPX-10GC28). The broad frequency noise spectrum of the slave laser is evidenced by the electrical spectrum of the free-running beat note in Fig. 2(a), which is as large as 2.6 MHz over 1 ms when fitted with a Voigt profile.

To achieve phase cloning in the coincidence locking regime, f_{beat} was kept between 220 and 470 MHz to comply with the limited working range of the 2-way 90° hybrid coupler (Minicircuits ZX10Q-2-5+) driving the two fast electro-optic inputs of the MZM (Covega Mach 10-060). In the offset frequency locking scheme, f_{beat} was kept at around 1 GHz to comply with the RF amplifier bandwidth (Minicircuits ZHL-2-8-S; 35 dB, 29 dBm, from 10 MHz to 1 GHz) and shifted down by mixing it with an LO between 500 and 800 MHz, in order to drive the MZM with a signal $(f_{\mathrm{beat}} - f_{\mathrm{LO}})$ in the working range of the 90° coupler. The out-of-loop (OOL) frequency and phase noise measurement setup for characterizing phase cloning performance under both coincidence and offset locking conditions will be discussed alongside the experimental results hereafter.

For measuring the phase noise in the coincidence locking regime, the master laser was frequency offset from the MZM output by 30 MHz using an acousto-optic modulator, and their beat note was acquired by a balanced detector (Thorlabs PDB 150 C, DC-150 MHz) to reject amplitude noise [Fig. 1(b)]. This was not possible in the offset locking scheme due to the higher beat-note frequency, so that a simple, yet noisier, homemade 1-GHz detector was used. The spectral analysis of the beat-note signal (Figs. 2 and 3) was performed by a low-noise spectrum analyzer (Rohde & Schwarz FSW-8) equipped with a phase noise measurement option.

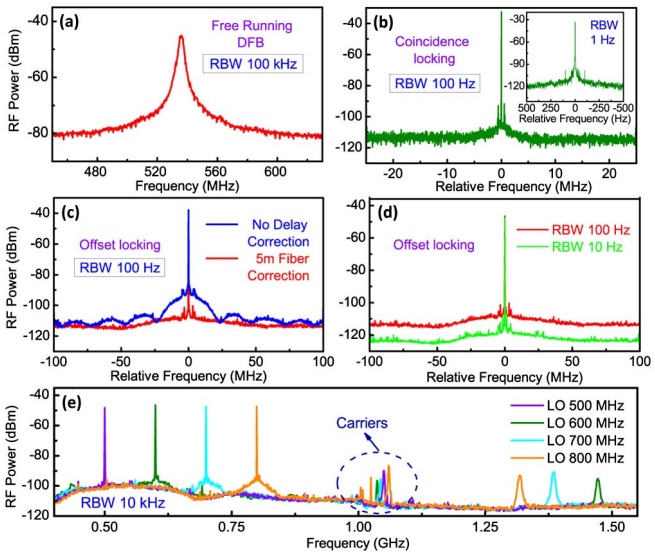

Fig. 2. Electrical spectrum of the beat notes between master and slave laser. (a) Free-running conditions. (b) Coincidence locking conditions. The beat-note linewidth collapses to an instrument-limited value of 1 Hz. (c) Offset locking conditions with (red) and without (blue) delay compensation in the slave propagation path. (d) Offset locking conditions with delay compensation. (e) Offset locking conditions: electrical spectra at different LO frequencies. RBW: spectrum analyzer resolution bandwidth.

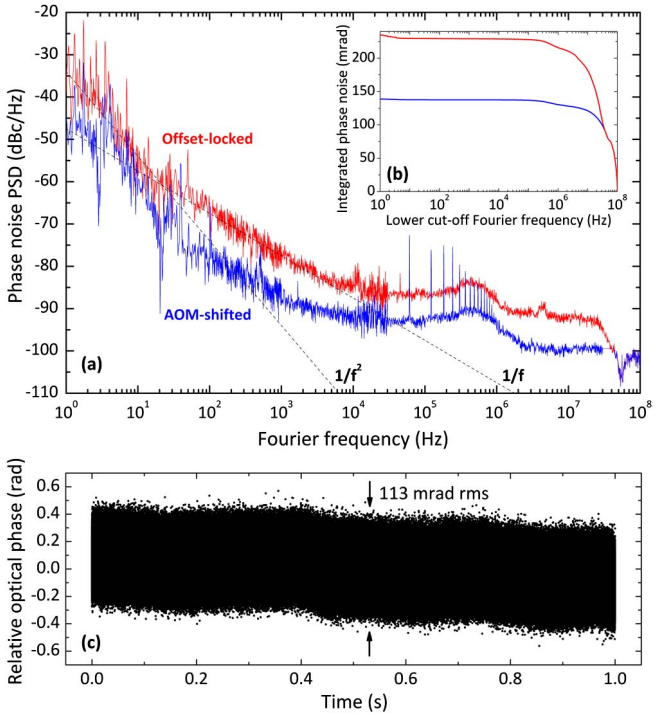

Fig. 3. Residual phase noise. (a) Single sideband phase noise in coincidence locking (blue) and offset locking (red) regimes, as acquired in an out-of-loop configuration. The curves are not corrected for detector and environment noise. (b) Rms phase noise integrated from a variable lower bound to 100 MHz. (c) Measured 1-s time series of the relative optical phase in coincidence locking conditions.

Figure 2(b) refers to the first case and shows the electrical spectrum of the beat signal between the MZM output and the 30-MHz acousto-optically-shifted replica of the master laser. With a resolution bandwidth (RBW) of 100 Hz, the carrier-to-background contrast attains a remarkable value of 80 dB, with no trace of servo bumps or bandwidth limitations over a span of 50 MHz. We deduce that 98.7% of the power was in the coherent carrier, which is consistent with a residual rms phase error as low as 114 mrad. At a 1-Hz RBW [inset of Fig. 2(b)], the carrier exhibits an instrument-limited linewidth with very weak low-frequency shoulders.

The blue trace in Fig. 2(c) shows over a wider frequency span of 200 MHz the beat-note spectrum acquired in offset-frequency locking conditions, with a free-running beating signal at around 1 GHz and an RF LO set at 550 MHz. Here, the spectrum is affected by an evident phase noise pedestal, and by the typical modulation that emerges in linewidth measurements when a short time delay is added between the branches of a self-homodyne Mach–Zehnder interferometer [19]. This lag originates from the phase delay introduced by the RF components and particularly from the pair of low-pass filters that have been introduced in the offset-frequency locking case to filter out the mirror frequency after the mixer. To first order, this delay can be compensated for by increasing the slave propagation path upstream the MZM. By adding a 5-m-long fiber patch, equivalent to about 25 ns, the electrical spectrum turns into the red trace reported in Fig. 2(c), which shows an efficient suppression of the noise pedestal around the carrier and to barely appreciable modulation signatures over a span of 200 MHz. Effective control bandwidths beyond this limit would be within reach by tighter control of time lags and the choice of dedicated RF components. Figure 2(d) shows that the carrier-to-background contrast inversely scales with RBW, as expected for a RBW-limited measurement.

To highlight the frequency tuning capability in the offset locking regime, Fig. 2(e) reports a wide view of the electrical spectrum of the beat note for different LO frequencies generated by an RF synthesizer. The LO frequency is the offset between MZM output and master source. This offset is independent of slave laser frequency within a capture range as large as 20 GHz, i.e., twice the bandwidth limit of our MZM device. Efficient line narrowing for the clone sideband is demonstrated, while carrier linewidth remains unaltered, and out-of-phase sideband linewidth doubles. These unwanted signals are suppressed by more than 30 and 35 dB, respectively.

Residual phase fluctuations were characterized in a bandwidth from 1 Hz to 100 MHz by processing the beating signal with the phase-noise analyzer. Figure 3 reports the single-sideband phase noise spectrum for both the coincidence locking (blue) and the offset locking (red) regimes. The two curves exhibit a similar behavior, with high noise suppression at frequencies higher than 10 Hz. Below this limit, they scale as $1/f^2$ random walk phase noise, partly due to out-of-loop fiber paths that were just thermally and mechanically isolated. The total integrated phase noise, from 1 Hz to 100 MHz (panel b), remains remarkably low, amounting to 139 mrad for coincidence locking.

This value was independently confirmed by the homodyne time-domain measurement of the relative optical phase without any acousto-optic frequency shift, which is reported in Fig. 3(c). This measurement indicates an rms phase noise of 113 mrad over 1 s and was obtained by superposing the unshifted MZM output with the master laser on the balanced detector [Fig. 1(b)]. The resulting homodyne interferometer signal was recorded at 200 Msample/s using a fast analog acquisition card (GAGE model CS1622). Voltage-to-phase conversion of the time series was then accomplished by converting the full-scale voltage swings to $\pm\pi/2$ phase excursions.

In the case of offset locking, a higher phase error of 235 mrad rms was found. This is related to the use of two low-pass filters and an additional amplifier with relatively poor noise figure, all of which exhibit nonflat amplitude and phase responses.

In order to test the viability of the approach for molecular spectroscopy at high spectral resolution and sensitivity, the MZM output was mode-matched to a high-finesse cavity [20] used as an optical scanning etalon [Fig. 1(b)]. The spectral width of cavity modes was about 950 Hz at 1610 nm, corresponding to a cavity finesse in excess of 4.5×10^5. A butterfly-packaged, polarization-maintaining booster optical amplifier (Covega BOA-1004) with 24-dB gain was inserted at the MZM output for achieving high scanned-cavity transmission signals on an InGaAs photodiode with 90 kΩ transimpedance gain. The cavity length was slowly modulated over the

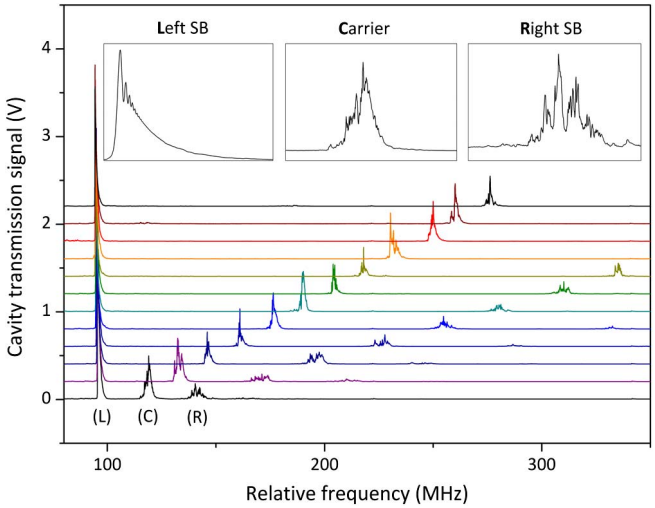

Fig. 4. Transmission of a scanning optical cavity (see Media 1 and Media 2 for the corresponding video). The vertically shifted traces correspond to different slave laser detunings. The carrier (C) and other sideband (R) were revealed by choosing suboptimal MZM working points. The feed-forward-corrected sideband (L) remains stable and narrow (see chirped oscillations in the upper left inset).

435-MHz cavity free spectral range by applying a triangular voltage to a piezoelectric actuator at rates ranging from 1 to 20 Hz. Periodic transmission transients at the cavity output were acquired, as those reported in Fig. 4.

For the noise-compensated sideband, strongly peaked, narrow, and stable transients are observed. Their position and height remains unaffected by slave laser frequency jumps within the capture range. They exhibit a typical chirped modulation structure that arises from the interference between the nearly monochromatic source and the intra-cavity radiation, which is Doppler-shifted by the moving cavity mirror [21]. In contrast, noisy transients are observed for the moving carrier and the complementary sideband, the latter moving twice as fast and being twice as broad because of the inverted-phase correction. The real-time tuning dynamics are illustrated by a short video provided as supplementary material.

To summarize, we have proposed and realized optical phase locking by MZM-based single-sideband modulation in a feed-forward configuration, and demonstrated coherence transfer from a highly stable sub-kHz reference laser to a noisy fiber-coupled DFB laser. An important advantage of the new method is that it can be generalized using an optical frequency comb, thereby allowing feed-forward phase cloning to slave lasers several hundreds of nanometers away [22]. Furthermore it requires only a few electronic and optic components that could be integrated on a chip, or at least packaged on a single device. This would reduce dimensions and bandwidth-limiting time lags to a minimal level, thereby increasing the overall performance while cutting costs and facilitating its use for the experimentalist. On the other hand, to extend the approach beyond the telecom range, a technological effort would be required for the design of dedicated modulators.

We acknowledge support from the Italian Ministry of Research and Education (ELI project—ESFRI Roadmap); LabexOSUG@2020 (ANR10 LABX56); Université Joseph Fourier (UJF) Pôle SMINGUE; Réseau FEMTO.

References

1. C. G. Parthey, A. Matveev, J. Alnis, B. Bernhardt, A. Beyer, R. Holzwarth, A. Maistrou, R. Pohl, K. Predehl, T. Udem, T. Wilken, N. Kolachevsky, M. Abgrall, D. Rovera, C. Salomon, P. Laurent, and T. W. Hänsch, Phys. Rev. Lett. **107**, 203001 (2011).
2. A. D. Ludlow, X. Huang, M. Notcutt, T. Zanon-Willette, S. M. Foreman, M. M. Boyd, S. Blatt, and J. Ye, Opt. Lett. **32**, 641 (2007).
3. C. W. Chou, D. B. Hume, J. C. J. Koelemeij, D. J. Wineland, and T. Rosenband, Phys. Rev. Lett. **104**, 070802 (2010).
4. B. Bloom, T. Nicholson, J. Williams, S. Campbell, M. Bishof, X. Zhang, W. Zhang, S. Bromley, and J. Ye, Nature **506**, 71 (2014).
5. G. M. Harry, H. Armandula, E. Black, D. R. M. Crooks, G. Cagnoli, J. Hough, P. Murray, S. Reid, S. Rowan, P. Sneddon, M. M. Fejer, R. Route, and S. D. Penn, Appl. Opt. **45**, 1569 (2006).
6. I. Coddington, W. C. Swann, L. Lorini, J. C. Bergquist, Y. Le Coq, C. W. Oates, Q. Quraishi, K. S. Feder, J. W. Nicholson, P. S. Westbrook, S. A. Diddams, and N. R. Newbury, Nat. Photonics **1**, 283 (2007).
7. K. Predehl, G. Grosche, S. M. F. Raupach, S. Droste, O. Terra, J. Alnis, T. Legero, T. W. Hänsch, T. Udem, R. Holzwarth, and H. Schnatz, Science **336**, 441 (2012).
8. T. Kessler, C. Hagemann, C. Grebing, T. Legero, U. Sterr, F. Riehle, M. Martin, L. Chen, and J. Ye, Nat. Photonics **6**, 687 (2012).
9. A. Ruehl, M. J. Martin, K. C. Cossel, L. Chen, H. McKay, B. Thomas, C. Benko, L. Dong, J. M. Dudley, M. E. Fermann, I. Hartl, and J. Ye, Phys. Rev. A **84**, 011806 (2011).
10. T. Sala, D. Gatti, A. Gambetta, N. Coluccelli, G. Galzerano, P. Laporta, and M. Marangoni, Opt. Lett. **37**, 2592 (2012).
11. S. Koke, C. Grebing, H. Frei, A. Anderson, A. Assion, and G. Steinmeyer, Nat. Photonics **4**, 462 (2010).
12. U. Gliese, T. Nielsen, M. Bruun, E. Lintz Christensen, K. Stubkjaer, S. Lindgren, and B. Broberg, IEEE Photon. Technol. Lett. **4**, 936 (1992).
13. S. Ristic, A. Bhardwaj, M. J. Rodwell, L. A. Coldren, and L. A. Johansson, J. Lightw. Technol. **28**, 526 (2010).
14. M. Lu, H. Park, E. Bloch, A. Sivananthan, A. Bhardwaj, Z. Griffith, L. A. Johansson, M. J. Rodwell, and L. A. Coldren, Opt. Express **20**, 9736 (2012).
15. R. A. Griffin and K. Katayama, Electron. Lett. **34**, 795 (1998).
16. M. Izutsu, S. Shikama, and T. Sueta, IEEE J. Quantum Electron. **17**, 2225 (1981).
17. T. Kawanishi, T. Sakamoto, T. Miyazaki, M. Izutsu, T. Fujita, S. Mori, K. Higuma, and J. Ichikawa, Opt. Express **14**, 4469 (2006).
18. J. Burkart, D. Romanini, and S. Kassi, Opt. Lett. **38**, 2062 (2013).
19. H. Ludvigsen, M. Tossavainen, and M. Kaivola, Opt. Commun. **155**, 180 (1998).
20. J. Burkart, D. Romanini, and S. Kassi, Opt. Lett. **39**, 4695 (2014).
21. J. Morville, D. Romanini, M. Chenevier, and A. Kachanov, Appl. Opt. **41**, 6980 (2002).
22. T. Sala, S. Kassi, J. Burkart, M. Marangoni, and D. Romanini, "Comb-assisted coherence transfer between laser fields," arXiv: 1412.1102 (2014).

4.3 Theoretical analysis of single-sideband-based phase cloning and offset locking

Supplementing the experimental demonstration in Article 2, a theoretical analysis of feed-forward phase coherence transfer and offset locking is provided in the following. It has been published as supplementary material to Article 2 [156].

To begin with, the beat note error signal for feed-forward single-sideband phase cloning of the reference laser field on the slave laser is formulated explicitly. Then, analytic expressions are provided for the electric fields inside the Mach-Zehnder modulator when this feed-forward correction is applied, demonstrating how single-sideband modulation arises with a full compensation of slave laser frequency offset and phase noise.

Subsequently, the extension of this scheme to frequency offset locking by mixing the correction signal beat note with a radio-frequency local oscillator (LO) is discussed. An overview of the necessary filtering of the mixer output, the appropriate sideband for noise suppression, as well as the direction of offset-tuning is provided as a function of sign and magnitude of the frequency offset between master and slave laser as well as LO frequency. A particular emphasis is given to the fact that this scheme provides direct control of both frequency and phase offset of the slave with respect to the master. This may be a crucial feature for light-matter interaction applications with several coherent light fields.

Finally, going beyond the idealization of immediate electric and optical signal propagation, an analyis of the impact of correction delays on phase noise suppression is made. In particular, the residual phase noise PSD of the feed-forward corrected slave laser is derived as a function of Fourier frequency and the correction delay, providing a simple expression for the correction bandwidth of the system. The study is closed by a discussion on the impact of phase noise contributions from unstabilized fiber paths in the optical setup and perspectives for monolithic integration of the phase cloner setup.

Optical phase cloning by an integrated dual-parallel Mach-Zehnder modulator: supplementary material

JOHANNES BURKART[1,2], TOMMASO SALA[3], SAMIR KASSI[1,2], DANIELE ROMANINI[1,2], AND MARCO MARANGONI[3,*]

[1]*Univ. Grenoble Alpes, LIPhy, F-38000 Grenoble, France*
[2]*CNRS, LIPhy, F-38000 Grenoble, France*
[3]*Physics Department of Politecnico di Milano and IFN-CNR, Piazza Leonardo da Vinci 32, 20133 Milano, Italy*
[*]*marco.marangoni@polimi.it*

Compiled September 3, 2014

This document provides supplementary information to "Optical phase cloning by an integrated dual-parallel Mach-Zehnder modulator," Optica *volume?*, first page? (2014). In the first part, we present a detailed theoretical analysis of optical phase cloning and offset-locking using a Mach-Zehnder modulator in a feed-forward configuration. In the second part, we briefly describe the supplementary video showing real-time experimental data on the transmission of a feed-forward-stabilized laser through a scanning high-finesse cavity.

OCIS codes: *(140.3425) Laser stabilization; (120.3930) Metrological instrumentation; (250.7360) Waveguide modulators.*

http://dx.doi.org/10.1364/optica.XX.XXXXXX

1. THEORETICAL ANALYSIS

The coherence of a reference laser field

$$E_{ref}(t) = E_{0r}\cos(\omega_0 t) \tag{1}$$

with amplitude E_{0r} and angular frequency ω_0, idealized here as perfectly monochromatic for the sake of simplicity, is to be transferred to a slave laser field

$$E_{in}(t) = E_0\cos[(\omega_0+\Delta\omega)t+\varphi(t)] \tag{2}$$

exhibiting phase noise $\varphi(t)$ and an angular frequency offset $\Delta\omega$, which is assumed to be positive without loss of generality. To clone the reference laser coherence on the slave laser, this phase noise has to be suppressed and the frequency offset corrected.
In feed-forward schemes [1, 2], this is accomplished by compensating the slave laser phase and frequency errors *a posteriori*, by first measuring and then correcting them. As the first step, the error may be measured as the beat note signal $S_{AC}(t)$ of the two laser fields on a photodiode

$$S_{AC}(t) = s_0\left\langle|E_{in}+E_{ref}|^2\right\rangle = s_0E_0E_{0r}\cos[\Delta\omega t+\varphi(t)] \tag{3}$$

$$s_0 = \eta c\epsilon_0 R A_{eff} \tag{4}$$

where η is the photodiode responsivity, c the speed of light, ϵ_0 the electric constant, R the transimpedance gain, and A_{eff} the effective detection surface. The angle brackets in (3) denote a time average over the photodiode response time. The time-independent photodiode signal component S_{DC} is discarded either by a high-pass filter or by an AC-coupled radio frequency (RF) amplifier.
In the second step, this amplifier with gain G supplies a sufficiently strong signal $V_{RF}(t)$ to drive the device actively correcting slave laser frequency and phase.

$$V_{RF}(t) = \sqrt{G}\cdot S_{AC}(t) \tag{5}$$

Here, we propose using a dual-parallel electro-optic Mach-Zehnder modulator (MZM) as a single-sideband generator to achieve this correction with unprecedented bandwidth. The nested interferometer lithium niobate ($LiNbO_3$) waveguide structure of the MZM is depicted in Fig. S1.

Three DC voltages are applied to set the working point of the Mach-Zehnder interferometers (MZIs) for single-sideband operation. The voltages V_1 and V_2 applied to the two child MZIs correspond to a static phase shift of π between their interferometer arms. This leads to optical carrier suppression by destructive interference. The third voltage V_3 corresponds to a static

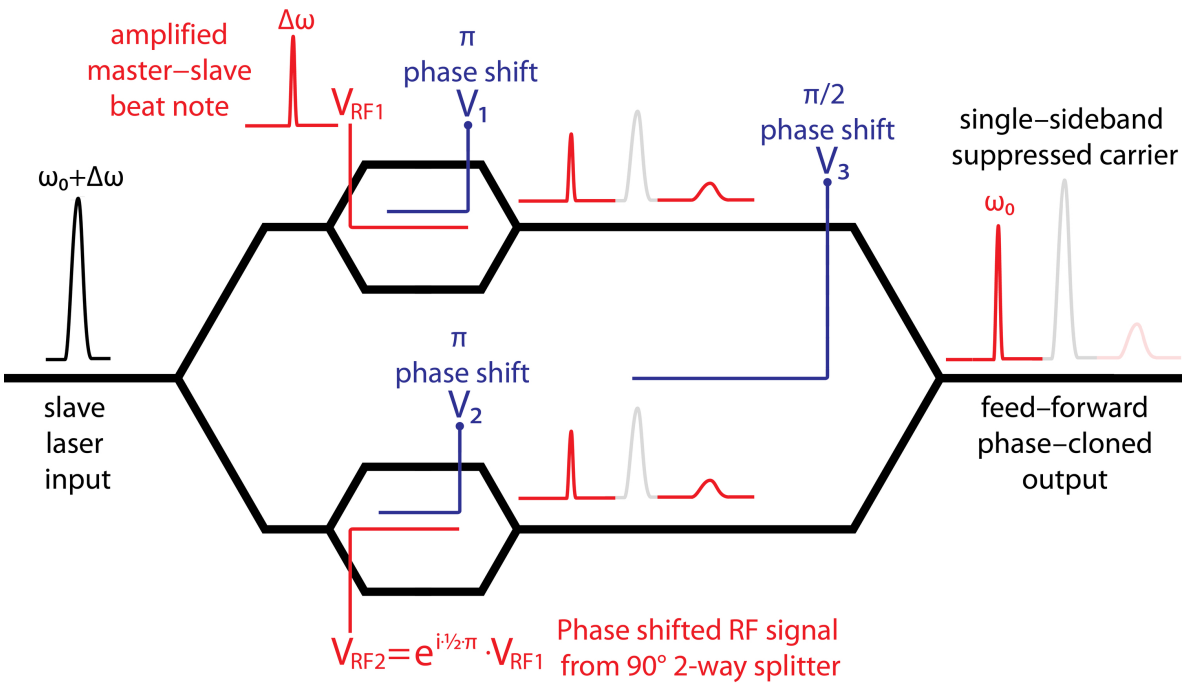

Fig. S1. Schematic sketch of feed-forward phase cloning using an MZM with nested Mach-Zehnder interferometer waveguide (black), RF electrodes (red) and DC electrodes (blue). The coherence of the master laser is transferred to the feed-forward-corrected single sideband (red), whereas the suppressed sideband is broadened (pale red) due to inverted-phase correction. The slave laser carrier (pale gray) is suppressed in the two child interferometers.

$\pi/2$ phase shift between the arms of the parent interferometer, which is the working point for interferometric single-sideband generation.

The amplified beat note signal $V_{RF}(t)$ is fed to a two-way 90° hybrid power splitter. Its two quadrature RF output signals are used for driving the travelling wave RF electrodes in the two child MZIs, leading to phase modulations $\varphi_1(t)$ and $\varphi_2(t)$ by the electro-optic Pockels effect:

$$\varphi_1(t) = \hat{\varphi}\cos\left[\Delta\omega t + \varphi(t)\right] \quad (6)$$

$$\varphi_2(t) = \hat{\varphi}\cos\left[\Delta\omega t + \varphi(t) + \frac{\pi}{2}\right] \quad (7)$$

$$\hat{\varphi} = \pi\cdot\frac{\sqrt{G s_0 E_0 E_{0r}}}{\sqrt{2}V_\pi} \quad (8)$$

V_π is the electro-optic half-wave voltage corresponding to a Pockels phase shift of π.

The timing of this active *a posteriori* phase noise compensation is an important issue. After beat note detection, the slave laser field takes a propagation time τ_2 to arrive at the MZM. The RF correction, in turn, is delayed by τ_1 due to propagation, amplification and the MZM response time. Consequently, the transformations $E(t) \to E(t-\tau_2)$ and $\varphi_{1/2}(t) \to \varphi_{1/2}(t-\tau_1)$ must be made. At the MZM input, the combination of both effects leads to an effective correction delay of $\tau = \tau_1 - \tau_2$.

Then, taking into account the static MZI phase shift of π typically realized in a push-pull configuration ($\pi = \frac{\pi}{2} - \left(-\frac{\pi}{2}\right)$), the superposition of waves at the output of child interferometer 1 yields

$$E_1(t) = \frac{E_0}{2}\Bigg(\cos\left\{(\omega_0+\Delta\omega)t + \varphi(t) + \frac{\pi}{2} + \hat{\varphi}\cos\left[\Delta\omega(t-\tau)+\varphi(t-\tau)\right]\right\} + \cos\left\{(\omega_0+\Delta\omega)t + \varphi(t) - \frac{\pi}{2} - \hat{\varphi}\cos\left[\Delta\omega(t-\tau)+\varphi(t-\tau)\right]\right\}\Bigg) \quad (9)$$

Using addition theorems, two terms of opposite sign cancel out, leaving

$$E_1(t) = -E_0\cos\left[(\omega_0+\Delta\omega)t + \varphi(t)\right] \times \sin\left\{\hat{\varphi}\cos\left[\Delta\omega(t-\tau)+\varphi(t-\tau)\right]\right\} \quad (10)$$

Expressing the nested trigonometric function in terms of its expansion in first-type Bessel functions J_k

$$\sin(z\cos\theta) = 2\sum_{k=0}^{\infty}(-1)^k J_{2k+1}(z)\cos\left[(2k+1)\theta\right] \quad (11)$$

one may drop $\mathcal{O}(\hat{\varphi}^3)$ terms, which can be made arbitrarily small for small modulation depths $\hat{\varphi}$, in a trade-off between output power and spectral purity. This yields

$$E_1(t) = -2J_1(\hat{\varphi})E_0 \cos\left[(\omega_0+\Delta\omega)t+\varphi(t)\right] \times \cos\left[\Delta\omega(t-\tau)+\varphi(t-\tau)\right] \quad (12)$$

$$= -J_1(\hat{\varphi})E_0\Big\{\cos\left[\omega_0 t+\varphi(t)-\varphi(t-\tau)+\Delta\omega\tau\right] + \cos\left[(\omega_0+2\Delta\omega)t+\varphi(t)+\varphi(t-\tau)-\Delta\omega\tau\right]\Big\} \quad (13)$$

Let us note that even-order sidebands are suppressed by destructive interference in the two child MZIs, just as the carrier. Analogously, one finds for the output of child interferometer 2

$$E_2(t) = J_1(\hat{\varphi})E_0\Big\{\sin\left[(\omega_0+2\Delta\omega)t+\varphi(t)+\varphi(t-\tau)-\Delta\omega\tau\right] - \sin\left[\omega_0 t+\varphi(t)-\varphi(t-\tau)+\Delta\omega\tau\right]\Big\} \quad (14)$$

The MZM output is found by adding $E_1(t)$ and $E_2(t)$, taking into account the static parent MZI phase shift of $\pm\pi/2 = \pm[\pi/4-(-\pi/4)]$:

$$\begin{aligned}E_{out\pm} = J_1(\hat{\varphi})E_0\times &\Big\{-\cos\left[\omega_0 t+\varphi(t)-\varphi(t-\tau)+\Delta\omega\tau\pm\frac{\pi}{4}\right]\\ &-\cos\left[(\omega_0+2\Delta\omega)t+\varphi(t)+\varphi(t-\tau)-\Delta\omega\tau\pm\frac{\pi}{4}\right]\\ &+\sin\left[(\omega_0+2\Delta\omega)t+\varphi(t)+\varphi(t-\tau)-\Delta\omega\tau\mp\frac{\pi}{4}\right]\\ &-\sin\left[\omega_0 t+\varphi(t)-\varphi(t-\tau)+\Delta\omega\tau\mp\frac{\pi}{4}\right]\Big\} \quad (15)\end{aligned}$$

Consequently applying addition theorems, the single-sideband suppressed-carrier MZM output is retrieved for left (-) and right (+) sideband:

$$E_{out+} = 2J_1(\hat{\varphi})E_0\times \cos\left[(\omega_0+2\Delta\omega)t+\varphi(t)+\varphi(t-\tau)-\Delta\omega\tau-\frac{3\pi}{4}\right] \quad (16)$$

$$E_{out-} = 2J_1(\hat{\varphi})E_0\cos\left[\omega_0 t+\varphi(t)-\varphi(t-\tau)+\Delta\omega\tau+\frac{3\pi}{4}\right] \quad (17)$$

The twofold amplitude as compared to plain phase modulation at equal modulation depth $\hat{\varphi}$ is due to constructive interference. In the idealized case $\tau = 0$ of zero correction delay, the left sideband

$$E_{out-} = 2J_1(\hat{\varphi})E_0\cos\left(\omega_0 t+\frac{3\pi}{4}\right) \quad (18)$$

completely compensates for slave laser frequency offset and phase noise and thus accomplishes reference phase coherence cloning on the slave laser field. Conversely, the out-of-phase correction on the right sideband E_{out+} in equation (16) leads to doubled frequency offset and phase noise. If $\Delta\omega$ is negative, the roles of left and right sidebands are inversed. Spurious signals from the imperfectly suppressed carrier and unwanted first-order sideband, as well as from resonant higher order sidebands are typically on the order of -30 dB [3].

This phase cloning can be generalized to coherent frequency- and phase-offset locking by mixing the original beat note signal (3) with a monochromatic RF signal and subsequent low- or high-pass filtering. With the RF local oscillator (LO) signal proportional to $\cos(\omega_{LO}t+\varphi_{LO})$, the feed-forward corrected output field acquires an angular frequency offset $\pm\omega_{LO}$ and a phase offset $\pm\varphi_{LO}$, while remaining phase locked to the reference. When $\Delta\omega<0$ or $\omega_{LO}>|\Delta\omega|$, the phase correction term $\varphi(t-\tau)$ (as in equations (6) and (7), for instance) changes sign. This inverts the direction of frequency and phase tuning, and switches the feed-forward-corrected sideband from left to right or vice-versa, depending on whether low- or high-pass filtering is used. An overview of the tuning behavior under offset-locking conditions, obtained from derivations analogous to the one detailed above, is given in Table S1.

Table S1. Tuning behavior for feed-forward offset locking when either low- or high-pass filtering is applied to the beat-note-and-LO-mixing signal. Letters: increasing LO frequency yields increasing ('**P**ositive') or decreasing ('**N**egative') optical frequency. Signs: left ('-') or right ('+') sideband accomplish feed-forward coherence transfer.

	Low-pass filtering		High-pass filtering	
	$\Delta\omega<0$	$\Delta\omega>0$	$\Delta\omega<0$	$\Delta\omega>0$
$\omega_{LO}<\lvert\Delta\omega\rvert$	N +	P -	P +	N -
$\omega_{LO}>\lvert\Delta\omega\rvert$	N -	P +	P +	N -

To give one concrete example, for $\Delta\omega<0$, $\omega_{LO}>|\Delta\omega|$, and high-pass filtering, the equivalent of equation (17) reads

$$E_{out+} = 2J_1E_0\cos\Big[(\omega_0+\omega_{LO})t+\varphi_{LO} + \varphi(t)-\varphi(t-\tau)+\Delta\omega\tau-\frac{3\pi}{4}\Big] \quad (19)$$

Thus enabling complete and automatable frequency and phase offset control, the method is well suited to a multitude of light-matter-interaction applications necessitating highly coherent laser fields.

In the following, let us consider the impact of non-negligible correction delay τ. For feed-forward frequency locking using an acousto-optic modulator, a similar analysis has been undertaken in [4]. The residual phase noise $\Delta\varphi(t)$ on the feed-forward-corrected sideband (17) is

$$\Delta\varphi(t) = \varphi(t)-\varphi(t-\tau) \quad (20)$$

To determine its power spectral density (PSD) $S_{\Delta\varphi}$, one may use the Wiener-Khinchin theorem linking it to the phase noise autocorrelation function $R_{\Delta\varphi}$:

$$S_{\Delta\varphi}(f) = \int_{-\infty}^{\infty} R_{\Delta\varphi}(t')\mathrm{e}^{-i2\pi ft'}\,\mathrm{d}t' \quad (21)$$

where f denotes the Fourier frequency of spectral components. Assuming that $\Delta\varphi(t)$ is an ergodic noise process, its autocorrelation may be written as

$$R_{\Delta\varphi}(t') = \langle\Delta\varphi(t)\Delta\varphi(t+t')\rangle_t \quad (22)$$

$$= \langle\varphi(t)\varphi(t+t')\rangle_t - \langle\varphi(t)\varphi(t+t'-\tau)\rangle_t - \langle\varphi(t+t')\varphi(t-\tau)\rangle_t + \langle\varphi(t-\tau)\varphi(t-\tau+t')\rangle_t \quad (23)$$

$$= 2R_\varphi(t') - R_\varphi(t'-\tau) - R_\varphi(t'+\tau) \quad (24)$$

The angle brackets with subscript t denote an average over time. Its translational symmetry has been exploited in the last step. Inserting the autocorrelation function (24) in (21) yields the phase noise PSD of the feed-forward-corrected signal at MZM output:

$$S_{\Delta\varphi}(f) = 2S_\varphi(f) - \mathrm{e}^{-i2\pi f\tau}S_\varphi(f) - \mathrm{e}^{i2\pi f\tau}S_\varphi(f) \quad \textbf{(25)}$$

$$= 2S_\varphi(f)\left[1-\cos\left(2\pi f\tau\right)\right] \quad \textbf{(26)}$$

$$= (2\pi f\tau)^2 S_\varphi(f) + \mathcal{O}\left((f\tau)^4\right) \quad \textbf{(27)}$$

The Fourier frequency f_{BW} for which the noise prefactor reaches unity is a useful measure for the correction bandwidth of the feed-forward system [4]:

$$f_{BW} = \frac{1}{2\pi\tau} \quad \textbf{(28)}$$

This inverse proportionality to the delay time unbalance τ illustrates the need for a well-balanced, low-delay system architecture for achieving efficient noise suppression at high Fourier frequencies. With electro-optic bandwidths well in excess of 10 GHz, MZMs are thus well suited for feed-forward phase cloning.

So far, phase noise due to the unstabilized fiber paths in the setup has been neglected in the analysis by assuming a constant delay time τ for the sake of simplicity. To take thermomechanical fiber noise into account, different delay times τ_1 and τ_2 need to be considered in the signal and correction branch, respectively. To a very good approximation, this can be described by an additional term $\varphi_{fiber}(t)$ in the argument of equation (2). Then, the phase noise power spectral density of the feed-forward-corrected output reads:

$$S_{\Delta\varphi}(f) = 2S_\varphi(f)\left[1-\cos\left(2\pi f\tau\right)\right] + S_{\varphi_{fiber}}(f) \quad \textbf{(29)}$$

For optimal phase cloning, as for any fibered frequency metrology application, it is therefore vital to keep all fiber paths as short and free from external perturbations as possible.
In a bench-top setup, this may be reached by actively stabilizing fiber paths using low-frequency servo loops. Another very promising way to accomplish this is monolithically implementing the whole MZM-based feed-forward phase cloning apparatus. All components – the optical splitters, the fibered photodiode, the MZM waveguide, the RF amplifier, as well as an RF mixer with an appropriate filter – could be integrated in a single package with cm dimensions, necessitating only an external power supply and RF source, as well as passive or active cooling.

2. VIDEO: SCANNING CAVITY TRANSMISSION

The video first gives a brief overview of the method and the experimental setup. Then, it shows experimental data on the transmission of a scanning high-finesse cavity in real time.
This transmission signal allows monitoring the MZM output in the frequency domain, as the length-scan driving voltage may be converted into optical frequency modulo one FSR by interpolating between two successive cavity modes. This provides a highly aliased, but nearly linear frequency scale (x axis) for optical spectral analysis. Cavity transmission (y axis) is proportional to optical power when laser linewidth is smaller than cavity modewidth. When linewidth increases beyond modewidth, transmission drops off rapidly as jitter inhibits coherent intensity buildup inside the cavity.

For this experimental demonstration, the MZM output was injected into a high-finesse cavity whose length was linearly modulated over more than one free spectral range at a rate of 5 Hz. To reveal the carrier and the inverted-phase sideband, the optimal MZM working points for single-sideband generation were intentionally left. Subsequently, frequency jumps of the carrier were abruptly triggered by manually changing the setpoint of the slave laser temperature stabilization.
Analogous to Fig. 4 and the corresponding discussion, the video illustrates how the phase-cloned sideband remains completely unperturbed while the broadened inverted-phase sideband moves at twice the pace of the noisy carrier.

REFERENCES

1. T. Sala, D. Gatti, A. Gambetta, N. Coluccelli, G. Galzerano, P. Laporta, and M. Marangoni, "Wide-bandwidth phase lock between a CW laser and a frequency comb based on a feed-forward configuration," Opt. Lett. **37**, 2592–2594 (2012).
2. S. Koke, C. Grebing, H. Frei, A. Anderson, A. Assion, and G. Steinmeyer, "Direct frequency comb synthesis with arbitrary offset and shot-noise-limited phase noise," Nature Photon. **4**, 462–465 (2010).
3. J. Burkart, D. Romanini, and S. Kassi, "Optical feedback stabilized laser tuned by single-sideband modulation," Opt. Lett. **38**, 2062–2064 (2013).
4. D. Gatti, T. Sala, A. Gambetta, N. Coluccelli, G. N. Conti, G. Galzerano, P. Laporta, and M. Marangoni, "Analysis of the feed-forward method for the referencing of a CW laser to a frequency comb," Opt. Express **20**, 24880–24885 (2012).

4.4 Article 3 - Feed-forward comb-assisted laser coherence transfer

The following manuscript reports proof-of-principle experiments on MZM-based feed-forward coherence transfer between lasers over vast spectral intervals, using an optical frequency comb as a transfer oscillator. This approach leads to the reproduction of the master laser comb offset on the slave laser, yet with respect to another tooth of the comb, which can be spaced tens or hundreds of nanometers afar. Importantly, the coherence transfer is not affected by common-mode noise of the frequency comb and does not necessitate $f - 2f$ self-referencing. A preliminary version of the manuscript is available online [157].

The article starts by introducing the generalization of the feed-forward stabilization scheme using two teeth of a frequency comb, as well as detailed aspects of its experimental implementation. Then, an experimental test of this scheme with a MHz-linewidth distributed feedback (DFB) slave laser spaced only a few comb modes apart from the sub-kHz master laser is reported, allowing a rigorous characterization of the coherence transfer through the comb. An RF power spectrum analysis of the beat note between master and feed-forward-corrected slave indicates sub-radian coherence transfer, limited by suboptimal characteristics of the components and the frequency comb used in the experiment. The locked slave laser light was subsequently injected into a high-finesse cavity acting as an optical spectrum analyser. The presence of coherent ringing signals in cavity transmission [130] independently confirmed the sub-kHz linewidth of the feed-forward corrected MZM output signal. Finally, the same experiment was repeated with a slave DFB laser almost 100 nm away from the master. The cavity transmission of the feed-forward-locked slave laser showed no appreciable degradation of the ringing transients, thus indicating an unspoiled coherence transfer, illustrating the enormous potential of the technique for applications in broadband, sub-kHz-resolution cavity-enhanced spectroscopy.

Applied Physics B manuscript No.
(will be inserted by the editor)

Feed–forward comb–assisted laser coherence transfer

Tommaso Sala[1], Samir Kassi[2,3], Johannes Burkart[2,3], Marco Marangoni[1], Daniele Romanini[2,3]

1) Physics Department of Politecnico di Milano and IFN-CNR, Piazza Leonardo da Vinci 32, 20133 Milano, Italy
2) Univ. Grenoble Alpes, LIPhy, F-38000 Grenoble, France
3) CNRS, LIPhy, F-38000 Grenoble, France
Corresponding author: daniel.romanini@ujf-grenoble.fr

Received: 1 July 2015 / Revised version: date

Abstract Transferring the coherence of a highly stable narrow–linewidth master laser to a widely tunable slave laser whose emission frequency may lie several THz away is an attracting perspective for precision and high–sensitivity spectroscopy. Here this transfer is accomplished through a particularly simple feed–forward locking scheme that makes use of a frequency comb as a transfer oscillator and of a dual–parallel Mach–Zehnder modulator as an extremely fast phase/frequency actuator. As a proof of principle, cavity ring–down transient decays obtained at 1617 nm out of an optical cavity with a finesse of 450 000 reveal no appreciable coherence loss with respect to those obtained directly from the master laser at 1521 nm, i.e. 12 THz away.

Highly coherent lasers with linewidth ranging from 1 kHz down to 1 Hz are exploited in several laboratories for high precision spectroscopy[1–3] and are now commercially available. Their stable and narrowband emission not only favors high spectral resolution and accuracy[4,5], but also leads to enhanced detection sensitivity in combination with optical cavities[3] down to $5 \times 10^{-13}/\mathrm{cm}/\sqrt{\mathrm{Hz}}$ for finesses in excess of 10^5[6]. However, the extensive application of such laser sources in gas phase spectroscopy is hampered by their limited frequency tunability.

In order to cover spectral gaps as large as several THz away from a high–coherence reference laser one may introduce a second broadly tunable source, such as a distributed feed-back (DFB) diode laser, and lock its phase to the highly coherent master laser through the interposition of a frequency comb[7]. This coherence transfer scheme, which relies on the possibility to generate a highly–coherent broadly–tunable source from a mode–locked laser[8,9], requires the development of several high–bandwidth feedback loops, typically one for the phase lock of the comb repetition frequency to the master laser[10,11], a second for locking the comb carrier envelope offset frequency to a stable radio-frequency (RF) synthesizer[12,13], a third to lock the probe slave laser to the comb. Each of these may actually involve two loops, one for slower and wider frequency corrections, the other for the faster corrections[14]. Less efforts are required with referencing schemes as that proposed by Telle and co-workers[15,16], where the carrier-envelope offset frequency fluctuations are electronically removed from the beat notes of the comb with the two lasers and these notes are subtracted from each other after proper frequency scaling. This reduces the amount of electronic circuitry, yet requires the availability of a direct digital synthesizer for the frequency scaling of the two notes. This scaling is necessary to get rid of the comb noise that is not common mode at the two frequencies (i.e. the differential phase noise between the two comb modes).

An even simpler coherence transfer scheme would be of broad interest in several precision spectroscopy experiments that do not require extremely low residual phase error but rather a widely tunable yet stable and narrow (kHz) source with a sufficient power fraction in the coherent carrier. After an initial investigation on a feed–forward transfer scheme based on an acousto–optic frequency actuator[17,18], we have recently demonstrated a powerful approach based on a dual–parallel Mach–Zehnder modulator (MZM) operated as a single sideband generator: thanks to its extremely fast response time, equivalent control bandwidths in the hundreds of MHz range are easily achieved, together with a GHz-level capture and tuning range[19].

We explore here the extension of that scheme to a multi-THz spectral gap between master and slave laser through interposition of a free-running frequency comb. Similarly to the Telle approach, but without frequency scaling and removal of the carrier–envelope offset frequency, the beat notes of slave and master lasers are simply electronically subtracted and applied to the MZM after amplification, which makes the slave laser frequency to reproduce that of the master field. This occurs with a phase error that remains ultimately limited by the comb noise that is not of common mode at the two fre-

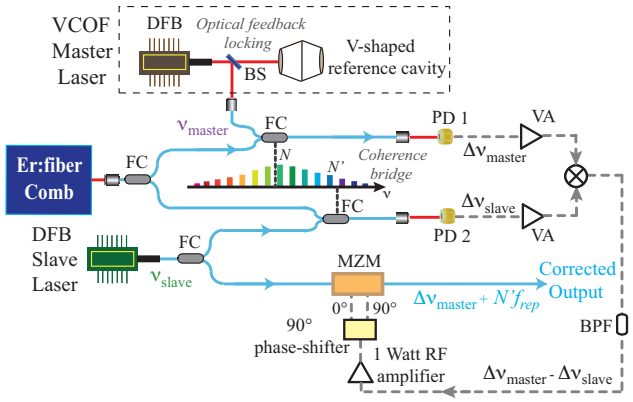

Fig. 1 Experimental scheme. VCOF is the sub-kHz linewidth master laser, DFB the slave distributed–feedback diode laser, OFC the self-referenced optical frequency comb, MZM the Mach-Zehnder electro–optic single–sideband modulator, PD1 and PD2 are photodiodes collecting the beat notes of both lasers with the OFC, filtered by diffraction gratings (DG). FC are single mode fiber combiners/splitters, VA are RF voltage amplifiers, BPF is a bandpass RF filter.

quencies. We applied this scheme to a slave laser wavelength (1521 nm) 12 THz away from that of the master (1617 nm), successfully reproducing the ring-down transients as clean as those observed with a slave close to the master wavelength, using of an optical cavity with a finesse as high as 450 000. This proof of principle demonstrates that cavity ring–down spectroscopy can be readily performed using the proposed scheme with no penalty for spectral resolution which is limited by the kHz width of the cavity modes.

The operation principle starts with the acquisition of the beat notes of slave and master laser with the frequency comb. Let us assume selecting with suitable RF band–pass filters the beat notes with the closest lower–frequency comb modes: $\Delta\nu_m = \nu_m - (f_0 + N f_{rep})$ for the master laser and $\Delta\nu_s = [\nu_s - (f_0 + N' f_{rep})]$ for the noisy slave laser, where f_0 and f_{rep} are the comb offset and repetition frequencies, respectively. An RF mixer provides their difference, $\Delta\nu_m - \Delta\nu_s = \nu_m - \nu_s + (N' - N) f_{rep}$, which is amplified and applied to the MZM, injected by a fraction of the slave laser radiation. In this way, after adjusting the MZM control bias voltages to produce only the upper sideband, the RF signal driving this sideband will subtract the slave laser frequency fluctuations relative to the comb modes and, at the same time, the common–mode comb frequency fluctuations on f_0. In equations, the MZM output is at frequency $\nu_c = \nu_s + [\nu_m - \nu_s + (N' - N) f_{rep}] = \Delta\nu_m + f_0 + N' f_{rep}$, thus being at the same comb offset as the master laser but relative to the comb mode N'. As the separation of slave from master is increased, the comb frequency fluctuations that are not common–mode at the two laser frequencies are expected to increase and to become a limiting factor for the coherence transfer. This effect is small and goes undetected in our proof-of-principle demonstration involving injection of a (very) high finesse CRDS cavity over a comb–wide frequency range. Also, as with active servo loops, the bandwidth of this feed–forward (FF) control is inversely proportional to time delays accumulated by both electrical and optical signals. However, the latter may be used to compensate the former provided a fiber patch of suitable length is added to the slave propagation path upstream the MZM correction unit[19]: To the first order this may lead to a zero net delay. The bandpass is then limited by photodetectors and RF components used to drive the MZM, and by the comb mode spacing.

Fig.1 illustrates our experimental implementation. Besides the V-cavity optical-feedback (VCOF) master source detailed elsewhere[20] and a standard fibered telecom DFB diode laser, a 100 MHz free-running Erbium fiber comb (Toptica FFS model) is used, with mode linewidth of about 10 kHz over 1 ms. A S/N of better than 25 dB could be obtained for the beat signals of both CW lasers, still modest relative to that obtained in [19] and likely a limiting factor here. The $\Delta\nu_s$ beat is kept below the 30 MHz cut-off frequency of a lowpass filter during several minutes thanks to the good stability of current and temperature controllers of the slave laser, whereas $\Delta\nu_m$ could remain for even longer times at around 70 MHz, at the center of a narrow bandpass filter, without servos on the master and on the comb. The sign of the beat notes is chosen in order to use the difference of these signals as the driving signal of the MZM (consistently with the equations above). RF amplification (∼25 dB for the slave and ∼40 dB for the master) brings up both $\Delta\nu_m$ and $\Delta\nu_s$ signals to the range where the mixer operates with negligible noise contribution. A bandpass filter selects the difference of the beat notes after the mixer. A 1 W RF amplifier boosts this signal up to a level adequate for the MZM to deliver ∼2% of the incident optical power in the first sideband. We should note that together with the carrier, destructive interference in the dual–MZM eliminates all even order sidebands as well[19]. The amplified signal is applied to the MZM via a 90° RF splitter operating in the range from 55 to 90 MHz.

As a first test we used a DFB diode tunable in the proximity of the master laser (1617 nm) allowing for a direct beating of the MZM output against the master. The result in the upper panel of Fig.2, shows an instrument–limited 300 kHz peak width for the upper sideband and a 4 MHz-wide peak for the lower sideband, i.e. twice as large as the carrier peak. To make this last signal visible, the MZM bias was intentionally unbalanced, inducing a change of the peak intensities of the carrier and of the uncorrected sideband while preserving their widths.

To quantify the width of the coherent peak with better resolution we downshifted the beat note via a frequency mixer in order to sample the signal using a 200 Msamples/s acquisition card (GAGE model CS1622, equipped with a 100 MHz low pass filter). By Fourier

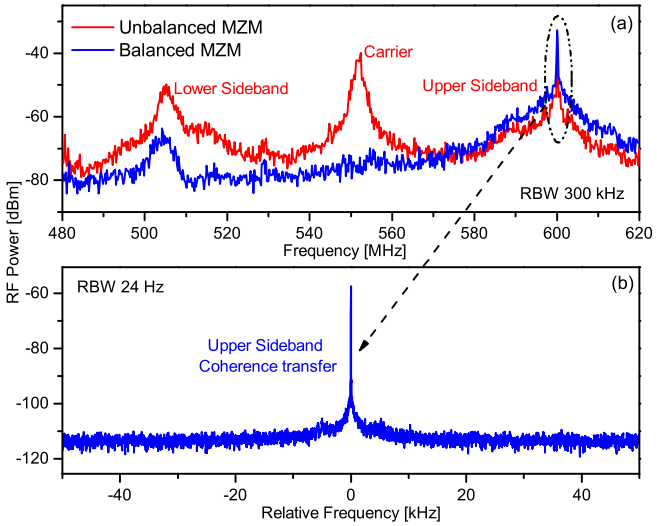

Fig. 2 Beat note of the MZM output with the VCOF master laser. Upper panel: Broad band view showing the carrier and the other sideband which are strongly suppressed after optimization of the MZM control DC bias levels. Lower panel: High resolution spectrum of the downshifted beat note, still limited by the instrumental resolution (24 Hz). 58% of the power is calculated to be in the carrier, corresponding to a phase noise of 0.75 rad rms.

transform this produces the higher resolution spectrum in the bottom panel of Fig.2, a beat note with Fourier–transform–limited 24 Hz width, lying 57 dB above a flat pedestal. By numerical integration over a span of 60 MHz, we estimate that about 58% of the power is in the carrier, corresponding to phase noise of 0.75 rad rms, much larger than the ∼0.1 rad rms reported in Ref.[19], where no comb was introduced in between slave and master lasers. This result cannot be attributed to non–common–mode noise of the comb which is negligible at such close–by frequencies, but it may result from the signal-to-noise ratio of the beat notes with the comb. The comb mode spacing of 100 MHz is another limitation of this proof-of-principle setup: it forces us to single out the comb–DFB beat note from the replicas due to the adjacent comb modes by means of a tight bandpass filter, thus slicing off a portion of the DFB noise spectrum rather than passing it over to the FF correction system. Using a comb with wider mode spacing (commercially available) effective control bandwidths exceeding 100 MHz would be available.

In order to test the coherence transfer over a broader spectral range an ideal solution would be the analysis of the beat signal between the slave laser and a second comb independently phase locked to the master by means of some fast feedback servo. Without the availability of such comb, and at the same time with the aim of verifying the viability of the proposed scheme for precision spectroscopy, we tested the coherence transfer over a multi-THz range using as an optical spectrum analyzer a high finesse optical cavity whose length was linearly scanned by a piezoelectric actuator. With a cavity length of 34.5 cm long (Free Spectral Range FSR=435 MHz) and a finesse of 450 000 around 1610 nm, the analyzer relies on 1 kHz wide resonances. We added a fibered optical amplifier at the MZM output to increase the cavity injection signal, followed by an optical isolator before mode–matched cavity injection. The cavity length was modulated at 1 Hz over one FSR delivering transmission transients as those reported in Fig.3. The upper panel refers to the slave laser discussed before, emitting at 1617 nm with a negligible gap from the master. The strong narrow peak corresponds to the upper sideband, while the weaker broad peak corresponds to the other sideband.

Smaller peaks in Fig.3 are due to transverse modes appearing due to imperfect mode matching (narrow or broad, depending on the sideband they correspond to). By zooming on the narrow sideband transient, a well–known chirped ringing pattern is visible, which can occur only if the incident field is spectrally narrower than the cavity mode[21] over the ∼ 0.5 ms duration of the passage through resonance. This is produced by the intracavity field buildup at the passage through resonance, which then exponentially decays and beats with the incident field that continues to weakly feed the cavity off-resonance. The chirp is due to the frequency scan of the cavity resonance. The other sideband does not show any ringing, as observed when injecting the uncorrected DFB laser directly into the cavity. The presence of a ringing pattern over a noisy pedestal demonstrates that a sizable fraction of the MZM output radiation fits inside a sub–kHz bandwidth, consistently with the above result from direct lasers beating (Fig.2). This pedestal is then filtered by the cavity and has no effect on the frequency resolution of ring–down measurements which are obtained by rapid switch off of the laser beam at resonance.

When replacing the slave DFB laser, the same cavity output patterns are observed up to the low wavelength edge of our comb. In particular, the bottom panel of Fig.3 shows signals from a 1521 nm DFB laser, which clearly appear equivalent to those from the 1617 nm laser. Therefore, at the kHz level of the scanning cavity mode width, the coherence transfer is as good for a laser at the VCOF frequency (186 THz) as for a laser at the comb edge (198 THz). Over this range the reflectivity of the cavity mirrors is almost constant, as is deduced from the exponential envelope of the coherent peaks in Fig.3 which display a decay constant of about 150 μs at both frequencies. In other words, if a degradation of the coherence transfer is present, it results into a slave laser narrowing to below 1 kHz (over 0.5 ms) across the whole 12 THz range allowed by our comb spectral span.

This result is consistent with the frequency noise analysis of Erbium combs previously reported[22]. In fact, comb noise is dominated around the optical carrier by environmentally–induced laser cavity length fluctua-

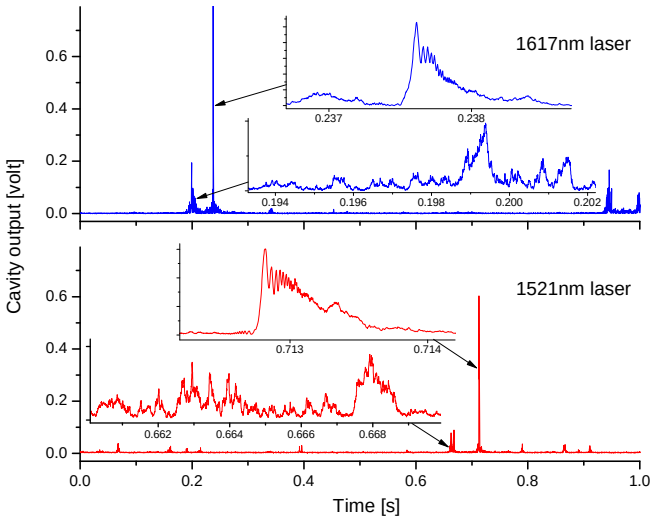

Fig. 3 A 450 000 finesse cavity used as an optical spectrum analyzer. 1 s on the horizontal scale is one cavity FSR (435 MHz). Top: coherence transfer applied to a DFB laser emitting close to the master VCOF laser. In the insets are detailed views of the narrow coherent peak from the upper sideband and the broad peak from the lower sideband. Bottom: Same observations when using a DFB laser lying at the far edge of the comb.

tions, which force the comb mode linewidth to increase by roughly a factor of 0.05 kHz per THz (at 1 ms observation time, longer than the photon decay time of our high–finesse cavity). Within the 12 THz frequency gap explored here, the non–common–mode frequency noise contribution can thus be assumed to influence the slave laser linewidth by about 0.6 kHz, thus barely appreciable with our swept–cavity linewidth analyzer. It is worth noting that this limitation from the comb noise, which is not appreciable with our setup, could be anyway overcome with a more refined referencing scheme, using a fast MZM-based frequency correction in combination with the transfer oscillator configuration by Telle and coworkers[15]. Alternatively one could resort to a simpler one–stage FF frequency correction as that demonstrated in Ref.[19] starting from a (more complex but less noisy) frequency comb with f_{rep} phase locked to the master and f_0 to an RF synthesizer[14].

In conclusion, we demonstrated a simple and robust FF approach for phase locking two CW single mode lasers beating with the same OFC, using a fast sideband modulator as the only optical control element. This approach was shown to lead to high quality and intense injection signals for a very high finesse cavity over the 12 THz spectral range of an Erbium fiber comb, which will allow cavity ring-down spectroscopy with high frequency precision (sub kHz). A set of cost–effective widely tunable telecom lasers can thus be used to interrogate molecular absorption in a high finesse cavity without any trade-off in terms of precision, sensitivity and spectral resolution, these being inherited from a single high coherence master. The power loss associated with phase–modulated sideband generation can in principle be compensated by an optical amplifier without penalty for the coherence transfer if the amplifier is inserted before the splitter feeding the modulator and the comb beating line. In contrast to existing high–end phase–frequency control loops, this technique is straightforward to implement in the telecom range, where fibered MZM modulators are readily available. We expect it to become eventually exploitable in the visible or mid–infrared regions thanks to progress with guided optics devices based on lithium–niobate or silicon technologies, respectively.

The authors acknowledge financial support by: Polo di Lecco - Politecnico di Milano, Institute of Photonics and Nanotechnology of CNR, LabexOSUG@2020 project (ANR10 LABX56), Pôle SMINGUE (Université Joseph Fourier), Femto network of CNRS.

References

1. L.-S. Ma, J. Ye, P. Dub, and J. L. Hall, J. Opt. Soc. Am. B **16**, 2255 (1999).
2. A. Foltynowicz, W. Ma, and O. Axner, Opt. Express **16**, 14689 (2008).
3. G.-W. Truong, K. O. Douglass, S. E. Maxwell, R. D. van Zee, D. F. Plusquellic, J. T. Hodges, and D. A. Long, Nat. Photon. **7**, 532 (2013).
4. T. Kessler, C. Hagemann, C. Grebing, T. Legero, U. Sterr, F. Riehle, M. J. Martin, L. Chen, and J. Ye, Nat. Photonics **6**, 687 (2012).
5. I. Galli, M. Siciliani de Cumis, F. Cappelli, S. Bartalini, D. Mazzotti, S. Borri, A. Montori, N. Akikusa, M. Yamanishi , G. Giusfredi, P. Cancio, and P. De Natale, Appl. Phys. Lett. **102**, 121117 (2013).
6. J. Burkart, D. Romanini, and S. Kassi, Opt. Lett. **39**, 4695 (2014).
7. A. Bartels, C. W. Oates, L. W. Hollberg, and S. A. Diddams, Opt. Lett. **29**, 1081 (2004).
8. M. J. Martin, S. M. Foreman, T. R. Schibli, and Jun Ye, Opt. Express **17**, 558 (2009).
9. A. Ruehl, M. Martin, K. Cossel, L. Chen, H. McKay, B. Thomas, C. Benko, L. Dong, J. Dudley, M. Fermann, I. Hartl, and J. Ye, Phys. Rev. A **84**, 011806 (2011).
10. E. Baumann, F. R. Giorgetta, J. W. Nicholson, W. C. Swann, I. Coddington, and N. R. Newbury, Opt. Lett. **34**, 638 (2009).
11. C. Benko, A. Ruehl, M. J. Martin, K. S. E. Eikema, M. E. Fermann, I. Hartl, and J. Ye, Opt. Lett. **37**, 2196 (2012).
12. J. J. McFerran, W. C. Swann, B. R. Washburn, and N. R. Newbury, Appl. Phys. B **86**, 219 (2007).
13. C.-C. Lee, C. Mohr, J. Bethge, S. Suzuki, M. E. Fermann, I. Hartl, and T. R. Schibli, Opt. Lett. **37**, 3084 (2012).
14. T. R. Schibli, I. Hartl, D. C. Yost, M. J. Martin, A. Marcinkevicius, M. E. Fermann, and J. Ye, Nat. Photon. **2**, 355 (2008).
15. H. R. Telle, B. Lipphardt, and J. Stenger, Appl. Phys. B **74**, 1 (2002).
16. I. Galli, S. Bartalini, P. Cancio, G. Giusfredi, D. Mazzotti, and P. De Natale, Opt. Express **17**, 9582 (2009).

17. T. Sala, D. Gatti, A. Gambetta, N. Coluccelli, G. Galzerano, P. Laporta, and M. Marangoni, Opt. Lett. **37**, 2592 (2012).
18. D. Gatti, T. Sala, A. Gambetta, N. Coluccelli, G. Nunzi Conti, G. Galzerano, P. Laporta, and M. Marangoni, Opt. Express **20**, 24880 (2012).
19. J. Burkart, T. Sala, S. Kassi, D. Romanini, and M. Marangoni, Opt. Lett. **40**, 816 (2015).
20. J. Burkart, D. Romanini, and S. Kassi, Opt. Lett. **38**, 2062 (2013).
21. J. Morville, D. Romanini, M. Chenevier, and A. A. Kachanov, Appl. Opt. **41**, 6980 (2002).
22. N. R. Newbury and W. C. Swann, J. Opt. Soc. Am. B **24**, 1756 (2007).

References

1. L.-S. Ma, J. Ye, P. Dub, and J. L. Hall, "Ultrasensitive frequency–modulation spectroscopy enhanced by a high–finesse optical cavity: theory and application to overtone transitions of C_2H_2 and C_2HD," J. Opt. Soc. Am. B **16**, 2255 (1999).
2. A. Foltynowicz, W. Ma, and O. Axner, "Characterization of fiber–laser–based sub-Doppler NICE-OHMS for quantitative trace gas detection," Opt. Express **16**, 14689 (2008).
3. G.-W. Truong, K. O. Douglass, S. E. Maxwell, R. D. van Zee, D. F. Plusquellic, J. T. Hodges, and D. A. Long, "Frequency–agile, rapid scanning spectroscopy," Nat. Photon. **7**, 532 (2013).
4. T. Kessler, C. Hagemann, C. Grebing, T. Legero, U. Sterr, F. Riehle, M. J. Martin, L. Chen, and J. Ye, "A sub-40-mHz–linewidth laser based on a silicon single–crystal optical cavity," Nat. Photonics **6**, 687 (2012).
5. I. Galli, M. Siciliani de Cumis, F. Cappelli, S. Bartalini, D. Mazzotti, S. Borri, A. Montori, N. Akikusa, M. Yamanishi , G. Giusfredi, P. Cancio, and P. De Natale, "Comb–assisted subkilohertz linewidth quantum cascade laser for high–precision mid-infrared spectroscopy," Appl. Phys. Lett. **102**, 121117 (2013).
6. J. Burkart, D. Romanini, and S. Kassi, "Optical feedback frequency stabilized cavity ring–down spectroscopy," Opt. Lett. **39**, 4695 (2014).
7. A. Bartels, C. W. Oates, L. W. Hollberg, and S. A. Diddams, "Stabilization of femtosecond laser frequency combs with subhertz residual linewidths," Opt. Lett. **29**, 1081 (2004).
8. M. J. Martin, S. M. Foreman, T. R. Schibli, and Jun Ye, "Testing ultrafast mode–locking at microhertz relative optical linewidth," Opt. Express **17**, 558 (2009).
9. A. Ruehl, M. Martin, K. Cossel, L. Chen, H. McKay, B. Thomas, C. Benko, L. Dong, J. Dudley, M. Fermann, I. Hartl, and J. Ye, "Ultrabroadband coherent supercontinuum frequency comb," Phys. Rev. A **84**, 011806 (2011).
10. E. Baumann, F. R. Giorgetta, J. W. Nicholson, W. C. Swann, I. Coddington, and N. R. Newbury, "High–performance, vibration–immune, fiber–laser frequency comb," Opt. Lett. **34**, 638 (2009).
11. C. Benko, A. Ruehl, M. J. Martin, K. S. E. Eikema, M. E. Fermann, I. Hartl, and J. Ye, "Full phase stabilization of a Yb:fiber femtosecond frequency comb via high–bandwidth transducers," Opt. Lett. **37**, 2196 (2012).
12. J. J. McFerran, W. C. Swann, B. R. Washburn, and N. R. Newbury, "Suppression of pump–induced frequency noise in fiber–laser frequency combs leading to subradian f_{ceo} phase excursions," Appl. Phys. B **86**, 219 (2007).
13. C.-C. Lee, C. Mohr, J. Bethge, S. Suzuki, M. E. Fermann, I. Hartl, and T. R. Schibli, "Frequency comb stabilization with bandwidth beyond the limit of gain lifetime by an intracavity graphene electro–optic modulator," Opt. Lett. **37**, 3084 (2012).
14. T. R. Schibli, I. Hartl, D. C. Yost, M. J. Martin, A. Marcinkevicius, M. E. Fermann, and J. Ye, "Optical frequency comb with submillihertz linewidth and more than 10 W average power," Nat. Photon. **2**, 355 (2008).

15. H. R. Telle, B. Lipphardt, and J. Stenger, "Kerr–lens, mode–locked lasers as transfer oscillators for optical frequency measurements," Appl. Phys. B **74**, 1 (2002).
16. I. Galli, S. Bartalini, P. Cancio, G. Giusfredi, D. Mazzotti, and P. De Natale, "Ultra–stable, widely tunable and absolutely linked mid-IR coherent source," Opt. Express **17**, 9582 (2009).
17. T. Sala, D. Gatti, A. Gambetta, N. Coluccelli, G. Galzerano, P. Laporta, and M. Marangoni, "Wide–bandwidth phase lock between a CW laser and a frequency comb based on a feed–forward configuration," Opt. Lett. **37**, 2592 (2012).
18. D. Gatti, T. Sala, A. Gambetta, N. Coluccelli, G. Nunzi Conti, G. Galzerano, P. Laporta, and M. Marangoni, "Analysis of the feed–forward method for the referencing of a CW laser to a frequency comb," Opt. Express **20**, 24880 (2012).
19. J. Burkart, T. Sala, S. Kassi, D. Romanini, and M. Marangoni, "Optical phase cloning by an integrated dual–parallel Mach–Zehnder modulator ," Opt. Lett. **40**, 816 (2015).
20. J. Burkart, D. Romanini, and S. Kassi, "Optical feedback stabilized laser tuned by single–sideband modulation," Opt. Lett. **38**, 2062 (2013).
21. J. Morville, D. Romanini, M. Chenevier, and A. A. Kachanov, "Effects of Laser Phase Noise on the Injection of a High–Finesse Cavity," Appl. Opt. **41**, 6980 (2002).
22. N. R. Newbury and W. C. Swann, "Low–noise fiber–laser frequency combs," J. Opt. Soc. Am. B **24**, 1756 (2007).

Part II

Optical feedback frequency-stabilized cavity ring-down spectroscopy (OFFS-CRDS)

Taking advantage of the highly stable sub-kHz linewidth laser source described in Part I, we will now turn to its application in ultra-sensitive, high-resolution molecular absorption spectroscopy. In particular, we present the novel Optical Feedback Frequency-Stabilized Cavity Ring-Down Spectroscopy (OFFS-CRDS) technique, which was developed in the framework of this thesis.

As a preface, let us first develop an elementary framework for absorption spectroscopy as the study of frequency-dependent light-matter interaction. Atoms and molecules interact with light by the coupling of the charges of their constituents to the electromagnetic field. Consequently, light with an appropriate frequency can trigger transitions between atomic or molecular quantum states, which correspond to different excitations of their respective internal motion. For molecules, the electronic motion needs to be distinguished from the motion of the atomic nuclei, which subdivides into vibration and rotation. A brief introduction on basic aspects of rotational-vibrational transitions of molecules will be given in Section 8.1.

For the moment, let us simply consider the fact that the excitation of an atomic or molecular transition by a light field converts at least one of its photons to internal energy of the excited entity. In a uniform sample, this leads to a continuous decrease in the intensity of the light field, which was first studied experimentally by Bouguer [158]. To first order, the decay of light intensity $I(z)$ along the propagation coordinate z is exponential:

$$I(z) = I_0 \mathrm{e}^{-\alpha z}, \tag{4.2}$$

where the decay rate of the exponential is the absorption coefficient α of the sample under study. With reference to the follow-up studies by Lambert [159] and Beer [160], this relation is commonly called Beer-Lambert or Bouguer-Beer-Lambert law.

However, in a certain analogy to Ohm's "law", one should rather consider Eq. (4.2) as a local definition of the absorption coefficient α, which might be a function of spatial coordinates in an inhomogeneous medium, and of light intensity as soon as nonlinear effect come into play (cf. Chapter 9). Then, in a one-dimensional setting, the absorption coefficient is defined as the relative intensity decay rate by the following equation:

$$\frac{\mathrm{d}I}{\mathrm{d}z} = -\alpha I \tag{4.3}$$

In the general case, where α is a function $\alpha(z, I)$ as discussed above, the shape of the intensity decrease $I(z)$ is found as the solution to the differential equation (4.3). Note that $\alpha < 0$ can also be physical, in a gain medium with population inversion. For $\alpha(z, I) = \text{const.} > 0$, the exponential decay Eq. (4.2) solves the differential equation (4.3), and the simple Bouguer-Beer-Lambert relation is retrieved.

On this basis, let us turn to the dependence of the absorption coefficient on light frequency ν, as $\alpha(\nu)$, which lies at the very heart of absorption spectroscopy. As all absorbers contribute, the absorption coefficient is proportional to absorber concentration, as first pointed out explicitly by Beer [160]. The degree of absorption is further determined by the transition probability of each individual molecule contributing to it. In the framework of quantum mechanics, this means that the absorption coefficient is also proportional to the transition matrix element squared [161]. Finally, various physical mechanisms, such as the Heisenberg uncertainty principle and others discussed later, spread out the absorption due to a transition over a finite range of frequencies.

The essence of this is that the frequency-dependent absorption coefficient $\alpha(\nu)$ in a molecular sample with volume density N/V and a transition at frequency ν_0 can be written

as

$$\alpha(\nu) = k \cdot \frac{N}{V} \cdot p(\nu - \nu_0) \tag{4.4}$$

Therein, k is the so-called line strength of the molecular transition, which is a temperature-dependent property depending on molecular structure according to first principles. The absorption line profile $p(\nu - \nu_0)$ describes the shape of the absorption feature. Concerning units, the most common practice in molecular spectroscopy is to express frequencies in terms of wavenumbers in cm^{-1} (cf. Chapter 2) and to give $\frac{N}{V}$ in molecules/cm^3. Consequently, k is expressed in cm/molecule and p in cm. By convention, the line shape function $p(\nu)$ is normalized:

$$\int_{-\infty}^{\infty} p(\nu)\mathrm{d}\nu = 1, \tag{4.5}$$

Different line profile models with an increasing degree of sophistication will be discussed in Section 8.1.2. Thanks to profile normalization (4.5), Eq. (4.4) implies the following simple expression for the integrated absorption S_α due to a molecular transition:

$$S_\alpha = \int_{-\infty}^{\infty} \alpha(\nu)\mathrm{d}\nu = k\frac{N}{V} \tag{4.6}$$

The fundamental relationships (4.4) and (4.6) clearly illustrate how absorption spectroscopy provides a wealth of information about the sample in particular, the molecule in general, and the environmental conditions. Very generally speaking, k gives access to molecular structure and fundamental physics, N/V yields the concentration of a substance, and p carries information on pressure and temperature as well as subtle signatures of intermolecular interaction processes.

Chapter 5

State of the art in ultra-sensitive and frequency-stabilized cavity ring-down spectroscopy

The origins of cavity ring-down spectroscopy (CRDS) can be traced back to the mirror reflectometer based on optical cavity decay time by Anderson, Frisch and Masser [162]. The authors demonstrated how the transmission intensity decay time of an optical cavity provides a precise and straightforward measurement of the reflectivity of its low-loss, highly reflective cavity mirrors. To acquire an unperturbed transmission decay signal, they used an electro-optic Pockels cell between two crossed polarizers as a fast optical switch for shutting off the continuous-wave laser injecting the optical cavity. The authors pointed out that their technique had the counter-intuitive advantage of gaining in precision the closer the mirror reflectivities were to one. In the first experimental realization, a mirror loss resolution of $5 \cdot 10^{-6}$ was achieved.

This conceptually simple, yet powerful technique was rapidly picked up by absorption spectroscopists for monitoring the frequency-dependent losses inside a resonator. Importantly, in addition to the inherent precision offered by time-domain measurements, the long lifetime of light in a cavity composed of highly reflective mirrors provides the further benefit of strongly enhancing the interaction between light and an absorbing sample, as light is trapped travelling back and forth through the sample in the resonator. The decay time τ of a cavity with length L then takes the form

$$\frac{1}{\tau} = \frac{1}{\tau_0} + \frac{\alpha c}{n} \tag{5.1}$$

where c is the speed of light in vacuum, n the refractive index of the sample, α its absorption coefficient, and τ_0 the decay time of the cavity without the sample. This fundamental relationship of CRDS will be discussed in the next section, in particular with the mirror-reflectivity-dependent explicit expression for τ_0 in Eq. 5.4.

The first cavity ring-down spectrometer based on these principles is due to O'Keefe and Deacon [163], who demonstrated the measurement of a weak electronic O_2 absorption band near 690 nm by probing the total cavity loss rate with a 15-ns-pulsed laser. The time-domain measurement provided the important advantage of making the absorption measurement insensitive to pulse-to-pulse intensity fluctuations of several percent.

Initially, it was widely believed that light pulses shorter than cavity round-trip time would not undergo interference inside the cavity and thus be transmitted through the cavity unperturbed by its discrete interferometric mode structure (cf. Section 2.4.1). However, contrary to this interpretation, Lehmann and Romanini demonstrated by a rigorous

theoretical analysis of pulsed CRDS in the frequency domain [164] that non-negligible light intensities inside the cavity only occur at frequencies corresponding to cavity resonances. This implies that only the overlap of absorption lines with cavity resonances can be measured in a simple pulsed CRDS scheme. Another issue for quantitative absorption spectroscopy was excess absorption noise due to the injection of pulse intensity into higher-order TEM_{mn} transverse modes of the cavity, whose losses can significantly differ from those of the fundamental TEM_{00} mode. Based on the frequency decomposition of intracavity light into the exclusive contributions from resonant cavity modes, Lehmann and Romanini pointed out that the instrumental apparatus function of a CRDS measurement is given by the cavity modewidth as long as only one mode is excited, and this in spite of a potentially noisy probe laser.

This insight paved the way to the realization of a continuous-wave cavity ring-down spectrometer (CW-CRDS) by Romanini and co-workers [41]. The basic working principle of this highly successful technique, illustrated by the simplistic sketch in Fig. 5.1, still is the foundation for most of today's state-of-the-art CRD spectrometers.

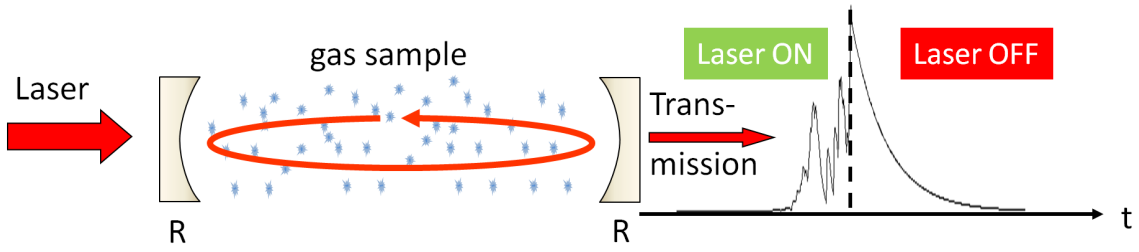

Figure 5.1 Schematic illustration of continuous-wave cavity ring-down spectroscopy (CW-CRDS). A CW laser is injected into a high-finesse cavity of mirror reflectivity R containing a gas sample. As soon as a certain cavity transmission threshold is reached, the injection is shut off by a fast optical switch, leading to an exponential decay of transmitted light intensity. The time constant of this decay provides a measure of intracavity losses, including sample absorption, according to Eq. (5.1).

In CW-CRDS, a tunable single-frequency CW laser is spatially mode-matched to a TEM_{00} mode of a high-finesse optical cavity. Then, the laser is tuned to a TEM_{00} mode frequency, or vice-versa, so that a resonant build-up of intracavity intensity is reached. If the laser linewidth is bigger than the cavity modewidth, this intensity build-up is noisy and less efficient due to laser frequency jitter [130], as illustrated in Fig. 5.1. When cavity transmission reaches a predetermined threshold, a fast optical switch, typically an acousto-optic modulator (AOM), is triggered for abruptly interrupting cavity injection by the CW laser. Consequently, the continuous leakage of intracavity light through the cavity mirrors can be measured, yielding an exponential decay signal. Its ring-down time τ can be measured at successive spectral points by jointly tuning laser and cavity mode, thus allowing high-resolution absorption spectroscopy according to Eq. (5.1), unlimited by the free spectral range of the ring-down cavity.

In this chapter, we shall first explore two distinct theoretical approaches to cavity ring-down, namely the most common simple one-dimensional analyis as well as an alternative genuinely three-dimensional derivation via the field energy in the cavity TEM_{00} mode. This latter strategy will be indispensable for the theoretical treatment in Section 9.2.3. Next, we will review some of the recent developments in ultra-sensitive and frequency-stabilized CRDS. These specific, yet broad branches of CRDS are highly relevant to the

discussion of the OFFS-CRDS technique put forward in this thesis, which is itself both frequency-stabilized and ultra-sensitive. Finally, some exciting current trends in cavity-ring-down spectroscopy and closely related techniques will be portrayed.

5.1 Two theoretical approaches to CRDS

Most commonly, the fundamental equation (5.1) for the cavity ring-down time is derived in a 1-dimensional model by considering the intracavity light intensity $I(k)$ after a discrete number k of round-trips in a cavity of length L, given by

$$I(k) = \left(R^{2k} \cdot \mathrm{e}^{-\alpha 2kL}\right) \cdot I(0) \tag{5.2}$$

with the mirror reflectivity R. Replacing the discrete variable k by the time $t = 2nL/c \cdot k$ needed for k cavity round-trips in a medium with refractive index n yields the time-dependent intracavity intensity $I(t)$ as

$$I(t) = I(0) \cdot \mathrm{e}^{-\left(\frac{(1-R)c}{nL} + \frac{\alpha c}{n}\right) \cdot t} \tag{5.3}$$

using the approximation $\ln R \approx R - 1$ for $R \Rightarrow 1$. Comparing to Eq. (5.1), one identifies the baseline ring-down time τ_0 as

$$\tau_0 = \frac{nL}{(1-R)c} \tag{5.4}$$

Let us note that this consideration is only valid for losses exclusively due to mirrors and absorption. As soon as elastic and inelastic scattering or diffraction effects come into play, Eq. (5.4) only holds approximately, and τ_0 becomes a global baseline encompassing all broad-band intracavity loss processes. In that case, it may be difficult to distinguish broad-band absorption features from the baseline, and great care is needed for establishing correct values for both τ_0 and α.

In the following, we will explore a different approach for deriving Eq. (5.1) for CW-CRDS, based on the time-dependent total energy $W(t)$ of the intracavity electromagnetic field. While the first approach is intuitive and captures the essential physical mechanisms, this second one has the virtue of being more rigorous and genuinely 3-dimensional, by correctly representing the spatial light intensity distribution inside the ring-down cavity. In Chapter 9, we will see that this feature is indispensable for deriving the cavity ring-down behavior in a saturated-absorption regime with an intensity-dependent absorption coefficient. In that case, α becomes a function of at least two spatial coordinates and time, and the aforementioned simple 1-dimensional approach breaks down.

Let us begin by considering the total energy W of the EM field $E(x, y, z)$ inside the cavity:

$$W = n^2 \epsilon_0 \int_V E^2(x, y, z) \mathrm{d}V \tag{5.5}$$

For an optical coupling of the laser beam into the cavity, CW-CRDS typically uses the fundamental TEM_{00} spatial mode of the cavity. The standing wave constituting the resonant TEM_{00} mode can be decomposed into two waves travelling into opposite directions along the z axis, each carrying half of the total field energy. As we are considering a symmetric cavity with two identical mirrors here, we may limit our treatment to the rightward-travelling wave without loss of generality. Its electric field amplitude $E(x, y, z)$

is given by Eq. (2.26), as discussed in Section 2.4:

$$E^2(x,y,z) = \frac{{E_0}^2}{1+z^2/{z_R}^2} \mathrm{e}^{-\frac{2\left(x^2+y^2\right)}{{w_0}^2\left(1+z^2/z_R^2\right)}} \cos^2\left(kz - \omega t - \arctan\left(\frac{z}{z_R}\right) + \frac{k(x^2+y^2)}{2z\left(1+{z_R}^2/z^2\right)}\right) \tag{5.6}$$

Inserting this squared electric field into the volume integral (5.5) expressed in cylindrical coordinates with $r^2 = x^2 + y^2$, the rapidly varying $\cos^2(kz - \omega t + ...)$-term averages to $\frac{1}{2}$ in very good approximation. Using the identity

$$\int \mathrm{e}^{-ax^2} x \mathrm{d}x = -\frac{1}{2a}\mathrm{e}^{-ax^2} \tag{5.7}$$

one finds

$$W = n^2\epsilon_0 \int_0^\infty \int_0^{2\pi} \int_{-L/2}^{L/2} E^2(r,z) r \mathrm{d}r \mathrm{d}\varphi \mathrm{d}z = \frac{1}{4} n^2 \epsilon_0 {E_0}^2 \pi {w_0}^2 L \tag{5.8}$$

This is the total energy content of the rightward-travelling EM field in the TEM_{00} mode of the cavity. The cavity ring-down event consists in a diminution of this energy over time due to the various intracavity loss processes.

First, we shall quantify the energy loss $(\mathrm{d}W)_m$ due to the cavity mirrors. It is equal to the non-reflected fraction $1-R$ of the power P_m incident on the mirror surface, integrated over the infinitesimally short time interval $\mathrm{d}t$:

$$(\mathrm{d}W)_m = -(1-R)P_m \mathrm{d}t \tag{5.9}$$

P_m is given by the surface integral of the light intensity $I(x,y,L/2) = \epsilon_0 cn E^2(x,y,L/2)$ [165] directed at the mirror surface. P_m can be written in polar coordinates using Eq. (5.6), again taking advantage of the rotational symmetry of the TEM_{00} mode and time-averaging over the rapidly varying $\cos^2(kz - \omega t + ...)$-term:

$$P_m = \int_0^\infty \int_0^{2\pi} I(r, L/2) r \mathrm{d}r \mathrm{d}\varphi = \frac{1}{4}\epsilon_0 cn E_0^2 \pi {w_0}^2 \tag{5.10}$$

Inserting this result in Eq. (5.9) yields the energy loss rate $\left(\frac{\mathrm{d}W}{\mathrm{d}t}\right)_m$ due to mirror reflections as

$$\left(\frac{\mathrm{d}W}{\mathrm{d}t}\right)_m = -\frac{1}{4}(1-R)\pi {w_0}^2 cn\epsilon_0 {E_0}^2 = -\frac{(1-R)c}{nL} \cdot W \tag{5.11}$$

where the last equality is obtained by comparison with Eq. (5.8). The time constant of this first-order ordinary differential equation (ODE) is the baseline ring-down time τ_0 from Eq. (5.4).

Now, let us turn to the energy loss $(\mathrm{d}W)_a$ due to absorption. In Section 9.2, the more general case of a space- and time-dependent absorption coefficient will be discussed. Here, we shall limit the discussion to the simple case of a sample with uniform α. We consider the absorption of light travelling over the infinitesimally short distance $\mathrm{d}l = c/n\mathrm{d}t$, for each volume element $\mathrm{d}V$ inside the cavity:

$$(\mathrm{d}W)_a = -\int_V n^2\epsilon_0 E^2(x,y,z)\alpha \cdot (c/n\mathrm{d}t)\mathrm{d}V \tag{5.12}$$

The coordinate-independent α in this simple case can be drawn out of the integral together with the other constants. Comparison of Eqs. (5.12) and (5.5) shows that the energy loss rate $\left(\frac{\mathrm{d}W}{\mathrm{d}t}\right)_a$ due to absorption can be written as

$$\left(\frac{\mathrm{d}W}{\mathrm{d}t}\right)_a = -\frac{\alpha c}{n} \cdot W \tag{5.13}$$

Summing up $\left(\frac{\mathrm{d}W}{\mathrm{d}t}\right)_m$ and $\left(\frac{\mathrm{d}W}{\mathrm{d}t}\right)_a$, the total energy loss rate is

$$\left(\frac{\mathrm{d}W}{\mathrm{d}t}\right) = \left(\frac{\mathrm{d}W}{\mathrm{d}t}\right)_m + \left(\frac{\mathrm{d}W}{\mathrm{d}t}\right)_a = -\left(\frac{(1-R)c}{nL} + \frac{\alpha c}{n}\right) \cdot W \tag{5.14}$$

In complete analogy to Eq. (5.3), the solution of this first-order ODE is an exponential decay

$$W(t) = W(0) \cdot \mathrm{e}^{-\left(\frac{(1-R)c}{nL} + \frac{\alpha c}{n}\right) \cdot t} \tag{5.15}$$

with the ring-down time

$$\tau = \left(\frac{(1-R)c}{nL} + \frac{\alpha c}{n}\right)^{-1}. \tag{5.16}$$

5.2 Ultra-sensitive continuous-wave CRDS

To begin our literature review on state-of-the-art techniques, let us first focus on ultra-sensitive CW-CRDS techniques which do not contain dispositions for tight laser or cavity frequency stabilization. We will turn to the latter in the following section. This somewhat artificial separation is not intended to imply that frequency-stabilized techniques cannot reach outstanding sensitivity levels, but an attempt to structure the discussion in an intelligible manner.

To clarify the terms used in the following, let us define some figures of merit which are commonly used for characterizing the performance of absorption spectrometers. An absorption signature smaller than the root-mean-square noise on the spectrometer baseline cannot be reliably detected. Consequently, that noise is taken to be the detection limit α_{min} of the spectrometer. With Eq. (5.1) in the limit $\alpha \to 0$, it can be written as

$$\alpha_{min} = \lim_{N\to\infty} \sqrt{\sum_{i=1}^{N} \left(\frac{1}{N-1}\left(\frac{1}{c\tau_{0_i}} - \frac{1}{c\overline{\tau_0}}\right)^2\right)}, \tag{5.17}$$

estimated in practice by a sufficient number N of baseline ring-down time measurements τ_{0_i} with arithmetic mean $\overline{\tau_0}$.

Another important concept is the so-called detectivity of an absorption spectrometer, which measures how fast a certain detection limit can be reached. This explicitly takes the important issue of averaging time into consideration. For N measurements of an absorption coefficient α with normally distributed white noise, the variance $\sigma_{\overline{\alpha}}^2$ of its arithmetic mean $\overline{\alpha}$ is the variance σ_α^2 of an individual measurement divided by N:

$$\sigma_{\overline{\alpha}}^2 = \frac{\sigma_\alpha^2}{N}, \tag{5.18}$$

according to elementary Gaussian error propagation. Then, if measurements are made at a frequency f the total averaging time is $T = N/f$. Consequently, the standard deviation of the mean $\overline{\alpha}$ can be written as

$$\sigma_{\overline{\alpha}} = \frac{\sigma_\alpha}{\sqrt{fT}} = \frac{\sigma_\alpha}{\sqrt{f}}\frac{1}{\sqrt{T}} = \frac{D}{\sqrt{T}} \tag{5.19}$$

thus defining the spectrometer detectivity D, which is typically specified in $\mathrm{cm}^{-1}/\sqrt{\mathrm{Hz}}$. Taking the measurement repetition rate into account, it provides a quantitative measure for how precise an absorption measurement made with a given spectrometer can be in a

given interval of time, typically one second. The inverse scaling of $\sigma_{\overline{\alpha}}$ with the square root of averaging time is the well-known $T^{-1/2}$-slope of the Allan deviation discussed in Section 2.1. The utility of an Allan-deviation approach for characterizing the stability and averaging behavior of an absorption spectrometer was pointed out by Werle and co-workers [80, 81]. Consequently, this powerful and widely used tool is also commonly known as Allan-Werle deviation in this context. Figure 3 in Article 4 on page 90 and Fig. 4 in Article 5 on page 160 are typical examples for such an analysis.

Let us underscore that a common pitfall in the interpretation of detectivity values is the implicit assumption that the division of a single-shot noise value by the square root of repetition rate yields a faithful picture of the averaging behavior of an absorption spectrometer. By contrast, the assumption of white noise in Eq. (5.18) is not always fulfilled. Especially at longer timescales, drifts, sinusoidal modulations, flicker or random walk noise contributions may affect the absorption measurement and hamper averaging performance. Consequently, the detectivity should not be used lightly to extrapolate spectrometer noise levels according to Eq. (5.19). Instead, a full stability and averaging analysis based on an Allan-Werle deviation approach should be carried out.

Now turning to specific experimental realizations of CW-CRDS with exceptionally high detectivities and low detection limits, let us take a closer look at an experimental setup at LIPhy which has been used for a wide range of investigations into very weak absorption features in the near-infrared spectral region between 1.25 and 1.7 µm in the last years. This range is seamlessly covered by over 80 telecom-type butterfly-packaged fibered distributed feedback (DFB) laser diodes, which can be easily swapped, thus conferring a high degree of versatility on the experimental setup, which is shown in Fig. 5.2. Each laser can

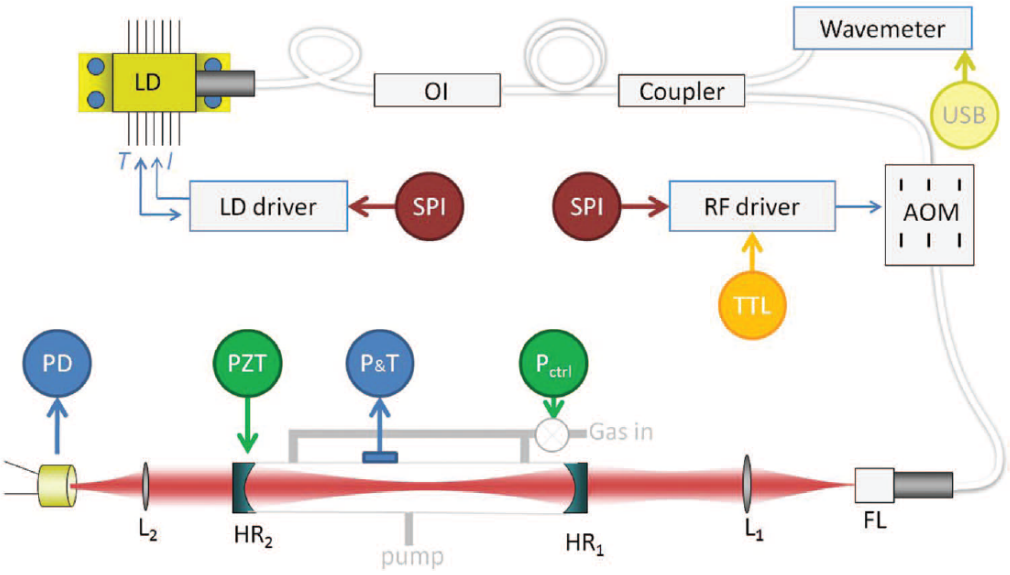

Figure 5.2 Experimental setup for ultra-sensitive CW-CRDS using fibered distributed-feedback (DFB) lasers at LIPhy by Kassi and co-workers [44, 166]. Adapted from [44] (Figure 1).

be frequency-tuned over roughly 30 cm^{-1} by changing its temperature at constant current using home-made low-noise laser temperature control and current driver electronics. As in most CW-CRDS setups, an acousto-optic modulator is used as a fast and high-extinction optical switch for triggering ring-down events. Transmission through the cavity is accomplished by means of triangular cavity length scans, usually over slightly more than one free spectral range of the cavity, by means of the cavity end mirror mounted on a piezo-electric

actuator, yielding at least one coincidence of laser frequency and a TEM_{00} resonance of the cavity per slope. The cavity itself is 140 cm long and equipped with highly reflective dielectric mirrors providing a finesse up to 500,000 and record-holding ring-down times in excess of 700 µs. The frequency axis of the spectrometer is established by diverting ten percent of laser power to a Fizeau-type wavemeter with a short-term resolution at the MHz-level and a long-term stability better than 20 MHz over several days.

The typical absorption detectivity of this spectrometer was found to be a photodetector-noise-limited $1.3 \cdot 10^{-11}\,\mathrm{cm}^{-1}/\sqrt{\mathrm{Hz}}$, and an Allan-Werle analysis showed that thermo-mechanical drifts of the absorption measurement limited the optimal averaging time to roughly 10 s [44]. Consequently, for decreasing absorption noise levels in spite of this limitation, an approach based on the averaging of successive individual spectra originally demonstrated by Kassi and co-workers [166] was chosen. If the measurement of individual spectra is sufficiently fast, the drift-related limitations to averaging discussed by Werle [81] no longer apply, as a vertical offset of the spectrometer baseline does not affect the absorption measurement by CRDS.

Averaging spectra for almost five days, no fundamental limitation of this approach could be evidenced and a $5 \cdot 10^{-13}\,\mathrm{cm}^{-1}$ baseline absorption noise level was reached [44]. This unique performance allowed the detection of the electric quadrupole 3-0 S4 overtone transition of N_2 shown in Fig. 5.3. With a line strength of about $1.5 \cdot 10^{-31}$ cm/molecule, this is the weakest line ever measured by absorption spectroscopy to the best of our knowledge.

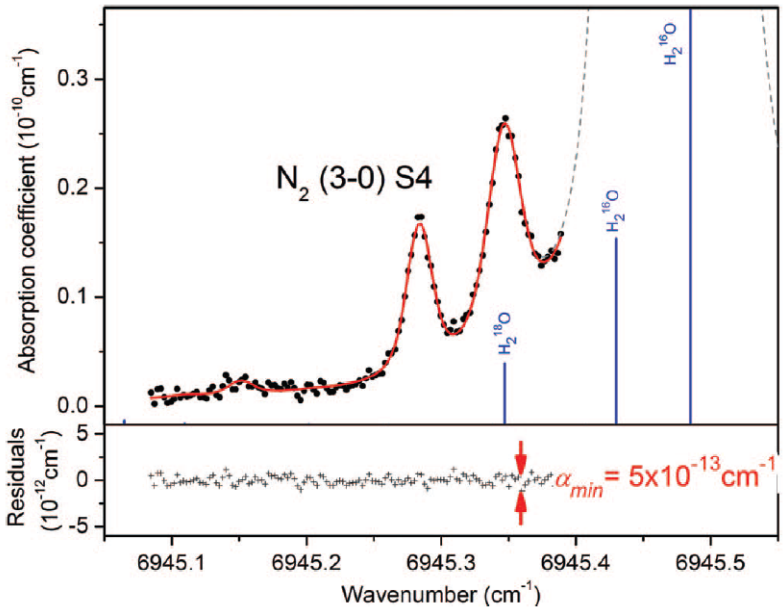

Figure 5.3 First detection of the 3-0 S4 line in N_2 in absorption by Kassi and Campargue [44], at a record-breaking root-mean-square noise level of $5 \cdot 10^{-13}\,\mathrm{cm}^{-1}$. Adapted from [44] (Figure 8).

In conclusion, the near-infrared CW-CRDS setup at LIPhy can stand as an example for illustrating the key ingredients for achieving ultra-high sensitivity. Firstly, efforts must be directed at lowering detector noise and parasite fringe amplitudes by a careful electronic and optical setup. Secondly, long ring-downs herald precise decay time measurements and, at the same time, limit the systematic impact of parasite fringes. On this latter aspect, the reader is referred to the discussion in Section 7.8. Finally, averaging of successive

spectra is a powerful tool for achieving a substantial reduction of detection limits in spite of long-term baseline drifts of the spectrometer.

As another important fundamental spectroscopic application, this setup was used by Kassi and co-workers for detecting very weak first-overtone electric quadrupole transition of H_2 [12] and D_2 [167]. These simplest neutral molecules are a fascinating and highly significant testbed for *ab initio* quantum-electrodynamics, and the experimental line positions and intensities were in very good agreement with the calculated values.

With a CW-CRDS setup similar to the one discussed above, yet using an active temperature stabilization of the ring-down cavity and an Invar baseplate for mounting the optical setup to limit thermo-mechanical drifts (cf. Chapter 7), Huang and Lehmann have demonstrated the detection of methane traces in nitrogen at a sub-parts-per-billion level near 1650 nm, based on a careful analysis of residual cavity-loss drifts and an optimal choice of averaging times [168].

5.3 Frequency-stabilized CRDS

As discussed in the last section, absorption measurements by CW-CRDS can be staggeringly precise. Furthermore, as the fundamental relation (5.1) of CRDS gives direct access to the absorption coefficient, this precision can be turned into accuracy without external calibration, provided that systematic bias sources are carefully avoided (see Chapter 7).

However, *a priori*, this high precision and accuracy only concerns one of the two dimensions of absorption spectroscopy, while the stability and linearity of the spectrometer frequency axis is just as crucial for retrieving accurate absorption line shapes and line strength measurements. This issue has first been addressed by Hodges and co-workers in their pioneering contribution [140] by referencing the ring-down cavity mode frequencies to a stable external reference, introducing what they called a frequency-stabilized cavity ring down spectrometer (FS-CRDS).

The crucial innovative feature of this setup was a ring-down cavity with dichroic mirrors, providing a high-finesse window with $1-R < 1.5\cdot10^{-5}$ around 935 nm for CRDS measurements with an external cavity diode laser (ECDL) [140, 169], and a low-finesse region at 633 nm with $R = 0.95$ for locking a TEM_{00} cavity resonance to a frequency-stabilized Helium-Neon (HeNe) laser by means of a first-derivative approach using phase-sensitive detection in cavity transmission (see [170], for instance). This HeNe-laser-based frequency stabilization scheme is depicted on the left of Fig. 5.4. An acousto-optic modulator in the HeNe laser beam path before injecting the cavity was used for generating the laser frequency modulation needed for phase-sensitive detection. In addition, the AOM adds frequency-tunability to the spectrometer by inducing cavity-length changes by the servo loop, thus conferring an essentially arbitrary frequency tunability to the setup within the precision of the HeNe reference laser. In practice, its stability was found to be better than 1 MHz over 24 h by means of a comparison to an iodine-stabilized HeNe laser.

An early application of FS-CRDS consisted in precision measurements of H_2O lines near 925 nm [171], harnessing the stability and linearity of its frequency axis for detecting subtle line-shape effects beyond the Voigt profile and for retrieving accurate pressure broadening and shifting coefficients (cf. Section 8.1.2). An example spectrum from this study is shown on the right of Fig. 5.4. Its inset b) shows that a saturated-absorption Lamb dip could be discerned at the center of a water line at Pa-level pressures by using sub-MHz laser frequency stepping. Related studies will be discussed in more detail in Section 9.1.

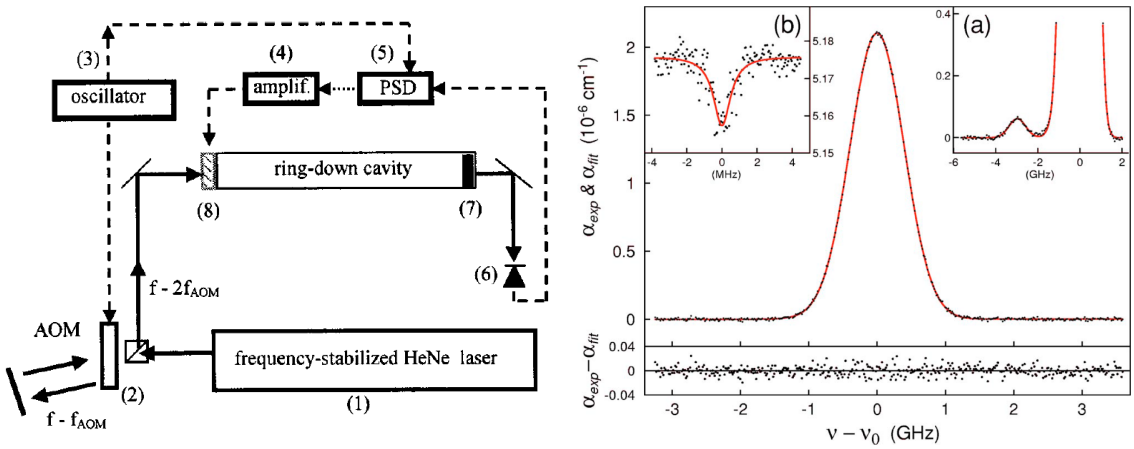

Figure 5.4 Left: Schematic sketch of the ring-down cavity length stabilization scheme in the first realization of FS-CRDS by Hodges and co-workers [140]. Adapted from [140] (Figure 1). Right: FS-CRDS spectrum of the water absorption line at 10687.3621 cm^{-1} measured by Lisak and co-workers [171]. The insets show a saturated-absorption Lamb-dip at the line center and a weak neighboring transition, respectively. Adapted from [171] (Figure 1).

The technique being used for a broad range of fundamental and sensing applications [172], FS-CRDS performance was further improved in the course of time, yielding notably a detectivity of $2.5 \cdot 10^{-10}\,\mathrm{cm}^{-1}/\sqrt{\mathrm{Hz}}$, as characterized by an Allan-Werle analysis [173]. In this study, weak oxygen quadrupole transitions near 765 nm were measured and a detection limit down to $1.8 \cdot 10^{-11}\,\mathrm{cm}^{-1}$ was demonstrated by averaging 100 successive spectra.

In these recent FS-CRDS experiments, ring-down events were obtained by a loose locking of probe laser frequency to cavity TEM_{00} resonances [169]. The scheme was based on maximizing the incidence of transmission events due to the noisy high-finesse cavity injection [130] by the MHz-level linewidth ECDL laser. For obtaining a transmission-event histogram, triangular ECDL frequency sweeps were employed, covering first broad, then narrow frequency intervals around the cavity mode. In this fashion, robust frequency tuning and ring-down event generation were achieved, essentially equivalent to conventional CW-CRDS setups. The absorption sensitivity of the spectrometer, however, remained impaired by the adverse effects of laser frequency jitter. With respect to this limitation, the full potential of a tight lock between laser and cavity for high repetition rates, low detection noise and high intracavity intensities for saturated absorption was already pointed out as a perspective in the original contributions on FS-CRDS [140, 169].

The first CRD spectrometer with a servo loop locking laser and ring-down cavity into resonance was realized years before by Paldus and co-workers [174]. They used the Pound-Drever-Hall (PDH) locking technique (see Section 2.4.3) to stabilize the length of a low-finesse ring-down cavity to the frequency of a continuous-wave ECDL. In particular, they used two orthogonal beam polarizations, one for maintaining a continuous PDH lock in spite of laser frequency tuning, and the other one for generating ring-down events for CRDS. In this fashion, the authors achieved ring-down repetition rates of 50 kHz at ring-down times on the order of 1 µs. A modified and optimized system using a narrowband CW Nd:YAG laser now locked to the cavity was realized by the same group [175]. To handle ring-down repetition rates of tens of kHz, a scheme based on logarithmic and differentiating amplifiers was used for a direct analog determination of ring-down times. At frequency scanning rates up to 500 MHz/s, the setup reached a long-standing record

detectivity of $10^{-12}\,\mathrm{cm}^{-1}/\sqrt{\mathrm{Hz}}$, and was used for measuring a CO_2 line in the narrow accessible spectral interval around 1064 nm.

Another CRD spectrometer with the probe laser tightly Pound-Drever-Hall-locked to ring-down cavity TEM_{00} resonance was realized by Martínez and co-workers [176]. Using a widely tunable CW Ti:Sa ring laser, they achieved typical ring-down repetition rates of 10 kHz and a detectivity of $1.4\cdot10^{-11}\,\mathrm{cm}^{-1}/\sqrt{\mathrm{Hz}}$. However, as for all the PDH-locked CRDS techniques discussed so far, no particular effort was made by Martínez *et al.* for stabilizing the length of the ring-down cavity itself, which defines the spectrometer frequency axis. By monitoring the integrator output of the PDH-servo loop on laser frequency, the authors estimated that their cavity resonance frequencies were subject to drifts on the order of 50 kHz/s.

Uniting the benefits of tight laser-cavity locking and cavity length stabilization, Cygan and co-workers have realized the initial vision of a Pound-Drever-Hall-locked FS-CRD spectrometer [177]. They used a 73-cm long cavity with dichroic mirrors for the HeNe reference laser at 633 nm and ring-down measurements around 687 nm with $1-R = 2.5\cdot10^{-4}$. The probe laser, a continuous-wave ECDL with a free-running linewidth on the order of 200 kHz, was modulated at 20 MHz by a free-space electro-optic modulator generating the phase modulation sidebands for PDH-locking. The resulting PDH error signal was fed to a fast commercial servo controller with 10 MHz bandwidth for narrowing the linewidth of the ECDL by tightly locking it to successive TEM_{00} cavity resonances. The authors demonstrated essentially flat cavity transmission traces with a noise level of a few percent, indicating a near-optimal transmission of light through the cavity. Figure 5.5 shows a comparison of ring-down event time series in the PDH-locked regime and for conventional FS-CRDS, respectively. The histogram-based loose lock of the probe laser to the cavity

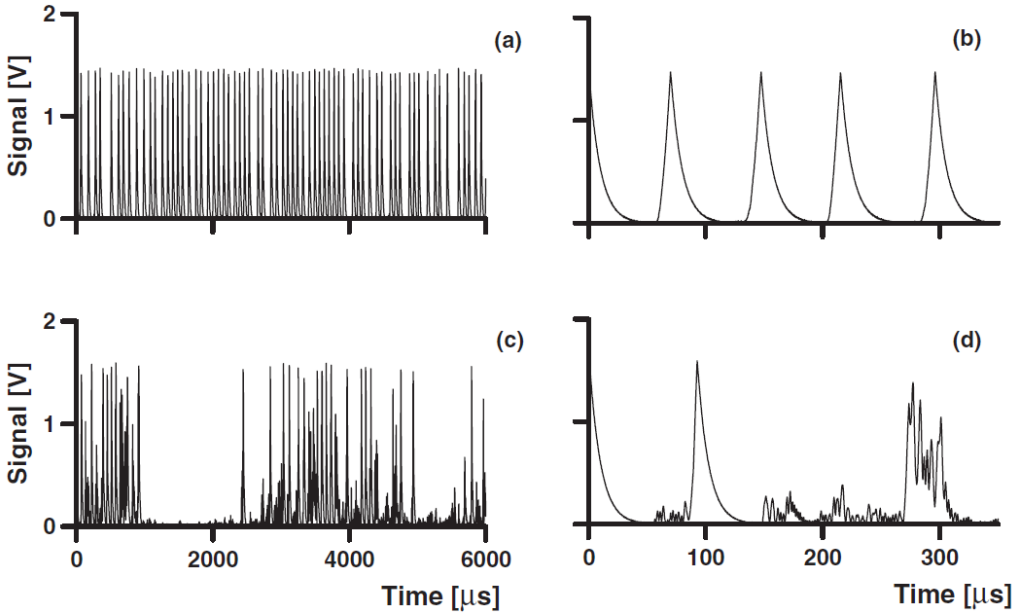

Figure 5.5 Comparison of ring-down acquisition in Pound-Drever-Hall-locked (panels a) and b)) and conventional (panels c) and d)) FS-CRDS experiments by Cygan and co-workers [177]. Note that a three times higher photodetection gain was used for the conventional FS-CRDS measurements. Adapted from [177] (Figure 6).

in classical FS-CRDS (panels c) and d)) leads to noisy cavity injection and, consequently, erratic ring-down triggering at random peak cavity transmission events. By contrast, the ring-down time series of the PDH-locked spectrometer (panels a) and b)) shows regular

ring-up and ring-down events at drastically improved repetition rates of up to 14 kHz. Together with the beneficial effect of higher cavity transmission on ring-down detection noise, this led to an enhancement of absorption detectivity to $7.5 \cdot 10^{-11}\,\mathrm{cm}^{-1}\sqrt{\mathrm{Hz}}$. As a demonstration in the original study [177], O_2 lineshape measurements with a single-scan signal-to-noise ratio on the order of 5000 were reported, three times better than in conventional FS-CRDS.

Employing this PDH-locked FS-CRDS setup in conjunction with the spectrum-averaging approach discussed in the preceding section, an unprecedented signal-to-noise ratio of 220,000 was demonstrated on absorption lineshape measurements in the O_2 band near 689 nm [178]. To this end, 1040 individual spectra were averaged over 33 h and two parasite fringes were fitted to the measured spectra. The minimum detectable absorption in this experiment was evaluated as $2.4 \cdot 10^{-11}\,\mathrm{cm}^{-1}$. A review of several PDH-locked FS-CRDS experiments is given in [179]. Recently, a comprehensive analysis of PDH-locked FS-CRDS lineshape measurements in the R-branch of the same O_2 band by means of a multi-spectrum fit procedure was carried out by Domysławska and co-workers [180]. Besides line parameters for several sophisticated line-shape models, the study also yielded 11 O_2 transitions with sub-MHz accuracy by referencing the PDH-locked FS-CRD spectrometer to an optical frequency comb. The emerging and rapidly developing fields of comb-assisted and comb-locked CRDS will be discussed briefly in the following section.

5.4 Recent trends in CRDS

Certainly falling short of completeness, the objective of this Section is to provide a succinct overview on some ongoing trends in CRDS with promising perspectives. For the sake of conciseness, the physical principles of these techniques will be presented without an in-depth discussion of their technical details, which would be beyond the scope of this thesis.

A first direction of development concerns the scanning speed of CW-CRDS, which is often considered slow with respect to other techniques, such as Fourier-transform infrared (FTIR) spectroscopy [181]. For CRDS, effective scanning speeds for low-noise, high-resolution spectra typically range from 1 [182] to $30\,\mathrm{cm}^{-1}$ [44] in one hour.

A drastically accelerated scanning scheme based on sideband-tuning with an electro-optic modulator (EOM) was introduced by Truong and co-workers [183]. For the original setup, which they called frequency-agile rapid-scanning (FARS) spectroscopy, the carrier frequency of a narrow-linewidth fiber laser was fixed at a stable offset to the cavity TEM_{00} mode by referencing it to a self-referenced optical frequency comb, while the cavity was stabilized against an iodine-referenced HeNe laser. Phase-modulation sidebands from the EOM are then resonantly injected into successive cavity TEM_{00} modes by changing the driving radio frequency from an ultrafast synthesizer with a bandwidth of 20 GHz and a switching time of 0.1 ms. This frequency-agile rapid-scanning scheme is illustrated on the left of Fig. 5.6. At a detectivity of $2 \cdot 10^{-11}\,\mathrm{cm}^{-1}\sqrt{\mathrm{Hz}}$, the original setup was used for a proof-of-principle study of CO_2 in ambient air, with a 2-s scan over a spectral interval of $2\,\mathrm{cm}^{-1}$.

In a follow-up study [184] using an external cavity diode laser (ECDL), the complex double-referencing to frequency comb and HeNe laser was simplified by directly PDH-locking the ECDL to the ring-down cavity. For obtaining a robust and tight lock in spite of rapid frequency scanning, an approach analogous to the one by Paldus *et al.* [174], discussed in the preceding section, was chosen. One linear polarization of the probe laser was always on for steady PDH-locking, reaching a relative linewidth between cavity and

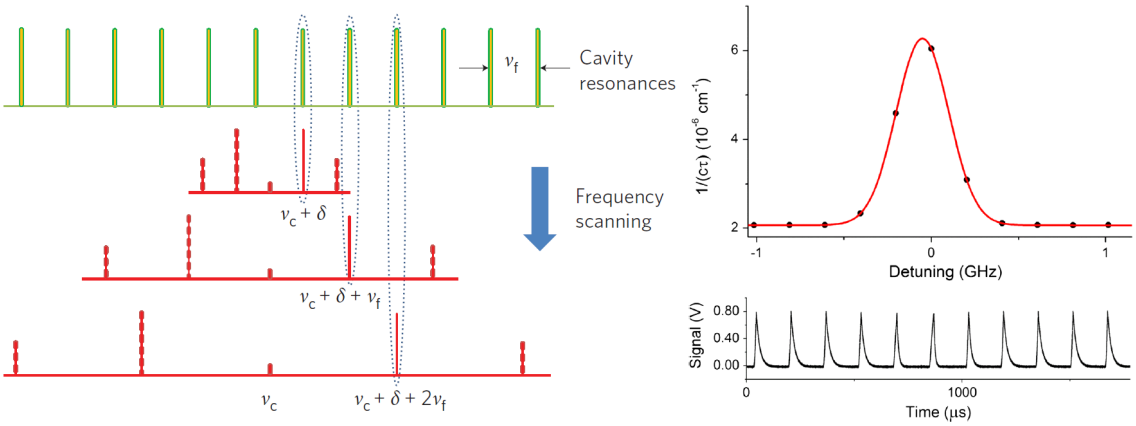

Figure 5.6 Left: Illustration of the working principle of frequency-agile rapid scanning cavity ring-down spectroscopy (FARS-CRDS) by Truong and co-workers [183]. Adapted from [183] (Figure 1). Right: CO_2 line spectrum at 6336.24 cm^{-1} (upper panel) measured by FARS-CRDS with an ECDL in 2 ms by Long *et al.* [184], by recording subsequent ring-down events (lower panel) at a frequency spacing of one cavity FSR[184]. Adapted from [184] (Figure 4).

ECDL of 130 Hz. The orthogonal polarization was used for rapid sideband frequency tuning and the generation of ring-down events. The potential of this approach is illustrated by the CO_2 spectrum on the right of Fig. 5.6, where the probe laser sideband was stepped from one TEM_{00} cavity mode to the next at each single ring-down event, thereby leading to a spectrum acquisition in only 2 ms. The detectivity of this ECDL-based FARS-CRDS scheme attained $2 \cdot 10^{-12}$ cm$^{-1}\sqrt{\text{Hz}}$.

While FARS-CRDS provides ultra-fast scanning on a narrow zone at a limited spectral resolution for time-critical applications such as trace gas monitoring at atmospheric conditions, broadband spectroscopy for fundamental molecular spectroscopy studies remain of prime interest. To extend the coverage of our ultra-sensitive CW-CRDS spectrometer at LIPhy (cf. Section 5.2) based on fibered DFB lasers between 1.25 and 1.7 µm with ever-increasing precision, a very similar spectrometer was developed with a fiber-coupled ECDL by Kassi and co-workers, covering a gap-free wavelength interval from 1.2 to 1.26 µm with a single diode [185]. Using an automated diffraction grating and pump current control, mode-hop free tuning over 0.8 cm^{-1} is achieved, and broadband spectra can be readily obtained by concatenating the individual mode-hop free scans. With ring-down times on the order of 200 µs, the spectrometer was used for measuring weak electric quadrupole transitions in the first rovibrational overtone band of H_2 at different pressures, in order to retrieve line positions and intensities, as well as pressure shift and collision-induced-absorption [186] coefficients.

The new setup was equally applied to a systematic broadband study of line positions and intensities in the 4-0 rovibrational band of CO from 8094 to 8317 cm^{-1} [187]. Compared to conventional CW-CRDS with DFB lasers at a linewidth of about 2 MHz, the new setup evidently benefits from the improved light injection of the 100-kHz linewidth ECDL into the cavity with a finesse well over 100000. The resulting lower photodetection noise allowed a spectrometer baseline detection limit of $5 \cdot 10^{-12}$ cm^{-1} to be reached on a regular basis at a typical frequency stepping resolution of 25 MHz, which corresponded to a tuning speed on the order of 16 cm^{-1}/h. In the future, the spectral coverage of this scheme is expected to be further expanded by exchanging the 1.2-µm laser diode currently installed in the commercial ECDL module.

Let us now turn to conceptually intriguing techniques which replace or complement ring-down time measurements by a spectroscopic characterization of the TEM_{00} mode structure of the ring-down cavity itself. While these approaches cannot qualify as CRDS techniques strictly speaking, they are nevertheless highly related by the fundamental principles of Fourier transformation and the Kramers-Kronig relations, which link absorption and dispersion and follow from electromagnetism and causality [188–190].

The first of these approaches is based on the fact that the width Γ of a cavity mode is related to the ring-down time τ of a light field in that mode by

$$\tau = \frac{1}{2\pi\Gamma} \tag{5.20}$$

This relation can be deduced from Eqs. (2.36), (2.32) and (5.4) and corresponds to the fundamental equivalence of a description of ring-down signals in the time-domain or by the cavity mode structure in the frequency domain, linked by Fourier transformation. The mode width Γ can be determined experimentally by measuring and fitting the Airy-shaped cavity transmission spectrum (2.34), which reduces to a Lorentzian (2.35) in the high-finesse limit. Then, the ring-down time τ of this mode can be retrieved according to Eq. (5.20) and the circle to CRDS closes. This is the principle of cavity mode-width spectroscopy (CMWS). Following an initial proposal and proof-of-principle demonstration by Long and co-workers in their contribution on ECDL-based FARS-CRDS discussed above [184], the technique was explicitly introduced and studied by Cygan and co-workers [191]. Its principle and the experimental setup are illustrated in Fig. 5.7.

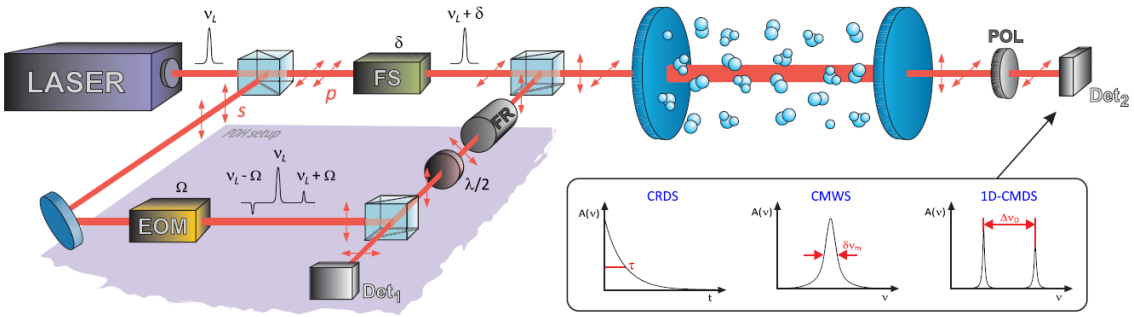

Figure 5.7 Schematic sketch of an experimental setup by Cygan *et al.* [192], which can be used for cavity ring-down (CRDS), cavity-modewidth (CMWS) and one-dimensional cavity-mode dispersion spectroscopy (CMDS). Adapted from [192] (Figure 3).

The cavity length was stabilized to a HeNe laser as in the FS-CRDS experiments discussed in the preceding section. An external cavity probe laser is tightly PDH-locked to a TEM_{00} mode of the cavity using one linear polarization. The cavity mode spectrum is then measured using the orthogonal polarization and an acousto-optic modulator as a frequency shifter for tuning through adjacent TEM_{00} cavity modes while recording the resulting transmission signal.

The same measured cavity transmission signal can be equally used for one-dimensional cavity-mode dispersion spectroscopy (1D-CMDS). This second technique, which was first realized by Cygan and co-workers [192], is also illustrated in Fig. 5.7. The approach here is even more radical in that it reduces the full information of an absorption spectrum to the measurement of only one physical quantity, namely the frequency of cavity TEM_{00} modes. An absorption of the intracavity sample is accompanied by a dispersion of its refractive index which is governed by the Kramers-Kronig relations [58, 188–190]. They state that absorption and dispersion are fully equivalent quantities, so that knowledge of one implies

knowledge of the other. The local cavity free spectral range, that is the spacing between successive TEM_{00} modes of the cavity can also be determined from the measured cavity transmission spectrum discussed above. As the dispersion of cavity mode frequencies has a characteristic first-derivative shape with respect to the absorption signal, the difference between mode locations follows a second-derivative behavior. Plotting these frequencies differences against the absolute optical mode frequencies thus yields a spectrum with two frequency axes. Let us underscore again that this dispersive frequency-frequency spectrum is fundamentally equivalent to the absorption spectrum as measured by CRDS.

The performance of the different techniques was compared on a CO absorption line at $6201\,\mathrm{cm}^{-1}$, achieving a ratio of peak absorption to root-mean square fit residuals of roughly 10200 for CRDS, 7200 for CWMS and 1600 for CMDS. Line intensities and collisional broadening from fitting the CMW spectrum were in good sub-percent agreement with CRDS-based values. After resolving PDH-lock-point-related issues, CMDS-based fit parameters showed percent-level agreement with CRDS. Due to the stronger profile-dependency of fit parameters in dispersive spectra, this already constituted a remarkable agreement between dispersive and absorptive spectra in practice. Holding the promise of further performance improvements, the main challenge to CMWS and CMDS is the time-consuming measurement procedure which requires the measurement of one narrowband cavity transmission spectrum for each single point of the absorption spectrum. Nevertheless, beyond their unarguable conceptual appeal, the techniques have intrinsic advantages, such as a reduced sensitivity to detection nonlinearities (cf. Section 7.3) in CMDS, for instance. CMWS is complementary to CRDS in that it avoids the need for measuring very short decays at high absorptions, which lead to dramatically increased noise levels according to Eq. (6.35) and raise bandwidth issues (cf. Section 7.4). In CMWS, broadening of cavity modewidths at high absorption help precision and partially balance the loss of cavity transmission intensity. Consequently, it could be an interesting perspective to use a CMWS approach at very high absorption levels to increase the dynamic range of the OFFS-CRD spectrometer presented in the following chapter to well beyond the 10^6 mark.

The revolution of frequency metrology brought about by the emergence of self-referenced optical frequency combs, as discussed in Section 2.5, has also fostered a broad range of experimental developments in molecular spectroscopy in general, and in CRDS in particular.

A first important group of CRDS techniques with an optical frequency comb can be qualified as comb-assisted in that they combine a conventional spectroscopy scheme with an absolute referencing of the spectrometer axis to the optical frequency comb. In this manner, such techniques can provide spectral line data of unprecedented frequency accuracy, for databases and semi-empirical effective Hamiltonian models and for validating state-of-the-art computational physics studies based on first principles, for instance.

Comb-assisted, PDH-locked FS-CRDS was first reported by Domysławska and coworkers, with the experimental setup shown in Fig. 5.8. The spectroscopic part corresponds to the one discussed in the previous section. The absolute frequency measurement is accomplished according to the procedure laid out in Section 2.5, using the beat note of frequency comb and probe laser as well as a wavemeter-based approximate frequency reading for the latter. A very similar experimental scheme was used by Truong and coworkers for an absolute CO_2 transition frequency measurement at 1.57 µm with a combined uncertainty of 9 kHz [193]. The comb-assisted PDH-locked FS-CRDS CO_2 frequency measurements near 1.6 µm by Long *et al.* [194] will be discussed in detail in Article 6 on page 192.

In parallel to the realization of the comb-assisted OFFS-CRD spectrometer devel-

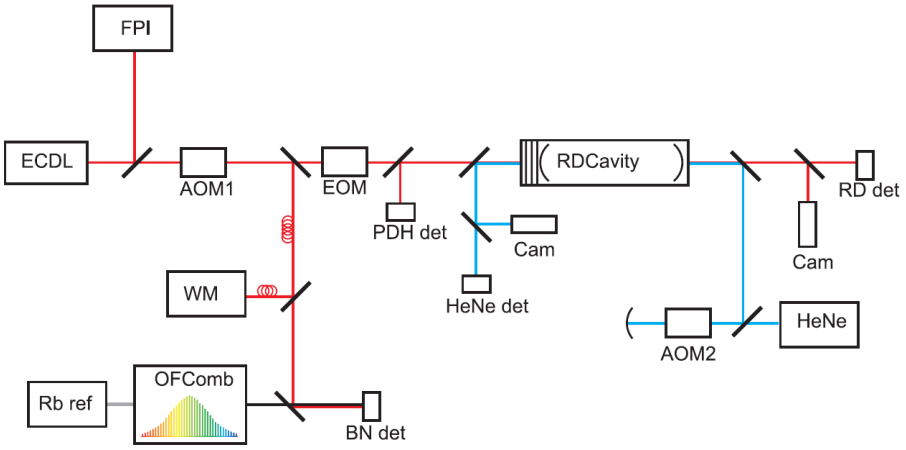

Figure 5.8 Schematic of comb-assisted, Pound-Drever-Hall-locked FS-CRDS by Domysławska *et al.* [180]. Blue light paths on the right: HeNe-laser-based cavity length stabilization and tuning using an acousto-optic modulator (AOM2). Red light paths: External-cavity diode probe laser (ECDL), PDH-locked to ring-down cavity and frequency-monitored by means of a wavemeter (WM) and the optical frequency-comb beat note (BN). Adapted from [180] (Figure 1).

oped in the framework of this thesis (see Chapter 9), the classical DFB-based CW-CRDS experiments at LIPhy were adapted for a comb-assisted absolute frequency calibration by Mondelain and co-workers [195]. To this end, a portion of probe laser light was superposed with an automatedly grating-selected portion of a self-referenced frequency comb. The resulting beat notes combined with a wavemeter reading provided measurements of the instantaneous absolute frequency of the noisy DFB laser at a refresh-rate of 3 kHz. Compared to high-bandwidth locking approaches, this conceptually simple on-the-fly frequency-calibrated ring-down acquisition scheme provides a straightforward upgrade for existing CW-CRDS spectrometers, while preserving easy broadband tunability on an absolute frequency axis. The technique was used for an extensive survey study of the absorption spectrum of CO between 6173 and 6418 cm^{-1}. With a detectivity of $1 \cdot 10^{-11}\,\mathrm{cm}^{-1}/\sqrt{\mathrm{Hz}}$, absolute line center frequencies could be measured at line strengths below $10^{-28}\,\mathrm{cm/molecule}$, including lines from hot bands and minor isotopologues. The transition frequencies in the main 3-0 overtone band of $^{12}\mathrm{C}^{16}\mathrm{O}$ were retrieved with an average line center accuracy of 300 kHz up to rotational quantum numbers over 30.

Comb-locked CRDS, which is a distinctly different approach to CRDS with absolute frequency calibration, was recently introduced by Gatti and co-workers [196]. In CL-CRDS, an ECDL probe laser is stabilized to a tooth of a self-referenced frequency comb by means of a feed-forward coincidence locking scheme using an acousto-optic modulator (see Chapter 4). Consequently, the absolute frequency comb itself becomes the clock for the whole spectroscopic setup. Frequency tuning is accomplished by slightly varying the comb repetition rate using an RF synthesizer while keeping the probe laser feed-forward-locked. Finally, an FPGA-controlled PZT-tracking scheme is used for loosely locking the ring-down cavity length to resonance with the probe laser. In this manner, an absolute CRDS frequeny axis is accomplished without a HeNe laser for cavity length stabilization, as in FS-CRDS, or a real-time frequency monitoring of laser jitter, as in the on-the-fly calibration scheme discussed above. The single-scan absorption detection limit of the first CL-CRDS setup was found to be $5.7 \cdot 10^{-11}\,\mathrm{cm}^{-1}$. A full Allan-Werle analysis showed that an intrinsic detectivity of $3.9 \cdot 10^{-12}\,\mathrm{cm}^{-1}/\sqrt{\mathrm{Hz}}$ was impaired by short-term drift mechanisms of unknown origin. As a spectroscopic application testing instrument performance, a CO_2 line at 1.57 µm was measured with a combined uncertainty of 3 kHz, thus

independently confirming the value measured by Truong *et al.* [193].

Without going into any detail, let us still mention the interesting developments in CRDS schemes based on fiber-optic resonators made from optical fibers and directional couplers. Proof-of-principle experiments on bend-induced fiber loss and absorption in solutions [197, 198] as well as magnetic field sensing [199] were carried out both in more conventional time-domain measurement configurations [197] and in spatial-domain ring-down schemes based on frequency-shifted interferometry [198, 199]. Typically, the evanescent wave around a narrow fiber taper inside the fiber resonator is used for probing the absorption of a sample outside the taper. While the detectivity of fiber-resonator CRDS schemes generally falls short of free-space CRDS performance by many orders of magnitude due to high intrinsic losses, these techniques have application perspectives based on their compactness, low cost and the possibility for extreme resonator lengths well beyond the km-level with multiple sensors at different locations for spatially resolved distributed sensing.

For a discussion on ultra-high resolution CRDS techniques based on saturated absorption, the reader is referred to Section 9.1 in Part III dedicated to this topic.

Chapter 6

OFFS-CRDS - method, setup and automation

Designed for ultra-sensitive absorption spectroscopy with extreme frequency resolution and stability, OFFS-CRDS builds on the development of highly coherent single-sideband-tuned **O**ptical **F**eedback **F**requency **S**tabilized laser sources in particular, and on a broad fundament of powerful state-of-the-art **C**avity **R**ing-**D**own **S**pectroscopy techniques (cf. Chapter 5) in general.

To briefly summarize the objectives and principles of OFFS-CRDS, let us quote from Article 5 on page 160, which captures the essence of the new spectroscopic technique:

> In particular, OFFS-CRDS was designed to meet the following five intimately related requirements: (1) a sensitivity on a par with state-of-the-art CW-CRDS setups, (2) a highly stable and linear frequency axis, (3) the absence of excess absorption noise due to frequency jitter conversion on slopes, (4) an arbitrary frequency stepping resolution for resolving delicate features of advanced Doppler-broadened line shapes or even sub-Doppler features, and, in turn, (5) very high intracavity power for saturating even weak transitions in the near infrared. (1) and (5) call for the resonant excitation of a very high-finesse cavity which guarantees long, well-defined RD events and strong passive intracavity power amplification. (2) and (3) necessitate a highly stable optical length of the RD cavity, while (4) combined with (2) suggests working in the radio frequency (RF) domain, where sub-Hz frequency accuracy and resolution are readily achievable.
>
> Fulfilling all five conditions, our approach consists in tightly locking a high finesse RD cavity to a sub-kHz linewidth stable laser finely tunable by means of electrooptic single-sideband modulation. Among the key elements of this setup are the optical feedback frequency-stabilized laser using a highly stable V-shaped reference cavity and single-sideband modulation with a dual-parallel Mach-Zehnder modulator (MZM), as well as a modified fibered Pound-Drever-Hall-locking scheme for tight locking of a high-finesse RD cavity. These methodological advances provide high cavity transmission for low-noise photodetection and guarantee an unbroken stability transfer chain from the V-shaped reference cavity to the absorption spectrum frequency axis.

Before moving on to specific technical and experimental details on the ring-down cavity design for OFFS-CRDS, its temperature stabilization and vacuum system, MZM-tuning as well as data processing and experimental automation, let us begin with the article OFFS-CRDS was first reported in.

6.1 Article 4 - Optical feedback frequency-stabilized cavity ring-down spectroscopy

After a general introduction, the following article [200] begins with a description of the experimental setup for OFFS-CRDS, with a particular focus on Mach-Zehnder-modulator-based single-sideband frequency tuning. Then, Pound-Drever-Hall locking of the ring-down cavity and the automation of the experimental setup are discussed. Characterizing the quality of ring-down acquisition, experimental ring-down fit residuals are presented subsequently. The precision of ring-down measurements is characterized in terms of an Allan plot, and a broadband spectrum of CO_2 near 1.6 µm is reported as a first application in molecular spectroscopy. Characterizing the detection limit of the technique, a detailed analysis of the spectrometer baseline structure is conducted in view of parasite fringes. The article concludes on two further proof-of-principle applications, namely the study of an absorption line profile with high signal-to-noise ratio and the observation of a saturated absorption Lamb dip.

In complement to Fig. 1 of the following article, a more comprehensive schematic of the experimental setup for OFFS-CRDS is provided in Fig. 1 of Article 5 on page 160. Some readers may prefer reading Articles 4 and 5 consecutively before moving on to the technical and experimental details in the following sections of this chapter.

Optical feedback frequency stabilized cavity ring-down spectroscopy

Johannes Burkart,[1,2] Daniele Romanini,[1,2] and Samir Kassi[1,2,*]

[1]*Université Grenoble Alpes, LIPhy, F-38000 Grenoble, France*

[2]*CNRS, LIPhy, F-38000 Grenoble, France*

**Corresponding author: samir.kassi@ujf-grenoble.fr*

Received April 18, 2014; revised June 23, 2014; accepted July 2, 2014;
posted July 3, 2014 (Doc. ID 210508); published August 6, 2014

We introduce optical feedback frequency stabilized cavity ring-down spectroscopy (OFFS-CRDS), a near-shot-noise-limited technique that combines kilohertz resolution with an absorption detection sensitivity of 5×10^{-13} cm^{-1} Hz$^{-1/2}$. Its distributed feedback laser source is stabilized to a highly stable V-shaped reference cavity by optical feedback and fine-tuned by means of single-sideband modulation. The stability of this narrow laser is transferred to a ring-down (RD) cavity using a new fibered Pound–Drever–Hall (PDH) locking scheme without a dedicated electro-optic phase modulator, yielding several hundred RD events per second. We demonstrate continuous coverage of more than 7 nm with a baseline noise of 5×10^{-12} cm^{-1} and a dynamic range spanning six decades. With its resonant intracavity light intensity on the order of 1 kW/cm^2, the spectrometer was used for observing a Lamb dip in a transition of carbon dioxide involving four vibrational quanta. Saturating such a weak transition at 160 μW input power, OFFS-CRDS paves the way to Doppler-free molecular overtone spectroscopy for precision measurements of hyperfine structures and pressure shifts.

OCIS codes: (300.6190) Spectrometers; (300.6320) Spectroscopy, high-resolution; (300.1030) Absorption; (300.6260) Spectroscopy, diode lasers; (300.6390) Spectroscopy, molecular; (300.6460) Spectroscopy, saturation.
http://dx.doi.org/10.1364/OL.39.004695

Continuous-wave cavity ring-down spectroscopy (CW-CRDS) [1] is a widely used, powerful tool for ultrasensitive laser absorption spectroscopy. It yields the absorption coefficient α of a sample in an optical cavity in terms of the cavity exponential decay time τ as $\alpha c = \tau^{-1} - \tau_0^{-1}$, where c is the speed of light and τ_0 is a baseline incorporating mirror transmission and losses as well as scattering and diffraction losses. By combining the benefits of cavity enhanced light-matter interaction with the precision of time-domain based measurements, CW-CRDS is capable of achieving detection limits down to a few 10^{-13} cm^{-1} [2]. In recent years, frequency stabilized CRDS techniques [3,4] have responded to a growing need for unbiased high-precision measurements of both shape and integrated area of molecular absorption lines. Applications of absorption line metrology include comparison with *ab initio* line shapes [5,6] and intensities [7] and measurement of isotopic ratios highly relevant to environmental sciences [8,9], as well as fundamental measurements, for instance, a redetermination of the Boltzmann constant [10,11] in view of the imminent redefinition of the Kelvin. Recent advances [12,13] achieving cavity-mode-width-limited apparatus functions on the order of 10 kHz underline the significant interest in the development of ultrasensitive ring-down (RD) spectroscopy techniques with high frequency stability. In this Letter, we introduce a conceptually different experimental approach: optical feedback frequency stabilized CRDS (OFFS-CRDS). It features a unique combination of kilohertz frequency resolution and stepping, shot-to-shot RD time fluctuations as low as 1.5×10^{-5}, and kW/cm^2 level intracavity light intensity.

In OFFS-CRDS, the RD cavity length is stabilized to resonance with the laser source using a modified fibered Pound–Drever–Hall (PDH) locking scheme. The laser derives its frequency stability from a highly stable V-shaped reference cavity, to which it self-locks by optical feedback. Arbitrarily fine, adaptive tunability is accomplished using optical single-sideband modulation [14]. Thanks to this direct stability transfer chain, the RD cavity length is referenced to the highly stable V-shaped cavity. Consequently, the frequency axis linearity of OFFS-CRDS is not affected by optical path length changes induced by absorption features according to the Kramers–Kronig relations.

The experimental setup for OFFS-CRDS is depicted in Fig. 1. A distributed feedback diode laser emitting between 1608 and 1616 nm is optical feedback locked to an evacuated, temperature stabilized, ultralow-expansion glass and Super Invar composite V-shaped cavity with a free spectral range of 491.38 MHz and a finesse in excess of 2×10^5. This laser source with sub-kilohertz linewidth and drift rates below 20 Hz/s is discussed in detail in [14]. The laser locks to successive modes ν_n of the V-shaped cavity when its current or temperature is changed. This coarse frequency tuning is complemented by frequency shifting over more than 1 GHz with millihertz accuracy by means of a fibered Mach–Zehnder modulator (MZM) working as an optical single-sideband frequency shifter [14].

In addition to arbitrarily fine-tuning, using a MZM has two further important benefits for CRDS. First, RD events can be triggered using a fast switch cutting the MZM driving radio frequency (RF) ν_{RF} to −80 dB within 20 ns. This is a significant improvement on conventionally used acousto-optic modulators, whose inferior extinction ratio and switching bandwidth may degrade the quality of RD measurements [15]. Second, phase modulation (PM) sidebands on the frequency shifted MZM output can be generated by supplying a phase modulated RF carrier at the MZM input. Therefore, the modified PDH scheme we propose (Fig. 1) goes without an additional electro-optic modulator. The beam reflected by the RD cavity is detected with a fibered photodiode using a

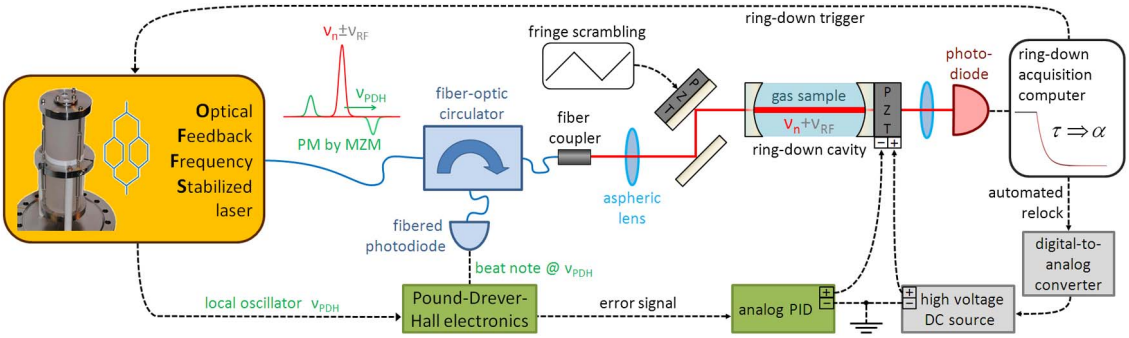

Fig. 1. Experimental setup for OFFS-CRDS. The laser source is optically locked to a highly stable V-shaped reference cavity and fine-tuned using single-sideband modulation [14]. Curved lines, polarization-maintaining optical fibers; straight lines, laser beam; dashed lines, electrical signals.

fiber-optic circulator. Its return loss around −50 dB generates an optical fringe. This parasite etalon can be averaged out by rapidly varying circulator-cavity distance with a piezoelectric transducer (PZT)-mounted steering mirror. A PDH local oscillator frequency ν_{PDH} around 400 kHz was chosen in order to minimize electronic noise and RF parasite radiation. The resulting error signal is used to control the RD cavity length by moving the output mirror mounted on a PZT. The latter is glued on a massive 33 cm long aluminum hollow cylinder of 50 mm outer and 8 mm inner diameter. For tuning this cavity into resonance with the laser, a relative stability on the PZT high voltage (HV) supply on the order of the inverse RD cavity finesse $F \asymp 450,000$ is needed. This criterion has been met by means of the split voltage driving scheme shown in Fig. 1. Two signals with a common ground are connected to the PZT: a DC offset from a homemade low-noise HV source controlled by an optocoupled digital signal, and a component from a commercial analog servo controller with a bandwidth of 7 kHz.

The OFFS-CRDS spectrometer is fully automated using a LabVIEW program. For instance, PDH lock of the RD cavity onto the laser is automatically acquired within a fraction of a second and maintained by updating the appropriate DC voltage offset on the PZT. This robust lock is not perturbed by switching off the laser at kilohertz rates for generating RD events. Laser current and temperature changes are synchronized with MZM driving RF steps for frequency tuning, while reference cavity mode jumps are counted using a 60 MHz resolution Michelson-type wavemeter. RD events are triggered, acquired, and fitted in real time with adaptive acquisition parameters. The spectrometer can thus operate completely autonomously and is able to realize broadband scans with adaptive resolution, as well as long-term averaging of spectra over several days.

RD events are recorded at 650 kHz sampling rate using an 18-bit analog-to-digital converter (ADC). Its 13 μV RMS noise level is evidenced by the tail of the exponential fit residuals shown in Fig. 2.

Long-term averaging of successive fit residuals reveals an underlying static pattern, which does not change with increasing averaging time. It is therefore attributed to ADC nonlinearity and its amplitude is well within the acquisition card specification. The front part of single event fit residuals exhibits an exponential noise envelope decaying at twice the RD time. It is due to photon shot noise and constitutes the quantum limit for the definition of a RD signal. The two RD noise components together determine the measurement precision, which can be characterized in terms of an Allan plot [16]. The result is shown in Fig. 3, derived from the RD time series depicted in the inset. At 260 RD events per second, the absorption Allan deviation without any etalon scrambling reaches 1.9×10^{-13} cm^{-1} after 1 s by averaging down as white noise, within a factor of 1.5 from the fundamental shot-noise limit as given by analytical error propagation in an ideal exponential fit. The remaining difference is due to ADC noise (Fig. 2). During fringe scrambling, 518 RD events per second are reached, as a shorter RD acquisition time can be chosen without increasing shot-to-shot fluctuations. This is the realistic case for spectroscopic scans, as varying frequency reveals the circulator-cavity etalon. The result shows that this fringe is averaged out efficiently by varying the corresponding distance. The averaging behavior is well understood by means of a Monte-Carlo-type simulation, which gives the Allan deviation for virtual RD events (red curve), taking into account the relevant experimental values, such as RD repetition rate, scrambling frequency, and fringe amplitude, for instance. The resulting detection sensitivities with and without etalon scrambling are 5×10^{-13} cm^{-1} Hz$^{-1/2}$ and 1.9×10^{-13} cm^{-1} Hz$^{-1/2}$, respectively.

As a first spectroscopic application and performance test, the broadband spectrum of 10 Pa of CO_2 shown

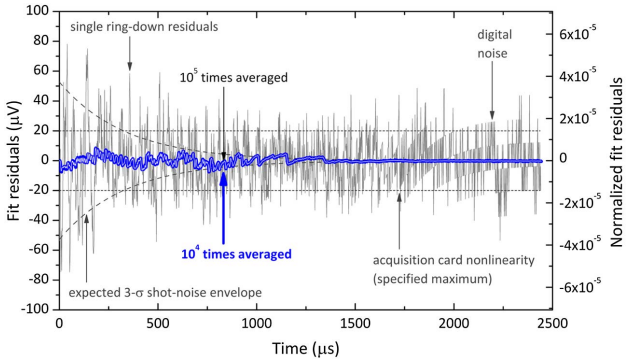

Fig. 2. Exponential fit residuals of a single RD event exhibit photon shot noise. Averaging over many residuals reveals an integrated acquisition card nonlinearity of a few parts per million.

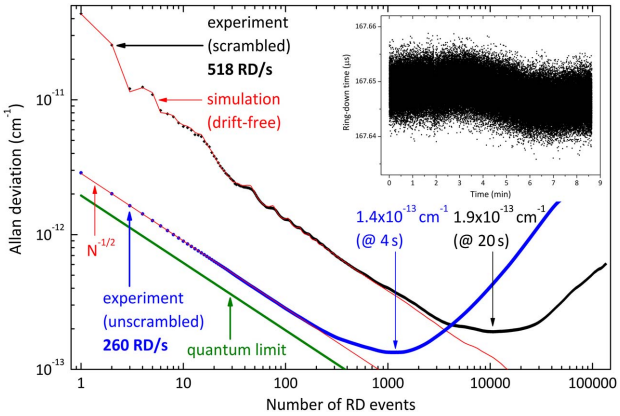

Fig. 3. Absorption measurement stability without modulation of the circulator-cavity distance is close to the fundamental shot-noise limit at short averaging times. The inset shows the corresponding RD time series. Absorption noise during circulator-cavity fringe scrambling averages out rapidly in a characteristic manner shown by the simulated line.

in Fig. 4 was recorded during a 17 h scan with 2.5 s averaging time per point. It features a spectral coverage of 28.5 cm^{-1} with a baseline RMS absorption noise around 5×10^{-12} cm^{-1}. The strongest measured absorption of 3.4×10^{-6} cm^{-1} therefore accounts for a dynamic range of 7×10^5. A rigorous baseline structure analysis revealing residual etalon effect contributions is vital for retrieving unbiased line parameters and uncertainties [17]. Therefore, the cavity was evacuated to record the line-free baseline section shown in the upper panel of Fig. 5. The Fourier transform of the linearly corrected baseline reveals a parasite etalon between photodiode and RD cavity and a residual contribution from the scrambled circulator-cavity fringe. Integrating over the corresponding sections of this absorption noise power spectral density (PSD) (lower panel of Fig. 5) shows that the two fringes represent one-half and one-quarter, respectively, of the total 2×10^{-23} cm^{-2} absorption baseline variance. Their amplitude scales with the inverse cavity finesse. This is an important advantage of high-finesse-cavity-based methods compared to sensitive but low finesse techniques such as [18].

OFFS-CRDS was used for studying the isolated line at 6214.5877 cm^{-1} in 2 Pa of CO_2. Figure 6 shows the profile recorded in a single 4 min scan with adaptive resolution, gradually increasing from 435 MHz on the baseline to

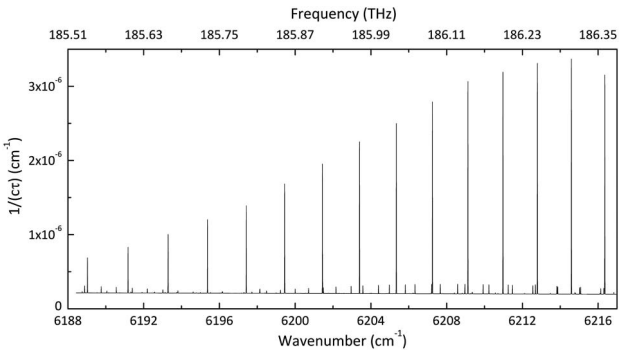

Fig. 4. Absorption spectrum of 10 Pa of CO_2 without any baseline correction recorded at frequency steps of 50 MHz.

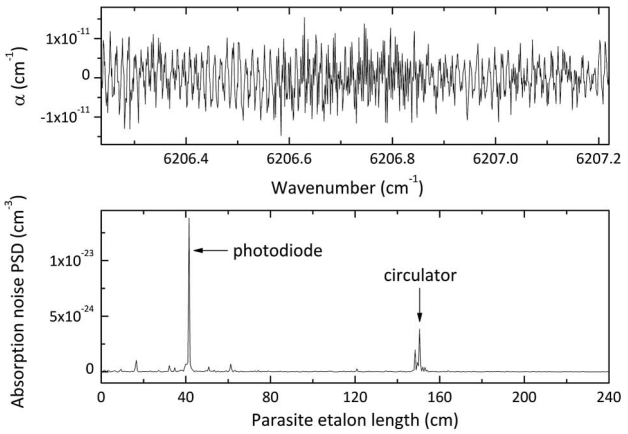

Fig. 5. Spectrometer baseline in the absence of absorption features recorded at frequency steps of 10^{-3} cm^{-1} after linear correction (upper panel). The corresponding absorption noise PSD reveals two interference fringes (lower panel). On the x axis, the frequency space period f of spectral components is expressed in terms of the corresponding etalon length $c/(2f)$.

10 MHz on top of the line. Even at this low pressure, the residuals from fitting with a Doppler profile reveal a clear w-shaped signature due to collisional broadening. This is correctly accounted for by a standard Voigt profile, which yields flat residuals corresponding to a single-scan signal-to-noise ratio (SNR) of 3×10^4, dominated by the excess noise from the shorter RDs at high absorption on the line center. Fitting with the Voigt profile yields a Doppler temperature of (295.96 ± 0.06) K, in good agreement with the RD cavity temperature stabilized at (296.1 ± 0.1) K.

Finally, at even lower pressure, the Lamb dip shown in Fig. 7 has been observed at the center of the same CO_2 line. The saturated absorption regime is attained with 160 µW input power yielding approximately 10 W resonant intracavity power (1 kW/cm^2). With an Einstein A coefficient of 7.3×10^{-3} Hz, the transition probed here is 2–4 orders of magnitude weaker than the ones measured in previous saturated CRDS studies [19,20]. The

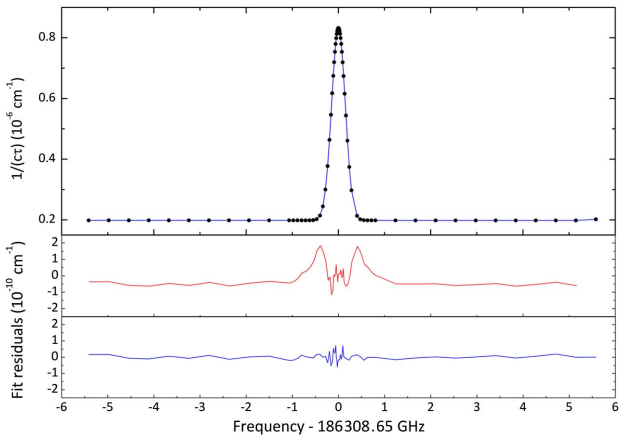

Fig. 6. Isolated $30^01(3) \leftarrow 00^00$ P(16) line in 2 Pa of CO_2 recorded with adaptive resolution. Upper panel: experimental data points and adjusted Voigt profile. Lower panel: fit residuals from fits with a Gaussian (top) and a Voigt profile (bottom).

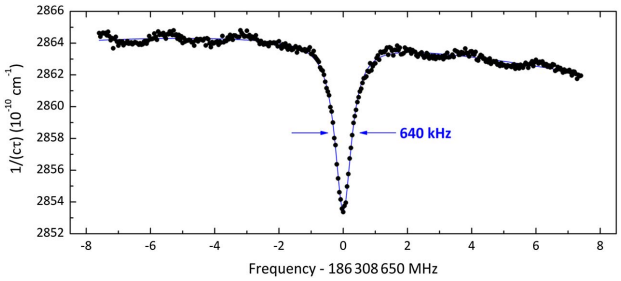

Fig. 7. Lamb dip on the $30^0 1(3) \leftarrow 00^0 0$ P(16) line of CO_2 at 0.25 Pa recorded at frequency steps of 40 kHz. Blue line: Lorentzian fit with quadratic baseline.

Lamb dip SNR of 50 allows a line center retrieval at 2 kHz precision for a measurement time below 1 min. The Lamb dip width is dominated by transit time broadening. The baseline tilt is due to an increase in CO_2 concentration by outgassing. To determine correct absorption coefficients from the nonexponential RDs in the saturated regime, a retrieval algorithm similar to the one in [20] must be adopted for future quantitative studies.

Summing up, OFFS-CRDS is a novel absorption spectroscopy technique approaching the fundamental shot-noise limit. It features a RD cavity that is tightly locked to a single-sideband-tuned laser stabilized to a highly stable V-shaped reference cavity. Reaching a detection sensitivity of 5×10^{-13} cm^{-1} Hz$^{-1/2}$, it opens up a multitude of direct application opportunities in various fields. To cite a few examples, broadband scans can be carried out to measure accurate line positions and intensities for comparison to *ab initio* calculations. Isolated absorption lines can be measured with adaptive resolution for testing state-of-the-art line-shape models and retrieving precision line parameters. Combining kilohertz resolution with high resonant intracavity power, OFFS-CRDS is ideally suited for studying sub-Doppler absorption features by saturating even weak molecular transitions. This should allow resolving hyperfine structures, retrieving pressure shifts with increased precision and, in a comb-assisted setup, making many new absolute optical frequency references available. Finally, with its small sample volume on the order of 10 ml and its footprint inherently below 1 m^2 and 50 kg, OFFS-CRDS holds a considerable potential for building highly sensitive, mobile instruments for field measurements of isotopic ratios for atmospheric and climate science.

This work was performed in the framework of Labex-OSUG@2020 (ANR10 LABX56) and was supported by Pôle SMINGUE (Université Joseph Fourier).

References

1. D. Romanini, A. Kachanov, N. Sadeghi, and F. Stoeckel, Chem. Phys. Lett. **264**, 316 (1997).
2. S. Kassi and A. Campargue, J. Chem. Phys. **137**, 234201 (2012).
3. A. Cygan, D. Lisak, P. Masłowski, K. Bielska, S. Wójtewicz, J. Domysławska, R. S. Trawiński, R. Ciuryło, H. Abe, and J. T. Hodges, Rev. Sci. Instrum. **82**, 063107 (2011).
4. D. A. Long, A. Cygan, R. van Zee, M. Okumura, C. Miller, D. Lisak, and J. Hodges, Chem. Phys. Lett. **536**, 1 (2012).
5. J.-M. Hartmann, H. Tran, N. H. Ngo, X. Landsheere, P. Chelin, Y. Lu, A.-W. Liu, S.-M. Hu, L. Gianfrani, G. Casa, A. Castrillo, M. Lepère, Q. Delière, M. Dhyne, and L. Fissiaux, Phys. Rev. A **87**, 013403 (2013).
6. P. Wcisło, A. Cygan, D. Lisak, and R. Ciuryło, Phys. Rev. A **88**, 012517 (2013).
7. A. Campargue, S. Kassi, K. Pachucki, and J. Komasa, Phys. Chem. Chem. Phys. **14**, 802 (2012).
8. D. Long, M. Okumura, C. Miller, and J. Hodges, Appl. Phys. B **105**, 471 (2011).
9. Y. Chen, K. K. Lehmann, J. Kessler, B. S. Lollar, G. L. Couloume, and T. C. Onstott, Anal. Chem. **85**, 11250 (2013).
10. C. Daussy, M. Guinet, A. Amy-Klein, K. Djerroud, Y. Hermier, S. Briaudeau, C. Bordé, and C. Chardonnet, Phys. Rev. Lett. **98**, 250801 (2007).
11. L. Moretti, A. Castrillo, E. Fasci, M. D. De Vizia, G. Casa, G. Galzerano, A. Merlone, P. Laporta, and L. Gianfrani, Phys. Rev. Lett. **111**, 060803 (2013).
12. G.-W. Truong, K. Douglass, S. Maxwell, R. van Zee, D. Plusquellic, J. Hodges, and D. Long, Nat. Photonics **7**, 532 (2013).
13. A. Cygan, S. Wójtewicz, J. Domysławska, P. Masłowski, K. Bielska, M. Piwiński, K. Stec, R. Trawiński, F. Ozimek, C. Radzewicz, H. Abe, T. Ido, J. Hodges, D. Lisak, and R. Ciuryło, Eur. Phys. J. Spec. Top. **222**, 2119 (2013).
14. J. Burkart, D. Romanini, and S. Kassi, Opt. Lett. **38**, 2062 (2013).
15. H. Huang and K. Lehmann, Appl. Phys. B **94**, 355 (2009).
16. P. Werle, R. Mücke, and F. Slemr, Appl. Phys. B **57**, 131 (1993).
17. S. Kassi, D. Romanini, A. Campargue, and B. Bussery-Honvault, Chem. Phys. Lett. **409**, 281 (2005).
18. P. Ehlers, I. Silander, J. Wang, A. Foltynowicz, and O. Axner, Opt. Lett. **39**, 279 (2014).
19. D. Lisak and J. T. Hodges, Appl. Phys. B **88**, 317 (2007).
20. G. Giusfredi, S. Bartalini, S. Borri, P. Cancio, I. Galli, D. Mazzotti, and P. De Natale, Phys. Rev. Lett. **104**, 110801 (2010).

6.2 Technical and experimental details

6.2.1 Ring-down cavity design

Striving for a tight Pound-Drever-Hall (PDH) lock of ring-down cavity length and an optimal noise level of the OFFS-CRD spectrometer, several cavity designs were planned, realized and tested in the framework of this thesis. First PDH-locking tests in [58] clearly indicated that the mechanical stability of a conventional ring-down cavity with breadboard-mounted mirrors was insufficient for achieving a robust and tight lock.

For illustrating the difficulty of the endeavor, let us recall that locking the CRDS cavity length onto the VCOF laser implies a resonance frequency stability on the order of the cavity modewidth $\delta\nu$. Rewriting $\delta\nu$ using the free spectral range definition (2.32), it can be translated into the associated cavity length stability δL according to Eq. (2.38), yielding the intuitive result

$$\delta L = -\frac{1}{F} \cdot \frac{\lambda}{2} \tag{6.1}$$

At $\lambda = 1.6\,\mu$m and with a cavity finesse $F = 450000$, this corresponds to

$$|\delta L| = 1.8\,\text{pm} \tag{6.2}$$

A substantial technical effort was required to meet this challenging criterion. The electronic part considering the piezo-electric actuator, on which the cavity end mirror was mounted, will be discussed in the following section.

Here, we shall focus on the considerations concerning the mechanical stability of the main body of the ring-down cavity. In view of the good experiences made with the V-shaped cavity mirror holders intrinsically aligned by precision machining (see Article 1 on page 32 and [58] for a detailed account), a massive monolithic cavity design with two mirrors tightly contacted to polished metal surfaces was chosen as the fundamental design principle. The most recent ring-down cavity we have designed and developed on this basis is shown in Fig. 6.1. The corresponding technical drawing is reported in Fig. 6.3. Aluminium was chosen as the cavity material for its ease of machining, rigidity and high thermal conductivity. The latter makes it compatible with stabilizing the ring-down cavity at a well-defined, uniform and stable temperature. This is crucial for many metrological applications of CRDS and will be discussed in more detail in Section 6.2.3. Consequently, the classical choice of stainless steel as a material was ruled out from the start on account of its poor thermal conductivity.

To first order, the cavity is a hollow cylinder with 76 mm outer diameter and 8 mm inner diameter. This massive body was chosen for enhancing the cavity's mechanical stability, and to provide it with a considerable thermal inertia enabling an efficient thermalization of the intracavity sample. The rather spacious central bore ensures that diffraction losses are completely negligible for light in the TEM_{00} cavity mode. On one side of the cavity, a half-inch mirror support is machined into the cavity bulk. The highly reflective front facet of the mirror is tightly contacted to a precision-machined polished aluminium surface. The mirror is held in this position by a Viton fluoroelastomer o-ring and a stainless steel disk tightened using four M3 $\times$ 0.5 screws. On the other side of the cavity, another Viton o-ring and a stainless steel disk tightened with four M2 $\times$ 0.4 screws provides the vacuum seal. Using the ultra-low-vapor-pressure epoxy resin TorrSeal, a stack-type piezoelectric actuator (PZT, Physik-Instrumente P-016.10H) is glued onto this disk. A two-part stainless steel mirror mount, in turn, is glued onto the other side of the stack PZT. The second mirror is contacted to the mount using another Viton o-ring tightened by a stainless steel ring. The completely mounted mirror-PZT assembly is shown in Fig. 6.2.

Figure 6.1 Most recent ring-down cavity machined in a monolithic aluminium cylinder. Mirrors, O-rings, adjustment screws and PZT-assembly are not yet mounted on this photography.

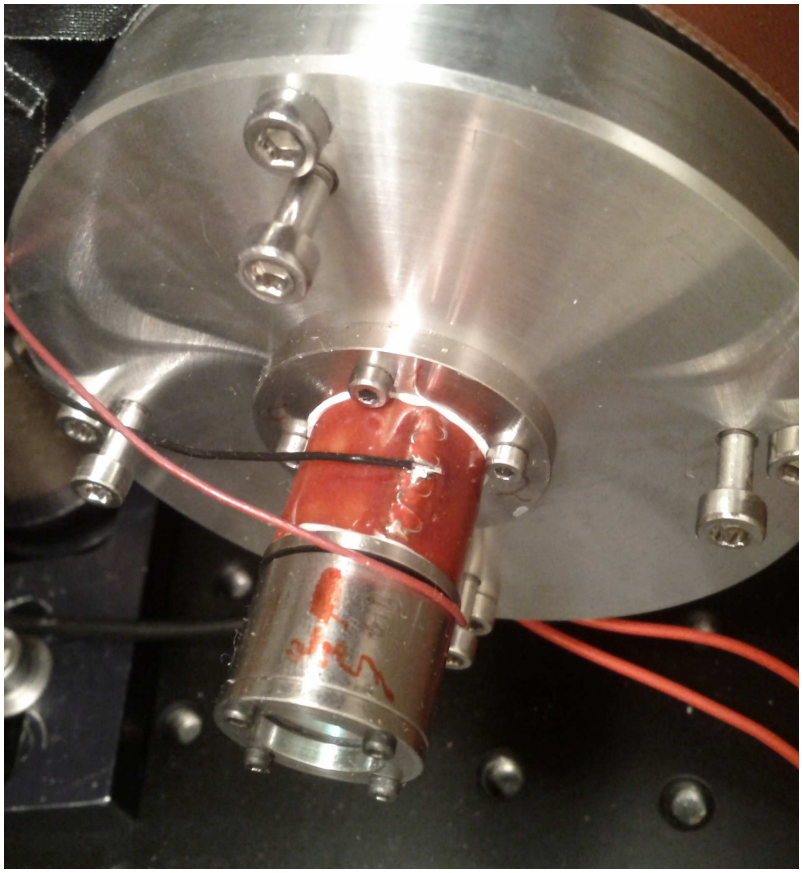

Figure 6.2 Fully mounted mirror-PZT assembly installed at cavity output. Eight mirror orientation adjustment screws are also visible.

One of the crucial features of this monolithic cavity is that it allows fine adjustments of mirror orientation. This is realized by cutting two 6-mm-deep trenches into the cavity bulk on a lathe, leaving a wall thickness of only 0.6 mm at the thinnest point. This creates two soft spots close to the mirror supports, which can be deformed using strong torques from 8 M3 $\times$ 0.5 adjustment screws on each side of the cavity, thereby enabling a slight

controllable mirror tilt with respect to the symmetry axis of the cavity. The adjustment screws on each side are organized in four pairs along two orthogonal axes, each pair containing one screw pushing outwards and one screw pulling inwards. The redundant degrees of freedom in this screw-based cavity deformation approach are useful in two ways. Firstly, they allow distributing the considerable forces occuring under deformation to several threads. Secondly, one can use them to apply forces acting in opposite directions, thereby efficiently freezing the deformation in its current state.

Since the first 15-cm-long cavity prototype, the cavity length has been progressively increased up to the current 34.5 cm over the subsequent design versions. At each step, the PDH-locking behavior of the cavity was tested. The result was always positive, indicating that moving towards a cavity length of 50 cm should be possible in the near future, while being able to maintain a sturdy lock.

In order to facilitate the measurement of intracavity pressure and to open the possibility of working with samples in a continuous flow, the cavity features two vacuum connection ports. After repeated leakage problems with national-pipe-thread (NPT) or Swagelok tube fitting connections, two female Swagelok VCR-type threads were machined into the cavity bulk for ensuring leak-tight operation. Finally, six 3-mm bores were drilled 2-cm-deep into the cavity bulk to host temperature probes allowing a reliable and spatially resolved characterization of cavity temperature. The probe sites are located at angles of 120° around the cylindrical symmetry axis of the cavity and divide its length into three equal parts.

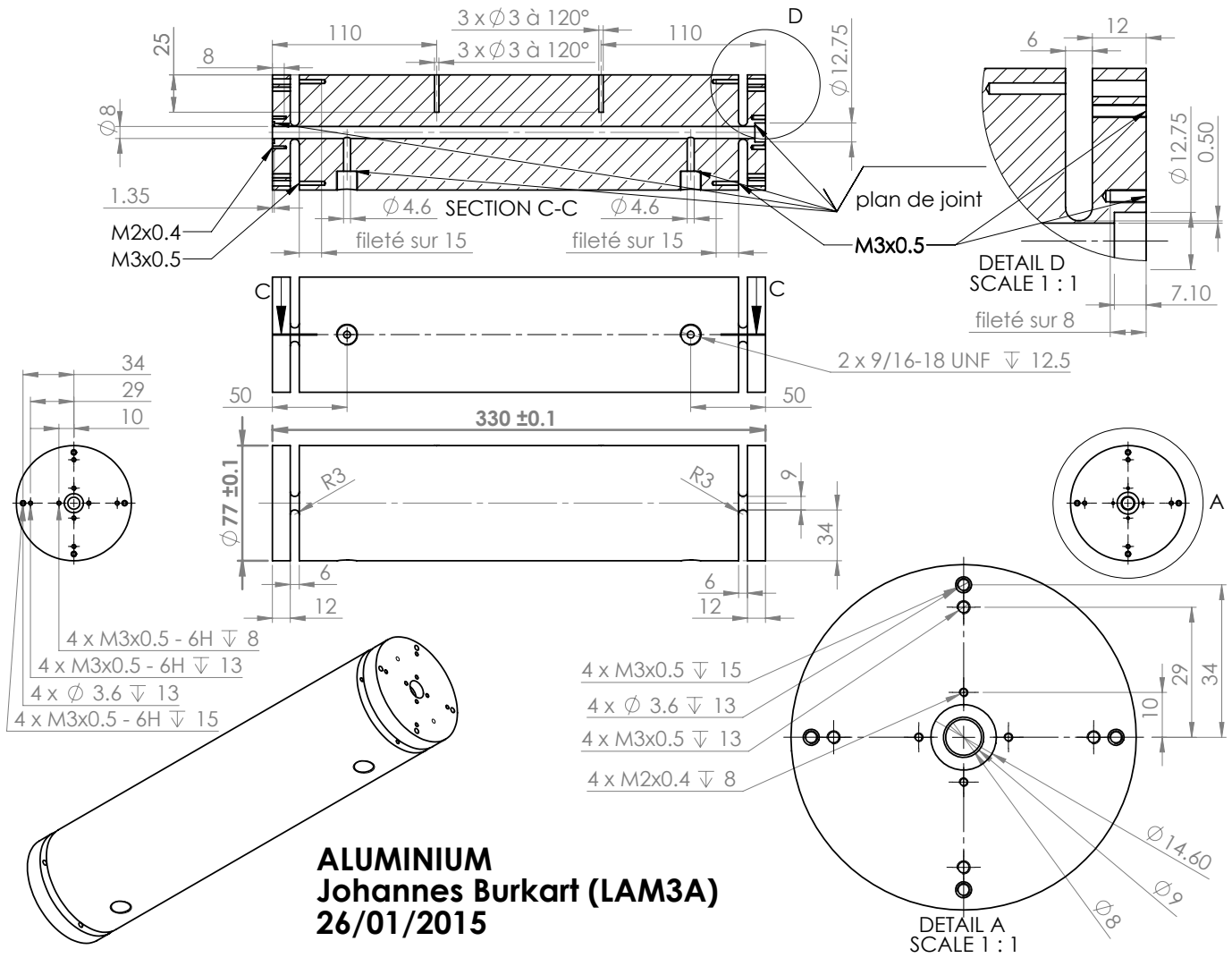

Figure 6.3 Technical drawing of the most recent ring-down cavity for Pound-Drever-Hall-locked OFFS-CRDS.

6.2.2 Low-noise, high-voltage cavity length servo loop

Tightly locking the ring-down cavity TEM_{00} mode onto the stable, but tunable VCOF laser is a key feature of OFFS-CRDS. It guarantees an unbroken stability transfer chain from the V-shaped reference cavity to the CRD spectrometer frequency axis. Physically, this lock is realized in terms of a servo loop on the ring-down cavity length controlled by a moving cavity end mirror mounted on a piezo-electric actuator (PZT). To begin with, let us examine the voltage stability needed on the PZT for this purpose. To first order, the PZT displacement δL is proportional to its driving voltage change δV and reaches one free-spectral range of the cavity at model-dependent characteristic voltage V_{FSR}:

$$\delta L = \frac{\delta V}{V_{FSR}} \cdot \frac{\lambda}{2} \tag{6.3}$$

Inserting this PZT property into the cavity length condition (6.1) one obtains the voltage stability criterion

$$\left| \frac{\delta V}{V_{FSR}} \right| = \frac{1}{F} \tag{6.4}$$

Again, this is a very intuitive result, stating that the voltage stability normalized to the FSR voltage must be better than the inverse cavity finesse. For the present case of a high-finesse CRDS cavity with $F \approx 450000$ this applies a voltage stability on the order of $2 \cdot 10^{-6}$ for voltages well over 100 V.

To meet this challenging voltage stability criterion, we developed the dedicated electric setup depicted in the schematic in Fig. 6.4. The heart of this innovative approach to PDH-locking of a high-finesse cavity lies in that the PZT is driven by the potential difference between the outputs of a computer-controlled low-noise high voltage source and a commercial analog servo controller (Toptica PID 110) operated in low-voltage mode. The effective voltage range typically used on both sources was 10 V to 150 V and ±1 V, respectively.

First, let us discuss the high voltage offset applied to the PZT plus pole. It is supplied by a home-made high-voltage (HV) amplifier with a constant voltage gain of 45. It uses a standard LM741 operational amplifier and has a very low intrinsic noise level, as will be shown further below. The HV setpoint, divided by the factor of 45, is provided as an analog voltage signal from a digital-to analog converter. The device serving this purpose in the present setup is a Texas Instruments DAC-1220-EVM, which provides an output voltage between 0 and 5 Volts with 20-bit resolution and a root-mean-square (rms) noise level on the order of 7 μV according to the datasheet. This high performance comes at the expense of a low effective bandwidth on the order of 300 Hz, limiting the rate at which the high voltage level can be effectively updated. Finally, to send a new voltage setpoint from the computer controlling the experiment to the DAC-1220, a National Instruments USB-8540 USB (universal serial bus) to SPI (serial-peripheral-interface) communication interface is used. To achieve the necessary ultra-low noise level at DAC-1220 output, the USB-8540 and DAC-1220 grounds needed to be galvanically separated by transmitting the SPI communication through digital optocouplers (Fairchild FODM8061). These integrated components contain a light-emitting diode (LED) and a receiving photodiode for transmitting a pulsed signal without galvanic contact between the emitting and receiving circuits.

The noise level eventually obtained with this custom-made high-voltage supply scheme was on the order of 0.3 mV rms at 20-kHz bandwidth for a 180 V output signal, thus satisfying the strict voltage stability criterion (6.4). Taking the voltage gain of 45 into account, this noise level is in good agreement with the 7 μV DAC-1220 rms noise, indicating that

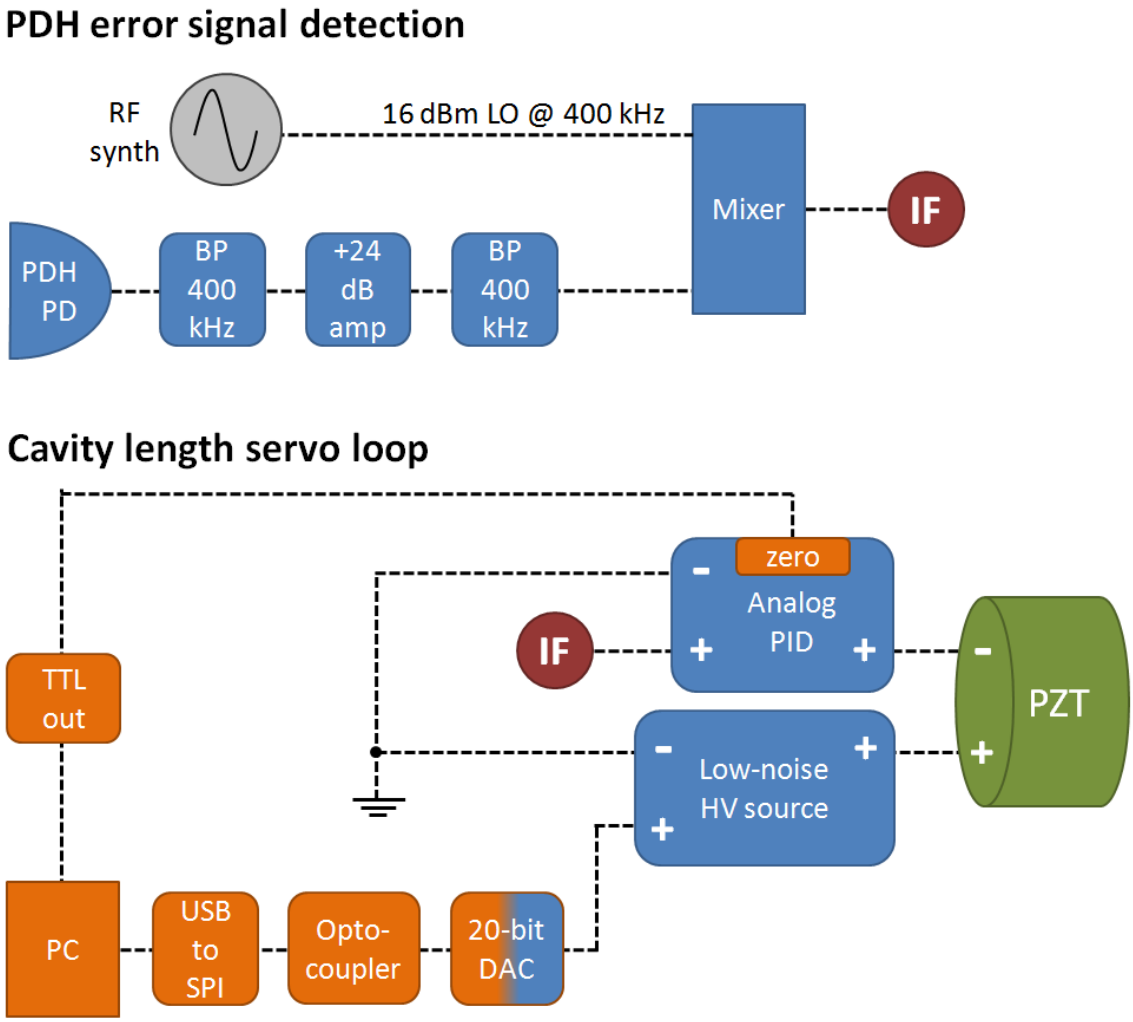

Figure 6.4 Schematic of the electronic setup for Pound-Drever-Hall(PDH)-locked OFFS-CRDS. Analog components are depicted in blue, digital ones in orange. PZT: Piezo-electric actuator controlling ring-down cavity length, PD: photodiode, BP: band-pass filter, RF: radio frequency, amp: amplifier, synth: synthesizer, PC: personal computer, USB: universal serial bus, SPI: serial-peripheral-interface, DAC: digital-to-analog converter, TTL: transistor-transistor logic, HV: high voltage, PID: proportional-integral-derivative controller, IF: RF mixer intermediate frequency output, LO: local oscillator.

the home-made HV source only negligibly contributes to the total noise level. It is important to note that the performances reported here could only be attained by meticulously eliminating ground loops between the different parts of the setup, which would lead to oscillatory parasite signals. Furthermore, a pair of 12 V-accumulators was used as a power supply for the OFFS-CRDS instrument, thus avoiding any parasite common-mode signals related to the three-phase laboratory power grid.

Now, let us turn to the fast signal applied to the PZT minus pole by the analog servo controller. It is based on the error signal obtained by means of a Pound-Drever-Hall (PDH) scheme using the MZM and a fiber-optic circulator. This modified PDH-locking scheme was proposed and treated in detail in [58]. Its working principle is also discussed in Articles 4 and 5. To implement it, we chose high-end commercial components wherever possible. Before and after 24 dB amplification by a low-noise amplifier (Minicircuits ZFL-500LN+), the signal from the PDH photodiode is filtered by a 350-450 kHz band-pass filter

(MiniCircuits ZFBP-400K+), keeping only the frequency band carrying the PDH error signal. The latter is obtained using a 17-dBm level RF mixer (MiniCircuits ZP-3H+) by demodulating the PDH photodiode signal using a local oscillator sine wave supplied by the RF synthesizer. The resulting PDH signal was wired directly to the error signal input of the analog servo controller. The maximum servo bandwidth of this Toptica 110 controller is on the order of 7 kHz here, well-matched with the in-phase response bandwidth of the PZT, which was evaluated experimentally to be superior to 6 kHz. In practice, best locking results were obtained when using the maximum 7-kHz servo bandwidth on the Toptica 110. In a standard PDH setup, a low-pass filter needs to be inserted between RF mixer and servo controller in order to filter out the PDH signal component at twice the modulation frequency. In the present setup, the intrinsic bandwidth of the Toptica 110 was seen to serve this purpose perfectly, and any addition of supplementary low-pass filters negatively affected lock quality.

Summing up, the PZT plus pole is kept at a constant high potential by the home-made low-noise HV source. The potential at the minus pole, in turn, is given by the fast correction signal from the analog servo controller referenced to the same ground potential. In this manner, the analog PID controls the voltage applied to the PZT by shifting the reference potential of the HV offset. In this differential voltage-driving scheme, the servo controller can thus lock the cavity length with an output voltage close to zero.

A last important point concerns the method by which the HV offset value needed for finding the TEM_{00} cavity mode is determined. It is evident that this task is not trivial when comparing the analog servo locking range of $\pm 1\,V$ to the PZT FSR voltage $V_{FSR} \approx 90\,V$. To find the approximate PZT voltage corresponding to the TEM_{00} cavity mode automatically and reliably, a fast computer-based routine was developed. It first sets the analog servo output to $0\,V$ using its built-in reset functionality controlled by a $+5\,V$ TTL signal, as indicated in Fig. 6.4. Then, it carries out a 50-ms long voltage sweep by stepping the DAC-1220 through discrete voltage values covering more than one FSR of the cavity. The peak in the CRDS transmission signal recorded during this sweep corresponds to the TEM_{00} mode. Having localized the mode, a second scan with a narrower span is carried out centered around the approximate position of the mode. This procedure is typically repeated 7 times, leading to a determination of the TEM_{00} voltage much better than the required $\pm 1\,V$-level. Once this iterative procedure has converged to the adequate HV offset, the analog servo is switched back on by the computer. Now within the TEM_{00} locking range, it automatically locks the cavity to resonance with the VCOF laser. This automated cavity relock procedure takes approximately half a second at present and can be triggered on demand anytime. Finally, in order to always keep the analog servo output centered around its working point of $0\,V$, the HV offset is automatically updated by communicating a new offset value to DAC. Such a HV update event is triggered as soon as the analog servo output, monitored by the computer, leaves a narrow voltage interval around $0\,V$. In this case, the HV offset is changed by a small amount, typically $4\,mV$. If necessary, another step is made a few ms later. This automatic computer-controlled HV-offset tracking allows perpetual servo operation without breaking the cavity lock, thanks to the small voltage steps and the high correction bandwidth of the analog PID.

To conclude, let us note the astounding fact that triggering hundreds of ring-down events per second with the corresponding dark laser-off periods does not negatively affect the robust PDH-lock of the cavity. Ring-down cavity and VCOF laser therefore seem to be sufficiently stable for passively maintaining their resonance over the few-ms dark period during each ring-down event.

6.2.3 Ring-down cavity temperature measurement and stabilization

Keeping the ring-down cavity at a stable temperature during spectroscopic measurements is vital for two important reasons: First, it minimizes spectrometer baseline fluctuations due to thermo-mechanical drifts of empty-cavity losses. Second, it prevents absorption line intensities from changing due to molecular population redistribution related to temperature-dependent Boltzmann statistics (cf. Section 8.1.1). Consequently, a double-stage temperature stabilization approach was developed for OFFS-CRDS, trying to lock ring-down cavity temperature to a setpoint value while keeping temperature gradients inside the cavity as small as possible.

The ring-down cavity is installed inside the polystyrene enclosure shown in Fig. 6.5, which provides a stable environment by passively isolating the cavity from perturbations in the air-conditioned laboratory room. The air temperature inside the enclosure is actively

Figure 6.5 Peltier-stabilized polystyrene enclosure containing the OFFS-CRDS setup.

stabilized by means of a commercial two-fan air-air Peltier cooler SuperCool AA040-1222 with 41 W nominal cooling power, which can be seen at the upper left side of the box in Fig. 6.5. It stabilizes the reading from a 100 Ω platinum temperature probe (PT100) installed in the middle of the box. According to the European IEC751 standard, the accuracy of this probe can be conservatively estimated to 0.3 K.

As the second temperature stabilization stage, two resistive silicone rubber heating bands were tightly contacted to the ring-down cavity surface. They feature resistance values of 55 Ω and 107 Ω and dimensions of 30 cm × 5 cm and 30 cm × 2.5 cm, respectively. The current driver for this heating scheme is a home-made circuit with an OPA548 operational amplifier and a voltage gain of 2.4. By applying the same voltage to both heating bands, a roughly equal power density per surface area is delivered by both bands. The heating current is controlled by the experimental control computer, using a software PID

servo loop and an analog output between 0 and 10 V from a data acquisition card, as discussed below in Section 6.3.2. The basis for this second-stage stabilization is an accurate and spatially resolved measurement of cavity temperature. It is provided by six 1000 Ω platinum temperature probes (PT1000) with a specified accuracy of 0.1 K, installed in three 3-mm-diameter holes 2.5-cm-deep in the cavity bulk, as discussed in Section 6.2.1 above. A photo of the ring-down cavity with all temperature probes and both heating bands installed is shown in Fig. 6.6. The PT1000 resistance values are read by means of

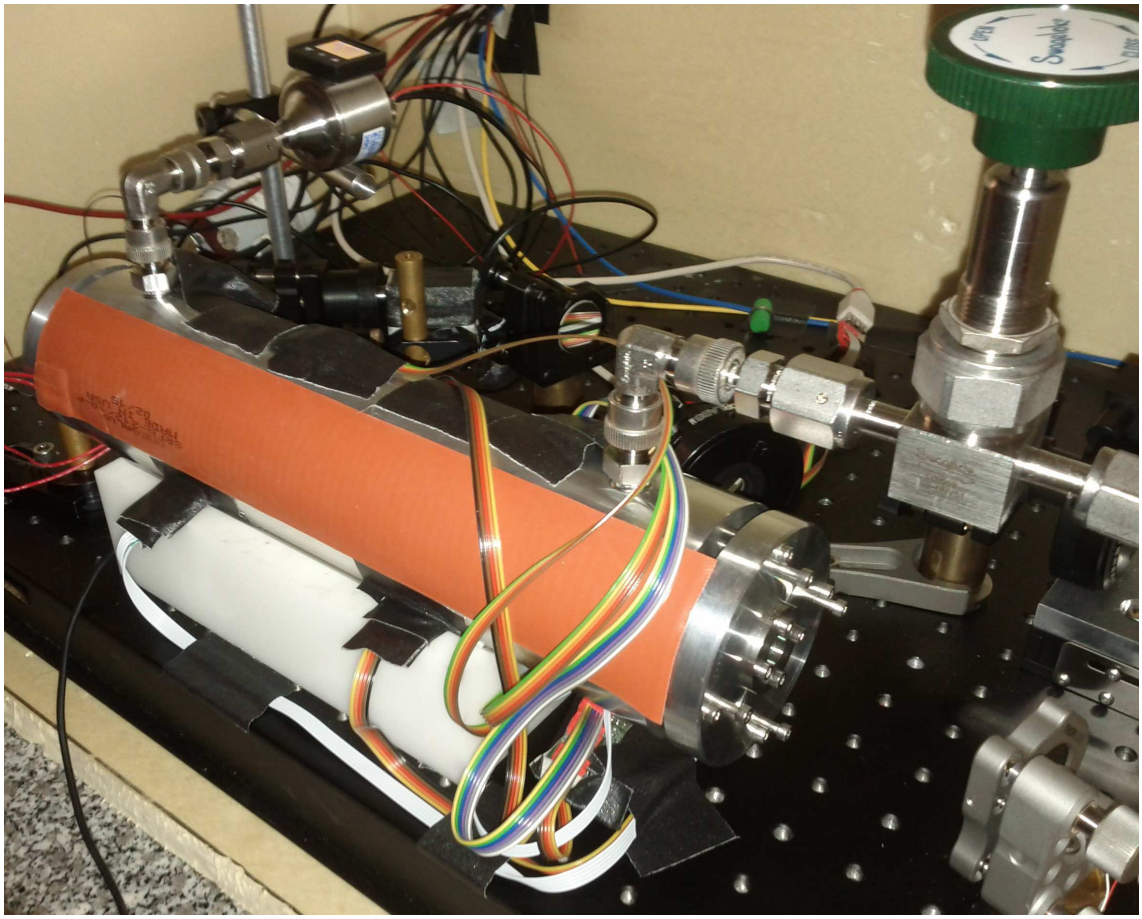

Figure 6.6 Ring-down cavity with heating bands and temperature probes installed on the breadboard with the optical setup for OFFS-CRDS.

six home-made Wheatstone-bridge circuits with a precision voltage reference. The resulting voltage signals are transferred to the experimental control computer by means of two analog-to-digital converters and USB communication interfaces. They are subsequently converted to temperature by the computer and used for the software servo loop mentioned above. The intrinsic technical noise of this temperature measurement scheme is very low, on the order of 100 μK, and up to 16 measurements can be made per second. The temperature measurement accuracy, however, is partially lost due to the uncertainties in the Wheatstone bridge resistances and, to a lesser extent, the voltage reference, leading to reading differences between uncalibrated probes on the order of a few 0.1 K.

Therefore, we carried out a calibration of the six PT1000 probes by equilibrating the ring-down cavity temperature using only the Peltier stabilization stage. Thanks to its massive design and its high thermal diffusivity, the ring-down cavity then acts as an effective thermal reservoir with minimal temperature gradients. Recording temperature measurements over several hours, the six probes were calibrated to the temperature measured by

the commercial PT100 probe of the Peltier cooler, thus used as a common temperature reference. The result of this measurement is shown in Fig. 6.7, with the respective calibration offset already added to the reading of each PT1000 probe for the sake of readability. The corresponding offset values for each probe are quoted in the legend. The curve from

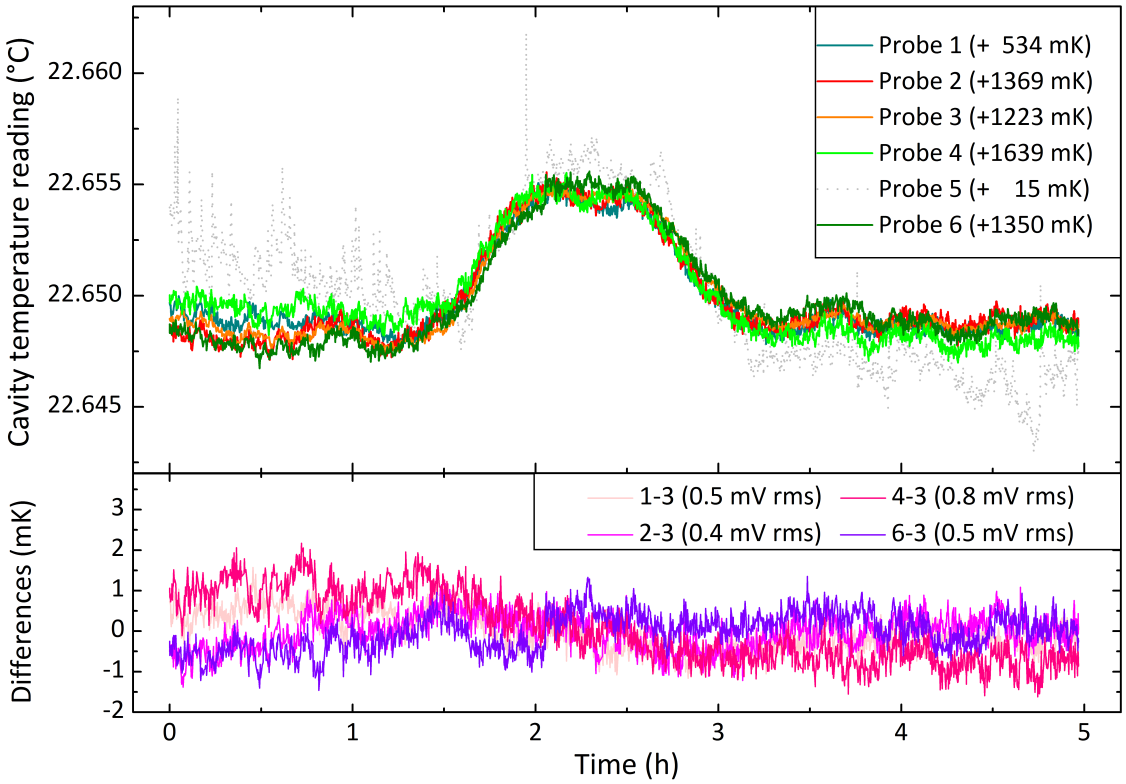

Figure 6.7 Upper panel: Temperature readings from the six PT1000 temperature probes installed at different sites in the cavity main body actively stabilized by the Peltier cooler. The temperature values were corrected for the offset shown in the legend for matching the reference PT100 temperature. Lower panel: Differences between the temperature readings from different probes. The root-mean-square fluctuations of these differences are reported in the legend.

probe 5 is shown in dotted gray, as it exhibits excess noise, significant drifts and, from time to time, measurement artifacts exhibiting sudden temperature jumps and spikes. In the light of these problems, the probe is considered unreliable, and its reading is not used for any purpose at present. Consequently, probe 5 and the respective readout circuit should be replaced in the next revision of the setup. The lower panel of Fig. 6.7 shows the evolution of the difference in temperature reading by the five operational probes, exhibiting an essentially flat behavior indicating a temperature uniformity at the sub-mK level inside the aluminium body of the cavity. Consequently, the arithmetic mean of the temperature readings from the five operational probes constitutes a very precise measure for cavity temperature.

Switching on the second-stage heating band stabilization, the average cavity temperature was increased to 26 °C and monitored over almost two days. The temperature readings by the five operational calibrated probes during this measurement are shown in Fig. 6.8. The root-mean-square temperature fluctuations of the actively-stabilized average temperature (blue curve) amount to only 260 μK. Three of the probes were within 5 mK from the setpoint, while the other two were at +18 mK and −22 mK, respectively. These

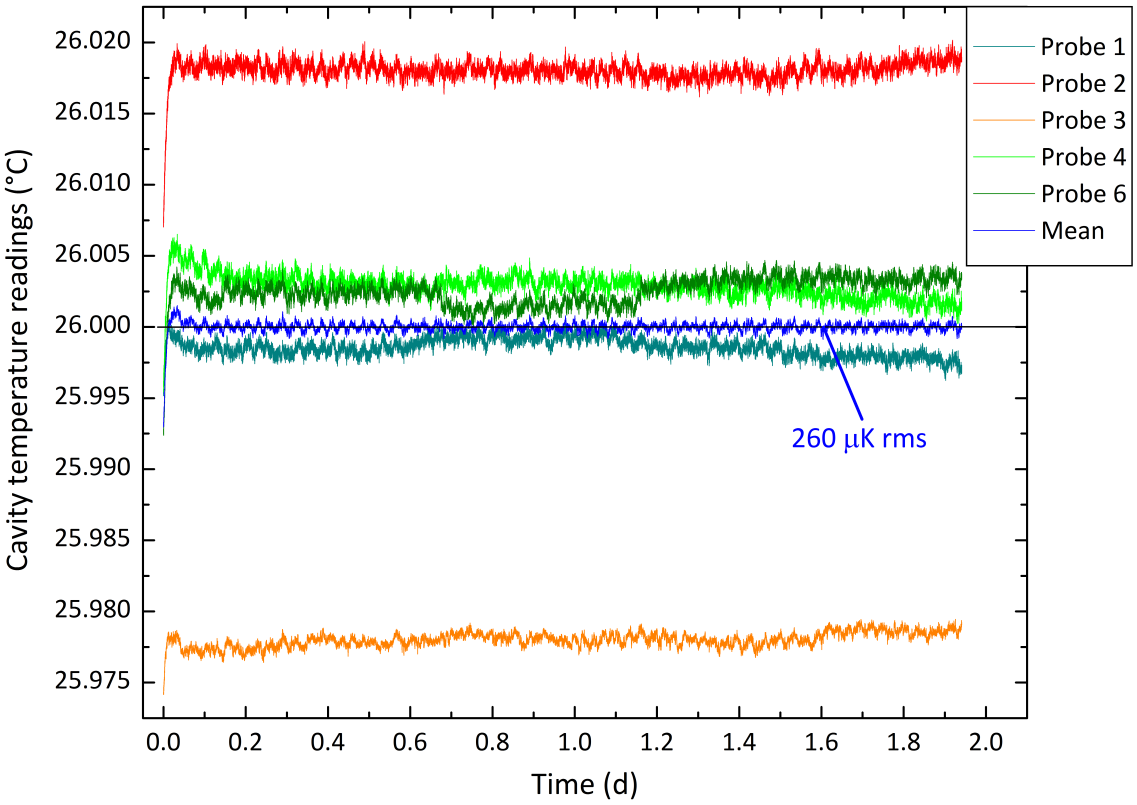

Figure 6.8 Evolution of ring-down cavity temperature over time during active double-stage stabilization, as measured by five PT1000 probes at different sites.

temperature differences are attributed to temperature gradients arising in the cavity under the effect of heating, which is not perfectly uniform and isotropic at present. This interpretation was confirmed by further increasing the cavity temperature, which lead to a roughly proportional growth of temperature differences, as expected. Let us note that a contribution from a temperature gradient effect on the Wheatstone bridge resistances cannot be excluded with certainty in the present setup. To improve this aspect, even longer wires may be used for the temperature probes in the future, thus completely separating the bridge circuit from the cavity. Finally, in future versions of the setup, a more complete and uniform coverage of the cavity surface with customized heating bands should allow further reducing temperature gradients inside the cavity body.

6.2.4 Vacuum system, pressure measurement and sample inlet

Ultra-sensitive techniques such as OFFS-CRDS are ideally suited for low-pressure and long-term measurements. To ensure well-defined and stable measurement conditions, the vacuum and sample inlet system must therefore comply with the highest possible standards in terms of pumping performance and leak tightness. With this objective in mind, Swagelok VCR and Ultra-Torr fittings for high-vacuum applications were chosen for the critical parts of the vacuum setup.

As discussed in Section 6.2.1, the ring-down cavity features two home-made quarter-inch Swagelok VCR-type vacuum ports. A VCR-to-6-mm-tube adapter was definitively installed in both, creating a gasket-free vacuum seal by the deformation of the cavity aluminium by the stainless steel VCR adapter. On one vacuum port, an MKS Baratron 626C capacitance manometer with a full range of 10 Torr (13.3 mbar) for intracavity pressure measurements is installed using an quarter-inch Swagelok Ultra-Torr elbow and a

6-mm-to-KF25 vacuum adapter for connecting the gauge. On the second port, a Swagelok Ultra-Torr elbow and a 6-mm-tube-to-VCR adapter are installed for connecting a manual Swagelok SS-BNV51 high-purity bellows-sealed valve, which is used for isolating the cavity from the pumping and gas inlet circuit connected to the valve by a quarter-inch Swagelok VCR bellow. This flexible bellow leaves the temperature-stabilized enclosure (cf. Section 6.2.3) and, via another Ultra-Torr adapter, links the system to the pumping and gas inlet circuits by means of a Swagelok 6-mm tube-fitting tee. On the gas inlet side, a manual Swagelok SS-1RS6MM precision needle valve is placed for manually controlling the sample inflow and for isolating the vacuum system from atmospheric pressure when the sample gas bottle is changed. On the pumping side, a full-opening KF25 gate valve is placed to allow isolating the system from the turbomolecular pump (Pfeiffer Vacuum HiPace 80) when necessary. This turbo pump operates at 1500 revolutions per second and has an ultimate pressure below 10^{-7} mbar. It is backed by a dry scroll pump (Varian SH-110) with a typical ultimate backing pressure on the order of $2 \cdot 10^{-2}$ mbar.

In order to obtain accurate pressure readings with the Baratron gauge, its zero pressure signal must be calibrated by evacuating the cavity to well below the minimum pressure which can be detected with the gauge, that is 10^{-2} Pa for the present model. With an MKS 925 Micro-Pirani gauge, we independently checked that the ring-down cavity can be evacuated to below 10^{-3} Pa without problems. While thus evacuated, the zero pressure calibration shown in Fig. 6.9 was carried out. Based on this measurement,

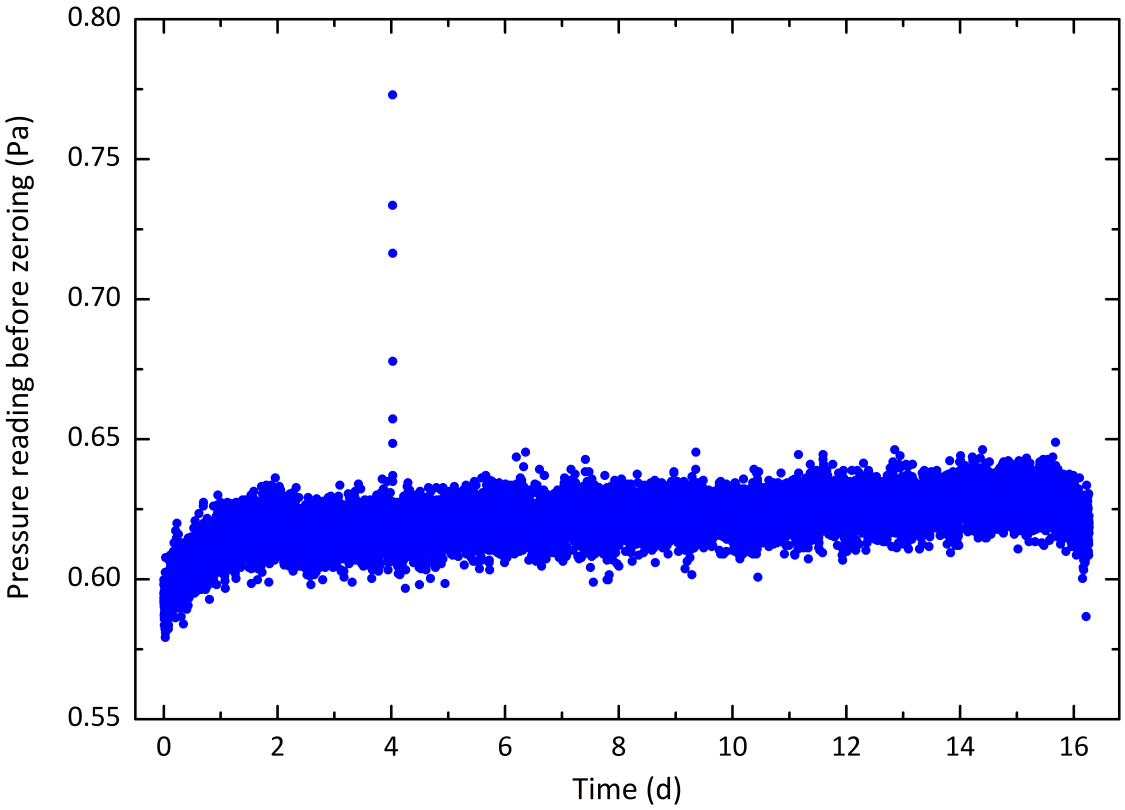

Figure 6.9 intracavity pressure reading before gauge zero setting. During this measurement, the cavity was evacuated to less than 10^{-3} Pa.

the zero-pressure value of the gauge was set to 0.62 Pa. The observed apparent pressure fluctuations are attributed to the impact of temperature variations in the laboratory room. They indicate that an accuracy better than 0.1 Pa cannot be reliably expected under the present conditions. With this zero-pressure calibration, the calibrated Baratron gauge has

an accuracy on the order of 0.1 Pa plus 0.3% of the pressure reading.

For characterizing the vacuum properties of the ring-down cavity, it was isolated from the pumps using the valve. The resulting intracavity pressure evolution over one day measured by the Baratron gauge is shown as the blue curve in Fig. 6.10. For comparison,

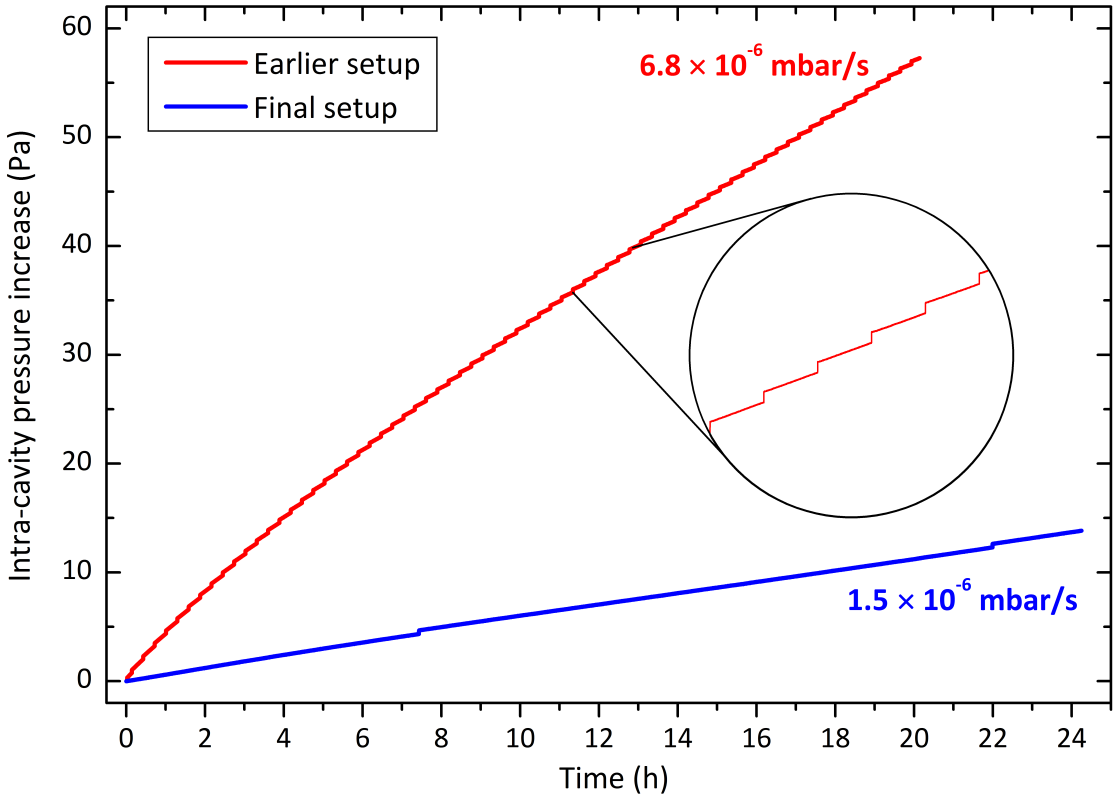

Figure 6.10 Comparison of the pressure increase in the isolated ring-down cavity over time for two ring-down cavities of different vacuum design, but equal volume. The effective leak rates are indicated for both curves. The circular inset shows a zoom on periodically occuring discrete leakage events.

the red curve shows the pressure behavior of an OFFS-CRDS ring-down cavity from an earlier revision, using a vacuum-greased quarter-inch conical NPT (national pipe thread) vacuum connector and Swagelok tube fittings for the vacuum line. Its pressure increase is 4.5 times faster than in the current setup. Furthermore, it exhibits discrete leakage events of unknown origin, shown by the circular inset in Fig. 6.10. They periodically occur at quite regular 17 min intervals and lead to a pressure increase by about 0.3 Pa each. Using the relations (6.5) and (6.6) below, this single-event pressure increase corresponds to a gas volume of 0.06 mm^3 at atmospheric pressure. Accumulating events over one day then yields a total volume of 5 mm^3. No trapped gas volume inside the cavity could explain this phenomenon, which was observed unaltered over several weeks. Therefore, it must be considered to originate from a genuine, external leak with some sort of periodic inlet mechanism. Looking closely at the blue curve for the current setup, one discerns that a similar phenomenon occured twice, separated by over 14 hours. In this light, the sharp signal peak in Fig. 6.9 is understood not to be a measurement artifact, but rather another discrete leakage event, which is rapidly absorbed back to zero pressure by the pumping system.

As indicated in Fig. 6.10, the blue curve implies an effective pressure increase rate $\dot{P} = 1.5{\cdot}10^{-6}$ mbar/s for the new, optimized ring-down cavity vacuum setup. To determine

the corresponding leak rate, let us consider the ring-down cavity volume

$$V_{cav} = \pi(0.4\,\mathrm{cm})^2 \cdot 34.5\,\mathrm{cm} = 17.3\,\mathrm{ml} \tag{6.5}$$

This value should be rounded up to $\tilde{V}_{cav} \approx 20\,\mathrm{ml}$, as a rough estimate for the tubing and pressure gauge volumes. Then, the observed pressure increase $\dot{P}$ corresponds to a leak rate

$$R = \tilde{V}_{cav}\dot{P} \approx 3 \cdot 10^{-8}\,\frac{\mathrm{mbar} \cdot \mathrm{l}}{\mathrm{s}} \tag{6.6}$$

Before quantitatively discussing this result, let us note that the composition of gases contributing to this leak rate was studied spectroscopically by OFFS-CRDS near $6198\,\mathrm{cm}^{-1}$. Water, carbon dioxide and methane concentrations were probed in this manner, showing that approximately 30% of the observed pressure increase was due to water. This result indicating significant water outgassing from the cavity walls was expected, as the cavity had never been baked out. Carbon dioxide and methane were present in traces at the permil level. Importantly, the observed increase in CO_2 partial pressure was continuous, hinting that CO_2 is being adsorbed on cavity walls and into Viton O-rings. In view of the temperature-dependent dynamic equilibrium between adsorption and desorption and the slow time constants in play, a certain degree of partial pressure fluctuations over time is therefore expected in any static sample measurement on CO_2 in the present setup.

Substracting roughly 30% of water outgassing from the effective leak rate (6.6), a potential external leak of roughly $2 \cdot 10^{-8}\,\mathrm{mbar} \cdot \mathrm{l/s}$ remains to be accounted for. Let us therefore consider the Swagelok VCR connections with silver-plated Nickel gaskets and the Ultra-Torr connections with elastomer O-rings in the system. According to the specifications, the leak rate of each such connection is guaranteed to be better than $4 \cdot 10^{-9}\,\mathrm{mbar} \cdot \mathrm{l/s}$. As there are currently eight such or equivalent connections in total, the tolerable leak rate of the system has an upper bound of $3 \cdot 10^{-8}\,\mathrm{mbar} \cdot \mathrm{l/s}$. Although this tolerance in itself could already account for the observed effective leak rate, leaks in the valve or the ring-down cavity itself are not excluded, for example related to the four O-ring seals. A Helium leak detector (Alcatel ASM-120h) was used to test this hypothesis, but no leakage signal was found even at very high flow rates of He outside the cavity. In principle, this means that external leaks of the ring-down cavity should be smaller than $10^{-9}\,\mathrm{mbar} \cdot \mathrm{l/s}$. In practice, the measurement can not be considered to be quantitatively reliable, as the leak detector calibration period had expired.

In view of these findings and the effective ring-down cavity leak rate of $3 \cdot 10^{-8}\,\mathrm{mbar} \cdot \mathrm{l/s}$, the vacuum system can be qualified as very tight according to common standards for vacuum systems [201] already at present. Nevertheless, the origin of the rare, but periodic leakage events is still unclear. It should be elucidated and remedied in future generations of ring-down cavities for OFFS-CRDS. As an order-of-magnitude improvement in performance is probably unrealistic with the current design and materials, we have identified several strategies for further improving the ring-down cavity vacuum system properties in future realizations.

First and foremost, the many fluoroelastomer seals in the current system may lead to micro-leaks due to their permeation properties and are expected to contribute to outgassing and memory effects by storing molecules from previous gas samples and ambient air. In future setups, they could be replaced by O-rings from materials such as silicone or PEEK (polyether ether ketone), which are expected to have better high-vacuum properties. A hydrophobic coating of the cavity walls could be used to decrease adsorption affinities in particular of water, but its effect on the adsorption of apolar molecules such as CO_2 is still unclear. Finally, inaccessible volumes around the mirrors and in the PZT-mounting assembly should be further reduced in order to minimize virtual leaks. If these

improvements can reduce intracavity pressure rise rates to well below the 10^{-6} mbar/s level, truly long-term spectroscopic measurements over several days come into reach even in the low-pressure regime needed for saturated absorption studies, such as in Section 3.2.2 and Chapter 9.

6.2.5 Further improvements in single-sideband frequency tuning

Within the electro-optic bandwidth of the Mach-Zehnder modulator (MZM), typically ranging from DC to between 13 and 20 GHz, the single-sideband tuning range is typically limited by the radio frequency (RF) equipment and components used for supplying its input signals. In the first realization of a single-sideband-tuned VCOF source in Article 1 on page 32 above and in [58], the necessary criterion was that SSB tuning must be able to cover more than one free spectral range (FSR) of the V-cavity to enable arbitrarily fine frequency tuning for spectroscopy without spectral gaps. This was achieved with a Rohde&Schwarz SMB100A RF synthesizer supplying up to 30 dBm for frequencies up to 2.2 GHz and a Minicircuits ZX10Q-2-19+ quadrature two-way splitter operating on the RF interval from 1.1 to 1.925 GHz, thus covering almost two V-cavity FSRs by SSB tuning. In practice, satisfactory MZM extinction ratios were also obtained for frequencies below 1.1 GHz, and the setup could be used for covering up to three FSRs by RF.

For fast spectroscopic scans, however, it is desirable to exploit the full potential of the MZM, with RF components allowing to work over a much broader spectral interval. This has the further advantage that whole spectral lines can be recorded using only RF tuning, without changing the VCOF mode. In such a situation, any doubt on the uniformity of the V-cavity FSR at the sub-kHz level does not impact the spectroscopic measurement. For achieving such an advantageous situation by upgrading the MZM driving system, we have targeted the tuning interval from 2 to 18 GHz. To this end, suitable RF equipment was identified and acquired. A Rohde&Schwarz SMF100A RF synthesizer which supplies power levels over 25 dBm up to 22 GHz was chosen to replace the SMB100A. As a 90° hybrid splitter, Narda model 4356 was chosen. Beyond frequency tuning, the SSB also automatically serves the purpose of triggering ring-down events by cutting the RF power driving the MZM. To this end, a very fast and highly absorptive RF switch is needed. For the previous low-frequency setup, this was carried out by a Minicircuits ZASWA-2-50DR+ operating from DC to 5 GHz with a switching time of 10 ns and a typical attenuation of 90 dB or better for RFs below 2 GHz. This switch was replaced by a Hittite HMC-C019 model working from DC up to 20 GHz with an isolation better than 75 dB up to 16 GHz, and even faster switching times below 10 ns. Finally, all SMA (sub-miniature version A) cable assemblies used for connecting the components were replaced by high-frequency versions compatible with RFs up to 26 GHz.

In spite of adequate components and a meticulous mounting procedure for all SMA connectors, moving to higher RFs approaching 20 GHZ comes at the price of reduced available power levels. The insertion losses of the hybrid splitter only slightly increased from 0.8 dB to 1 dB, but the fast switch contributes an insertion loss increase from roughly 2 dB to between 3 dB and 4 dB depending on RF. Furthermore, even the highest quality cables have insertion losses exceeding 2 dB/m at 20 GHz. Overall, the SSB power available for OFFS-CRDS decreased by a factor of two to three in this upgraded high-frequency setup.

Nevertheless, the advantages of the broad RF tuning range largely outweigh this power loss which may be compensated using an optical amplifier or a transimpedance gain at the ring-down detection photodiode. Fig. 6.11 shows a typical CRDS cavity transmission signal at zero absorption, in terms of the transmission photodiode voltage at a tran-

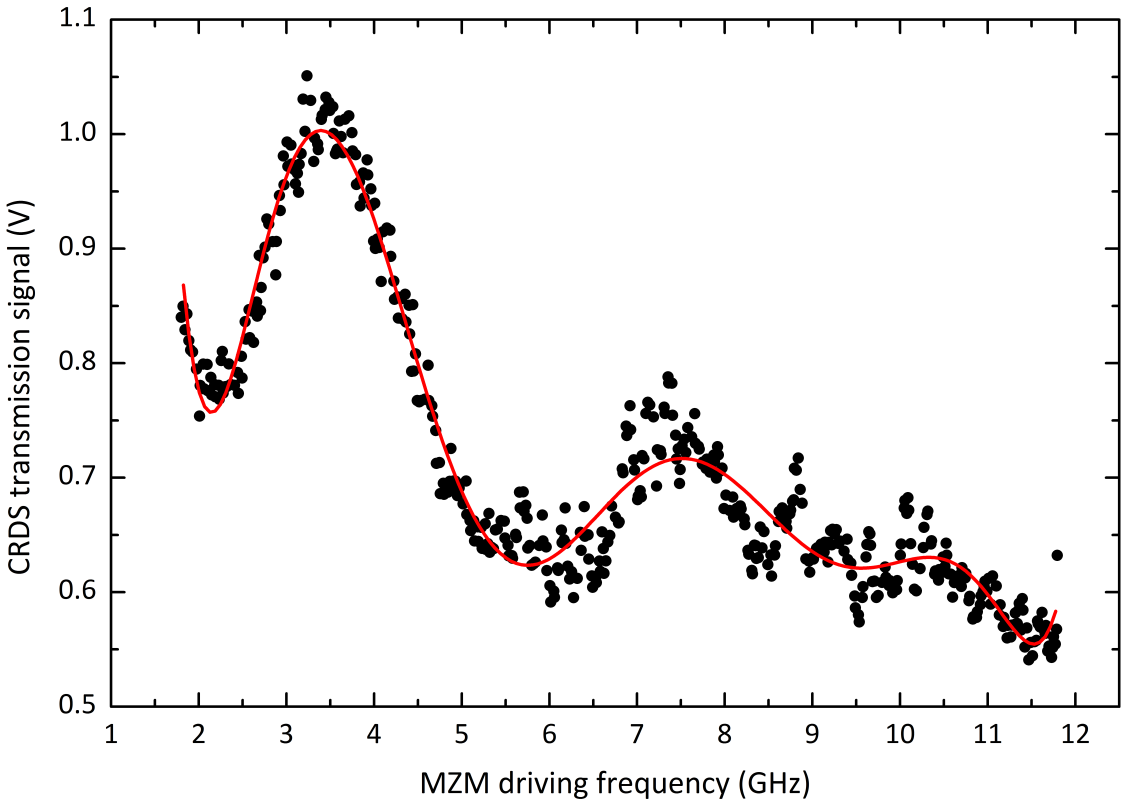

Figure 6.11 Typical CRDS cavity transmission signal as a function of MZM driving frequency using the new high-bandwidth single-sideband-tuning setup. The red curve is a phenomenological nineth-order polynomial fit used for optimizing the PDH error signal.

simpedance gain of 91 kΩ. The red fit curve is a nineth-order polynomial fit of the signal which phenomenologically yields an analytic relationship $S(f)$ between SSB-tuning RF and cavity transmission.

Experience shows that this polynomial $S(f)$ is useful for actively controlling the phase modulation (PM) depth for PDH error signal detection, in order to obtain a PDH lock in the same dynamic regime and, consequently, of the same quality, by compensating the global power change on the physical signal by a factor of two. To this end, a simple physical scaling can be set up noting that a SSB power variation changes the strength of the detected PDH signal and, consequently, the effective gain of the cavity length servo loop. Quantitatively speaking, the PDH signal strength should be proportional to the product of the global power signal $S(f)$ and the PM depth $\Delta\varphi$:

$$S(f)\Delta\varphi(f) = \text{const.} \tag{6.7}$$

This proportionality can be used for choosing a reference signal $S(f_0)$ at RF f_0, at which a good PDH lock is achieved for a PM depth $\Delta\varphi_0$. Then, following the proportionality relation (6.7), the optimal phase modulation depths $\Delta\varphi(f)$ at all other frequencies should be given by

$$\Delta\varphi(f) = \frac{S(f_0)}{S(f)}\Delta\varphi_0 \tag{6.8}$$

where the reference transmission signal shown in Fig. 6.11 can be inserted as $S(f)$. This automatic phase modulation depth compensation of signal power changes works well in practice and yields a stable and tight PDH lock of the ring-down cavity over the whole RF tuning range.

6.3 Data processing and experimental automation

6.3.1 Exponential ring-down fitting

To handle the fitting of hundreds of ring-down events per second in real-time, a fast exponential fit algorithm developed by Prof. Marco Prevedelli from Università di Bologna was used as a starting point. It is based on the following ansatz for a discrete ring-down signal time series y_i with N data points $i = 0..N-1$:

$$y_i = Ap^i + b \tag{6.9}$$

with the ring-down amplitude A, the per-point intensity loss factor p and a constant offset b. With the sampling period t_S between two data points, p is related to the ring-down time τ by

$$p = \mathrm{e}^{-\frac{t_S}{\tau}} \tag{6.10}$$

The original algorithm followed an approach implicitly assuming an equal precision level for all data points, which is the case for a signal limited by a constant level of technical white noise. As discussed in Articles 4 on page 90 and 5 on page 160, however, this condition is no longer met in a regime where the fundamental photo-electron shot noise becomes a limiting factor. Hence, we developed an extension of Prevedelli's algorithm in order to perform a weighted exponential fit, which shall be detailed in the following.

Introducing a noise level σ_i for each data point, elementary statistics [202] shows that the decisive measure for fit quality are the squared deviations of the data points from the model normalized by σ^2. By the maximum-likelihood principle, an optimal fit must be the model yielding the highest possible probability for observing the y_i which were indeed measured. One can show that such a fit minimizes the sum of squared and normalized fit residuals given by

$$\chi^2 = \sum_i w_i \left(y_i - \left(Ap^i + b\right)\right)^2 = \sum_i w_i \left(y_i^2 + A^2p^{2i} - 2Ay_ip^i + 2Abp^i - 2by_i + b^2\right), \tag{6.11}$$

with the weights $w_i = \alpha{\sigma_i}^{-2}$ and an arbitrary factor $\alpha > 0$. Minimization of χ^2 implies the following three necessary conditions:

$$\frac{\mathrm{d}\chi^2}{\mathrm{d}b} = \frac{\mathrm{d}\chi^2}{\mathrm{d}A} = \frac{\mathrm{d}\chi^2}{\mathrm{d}p} = 0 \tag{6.12}$$

The weight normalization factor α is therefore arbitrary, as it does not impact on any of these conditions. For the sake of compatibility with the unweighted fitting algorithm, we shall always choose α in a way that $c_0 = \sum_i w_i = N$ in the following. Sytematically evaluating the above conditions explicitly, one obtains the following equations for b, A and p:

$$b = \frac{s_1 - Ac_1}{c_0} = \frac{s_1 - Ac_1}{N} \tag{6.13}$$

$$A = \frac{s_2 - bc_1}{c_2} \tag{6.14}$$

$$f(p) = s_1\left(c_2c_3 - c_1c_4\right) + s_2\left(c_0c_4 - c_1c_3\right) + s_3\left({c_1}^2 - c_0c_2\right) = 0 \tag{6.15}$$

with the abbreviated sums

$$c_0 = \sum_i w_i = N \tag{6.16}$$

$$c_1 = \sum_i w_i p^i \tag{6.17}$$

$$c_2 = \sum_i w_i p^{2i} \tag{6.18}$$

$$c_3 = \sum_i i w_i p^{i-1} \tag{6.19}$$

$$c_4 = \sum_i i w_i p^{2i-1} \tag{6.20}$$

and

$$s_1 = \sum_i w_i y_i \tag{6.21}$$

$$s_2 = \sum_i w_i y_i p^i \tag{6.22}$$

$$s_3 = \sum_i i w_i y_i p^{i-1} \tag{6.23}$$

All the above equations only depend on the input data y_i and w_i as well as the fit parameter p. Inserting the quantities (6.16) through (6.23) in Eqs. (6.13), (6.14) and (6.15), one sees that all of them are functions of the single free parameter p only. After some simple algebra, one finds the explicit relationships

$$b = \frac{s_1 c_2 - c_1 s_2}{c_0 c_2 - {c_1}^2} \tag{6.24}$$

$$A = \frac{c_0 s_2 - c_1 s_1}{c_0 c_2 - {c_1}^2} \tag{6.25}$$

This result demonstrates the first enormous advantage of the algorithm: it reduces a seemingly three-dimensional optimization problem to a one-dimensional one. After convergence, the optimal b and A parameter values simply follow without ambiguity by inserting the optimal p in Eqs. (6.24) and (6.25).

Consequently, the initial problem of finding a maximum-likelihood exponential fit is now reduced to finding the root of Eq. (6.15). For fast convergence of the fit, the quadratically converging Newton method is chosen. The iterations p_k thus take the form

$$p_{k+1} = p_k - \frac{f(p_k)}{f'(p_k)} \tag{6.26}$$

$f(p_k)$ can be evaluated using the findings above. For a fast and precise computation, an analytic form is preferred for the derivative $f'(p)$. Obtained by differentiation $f(p)$ in (6.15), it reads

$$f'(p) = s_1 (c_2 c_5 + c_3 c_4 - c_1 c_6) + s_2 \left(c_0 c_6 - {c_3}^2 - c_1 c_5\right) + s_3 (c_1 c_3 - c_0 c_4) + s_4 \left({c_1}^2 - c_0 c_2\right) \tag{6.27}$$

with the new quantities

$$c_5 = \sum_i i(i-1) w_i p^{i-2} \tag{6.28}$$

$$c_6 = \sum_i i(2i-1) w_i p^{2i-2} \tag{6.29}$$

To avoid any danger of divergence in the Newton iteration, the algorithm verifies after each iteration whether the absolute value of $f(p)$ has decreased. If not, the last Newton step p_{k-1} is abandoned, and an only linearly converging, but much more robust interval bisection scheme is adopted for the next iteration p_k. Finally, the algorithm is considered to have converged to a root of Eq. (6.15) as soon as $|f(p)| < \epsilon$, with a predetermined precision goal ϵ.

For the sake of completeness, let us note that in the special case of equal weights, $w_i = 1 \forall i$, the c_j in Eqs. (6.16) to (6.20) as well as (6.28) and (6.29) can be written as geometric sums or related formulae, such as

$$c_3|_{w_i=1} = \frac{1}{p}\sum_{i=0}^{N-1} ip^i = \frac{(N-1)p^N - Np^{N-1} + 1}{(1-p)^2} = \frac{1 + p^N\left(N - 1 - \frac{N}{p}\right)}{(1-p)^2} \tag{6.30}$$

for instance. This substitution of lengthy sums by simple analytic expressions is the second reason for the outstanding speed of the original algorithm. With variable weights, an iterative determination of the c_j is inevitable. Fortunately, an optimized strategy, which strictly avoids any division or redundant floating point operation, can limit the additional computational cost to a very reasonable level. We have checked that, on a personal computer and in one second, the new algorithm can still fit several thousands of ring-down events consisting of over 1000 data points. This is roughly two to three times slower than the original algorithm, but completely suffices for real-time CRDS operation in practice, even at the highest repetition rates.

The algorithm elaborated here was implemented in terms of the C source code given in the Appendices, on page 211. This fitting routine, which is downward-compatible with previous versions, was compiled as a dynamic link library (dll) and subsequently embedded in LabVIEW. This allowed its straightforward integration into existing and new CRDS experimental control, automation and simulation routines.

From a practical point of view, it is not trivial to determine the correct noise level σ_i values for each point of an unknown ring-down event with previously unknown characteristics. To address this issue, here we propose a semi-analytic approach developed for ring-downs which combine statistically independent contributions from technical noise and shot noise. Technical noise is due to the measurement apparatus and equal for all data points, $\sigma_{T_k} = \sigma_T$. Shot noise, on the contrary, is a fundamental physical process due to the Poissonian number statistics of the light field and the photo-electron excitation process. Following the detailed derivation in Section 3.1 of Article 5 on page 160, it is proportional to the square root of the ring-down signal:

$$\sigma_{SN_k} = \sqrt{\frac{eRV_0}{t_g}} \mathrm{e}^{-\frac{kt_S}{2\tau}} \tag{6.31}$$

With the elementary charge e and the known values for the photodiode amplifier transimpedance gain R, the sampling period t_S and the analog-to-digital converter gate time t_g, only the initial signal voltage V_0 and the ring-down time τ still need to be determined to obtain the theoretical shot-noise level of the signal over time. Returning to the observed ring-down signal, a simple unweighted exponential fit yields very precise estimates for V_0 and τ. This realization is the basis for the approach proposed here.

First, a simple exponential fit of the ring-down signal is carried out. With the resulting V_0 and τ, the shot noise level is calculated according to Eq. (6.31). The technical noise σ_T is taken as the root-mean-squared noise on the tail of the ring-down signal, assuming that

a sufficiently long ring-down acquisition had been chosen by the user or by an automated routine. Adding the empirical σ_T and the semi-analytic σ_{SN_k} for the two independent statistical processes thus yields the best-effort noise estimate

$$\sigma_k^2 = \sigma_T^2 + \sigma_{SN_k}^2 \tag{6.32}$$

With this result and the corresponding normalized weights $w_k = \alpha {\sigma_k}^{-2}$, a true maximum-likelihood exponential fit following the above algorithm is carried out as a second pass to obtain an optimal precision in τ.

We have implemented this double-pass semi-analytic-weights maximum-likelihood fit procedure for partially shot-noise limited ring-down signals as a LabVIEW routine. Taking a ring-down signal with 1200 data points as a benchmark test, the program performed 5870 fits per second on an Intel i5-3317U notebook at 1.7 GHz. Using this fitting routine, the single-ring-down precision attainable by OFFS-CRDS was $3 \cdot 10^{-12}\,\mathrm{cm}^{-1}$ in absorption units, as given by the first point of the Allan-Werle plots in Fig. 3 of Article 4 and Fig. 4 of Article 5. When using an unweighted exponential fit, on the contrary, precision was never better than $6 \cdot 10^{-12}\,\mathrm{cm}^{-1}$ per ring-down. This clearly illustrates how a fast exponential fitting procedure with adequate weights, such as the one presented here, is crucial for attaining ultimate precision by CRDS in a shot-noise-limited regime.

6.3.2 Looped automated measurement routines

Owing to its increased complexity as compared to classical CW-CRDS setups, several new experimental control tasks arise in OFFS-CRDS. In the framework of this thesis, all necessary functionalities and several different types of automated measurement programs were developed, targeting a full automation of the experimental setup. All programs and routines were implemented as LabVIEW virtual instruments. As discussed in Section 6.3.1 above, the fast ring-down fitting algorithm was programmed in C and embedded in LabVIEW using a dynamic link library.

Here, we shall first discuss the experimental control routines needed for OFFS-CRDS in more profound detail. The control tasks arising from the temperature stabilization of the V-shaped reference cavity vacuum cell were treated in the framework of [58]. For historical reasons, these tasks are carried out by an independent computer in the current realization of OFFS-CRDS, although all tasks could be carried out by a single computer without problem. If V-cavity transmission is above a certain threshold, the VCOF laser can be considered locked. In this case, a +5 V signal is transmitted to the digital input port of a National Instruments PCI-6281 acquisition card of the OFFS-CRDS control computer.

Via USB, that computer reads the VCOF carrier frequency measured by a wavemeter. At the beginning of an experiment, the frequency of the TEM_{00} mode the laser is locked to is measured and logged. The arbitrary mode number 0 is then assigned to that V-cavity mode. From then on, a background routine converts the wavemeter frequency reading to the corresponding mode number, while assuring that the VCOF laser is really locked to a TEM_{00} mode of the V-cavity. For applications not necessitating any absolute frequency referencing, a low-finesse etalon could be used for counting VCOF modes instead of a costly high-end wavemeter. With the constantly updated information on the present VCOF mode number, another routine carries out laser current sweeps until the target VCOF mode is reached. The corresponding PCI-6281 analog output signal is connected to the DC-coupled modulation input of the VCOF laser current driver. With a ± 10 V voltage swing, a spectral interval of almost 20 GHz, corresponding to roughly 40 VCOF modes, can be covered in this fashion. When the limit of this current-tuning range is reached,

another routine can be called to change the temperature of the laser chip via serial-peripheral-interface (SPI) communication with a home-made temperature control servo card. A typical temperature-to-frequency conversion factor is on the order of 15 GHz/K for a DFB laser at 1600 nm. Frequency fine-tuning by MZM-single-sideband modulation is carried out by communicating with the radio-frequency (RF) synthesizer by VISA (Virtual Instrument Software Architecture) over ethernet. At each new spectral point, the radio frequency (RF), RF power level, as well as phase-modulation depth and rate are updated on the synthesizer if necessary.

As described in Section 6.2.2 above, PDH lock of the cavity onto the VCOF single-sideband can be automatically acquired by a computer-controlled hybrid analog-digital PZT voltage driving scheme within a fraction of a second. Such relock events are triggered by the OFFS-CRDS software whenever necessary, for instance when the lock is broken due to a strong external perturbation. When the laser frequency is changed by exactly one free spectral range (FSR) of the ring-down cavity, the cavity is always resonant and the lock is not broken. Therefore, it is advantageous to change the MZM-tuning radio frequency (RF) by exactly one FSR within the tuning range of the RF components. A spectrum with higher frequency stepping resolution can nevertheless be obtained by rearranging the spectral points into several chains with successive points separated by exactly one FSR. These chains can be measured subsequently and eventually yield the complete spectrum. This highly advantageous spectral interlacing approach considerably increases measurement speed by avoiding redundant PDH-relock events and is chosen wherever possible.

On demand, an adequate ring-down threshold is determined by recording the PDH-locked CRDS cavity transmission for some tens of milliseconds. All subsequent ring-down events at the given spectral point are then triggered using that signal threshold. A typical result of such a ring-down threshold calibration plotted against the MZM-tuning radio frequency using spectral interlacing is shown in Fig. 6.11 of Section 6.2.5.

During ring-down acquisition, the scrambling PZT position is automatically changed using a PCI-6281 analog output, according to the scrambling schemes discussed briefly in Article 4 above and comprehensively in Article 5 on page 160. With another analog output and a second scrambling PZT, we have recently realized discrete fringe scrambling also between cavity output and the detection photodiode, thereby neutralizing any small residual fringe related to light scattered by the detection photodiode. Additional OFFS-CRDS routines, which were implemented for choosing optimal acquisition parameters and for quality checking acquired signals, will be discussed in detail in the following section.

On the fundament of all these basic functionalities for OFFS-CRDS, a multitude of automated programs for spectoscopic measurements of different types was realized. As an example, the graphical user interface of one such software is shown in Fig. 6.12. This particular program is intended for the automated scan of predetermined target lines under changing experimental conditions. A typical application would be the recording of many absorption lines with different J values from the same rovibrational band at different pressures for subsequent determination of physically relevant and reliable line parameters by a multi-spectrum-fitting approach [203, 204]. The program was used for alternatingly measuring one water and one carbon dioxide absorption line with surrounding methane lines for the monitoring of intracavity gas composition during outgassing, as mentioned in Section 6.2.4 above. One key feature of the program lies in that it is capable of reading a list of lines to be measured in HITRAN format. It then automatically determines which VCOF mode the laser should lock to for measuring each line. For each line, a measurement grid is automatically set up, and the corresponding radio frequencies for driving the MZM are calculated, depending on whether the lower or the upper single-sideband is used, and whether an upward or a downward scan in frequency is desired. After each spectrum,

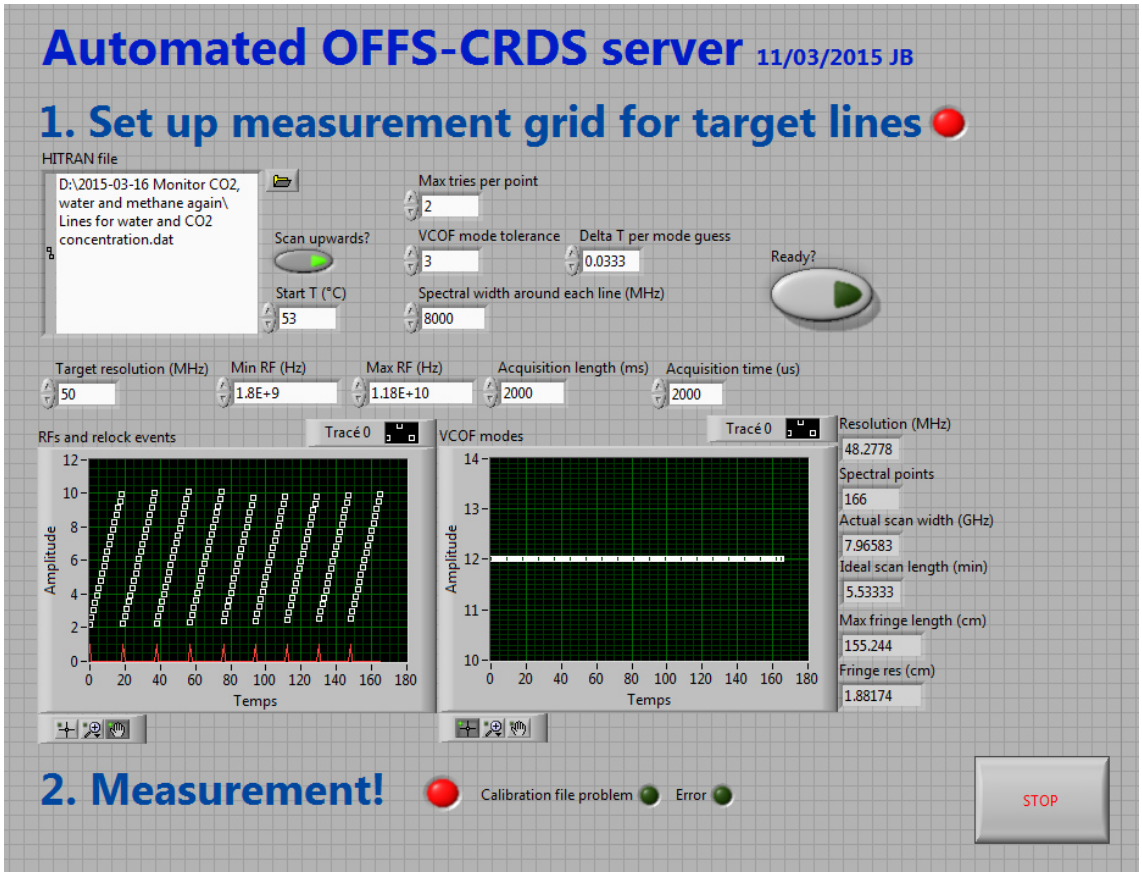

Figure 6.12 Typical user interface for one type of automated OFFS-CRDS measurement.

the laser temperature is automatically changed to reach the VCOF mode corresponding to the next absorption line. At each spectral point, a new ring-down trigger threshold is determined. The program can thus handle decreasing cavity transmission levels due to increasing absorption, for example if additional sample was introduced into the cavity by the user in the course of a multi-pressure measurement.

A similar automated OFFS-CRDS measurement program was developed for the subsequent and repeated measurement of predetermined Lamb dips on top of absorption lines with very well-known relative positions. It was notably used for carrying out the triple-dip VCOF-cavity drift measurement described in Section 3.2.2. This program first sets up a predetermined measurement grid around each Lamb dip in the HITRAN-type line list provided by the user. Let us point out that HITRAN-grade transition frequency precision is generally insufficient for obtaining symmetric measurement windows around each dip, as a typical measurement interval around the sub-MHz-width Lamb dip typically spans only 5 to 10 MHz. If no more precise transition frequency data is available, the positions in the line list may be adjusted by hand to obtain centered Lamb dips. This, in turn, can yield a measurement of their frequency separation with kHz-level accuracy, as discussed in Section 3.2.2. After setting up the measurement grid, contrarily to the routine discussed above, the software first conducts a ring-down threshold calibration procedure, which is carried out once for each spectral point. The corresponding trigger threshold values are then used for all subsequent measurements. For measurements over many hours or even days, this approach is very economical from a measurement-time point of view and widely used in OFFS-CRDS software. After successful ring-down threshold calibration, the program starts recording the selected Lamb dip spectra in an infinite loop eventually stopped manually by the user. An extract of the LabVIEW diagram structure for this program

is shown in Fig. 6.13. In order to compensate for any long-term drift of laser power, for

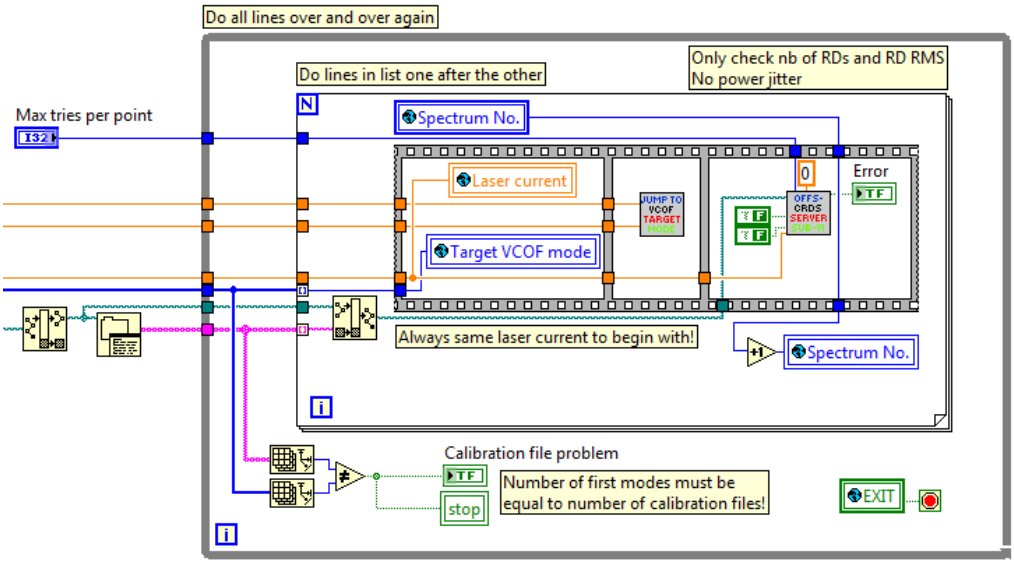

Figure 6.13 Main loop structure of the LabVIEW program for automated sequential and repetitive measurements of predetermined Lamb dip targets by OFFS-CRDS.

instance due to a progressive misalignment of the VCOF fiber coupling, the wavemeter power reading is used to update the predetermined ring-down trigger threshold levels by multiplying them with the corresponding factor at the beginning of each new spectrum acquisition. In this way, global power fluctuations do not adversely affect the automated spectrometer operation.

Further OFFS-CRDS operating software was developed for specific measurement applications, such as repeated measurements of the spectrometer baseline or high-signal-to-noise absorption line profiles with adaptive acquisition parameters, for instance. These programs are conceptually similar to the ones presented above, and discussing them in great detail is beyond the scope of this thesis.

Finally, the only experimental aspect which has not been automated yet is sample treatment, comprising tasks such as gas inlet, pressure or flow regulation and automatic cavity flushing cycles with dry nitrogen. These tasks are so far carried out manually by the experimenter, as described above in Section 6.2.4. A complete automation of these functions is planned for the near future and currently ongoing. Once accomplished, it will in particular enable a full remote control of OFFS-CRDS, allowing even new scans and measurements to be launched at a distance, for instance via internet.

6.3.3 Adaptive acquisition parameters and ring-down quality checking

Several automated routines of the OFFS-CRDS automation software ensure that optimal acquisition parameters are chosen for the ring-down measurements at each spectral point, and, subsequently, that the acquired signals are of good quality.

To optimize the ratio of signal to technical noise, the smallest possible analog-to-digital converter (ADC) voltage on the ring-down acquisition card (NI PCI-6281) is chosen among $\pm 0.5\,\mathrm{V}$, $\pm 1\,\mathrm{V}$, $\pm 2\,\mathrm{V}$, $\pm 5\,\mathrm{V}$ and $\pm 10\,\mathrm{V}$, depending on the predetermined ring-down trigger threshold. As short ring-down events correspond to low cavity transmission, the threshold can also be used to determine whether the integrated 40-kHz low-pass filter of the acquisition card may be used. This filter dramatically decreases the technical noise level at the expense of a systematic bias for short ring-down times (cf. Section 7.4.2). To avoid any danger of an ADC-bandwidth-related bias of the CRDS measurement, using

the filter was abandoned at an early stage, and this functionality is obsolete in all current versions of the operating software.

Some versions of the OFFS-CRDS operating software include the possibility of carrying out a rapid survey-type scan in order to analyze the spectral zone under study. In a second step, the measured spectrum is fitted in order to determine an optimal sample and measurement time distribution. This approach was used, for instance, for the ultraprecise lineshape measurements in Article 5 on page 160. The number of samples per ring-down acquisition is chosen to be a multiple of the ring-down time at each point, typically between 10 and 15 times the ring-down time depending on the precision goal. Another important parameter is the number of samples recorded for each spectral point. In order to choose an optimal averaging length, one needs to consider the averaging behavior of the OFFS-CRDS setup, as given by the Allan-Werle plots in Fig. 3 of Article 4 and Fig. 4 of Article 5, compromising between measurement speed and accuracy. Qualitatively speaking, longer averaging times T are needed at short ring-down times τ, as the signal-to-noise-ratio is lesser, and because there are less points available for fitting, which actually carry a physical signal. Following the derivation of Eq. 7 in Article 5, the shot-noise σ_α in absorption scales with the ring-down time as

$$\sigma_\alpha \sim \tau^{-\frac{3}{2}} \tag{6.33}$$

Averaging a number N of ring-down events, this random white noise averages as

$$\sigma_{\alpha N} \sim \tau^{-\frac{3}{2}} N^{-\frac{1}{2}} \tag{6.34}$$

Imposing a constant noise level after averaging for all spectral points in spite of lower per-shot precision thus implies

$$\tau^{-\frac{3}{2}} N^{-\frac{1}{2}} = \text{const.} \Leftrightarrow N \sim \tau^{-3} \tag{6.35}$$

Consequently, one needs to average eight times more ring-down events if ring-down times are two times shorter. This hefty scaling has less drastic consequences in the case of a tightly locked CRDS where the ring-down repetition rate f ideally scales as $f \sim \tau^{-1}$. Expressing the number of ring-down events $N = fT$ in terms of the averaging duration T, Eq. (6.35) reads

$$T \sim \tau^{-2} \tag{6.36}$$

In an ideal tightly locked OFFS-CRDS experiment, one should choose T according to Eq. (6.36) for each spectral point. Such a scaling was used for the lineshape measurements with very high signal-to-noise ratio shown in Fig. 7 of Article 5.

To check the quality of the acquired ring-down signals, several criteria were implemented. If the acquired ring-down signal data at a spectral point do not meet the quality requirements that point is rejected. Depending on the scan strategy, it is then either repeated or the measurement continues at the next spectral point. One main reason for the strict quality control was the theoretical possibility of a parasitic injection of the residual VCOF carrier and second sideband into the TEM_{00} mode or higher-order transverse modes of the cavity. In practice, this was virtually never observed thanks to the high MZM parasite signal extinction of almost 30 dB, the excellent mode matching of the laser beam to the TEM_{00} mode, with an injection of less than 0.5 percent of the TEM_{00} intensity for all other TEM_{mn} modes, and, most importantly, the cavity finesse of 450000, which implies a very small *a priori* probability of 450000^{-1} for finding a cavity mode by pure chance. In any case, if an accidental injection coincidence or another experimental perturbation nevertheless happened, it should be detected by the following ring-down quality checking scheme:

The most important quality criterion are the ring-down fit residuals. If they reveal a non-exponential structure or exhibit excess noise, the ring-down acquisition must have been perturbed by some parasite or spurious signal. Consequently, if the fit residual rms exceeds a certain value depending on the acquisition parameters, the corresponding ring-downs are rejected. Furthermore, the quality checking routine verifies that a sufficient number of ring-down events was recorded for each spectral point. The inverse case inevitably leads to an increased noise level for the respective spectral point and might thus create a spike in the spectrum. A typical reason for an insufficient number of ring-down events at a spectral point is an unlocking of the cavity lock due to an external perturbation. Too big differences in the ring-down times measured at one spectral point, quantified by the root-mean-square variation about their mean, are also used as an indicator for a potential issue with the measurement. If the root-mean-squared ring-down noise is too high, the corresponding events are discarded. In the special case of discrete fringe scrambling as discussed in Article 5 on page 160, an additional criterion is introduced. A certain degree of uniformity in the ring-down-number distribution on the four scrambling positions is required. Otherwise, this might again lead to an abnormally high noise-level and a spike at the respective spectral point.

Owing to the experience that distorted, perturbed ring-down events virtually never occur in practice, later versions of the OFFS-CRDS software generally only check for the minimum number of RD events and for their uniform distribution over the discrete scrambling steps. This dual criterion ensures a uniform noise level over the entire spectrum and avoids spikes due to single, noisy spectral points.

6.4 Spectrum averaging and detection limits

In Section 5.2, we elaborated why averaging absorption spectra rather than ring-down events is a beneficial strategy for lowering spectrometer detection limits in the long term. Examples from the literature were discussed where this approach was applied to reach unprecedented minimum detectable absorption levels and signal-to-noise ratios. Consequently, complementarily to the exhaustive spectrometer performance characterization studies reported in Articles 4 on page 90 and Article 5 on page 160, we have also tested the long-term spectrum averaging behavior of the OFFS-CRDS instrument.

To this end, the cavity was kept evacuated to below 10^{-3} Pa, and repeated automated spectrometer scans were carried out at a fixed frequency stepping resolution on a given spectral interval. Experience shows that two types of measurements need to be distinguished: a first group of 229 spectra was recorded on a broad span of 4700 MHz at frequency steps of 39.5 MHz, taking 7.4 min per spectrum on average. Such a scan configuration typically corresponds to a precision measurement of one Doppler-broadened absorption line up to its far wings, for instance. A second group of 202 spectra was measured on a 10 MHz span at 50 kHz intervals between spectral points in an average 7 min per spectrum. Such a scan, in turn, corresponds to a configuration for measuring high-resolution sub-Doppler saturated absorption spectra (cf. Chapter 9).

Spectrum averaging was carried out in both cases by involving a growing number N of spectra in the averaging. A linear slope was removed from each averaged spectrum to compensate for the mirror baseline. The resulting root-mean-square baseline noise corresponds to the OFFS-CRDS detection limit α_{min} after averaging N spectra. The result of this analysis is reported in Fig. 6.14, both for the broad and narrow span measurements.

Averaging of the spectra acquired at a span of 4700 MHz is drastically slower than the $1/\sqrt{N}$-scaling expected for a signal limited by random white noise and stops progressing

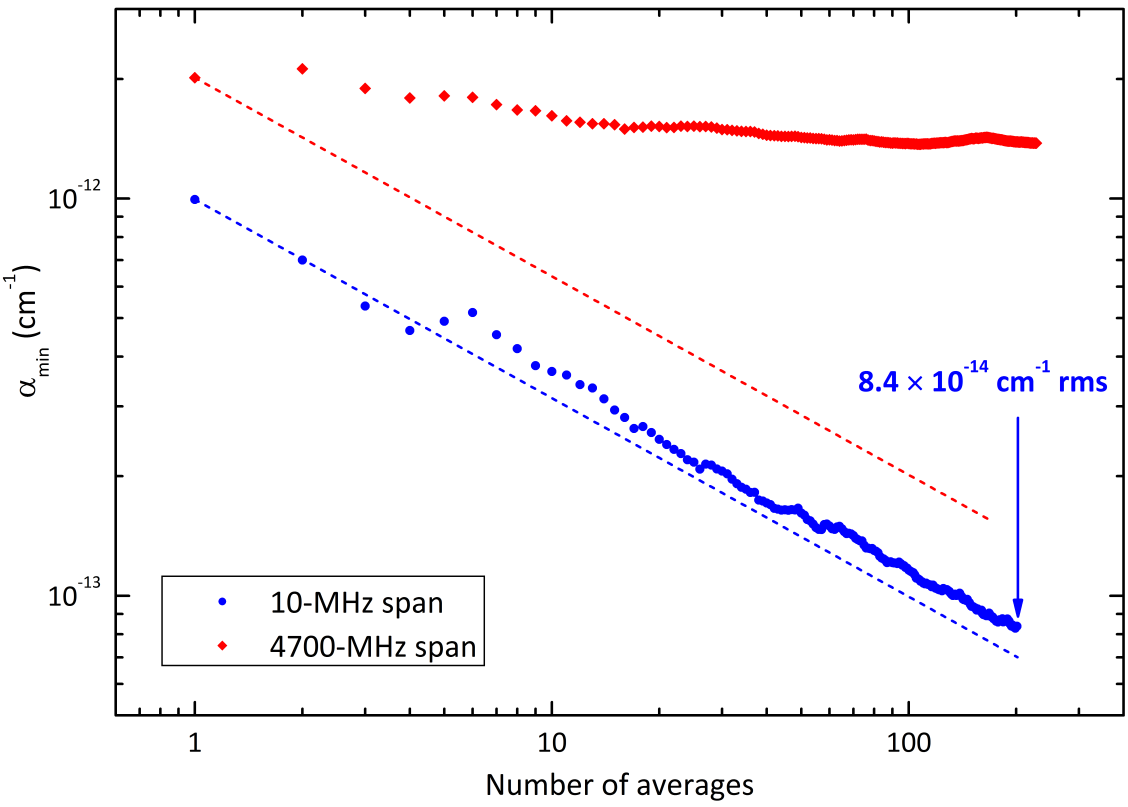

Figure 6.14 Absorption detection limit α_{min} by OFFS-CRDS on two different spectral intervals as a function of the number N of averaged spectra. Dashed lines indicate the $1/\sqrt{N}$ scaling of random white noise.

after roughly 100 averages. This impeded averaging behavior is attributed to the fact that the OFFS-CRD spectrometer baseline on a broader spectral interval is limited by tiny, slow periodic variations notably due to residual parasite interference fringes (cf. Section 7.8), as analyzed in detail in Fig. 5 of Article 5 on page 160 and the corresponding discussion therein. Fluctuating losses due to the influence of higher-order TEM_{mn} modes near the TEM_{00} mode, as discussed in Section 7.6, are also a potential issue. Consequently, the minimum detectable absorption in OFFS-CRDS on such a spectral interval is limited to $1 \cdot 10^{-12}\,\mathrm{cm}^{-1}$ at present, as long as no post-treatment such as a subtraction of a quasi-static baseline background is carried out.

The averaging on a 10-MHz span is in stark contrast with the aforementioned observations. Here, the full potential of OFFS-CRDS is unleashed, and a near-ideal white-noise averaging behavior is observed. In this way, an unprecedented minimum detectable absorption level of $8.4 \cdot 10^{-14}\,\mathrm{cm}^{-1}$ was achieved. Small deviations from the white noise $1/\sqrt{N}$-averaging behavior indicate that the data cannot be described in terms of a purely white noise process with a constant spread. Instead, the deviations from the straight dashed line in Fig. 6.14 are mainly due to fluctuations of single-scan rms noise over time and from spectrum to spectrum. The 111$^{\mathrm{th}}$ spectrum was excluded from the averaging analysis, as it was affected by a pressure-related spike (cf. Section 6.2.4). Importantly, no substantial slowdown in averaging was evidenced during the whole day-long measurements and no sign for a fundamental limitation of further averaging can be perceived at this stage.

This drastic improvement with respect to the broad-span spectra is attributed to the fact that optical path length differences of 100 m and beyond would be needed for generat-

ing parasite fringes with a periodicity prone to affect a spectrum on a 10 MHz interval. As such distances do not exist in the OFFS-CRDS setup, no periodic structures are observed on the single-scan and averaged baseline spectra on the 10 MHz interval. This result is shown in Fig. 6.15.

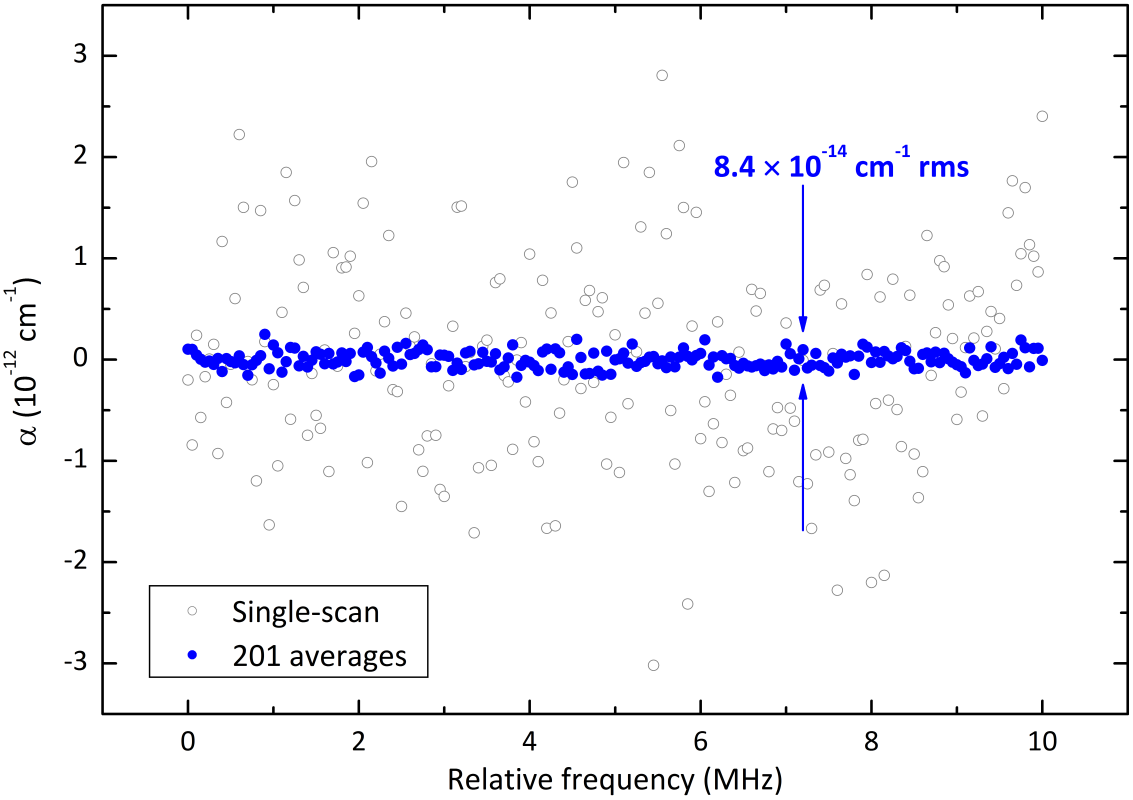

Figure 6.15 OFFS-CRDS baseline spectra on a 10 MHz interval at 50 kHz frequency steps after linear slope correction. A single scan exhibits a root-mean-square noise of 10^{-12} cm^{-1}, whereas the averaged baseline reaches the unprecedented detection limit indicated in the figure.

This record-breaking 10^{-14} cm^{-1}-level baseline noise after averaging for less than one day is an important and precious result in itself, as it paves the way to saturated-absorption Lamb dip spectroscopy with signal-to-noise ratios higher than 1000, which have so far only been reached for Doppler-broadened lines. Beyond that, it also hints at a considerable potential for yet higher OFFS-CRDS performance on broad spectral intervals, which might be reached by subtle improvements in the optical setup aimed at further reducing the impact of optical fringes (cf. Section 7.8) and of the higher-order transverse mode structure of the ring-down cavity (cf. Section 7.6).

Chapter 7

Systematic biases and error sources in CRDS

A generally acclaimed feature of CRDS is that it yields auto-calibrated absorption coefficient measurements in very good approximation. However, this does not mean that the accuracy of a CRDS measurement may simply be equated to its precision, as there are a multitude of systematic effects which can bias RD time measurements and, consequently, impair the absorption accuracy of CRDS. Consequently, the objective of this chapter is to give an overview about potential bias effect in CRDS, trying to be as exhaustive as possible without the pretention of completeness. To this end, literature reviews are interweaved with original results from this thesis throughout the chapter.

First, error sources related to an over-simplified usage of the basic relationship between ring-down time and absorption coefficient are analyzed. Then, limitations in ring-down signal acquisition are discussed. Subsequently, real deviations of the ring-down signal from an ideal exponential function as well as their physical sources and their impact are analyzed. Finally, spectroscopic error sources related to the spectrometer baseline are brought into focus.

7.1 Acquisition card timebase error

For quantifying absorption, CRDS substitutes a light intensity loss measurement by a decay time measurement. Consequently, the accuracy of the measurement is fundamentally limited by that of the underlying timebase. An inaccurate clock can formally be introduced into the fundamental equation (5.1) of CRDS in terms of a time dilation factor γ:

$$\frac{1}{(1+\gamma)\tau} = \frac{1}{(1+\gamma)\tau_0} + \frac{\alpha c}{n} \tag{7.1}$$

Inserting the observed biased ring-down times $(1+\gamma)\tau$ and $(1+\gamma)\tau_0$ into Eq. (5.1) yields the timebase-biased absorption coefficient $\tilde{\alpha}$

$$\tilde{\alpha} = \frac{1}{1+\gamma}\alpha \tag{7.2}$$

Consequently, the systematic error $\delta\alpha = \tilde{\alpha} - \alpha$ can be expressed in terms of the relative inaccuracy γ of the CRDS timebase as

$$\frac{\delta\alpha}{\alpha} = -\gamma \tag{7.3}$$

This result, namely that the relative absorption error is equal to the relative timebase error, is trivial from a physical point of view. The inaccurate timebase defines a biased

pseudo-second which, by the definition of the meter in terms of the speed of light, translates into a biased pseudo-meter. The absorption coefficient, which is defined as the relative intensity loss per unit length, is altered accordingly.

Although this effect is small in practice, it is not necessarily negligible for the error budget of state-of-the-art measurements. For the present OFFS-CRD spectrometer, for instance, the accuracy of the internal timebase of the National Instruments PCI-6281 acquisition card is specified to $5 \cdot 10^{-5}$. For measurements with a signal-to-noise ratio approaching 10^5, such as the line profile in Fig. 7 of Article 5 on page 160, the systematic timebase error therefore leads to a bias bigger than random noise.

In conclusion, the CRDS signal acquisition system must be referenced to the SI second to ensure a traceable, unbiased measurement. In practice, this can be realized by locking the analog-to-digital converter internal clock to a 10 MHz signal from a GPS-disciplined Rubidium timebase.

7.2 Sample refractive index

It is intuitively clear that the refractive index n must influence the CRDS absorption measurement, as the presence of a medium alters the phase velocity of light, thereby prolonging its lifetime inside the cavity. This is confirmed by the explicit n-dependence of the ring-down time τ derived in Section 5.1:

$$\tau = \left(\frac{1}{\tau_0} + \frac{\alpha c}{n} \right)^{-1} = \left(\frac{(1-R)c}{nL} + \frac{\alpha c}{n} \right)^{-1} \tag{7.4}$$

In practice, however, n is often implicitly neglected by using $n = 1$ in (7.4). While this is a good approximation for very dilute samples, the impact of n is non-negligible at higher pressures, and the full equation (7.4) must be used.

Quantitatively speaking, the error made by setting $n = 1$ depends on whether the baseline ring-down time τ_0 is measured with an empty cavity or determined as a fitting baseline when analyzing the absorption spectrum.

In the first case, when τ_0 is measured, setting $n = 1$ in Eq. (7.4) leads to the following determining equation for the biased absorption coefficient $\tilde{\alpha}$:

$$\tau^{-1} = \frac{(1-R)c}{nL} + \frac{\alpha c}{n} = \frac{(1-R)c}{L} + \tilde{\alpha} c \tag{7.5}$$

For gas samples at atmospheric pressures or below, the refractive index is close to one and can be written as $n = 1 + \epsilon$ with $\epsilon \ll 1$ in very good approximation. Then, Eq. (7.5) and some simple algebra, dropping higher orders of ϵ yields

$$\delta\alpha = -\epsilon \cdot \frac{1}{c\tau} \tag{7.6}$$

for the absorption error $\delta\alpha = \tilde{\alpha} - \alpha$ due to neglecting the refractive index. In this case, the systematic absorption coefficient error thus amounts to the fraction ϵ of total intracavity losses per length.

In the second case, when τ_0 is determined by fitting, the baseline is not biased by setting $n = 1$. The biased absorption coefficient $\tilde{\alpha}$ then follows from the simpler equation

$$\tau^{-1} = {\tau_0}^{-1} + \frac{\alpha c}{n} = {\tau_0}^{-1} + \tilde{\alpha} c \tag{7.7}$$

which yields

$$\frac{\delta\alpha}{\alpha} = -\epsilon \tag{7.8}$$

Here, even more intuitively, the relative systematic error in the absorption coefficient is just equal to $1 - n$.

Let us evaluate an order of magnitude of this effect for the present OFFS-CRD spectrometer. Absorption-related refractive index changes according to the Kramers-Kronig relations (cf. Section 5.4) are also governed by Eqs. (7.6) and (7.8), but shall not be treated here explicitly. Instead, the impact of the global off-resonant refractive index shall be considered. In most applications, the baseline is determined from a fit of the measured absorption spectrum, and Eq. (7.8) applies. As an example value for the refractive index near 1.6 µm, CO_2 has $n = 1+4.4\cdot10^{-4}$ at 1 atm [205]. The effect of this refractive index on the ring-down time measurement must then be taken into account for pressures in excess of

$$P_{lim} = p \cdot 230\,\mathrm{Pa} \tag{7.9}$$

where p is the relative accuracy target in ppm for the absorption coefficient.

For specific applications, such as the measurement of absorption continua, however, the baseline τ_0 cannot be determined from fitting, but must be measured for the evacuated cavity. In this case, Eq. (7.6) applies and the impact of the bias due to the refractive index can be much bigger. Still in the case of CO_2 near 1.6 µm, and for an empty-cavity ring-down time of approximately $\tau_0 = 168\,\mu$s, the absolute absorption error $\delta\alpha$ as a function of P in the limit of very weak absorption signals $\tau \approx \tau_0$ can be written as

$$\delta\alpha(P) = -8.7 \cdot 10^{-11}\,\mathrm{cm^{-1}atm^{-1}} \cdot P \tag{7.10}$$

while the relative error diverges towards infinity for $\alpha \to 0$.

7.3 Nonlinearities

Nonlinearities can arise at many steps of the ring-down signal detection and acquisition chain. They can originate from the photodiode itself, its amplifier circuit as well as the analog-to-digital converter (ADC) acquisition card. Characterizing these influences separately by separating them systematically and measuring them with respect to some reference of higher linearity is a task necessitating meticulous experimental work.

This quest is complicated by the fact that nonlinearities due to intensity-dependent losses may even arise in the ring-down phenomenon itself. Then, they carry physical information such as in the case of saturated absorption analyzed in great detail in Chapter 9. Another potential mechanism could be a temperature-dependent loss variation in the highly reflective dielectric coating of the cavity mirrors, due to the exponential decrease of dissipated power in the coating during each ring-down event. This effect most probably exists, but should be tiny, as it has not yet been observed in CRDS to the best of our knowledge.

In order to analyze the impact of nonlinearities on the determination of the ring-down time quantitatively, let us consider the following unique property of an exponential signal:

$$y(t) = y(0)\mathrm{e}^{-\frac{t}{\tau}} \Leftrightarrow \tau = -\frac{y(t)}{\dot{y}(t)} \tag{7.11}$$

Therefore, an easy analytic estimation of the ring-down time τ is possible in terms of the instantaneous apparent ring-down time $\tilde{\tau}(t)$ for a nearly exponential signal $\tilde{y}(t)$:

$$\tilde{\tau}(t) = -\frac{\tilde{y}(t)}{\dot{\tilde{y}}(t)} \tag{7.12}$$

Assuming $\tilde{\tau} = \tau$ without considering any details of the exponential fitting procedure used for determining the ring-down time is clearly simplistic. However, Eq. (7.12) evaluated at the starting point of the exponential fit generally provides an approximate, yet faithful reproduction of the ring-down time found by the fit. This is due to the fact that the fit is overwhelmingly dominated by the strong-signal at the beginning of the ring-down event. Consequently, this approach is a powerful tool for capturing the essential physical features of the ring-down time measurement in simple analytic expressions and will be used also in the following Sections 7.4, 7.6 and 7.7.

On this basis, let us study an ideal exponential intensity decay $I(t) = I_0 \mathrm{e}^{-t/\tau}$ with peak intensity I_0. We may then introduce a nonlinearity of the detection and acquisition setup by writing the resulting ring-down signal $\tilde{y}(t)$ as

$$\tilde{y}(t) = rI(t) \cdot (1 + \beta I(t)) \tag{7.13}$$

with a proportionality constant r and the coefficient β characterizing the magnitude of the first-order nonlinearity. Next, Eq. (7.12) may be used for quantifying the impact of β on the ring-down time measurement. Inserting the nonlinearity-affected signal (7.13) in Eq. (7.12) thus yields

$$\tilde{\tau}(t) = \tau \cdot \frac{1 + \beta I_0 \mathrm{e}^{-\frac{t}{\tau}}}{1 - 2\beta I_0 \mathrm{e}^{-\frac{t}{\tau}}} \tag{7.14}$$

As expected, the effect of the nonlinearity vanishes for $t \to \infty$ as $I \to 0$, and $\tilde{\tau} \to \tau$. Now, for a reasonably designed system, the nonlinearity bias is much smaller than the signal itself, $\beta I(t) \ll 1$. Consequently expanding Eq. (7.14) to first order in $\beta I(t)$ and evaluating the apparent ring-down time at $t = 0$ yields

$$\tilde{\tau}(t = 0) = \tau \left(1 - \beta I_0\right) \tag{7.15}$$

In this first-order analysis, the relative error in the ring-down time determination is thus identical to the dimensionless nonlinearity parameter βI_0.

Let us examine the propagation of this error to a biased absorption coefficient $\tilde{\alpha}$ according to the basic equation (5.1) of CRDS by inserting the nonlinearity-affected apparent ring-down times $\tilde{\tau}$ with sample absorption and $\tilde{\tau}_0$ on the baseline as in Eq. (7.15):

$$\tilde{\alpha} c = \frac{1}{\tilde{\tau}} - \frac{1}{\tilde{\tau}_0} = \frac{1}{\tau \left(1 - \beta I_0\right)} - \frac{1}{\tau_0 \left(1 - \beta I_0'\right)} \tag{7.16}$$

This is the general result when τ and τ_0 are determined from ring-down events with different peak intensities I_0 and I_0', respectively, which is the typical case when studying strong absorption features. For the sake of simplicity, we shall limit our further discussion to the case of weak absorption, where $I_0 \approx I_0'$ in good approximation. In this case, the relative absorption error σ_α / α in the limit $\beta I(t) \ll 1$ simply reads

$$\frac{\sigma_\alpha}{\alpha} = \frac{\tilde{\alpha} - \alpha}{\alpha} = \beta I_0 \tag{7.17}$$

This result implies that the systematic absorption coefficient error in the limit of weak absorption is simply equal to the relative nonlinearity βI_0 in the ring-down detection and acquisition system.

The National Instruments PCI-6281 data acquisition card used in OFFS-CRDS is specified at an integrated nonlinearity of 10 ppm, which can be identified with the term βI_0 from the present analysis to first order. Consequently, a systematic error on that order due to ADC nonlinearity has to be expected in OFFS-CRDS. The acquisition card specifications are in good agreement with the static µV-level structures observed in the averaged

ring-down fit residuals reported in Fig. 2 of Article 4 on page 90 and Fig. 3 of Article 5 on page 160. A dedicated experimental study confirming that the nonlinearities of the cavity transmission photodiode and its transimpedance amplifier circuit are negligible in OFFS-CRDS still needs to be carried out. However, no experimental evidence for such nonlinearities was found so far when the laser beam intensity was distributed uniformly over the full photodiode front facet surface.

The impact of ADC nonlinearity as a systematic error source in molecular line strength measurements was studied using PDH-locked FS-CRDS by Wójtewicz and co-workers [206]. The authors compared two ADC digitizer cards, one with nonlinearities at the percent level (ADC1, Gage Applied model CompuScope Octopus 8327) and one whose linearity properties are significantly better (ADC2, Gage Applied model CompuScope 14200). Having discussed the propagation of nonlinearity-biases from absorption coefficients to line strengths based on Eq. (4.4), the authors used both acquisition cards to record the same O_2 absorption line, determining ring-down times on several different fitting intervals. The comparison of line strength values deduced from the spectra obtained in this manner is shown in Fig. 7.1.

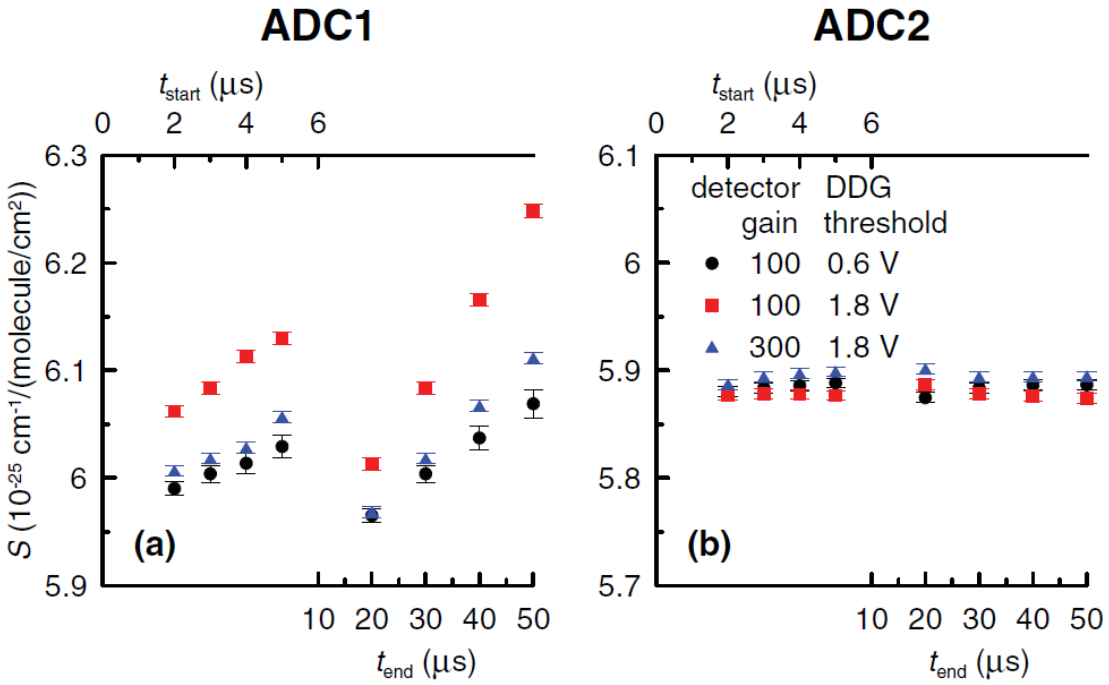

Figure 7.1 Line intensities for the O_2 B-band line near 14546.01 cm^{-1} measured by PDH-locked FS-CRDS with two distinct analog-to-digital converters and for different fitting intervals by Wójtewicz and co-workers [206]. Adapted from [206] (Figure 4).

As expected for a reliable ring-down detection and acquisition system, the line strength values measured using ADC2 do not exhibit any significant dependency on the experimental parameters. In stark contrast, the line strengths deduced from measurements with ADC1 exhibit systematic trends with the time interval used for ring-down fitting, providing further strong evidence for acquisition card nonlinearities. The line strength values with ADC1 are systematically biased by up to 5%. This is consistent with the percent-level nonlinearities observed on the exponential fit residuals for this digitizer card.

To conclude, let us point out that the outstanding exponentiality of the ring-down signal may be an important asset for further improving data acquisition. After an initial

experimental study for ensuring that both photodiode and ring-down cavity are operating in a regime where intensity-dependent nonlinearities are completely negligible, and with an excellent polarization matching of the input laser beam to a polarization eigenmode of the ring-down cavity (cf. Section 7.7), one may attempt to calibrate the acquisition card itself using the nearly ideally exponential ring-down signals. First promising tests aiming at such an experimental acquisition-card nonlinearity calibration were made by recording full-scale ring-down events over several days for generating a look-up table containing the voltage error for every bit of the ADC.

7.4 Bandwidth limitations

Cavity ring-down spectroscopy converts an intensity loss measurement into a decay measurement in the time domain. As discussed in Chapter 5 and Section 6.2.5, an optical switch turning off the input laser field many orders of magnitude faster than the response time of the cavity is a necessary requirement for this purpose [162] (cf. discussion in Section 7.5). Then, the light field leaking out the cavity provides a nearly perfect exponential decay, although several limitations and restrictions apply, as discussed in the following sections.

On this basis, an idealized ring-down signal $y(t)$ triggered at time t_0, as seen by a photodiode with an ideally linear, immediate response, can be written as

$$y(t) = \begin{cases} 1 & t < t_0 \\ \mathrm{e}^{-\frac{t-t_0}{\tau}} & t \geq t_0 \end{cases} \tag{7.18}$$

with ring-down time τ and an initial signal normalized to 1 without loss of generality for the sake of simplicity.

Let us now introduce a limited bandwidth somewhere in the detection system, in terms of a first-order low-pass filter with cut-off frequency ν_c which is represented by the transfer function

$$H(s) = \frac{1}{1 + \frac{s}{\omega_c}} \tag{7.19}$$

where $s = \sigma + i\omega$ is the complex Laplace transform variable and $\omega_c = 2\pi\nu_c$ is the angular cut-off frequency of the first-order low-pass. At the cut-off frequency, the power of a signal transmitted through such a filter is reduced by a factor of two, that is 3 dB. For frequencies higher than ν_c, the signal strength vanishes at the characteristic first-order roll-off slope of -6 dB per octave. The Laplace transform of a function $f(t)$ is defined as

$$F(s) = \int_0^\infty f(t)\mathrm{e}^{-st}\mathrm{d}t \tag{7.20}$$

The convolution theorem of Laplace transformation states that the effect of the low-pass filter on the signal is given by the product of their Laplace transforms:

$$\tilde{Y}(s) = H(s) \cdot Y(s) \tag{7.21}$$

This simple relationship justifies the enormous utility of a Laplace-transformation approach for an analytic treatment of bandwidth-limitation effects. After having taken the action of the low-pass into account according to (7.21), one may retrieve the altered signal $\tilde{y}(t)$ by returning to the time domain by means of an inverse Laplace transformation.

Therefore, let us begin by transforming $y(t)$ to the Laplace domain according to Eq. (7.20), using the linearity of the transformation:

$$Y(s) = \int_0^{t_0} \mathrm{e}^{-st}\mathrm{d}t + \int_{t_0}^{\infty} \mathrm{e}^{-\frac{t}{\tau}}\mathrm{e}^{-st}\mathrm{d}t = \frac{1-\mathrm{e}^{-st_0}}{s} + \frac{\mathrm{e}^{-st_0}}{s+\frac{1}{\tau}} \tag{7.22}$$

Then, introducing the limited bandwidth according to Eqs. (7.19) and (7.21) yields

$$\begin{aligned}\tilde{Y}(s) &= \frac{1}{1+\frac{s}{\omega_c}}\left(\frac{1-\mathrm{e}^{-st_0}}{s} + \frac{\mathrm{e}^{-st_0}}{s+\frac{1}{\tau}}\right) \\ &= \frac{1}{s}\frac{1}{1+\frac{s}{\omega_c}} - \mathrm{e}^{-st_0}\frac{1}{s}\frac{1}{1+\frac{s}{\omega_c}} + \mathrm{e}^{-st_0}\frac{\omega_c}{s^2+\left(\omega_c+\frac{1}{\tau}\right)s+\frac{\omega_c}{\tau}}\end{aligned} \tag{7.23}$$

This signal in the Laplace domain needs to be transformed back to the time domain. To this end, one may treat the three terms in (7.23) one by one thanks to the linearity of the transformation. Without going into smaller details, let us indicate the most important identities and Laplace transformation properties, which were used for the evaluation of $\tilde{y}(t)$. The inverse transformation of the first term in (7.23) can be carried out using

$$\frac{1}{s}F(s) \leftrightarrow \int_0^t f(u)\mathrm{d}u \tag{7.24}$$

and the following correspondence between Laplace and time domain:

$$\frac{1}{s+a} \leftrightarrow \mathrm{e}^{-at} \tag{7.25}$$

For the second term, one may reuse the result for the first term, together with the time-shifting property of the Laplace transformation,

$$\mathrm{e}^{-t_0 s}F(s) \leftrightarrow f(t-t_0)\Theta(t-t_0), \tag{7.26}$$

where $\Theta(t)$ is the Heaviside step function, which is 0 for $t < 0$ and 1 otherwise. Finally, to transform the third term back to the time domain, one may rely on the Laplace transformation pair

$$\mathrm{e}^{at}\sinh(bt) \leftrightarrow \frac{b}{(s-a)^2-b^2} \tag{7.27}$$

and the time-shifting relation (7.26). Inserting $\sinh x = 1/2\,(\mathrm{e}^x - \mathrm{e}^{-x})$ leads to a considerable simplification of the result here.

With all this, summing up the three terms of Eq. (7.23) transformed back into the time domain yields

$$\tilde{y}(t) = \begin{cases} 1 & t < t_0 \\ \frac{1}{1-\frac{1}{\omega_c\tau}}\mathrm{e}^{-\frac{t-t_0}{\tau}} + \left(1-\frac{1}{1-\frac{1}{\omega_c\tau}}\right)\mathrm{e}^{-\omega_c(t-t_0)} & t \geq t_0 \end{cases} \tag{7.28}$$

which can be further simplified to yield the final result for the bandwidth-limited ring-down signal $\tilde{y}(t)$ as

$$\tilde{y}(t) = \begin{cases} 1 & t < t_0 \\ \frac{1}{\omega_c\tau-1}\left(\omega_c\tau\mathrm{e}^{-\frac{t-t_0}{\tau}} - \mathrm{e}^{-\omega_c(t-t_0)}\right) & t \geq t_0 \end{cases} \tag{7.29}$$

Naturally, for an infinite system bandwidth $\omega_c\tau \to \infty$, $\tilde{y}(t) = y(t)$ and the unbiased signal of Eq. (7.18) is retrieved. It is important to note that the first derivative at $t = t_0$ vanishes for any value of ω_c and τ: $\dot{y}(t)|_{t=t_0} = 0$. This means that the introduction of a finite

bandwidth, which is present in any real physical system, does away with the unphysical non-differentiable behavior of the idealized ring-down signal in (7.18) at $t = t_0$.

To understand the bias of a finite system bandwidth on cavity ring-down time measurements quantitatively, let us use the notion of instantaneous apparent ring-down time $\tilde{\tau}$ developed in Section 7.3, according to Eq. (7.12):

$$\tilde{\tau}(t) = -\frac{y(t)}{\dot{y}(t)} = \frac{\tau \mathrm{e}^{-\frac{t}{\tau}} - \frac{1}{\omega_c}\mathrm{e}^{-\omega_c t}}{\mathrm{e}^{-\frac{t}{\tau}} - \mathrm{e}^{-w_c t}}, \tag{7.30}$$

where $t_0 \equiv 0$ was assumed for the sake of simplicity, without loss of generality. Equation (7.30) exhibits a strong t-dependence of the apparent instantaneous ring-down time due to the fading of the limited-bandwidth effect with growing t. It is most useful to express this bias in terms of a relative systematic error ξ:

$$\xi = \frac{\tilde{\tau} - \tau}{\tau} = \frac{1 - \frac{1}{w_c \tau}}{\mathrm{e}^{\left(\omega_c - \frac{1}{\tau}\right)t} - 1} \tag{7.31}$$

Let us now introduce an accuracy target p, requiring a relative systematic bandwidth-related error $\xi < p$ for the ring-down measurement. Then, Eq. (7.31) implies a minimal waiting time t_w between the ring-down trigger at $t = 0$ and the ring-down time determination at $t \geq t_w$, typically by means of an exponential fit. Letting $\xi = p$ in Eq. (7.31) yields the following relationship between p, τ, t_w and ω_c:

$$\left(\omega_c - \frac{1}{\tau}\right) t_w = \ln\left(\frac{1 - \omega_c \tau}{p} - 1\right) \tag{7.32}$$

In the limiting case of an accurate measurement $p \ll 1$ in a well-designed system $\omega_c \tau \gg 1$, whose bandwidth is big compared to the ring-down time, the result can be simplified using first-order expansions in these parameters, yielding the succinct expression

$$t_w \approx -\frac{\ln p}{2\pi\nu_c} \tag{7.33}$$

This provides the interesting and useful insight that t_w is nearly independent of τ as long as $\omega_c \tau \gg 1$ is fulfilled. Furthermore, by combining Eq. (7.33) and Eq. (7.18), the accuracy may be related to the relative fitting threshold $y(t_w)/y(0)$ through

$$p \approx \left(\frac{y(t_w)}{y(0)}\right)^{2\pi\nu_c\tau} \tag{7.34}$$

In the light of the findings, typical potential bandwidth limitations in cavity ring-down spectroscopy shall be discussed quantitatively in the following, on the concrete example of the OFFS-CRD spectrometer presented in this thesis.

7.4.1 Photodiode bandwidth

The ring-down detection photodiode and amplifier circuit are at the heart of cavity ring-down measurements and their noise, linearity and bandwidth properties often direclty limit those of the cavity ring-down measurement. We have therefore measured the bandwidth of the detection photodiode setup used for OFFS-CRDS to ensure that it is sufficient for guaranteeing accurate ring-down measurements.

The setup consists of an indium gallium arsenide (InGaAs) photodiode with a home-made transimpedance amplifier whose gain can be switched to either 91 kΩ, that is two resistors of 91 kΩ and 1 MΩ, respectively, in parallel, or 1 MΩ using an optocoupled switch and a $0/+5$ V TTL (transistor-transistor logic) control signal. The bandwidth measurement was carried out by focussing the light from an infrared LED (light-emitting diode) on the photodiode, while modulating the LED driving current at different frequencies. The modulation bandwidth of the LED was well over 10 MHz in this experiment. To reveal the bandwidth limitation of the photodiode-amplifier system, a 1-s-long logarithmic frequency sweep spanning five decades was programmed on an arbitrary waveform generator and fed to the LED current driver modulation input. The resulting LED output power modulation was picked up by the photodiode, and the voltage output signal from its transimpedance amplifier circuit was recorded at a sampling rate of 1 GHz by means of an AC-coupled Tektronix digitizer oscilloscope. The result of this measurement at two different transimpedance amplifier gain values is shown in Fig. 7.2, with the AC-coupled voltage signal normalized to its maximum value. The first-order bandwidth of the photodiode-amplifier

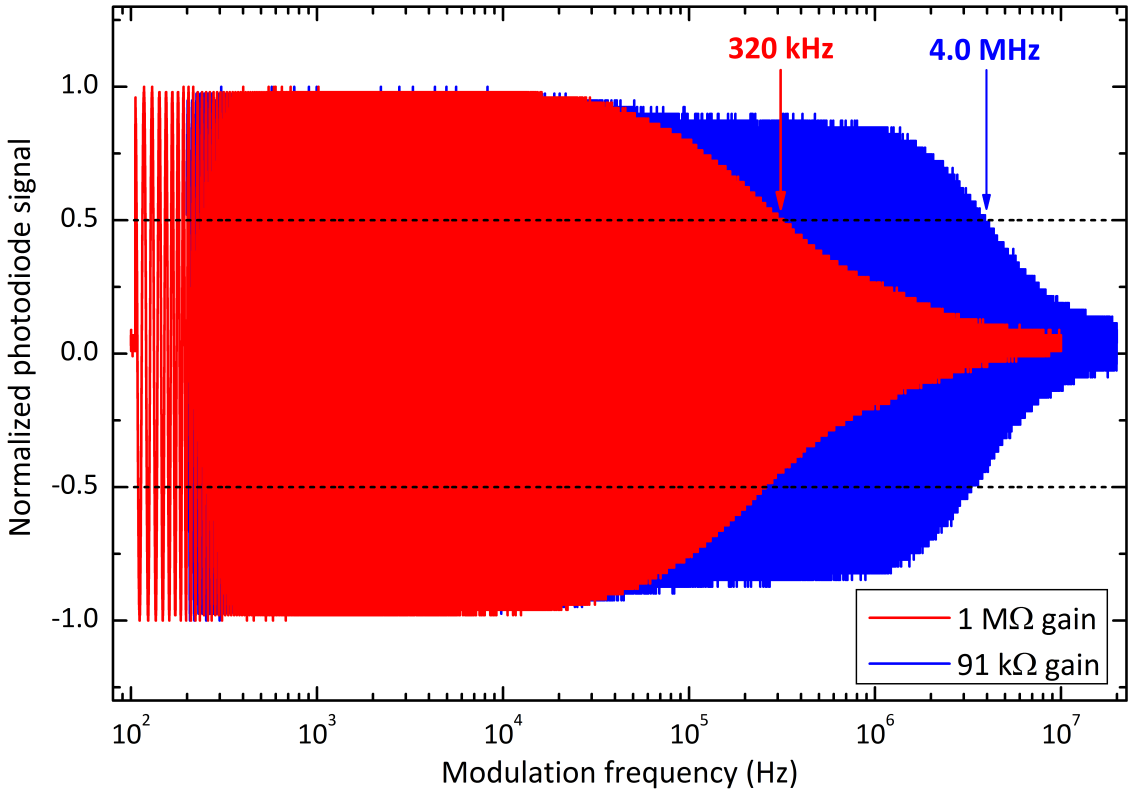

Figure 7.2 AC-coupled photodiode signal for an intensity-modulated LED undergoing a one-second logarithmic modulation frequency chirp. One measurement was carried out for each of two transimpedance amplifier gain values (red and blue curves). The resulting effective photodiode bandwidth frequencies $\nu_{c_{91\,\mathrm{k}\Omega}}$ and $\nu_{c_{1\,\mathrm{M}\Omega}}$ are reported in the figure.

system follows from the experimental curves by locating the half-maximum intersection of the signal envelope, which monotonously decreases with modulation frequency. This -3 dB criterion for finding ν_c is illustrated by the dashed lines in Fig. 7.2 and yields a bandwidth of 320 kHz at 1 MΩ and 4.0 MHz at 91 kΩ. The latter is slightly higher than the 3.5 MHz expected for a constant gain-bandwidth product.

Finally, let us turn to the implications of these results for our OFFS-CRDS setup. According to Eq. (7.33), a 10^{-6}-accuracy level ring-down time measurement requires

waiting times $t_{w_{91\,\mathrm{k}\Omega}} = 0.5\,\mu$s and $t_{w_{1\,\mathrm{M}\Omega}} = 7\,\mu$s, respectively. Therefore, even the high-gain bandwidth is sufficient for making highly accurate ring-down measurements, provided that a waiting time of approximately 7 µs before exponential fitting is respected. For strong intracavity absorption, this becomes a non-negligible fraction of the ring-down time, implying a maximum fitting threshold of 50% of the peak signal for a typical very low ring-down time of 10 μs, for instance. In practice, all metrology-grade OFFS-CRDS measurements were carried out at a transimpedance gain of 91 kΩ. The corresponding waiting time of 0.5 µs is three times shorter than the shortest sampling interval of the National Instruments PCI-6281 card used for ring-down signal acquisition. By virtue of this fact and according to Eq. (7.33), working at a transimpedance gain of 91 kΩ guarantees that there is no deterioration of ring-down time accuracy in OFFS-CRDS due to photodiode-bandwidth effects.

7.4.2 Low-pass filtering

Inserting a low-pass filter before analog-to-digital conversion is imperative for avoiding aliasing of higher-frequency noise components in the discrete digitized signal. Furthermore, a low-pass filter reduces the bandwidth of white technical noise, leading to a proportional reduction in noise variance. While an analog low-pass filter before the ADC is thus necessary and beneficial, care must be taken to avoid the bandwidth issues in ring-down time determination discussed above.

In OFFS-CRDS, the analog bandwidth of the National Instruments PCI-6281 card used for ring-down acquisition amounts to 750 kHz by default. In this case, Eq. (7.33) requires a waiting time of 3 μs between ring-down triggering and exponential fitting for an accuracy of 10^{-6}. If a photodiode gain of 1 MΩ is chosen, that bandwidth limitation dominates. Therefore, let us focus on the case of 91 kΩ, where transmission photodiode signal levels typically allow measuring ring-down times down to 60 μs. Consequently, a waiting time of 3 μs corresponds to a fitting threshold of over 95%, which is entirely sufficient for precise ring-down measurements. The PCI-6281 acquisition card also features a built-in low-pass filter with $\nu_c = 40$ kHz, which is a very attractive choice for ultra-low-noise ring-down measurements. When it is activated, the resulting noise level reduction allows working at the digitized noise of the acquisition card with effective 18-bit resolution, corresponding to observed photodiode signal dark voltage root-mean-square noise levels down to 13 μV. However, when accuracy is an issue, using this low-pass filter becomes problematic. Inserting $p = 10^{-6}$ and $\nu_c = 40$ kHz in Eq. (7.33), one obtains a waiting time $t_w = 55\,\mu$s. For the case of $\tau = 60\,\mu$s discussed above, this would correspond to very low fit threshold of 40% in order to meet the accuracy goal. This can be sufficient under certain conditions, and the accuracy criterion may be enforced by discarding the number of first ring-down data points corresponding to the respective waiting time. In practice, all metrology-grade absorption spectra by OFFS-CRDS were recorded at full 750-kHz bandwidth, again excluding any deterioration of accuracy by bandwidth limitations.

7.5 Imperfect signal extinction

Theoretical treatments of CRDS in textbooks and in the literature, but also the ones in this thesis, generally assume - either implicitly or explicitly - an ideal interruption or switch-off of the light source used for injecting light into the ring-down cavity before triggering the ring-down event. This idealization is twofold, requiring both an infinitely fast switch-off at $t = 0$ and a signal that drops to strictly zero, corresponding to an infinite extinction ratio, as described mathematically by a Heaviside step function $\Theta(-t)$. In reality,

this picture is naturally only partially fulfilled and the elements of the experimental setup lead to a finite switch-off time of the light source down to a finite signal extinction ratio. Then, the residual cavity injection interferes with the resonant intracavity field, leading to fluctuations of the ring-down signal, which bias the ring-down time determination by exponential fitting.

The condition of switching off the input field much faster than the cavity ring-down time was analyzed theoretically in the seminal paper by Anderson, Frisch and Masser [162], whose decay-time mirror reflectometer was the foundation for all future CRDS developments. The impact of finite extinction, in turn, was studied both theoretically and experimentally by Huang and Lehmann [207]. They considered the general case $\Delta\nu_L\tau \gg 1$ of a noisy laser whose linewidth $\Delta\nu_L$ is big compared to the cavity modewidth $\Delta\nu_C = 1/(2\pi\tau)$, here expressed in terms of the cavity ring-down time τ. Consequently, the authors carry out a statistical analysis of the random process of cavity injection and present an explicit treatment of effects due to the sweeping of the laser through cavity resonance with the cavity, or vice-versa. Due to the noisy cavity injection in this limit discussed in greater detail in [164], the transmitted-intensity threshold for triggering a ring-down event I_{th} can be bigger than the time-averaged transmitted intensity I_0. The ratio between the two values should not be much bigger than unity, as ring-down events become less frequent with growing I_{th}.

On this basis, the authors deduce the single-shot root-mean-square noise σ_k in the cavity decay rate $k = \tau^{-1}$ as a function of the inverse power extinction ratio ϵ_r of the light switch used for generating ring-down events, with $\epsilon_r \ll 1$. In the case of ring-down fitting with equal weights for all data points, which is appropriate in a technical-noise-limited regime (cf. Section 6.3.1), they find

$$\left(\frac{\sigma_k}{k}\right)^2 = \frac{64}{27}\frac{I_0}{I_{th}}\epsilon_r \tag{7.35}$$

The effect scales with the amplitude of the residual cavity injection proportional to $\sqrt{\epsilon_r}$, as intuitively expected for a ring-down signal deformed by heterodyne interference. In the case of shot-noise-limited ring-down acquisition, where a weighted least-squares fit of the decay signal must be carried out (cf. Section 6.3.1), the prefactor of the result is slightly different:

$$\left(\frac{\sigma_k}{k}\right)^2 = 4\frac{I_0}{I_{th}}\epsilon_r \tag{7.36}$$

In [207], Huang and Lehmann also report CRDS experiments with variable laser-off extinction ratio ϵ_r for verifying these results experimentally. They use a standard continuous-wave CRDS setup with an acousto-optic modulator (AOM) acting as a fast switch for triggering ring-down events. The radio frequency (RF) signal driving the AOM is generated using a dedicated setup composed of two RF switches, a step attenuator, a power splitter and an amplifier, allowing full experimental control over the effective RF attenuation during the laser-off period for the ring-down measurement. In this manner, ϵ_r was varied in steps of 5 dB, while ring-down time shot-to-shot noise was characterized at each ϵ_r value by recording 400 ring-down events. The result of this experiment is shown in Fig. 7.3. The experimental curves are in excellent agreement with the prediction of Eq. (7.35). At high extinction ratios, the ring-down time noise levels off, indicating that it is no longer limited by poor input laser extinction, but by the intrinsic technical noise of the CRD spectrometer detection and data acquisition system.

In view of these findings, great care was taken in the setup of the OFFS-CRD spectrometer to guarantee sufficient extinction ratios for unbiased and low-noise ring-down

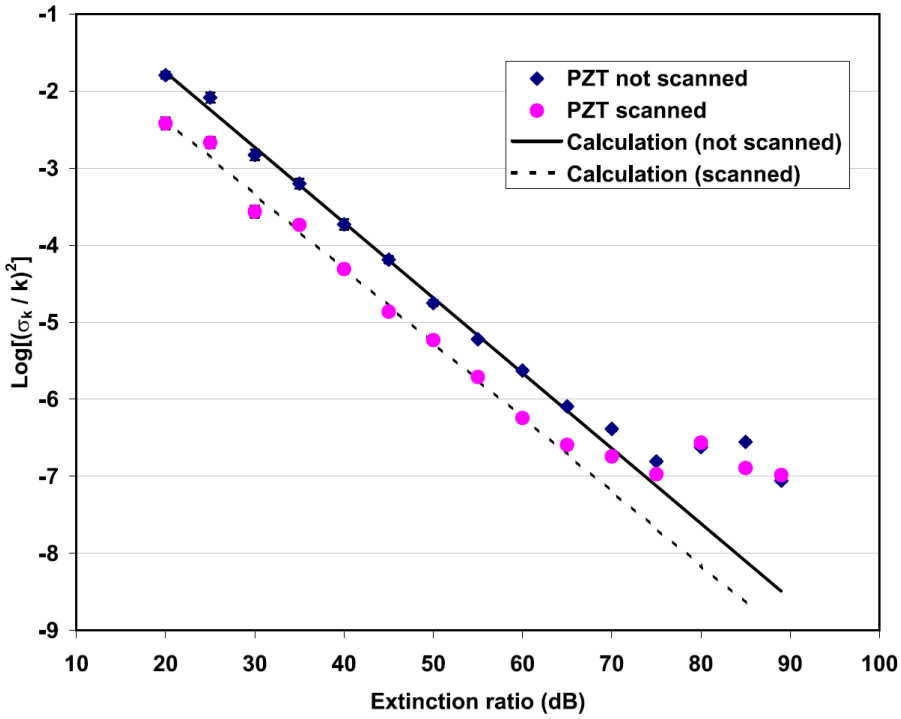

Figure 7.3 Relative variance of ring-down times measured at different laser-off extinction ratios and comparison to theoretical predictions by Huang and Lehmann. Adapted from [207] (Figure 2).

detection. The Mach-Zehnder modulator (MZM) proved to be an ideal tool to this end. With its electro-optic bandwidth in excess of 10 GHz, it features intrinsic sub-ns switching times. Furthermore, the absence of a driving RF unambiguously guarantees that no single sideband exists. Therefore, the problem of optical switching with the MZM reduces to finding a RF switch with sufficient suppression ratio and switching time. As discussed in Section 6.2.5, two such switches were used for OFFS-CRDS so far, a Minicircuits ZASWA-2-50DR+ with a typical extinction of 90 dB in the lower GHz range and a Hittite HMC-C019 whose extinction still reaches 75 dB at 16 GHz. Their switching times of 10 ns or better are completely negligible in view of the digitizer sampling interval of at least 1.5 µs used in OFFS-CRDS so far.

With $\epsilon_r \approx 10^{-9}$ for the ZASWA-2-50DR+ switch, Eq. (7.36) provides a quantitative estimation of ring-down time noise in OFFS-CRDS due to imperfect laser-off extinction. For the PDH-locked system, the ring-down trigger threshold is essentially identical to the continuous locked maximum transmission level and $I_0 \approx I_{th} \approx 1$. With these values, Eq. (7.36) implies $\sigma_k/k = 6.3 \cdot 10^{-5}$. Switching to absorption units, and for typical spectrometer baseline losses of $2 \cdot 10^{-7}\,\mathrm{cm}^{-1}$ this corresponds to an extinction-related absorption noise prediction of $1.3 \cdot 10^{-11}\,\mathrm{cm}^{-1}$. This value is significantly higher than the single-shot ring-down noise as low as $3 \cdot 10^{-12}\,\mathrm{cm}^{-1}$ really observed, as reported in Fig. 3 of Article 4 on page 90 and Fig. 4 of Article 5 on page 160.

We suspect that this discrepancy can be attributed to the fact that the ring-down cavity length is locked to the stable VCOF laser in OFFS-CRDS. Therefore, to first order, there are no frequency fluctuations leading to intensity fluctuations due to noisy cavity injection. Instead, a tiny but continuous background transmission signal of the cavity is expected, which should not bias the ring-down time determination. An experimental study similar to the one by Huang and Lehmann [207] should be carried out in the future to confirm this continuous-background hypothesis. If confirmed, this would further underline the benefits

of OFFS-CRDS for obtaining extreme detection sensitivity. Let us note that for obtaining the single-ring-down precision down to $3 \cdot 10^{-12}\,\mathrm{cm}^{-1}$ demonstrated by OFFS-CRDS, a challenging extinction ratio of almost 100 dB would be necessary in a noisy-laser scenario according to Eq. (7.36), for the typical value $I_0/I_{th} = 2.5$ used in [207].

7.6 Transverse mode coincidences

An intriguing phenomenon occasionally occuring in CRDS is intimately linked to the transverse mode structure of a high-finesse cavity [113]. At some temperatures or gas pressures the baseline loss and single-shot ring-down noise increase. When the effect is marked, a clear decrease in cavity transmission is also observed, hinting to an increase in intracavity losses. Huang and Lehmann [182] explained this phenomenon in terms of the coincidence of the resonance frequency of the TEM_{00} mode used for high-sensitivity CW-CRDS with the one of another TEM_{mn} mode, with $m + n \gg 1$ in general.

Recalling the transverse mode resonance frequencies (2.31) of the TEM_{mn} modes of an ideal Fabry-Pérot resonator of length L in the paraxial approximation

$$\nu_{lmn} = \frac{c}{2n_0 L} \cdot \left(l + \frac{m+n+1}{\pi} \cdot \arccos g \right) \tag{7.37}$$

with the intracavity refractive index and the resonator parameter g from Section 2.4, one sees that coincidences of TEM_{mn} mode frequencies with those of TEM_{00} modes of arbitrary longitudinal mode number l occur when the second term in the (7.37) is an integer j:

$$m + n = j \cdot \frac{\pi}{\arccos g} \tag{7.38}$$

The precision needed for a coincidence to occur is given by the width of the cavity modes, and thus the cavity finesse. However, the finesse for higher-order modes is much lower than for the TEM_{00} mode due to increased losses, thereby facilitating the occurrence of coincidence events. Furthermore, mirror astigmatism and polarization effects [113–115] lift the frequency degeneracy of modes with same $m + n$ in real resonators, giving rise to multiplets with $2(m + n + 1)$ individual modes with various splittings. Consequently, the simplistic Eq. (7.37) can only provide an approximate picture of the occurence of coincidence events in high-finesse resonators.

One way of approaching the effect of transverse mode excitation in the vicinity of a TEM_{00} mode is to write down the photodiode signal $y(t)$ for a light field containing a main TEM_{00} contribution with amplitude A and a tiny contribution ϵA with $\epsilon \ll 1$ from a higher-order mode in terms of the ansatz

$$y(t) = A\mathrm{e}^{-\frac{t}{\tau}} + 2\epsilon A \epsilon \mathrm{e}^{-\left(\frac{1}{2\tau}+\frac{1}{2\tau'}\right)t} \cos\left(\Delta t + \varphi\right) \tag{7.39}$$

where τ and τ' are the ring-down times for the TEM_{00} and the higher order term, respectively, Δ is the frequency separation between the nearly degenerate modes, and φ is the phase difference of the fields of the two modes. The second-order term in ϵ was dropped in Eq. (7.39). Assuming a non-zero beat note between the two modes with $\epsilon \neq 0$ is justified when the orthogonality between the TEM_{mn} is lifted by the limited integration bounds corresponding to spatial clipping of the higher order mode. Such an aperture insufficiency may occur for instance on the detection photodiode, as the radial size of a TEM_{mn} mode scales as $\sqrt{m+n+1}w_0$ with the TEM_{00} waist radius w_0 [182]. In addition, the eigenmodes of a real resonator with mode-dependent losses are only nearly orthogonal [108].

The ring-down signal y(t) in (7.39) may be inserted into Eq. (7.12) for estimating the apparent ring-down time $\tilde{\tau}$ at $t = 0$ in the mode beating regime:

$$\tilde{\tau}(t=0) = -\frac{y(0)}{\dot{y}(t)|_{t=0}} = \tau \frac{1 + 2\epsilon \cos\varphi}{1 + (1 + \frac{\tau}{\tau'})\,\epsilon \cos\varphi + 2\epsilon\Delta\tau \sin\varphi} \tag{7.40}$$

This expression can be further simplified by expanding to first order in $\epsilon \ll 1$ again. Then, the relative ring-down bias due to transverse mode beating reads

$$\frac{\tilde{\tau} - \tau}{\tau} = -\epsilon \cdot \left(\left(\frac{\tau}{\tau'} - 1 \right) \cos\varphi + 2\Delta\tau \sin\varphi \right) \tag{7.41}$$

For $\varphi \ll 1$, this result thus predicts a decrease in ring-down time, as $\tau' < \tau$ in general. Huang and Lehmann have observed such mode-beatings on experimental ring-down signals and obtained a good fit with a function equivalent to the one in 7.39, yet without dropping the ϵ^2-term [182]. This result is shown in Fig. 7.4.

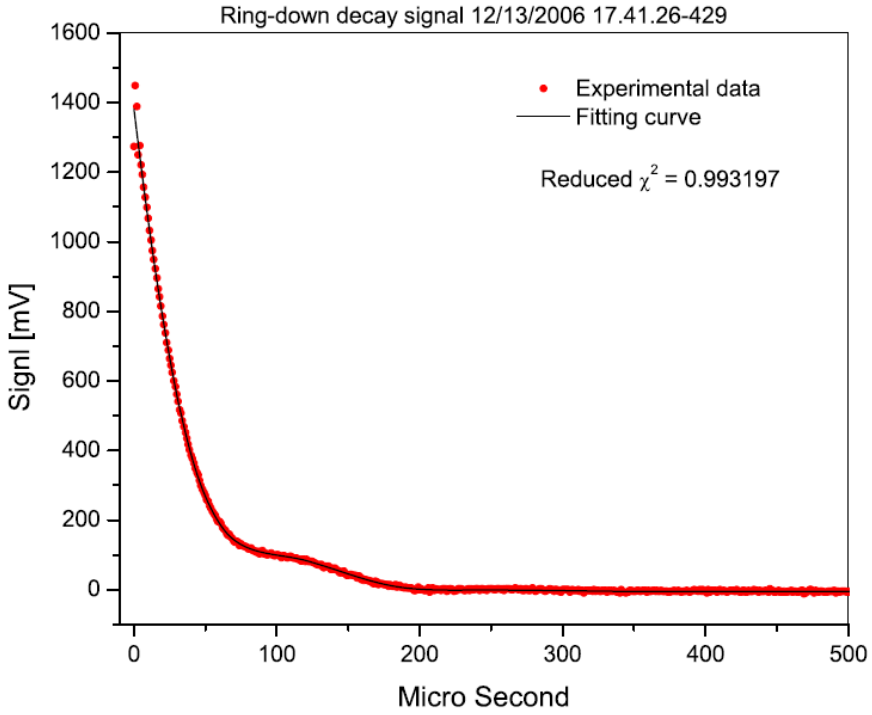

Figure 7.4 Ring-down signal measured in CW-CRDS by Huang and Lehmann [182], carrying a heterodyne beat note between a TEM_{00} and a higher-order TEM_{mn} mode. The excellent fit (black curve) is based on a mode-beating function similar to Eq. (7.39). Adapted from [182] (Figure 5).

Note that mode beating alone cannot account for the global drop in signal intensity observed during coincidence events. In [182], Huang and Lehmann propose that the phenomenon bears some analogy to an avoided crossing between the energies of a two-level system with two quantum states linked by an off-diagonal coupling term. In the case of the cavity, such a coupling between modes arises from diffuse diffraction by mirror imperfections leading to an interferential speckle pattern [208], which couples energy into other cavity modes according to projection-integral theory [106]. This coupling mechanism was initially proposed and studied by Klaassen and co-workers [209]. They demonstrated experimentally how the coupling leads to mode-broadening and transmission reduction when approaching degeneracy. Contrary to the interpretation by Klaassen and co-workers, we hold that the mixing of TEM_{00} and TEM_{mn} properties in the new eigenmodes arising

from the coupling term can lead to a significant reduction in ring-down time, due to the fact that the bigger TEM_{mn} mode samples the imperfections of the mirror surface, whereas the small TEM_{00} mode is generally aligned to the zone of lowest losses by the experimenter. Consequently, as the coupling between the modes becomes stronger as they approach degeneracy, losses in the new eigenmode increase and the ring-down time decreases. Therefore, and in the light of the findings by Huang and Lehmann [182], the conclusion drawn by Klaassen and co-workers [209]

> These effects *cannot* be observed by cavity ringdown experiments; this should serve as a warning to experimentalists.

is not correct, unfortunately for cavity ring-down absorption spectroscopists.

Systematic effects on absorption measurements due to transverse mode coincidences were also observed in NICE-OHMS (noise-immune cavity-enhanced optical heterodyne molecular spectrometry) by Silander and co-workers [210]. In all three studies, on the fundamentals of transverse mode coupling [209], its impact on CW-CRDS [182] and on NICE-OHMS [210], the mode-broadening and loss-enhancement effects could be drastically reduced by inserting an aperture with small diameter a into the cavity, thereby efficiently suppressing the propagation of big higher-order TEM_{mn} modes with their $\sqrt{m+n+1}$ size scaling. The diffraction limit is characterized by the Fresnel number $N_f = a^2/(\lambda L)$, where λ is the wavelength. A rough estimate for the highest-order modes which can still propagate in the cavity is then given by $m + n \leq \pi N_f$ [108]. Therefore, restricting the cavity diameter is an efficient means of increasing losses for higher-order modes, thereby minimizing their coupling with the TEM_{00} mode.

Although no quantitative systematic analysis was made, several observations indicate that transverse mode coupling effects are also a key limitation for OFFS-CRDS. When varying the temperature of the ring-down cavity, periodic episodes of decreased ring-down times and cavity transmission are observed, as illustrated by the measurement shown in Fig. 7.5. The active heating and cooling of the ring-down cavity (red curve) was carried out using the Peltier system (cf. Section (6.2.3)). The temperature changes by up to 5 °C lead to relative cavity length variations of 10^{-4} in view of the coefficient of thermal expansion of aluminium, which amounts to roughly $2{\cdot}10^{-5}K^{-1}$. Under these drastic cavity length drifts, Pound-Drever-Hall locking of the cavity on the laser would be instable due to failure of the high-voltage tracking scheme (cf. Section (6.2.2)). Therefore, ring-down times (black curve) were measured using simple PZT-triangle scans of slightly more than one FSR yielding one or two ring-down events per slope as in classical CW-CRDS. To obtain a reasonable transmission signal in spite of this inefficient cavity injection scheme, the unshifted VCOF laser light was used by bypassing the Mach-Zehnder modulator. The measured ring-down times reveal a plenitude of intracavity loss increase events of different amplitude, reducing ring-down times down to below 140 µs for a normal empty-cavity loss level corresponding to about 162 µs. The inversion of the temperature change in the second half of the measurement reveals the reproducibility of the loss-increase events and provides strong evidence for their interpretation on the grounds of transverse mode coupling. The strong delay between the cavity temperature measured by five platinum probes in the cavity bulk (cf. Section (6.2.3)) naturally does not challenge causality, but is due to the big temperature gradients between air from Peltier cooler heating the cavity surface and interior of the cavity. It hints at a disalignment-based component of the cavity length changes leading to the transverse mode coincidences. This interpretation is supported by the strong hysteresis of the ring-down time evolution, which exhibits a much faster succession of loss events when going from high to low temperatures than vice-versa.

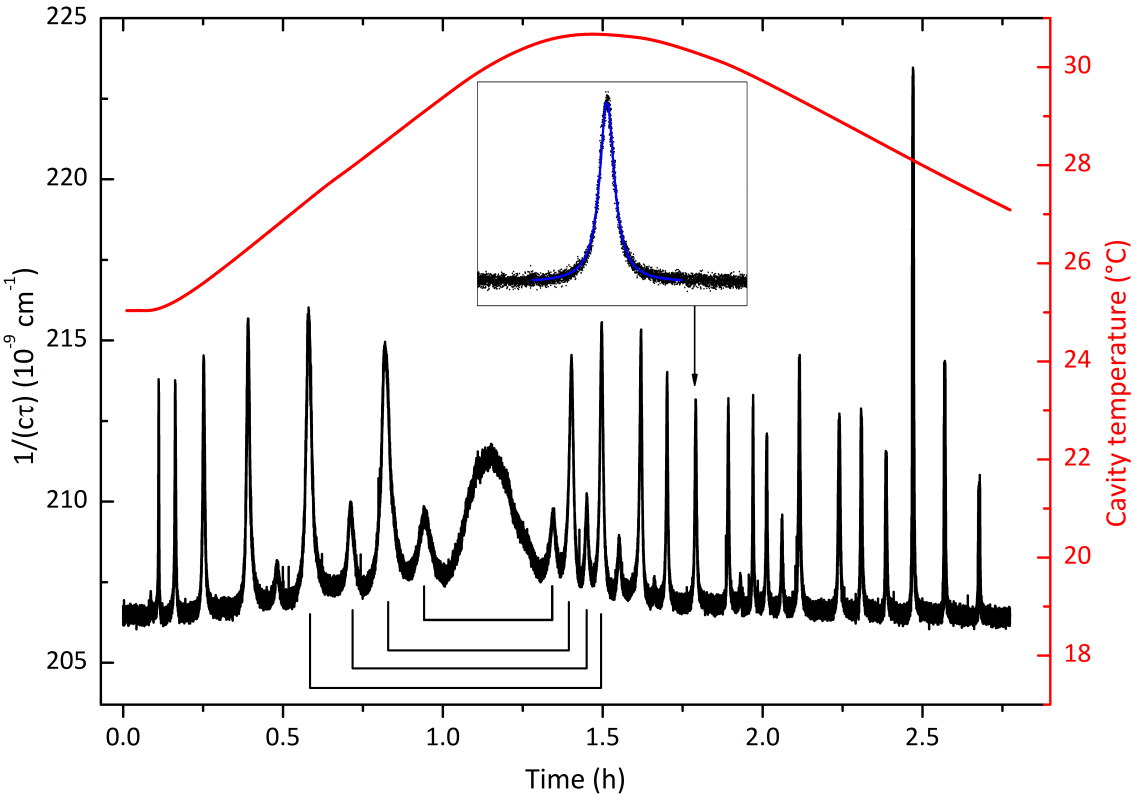

Figure 7.5 Ring-down time evolution (black curve) for an empty cavity undergoing a temperature change (red curve), exhibiting recurring Lorentzian loss-increase events attributed to spectral coincidence of higher order TEM_{mn} modes of the ring-down cavity with the TEM_{00} mode. A zoom on one of the events is shown in the inset, together with a Lorentzian fit (blue curve). Brackets indicate the reproducibility of the loss events for some example pairs corresponding to the same coincidence. Note that five additional pairs of corresponding coincidences are visible in the figure.

The most recent ring-down cavity (cf. Section 6.2.1) used for recording the data in Fig. 7.5 consists of two mirrors with $r = 100\,\mathrm{cm}$ radius of curvature spaced $L = 34.5\,\mathrm{cm}$ apart, corresponding to a resonator parameter $g = 0.655$ according to Eq. (2.30). Consequently, Eq. (7.38) predicts a transverse mode coincidence within $2 \cdot 10^{-3}$ of the cavity FSR for $j = 3$ and at the mode index $m + n = 11$, a coincidence within $4 \cdot 10^{-3}$ for $j = 6$ and $m + n = 22$, and so on. According to Eq. (7.37) this would be sufficient to avoid coincidence effects in view of the cavity finesse of 450000. However, the mirror curvature radius value is not known to better than 1%, so that immediate coincidence cannot be excluded. Even worse, the degeneracy lifting of TEM_{mn} modes, giving rise to multiplets of $2 \cdot (m + n + 1)$ modes due to astigmatism and polarization as discussed above, tears this simple picture down definitively. In the case of the TEM_{10} and TEM_{01} modes studied by Huang and Lehmann [182], for instance, an astigmatism-related splitting of $7 \cdot 10^{-4}$ in units of the cavity FSR was found, corresponding to sub-percent imperfections in the mirror curvature. To first order, this effect is expected to scale with $m + n$, leading to TEM_{mn} multiplets of considerable frequency extension. The current OFFS-CRDS cavity inner diameter 8 mm has a Fresnel number of $N_f = 29$, implying that cavity modes with $m + n \leq \pi N_f \approx 91$ can propagate in the cavity without huge diffraction losses. Consequently, the transverse mode structure of the present cavity provides an extremely unfavorable configuration for OFFS-CRDS, as confirmed by the observed dense pattern of transverse mode coincidences shown in Fig. 7.5.

For a quantitative analysis of this mode structure leading to a precise determination of the mirror parameters and a cavity mode assignment of the observed coupling resonances, some meticulous work is still necessary for thoroughly representing the complex transversal mode frequency structure of a real cavity to high orders in TEM_{mn}, taking both scalar-field astigmatism splittings [113] and polarization-related splittings [114, 115] into account. While certainly cumbersome, such an analysis would have the benefit of providing one of the most stringent experimental tests of optical resonator physics beyond the paraxial approximation to date [114].

To conclude, let us discuss a pragmatic strategy to try and remedy biases related to transverse mode coincidences in future versions of OFFS-CRDS. Firstly, a pinhole of 3.2 mm diameter could be inserted at the middle of the cavity, reducing the Fresnel number of the system to $N_f = 4.6$, allowing only transverse modes with $m + n \leq 14$ to propagate in the cavity with negligible diffraction losses. Secondly, one may tailor the transverse mode frequency structure of the cavity in order to avoid coincidences of the TEM_{00} mode with any of the multiplets with $m + n \leq 14$ by setting $\arccos g/\pi$ in Eq. (7.37) to 0.93, for instance. In practice, such a near-concentric cavity configuration can be realized with two $r = 25\,\mathrm{cm}$ mirrors and a cavity length of $L = 49.4\,\mathrm{cm}$. With a mirror curvature precision better than 1%, such a cavity is stable and should render transverse mode coincidences with non-negligible impact impossible.

7.7 Polarization mode mismatch

In Section 3.2.1, an experiment resolving the polarization splitting of the TEM_{00} mode of a macroscopic high-finesse Fabry-Pérot resonator was presented. Here, we shall discuss the impact of such splittings on CRDS.

In the literature, Huang and Lehmann have carried out a systematic study of linear birefringence- and polarization-dependent losses of CRDS mirrors [148]. Importantly, the authors confirmed that stress-induced birefringence is the dominant mechanism lifting the polarization degeneracy of the TEM_{00} mode of macroscopic high-finesse cavities, typically used in highly sensitive CRDS experiments. Modelling the birefringence and polarization-dependent losses of the mirrors using a Jones matrix formalism [211], they derived an analytic expression for the polarization mode splitting of the two nearly linear polarization eigenmodes with slightly different losses. The authors validated their analysis with an extensive experimental study on the dependency of output polarization and measured ring-down times on cavity mirror orientation and input polarization. However, an explicit deformation of the ring-down signal due to the heterodyne beating between light fields from the two polarization eigenmodes of the cavity could not be observed directly in the study by Huang and Lehmann. This was attributed to the fact that the TEM_{00} frequency splitting was too small [148].

Here, we shall focus on a direct analysis of the impact of polarization mode beating on ring-down determination. First, a theoretical treatment is made for obtaining an explicit expression for a ring-down signal originating from light from both polarization eigenmodes of a cavity. Second, we present an experimental study providing, to the best of our knowledge, the first direct observation of polarization mode-beating in CRDS. Then, a measurement of related ring-down time biases is reported and compared with the theoretical description. Finally, a simple experimental protocol for ensuring an optimal matching of

the input laser polarization to one of the cavity TEM_{00} polarization eigenmodes is given, and its effectiveness for eliminating polarization biases in CRDS is demonstrated.

7.7.1 Theoretical analysis

A theoretial framework for the description of the two polarization eigenmodes $\mathbf{e_1}$ and $\mathbf{e_2}$ was provided by Huang and Lehmann in [148]. Here, let us denote the frequency splitting of the TEM_{00} mode doublet by Δ and their Lorentzian full-width-at-half-maximum as Γ_1 and Γ_2, respectively. Recalling Eq. (5.20), these cavity modewidths are related to the ring-down times $\tau_{1,2}$ by

$$\tau_{1,2} = \frac{1}{2\pi\Gamma_{1,2}} \tag{7.42}$$

As the difference in losses for both modes is small [148], it is useful to introduce the small parameter γ loss difference γ so that

$$\Gamma_2 = \Gamma_1 + \gamma \tag{7.43}$$

quantifying the difference in losses between both polarization modes.

On this basis, let us now study the shape of a ring-down signal when the light field exciting the ring-down cavity is not in one of the two polarization eigenstates of the cavity. One may arbitrarily choose the mode of lower frequency ν to have $\tau = \tau_1$ and $\Gamma = \Gamma_1$ without loss of generality. Furthermore, let us assume that the polarization state of the exciting laser field is close to this polarization eigenmode of the cavity. Then, the electric field amplitudes transmitted through the cavity during a ring-down event can be written as

$$E_1 = \hat{E}\mathrm{e}^{-\frac{1}{2}\frac{t}{\tau}}\mathrm{e}^{-i2\pi\nu t} \tag{7.44}$$

$$E_2 = \kappa\hat{E}\mathrm{e}^{-\frac{1}{2}\frac{t}{\tau}}\mathrm{e}^{-\pi\gamma t}\mathrm{e}^{-i2\pi(\nu+\Delta)t+\varphi_0} \tag{7.45}$$

where $\hat{E}$ and $\kappa\hat{E}$ are the amplitudes in the first and second polarization mode, respectively, and κ is a real number between 0 and 1. Let us note that, due to the overlap of the Lorentzian modes of the doublet (cf. Section 3.2.1), a non-zero amplitude fraction $\kappa \ll 1$ can be present in the second mode even for an infinitely narrow laser perfectly locked to the peak of the main polarization mode. An explicit study of the mode excitation process with an expression for κ and the relative phase φ_0 between the two fields at $t = 0$ is beyond the scope of this analysis.

On the CRDS detection photodiode, the electric fields from both modes of the polarization doublet interfere, yielding a photodiode signal $S(t)$ which reads

$$S(t) \sim \left(\mathrm{Re}(E_1\mathbf{e_1}) + \mathrm{Re}(E_2\mathbf{e_2})\right)^2 = \left(\mathrm{Re}\left(E_1\right)\right)^2 + \left(\mathrm{Re}\left(E_2\right)\right)^2 + 2\mathrm{Re}\left(E_1\mathbf{e_1}\right)\cdot\mathrm{Re}\left(E_2\mathbf{e_2}\right) \tag{7.46}$$

In spite of the losses in the system leading to $\mathbf{e_1}\cdot\mathbf{e_2} \neq 0$, this signal is generally very weak, as an approximate orthogonality between both polarization modes still holds [148]. Therefore, let us consider the case where a linear polarizer with transmission axis $\mathbf{e_0}$ is introduced between the cavity and the photodiode. In this special case, which will be important in the next section, the expression for the photodiode signal takes the altered form

$$\begin{aligned} S(t) &\sim \left(\mathrm{Re}(E_1\mathbf{e_1}\cdot\mathbf{e_0}) + \mathrm{Re}(E_2\mathbf{e_2}\cdot\mathbf{e_0})\right)^2 \\ &= \left(\mathrm{Re}\left(E_1\mathbf{e_1}\cdot\mathbf{e_0}\right)\right)^2 + \left(\mathrm{Re}\left(E_2\mathbf{e_2}\cdot\mathbf{e_0}\right)\right)^2 + 2\mathrm{Re}\left(E_1\mathbf{e_1}\cdot\mathbf{e_0}\right)\mathrm{Re}\left(E_2\mathbf{e_2}\cdot\mathbf{e_0}\right) \end{aligned} \tag{7.47}$$

To illustrate the difference between both cases, let us consider the example of two orthogonal linear polarizations and the polarizer oriented at 45° with respect to both. Then Eq. (7.46) yields $S(t) \sim (\mathrm{Re}\,(E_1))^2 + (\mathrm{Re}\,(E_2))^2$, whereas Eq. (7.47) yields $S(t) \sim 1/2\left[(\mathrm{Re}\,(E_1))^2 + (\mathrm{Re}\,(E_1))^2 + 2\mathrm{Re}\,(E_1)\,\mathrm{Re}\,(E_2)\right]$.

As the following derivation is analogous in both cases, let us concentrate on the important second case with a polarization analyzer here. Inserting the expressions (7.44) and (7.45) for the electric field amplitudes into Eq. (7.47), the photodiode signal can be written as

$$S(t) \sim \frac{1}{2}\hat{E}^2 \mathrm{e}^{-\frac{t}{\tau}} \left(p_1^2 + \kappa^2 p_2^2 \mathrm{e}^{-2\pi\gamma t} + 2\kappa p_1 p_2 \mathrm{e}^{-\pi\gamma t} \cos\left(2\pi\Delta t + \varphi_0 + \varphi_2 - \varphi_1\right)\right) \tag{7.48}$$

where the polarization scalar products have been expressed as $\mathbf{e_1}\cdot\mathbf{e_0} = p_1 \mathrm{e}^{i\varphi_1}$ and $\mathbf{e_2}\cdot\mathbf{e_0} = p_2 \mathrm{e}^{i\varphi_2}$ and rapidly oscillating terms such as $\cos^2(2\pi\nu t)$ have been replaced by their time average 1/2. Abbreviating the phase $\varphi = \varphi_0 + \varphi_2 - \varphi_1$ of the oscillating term, introducing the signal amplitude $A \sim 1/2\hat{E}^2 p_1^2$ and the coupling parameter $\epsilon = p_2/p_1\kappa$, one retrieves the following expression for the photodiode signal:

$$S(t) = A\mathrm{e}^{-\frac{t}{\tau}} \left(1 + \epsilon^2 \mathrm{e}^{-2\pi\gamma t} + \epsilon \mathrm{e}^{-\pi\gamma t} \cos\left(2\pi\Delta t + \varphi\right)\right) \tag{7.49}$$

Therefore, in the presence of light from both polarization eigenmodes of the cavity and a polarization analyzer projecting the two polarization onto a common axis, oscillations at a frequency equal to the mode splitting Δ appear on the ring-down signal, which is no longer a pure exponential. In the case without a linear polarizer behind the cavity, the factor ϵ^2 in Eq. (7.49) needs to be replaced by an additional independent parameter. However, as discussed above, the effect on the ring-down signal is generally much smaller in this case.

To conclude, let us examine the impact of the non-exponential signal $S(t)$ in (7.49), exhibiting polarization-related oscillations, on the determination of the cavity ring-down time τ by exponential fitting. As discussed in Section 7.3, a simple analytic approximation for the apparent ring-down time of a nearly exponential signal is given by Eq. (7.12). Inserting the signal (7.49) which exhibits polarization oscillations, one obtains the following rough estimate for the apparent ring-down time $\tilde{\tau} \equiv \tilde{\tau}(t = 0)$:

$$\tilde{\tau} = \left(\tau^{-1} + \frac{4\pi^2\Delta\epsilon \sin\varphi}{1 + \epsilon^2 + 2\epsilon\cos\varphi}\right)^{-1} \tag{7.50}$$

In the special case of orthogonal linear polarization eigenmodes of the cavity, the two polarization projections in Eq. (7.48) can be written as $p_1 = \cos\vartheta$ and $p_2 = \sin\vartheta$ in terms of the orientation ϑ of the polarization analyzer with respect to the polarization of the first cavity eigenmode. Inserting these expressions into the coupling parameter ϵ yields

$$\epsilon = p_2/p_1\kappa = \kappa\tan\vartheta \tag{7.51}$$

To obtain a simple analytic expression, we will exclude the divergent case $\vartheta \to 90°$ in the following by requiring $\epsilon \ll 1$. This implies $\kappa \ll 1$, that is an injecting laser field which is almost polarization-matched to the first eigenmode of the cavity. To first order in ϵ, the denominator of Eq. (7.50) can then be taken as unity, yielding

$$\tilde{\tau} = \frac{\tau}{1 + 4\pi^2\kappa\Delta\tau \sin\varphi\tan\vartheta} \tag{7.52}$$

Finally, one may again use $\epsilon = \kappa\tan\vartheta \ll 1$ for a series expansion of the denominator to first order, yielding the final result for the approximate biased ring-down time $\tilde{\tau}$:

$$\tilde{\tau} = \tau\left(1 - 4\pi^2\kappa\Delta\tau\sin\varphi\tan\vartheta\right) \tag{7.53}$$

The apparent ring-down time $\tilde{\tau}$ is thus expected to exhibit a bias scaling as $\tan\vartheta$ under a variation of the polarization analyzer angle ϑ.

7.7.2 Experimental results and polarization matching

For obtaining optimal cavity transmission in OFFS-CRDS, one generally aligns the polarization-maintaining fiber carrying the VCOF laser beam so that it mostly injects one of the two polarization eigenmodes of the cavity. In this case $\kappa \ll 1$ of weak coupling into the second polarization mode and with the approximate orthogonality of the two modes $|\mathbf{e_1} \cdot \mathbf{e_2}| \ll 1$ the non-exponential perturbation signal in Eq. (7.46) is very small. Under certain conditions, it can be discerned as a structure in the fit residuals after averaging hundreds of ring-down events, which is often still compatible with acquisition card nonlinearity specifications.

As discussed in the previous Section, one may place a linear polarizer between ring-down cavity and detection photodiode in order to enhance and study polarization-dependent effects and biases in CRDS. The polarizer projects the electric field amplitudes from the two polarization modes of the TEM_{00} doublet onto a common axis for maximizing their interference signal. Such an experiment with our OFFS-CRDS setup is shown in Fig. 7.6, using a photodiode transimpedance gain of 1 MΩ to compensate for the strong signal attenuation by the polarization analyzer rotated by 70° with respect to maximum transmission.

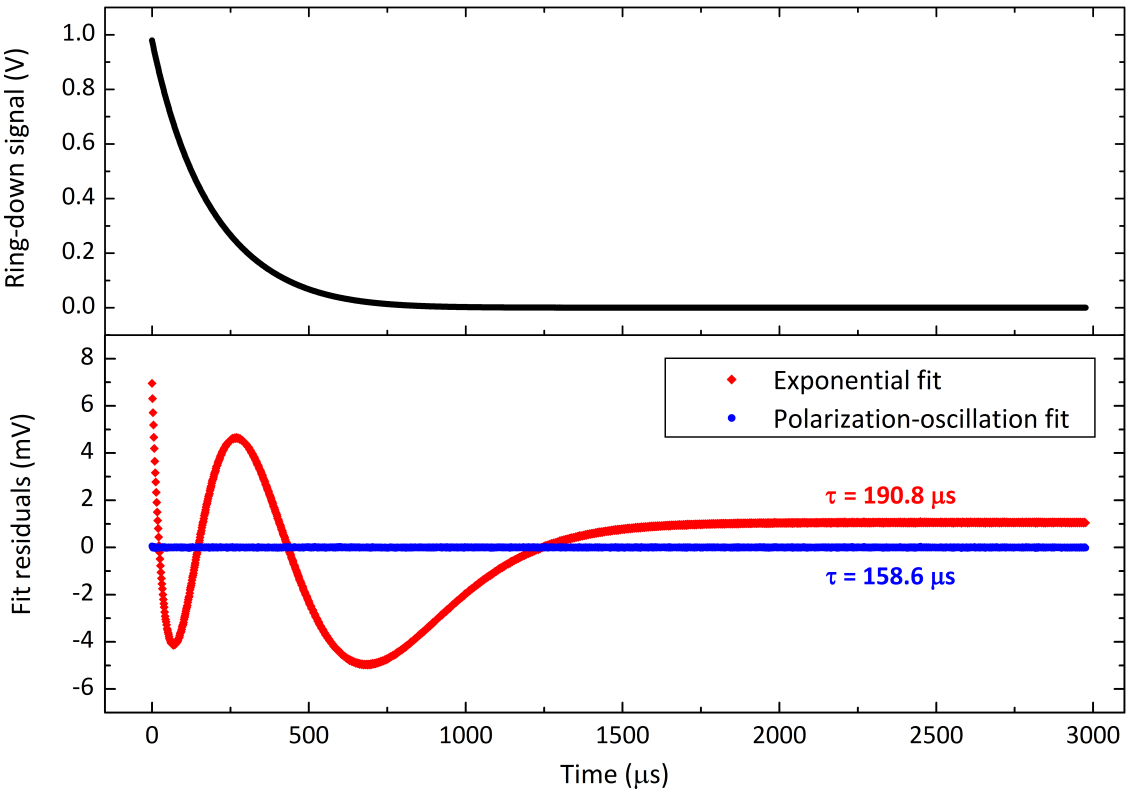

Figure 7.6 Experimental cavity ring-down signal with a linear polarizer placed between cavity and photodiode (upper panel). Residuals for a simple exponential fit and a fit using the function in Eq. (7.49), which takes into account the effect of polarization (lower panel). The ring-down times resulting from both fits are indicated in the figure.

Its upper panel shows a ring-down signal with sampling intervals of 1.5 μs obtained by

averaging 3000 individual events at equal trigger threshold. The oscillating fit residuals from a simple exponential fit (red diamonds) reveal a drastic deformation of this ring-down signal by the beating signal of the two polarization modes. Consequently, this fit with an inadequate model yields a strongly biased ring-down time $\tilde{\tau} = 190.8\,\mu$s. In contrast, the residuals from fitting with the polarization-affected ring-down signal of Eq. (7.49) (blue circles) are perfectly flat at a root-mean-square noise level of $15\,\mu$V. Importantly, this fit yields the following realistic physical parameters:

$$\tau = (158.64 \pm 0.04)\,\mu\text{s} \tag{7.54}$$

$$\Delta = (734 \pm 1)\,\text{Hz} \tag{7.55}$$

$$\epsilon = (1311 \pm 3) \cdot 10^{-4} \tag{7.56}$$

The uncertainties given above are statistical and based on an error propagation in the fit procedure. The fit according to Eq. (7.49) thus provides a very precise measurement of the polarization mode splitting of the ring-down cavity. Expressed relative to the cavity modewidth, which is $\Gamma = (2\pi\tau)^{-1} = (1003.3 \pm 0.3)\,\text{Hz}$ here, this splitting amounts to $\Delta/\Gamma = 0.732 \pm 0.001$, indicating a significant overlap of the two polarization modes. Their separation is on the same order of magnitude as the $\Delta/\Gamma = 3.453 \pm 0.004$-splitting observed for the TEM_{00} polarization doublet of the high-finesse etalon in Section 3.2.1. Let us emphasize that splittings are expected to vary from cavity to cavity depending on the birefringence-inducing stress on the cavity mirrors and the relative orientation of their polarization main axes.

In another measurement with different input polarization, yet still roughly matched to one ring-down cavity mode by turning the polarization-maintaining fiber port, the polarization-induced bias on ring-down time was studied as a function of the polarization analyzer angle ϑ. To this end, the analyzer was turned in steps of 10° and several hundred ring-down events were averaged at each angle. The ring-down times resulting from a simple exponential fit and from a fit according to Eq. (7.49) are reported in Fig. 7.7 as the red diamonds and blue circles, respectively.
The fit taking polarization into account yields an unbiased RD value of $\tau = (158.8 \pm 0.1)\,\mu$s. In contrast, the red curve exhibits a strong $\tan\vartheta$-dependency, following its theoretical shape (7.53), as indicated by the fit equation reported in Fig. 7.7. The offset of the red curve zero crossing at $\tilde{\tau} = (158.1 \pm 0.1)\,\mu$s with respect to the unbiased value hints to the presence of an elliptic polarization contribution. Averaging over all polarizer orientations ϑ, the measurement in Fig. 7.7 also yields a supplementary measurement of the TEM_{00} polarization mode splitting

$$\Delta = (730 \pm 20)\,\text{Hz}, \tag{7.57}$$

in good agreement with the result (7.55). The statistical uncertainty in (7.57) is due to the spread of the individual measurements.

To minimize the bias due to polarization mode beating in CRDS, the polarization of the probe laser field must be matched to one polarization eigenmode of the cavity. Then $\kappa = 0$ and the electric field E_2 in Eq. (7.45) vanishes, so that no heterodyne beating signal can arise.

In practice, an experimenter can obtain full polarization control with high purity by inserting a combination of linear polarizer and quarter-wave plate before the cavity. Then, a polarization analyzer placed behind the cavity serves as an excellent discriminator for tailoring the input polarization to an eigenmode of the TEM_{00} doublet: maximizing the mode-beating signal by turning the polarizer by typically 70° with respect to its maximum transmission axis, one may readily adjust the input polarization by hand until the beating

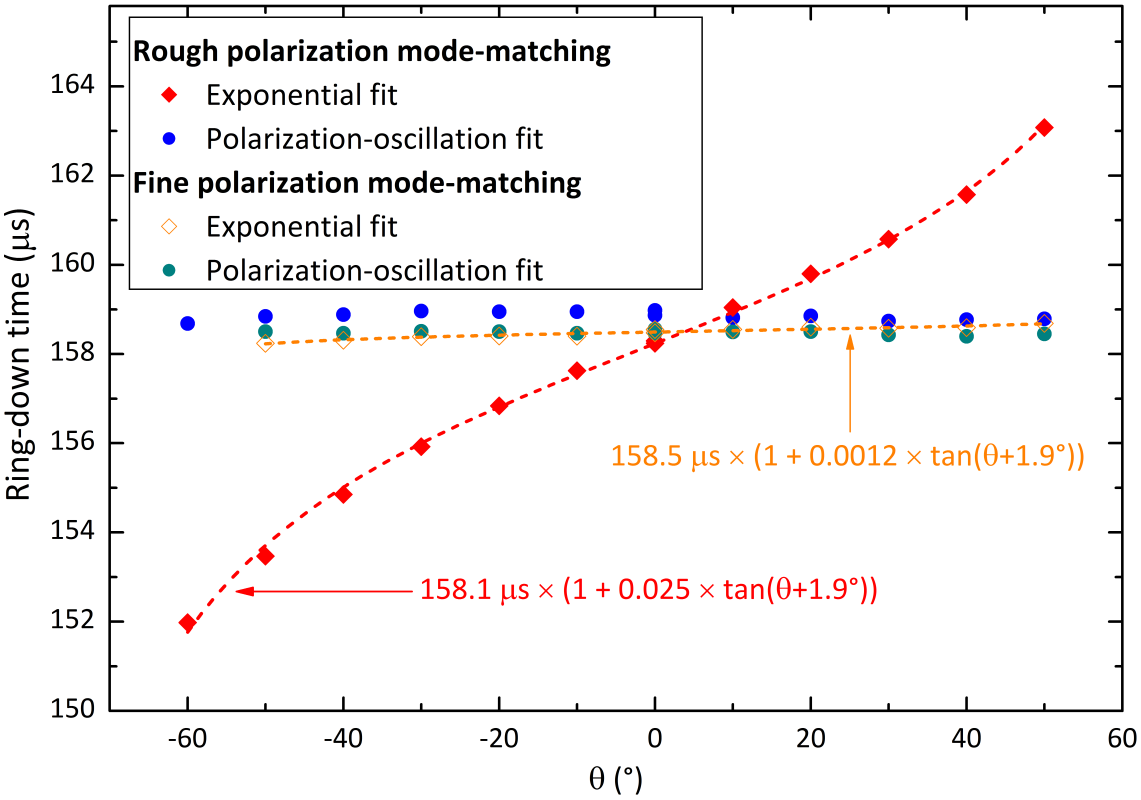

Figure 7.7 Difference in ring-down times obtained by fitting with a pure exponential and with the function of Eq. (7.49) for two different degrees of polarization-matching between laser field and ring-down cavity. The dashed lines are fits of Eq. (7.53) to the data, with the results indicated in the figure.

signal vanishes. This situation corresponds to a near-perfect polarization-state matching of probe laser and ring-down cavity.

The beneficial effect of polarization mode-matching for retrieving unbiased ring-down times is clearly visible in Fig. 7.7. The data points from fitting with a simple exponential (empty orange diamonds) show but a very slight systematic dependence on the polarization analyzer angle ϑ, as indicated by the dashed fit curve according to 7.53. In view of the small effect, the polarization analyzer zero angle $\vartheta_0 = 1.9°$ in the fit was fixed to the more precise value deduced from the previous experiment with approximate polarization matching, where the effect was much bigger. Comparing the fit equations in the roughly and finely polarization-matched equations, one obtains the ratio of the respective coupling coefficients κ_r and κ_f as $\kappa_r/\kappa_f \approx 21$. The polarization beat signal is due to the heterodyne interference between two fields and the effect therefore scales as κ. However, the power in the second polarization mode scales as κ^2, implying that the polarization matching of laser and cavity in the finely adjusted case was improved by a factor of 440 with respect to the roughly adjusted case.

This square-root-scaling of ring-down time biases with polarization matching illustrates the difficulty of near-perfect polarization matching in practice. The manual adjustment of the injection polarization optics is extremely sensitive and large-diameter rotation mounts should be used. Furthermore, even very small thermomechanical drifts in the polarization optics orientation or tiny depolarization effects due to diffuse scattering lead to the coupling of light into the second mode. Tiny effects can then still be visible in the presence of a polarization analyzer when using a low-noise detection photodiode and signal averaging, as demonstrated by Fig. 7.7.

Finally, without surprise, the ring-down times retrieved from the advanced ring-down fit according to Eq. (7.49), shown as turquoise circles in Fig. 7.7, yield an unbiased value of $\tau = (158.48 \pm 0.04)\,\mu$s also in the case of near-perfect polarization matching. Let us note that small differences in the ring-down times deduced from the three independent measurements in this Section are not in contradiction, but simply due to slow drifts in ring-down cavity losses over the total measurement period of several hours during which the cavity was not temperature-stabilized due to the ongoing manual polarization adjustments.

7.8 Interference fringes due to parasite reflections and diffuse scattering

A very common limitation of the detectivity, noise level and accuracy of absorption spectrometers originates from periodic sinusoidal signal modulations known as etaloning, optical fringes or parasite fringes depending on authors and sources. They are due to interferences of the probe field with light fields of much smaller amplitude due to parasite reflections or diffuse scattering somewhere in the optical setup. Consequently, the periodicity of the sinusoidal modulation signature corresponds to the optical path differences between both interfering waves and can be used for identifying location and origin of each parasite reflection. Experimental examples for such interference fringes can be seen in the spectrometer baselines and the corresponding Fourier spectra of Fig. 5 of Article 4 on page 90 and Fig. 5 of Article 5 on page 160, which also illustrate how parasite fringes limit the performance of OFFS-CRDS.

To develop a quantitative picture on the origin and the impact of optical fringes, one may consider the output of a high-finesse cavity with mirror reflectivity $R = r^2$ in the limit $R \to 1$, where r is the amplitude reflection coefficient, assuming a loss-free mirror transmission $T = 1-R$ for the sake of simplicity. Let us place a parasite reflection site with a tiny amplitude reflectivity coefficient ρ in the limit $\rho \to 0$ and a transmission $\theta^2 = 1-\rho^2$ at a distance D before the cavity input mirror. For reasons which will be discussed in detail below it is useful to also introduce an additional round-trip amplitude loss factor κ with $0 \leq \kappa \leq 1$ between parasite reflection site and cavity. Let us designate the one-way phase shift of light in the cavity as $\varphi = kL$ where k is the wave vector and L is the cavity length. Analogously, $\Phi = kD$ shall be the one-way phase shift for a light wave travelling between the cavity input mirror and the parasite reflection site.

On this basis, one may examine the impact of the parasite reflection ρ and the loss factor κ on the transmission of this coupled system of one low-finesse and one high-finesse cavity as a generalization of the derivations of the Airy function (2.34) (cf. [116], for instance). The following derivation sets aside the effect of absorption for the sake of simplicity, but it can readily be generalized to take absorption α into account by inserting the appropriate multiplicative terms such as $\mathrm{e}^{-\alpha L}$ in the ansatz (7.58).

In the steady state, the field amplitude E_{out} transmitted by the high-finesse cavity can be written in terms of the incoming amplitude E_{in} before the parasite reflection site as

$$\frac{E_{out}}{E_{in}} = \theta \mathrm{e}^{i\Phi} \left(1 - r\kappa\rho \mathrm{e}^{i2\Phi} + \left(-r\kappa\rho \mathrm{e}^{i2\Phi}\right)^2 + ...\right) t^2 \mathrm{e}^{i\varphi} \left(1 + r^2 \mathrm{e}^{i2\varphi} + (r^2 \mathrm{e}^{i2\varphi})^2 + ...\right) \tag{7.58}$$

In words, the transmission of the cavity is the infinite sum of amplitude contributions from a growing number of round-trips inside the cavity, and this, in turn, for an infinite sum of input amplitude contributions due to the parasite reflection. The corresponding terms can be factored out, as all of these input amplitude contributions eventually perform the

same round-trip pattern in the cavity. The infinite sums in Eq. (7.58) are geometric series, leading to the following simplification in terms of analytic expressions:

$$\frac{E_{out}}{E_{in}} = \frac{\theta t^2 \mathrm{e}^{i\Phi}\mathrm{e}^{i\varphi}}{(1 + r\kappa\rho\mathrm{e}^{i2\Phi})(1 - r^2\mathrm{e}^{i2\varphi})} \tag{7.59}$$

The light intensity transmitted through the cavity is proportional to the absolute value squared of Eq. (7.59). It is useful to introduce $\epsilon = 1 - R$ with $\epsilon \ll 1$ in the present high-finesse limit, which also implies $\varphi \ll 1$ for non-zero cavity transmission. Then, various fractional and trigonometric expressions can be expanded to leading order in the small quantities ρ, φ and ϵ, leading to considerable simplifications after some lengthy algebra which shall be omitted here. Eventually, one finds the transmissivity of the cavity as

$$\left|\frac{E_{out}}{E_{in}}\right|^2 \sim \frac{1}{\varphi^2 + \frac{1}{4}\frac{\epsilon^2}{1-\epsilon+2\kappa\rho\cos(2\Phi)}}, \tag{7.60}$$

which is a Lorentzian function in φ with a full width at half maximum (FWHM) of

$$\Delta\varphi_{FWHM} = \sqrt{\frac{\epsilon^2}{1 - \epsilon + 2\kappa\rho\cos(2\Phi)}} \tag{7.61}$$

The resulting cavity modewidth is then retrieved using the dispersion relation $\phi = kL = 2\pi L\nu/c$:

$$\Delta\nu_{FWHM} = \Delta\varphi_{FWHM} \cdot \frac{c}{2\pi L} \tag{7.62}$$

and the corresponding cavity ring-down time $\tau = 1/(2\pi\Delta\nu_{FWHM})$ reads

$$\tau = \tau_0 + \frac{\kappa\rho L}{\epsilon c}\cos(2kD) \tag{7.63}$$

with the ring-down time of the isolated cavity τ_0 given by Eq. (5.4), after expansion to first order in ϵ in the present high-finesse limit. Equation (7.63) thus describes an optical parasite fringe on the ring-down time with a period $\lambda/2$ when varying the distance D. According to the dispersion relation $k = 2\pi\nu/c$, the fringe period with respect to a frequency change of the laser equals $\Delta\nu_{fringe} = c/(2D)$, which is the optical fringe analogon of the free spectral range in Eq. (2.32). The amplitude $\hat{\tau} = \frac{\kappa\rho L}{\epsilon c}$ of this fringe is best expressed in relative units, yielding

$$\frac{\hat{\tau}}{\tau_0} = \kappa\rho \tag{7.64}$$

in the limit $R \to 1$. With $\kappa = 1$ when there is no obstacle between parasite reflection site and cavity, this astonishingly simple result yields a direct estimate for the parasite reflectivity corresponding to a certain fringe amplitude and vice-versa. For instance, the optical circulator used in OFFS-CRDS (AFW model CIR-PM-1590-C-5-2), as discussed in Article 4 on page 90 and in Article 5 on page 160, has specified return losses better than -50 dB, implying $\rho = \sqrt{10^{-5}}$. For a spectrometer baseline of $\alpha_0 \approx 2 \cdot 10^{-7}\,\mathrm{cm}^{-1}$ expressed in absorption units, this corresponds to a fringe amplitude of $6 \cdot 10^{-10}\,\mathrm{cm}^{-1}$, perfectly matching the observations. The amplitude of this circulator fringe exhibits variations over time, hinting to an interferometric phenomenon inside the circulator leading to a modulation of effective return losses. Inserting a neutral density filter with an optical depth of 0.5, corresponding to an intensity loss by a factor of three per passage, the fringe amplitude could be reduced by that same factor, as expected according to Eq. (7.64) with $\kappa = \sqrt{(1/3)^2} = 1/3$ for two passages through the density filter per fringe-etalon round-trip. For experiments with sufficient input power level, this proved to be a beneficial choice

allowing a considerable reduction of the averaging times needed for both fringe-scrambling schemes discussed in detail in Article 5 on page 160.

In the case of a neutral density filter, κ is due to a bidirectional signal attenuation and reduces the fringe amplitude at the expense of a loss in optical power by the same factor, as indicated above. However, $\kappa < 1$ can also be implemented by means of an optical isolator. Equation (7.64) illustrates how high-end double-stage isolators with $\kappa \leq 10^{-3}$ lead to a very efficient suppression of parasite fringes. Unfortunately, this would come at the expense of losing the Pound-Drever-Hall signal in cavity reflection in a setup based on a fibered circulator, such as the current realization of OFFS-CRDS. In such a situation, fiber-coupled PDH-detection could be abandoned by inserting an adequate free-space optical isolator, whose lateral exit port provides the cavity reflection beam for free-space PDH signal detection.

7.9 Spectroscopic interference from unresolved absorption background structures

A very important bias source in practice does not come from the CRD measurement system itself, but from real physical background loss structures with a seemingly chaotic spectrum. We suspect that such background spectra might be due to the presence of heavier, probably organic molecules exhibiting a complex, partially resolved near-infrared spectrum. An impressive experimental observation of this effect by OFFS-CRDS is shown in Fig. 7.8.
The right side of the spectrum, before the pumping event evacuating the cavity, is the measured CRD spectrum of 4 Pa CO_2 in 44 Pa of a gas of unknown composition due to outgassing and periodic leakage into the cavity (cf. Section 6.2.4). In the middle of the 44-min scan, the valve isolating the cavity from the pumping system was opened, leading to a rapid pressure drop back towards zero inside the cavity. The spikes in pressure and absorption which are visible in the vicinity of the pumping event are due to the fact that the spectrum was not recorded with monotonously decreasing frequency, but with the spectral interlacing approach discussed in Section 6.3.2. The most immediate effect visible on the left side of the spectrum, after pumping, is a strong reduction of intracavity losses by the elimination of a continuous absorption background due to the intracavity gas. It is interesting to note that the spectrum provides real-time monitoring information on the residual CO_2 concentration in the cavity during the pump-down process: The CO_2 line at $6214.0\,\mathrm{cm}^{-1}$ has an observed peak absorption of $2.7 \cdot 10^{-11}\,\mathrm{cm}^{-1}$, corresponding to a CO_2 partial pressure of 3 Pa. This is higher than the measured total pressure of 0.6 Pa, thereby indicating a strong pressure gradient during pump-down between cavity and pressure gauge, as expected for the older cavity version with only one vacuum port used in this measurement (cf. Section 6.2.4). Five minutes later, at the much stronger line at $6213.87\,\mathrm{cm}^{-1}$, no absorption signal can be descerned beyond the baseline noise level of $5 \cdot 10^{-12}\,\mathrm{cm}^{-1}$. This yields an upper bound for CO_2 partial pressure of 0.5 mPa.

Most important for the present consideration, however, is the astounding decrease in (pseudo-)noise on the absorption baseline by a factor of ten after the pumping event. This reveals that the baseline structure before pumping was not limited by random noise or optical fringes, but by a real absorption signature with a very complex, yet partially resolved structure. The size of the measurement bias due to this effect is hard to predict in advance, but the measurement demonstrates that it can easily introduce a systematic error ten times as big as the intrinsic spectrometer noise level. Consequently, spectroscopic interference from such parasite background structures may constitute the dominant

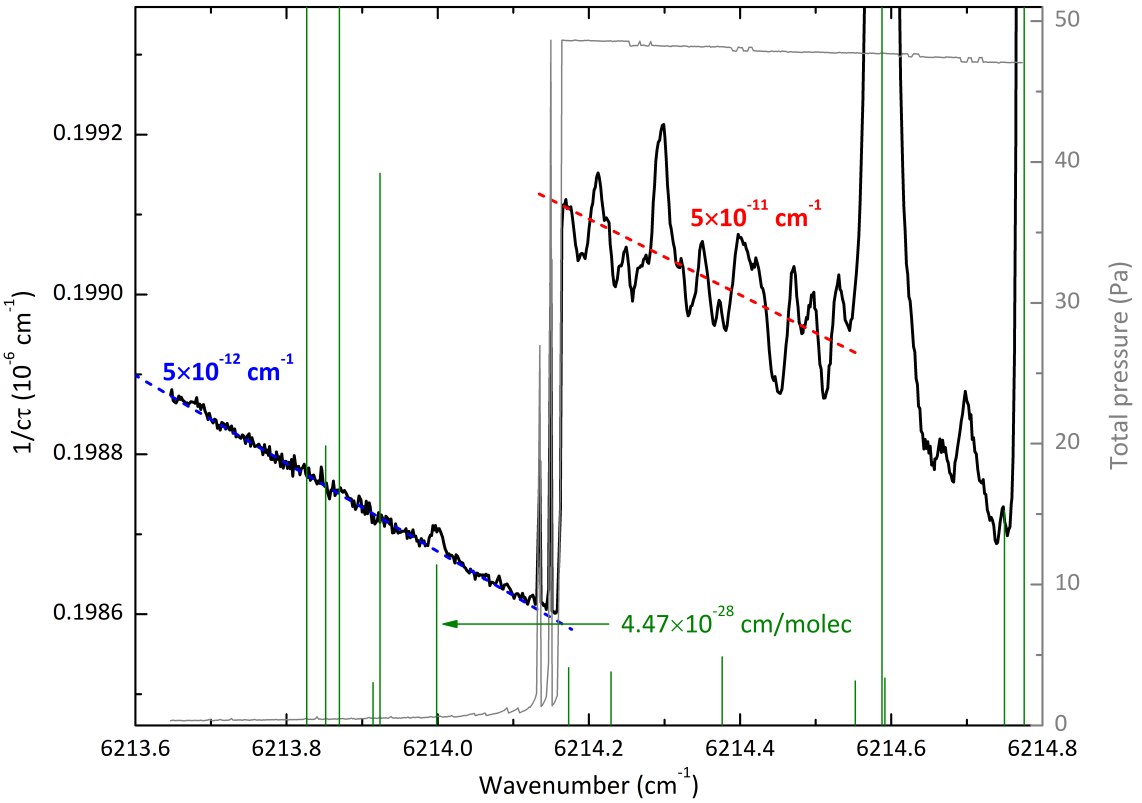

Figure 7.8 CRDS spectrum (black curve) with a frequency stepping resolution of $1.7 \cdot 10^{-3}\,\mathrm{cm}^{-1}$, showing a drastic baseline change when evacuating the cavity. Before pumping, the cavity contained 4 Pa of CO_2 in 44 Pa of an unknown gas mixture due to outgassing or potential leakage. The intracavity pressure is reported as the gray curve (right axis). CO_2 absorption line strengths in this spectral interval according to the HITRAN 2012 database [212] are indicated as vertical bars. The root-mean-square noise levels on the baseline before and after pumping are indicated above the spectrum.

contribution to total systematic uncertainty in linewidth or integrated absorption measurements under certain conditions. The effect must imperatively be taken into account in the error analysis and budget for any metrological application, as overfitting of absorption lines might erroneously assimilate the background structure into an advanced line profile, thereby biasing its physical parameters.

Several strategies for limiting the impact of this bias source can be envisaged. From an empirical point of view, one may observe the fingerprint spectrum arising over time with increasing pressure to subtract it from the measured spectra in later measurements. This approach, however, is prone to fail as soon as the gas composition leading to the background spectrum changes, rendering the measured fingerprint obsolete. Working in a steady flow of sample gas is an efficient experimental solution tackling the problem at its origin. Unfortunately, it is not applicable to all experimental circumstances, for example in the case of a very precious, small sample. Finally, a hard but rewarding approach to minimizing the effect lies in optimizing the vacuum system, by eliminating outgassing sources as well as virtual and external leaks (cf. Section 6.2.4). Indeed, the effect discussed here was observed to be much smaller in the most recent ring-down cavity with the optimized vacuum setup discussed in Section 6.2.4.

Part III

Spectroscopic applications of OFFS-CRDS

Chapter 8

Broadband rovibrational spectroscopy and advanced absorption line shapes

In this chapter, some proof-of-principle applications of OFFS-CRDS in molecular spectroscopy will be presented. Here, a main focus is put on broadband spectroscopy over a spectral interval of several nanometers on the one hand and on a precision study of an isolated absorption line shape on the other hand. Saturated-absorption experiments which were made by OFFS-CRDS, in particular applied to kHz-accuracy line center frequency measurements for CO_2, will be discussed in great detail in the dedicated Chapter 9.

Here, we will begin by introducing some very basic notions of molecular absorption spectroscopy. This discussion is intended to lay the foundation for this and the following chapters. Clearly, it can neither outstrip nor substitute the systematic and exhaustive treatments made in classical textbooks on the matter [161, 213, 214], which are highly recommended to the novice reader for further study. In the second part of this chapter, an article targeting metrological applications of OFFS-CRDS in absorption spectroscopy is presented. It contains the proof-of-principle measurements mentioned above, and an analysis of the experimental techniques needed for putting them into practice with supreme precision. Perspectives for specific applications beneficial to various currently open research questions are discussed in the foreword preceding the article.

8.1 Some basics of rovibrational absorption spectroscopy

A molecule is a bound system composed of atomic nuclei and electrons. In view of the proton-to-electron mass ratio $m_p/m_e \approx 1836$, their masses are separated by three orders of magnitude. In their seminal contribution [215] on the quantum theory of molecules, Max Born and Robert Oppenheimer showed that this mass disparity naturally gives rise to an energy hierarchy of molecular motion in terms of an expansion in powers of $\sqrt[4]{m_e/m_{nuc}}$, where m_{nuc} is an average nuclear mass. They demonstrated that the Hamiltonian governing the motion of molecules can thus be decomposed in good approximation as

$$H = H_{el} + H_{vib} + H_{rot} \tag{8.1}$$

in the rest frame of the molecule. The energy contribution H_{el} of electronic motion dominates, while the nuclear motion Hamiltonians H_{vib} for vibration and H_{rot} for rotation correspond to higher orders of the aforementioned expansion.

Transitions between energy eigenstates of the Hamiltonian (8.1) separated by ΔE give rise to the absorption or emission of a photon, a discrete quantum of light obeying Einstein's frequency-energy relation

$$\Delta E = h\nu = \frac{hc}{\lambda} = hc\tilde{\nu} \tag{8.2}$$

with Planck constant h, speed of light c, frequency ν, wavelength λ and wavenumber $\tilde{\nu}$. The second equality in Eq. (8.2) is based on the dispersion relation (2.2).

To provide very rough orders of magnitude for the energies in play, transitions between electronic energy levels typically correspond to a photon energy between 1 and 10 eV, placing them in the visible or ultraviolet range of the electromagnetic spectrum. Vibrational transitions are generally found for spacings between 0.1 and 1 eV in the near- and mid-infrared, whereas rotational transitions are associated with microwave photons with typical energies between 0.1 meV and 0.1 eV. A practical rule of thumb for converting energies to wavenumbers and vice-versa is $1\,\mathrm{meV} \approx hc \cdot 8\,\mathrm{cm}^{-1}$.

In the following, we will focus on studies in the near infrared, where so-called rovibrational transitions are located, which combine both vibrational and rotational excitation. A basic description of the rotational energy levels of a linear molecule can be obtained by considering a rigid rotor, as illustrated on the left of Fig. 8.1.

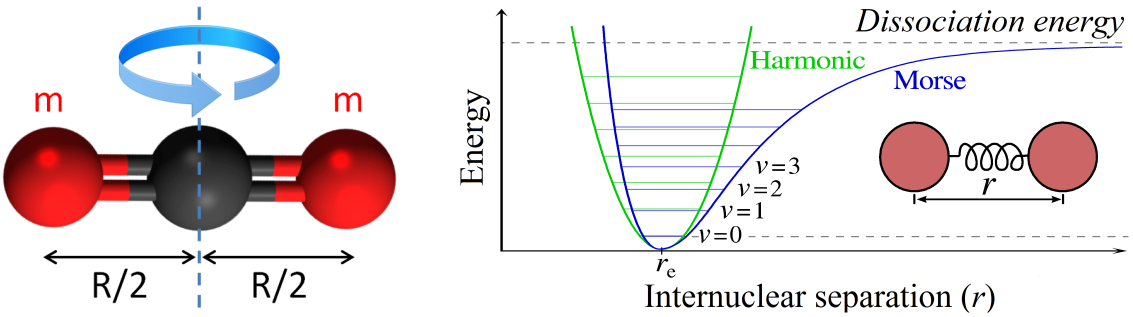

Figure 8.1 Left: Simple classical picture of molecular rotation for a linear diatomic or triatomic molecule, such as CO_2. Right: Harmonic oscillator potential as a first-order framework for describing molecular vibration. The anharmonic Morse potential [214] comes closer to reality by taking the diverging repulsion at zero separation and the unbound asymptotic state at infinite internuclear separation into account. Figure based on [216].

The classical expression for the kinetic energy of such a rigid rotor with two masses m at a separation R, rotating at an angular momentum L, is given by the Hamiltonian

$$H_{rot} = \frac{L^2}{2I} \tag{8.3}$$

where I is the moment of inertia $I = \mu R^2$ of the rotor, with the reduced mass $\mu = m/2$. Replacing the angular momentum L by a quantum-mechanical operator $\hat{L}$ with canonical commutation relations [217], the absolute value squared of the angular momentum can only take on values $L^2 = \hbar^2 J(J+1)$, with a rotational quantum number J [217]. By the correspondence principle, the energy eigenvalues of the quantum mechanical rigid rotor governed by the Hamiltonian (8.3) thus read

$$E_{rot} = \frac{\hbar^2}{2I} J(J+1) \tag{8.4}$$

The $(2J+1)$-fold degeneracy of these energy levels corresponding to different orientations of the rotor can be lifted by applying an external magnetic field.

Naturally, the picture of an infinitely rigid rotor is an idealization. In practice, the internuclear separation increases with growing J. This distortion of the molecule increases R, thus lowering the E_{rot} in Eq. (8.4). A rigorous quantum-mechanical treatment of the non-rigid rotor confirms this qualitative analysis and yields the refined energy levels as a series expansion in $J(J+1)$ [161]:

$$E_{rot} = hc\left(BJ(J+1) - DJ^2(J+1)^2 + HJ^3(J+1)^3 + LJ^4(J+1)^4 + ...\right) \tag{8.5}$$

with the so-called spectroscopic constants B, D, H and L, which were defined in wavenumber units in Eq. (8.5). D is the distortion constant and H and L correspond to higher-order corrections.

On the right of Fig. 8.1, the potential energy of two nuclei is traced along their spatial separation coordinate. Due to the presence of binding electrons, a minimum of potential energy exists and discrete bound states emerge. Around this minimum, the potential can be approximated by a quadratic harmonic oscillator potential. A quantum-mechanical harmonic oscillator [217] has the unique property of equidistant energy eigenvalues:

$$E_{vib} = h\nu \cdot \left(v + \frac{1}{2}\right) \tag{8.6}$$

with a vibrational quantum number v labelling the states and a zero-point energy $h\nu/2$. By the dominant electric dipole interaction [165], only transitions changing the vibrational quantum number v of the harmonic oscillator by ± 1 are allowed, and $\Delta v = \pm 1$. However, as shown in Fig. 8.1, the potential energy of a real molecule is not harmonic, as repulsion becomes infinite at small distances and attraction goes to zero at infinite distances. Due to the anharmonicities of the potential energy surface, the selection rule $\Delta v = \pm 1$ only holds approximately, and overtones with $\Delta v = \pm 2, \pm 3, ...$ exist, yet suppressed by several orders of magnitude with respect to the fundamental.

The nuclear motion in the vibrational state v slightly changes the average molecular geometry. As the moment of inertia in Eq. (8.3) depends on the internuclear spacing, the spectroscopic constants become functions of v, as denoted by indices in B_v, D_v, H_v and L_v. Thus taking the interaction between rotation and vibration into account, the rovibrational energy levels can be written as

$$E_{rovib} = hc\left(G_v + B_vJ(J+1) + D_vJ^2(J+1)^2 + H_vJ^3(J+1)^3 + L_vJ^4(J+1)^4 + ...\right) \tag{8.7}$$

with the vibrational energy hcG_v of the anharmonic oscillator in the vibrational state v measured with respect to the zero-point energy, so that $G_0 \equiv 0$ without loss of generality.

8.1.1 Band structure and line strength

For examining the structure of rovibrational absorption bands, let us drop higher-order rotational terms in Eq. (8.7) in the following for the sake of simplicity. With Eq. (8.2), a transition from a lower state v'', J'' to an upper state v', J' thus occurs at the wavenumber $\tilde{\nu}_{v',J' \leftarrow v'',J''}$ given by

$$\tilde{\nu}_{v',J' \leftarrow v'',J''} = (G_{v'} - G_{v''}) + B_{v'}J'\left(J'+1\right) - B_{v''}J''\left(J''+1\right) \tag{8.8}$$

As discussed above, no strict selection rule relating v' and v'' holds for the anharmonic oscillator. By contrast, the change in rotational angular momentum $\Delta J = J' - J''$ for

rovibrational electric-dipole transitions is subject to the following selection rule in most cases:

$$\Delta J = \pm 1 \tag{8.9}$$

This rule gives rise to two distinct branches of a rovibrational absorption band, the P-branch with $\Delta J = -1$ and the R-branch with $\Delta J = +1$. In the case of degenerate bending-type vibrations in polyatomic molecules or in the presence of additional angular momentum due to electronic motion, a Q-branch with $\Delta J = 0$ is also allowed.

Adopting the selection rule (8.9), let us focus on the structure of a rovibrational band with P- and R-branch by inserting $J' = J'' \pm 1$ in Eq. (8.8). By defining the running index m as $m = J'' + 1$ for R-branch transitions and $m = -J''$ for P-branch transitions, the following unified description for the transition wavenumbers over the whole absorption band is obtained, comprising both branches:

$$\tilde{\nu}_{v' \leftarrow v'',m} = (G_{v'} - G_{v''}) + (B_{v'} + B_{v''}) \cdot m + (B_{v'} - B_{v''}) \cdot m^2 \tag{8.10}$$

This means that the transition frequencies in a rovibrational band can be described by a so-called Fortrat parabola in m to good approximation. If the higher-order terms with D_v, H_v and L_v in the rotational energy expansion (8.5) are taken into account, an equation analogous to (8.8) holds. The P- and R-branch frequencies can then still be stated as a polynomial in m, which is of order 8 if the spectroscopic constants up to L_v are included. This lengthy expression shall be omitted here. It is provided in [9], for instance.

Now, let us still examine the distribution of absorption line strength k, as defined in Eq. (4.4), in a rovibrational absorption band such as the one in Eq. (8.10). The integrated absorption due to a transition was found to be

$$S_\alpha = k \frac{N}{V} \tag{8.11}$$

with the molecular number density N/V. However, only molecules in the lower state of the transition under study contribute to its absorption. Consequently, the line strength k must reflect the fraction of molecules which are in that lower state, which is governed by elementary Boltzmann statistics in thermal equilibrium at temperature T. Accordingly, the number $N_{v'',J''}$ of molecules in the lower vibrational state v'' with rotational quantum number J'' obeys the distribution

$$\frac{N_{v'',J''}}{N_{0,0}} = \mathrm{e}^{-\frac{hcG_{v''}}{k_B T}} \cdot (2J'' + 1)\, \mathrm{e}^{-\frac{hcB_{v''}J''(J''+1)}{k_B T}} \tag{8.12}$$

The first factor in (8.12) is the Boltzmann factor due to vibrational energy, with the Boltzmann constant k_B. Vibrational energies for $v > 0$ are usually large compared to thermal energy $k_B T$, which amounts to 25 meV at room temperature. Consequently, so-called hot bands, which consist of transitions starting from a vibrationally excited level, are normally much weaker than transitions from the vibrational ground state at room temperature. The factor $(2J'' + 1)$ is due to the degeneracy of the rotational levels and contributes, together with the Boltzmann factor due to rotational energy, to the characteristic shape of rovibrational bands, which can be seen on the CO_2 spectrum shown in Figure 6a of Article 5 on page 160, for instance. Higher-order rotational constants were neglected in the rotational Boltzmann factor to very good approximation. Due to the temperature dependence of Eq. (8.12), spectra at very low or very high temperatures appear completely different, although they originate from the same molecular species with unchanged energy levels.

It is important to note that line strengths are often also weighted to reflect the natural abundances of different isotopologues of a molecular species. This is the case in the HITRAN database [212], for instance. This has the practical advantage that spectra can be simulated or evaluated without dealing with abundances explicitly. In exchange, care must be taken when using such line strength values in studies on isotopically enriched or depleted samples.

In view of the upcoming discussions on spectroscopic results on CO_2 in the following chapters, let us point out that the vibrational states of CO_2 will be labeled using a common five-digit nomenclature [218] in the following, 00001 denoting the vibrational ground state. Transitions are identified using the upper and lower vibrational state, the branch of the rovibrational band, as well as the rotational quantum number J'' of the lower state. For an absorption from the vibrational ground state at $J'' = 16$ to the 30013 state at $J' = 15$, this yields 30013←00001 P16, for instance. A detailed discussion on the physics and the labelling of the vibrational modes of CO_2 would be beyond the scope of this brief introduction and is provided in [213, 218], for instance.

Likewise, for a detailed discussion on the impact of nucleus-exchange symmetry and nuclear spin with regard to the symmetrization postulate of quantum mechanics, the reader is referred to classical textbooks on the matter [161, 214]. Here, let us just point out that every second line in the rovibrational bands of $^{12}C^{16}O_2$ is missing due to the presence of two undistinguishable ^{16}O nuclei with zero nuclear spin.

8.1.2 Absorption line profile models

In the preface of Chapter 5, the frequency-dependent absorption coefficient $\alpha(\nu)$ due to a transition at frequency ν_0 was written as

$$\alpha(\nu) = k \cdot \frac{N}{V} \cdot p(\nu - \nu_0) \tag{8.13}$$

with line strength k, molecular number density N/V, integrated absorption $S_\alpha = k \cdot N/V$ and a normalized absorption profile or line shape $p(\nu - \nu_0)$ with $\int_{-\infty}^{\infty} p(\nu)\mathrm{d}\nu = 1$. Now turning to explicit formulations of the profile function $p(\nu)$, we shall first discuss the Lorentzian profile, then derive the Doppler and Voigt profiles and eventually turn to a qualitative discussion on advanced analytic line shape models.

The Lorentzian profile, named after Hendrik Antoon Lorentz, is given by

$$p_L(\nu - \nu_0) = \frac{1}{\pi} \frac{\frac{\gamma}{2}}{(\nu - \nu_0)^2 + \frac{\gamma^2}{4}} \tag{8.14}$$

and has a full-width-at-half-maximum (FHWM) of $\Delta_L = \gamma$. This profile is the frequency-domain equivalent, that is the Fourier transform, of a sinusoidal at frequency ν_0 whose signal envelope exponentially decays at a rate γ. Consequently, the Lorentzian describes the natural linewidth γ_{nat} of a transition, which is due to the finite lifetime γ_{nat}^{-1} of its upper state. Beyond that, an exponentially decaying signal can also be caused by the decoherence induced by intermolecular collisions, which progressively randomize the phase between individual absorbing or emitting molecules. In the frequency domain, this leads to a Lorentzian of FWHM γ_P, which is proportional to pressure:

$$\gamma_P = \gamma^0 \cdot P \tag{8.15}$$

The pressure-broadening coefficient γ^0 depends on the collision partner. Typical coefficient values given in molecular line databases such as HITRAN [212] are the half-width

coefficients $\gamma^0_{air}/2$ for broadening by air and $\gamma^0_{self}/2$ for broadening by the absorbing gas itself. As the convolution of two Lorentzians with γ_1 and γ_2 is another Lorentzian with $\gamma_1 + \gamma_2$, the broadening effects of natural lifetime and collisional dephasing add up to

$$\Delta_L = \gamma = \gamma_{nat} + \gamma_P \tag{8.16}$$

For the weak transitions in the near infrared, γ_{nat} is usually negligible compared to γ_P, even at low sub-Pa pressures.

The Doppler profile arises when considering a sample in the gas phase, whose translational molecular velocities follow the Maxwell-Boltzmann distribution of thermal motion. Along any arbitrary one-dimensional axis, this distribution reads

$$F(v) = \left(\frac{m}{2\pi k_B T}\right)^{\frac{1}{2}} \mathrm{e}^{-\frac{mv^2}{2k_B T}} \tag{8.17}$$

as a function of velocity v, with the molecular mass m, the Boltzmann constant k_B and the temperature T. According to $F(v)$, the contribution $\frac{\mathrm{d}N}{V}$ to number density by absorbers from the velocity interval $[v, v + \mathrm{d}v]$ is

$$\frac{\mathrm{d}N}{V} = \frac{N}{V} F(v)\mathrm{d}v \tag{8.18}$$

For these absorbers at speed v, the Doppler effect leads to a frequency shift of the exciting light field by

$$\Delta\nu = \frac{v}{c} \cdot \nu + \mathcal{O}\left(\left(\frac{v}{c}\right)^2\right), \tag{8.19}$$

where v was taken to be negative along the propagation direction of the light field. Consequently, in their rest frame, the individual molecules see a Doppler-shifted light field at frequency ν_v:

$$\nu_v = \nu_0 \left(1 + \frac{v}{c}\right). \tag{8.20}$$

To determine the absorption line shape resulting from this interplay of Doppler effect and Maxwell-Boltzmann distribution, let us set aside the Lorentzian contribution from intermolecular collisions for the moment. In that case, the natural linewidth of a molecular transition in the near infrared is many orders of magnitude smaller than the Doppler width. Therefore, one may consider the contribution $\mathrm{d}\alpha_{v'}(\nu)$ to absorption at the frequency ν by the velocity class v' as monochromatic in very good approximation:

$$\mathrm{d}\alpha_{v'}(\nu) = k\frac{\mathrm{d}N_{v'}}{V}\delta(\nu - \nu_{v'}) = k\frac{N}{V}\delta(\nu - \nu_{v'})F(v')\mathrm{d}v' \tag{8.21}$$

with the delta function $\delta(\nu - \nu_{v'})$ imposing resonance with the molecular transition for each velocity class. In the second step, Eq. (8.18) was inserted. Integrating over the absorption contributions (8.21) from all velocity classes under the substitution $v' = c/\nu_0(\nu_{v'} - \nu_0)$ based on the Doppler shift relation (8.20), one obtains the frequency-dependent absorption coefficient as

$$\alpha(\nu) = k\frac{N}{V}\int_{-\infty}^{\infty} \delta\left(\nu - \nu_{v'}\right) F\left((\nu_{v'} - \nu_0)\frac{c}{\nu_0}\right)\frac{c}{\nu_0}\mathrm{d}\nu_{v'} \tag{8.22}$$

which straightforwardly yields

$$\alpha(\nu) = k\frac{N}{V}\frac{c}{\nu_0}F\left((\nu - \nu_0)\frac{c}{\nu_0}\right) \tag{8.23}$$

Finally, identifying the line profile according to Eq. (4.4) and inserting $F(v)$ from Eq. (8.17) yields the Doppler profile $p_D(\nu-\nu_0)$ of gas-phase absorption lines at very low pressures:

$$p_D(\nu-\nu_0)=\frac{c}{\nu_0}F\left((\nu-\nu_0)\frac{c}{\nu_0}\right)=\left(\frac{mc^2}{2\pi k_BT\nu_0^2}\right)^{\frac{1}{2}}\mathrm{e}^{-\frac{mc^2}{2k_BT\nu_0^2}(\nu-\nu_0)^2}. \tag{8.24}$$

It is a normalized Gaussian bell curve centered at ν_0, with full-width-at-half-maximum

$$\Delta_D=\nu_0\sqrt{8\ln 2\frac{k_BT}{mc^2}} \tag{8.25}$$

On this basis, let us derive the so-called Voigt profile by revisiting Eq. (8.21) of the above derivation. There, the simplifying assumption of a monochromatic resonance described by a δ-distribution eventually gave rise to the Doppler profile. We shall now generalize this ansatz by replacing $\delta(\nu-\nu_{v'})$ by the Lorentzian profile $p_L(\nu-\nu_{v'})$ due to natural lifetime and collisional broadening. Then, the contribution $\mathrm{d}\alpha_{v'}(\nu)$ to absorption at the frequency ν by the velocity class v' reads

$$\mathrm{d}\alpha_{v'}(\nu)=p_L\left(\nu-\nu_{v'}\right)k\frac{N}{V}F\left(v'\right)\mathrm{d}v' \tag{8.26}$$

Integrating over these contributions by again using the substitution $v'=c/\nu_0(\nu_{v'}-\nu_0)$ yields

$$\alpha(\nu)=k\frac{N}{V}\int\limits_{-\infty}^{\infty}p_L\left(\nu-\nu_{v'}\right)\frac{c}{\nu_0}F\left(\frac{c}{\nu_0}\left(\nu_{v'}-\nu_0\right)\right)\mathrm{d}\nu_{v'} \tag{8.27}$$

In Eq. (8.27), the Doppler profile $p_D\left(\nu_{v'}-\nu_0\right)$ can be identified using Eq. (8.24). With this simplification and the detuning variable $\Delta'=\nu_{v'}-\nu_0$, the new line profile $p_V\left(\nu-\nu_0\right)$ reads

$$p_V\left(\nu-\nu_0\right)=\int\limits_{-\infty}^{\infty}p_L\left(\left(\nu-\nu_0\right)-\Delta'\right)p_D\left(\Delta'\right)\mathrm{d}\Delta'=\left(p_L*p_D\right)\left(\nu-\nu_0\right) \tag{8.28}$$

This is the well-known result that the molecular absorption lineshape in the presence of both homogeneous and Doppler broadening is the convolution p_L*p_D of a Lorentzian profile with a Gaussian profile. This Voigt profile [219], named after Woldemar Voigt, is also normalized, as one easily verifies using the normalization of both $p_L(\nu)$ and $p_D(v)$:

$$\int\limits_{-\infty}^{\infty}p_V\left(\nu-\nu_0\right)\mathrm{d}\nu=\int\limits_{-\infty}^{\infty}p_D\left(\nu'-\nu_0\right)\left(\int\limits_{-\infty}^{\infty}p_L\left(\nu-\nu'\right)\mathrm{d}\nu\right)\mathrm{d}\nu'=1 \tag{8.29}$$

The Voigt profile is a good approximation if velocity changes due to collisions are negligible in the thermal motion giving rise to the Gaussian profile, and if statistical correlations between this thermal motion and the internal quantum-state evolution underlying the Lorentzian profile are negligible, too. These prerequisite assumptions are inherent to the ansatz in Eq. (8.26), but not sufficiently well fulfilled in reality at higher pressures, where intermolecular collision effects become important.

A first effect which needs to be taken into account for going beyond the Voigt profile are velocity-changing collisions, as opposed to the internal-phase-changing collisions, which

lead to collisional broadening. Dicke showed by elementary theoretical consideration that the velocity-averaging effect due to collisions can narrow the width of Doppler-broadened lines [220], a phenomenon consequently called Dicke narrowing. For molecular hydrogen, this effect is particularly strong, as illustrated by the experimental result from LIPhy [12] shown in Fig. 8.2. The effect of velocity-changing conditions can be studied in two limiting

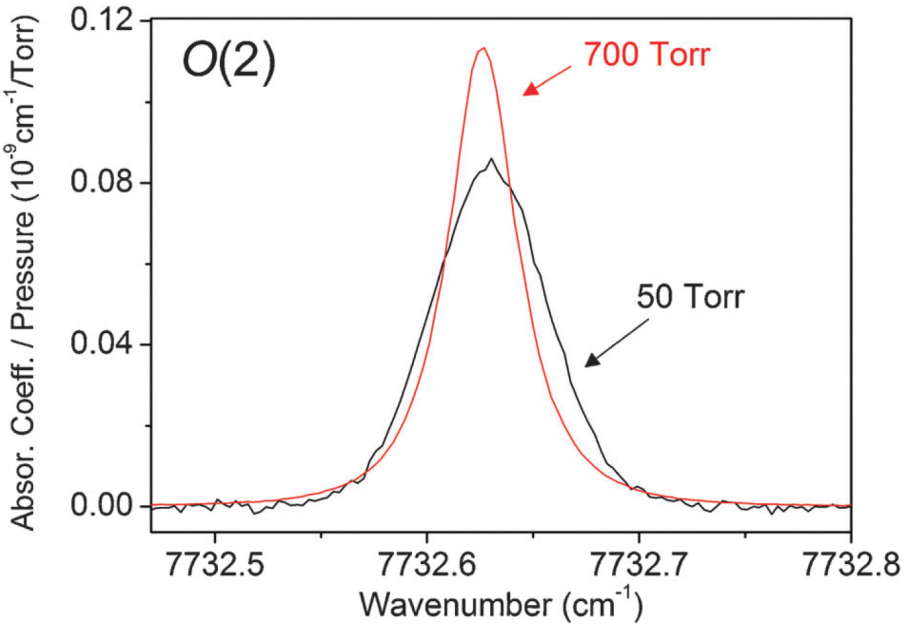

Figure 8.2 Pressure-normalized experimental CRDS spectrum of the electric-quadrupole transition $2 \leftarrow 0$ O2 of H_2 with $\Delta J = -2$, measured at two different pressures by Campargue and co-workers [12]. A strong Dicke narrowing due to velocity-changing collisions and a pressure shift on the order of $-3 \cdot 10^{-3}\,\mathrm{cm}^{-1}$ can be observed on the higher-pressure line. Note that 1 Torr equals approximately 133 Pa. Adapted from [12] (Figure 1).

cases leading to different absorption profiles. On the one hand, there is the hard-collision limit, where the velocity of an absorbing molecule is fully randomized by a collision event. This gives rise to hard collision profile, which is also commonly called Nelkin-Ghatak profile [221]. On the other hand, a soft-collision setting, where molecular velocity undergoes only a slight change at each collision, leads to the so-called Galatry profile [222]. Both these profiles introduce one additional parameter representing the effective frequency of velocity-changing collisions. Under certain conditions, it can be related to the mass-diffusion coefficient of the molecular sample and typically has the same order of magnitude as the latter [223].

A further effect of collisions is a perturbation of the intramolecular potential which modifies the energy eigenstates of the molecule and leads to a line center frequency shift proportional to pressure [223]. As pointed out by Rautian and Sobel'man [224], Doppler broadening and collisional broadening are only statistically independent if the collisional broadening and shifting coefficients are independent of the velocity of the absorbing molecule. In the opposite case where statistical independence does not hold, a speed-dependence of these parameters arises, and the line profile becomes asymmetric [224].

The impact of speed-dependent collisional width and shift parameters was theoretically studied by Berman [225]. Based on an inverse power law potential in the intermolecular separation, he derived an asymmetric, speed-dependent extension of the Voigt profile, the so-called speed-dependent Voigt profile. To simplify calculations, a quadratic approxi-

mation of this speed dependence is generally made. The reliability of this widespread approach was characterized by De Vizia and co-workers [226], for instance, by comparing the quadratic approximation with the more sophisticated hypergeometric dependence. The aforementioned effects of velocity-changing collisions and speed-dependent pressure broadening and shifting can be combined in terms of the speed-dependent Nelkin-Ghatak [227] and Galatry [228] profiles.

By also taking temporal correlations between velocity-changing and state-changing collisions into account in terms of one additional parameter, the partially-correlated quadratic-speed-dependent hard-collision model is obtained [27, 226]. It provides a comprehensive coverage of the various effects induced by molecular collisions and features two pressure-independent parameters and five parameters which are proportional to pressure. The computational cost of this profile can be drastically reduced by decomposing it into basic complex Voigt profiles [229], for the approximate calculation of which fast algorithms exist [230]. The combination of all these properties make this profile an excellent compromise for multi-fit analyses over whole vibrational bands and in different pressure ranges [27], which is the most promising approach to date for retrieving physically meaningful fit parameters and for evidencing potential systematic deviations of the experimental data from the model profile.

Consequently, the IUPAC (International Union of Pure and Applied Chemistry) task group on "Intensities and line shapes in high-resolution spectra of water isotopologues from experiment and theory" has recently issued a recommendation that the partially-correlated quadratic-speed-dependent hard-collision profile should supersede the Voigt profile in spectroscopic databases [231], stating that

> The Task Group recommends that the partially Correlated quadratic-Speed-Dependent Hard-Collision profile (pCqSD-HCP) should be adopted as the appropriate model for high-resolution spectroscopy. For simplicity this should be called the Hartmann-Tran profile (HTP). The HTP is sophisticated enough to capture the various collisional contributions to the isolated line shape, can be computed in a straightforward and rapid manner, and reduces to simpler profiles, including the Voigt profile, under certain simplifying assumptions.

Indeed, the inadequacies of the Voigt profile have become a pressing issue for many applications of spectroscopic data, such as remote sensing and radiation transfer calculations in atmospheric sciences, where the use of a Voigt profile was shown to lead to considerable errors [232].

In conclusion, advanced analytic absorption line models in general, and the Hartmann-Tran profile in particular, can provide precious insights into the properties of the molecular system under study, as they reflect interaction mechanisms at a microscopic level. However, the deviations from the Voigt profile are usually not very large, and the many parameters of most sophisticated models come at the price of correlations between these fit parameters or potential over-fitting of noise signatures. Therefore, state-of-the-art absorption spectrometers with unimpeachable precision and linearity on both axes are needed for carrying out molecular absorption lineshape studies and multi-fit analyses at very high signal-to-noise ratios.

8.2 Article 5 - Absorption line metrology by optical feedback frequency-stabilized cavity ring-down spectroscopy

To begin with, the following article [233] focusses on a detailed description of the methodology and experimental setup for OFFS-CRDS, thus complementing the discussion in Chapters 3 and 6. In particular, a precision measurement of the V-shaped reference cavity free spectral range is reported and the Pound-Drever-Hall locking behavior in the ring-down regime is characterized. This is followed by an in-depth discussion of the limitations of spectrometer performance due to photo-electron shot noise and parasite interference fringes. Experimental results evidencing the impact of both mechanisms in OFFS-CRDS are presented, and a detailed analysis of two efficient fringe cancellation schemes is provided.

On this basis, the application of the OFFS-CRD spectrometer to the measurement of a broadband spectrum of CO_2 between 6188 and 6217 cm^{-1} with a dynamic range approaching $8 \cdot 10^5$ is reported. Importantly, the spectrum confirmed the need for a revision of the 40013 $\leftarrow$ 10001 hot band line center frequencies for $^{12}C^{16}O_2$ in the HITRAN 2012 database [212]. Eventually, an application of the spectrometer to an absorption line shape study of $^{12}C^{16}O_2$ broadened by N_2 with a signal-to-noise ratio of $8 \cdot 10^4$ is presented. At this high precision, only line profile models taking both velocity-changing collisions and speed-dependent broadening and shifting parameters (cf. Section 8.1.2) into account were able to reproduce the data with flat, unstructured fit residuals.

Let us comment on some application perspectives of OFFS-CRDS in rovibrational spectroscopy, which ensue from the comprehensive proof-of-principle experiments reported in the article below.

The fact that the Doppler temperature retrieved with the Hartmann-Tran profile (HTP) was in good agreement with the platinum resistor temperature measurement supports the applicability of OFFS-CRDS and the HTP to Doppler thermometry. A calibrated temperature probe with an accuracy well below the 100 mK-level should be used in a long-term Doppler temperature measurement at different temperatures for a rigorous validation of the precision, accuracy and reliability of Doppler thermometry by OFFS-CRDS.

Another exciting application of OFFS-CRDS, equally building on its high precision and stability on both axes and the versatility of the automated setup, is the measurement of absorption lines up into the very far Lorentzian wings of the lineshape. Adaptive frequency steps eventually attaining one free spectral range of the ring-down cavity could be used for speedy scanning to quickly cover broad spectral intervals with a slowly varying absorption signal. Such a measurement could provide a precious direct experimental test of the physical validity and significance of the $\pm 25\,cm^{-1}$-truncation of Lorentzian profiles which is commonly used in absorption continuum studies [234–236].

Let us underscore the wealth of absolute frequency information on hot bands and minor isotopologues contained in broadband spectra such as the CO_2 spectrum near 1.6 µm shown in Figure 6 of the article. An absolute frequency axis calibration for spectra in this region can be carried out thanks to the kHz-accuracy CO_2 reference frequencies presented in Section 9.4 and Article 6 therein. In this manner, transition frequency measurements with sub-MHz accuracy should be possible without an optical frequency comb and even for weak lines.

Finally, as discussed in the article, the OFFS-CRD spectrometer should be used for automated lines shape measurements on many lines of a rovibrational band repeated at different pressures, in order to enable a multispectrum fitting approach such as in [180], providing a stringent test of line-shape models and yielding physical line parameters.

Appl. Phys. B (2015) 119:97–109
DOI 10.1007/s00340-014-5999-3

Applied Physics B
Lasers and Optics

Absorption line metrology by optical feedback frequency-stabilized cavity ring-down spectroscopy

Johannes Burkart · Samir Kassi

Received: 31 October 2014 / Accepted: 22 December 2014 / Published online: 7 January 2015

Abstract Optical feedback frequency-stabilized cavity ring-down spectroscopy (OFFS-CRDS) is a near-shot-noise-limited technique combining a sensitivity of $2 \times 10^{-13}\,\mathrm{cm}^{-1}/\sqrt{\mathrm{Hz}}$ with a highly linear frequency axis and sub-kHz resolution. Here, we give an in-depth review of the key elements of the experimental setup encompassing a highly stable V-shaped reference cavity, an integrated Mach-Zehnder modulator and a tightly locked ring-down cavity with a finesse of 450,000. Carrying out a detailed analysis of the spectrometer performance and its limitations, we revisit the photo-electron shot-noise limit in CRDS and discuss the impact of optical fringes. We demonstrate different active schemes for fringe cancelation by varying the phase of parasitic reflections. The proof-of-principle experiments reported here include a broadband high-resolution spectrum of carbon dioxide at 1.6 μm and an isolated line-shape measurement with a signal-to-noise ratio of 80,000. Beyond laboratory-based absorption line metrology for fundamental research, OFFS-CRDS holds a considerable potential for field laser measurements of trace gas concentrations and isotopic ratios by virtue of its small sample volume and footprint, the robust cavity-locking scheme and supreme precision.

J. Burkart (✉) · S. Kassi
Univ. Grenoble Alpes, LIPhy, 38000 Grenoble, France
e-mail: johannes.burkart@ujf-grenoble.fr

J. Burkart · S. Kassi
CNRS, LIPhy, 38000 Grenoble, France

1 Introduction

Ultra-sensitive measurements of molecular absorption by means of continuous-wave-laser cavity ring-down spectroscopy (CW-CRDS) [1] have a multitude of applications in atmospheric trace gas concentration monitoring and the detection of extremely weak absorption features [2] for improving spectroscopic databases [3–5]. In recent years, the increasing demand for precision field measurements is reflected by a growing market for commercial CRDS field instruments [6] detecting various relevant molecules in situ at atmospheric concentrations. This process is accelerated by the rapidly developing field of spectroscopic isotopic ratio measurements [7], whose long-term objective is replacing bulky and expensive dual-inlet isotopic ratio mass spectrometers by compact, inexpensive and highly selective near- or mid-infrared laser instruments. Significant progress in measuring the isotopic anomalies of ^{2}H, ^{17}O, ^{18}O and ^{13}C has been made for important atmospheric constituents such as water vapor [8, 9], carbon dioxide [10] and methane [11], equally triggering the development of commercial devices [12].

In CRDS, the absorption coefficient α of a gas sample filling an optical cavity is obtained from a measurement of the exponential ring-down (RD) decay time τ via

$$\alpha c = \tau^{-1} - \tau_0^{-1} \tag{1}$$

c being the speed of light and τ_0 the RD time on the spectral baseline. Relying purely on time and frequency measurements, CRDS holds the promise of highly accurate, SI-traceable line strength measurements for validating *ab initio* calculations [13, 14], which could pave the way to absolute gas concentration measurements by laser spectroscopy [15]. Besides high sensitivity, a stable and linear

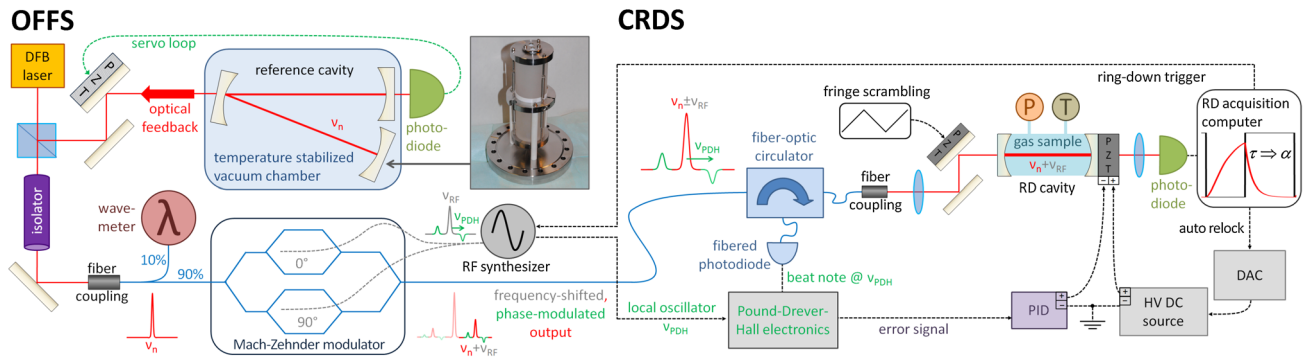

Fig. 1 Schematic of the experimental setup for optical feedback frequency-stabilized cavity ring-down spectroscopy (OFFS-CRDS)

frequency axis is vital for such precision measurements. This issue has been addressed by frequency-stabilized CRDS (FS-CRDS) [16, 17], which consists in locking the laser to a dichroic-mirror RD cavity stabilized by means of a helium-neon laser. The advent of FS-CRDS has fostered experimental development for high-fidelity line-shape measurements beyond the Voigt profile [18, 19], crucial for an accurate retrieval of line parameters and a physical understanding of intermolecular potentials and collision processes [20–22].

The recently developed optical feedback frequency-stabilized cavity ring-down spectroscopy (OFFS-CRDS) technique [23] follows a distinctly different route to CRDS frequency stabilization. It is based on tightly locking a high-finesse ring-down cavity on a narrow laser referenced to a highly stable resonator via a tunable radio frequency. Combining extreme sensitivity with an undistorted frequency axis, the method was conceived to address current and future challenges in high resolution and sensitivity molecular spectroscopy. It exhibits performances suitable for fundamental applications, such as an optical determination of the Boltzmann constant [24–26], as well as both robustness and limited complexity compatible with field measurements in demanding environments [27–29].

2 Method and experimental setup

In particular, OFFS-CRDS was designed to meet the following five intimately related requirements: (1) a sensitivity on a par with state-of-the-art CW-CRDS setups, (2) a highly stable and linear frequency axis, (3) the absence of excess absorption noise due to frequency jitter conversion on slopes, (4) an arbitrary frequency stepping resolution for resolving delicate features of advanced Doppler-broadened line shapes or even sub-Doppler features, and, in turn, (5) very high intracavity power for saturating even weak transitions in the near infrared. (1) and (5) call for the resonant excitation of a very high-finesse cavity which guarantees long, well-defined RD events and strong passive intracavity power amplification. (2) and (3) necessitate a highly stable optical length of the RD cavity, while (4) combined with (2) suggests working in the radio frequency (RF) domain, where sub-Hz frequency accuracy and resolution are readily achievable.

Fulfilling all five conditions, our approach consists in tightly locking a high-finesse RD cavity to a sub-kHz linewidth stable laser finely tunable by means of electro-optic single-sideband modulation. Among the key elements of this setup are the optical feedback frequency-stabilized laser using a highly stable V-shaped reference cavity and single-sideband modulation with a dual-parallel Mach-Zehnder modulator (MZM) [30], as well as a modified fibered Pound-Drever-Hall-locking scheme for tight locking of a high-finesse RD cavity [23]. These methodological advances provide high cavity transmission for low-noise photodetection and guarantee an unbroken stability transfer chain from the V-shaped reference cavity to the absorption spectrum frequency axis. An overview of the experimental setup for OFFS-CRDS is depicted in Fig. 1.

2.1 Optical feedback frequency stabilization and single-sideband modulation

A distributed-feedback (DFB) diode laser emitting between 1,608 and 1,616 nm is locked to a high-finesse V-shaped Fabry-Pérot cavity by optical feedback. The optical self-locking of diode lasers to an external feedback cavity [31, 32] relies on the stable frequency and phase of the resonant light field in the feedback cavity. When its backward transmission is reinjected into the laser medium, the stimulated emission by feedback photons counteracts the random walk of laser phase due to spontaneous emission. This leads to laser linewidth narrowing by several orders of magnitude and frequency locking to feedback cavity resonance. The optical-feedback-locking range is proportional to the square root of feedback power [32]. We therefore use a Glan-Taylor polarizing beam splitter to divert a

percent-level fraction of the total laser power toward the V-cavity. The feedback power is fine-tuned for obtaining a locking range equal to the free spectral range (FSR) between successive longitudinal modes of the cavity. The light not needed for optical feedback locking is coupled into a polarization-maintaining (PM) optical fiber carrying roughly 50 % of the initial laser power. As the relative phase of the feedback field gives rise to frequency pulling within the cavity modewidth, a sub-kHz-bandwidth servo-loop actively controlling the laser-cavity distance is needed to keep the laser locked to the center of a TEM_{00} resonance. The corresponding error signal is obtained by laser current modulation at a few kHz and phase-sensitive first-harmonic detection in cavity transmission.

The highly stable reference cavity [30] consists of a vertically mid-plane mounted 15-cm-long cylindrical ultra-low expansion (ULE) glass spacer with Super Invar mirror holders tightly contacted to both ends. These cavity flanges are precision-machined for holding three dielectric mirrors at appropriate angles for automatic and permanent V-shape alignment. The reference cavity is placed in a high-vacuum chamber pumped down to a few 10^{-7} mbar. The latter is temperature stabilized to better than 8 mK over its entire surface.

This optical feedback frequency-stabilized laser source features a linewidth below 530 Hz at 1 s and drift rates below 20 Hz/s. The laser locks to successive reference cavity modes when its current or diode temperature are changed, thereby enabling easy and fast mode-by-mode frequency tuning over 8 nm.

To cover the spectral gap between reference cavity modes, we have proposed fine-tuning by single-sideband modulation using a PM-fiber-coupled dual-parallel Mach-Zehnder modulator (MZM) [30, 33]. In its nested lithium niobate $LiNbO_3$ interferometer waveguide, phase-modulation sidebands generated via the electro-optic Pockels effect undergo DC-voltage-controlled destructive and constructive interferences yielding a single-sideband output. The optical carrier is suppressed by static destructive interference in the two inner Mach-Zehnder interferometers (cf. Fig. 1). The suppression ratios of unwanted spectral components are better than 28 dB [30]. The accuracy and resolution of this frequency-shifting mechanism are given by the RF synthesizer (Rohde&Schwarz SMB100A) referenced to a 10 MHz Rubidium timebase (SRS PRS10). The tuning range of the present setup was limited to approximately 1 GHz by the bandwidth of the 90° hybrid coupler (Mini-Circuits ZX10Q-2-19+) needed for driving the two RF electrodes of the MZM (Covega Mach-10-060). In a follow-up setup currently under preparation, a commercial 2–18 GHz broadband hybrid coupler will be used for achieving a 32-GHz tuning span around the optical feedback frequency-stabilized carrier.

Summing up, the optical frequency ν synthesized by the single-sideband-tuned optical feedback frequency-stabilized laser is

$$\nu = \nu_0 + k \times \mathrm{FSR} \pm \nu_{\mathrm{RF}} \tag{2}$$

where k is the number of the V-cavity mode the laser is locked to and ν_0 is the optical frequency of the arbitrarily chosen mode defined as $k = 0$. ν_0 and k are measured by monitoring ten percent of the optical feedback locked laser power on a Fourier-type wavemeter (Burleigh WA-1650). According to Eq. (2), this procedure limits the knowledge of ν to the wavemeter accuracy of ±20 MHz. This limitation could be readily overcome by monitoring the beat note of the stable laser with a self-referenced frequency comb [34]. The uncertainty of the MZM-generated frequency shift $\pm\nu_{\mathrm{RF}}$ is well below the Hz-level.

In view of Eq. (2), it is also essential to have a precise knowledge of the V-cavity FSR and its slight wavelength-dependence in order to record spectra by using its modes as a frequency grid. A precision measurement of this quantity was carried out by successively locking the laser to two distant modes of the V-cavity and recording its beat note with a self-referenced frequency comb (Toptica FFS1550) using a 200 MHz 16-bit acquisition card (GAGE model CS1622). Using a less precise value for the FSR from previous wavemeter-based measurements, the two V-cavity modes could be unambiguously numbered and the beat notes combined to yield an accurate measurement of their frequency spacing. Dividing it by the number of modes yields the Hz-level precision average FSR values for different laser wavelength intervals shown in Fig. 2. The linear trend at the limit of statistical significance can be attributed to mirror dispersion. For most applications, using the weighted average $\overline{\mathrm{FSR}} = 491,395,463(6)$ Hz over the entire spectral interval is sufficient in Eq. (2). Knowing the FSR, the V-shaped cavity finesse around 2.8×10^5 was determined by means of a ring-down measurement [35]. In the absence of technical noise, this would correspond to a sub-Hz laser linewidth under optical feedback locking [32].

2.2 Pound-Drever-Hall cavity-locking and ring-down measurement

The RD cavity used here consists of two highly reflective dielectric mirrors separated by a massive 33-cm-long aluminum hollow cylinder of 50 mm outer and 8 mm inner diameter with a lateral 1/4″-NPT vacuum fitting for pumping and gas inlet. The cavity output mirror mounted on a piezo-electric actuator (PZT) allows tuning the TEM_{00} mode of the cavity to resonance with the stable laser. This necessitates a relative voltage stability on the order of the inverse cavity finesse, which ranges from 425,500 at 1,616 nm to 462,200 at 1,608.5 nm here. For achieving

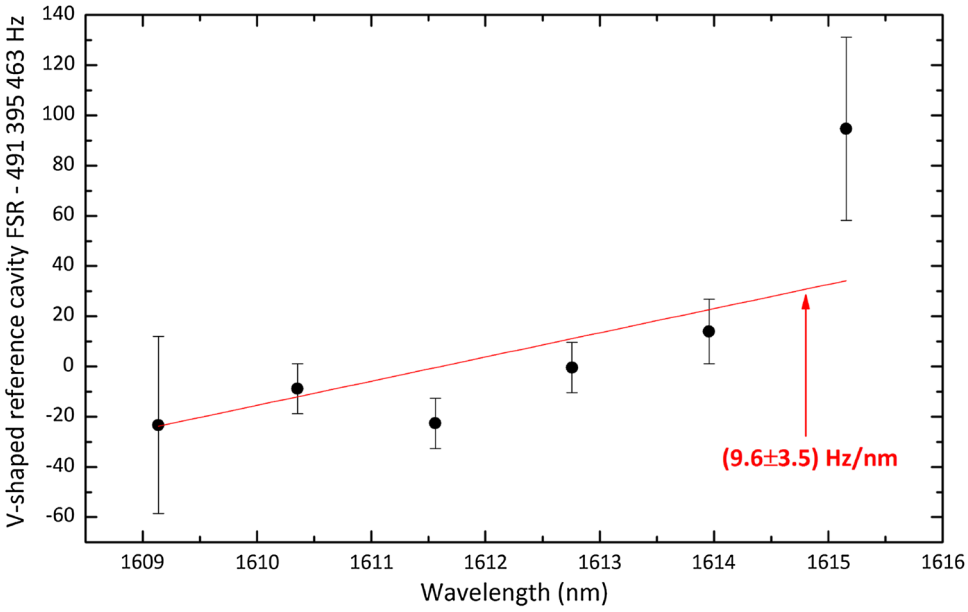

Fig. 2 Measured average reference cavity free spectral range for different laser wavelength intervals

this challenging stability goal, we realized the split voltage supply scheme illustrated in Fig. 1. The PZT electrodes are driven by two signals referenced to a common ground, one low-noise, low-bandwidth high-voltage component and one 7 kHz-bandwidth low-voltage signal from a commercial analog servo controller (Toptica PID110). This approach allows for a two-step automated relock procedure discussed in detail in Sect. 2.3.

To obtain an error signal for the analog servo loop, we set up an all-fibered, slightly modified Pound-Drever-Hall (PDH) locking scheme [36]. In PDH locking, a phase-modulation sideband pair serves as a phase- and frequency detector for the optical carrier in cavity reflection. Instead of adding an electro-optic modulator for generating these sidebands, we supply a phase-modulated RF at the MZM input, which generates a single-sideband frequency-shifted optical signal with small phase-modulation satellites. The resulting PDH signal in cavity reflection is detected on a fibered photodiode (PD) by means of a fiber-optic circulator. This robust locking scheme reduces experimental complexity and minimizes insertion losses. The RF driving the MZM is phase-modulated at $\nu_{\mathrm{PDH}} = 400$ kHz and the error signal retrieved with commercial general-purpose RF components, such as bandpass filters (Mini-Circuits ZFBP-400K+) and amplifiers (Mini-Circuits ZFL-500LN+).

As soon as a certain cavity transmission threshold is reached, RD events are triggered by a 5-V TTL (transistor-transistor logic) signal driving a broadband absorptive RF switch (Minicircuits ZASWA-2-50DR+). The switch cuts the MZM single-sideband output by attenuating the RF driving signal by more than 80 dB within tens of nanoseconds. In this scheme, contrary to classical CW-CRDS, an acousto-optic modulator with additional insertion losses and inferior switching characteristics is no longer needed. The RD signals on the transmission PD are acquired at a sampling rate of 650 kHz by an 18-bit analog-to-digital converter (ADC) card (NI PCI-6281). Figure 3 shows an example of a PDH-locked RD measurement with an acquisition time of 1.2 ms per RD, resulting in a RD event rate of approximately 400 Hz. As the robust locking is not perturbed by the RD events, switching the light back on leads to near-exponential transmission ring-up events, which exhibit random intensity noise features mainly due to residual frequency jitter at the sub-kHz level. Exponential least-squares fitting of the RD signals is carried out in real-time by an optimized C algorithm embedded in LabVIEW, which can handle RD event rates on the order of 10 kHz on a standard computer.

As shown in the lower panel of Fig. 3, the fit residuals from a single RD event exhibit an exponentially decaying shot noise component at the beginning of the ring-down. It is due to the Poissonian nature of the coherent laser field and dominates for the first few RD times after the trigger, indicating a near-shot-noise-limited measurement. Further evidence for this and a more detailed discussion of the shot-noise-limit are given in Sect. 3.1. Averaging over many fit residuals cancels the random shot-noise and ADC noise components and reveals a static pattern. This structure is stable in time and attributed to ADC nonlinearity well within the acquisition card specifications. The associated relative systematic error [37] amounts to 5×10^{-6} in the present case.

2.3 Automated spectrometer operation

In order to allow acquisition of broadband spectra and long-term averaging, the spectrometer operation has been

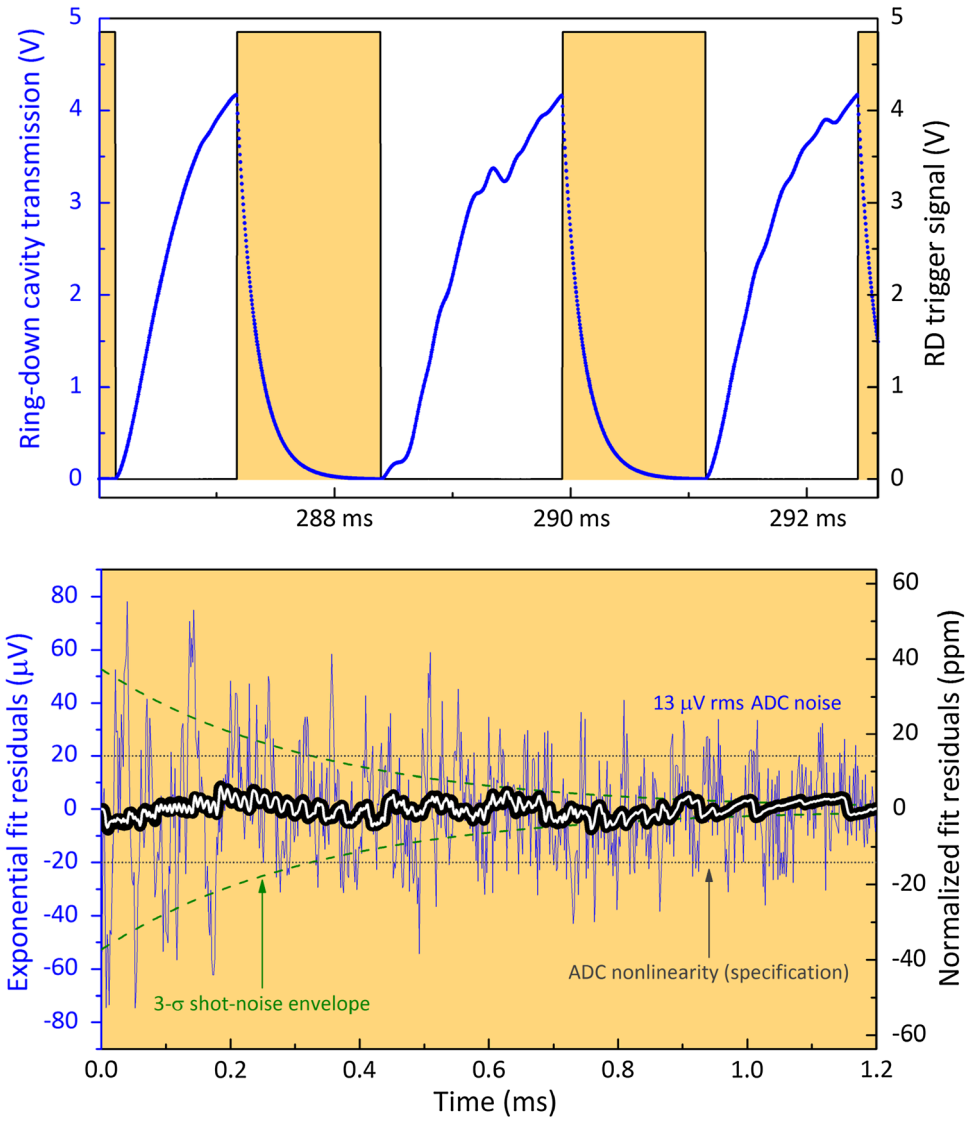

Fig. 3 *Upper panel* Ring-down cavity transmission under Pound-Drever-Hall-locking conditions with ring-down triggering by the *black* signal (*orange background*). *Lower panel* Residuals from exponential least-squares fit of a ring-down signal. Averaging of 10^4 (*black*) and 10^5 (*white*) successive fit residuals reveals a static pattern attributed to acquisition card nonlinearity

completely automated using a dedicated LabVIEW software. Its basic principle is to acquire an absorption spectrum by measuring many RD events at one laser frequency and subsequently stepping to the next frequency, while logging experimental parameters such as time, pressure and temperature. Looping this procedure yields time-resolved or averaged spectral information. An overview of the automatization tasks is given in the following.

The laser frequency is changed by means of an optimized combination of the elements of Eq. (2). Rapid fine-tuning by single-sideband modulation at the computer-controlled synthesizer frequency ν_{RF} is complemented by FSR-by-FSR tuning as soon as the RF tuning range is left. To change the V-cavity mode k, a laser current sweep controlled by a digital-to-analog converted (DAC) voltage is applied to the DC modulation input of the current driver. When the limit of current-based laser frequency tuning is reached after roughly 15 GHz, the system automatically stabilizes to a new laser diode temperature to connect the next current-scanning interval. This tuning scheme enables an arbitrary frequency stepping resolution limited only by laser drift and linewidth. One may choose uniform frequency steps for survey-type broadband spectra (cf. Sect. 3.2) or an adaptive measurement frequency grid in the case of known spectra, in particular for isolated lines (cf. Sect. 3.3). This allows choosing a distribution of points which optimizes the measurement precision for a given parameter, such as width or integrated absorption, and a given measurement time. For carrying out the latter type of measurement, the spectrometer first acquires a rapid survey spectrum at uniform frequency steps. The software then determines an adaptive measurement frequency grid which is subsequently used for repeatedly acquiring spectra of that spectral interval.

After tuning the laser frequency, Pound-Drever-Hall lock of the cavity is acquired by means of a DAC-controlled

PZT-voltage sweep which localizes the TEM_{00} mode of the ring-down cavity. The corresponding high-voltage offset is then kept constant, while the analog servo loop takes over and locks the system. Once lock is acquired within roughly half a second, ring-downs are triggered, acquired and fitted in real time at kHz-level rates. In order to average out the RD time bias due to an interference fringe from the return losses of the fiber-optic circulator, the distance between circulator and cavity is triangle-modulated by means of a PZT-mounted steering mirror. The impact of this active fringe cancelation scheme will be discussed in detail in Sect. 3.1. For known spectral regions, the length of the laser-off RD acquisition period is automatically adapted to be a fixed multiple of the RD time τ. At the RD signal-to-noise ratio (SNR) of Fig. 3, for instance, ten RD times are sufficient for optimal exponential fit precision. The quality of RD residuals is checked for ensuring that there is no resonant injection of the residual carrier or other sideband into cavity transverse modes, whose geometric overlap with the laser beam [38] is at the permil level. In practice, this situation virtually never arises due to the high-cavity finesse and the strong suppression of unwanted spectral components at the MZM output. For frequency steps exactly equal to one RD cavity FSR or smaller than the PDH locking range of $\pm\nu_{PDH}$, as in the case of saturated-absorption spectra [23], the system remains locked after changing the RF. As no relock procedure is required in these cases, they are chosen whenever very small or rather big (cf. baseline of Fig. 7) frequency steps are applicable.

In order to ensure well-defined experimental conditions, the ring-down cavity is actively temperature stabilized, currently by means of a stand-alone ventilated Peltier cooler (Laird AA-040-1222) regulating the reading from a 100 Ω platinum temperature probe (PT100) contacted to the cavity surface. For the follow-up setup under development, six 1 kΩ platinum probes (PT1000) will be deployed in a uniform distribution centimeter deep within the cavity bulk for low-noise temperature stabilization and residual temperature gradient monitoring.

The pressure inside the RD cavity is monitored using a 10 Torr Baratron gauge (MKS 626B). A completely automated pumping and gas inlet system based on solenoid and pneumatic valves is under development. Enabling completely automated spectrometer operation and remote control, this will notably allow for regular nitrogen flushing and cycling of calibration gas and sample gas for optical isotopic ratio measurements.

3 Results

The OFFS-CRDS prototype was used for a series of proof-of-principle experiments, which will be discussed in the following, characterizing its performance and illustrating its potential for absorption line metrology applications.

3.1 Absorption measurement precision, stability and fringe scrambling

The measurement stability can be characterized by means of a two-sample variance approach originally developed for estimating the stability of frequency standards by Allan [39]. The concept has been applied to absorption measurements by Werle et al. [40] to quantify the limitations of noise reduction by averaging in the presence of instrumental drifts. The Allan-Werle deviation for ring-down measurements by OFFS-CRDS, expressed in absorption coefficient units, as a function of averaging time is depicted in Fig. 4.

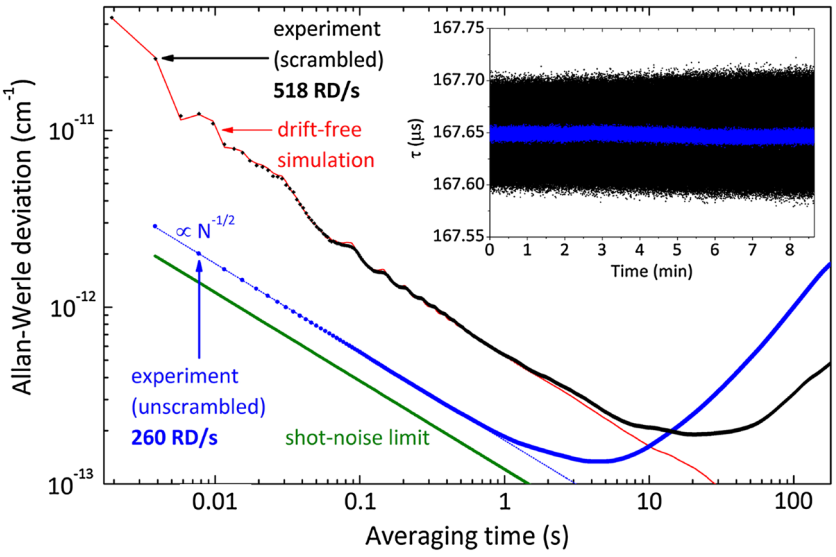

Fig. 4 Allan-Werle deviation characterizing the ring-down absorption measurement stability. The *x* axis corresponding to the number of averaged measurements *N* has been expressed in units of time here to facilitate comparison. The *inset* shows the time series of ring-down events corresponding to the respective experimental Allan-Werle deviations

The blue circles, corresponding to the time series shown in the inset, is the Allan-Werle deviation recorded without moving the circulator-cavity fringe-scrambling PZT. Starting at a single-shot precision of 3×10^{-12} cm^{-1}, it reaches its minimum at 1.4×10^{-13} cm^{-1} after 4 s. Beyond this point, the drift due to the circulator-cavity fringe becomes dominant. For shorter averaging times, the Allan-Werle deviation is inversely proportional to the square root of the number of averages N and remarkably close to the photoelectron shot noise (green line).

To derive this fundamental limit for CRDS [41], let us consider the photocurrent $I(t)$ during a RD event

$$I(t) = \frac{V_0}{R} \mathrm{e}^{-t/\tau} \tag{3}$$

yielding a voltage $V(t) = RI(t)$ at the transmission PD transimpedance amplifier gain resistance R. Sampling $V(t)$ by an ADC at time intervals t_s with a gate time t_g yields a discrete time series V_k related to the number Q_k of photoelectrons accumulated during the gate time. Expressing Q_k in terms of the photocurrent and the elementary charge e yields

$$Q_k = \frac{1}{e} \int_{kt_\mathrm{s}}^{kt_\mathrm{s}+t_\mathrm{g}} I(t)\mathrm{d}t \approx \frac{V_0 t_\mathrm{g}}{eR} \mathrm{e}^{-kt_\mathrm{s}/\tau} \tag{4}$$

The last equality holds in good approximation for $t_\mathrm{g} \ll \tau$. Q_k exhibits random fluctuations due to the quantum character of the coherent light field and the random nature of photo-electron generation. The standard deviation σ_{Q_k} of this Poissonian photo-electron shot noise process is

$$\sigma_{Q_k} = \sqrt{Q_k} \tag{5}$$

Determining the RD time τ by means of an exponential fit of the infinite digitized voltage time series V_k can be formulated as a linear regression on the natural logarithm of the dimensionless charge Q_k according to Eq. (4):

$$y_k \equiv \ln Q_k = \ln\left(\frac{V_0 t_\mathrm{g}}{eR}\right) - \frac{t_\mathrm{s}}{\tau} k \equiv A + Bk \tag{6}$$

Obtaining a maximum-likelihood estimate for τ implies minimizing the sum $\sum_{k=0}^{\infty} \left((y_k - \overline{y_k})/\sigma_{y_k}\right)^2$ of normalized differences between data y_k and model $\overline{y_k}$, with $\sigma_{y_k} = 1/\sqrt{Q_k}$ by simple error propagation of Eq. (5) in Eq. (6). This weighted least-squares fit has an analytic solution [42] which allows error propagation on the fit parameters A and B by using the geometric series and related expressions. Converting σ_B to σ_τ and expressing in absorption units σ_α through Eq. (1) yields the CRDS shot-noise limit

$$\sigma_\alpha = \sqrt{\frac{eR}{V_0 c^2 \tau^3} \frac{t_\mathrm{s}}{t_\mathrm{g}}} = \alpha \sqrt{\frac{eRt_\mathrm{s}}{V_0 \tau t_\mathrm{g}}} \tag{7}$$

In the present case, $t_\mathrm{s}^{-1} = 650$ kHz, $t_\mathrm{g} = 1$ µs, $V_0 = 1.4$ V, $R = 90,900\,\Omega$ and $\tau = 167$ µs lead to a shot-noise limit of 2×10^{-12} cm^{-1} for single-RD precision. An important practical consequence of this analysis is that a weighted exponential fit has to be employed in the near-shot-noise-limited regime to reach optimal precision. In practice, Allan-Werle deviations of RD time series from unweighted exponential fitting were up to 50 % higher than those based on a true maximum-likelihood estimate for the present setup.

The black diamonds in Fig. 4 are the Allan-Werle deviation derived from RD events under fringe-scrambling conditions, reaching a minimum of 1.9×10^{-13} cm^{-1} after 20 s. Exploring all possible values of the circulator interference fringe by varying its phase through the scrambling PZT position significantly increases RD time fluctuations, as clearly visible on the time series in the inset. This pseudo-noise is counterbalanced by a shorter RD acquisition period which increases the RD repetition rate, thereby leading to efficient averaging with a characteristic oscillatory behavior.

The shape of this Allan-Werle deviation can be modeled in terms of a Monte-Carlo simulation of fringe-scrambled RD measurements α_k based on the ansatz

$$\alpha_k = \alpha_0 + \Delta_\alpha \sin\left(2\pi d \times \mathrm{tri}(t_k, f_\mathrm{s}) + \varphi_s\right) + \epsilon_k \tag{8}$$

$$t_k = t_{k-1} + {f_\mathrm{RD}}^{-1} + \xi_k \tag{9}$$

where $\mathrm{tri}(t,f_\mathrm{s})$ is a symmetric triangle function with amplitude ± 1 and periodicity ${f_\mathrm{s}}^{-1}$ evaluated at time t. ε_k and ξ_k are random numbers with zero mean representing RD measurement noise and non-uniform RD timing, respectively. The scrambling frequency $f_\mathrm{s} = 17$ Hz and the RD event rate $f_\mathrm{RD} = 518$ Hz are imposed by the measurement conditions of Fig. 4. The fringe amplitude $\Delta_\alpha = 5 \times 10^{-11}$ cm^{-1}, the PZT-scrambling modulation depth $d \approx 2.5$ controlled by the high voltage applied to the PZT, as well as the 8.5×10^{-12} cm^{-1} standard deviation of ε_k were equally fixed to experimental values. The fringe offset $\varphi_s = 1.25$, $t_0 = 0$, and the range $|\xi_k| \leq 625$ µs of possible RD timing jitter values were manually adjusted to the data. The excellent agreement between the experimental Allan-Werle deviation and the one calculated from the simulated absorption coefficient time series α_k indicates that the averaging behavior under fringe-scrambling conditions is well understood in terms of the physical processes formalized by Eqs. (8) and (9).

An Allan-Werle plot such as the one in Fig. 4, based on measurements at one single frequency, can be misleading in the presence of optical fringes. Taken in itself, it is thus insufficient for characterizing frequency-scanned spectrometer performance. In this regime, a systematic analysis of spectrometer baseline structure is vital to

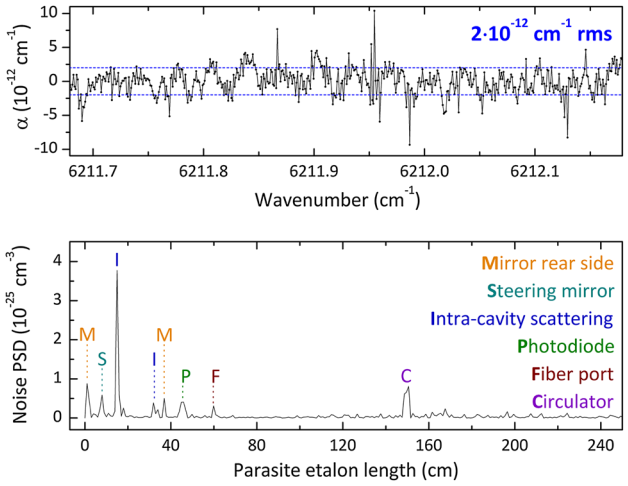

Fig. 5 Spectrometer baseline after linear correction (*upper panel*). The corresponding absorption noise power spectral density (*lower panel*) reveals interference by parasite reflections with different etalon lengths

analyze and minimize the impact of interference fringes due to parasite reflections. For the present OFFS-CRD spectrometer, the 0.5 cm^{-1} wide baseline section shown in the upper panel of Fig. 5 was recorded at frequency steps of 10^{-3} cm^{-1}. Measuring for 1.5 s at each point yielded 300 RD events on average, resulting in a baseline rms noise level of only 2×10^{-12} cm^{-1}. The improvement in comparison with the first demonstration [23] is due to a meticulous optimization of alignment and cleaning of all optics, the use of a quarter-wave plate between cavity and photodiode, as well as a more sophisticated fringe cancelation procedure.

This scheme exploits the fact that the RD time bias due to the interference fringe changes sign when the phase of the latter changes by $\pm\pi$. In analogy to Eq. (8), the bias Δ_α of the absorption measurement due to two fringes Δ_{α_a} and Δ_{α_b} may be generalized as

$$\Delta\alpha = \Delta_{\alpha_a} \sin\left(\frac{4\pi p}{\lambda} + \phi_a\right) + \Delta_{\alpha_b} \sin\left(\frac{8\pi p}{\lambda} + \phi_b\right) \quad (10)$$

by expressing the parameter d in terms of the scrambling PZT displacement p. In the paraxial approximation, d is roughly equal to $2p/(\lambda/2)$ for an interference fringe having its origin before the last steering mirror, represented by Δ_{α_b}, and $p/(\lambda/2)$ for parasite scattering by the steering mirror itself, represented by Δ_{α_a}.

In order to cancel the effect of both fringes, the PZT may therefore be stepped to four positions $p_j = j \times \lambda/8$ with $j = 0, \ldots, 3$, yielding fringe contributions with opposite signs. The arithmetic mean $\overline{\Delta_\alpha}$ of the corresponding Δ_{α_j} is thus zero, corresponding to complete fringe canceling:

$$\overline{\Delta_\alpha} = \frac{1}{4}\sum_{j=0}^{3} \Delta_{\alpha_j} = \frac{\Delta_{\alpha_a}}{4}\sum_{j=0}^{3} \cos\left(\phi_a + j\frac{\pi}{2}\right) + \frac{\Delta_{\alpha_b}}{4}\sum_{j=0}^{3} \cos\left(\phi_b + j\pi\right) = 0 \quad (11)$$

In practice, $\overline{\Delta_\alpha}$ is determined by averaging N_j RD measurements at each position p_j.

$$\Delta_{\alpha_j} = \frac{1}{N_j}\sum_{i=1}^{N_j} \Delta_{\alpha_{j_i}} \quad (12)$$

The random noise σ_α on the $\Delta_{\alpha_{j_i}}$ values propagates to $\overline{\Delta_\alpha}$ as

$$\sigma_{\overline{\Delta_\alpha}} = \frac{\sigma_\alpha}{4}\sqrt{\sum_{j=0}^{3}\frac{1}{N_j}} \quad (13)$$

via Eqs. (11) and (12). In the optimal case $N_j = N/4 \ \forall j$, this fringe cancelation method therefore yields a RD measurement precision equal to the one for N fringe-biased measurements at a single displacement p. In practice, care has to be taken to keep the number of RD events close to $N/4$ for all spectral measurement points, since noise increases considerably for a non-uniform N_j distribution according to Eq. (13). Small deviations from N_j-uniformity are irrelevant in a regime where RD acquisition noise is negligible compared with optical fringes. This is clearly the case for the present near-shot-noise-limited spectrometer with kHz-level repetition rates.

For the sake of generality, let us nonetheless note that the present scheme can be beneficially applied also in a regime where random acquisition noise dominates over interference fringes, even if the N_j are non-uniform. In this special case, the weighting in Eq. (11) should be modified to read

$$\overline{\Delta_\alpha} = \frac{\sum_{j=0}^{3} N_j \Delta_{\alpha_j}}{\sum_{j=0}^{3} N_j} \quad (14)$$

While this compensation strategy leads to only partial fringe cancelation, it has the benefit of not impairing the statistical noise reduction due to averaging.

As shown in the lower panel of Fig. 5, converting the baseline noise to a power spectral density (PSD) by Fourier transform clearly reveals several periodic contributions. With the help of the etalon length corresponding to these peaks in the PSD, the optics responsible for each parasite reflection may be identified. In the present case, small signatures of the FC-APC fiber out-coupling, the anti-reflection-coated, wedged rear side of the dielectric cavity mirrors, as well as the transmission photodiode can be discerned. A small residual from the scrambled circulator fringe is also still visible. The dominant 15 cm-fringe

is presumedly due to intra-cavity scattering losses. This hypothesis will be checked by means of the slightly different RD cavity design of a follow-up setup.

3.2 Broadband spectrum of CO_2 at 1.6 μm

OFFS-CRDS was used for acquiring the broadband, high-resolution spectrum of carbon dioxide around 1.6 μm shown in Fig. 6. This 17 h measurement was carried out for CO_2 at natural isotopic abundances and a partial pressure of 10 Pa for optimally exploiting the dynamic range of the spectrometer. Being defined as the ratio of the biggest signal to the noise on the baseline, this quantity amounts to almost 8×10^5 in the present case, with a baseline noise as low as 4×10^{-12} cm^{-1}. The inverted red curve in Fig. 6a shows a simulated spectrum based on the HITRAN 2012 database [43] for comparison.

For lines in the 40013 ← 10001 hot band of $^{12}C^{16}O_2$, the measured spectrum reveals significant disagreements with the center frequencies from the HITRAN database. For instance, the center of the R6 line shown in Fig. 6b was determined to be 6,210.7097(5) cm^{-1} and clearly disagrees with the HITRAN value of 6,210.7126 cm^{-1} given at an accuracy better than 10^{-3} cm^{-1}. Our value is in excellent agreement with previous CRDS measurements [5] (6,210.7094(10) cm^{-1}) and the position calculated from the band parameters by Miller and Brown [44] (6,210.7096(4) cm^{-1}), consequently underpinning the need for a revision of HITRAN values for this band.

A more comprehensive evaluation of the spectrum in Fig. 6 is in progress. It is expected to yield sub-MHz line center accuracies also for weak bands by using absolute frequency references at 1.6 μm.

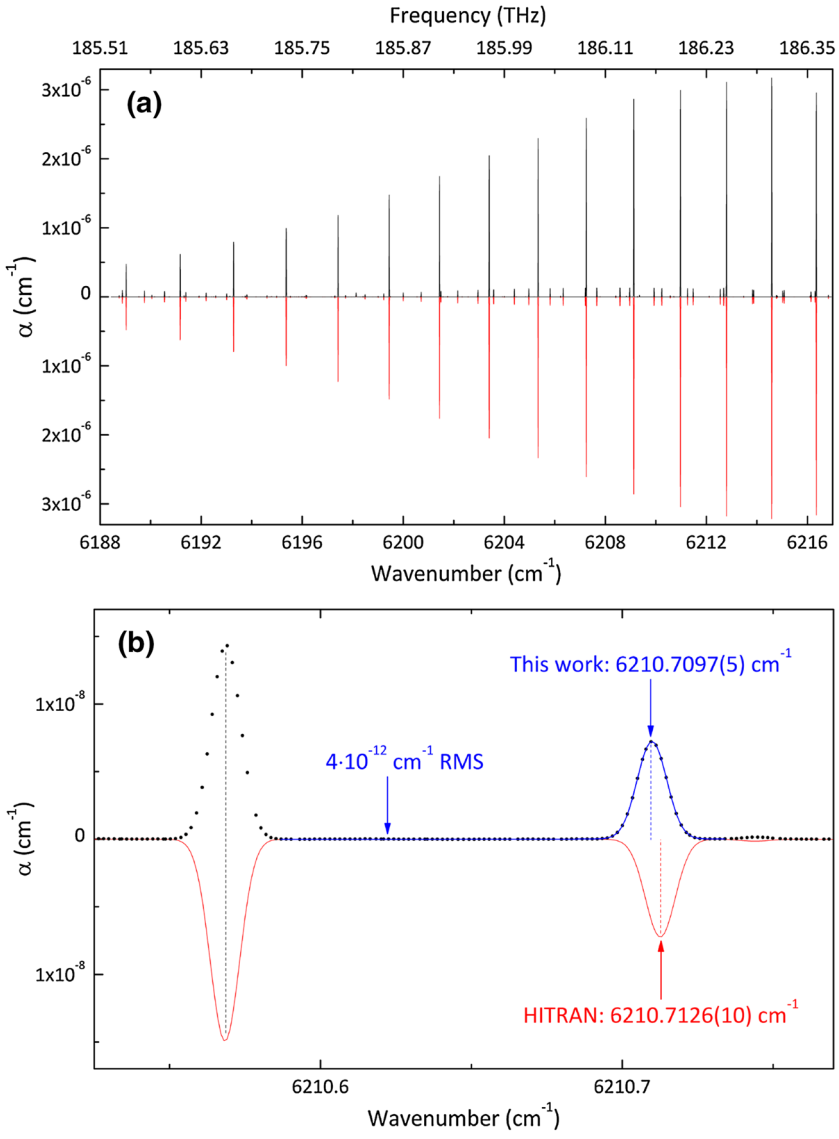

Fig. 6 **a** *Black curve* Measured broadband absorption spectrum in the P-branch of the 30013 ← 00001 band of CO_2 at 10 Pa and 296 K with second-order polynomial baseline correction. The frequency stepping resolution was 50 MHz, with several hundreds of RD events averaged for each point. *Red curve* Simulated HITRAN spectrum at identical conditions. **b** Zoom showing the individual data points and the spectrum baseline noise. The 40013 ← 10001 R6 line at 6210.71 cm^{-1} exhibits a significant frequency offset with respect to the HITRAN value

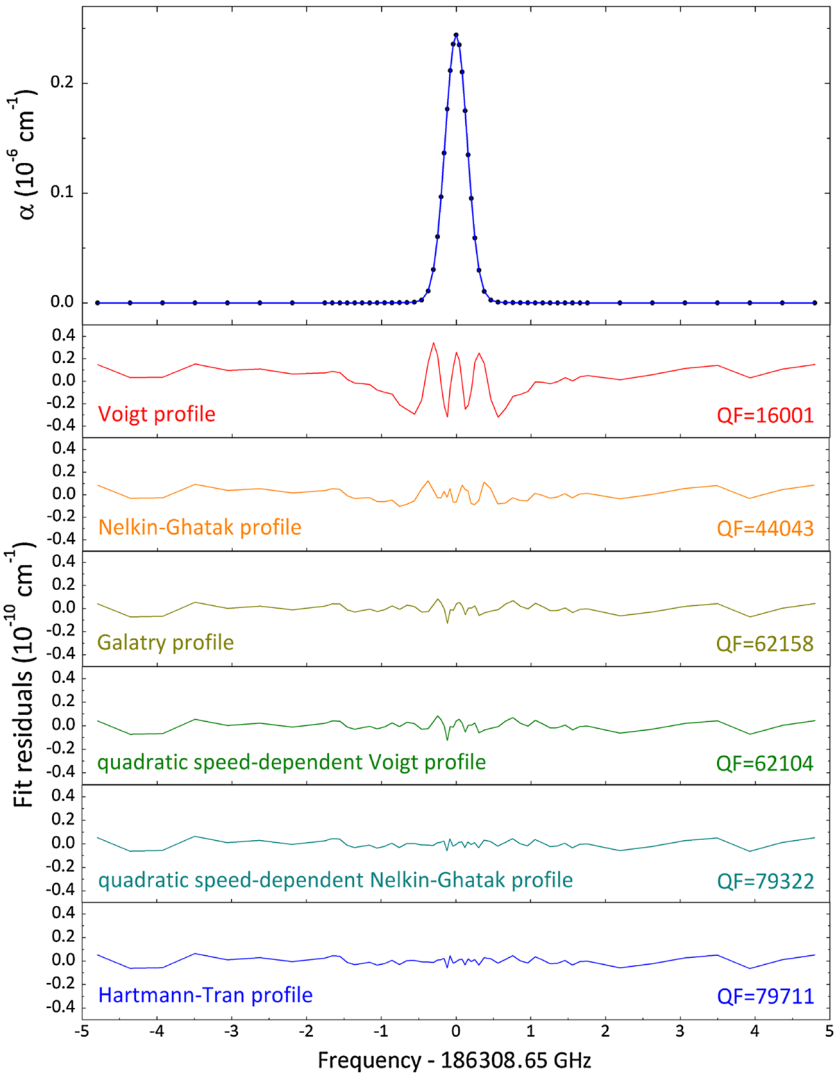

Fig. 7 Isolated 30013 ← 00001 P16 line of CO_2 at 6,214.588 cm^{-1} broadened by N_2 at a total pressure of 150 Pa and a CO_2 concentration of 5.04×10^{-3}, with first-order polynomial baseline correction. The *lower panels* show the fit residuals from different line profile models. Fit quality is indicated as the ratio QF of peak signal to rms fit residuals

3.3 Isolated line-shape study of CO_2 in N_2

A precision lineshape measurement of CO_2 broadened by N_2 was carried out at a temperature of 295.8 ± 0.1 K and a pressure of 150 Pa, with a CO_2 mole fraction of 5.04×10^{-3}. The 3.6 min single scan depicted in Fig. 7 was recorded with adaptive measurement parameters, such as the number of averaged RD events and the frequency stepping between 40 and 434.4 MHz. It exhibits a SNR of almost 8×10^4. The experimental data were fitted with various common line-shape models to compare their performance. In view of the high SNR, all parameter were kept floating during fitting. With the molecular mass m and the Boltzmann constant k_B, the fitted Doppler width Δ_D allows a critical comparison of the corresponding Doppler temperature $T_D = (\Delta_D/\nu)^2 mc^2/k_B$ to the measured RD cavity temperature. The fit residuals are shown in the lower panels of Fig. 7 and the deduced physical parameters are reported in Table 1. As a semi-quantitative indicator for fit quality, the quality figure (QF) defined as the ratio between peak signal and rms fit residuals [21] was adopted. Depending on the distribution of spectral points, QF may constitute a somewhat ambiguous measure. Nevertheless, it is a

Table 1 Comparison of the models used for fitting the line profile in Fig. 7.

Profile	QF	T_D (K)	$10^4\Gamma$ (cm^{-1})	$10^9 A$ (cm^{-2})
Voigt	16001	293.37	1.335	3.0590
NG	44043	294.56	1.353	3.0575
Galatry	62158	296.40	1.249	3.0564
qSD Voigt	62104	296.41	1.248	3.0564
qSDNG	79322	295.90	1.275	3.0567
pCqSDNG	79711	295.91	1.338	3.0567

QF fit quality figure, T_D Doppler temperature, Γ Lorentzian width, *A* integrated absorption, *NG* Nelkin-Ghatak, *qSD* quadratic speed-dependent, *pC* partially correlated

sensitive and meaningful fit quality indicator for the present study, as most measurement points were taken close to the line center.

The characteristic residuals from fitting with a Voigt profile clearly show its inadequacy even at this rather low pressure, underlined by the severely biased Doppler temperature (2.4 ± 0.1 K) below the true value.

As a first refinement beyond the Voigt profile, velocity-changing collisions leading to collisional (Dicke) narrowing [45] are often taken into account by means of the hard-collision Nelkin-Ghatak model [46]. In the present case, its fit residuals are significantly flatter than for the Voigt profile, but retain a considerable systematic structure. This is reflected by the biased Doppler temperature deduced from the fit, which is still wrong by 1.2 ± 0.1 K. The Galatry profile [47] is based on a complementary approach to collisional narrowing considering soft collision leading to only slight velocity changes. Here, it yields further improved fit residuals, which feature only little residual structure. Nonetheless, this seemingly good agreement is accompanied by a significantly biased Doppler temperature retrieval off by 0.6 K. These observations indicate that collisional narrowing alone is not sufficient to describe the physics underlying the observed lineshape.

Line-narrowing can also be due to the speed-dependence of the collisional width and shift. This is taken into account in a quadratic approximation by fitting with the quadratic speed-dependent Voigt profile. Although based on an entirely different physical mechanism, the residuals and parameters from this fit are very similar to those obtained with the Galatry profile. Combining both collisional narrowing and speed-dependence by the quadratic speed-dependent Nelkin-Ghatak (qSDNG) profile leads to a further, significant improvement in fit quality. Importantly, the Doppler temperature derived from this fit is consistent with the resistive temperature probe measurement. The residuals are flat over the whole scanning range, yielding the true SNR of the measurement, and indicating that the introduction of further parameters should create parameter correlations without improving the fit quality. This is the case when fitting with the so-called Hartmann-Tran profile (HTP) [48], which generalizes the qSDNG profile by including a partical correlation between velocity-changing and dephasing collisions (pCqSDNG). It has been suggested that this profile should supersede the Voigt profile in databases for atmospheric applications and radiative transfer models [49], as it preserves backward compatibility and features a very limited computational cost, with seven parameters which are either independent of or proportional to pressure. The HTP yields results in terms of fit quality and Doppler temperature which are very similar to those obtained with the qSDNG, but their Lorentzian broadenings Γ differ by almost 5 %. To resolve this ambiguity, a multi-fit procedure combining spectra at different pressures should be carried out, ideally from the Doppler-limited to near-Lorentzian regimes. By taking the physical scaling of parameters with pressure into account, this approach allows resolving the correlations between single-spectrum fit parameters [48] and is to be recommended for reliably retrieving physically meaningful quantities. Nevertheless, we have demonstrated here that a spectrometer with a very high signal-to-noise ratio distinguishes between the different physical broadening and narrowing processes in a remarkably efficient manner already on a single-line basis. The differences between the retrieved integrated absorption areas, which are at the 10^{-4} level even for profiles beyond Voigt, suggest the cautious use of advanced profiles for applications such as trace gas monitoring and isotopic ratio measurements.

4 Conclusions

OFFS-CRDS combines an adaptive resolution down to the kHz-level with a near-shot-noise-limited absorption sensitivity of $2 \times 10^{-13}\,\mathrm{cm}^{-1}/\sqrt{\mathrm{Hz}}$, and allows recording broadband spectra over a 1 THz span with an rms baseline noise as low as 2×10^{-12} cm^{-1}. This performance makes it a versatile, powerful tool for absorption line metrology. For achieving optimal performance, a thorough minimization of interference fringes due to parasite reflections is crucial. To this end, two active fringe cancelation schemes based on triangle-shaped and discrete piezoelectric mirror displacements were experimentally realized and theoretically described.

The OFFS-CRDS prototype was used for recording a high-resolution spectrum of CO_2, with a dynamic range approaching 800,000, between 6,188 and 6,217 cm^{-1}, confirming a need for improvement of the line center frequencies of the $^{16}O^{12}C^{16}O$ 40013 ← 10001 hot band in the HITRAN 2012 database. By linking OFFS-CRDS to absolute frequency references of any type, such high-resolution survey-type spectra should allow broadband line center frequency measurements with sub-MHz accuracy even for weak bands.

We measured the spectrum of an isolated transition of CO_2 broadened by N_2 with adaptive resolution and a signal-to-noise ratio of 80,000, clearly distinguishing line-narrowing effects beyond the Voigt profile at a pressure of 150 Pa. This performance opens the door to a systematic multi-fit analysis of line measurements over whole absorption bands and wide pressure ranges, for validating state-of-the-art lineshape models and retrieving accurate, physically meaningful line parameters. To harness this potential for applications in environmental sciences, we are currently developing an OFFS-CRD spectrometer dedicated to carbon dioxide isotopic ratios measurements.

Due to its tightly locked high-finesse ring-down cavity, OFFS-CRDS features kW/cm^2-level intracavity light intensity for input powers on the order of 100 µW. We demonstrated elsewhere [23] how this can be exploited for saturating weak CO_2 transitions around 1.6 µm involving four vibrational quanta. In a setup linked to a self-referenced frequency comb, such sub-Doppler Lamb dip measurements could pave the way to extensive near-infrared line center retrievals with sub-kHz-accuracy. This is expected to yield a multitude of new frequency references for precision spectroscopy and to contribute to the verification of state-of-the-art *ab-initio* energy level calculations.

Beside these promising lab-based applications, the relatively compact and rugged experimental setup, which uses fiber-optic components to a great extent, calls for mobile, field-deployable spectrometers. The development of such an OFFS-CRDS instrument for monitoring the concentration and isotopic composition of water vapor in Antarctic air is currently underway.

Acknowledgments The authors gratefully acknowledge Tommaso Sala, Marco Marangoni and Guillaume Méjean for the FSR measurement with a self-referenced frequency comb, Kevin K. Lehmann for his initial idea for an alternative fringe-scrambling scheme, Serge Béguier for his contribution to line fitting, David Terrier for precision machining, as well as Alain Campargue and Daniele Romanini for fruitful discussions and suggestions. This work was supported by Pôle SMINGUE, LabexOSUG@2020 (ANR10 LABX56), CNRS-INSU and Réseau FEMTO.

References

1. D. Romanini, A. Kachanov, N. Sadeghi, F. Stoeckel, Chem. Phys. Lett. **264**, 316 (1997)
2. S. Kassi, A. Campargue, J. Chem. Phys. **137**, 234201 (2012)
3. L. Brown, K. Sung, D. Benner, V. Devi, V. Boudon, T. Gabard, C. Wenger, A. Campargue, O. Leshchishina, S. Kassi, D. Mondelain, L. Wang, L. Daumont, L. Rgalia, M. Rey, X. Thomas, V.G. Tyuterev, O. Lyulin, A. Nikitin, H. Niederer, S. Albert, S. Bauerecker, M. Quack, J. OBrien, I. Gordon, L. Rothman, H. Sasada, A. Coustenis, M. Smith, T. C Jr, X.-G. Wang, A. Mantz, P. Spickler, J. Quant. Spectrosc. Radiat. Transf. **130**, 201 (2013)
4. S. Mikhailenko, D. Mondelain, S. Kassi, A. Campargue, J. Quant. Spectrosc. Radiat. Transf. **140**, 48 (2014)
5. B. Perevalov, S. Kassi, V. Perevalov, S. Tashkun, A. Campargue, J. Mol. Spectrosc. **252**, 143 (2008)
6. E. Crosson, Appl. Phys. B **92**, 403 (2008)
7. E. Kerstel, L. Gianfrani, Appl. Phys. B **92**, 439 (2008)
8. E.T. Kerstel, R. Iannone, M. Chenevier, S. Kassi, H.-J. Jost, D. Romanini, Appl. Phys. B **85**, 397 (2006)
9. J. Landsberg, D. Romanini, E. Kerstel, Opt. Lett. **39**, 1795 (2014)
10. D. Long, M. Okumura, C. Miller, J. Hodges, Appl. Phys. B **105**, 471 (2011)
11. Y. Chen, K.K. Lehmann, J. Kessler, B.S. Lollar, G.L. Couloume, T.C. Onstott, Anal. Chem. **85**, 11250 (2013)
12. A.L. Rizzo, H.-J. Jost, A. Caracausi, A. Paonita, M. Liotta, M. Martelli, Geophys. Res. Lett. **41**, 2382 (2014)
13. O.L. Polyansky, A.G. Császár, S.V. Shirin, N.F. Zobov, P. Barletta, J. Tennyson, D.W. Schwenke, P.J. Knowles, Science **299**, 539 (2003)
14. A. Campargue, S. Kassi, K. Pachucki, J. Komasa, Phys. Chem. Chem. Phys. **14**, 802 (2012)
15. A. Pogány, O. Ott, O. Werhahn, V. Ebert, J. Quant. Spectrosc. Radiat. Transf. **130**, 147 (2013)
16. J.T. Hodges, R. Ciuryło, Rev. Sci. Instrum. **76**, 023112 (2005)
17. D. Long, A. Cygan, R. van Zee, M. Okumura, C. Miller, D. Lisak, J. Hodges, Chem. Phys. Lett. **536**, 1 (2012)
18. D. Lisak, J.T. Hodges, Appl. Phys. B **88**, 317 (2007)
19. M.D. De Vizia, A. Castrillo, E. Fasci, P. Amodio, L. Moretti, L. Gianfrani, Phys. Rev. A **90**, 022503 (2014)
20. J.-M. Hartmann, H. Tran, N.H. Ngo, X. Landsheere, P. Chelin, Y. Lu, A.-W. Liu, S.-M. Hu, L. Gianfrani, G. Casa, A. Castrillo, M. Lepère, Q. Delière, M. Dhyne, L. Fissiaux, Phys. Rev. A **87**, 013403 (2013)
21. P. Wcisło, A. Cygan, D. Lisak, R. Ciuryło, Phys. Rev. A **88**, 012517 (2013)
22. P. Wcisło, H. Tran, S. Kassi, A. Campargue, F. Thibault, R. Ciuryło, J. Chem. Phys. **141**, 074301 (2014)
23. J. Burkart, D. Romanini, S. Kassi, Opt. Lett. **39**, 4695 (2014)
24. C.J. Bordé, Phil. Trans. R. Soc. A **363**, 2177 (2005)
25. C. Daussy, M. Guinet, A. Amy-Klein, K. Djerroud, Y. Hermier, S. Briaudeau, C. Bordé, C. Chardonnet, Phys. Rev. Lett. **98**, 250801 (2007)
26. L. Moretti, A. Castrillo, E. Fasci, M.D. De Vizia, G. Casa, G. Galzerano, A. Merlone, P. Laporta, L. Gianfrani, Phys. Rev. Lett. **111**, 060803 (2013)
27. S. Kassi, M. Chenevier, L. Gianfrani, A. Salhi, Y. Rouillard, A. Ouvrard, D. Romanini, Opt. Express **14**, 11442 (2006)
28. W.E. Wang, A.P.M. Michel, L. Wang, T. Tsai, M.L. Baeck, J.A. Smith, G. Wysocki, Rev. Sci. Instrum. **85**, 093103 (2014)
29. B. Tuzson, J. Mohn, M. Zeeman, R. Werner, W. Eugster, M. Zahniser, D. Nelson, J. McManus, L. Emmenegger, Appl. Phys. B **92**, 451 (2008)
30. J. Burkart, D. Romanini, S. Kassi, Opt. Lett. **38**, 2062 (2013)
31. B. Dahmani, L. Hollberg, R. Drullinger, Opt. Lett. **12**, 876 (1987)
32. P. Laurent, A. Clairon, C. Breant, IEEE J. Quant. Electron. **25**, 1131 (1989)
33. M. Izutsu, S. Shikama, T. Sueta, IEEE J. Quant. Electron. **17**, 2225 (1981)
34. T. Udem, R. Holzwarth, T.W. Hänsch, Nature **416**, 233 (2002)
35. D.Z. Anderson, J.C. Frisch, C.S. Masser, Appl. Opt. **23**, 1238 (1984)
36. R.W.P. Drever, J.L. Hall, F.V. Kowalski, J. Hough, G.M. Ford, A.J. Munley, H. Ward, Appl. Phys. B **31**, 97 (1983)
37. S. Wójtewicz, D. Lisak, A. Cygan, J. Domysławska, R. Trawiński, R. Ciuryło, Phys. Rev. A **84**, 032511 (2011)
38. D. Romanini, Appl. Phys. B **115**, 517 (2014)
39. D.W. Allan, Proc. IEEE **54**, 221 (1966)
40. P. Werle, R. Mücke, F. Slemr, Appl. Phys. B **57**, 131 (1993)
41. D. Romanini, K. Lehmann, J. Chem. Phys. **99**, 6287 (1993)
42. J. Taylor, *Introduction to Error Analysis, the Study of Uncertainties in Physical Measurements* (University Science Books, New York, 1997)
43. L. Rothman, I. Gordon, Y. Babikov, A. Barbe, D.C. Benner, P. Bernath, M. Birk, L. Bizzocchi, V. Boudon, L. Brown, A. Campargue, K. Chance, E. Cohen, L. Coudert, V. Devi, B. Drouin, A. Fayt, J.-M. Flaud, R. Gamache, J. Harrison, J.-M. Hartmann, C. Hill, J. Hodges, D. Jacquemart, A. Jolly, J. Lamouroux, R.L. Roy, G. Li, D. Long, O. Lyulin, C. Mackie, S. Massie, S. Mikhailenko, H. Mller, O. Naumenko, A. Nikitin, J. Orphal, V. Perevalov, A. Perrin, E. Polovtseva, C. Richard, M. Smith, E. Starikova, K. Sung, S. Tashkun, J. Tennyson, G. Toon, V. Tyuterev, G. Wagner, J. Quant. Spectrosc. Radiat. Transf. **130**, 4 (2013)
44. C.E. Miller, L.R. Brown, J. Mol. Spectrosc. **228**, 329 (2004)
45. R.H. Dicke, Phys. Rev. **89**, 472 (1953)
46. M. Nelkin, A. Ghatak, Phys. Rev. **135**, A4 (1964)

47. L. Galatry, Phys. Rev. **122**, 1218 (1961)
48. N. Ngo, D. Lisak, H. Tran, J.-M. Hartmann, J. Quant. Spectrosc. Radiat. Transf. **129**, 89 (2013)
49. J. Tennyson, P.F. Bernath, A. Campargue, A.G. Császár, L. Daumont, R.R. Gamache, J.T. Hodges, D. Lisak, O.V. Naumenko, L.S. Rothman, H. Tran, N.F. Zobov, J. Buldyreva, C.D. Boone, D. De Vizia, L. Gianfrani, J.-M. Hartmann, R. McPheat, D. Weidmann, J. Murray, N.H. Ngo, O.L. Polyansky, Pure Appl. Chem. **86**(12), 1931–1943 (2014)

Chapter 9

Saturated absorption

Absorption consists in an attenuation of the light field by transferring molecules from the lower to the upper state of a transition. For intense light fields, the fraction of molecules remaining in the upper state can become non-negligible. These molecules no longer contribute to absorption, and, on the contrary, lead to stimulated emission due to their interaction with the light field. Consequently, the absorption coefficient α becomes a monotonously decreasing function of the intensity I of the light field:

$$I \nearrow \Rightarrow \alpha \searrow \tag{9.1}$$

This phenomenon is called saturated absorption. In the limit of an infinitely strong light field $I \to \infty$, an equal number of molecules are in the upper and lower state of the transition, absorption and stimulated emission balance one another, and the medium becomes transparent: $\alpha \to 0$.

Mechanisms limiting this total equilibration of lower and upper population include the finite natural lifetime of the upper state, collisions with other molecules leading to dephasings or direct population redistribution, and transit effects, where molecules leave and enter the interaction zone due to their non-zero velocity according to the Maxwell-Boltzmann distribution in an ideal gas. For molecular overtone and combination tone spectroscopy, transition dipole moments are generally weak. Therefore, transferring a non-negligible fraction of the population to the upper state, before collisions and transit effects lead to a reequilibration, becomes challenging. As a consequence, very high light intensities are required to observe a measurable decrease in sample absorption.

The exceptional potential of OFFS-CRDS for saturated molecular absorption spectroscopy resides in its ability to coherently inject a laser into a resonator with very high finesse, yielding a passive intracavity intensity amplification by a factor of 10^5. With its ultra-high absorption sensitivity, it allows working at very low pressures, a necessary condition for obtaining narrow spectroscopic features with widths on the order of 100 kHz. OFFS-CRDS can then resolve these features with a negligible apparatus function due to its sub-kHz linewidth laser with negligible drifts.

Throughout this chapter, the perspectives of saturated OFFS-CRDS shall be explored on the basis of a thorough theoretical analysis validated by proof-of-principle experiments. First significant spectroscopic applications on the near-infrared spectroscopy of CO_2 are also presented and discussed in the later sections, in particular line center frequency measurements near 1.6 μm with previously unattained performance. Furthermore, we shall argue that saturation in CRDS should not be considered as a bias source, but rather as an additional physical property of the system under test. It is inherently contained in the measurement signal, thus adding an additional degree of freedom to spectroscopic studies. To this end we derive a closed, analytic expression for a ring-down signal in the

weakly saturated regime as a function of the relevant physical parameters. We demonstrate how such an approach yields an unbiased measurement of unsaturated absorption coefficients and lineshapes in a saturated-absorption regime, and how it opens the door to concentration-independent transition dipole moment measurements, which may yield precious insights into the very foundations of molecular physics.

In the literature, some previous CRDS studies are reported that have taken up the experimental challenge and successfully exploited saturated molecular absorption in the mid- and near-infrared spectral regions, thereby realizing previously practically impossible measurement applications.

9.1 Prior saturated-absorption measurements by CRDS

To the best of our knowledge, the first experimental demonstration of saturation effects in continuous-wave (CW) CRDS was made by Romanini and co-workers at Laboratoire de Spectrométrie Physique (LSP) in Grenoble [237]. With a single-mode CW titanium-sapphire (Ti:Sa) laser, mode-matched to the TEM_{00} mode of a cavity with ring-down times on the order of 100 µs, they achieved intracavity power levels on the order of 20 W at 800 nm. Virtually eliminating collisional decoherence effects by probing nitrogen dioxide molecules in a continuous supersonic planar jet, they were able to observe saturation Lamb dips in absorption, as shown in Fig. 9.1. The authors used the fact that during a ring-

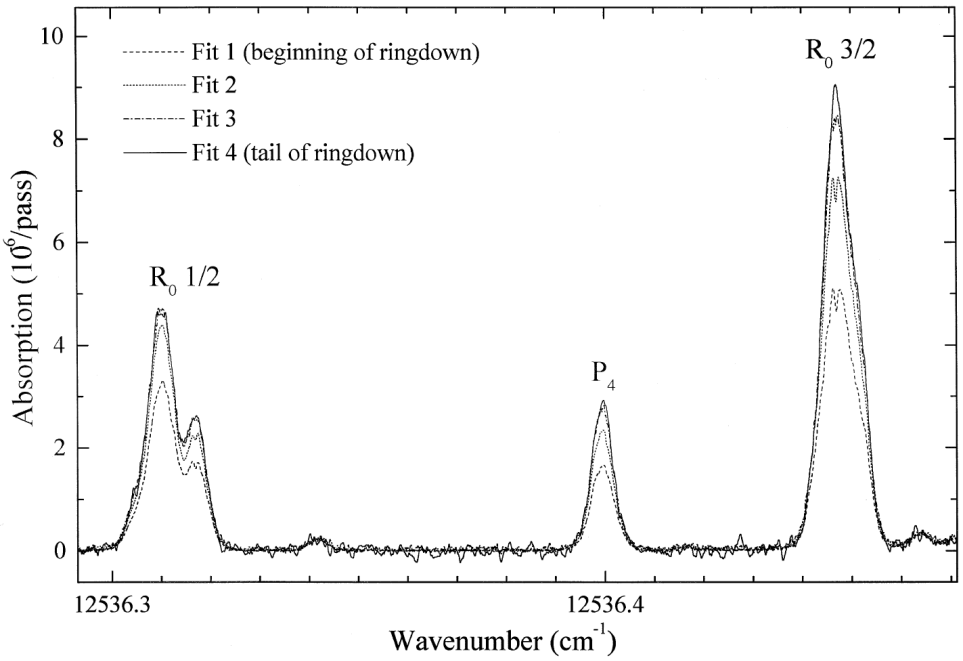

Figure 9.1 Saturated-absorption Lamb dips in a cavity ring-down spectrum of NO_2 in a supersonic slit jet by Romanini *et al.* [237]. The different curves correspond to exponential fitting of different parts of the ring-down signal. Adapted from [237] (Figure 1).

down event saturation fades out with the decaying intracavity intensity, thus allowing an approximate determination of the unsaturated absorption coefficient by fitting the tail of each ring-down event. A spectrum obtained in this manner is shown as the unbroken black line in Fig. 9.1. Inversely, taking into account the beginning of the ring-down event reveals strong saturation, manifesting itself through a decrease in absorption and the emergence of Doppler-free Lamb dips at the center of the lines. Beyond that, this supersonic-jet CRDS study also provided evidence for extremely narrow two-photon-transitions of NO_2

observed in a fluorescence signal acquired simultaneously with the cavity-transmission-based ring-down signal.

Let us cite a discussion paragraph from the article [237], which sums up very precisely the endeavor we undertake in Section 9.2 of this thesis, by developing an analytic theoretical framework for carrying out quantitative CRD spectroscopy explicitly encompassing saturation effects, opening the promising perspective of concentration-independent transition dipole measurements:

> We are not going further into the determination of the function $\alpha(I)$, however, all information should be available in order to write down a complete and accurate rate equation model. This should include the velocity distribution of the molecules and the intensity profile of the intracavity TEM field. Analytic or numerical integration would allow determining the exact ringdown profile. From an accurate measurement of the intracavity optical power density and the corresponding saturation observed in the ringdown, an estimation of the value of the transition moment should then be possible. This would allow to determine the absolute absorption intensities without knowledge of number density and partition function.

Another proof-of-principle experiment in saturated absorption CRDS was carried out on a strong ethylene transition at 10.6 µm by Bucher and co-workers [238]. Starting from a CO_2 laser with 10 W, they used a CdTe electro-optic modulator driven by 20 W of microwave power to obtain two times 1 mW of tunable sideband power. The length of the ring-down cavity was then tuned and locked into resonance with one of the sidebands by means of a piezoelectric actuator as well as a slow thermal-expansion-based cavity length servo for compensating bigger drifts. The corresponding error signal was obtained by sideband frequency modulation and phase-sensitive detection. With the resulting resonant intracavity amplification, the authors could demonstrate saturated absorption Lamb dips at the center of the studied C_2H_4 line. They quantitatively characterized the degree of saturation as well as the power broadening of the dip by recording spectra at several different sideband powers. Although the absorption coefficient could be considered constant during a ring-down event in their study due to the very short cavity decay time, which was small compared to population relaxation times, the authors conclude their article stating that

> An important feature to be studied is the degree to which the transients are nonexponential, inasmuch as this will provide a direct measure of the saturation of the optical absorption.

This outlook essentially matches the proposal by Romanini *et al.* in [237].

Exploiting saturated-absorption CRDS for quantitative spectroscopy, Lisak and Hodges studied four closely spaced water lines near 1.4 µm by FS-CRDS (cf. Section 5.3) [239]. Besides integrated-absorption measurements and error budget considerations for water vapor in nitrogen, they also investigated the case of very low water partial pressures originating from outgassing from the cavity walls. Due to the negligible impact of intermolecular collisions in this regime, saturation of transitions can be achieved at comparably low light intensities. Furthermore, the spectrometer frequency axis was referenced to a I_2-stabilized Helium-Neon laser, leading to kHz-level precision and resolution. Thanks to the combination of these factors, Lamb dips could be evidenced at the top of the four lines using narrow-span scans with high frequency stepping resolution. This result is shown in Fig. 9.2. The Doppler-free Lamb dips are three orders of magnitude narrower than the Doppler-broadened line. The authors demonstrated how this can be used for precise line center measurements, in spite of the limited signal-to-noise ratio of the dips. They report

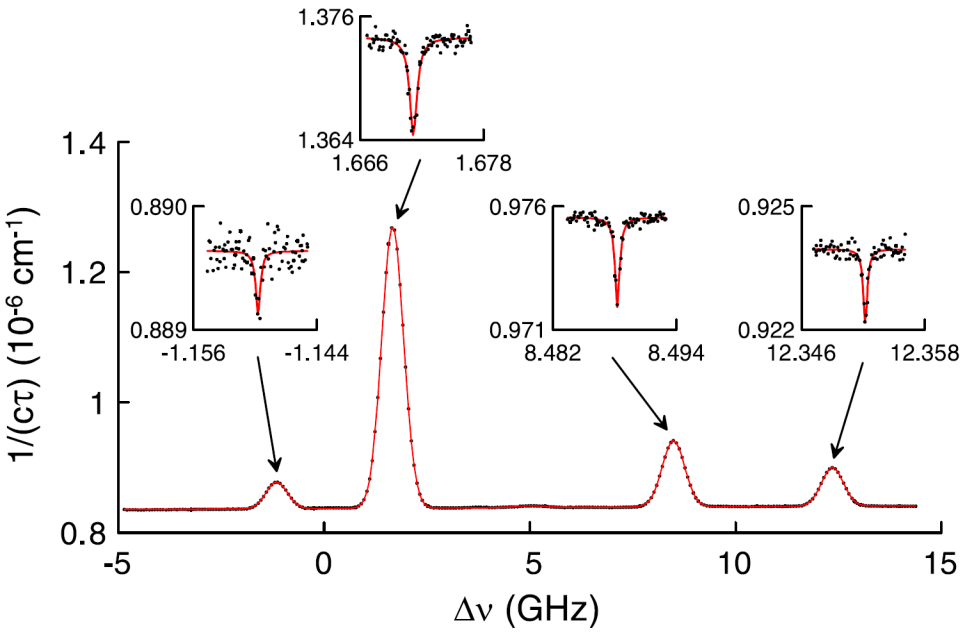

Figure 9.2 FS-CRDS spectrum of four water vapor absorption lines near 1392 nm at a total pressure of 38 mPa by Lisak and Hodges [239]. The insets show the Lamb dip at the center of each line measured with very small frequency steps on a narrow spectral interval at the top of the line. Adapted from [239] (Figure 3).

that the uncertainty in the relative position of the four lines is reduced by a factor of 3 to 8 by going from Doppler-limited to sub-Doppler measurements. Using the Lamb dips, the frequency spacings between the four water transitions could be determined at an accuracy of a few 100 kHz.

Taking advantage of the intense transitions in the mid-infrared, Giusfredi and co-workers have devised a CRDS technique dubbed SCAR (for saturated-absorption cavity ring-down), specifically dedicated to saturated-absorption measurements and capable of decoupling the ring-down spectrometer baseline from absorption signal [240]. In intuitive terms, its principle is to induce virtual transparence in the gas sample due to saturation at the beginning of the ring-down event. This allows a determination of the spectrometer baseline loss at each measurement point in spite of absorbing gas sample. The absorption coefficient due to the gas then builds up to its unsaturated level as intracavity intensity decays, and can thus be determined at the tail of each ring-down event. This measurement scheme makes SCAR immune to common CRDS bias sources such as optical fringes in principle and is illustrated in Fig. 9.3. The decay functions f essentially represent saturated absorption and are plotted for different initial saturation parameters G_0 in Fig. 9.3. The time-dependent saturation parameter satisfies a differential equation, which is solved numerically for fitting the experimental cavity ring-down photodiode signals during a SCAR measurement. A theoretical analysis of noise and detection limits in SCAR as a function of the initial saturation parameter has been undertaken by Lehmann [241]. To demonstrate the resolution of the SCAR spectrometer as well as its sensitivity in the strong saturation regime, Guisfredi and co-workers measured the Lamb dips and saturated-absorption crossover resonances at the top of an intense $^{17}O^{12}C^{16}O$ line in 0.2 Pa of CO_2 at natural abundance. More than one Lamb dip is observed on top of this line due to the electric quadrupole interaction of the ^{17}O spin-$\frac{5}{2}$-nucleus with the intramolecular electric field gradient at the nucleus position. This leads to a hyperfine splitting of the line into three components corresponding to different changes in the nuclear spin orienta-

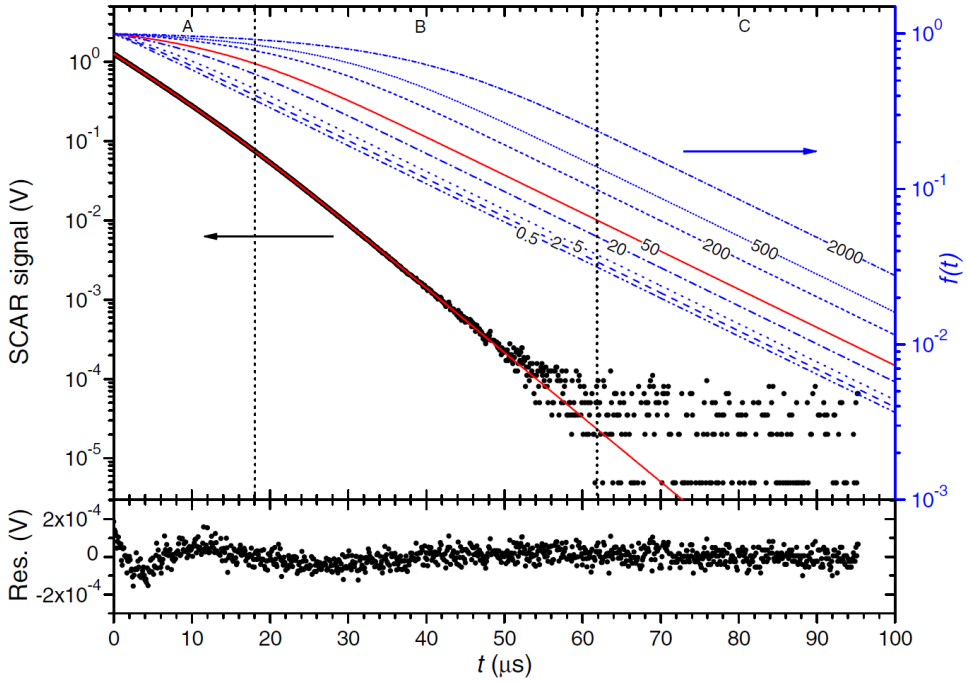

Figure 9.3 Illustration of the SCAR principle with an experimental saturated ring-down decay signal with fit residuals. SCAR decay functions $f(t)$ representing saturated sample absorption are shown for different values of the initial saturation parameter. Adapted from [240] (Figure 1).

tion with respect to the molecular rotation axis. With the difference-frequency-generated mid-infrared laser source referenced to an optical frequency comb, this study improved the knowledge of the fundamental rovibrational 00011 ← 00001 R0 transition frequency in the asymmetric stretching mode by three orders of magnitude. The SCAR technique was equally employed for the first radioactive carbon-14 concentration measurements in gaseous $^{14}C^{16}O_2$ samples at and below natural abundance ($^{14}C/C \approx 10^{-12}$), reaching a detection limit corresponding to a relative ^{14}C-abundance of $4.3 \cdot 10^{-14}$ [242].

In the next section, we follow an approach which is similar to the one in [240] but focus on the derivation of an analytic formula for a weakly saturated ring-down signal by means of a detailed theoretical analysis including the quantitative impact of the intensity distribution in the Gaussian TEM_{00} mode. Furthermore, we set out the experimental path to accurate concentration-independent transition dipole measurements using saturated-absorption CRDS.

9.2 Theoretical analysis of saturation effects in CRDS

Many detailed treatments of saturation effects in laser physics and absorption spectroscopy exist in the literature [243, 244], and considerable theoretical efforts were made to represent the saturated absorption lineshape with high fidelity [245, 246]. An exhaustive treatment is beyond the scope of this thesis. Instead, we will focus on points which are vital to saturated-absorption cavity ring-down spectroscopy in a regime of weak saturation. This special case is of primordial interest here, as it is typical when probing weak rovibrational molecular transitions in the near-infrared in a gas in thermal equilibrium.

First, we will give a brief overview of basic aspects of light-matter interaction giving rise to saturation as well as the relevant physical parameters. Then, we go on to discussing the differences between the homogeneous and inhomogeneous line broadening regimes and explaining the appearance of narrow absorption dips in the latter. Finally, we shall derive an analytic formula for the cavity ring-down signal due to a weakly saturated absorption line.

9.2.1 Homogeneous *versus* inhomogeneous saturation

Spectral lines are said to be homogenously broadened if the effective transition frequency ν_0 is the same for all molecules and each one contributes to the total absorption with the same line profile $p(\nu)$ (cf. Section 8.1.2). In this case, the absorbing ensemble behaves essentially equivalently to a single molecule, naturally scaled by the particle density N/V. From fundamental light-matter interaction considerations in a two-level system [247–249], one may show that the absorption coefficient then takes the Lorentzian form

$$\alpha = \frac{N}{V}\frac{k^*}{(\nu-\nu_0)^2 + \frac{\gamma^2}{4} + \tilde{k}I} \tag{9.2}$$

as a function of frequency ν, depending on the full linewidth of the transition γ as well as on the exciting light intensity I. By explicitly writing the two constants k^* and $\tilde{k}$ in terms of the relevant physical quantities, as given for instance in [58], Eq. (9.2) becomes

$$\alpha = \frac{N}{V}\frac{\nu_0\gamma\mu^2}{2c\epsilon_0\hbar}\frac{1}{(\nu-\nu_0)^2 + \frac{\gamma^2}{4}\left(1+\frac{I}{I_S}\right)} \tag{9.3}$$

with

$$I_S = \frac{c\epsilon_0 h^2\gamma^2}{4\mu^2} \tag{9.4}$$

This saturation intensity I_S is an intrinsic property of the physical system under study, depending essentially on the lifetime of the upper level and the strength of the transition dipole moment. It is common practice to define a saturation parameter G as

$$G = \frac{I}{I_S} \tag{9.5}$$

G is a dimensionless light intensity quantifying the degree of saturation for the transition in question at given experimental conditions. One can see from Eq. (9.3) that saturation in the homogeneous regime leads to a broadening of absorption lines proportional to the light intensity, and, simultaneously, to a drop in sample absorption. Let us now quantify its impact on the integrated absorption S due to the transition by integrating Eq. (9.3):

$$S = \int_{-\infty}^{\infty}\alpha(\nu)\mathrm{d}\nu = \frac{N}{V}\frac{\pi\nu_0\mu^2}{c\epsilon_0\hbar}\frac{1}{\sqrt{1+\frac{I}{I_S}}} \tag{9.6}$$

According to the basic formula $S = k\frac{N}{V}$ for integrated absorption, Eq. (4.6), the unsaturated line strength of the transition is

$$k_0 = \frac{\pi\nu_0\mu^2}{c\epsilon_0\hbar} \tag{9.7}$$

and the line strength diminished by saturation, which incorporates the explicit intensity dependence, then reads

$$k = \frac{k_0}{\sqrt{1+\frac{I}{I_S}}}, \tag{9.8}$$

Following from first principles, the transition dipole moment μ in Eqs. (9.3) through (9.8) is a fundamental physical property of the molecular system under study. Both S and I_S depend on it and can therefore be used for determining μ experimentally. However, S is also proportional to N/V and thus yields a concentration-dependent measurement, ultimately limited by the accuracy of the pressure gauge used for the measurement. I_S, on the contrary, holds the promise of a concentration-independent transition dipole measurement, a fascinating possibility towards which first steps shall be explored in Section 9.3.

The homogeneous saturation case could be hypothetically realized by trapping a single molecule or an ensemble of molecules in an optical lattice and performing spectroscopy on them. However, as discussed in Section 8.1.2, an absorption line in the gas phase is inhomogeneously broadened by absorption contributions at different Doppler-shifted frequencies due to the Maxwell-Boltzmann distribution $F(v)$ of molecular velocities v in thermal equilibrium. The impact of saturation in this inhomogeneous regime follows directly from the homogeneous case in Eq. (9.8) and the derivation of the Doppler profile in Section 8.1.2. Inserting $k(I)$ in Eq. (8.23) thus yields

$$\alpha(\nu) = k\frac{N}{V}\frac{c}{\nu_0}F\left((\nu-\nu_0)\frac{c}{\nu_0}\right)\frac{1}{\sqrt{1+\frac{I}{I_S}}} \tag{9.9}$$

Defining the unsaturated absorption $\alpha_0(\nu) = \alpha(\nu)|_{I=0}$, one may write

$$\alpha(\nu) = \frac{\alpha_0(\nu)}{\sqrt{1+\frac{I}{I_S}}} \tag{9.10}$$

This is the fundamental equation for the impact of saturation in the Doppler-broadened regime. As mentioned above, a weak light field is an important special case. Expanding Eq. (9.10) to first order in this weak saturation regime $I \ll I_S$ yields:

$$\alpha(\nu) = \alpha_0(\nu)\left(1-\frac{I}{2I_S}\right) + \mathcal{O}\left(\left(\frac{I}{I_S}\right)^2\right) \tag{9.11}$$

The linearity of the correction term in the weakly saturated regime shall prove very helpful in the following. Interesting phenomena arise when considering that the exciting light intensity I itself can become a function of frequency. These deviations from the simple Doppler profile due to inhomogeneous saturation shall be discussed in the following section.

9.2.2 Doppler-free Lamb dips

As discussed in the previous section, each velocity class saturates independently and contributes to the total inhomogeneously Doppler-broadened absorption. Importantly, only the light intensity which is effectively resonant with the transition may be taken as I in Eqs. (9.10) and (9.11). However, this exciting light intensity is no longer equal for all velocity classes in a configuration with collinear counter-propagating light beams. This is due to the fact that the Doppler effect changes sign depending on the direction of propagation of the light wave. When inverting the direction, the excitation switches from velocity class $+v$ to $-v$ and vice-versa.

Let us illustrate these considerations with the schematic setup in Fig. 9.4 a). Two nearly collinear counter-propagating light beams, commonly called pump and probe beam, are transmitted through an absorbing gas sample. Let us assume that they have equal intensity I and frequency ν for the sake of simplicity.

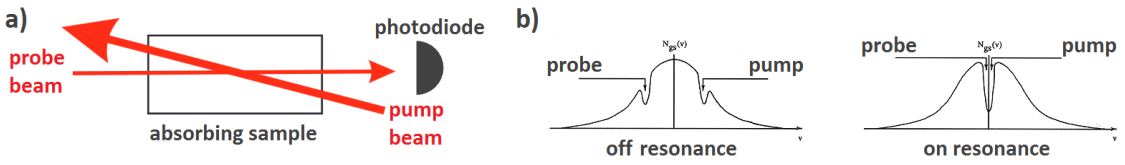

Figure 9.4 Basic saturation spectroscopy. a) Schematic sketch of the essential components of an experimental setup. b) Ground-state population as a function of frequency, for counter-propagating pump and probe laser beams of equal frequency off resonance with the molecular transition (left), or on resonance (right), giving rise to a Lamb dip at the center of the Doppler-broadened line.

If their frequency is not resonant with the transition frequency of the gas molecules but still lies within the inhomogeneously broadened Doppler profile, each beam excites molecules from one velocity class v_z and $-v_z$, respectively. The velocities, which are projections onto the optical axis of the system, fulfill the condition $v_z = \pm c(\nu/\nu_0 - 1)$ according to Eq. (8.19) and are symmetrically located with respect to the line center ν_0. For these two velocity classes, some of the gas molecules from the ground state of the transition are transferred to its excited state. The resulting population distribution for the ground state is illustrated on the left of Fig. 9.4 b).

If, however, the two beam frequencies resonantly coincide with the transition frequency of the molecules, $\nu = \nu_0$, then only the velocity class $v_z = 0$ satisfies the interaction condition and both the left- and right-propagating wave excite the molecular transition, leading to a two-fold increase in interacting light intensity. Consequently, as illustrated in Fig. 9.4 b), the resonant depopulation of the ground state for molecules with $v_z = 0$ is stronger than the one for the two velocity classes $\pm v_z \neq 0$ in the off-resonant case discussed above. By an excess depopulation of the transition ground state, the two-fold intensity increase on resonance with both beams thus leads to a decrease in absorption at the line center, as stated by Eq. (9.1).

This type of dip was first discovered by McFarlane, Bennett and Lamb as a decrease in light amplification at the center of the gain profile of a single-mode Helium-Neon laser [250]. Analogously to the discussion above, this dip is due to the fact that the resonant laser beam interacts with the same velocity class for both its counter-propagating intra-resonator waves, instead of benefiting from the population inversion in two independent velocity classes $+v_z$ and $-v_z$, as in the case of frequency pulling off the Neon line center by the laser resonator. Owing to the fact that Lamb predicted this gain-reduction phenomenon in his extensive theoretical treatise on laser physics [251], it is most commonly termed as Lamb dip in his honor.

In the case of saturated absorption, the effect translates into an increase in transmission through an absorber, which is also known as inverted Lamb dip [243]. In the framework of the present thesis, we are considering absorption coefficients. As increased transmission is equivalent to reduced absorption, we therefore encounter downward-oriented dip signatures in the absorption coefficient. Let us note that the special case of counter-propagating beams with equal frequency and intensity is highly significant here, as it corresponds to a high-finesse resonator with highly reflective mirrors. In the steady state and directly after switching off the light source injecting such a resonator, this is a completely symmetric system with a standing wave inside the cavity, which can be decomposed into two waves of equal intensity travelling into opposite directions.

For the sake of conceptual simplicity, the above discussion was made for an infinitely narrow homogeneous linewidth of the transition in question, leading to the interaction with a single perfectly monochromatic velocity class. This is obviously just an idealization, as

the number of absorbers in such an infinitely narrow velocity class is infinitesimally small. When taking the finite homogeneous linewidth into account, the Doppler profile gives way to the Voigt profile, which is a convolution of the Gaussian Doppler profile and the homogeneous Lorentzian profile, as discussed in Section 8.1.2.

On the basis of this consideration, it is clear that not only the infinitesimally narrow velocity class with $v_z = 0$ can interact with both of the counter-propagating beams, but all velocity classes within the bounds of their homogeneous profile $p(\nu)$. Introducing the full intensity-dependent homogeneous absorption coefficient from Eq. (9.3) into an ansatz like Eq. (8.26) leads to a complex expression with a rich behavior in the case of strong saturation. Such shapes of saturated absorption features under different conditions were analyzed in great detail in the literature (e.g. [243, 245, 246]).

Here, we shall choose a conceptually simpler, phenomenological approach, which is valid in the weak saturation regime. As $G \ll 1$ in this case, there are only small changes in the homogeneous absorption line shape $p(\nu)$ due to saturation. Under this condition, one can write the total light intensity effectively interacting with the molecular transition as

$$I_{tot}(\nu) = I\left(1 + \frac{p(\nu - \nu_0)}{p(\nu_0)}\right) \tag{9.12}$$

The factor in brackets is a dimensionless effective velocity parameter with the shape of the homogeneous line profile $p(\nu - \nu_0)$ and shall be called g here:

$$g(\nu - \nu_0) = 1 + \frac{p(\nu - \nu_0)}{p(\nu_0)} \tag{9.13}$$

It describes the degree of interaction with the two counter-propagating light beams, taking values between 1 and 2, with the limiting cases $g \to 1$ for $(\nu - \nu_0) \to \pm\infty$ and $g \to 2$ for $(\nu - \nu_0) \to 0$. Through its link to I via its definition (9.5), the saturation parameter G for two counter-propagating beams of equal intensity and frequency can thus be written as

$$G_{tot}(\nu) = G \cdot g\,(\nu - \nu_0)\,. \tag{9.14}$$

Inserting the frequency-dependent effectively interacting intensity I_{tot} from Eq. (9.12) into the absorption coefficient in Eqs. (9.10) and (9.11) qualitatively changes the inhomogeneous absorption profile as expected, by the appearance of a Lamb dip with shape $g(\nu - \nu_0)$ at the line center ν_0. The depth of this dip as compared to the absorption $\alpha_1(\nu) = \alpha_0(\nu)\,(1 - I/(2I_S))$ for excitation by a single light beam is given by

$$\Delta\alpha = \alpha_0(\nu_0)\left(1 - \frac{I}{2I_S}\right) - \alpha_0(\nu_0)\left(1 - \frac{g(0)I}{2I_S}\right) = \alpha_0(\nu_0)\frac{I}{2I_S}, \tag{9.15}$$

with $g(0) = 2$. Using the fact that terms quadratic in I/I_S are negligible in the case of weak saturation, one may reformulate this in terms of $\alpha_1(\nu)$ as follows:

$$\Delta\alpha \approx \alpha_1(\nu_0)\left(1 + \frac{I}{2I_S}\right)\frac{I}{2I_S} \approx \alpha_1(\nu_0)\frac{I}{2I_S} \tag{9.16}$$

In this regime, the saturation parameter can thus be readily determined from the observed depth of the Lamb dip:

$$G = 2\frac{\Delta\alpha}{\alpha_1(\nu_0)} \tag{9.17}$$

This strikingly simple and useful result is important for the evaluation of the CO_2 Lamb dip measurements discussed in Section 9.4, for instance.

9.2.3 Analytic formula for weak saturation

With the intensity-dependent saturated absorption coefficient $\alpha(I_{tot})$ of Eqs. (9.10) and (9.11) as well as the frequency-dependent effectively interacting light intensity $I_{tot}(\nu)$ of Eq. (9.12), we shall now turn to a theoretical description of a cavity ring-down event in the weakly saturated, inhomogeneously broadened regime. As stated above, the challenge lies in the varying degree of saturation both over the temporal and the spatial coordinates. This is due to the intensity decay during the ring-down event and the spatial intensity distribution in the TEM_{00} mode of the ring-down cavity, respectively.

For this analysis, let us revisit the second theoretical approach from Section 5.1, which consists in considering the energy loss of the ring-down cavity. We have seen that the total electromagnetic field energy stored in the travelling-wave TEM_{00} mode is given by

$$W = \frac{1}{4} n^2 \epsilon_0 {E_0}^2 \pi {w_0}^2 L \tag{9.18}$$

The energy loss rate $\left(\frac{\mathrm{d}W}{\mathrm{d}t}\right)_m$ due to the mirrors given by Eq. (5.11) is unaffected by the intensity-dependent $\alpha(I)$. To obtain a differential equation, and, eventually, an analytic formula for the saturated ring-down signal as a function of time, we need to reconsider the energy loss due to absorption:

$$(\mathrm{d}W)_a = -\int_V n^2 \epsilon_0 E^2(x,y,z) \alpha\left(g \cdot I(x,y,z)\right) \frac{c}{n} \mathrm{d}t \mathrm{d}V \tag{9.19}$$

Note that $\alpha(g \cdot I)$ can no longer be pulled out of the volume integral in Eq. (9.19) due to the dependence of I on the spatial coordinates. In writing $\alpha(I)$, we implicitly assume that there is a continuous re-equilibration of the upper and lower state population to a steady state at each I. This adiabatic approximation is valid if the ring-down time is much longer than the inverse homogeneous linewidth of the transition, a condition which is fulfilled in the low-pressure high-finesse CRDS studies targeted here. As a next step, we write the volume integral in Eq. (9.19) in cylindrical coordinates and insert the weakly saturated absorption coefficient from Eq. (9.11). Expressing the one-way intracavity intensity $I = \epsilon_0 n c E^2$ explicitly in terms of the electric field E, this yields the energy loss rate $\left(\frac{\mathrm{d}W}{\mathrm{d}t}\right)_a$ due to absorption as

$$\left(\frac{\mathrm{d}W}{\mathrm{d}t}\right)_a = -cn\alpha_0\epsilon_0 \int_0^{\infty}\int_0^{2\pi}\int_{-L/2}^{L/2} E^2(r,z) \cdot \left(1 - \frac{cn\epsilon_0 g \cdot E^2(r,z)}{2I_s}\right) \mathrm{d}r\mathrm{d}\varphi\mathrm{d}z \tag{9.20}$$

Comparing to Eq. (5.12), the first term in the above equation can be simplified by writing it in terms of the electromagnetic field energy W. The second term acquires an additional factor $\frac{1}{2}$ by time-averaging over the rapidly varying $\cos^2(kz - \omega t + ...)$-term, reflecting the fact that the molecular population distribution is not affected by intensity variations as fast as optical frequencies. In the volume integral, the trivial φ-integration yields 2π and the r-integration can be carried out using the identity (5.7). Once more identifying W in the result by completing with the cavity length L leads to

$$\left(\frac{\mathrm{d}W}{\mathrm{d}t}\right)_a = -\frac{\alpha_0 c}{n} W \left(1 - \frac{gcn\epsilon_0 {E_0(t)}^2}{2I_S} \frac{1}{2L} \int_0^{L/2} \frac{\mathrm{d}z}{1 + \frac{z^2}{z_R^2}}\right) \tag{9.21}$$

The z-integration yields an arctangent. Expressing the Rayleigh range z_R for a symmetric cavity with identical mirrors in terms of L and the mirror radius of curvature r as in Eq.

(2.28), one obtains

$$\left(\frac{\mathrm{d}W}{\mathrm{d}t}\right)_a = -W\frac{\alpha_0 c}{n}\left(1 - \frac{\frac{1}{4}gcn\epsilon_0 {E_0}^2\sqrt{\frac{2r}{L}-1}\arctan\left(\left(\frac{2r}{L}-1\right)^{-1/2}\right)}{2I_S}\right) \tag{9.22}$$

In this equation, one may identify the effective one-way light intensity

$$I_{eff} = \frac{1}{4}cn\epsilon_0 {E_0}^2\sqrt{\frac{2r}{L}-1}\arctan\left(\left(\frac{2r}{L}-1\right)^{-1/2}\right) \tag{9.23}$$

Then, the intracavity energy decay rate due to absorption takes on the simple form

$$\left(\frac{\mathrm{d}W}{\mathrm{d}t}\right)_a = -W\frac{\alpha_0 c}{n}\left(1 - \frac{gI_{eff}}{2I_S}\right) \tag{9.24}$$

It is remarkable that the complex intensity distribution inside the TEM_{00} cavity mode can eventually be completely absorbed into a mere effective, or pseudo-average, intracavity intensity. Its nontrivial geometric scaling factor $\sqrt{2r/L-1}\arctan\left((2r/L-1)^{-1/2}\right)$ goes to 1 for the limiting case of a cavity with flat mirrors. Then, the result $I_{eff} = 1/4cn\epsilon_0 {E_0}^2$ is very intuitive, corresponding to exactly half the time-averaged one-way peak intensity. Comparison of Eq. (9.24) with Eq. (5.13) shows that in CRDS weak saturation in an inhomogeneously broadened regime simply diminishes the absorption-related decay rate, and this proportionally to the effectively interacting light intensity. Importantly, the presence of the velocity parameter g in (9.24) implies that Lamb dips also can be observed in CRDS decay rates.

Combining the saturated absorption energy decay rate (9.24) with the mirror-loss-related decay rate from Eq. (5.11) one obtains a differential equation for W:

$$\frac{\mathrm{d}W}{\mathrm{d}t} = -W\left(\frac{(1-R)c}{nL} + \frac{\alpha_0 c}{n}\left(1 - \frac{gI_{eff}}{2I_S}\right)\right) \tag{9.25}$$

The first two terms on the right would yield the same linear ordinary differential equation (ODE) as for the unsaturated case in Eq. (5.14). The third term, however, is quadratic in I_{eff}, because I_{eff} as in Eq. (9.23) is proportional to the total intracavity energy W of Eq. (5.8). Therefore, it is straightforward to reformulate the differential equation (9.25) in terms of $I_{eff}(t)$:

$$\frac{\mathrm{d}I_{eff}}{\mathrm{d}t} = -\frac{1}{\tau_u}I_{eff} + k_S I_{eff}^2 \tag{9.26}$$

with the unsaturated ring-down time τ_u and a saturation factor k_S given by

$$ {\tau_u}^{-1} = \frac{(1-R)c}{nL} + \frac{\alpha_0 c}{n} \tag{9.27}$$

$$k_S = \frac{cg\alpha_0}{2nI_S} \tag{9.28}$$

The nonlinear differential equation (9.26) has an analytic solution which takes the form

$$I_{eff}(t) = I_0\frac{\mathrm{e}^{-\frac{t}{\tau_u}}}{1 - b\tau_u\left(1 - \mathrm{e}^{-\frac{t}{\tau_u}}\right)} \tag{9.29}$$

As expected, this is a slightly non-exponential function with initial intensity I_0 at $t = 0$. It exibits a slower decay at small times t due to saturation, represented by the new parameter

b. For big t, saturation fades away, and the decay time returns to the unsaturated ring-down time τ_u. b is proportional to the effectively interacting light intensity normalized to the saturation intensity, and thus carries fundamental information on the molecular transition and Lamb dip signatures in its frequency dependency:

$$b(\nu) = k_S I_{eff} = \frac{c\alpha_0(\nu)}{n} \frac{g(\nu) I_0(\nu)}{2 I_S} \tag{9.30}$$

In $b(\nu)$, $c\alpha_0(\nu)/n$ is directly given by τ_u through Eq. (9.27), which is equivalent to the basic equation (5.1) of CRDS. The peak intracavity intensity $I_0(\nu)$, in turn, can be determined experimentally by means of the ring-down photodiode signal S_{PD}. The link between both quantities is established as follows: The one-way intensity integrated over the output mirror surface gives rise to a directional power P_m which was derived in Equation (5.10). This power is transmitted through the cavity output mirror according to its transmission coefficient T.

$$P_{out}(t) = T P_m(t) = \frac{1}{4} \pi w_o^2 T c n \epsilon_0 E_0(t)^2 = \frac{T \pi w_0^2}{\sqrt{\frac{2r}{L} - 1} \arctan\left(\left(\frac{2r}{L} - 1 \right)^{-1/2} \right)} \cdot I_{eff}(t) \tag{9.31}$$

In the last step, Eq. (9.23) was used to express P_{out} in terms of $I_{eff}(t)$. This transmitted power P_{out} then experiences losses on its way into the photodiode semiconductor material due to various factors, including scattering, absorption, diffraction, reflection and clipping. One may globally combine all these processes in terms of a single loss factor $0 < \xi < 1$, whose frequency dependence may not be negligible in all cases. Here, it shall be treated as constant for the sake of simplicity. The photodiode then converts the incoming power ξP_{out} to a photocurrent $\eta \xi P_{out}$, with its power-to-current conversion sensitivity η typically given in A/W. Finally, the transimpedance amplifier circuit converts the photocurrent to the voltage signal S_{PD} through its transimpedance gain R_{gain}, yielding

$$S_{PD}(t) = R_{gain} \eta \xi P_{out}(t) = \frac{\eta \xi T \pi w_0^2 R_{gain}}{\sqrt{\frac{2r}{L} - 1} \arctan\left(\left(\frac{2r}{L} - 1 \right)^{-1/2} \right)} \cdot I_{eff}(t) \tag{9.32}$$

Using the relationship between beam waist and Rayleigh range from Eq. (2.29) and the explicit expression for z_R in Eq. (2.28), this simplifies to

$$I_{eff}(t) = \frac{2 \arctan\left(\left(\frac{2r}{L} - 1 \right)^{-1/2} \right)}{\eta \xi T R_{gain} \lambda L} \cdot S_{PD}(t) \tag{9.33}$$

For a sufficiently good knowledge of the system constants r, L, T, η, R_{gain} and ξ, which need to be predetermined experimentally in independent measurements, the photodiode signal thus constitutes a direct measure for the effective intracavity light intensity.

Having determined $b(\nu)$ from fitting the analytic function (9.29) to the saturated ring-down signal, $g(\nu)$ normalized to the yet unknown saturation intensity follows as

$$\frac{g(\nu)}{I_S} = \frac{2n}{c\alpha_0(\nu) I_0(\nu)} b(\nu) \tag{9.34}$$

As discussed above, $g(\nu)$ essentially has the shape of the homogeneous line profile. Therefore, fitting

$$g(\nu)/I_S = \left(1 + \hat{p}(\nu - \nu_0)\right)/I_S \tag{9.35}$$

with a Lorentzian $\hat{p}(\nu - \nu_0)$ of unitary amplitude and a scaling parameter $1/I_S$ allows retrieving both $g(\nu)$ and the molecular property I_S.

As discussed above, such a concentration-independent measurement is of high interest for fundamental molecular physics studies. The homogeneous linewidth γ can be retrieved from a fit of $g(\nu)$ in good approximation for weak saturation. Then, Eq. (9.4) can be inverted, yielding the experimentally determined concentration-independent molecular transition dipole moment by weakly-saturated CRDS as

$$\mu = \sqrt{\frac{c\epsilon_0 h^2 \gamma^2}{4 I_S}} \tag{9.36}$$

9.3 Non-exponential cavity ring-down spectroscopy

Using the findings described in the previous section it is a promising endeavour to not treat saturation as a source of bias, but to see it as a natural property of the ring-down signal, which can be determined experimentally by fitting the ring-down in the saturated regime with the appropriate slightly non-exponential function (9.29). For the present proof-of-principle measurements, saturated-absorption CRDS measurements were carried out on the 30013←00001 P18 line of CO_2 at 6212.795 cm^{-1}, at a partial pressure of 1 Pa. A 7-minute OFFS-CRDS scan was carried out on a span of 10 MHz around the line center, at an equidistant 50-kHz-spacing between measurement points. On the order of 300 individual ring-down events were averaged at each spectral point to obtain a good signal-to-noise ratio.

When attempting to fit the saturated ring-down signals from this scan with simple exponentials, one obtains non-flat fit residuals revealing their non-exponential features, as shown in Fig. 9.5. Oscillatory non-exponential signatures indicating a slower decay at the

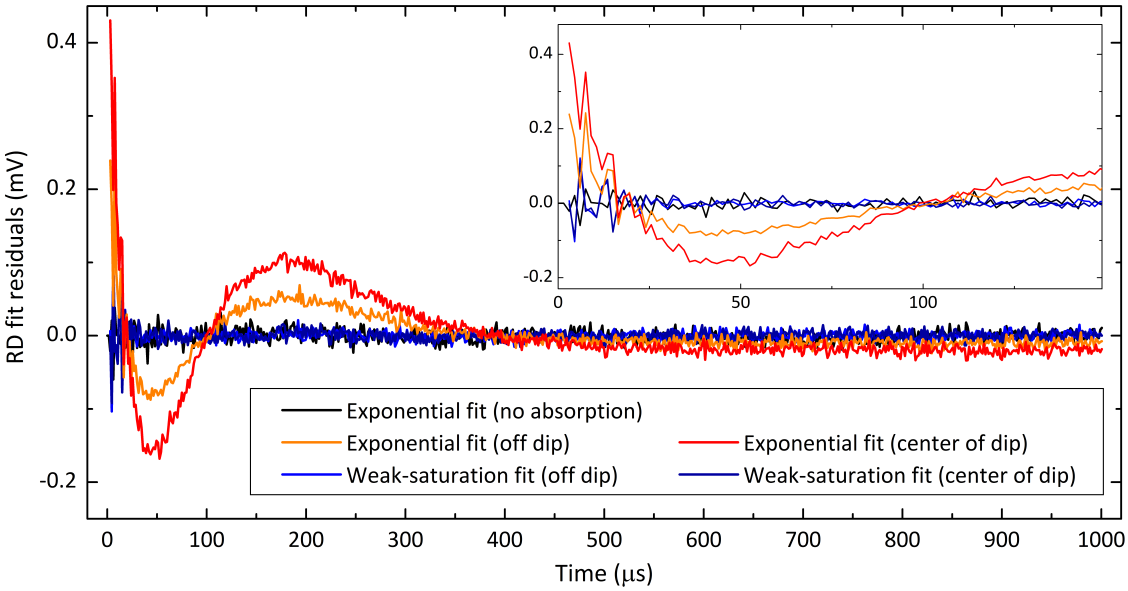

Figure 9.5 Comparison of residuals from fitting averaged ring-down events at different degrees of saturation with a simple exponential function and the slightly non-exponential ring-down function in the weakly saturated regime. Inset: Zoom onto the fit residuals at the beginning of the ring-down.

beginning, and a faster decay at the end of a ring-down event, respectively, are clearly visible on the orange and red traces. The orange one corresponds to a frequency close to the center of the Doppler-broadened line. The red trace exhibiting an even stronger

effect originates from ring-down events at the center of the Lamb dip, where saturation is twice as strong. This physics is captured by the weakly saturated ring-down function (9.29) from the previous section, which yields flat residuals during the whole ring-down event both on and off the Lamb dip resonance. These two cases are reported as the two curves in different shades of blue in Fig. 9.5. Fit residuals from ring-down events in the absence of any absorption are shown as the black curve for comparison.

Whether the simple exponential function or the analytic ring-down function (9.29) for weak saturation is used for fitting the ring-down signals clearly has an important impact on the retrieved absorption coefficient. The spectra resulting from the two approaches are shown in Fig. 9.6 for comparison. The simple exponential fit accounts for the reduced

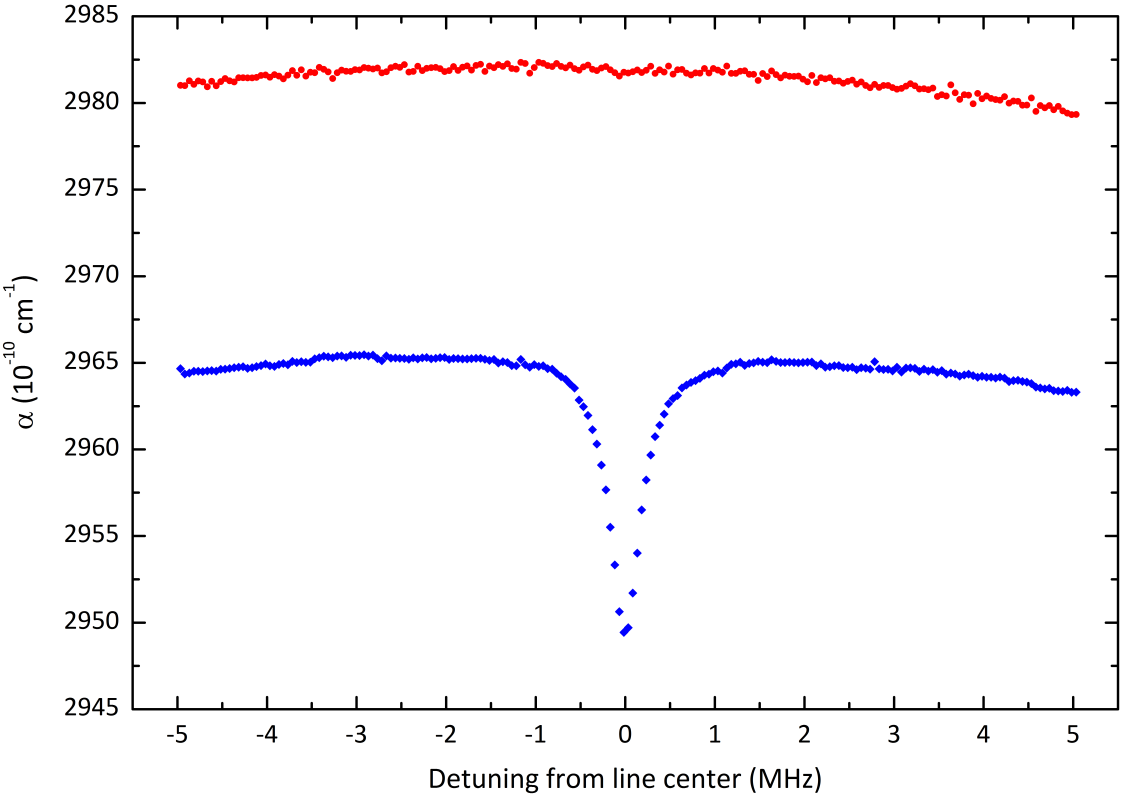

Figure 9.6 Absorption coefficients at the top of the CO_2 line at 6212.795 cm^{-1} determined by fitting ring-down events with a simple exponential (blue diamonds) and the non-exponential function (9.29) yielding unsaturated absorption coefficients in spite of weak saturation (red circles).

absorption and longer decay time due to saturation at the beginning of the ring-down event in terms of an averaged effective ring-down time. The saturation bias on the exponential decay constant is twice as strong in the Lamb dip, thus leading to a correct qualitative representation of the dip shown as blue diamonds in Fig. 9.6. The saturated ring-down function (9.29), however, explicitly contains the fit parameter τ_u, which corresponds to the ring-down time in the unsaturated limit of infinitesimally small laser power. Therefore, it yields an absorption spectrum unbiased by saturation effects, reported as the red circles in Fig. 9.6.

All saturation effects are entirely captured by the second fit parameter b, shown in Fig. 9.7 as a function of detuning around the line center, which measures the degree of saturation according to Eqs. (9.29) and (9.30). The parameter $b(\nu)$ is proportional to the frequency-dependent saturation parameter $G(\nu)$, but combines several other effects, too.

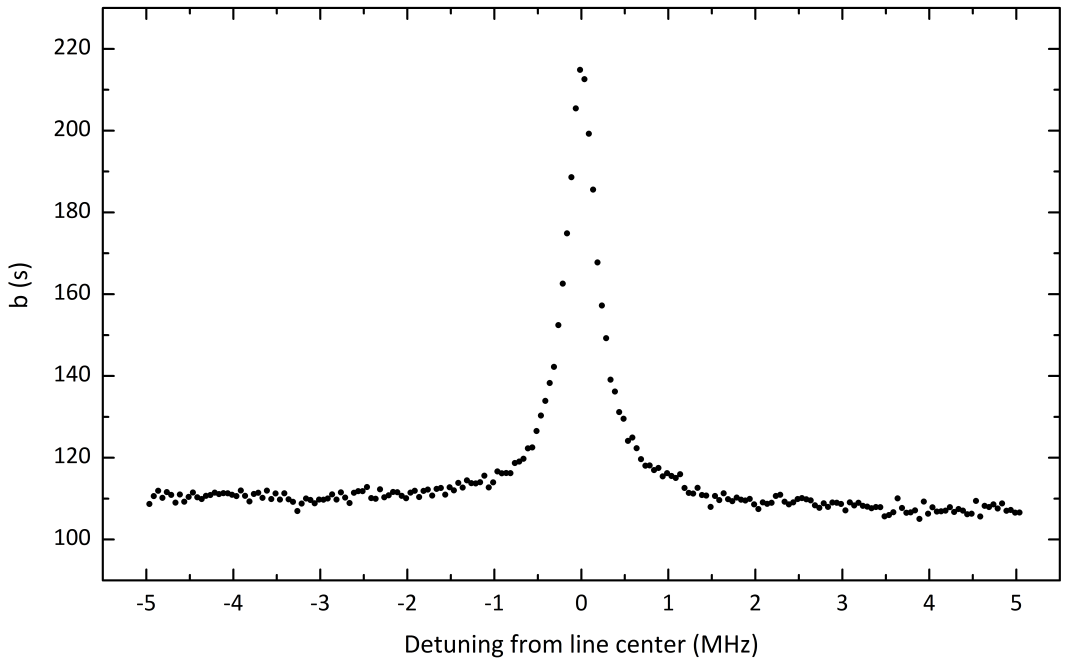

Figure 9.7 Saturation parameter b at the top of the CO_2 line at 6212.795 cm^{-1} from non-exponential ring-down fitting.

To retrieve the pure shape of the Lamb dip in terms of the velocity parameter $g(\nu)$ and the saturation intensity I_S using Eq. (9.34), one needs to take into account both changes in unsaturated absorption α_0 and laser intensity variations in $I_0(\nu)$.

As discussed in the previous section, using Eq. (9.33), $I_0(\nu)$ can be unambiguously determined from the photodiode signal S_0 at the ring-down trigger threshold. This signal, with units on the right axis, is shown in Fig. 9.8. This CRDS cavity transmission signal

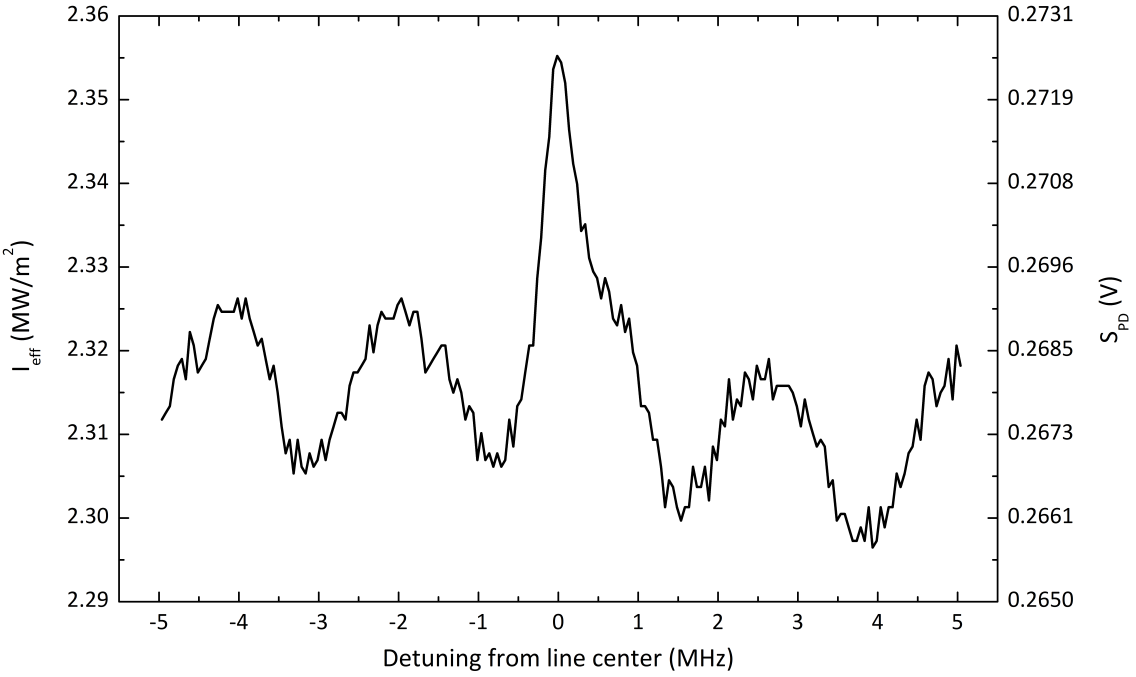

Figure 9.8 Effective one-way-travelling intracavity light intensity I_{eff} during the saturated CRDS measurement shown in Figs. 9.6 and 9.7. A proportionality to the ring-down cavity transmission photodiode signal S_{PD} holds to very good approximation in this case.

exhibiting an inverse Lamb dip is in itself an impressive illustration of the force of high-finesse cavity-enhanced absorption spectroscopy techniques featuring strong enhancement of the effective light-matter interaction path-length. The inverse Lamb dip signature is superposed on a sinusoidal 0.8-percent variation of intracavity power with a period of roughly 2.3 MHz. It is attributed to small variations of single-sideband generation efficiency by the Mach-Zehnder modulator or slight changes in the ring-down cavity lock point due to residual amplitude modulation (RAM) by the MZM [252]. On the left axis of Fig. 9.8, the photodiode signal has been converted to effective one-way intracavity intensity. Due to the extremely small change in λ, amounting to 10 MHz/186 THz $\approx 5{\cdot}10^{-8}$ during the scan across the dip, S_{PD} and I_{eff} may be considered proportional to each other in very good approximation, assuming similarly small variations in η, ξ and T. This justifies plotting a single curve on two y axes with different units in Fig. 9.8. To make the conversion from S_0 to I_0, experimentally determined or realistic values were inserted in (9.33). For the ring-down cavity used here $r = 1$ m and $L = 34.5$ cm, yielding a geometric factor $\arctan\left(\left(\frac{2r}{L} - 1\right)^{-1/2}\right)$ in Eq. (9.32) approximately equal to 0.4283. The factor $\sqrt{\frac{2r}{L} - 1}$ in Eqs. (9.23), (9.31) and (9.32), in turn, equals 2.190. The product of both is still close to unity and corresponds to a geometric correction with respect to a plane-mirror cavity configuration amounting to about 6 percent. A photodiode sensitivity $\eta = 0.9$ A/W was taken as a typical value for InGaAs photodiodes. The photodiode front facet was not antireflection-coated, and its Fresnel reflectivity at normal incidence was expected to be on the order of 30 percent based on its refractive index. This loss process outweighs all others, as direct absorption in air is negligible in the present spectral region, making $\xi = 0.7$ a good estimate. The value $T = 3.1 \cdot 10^{-6}$ for the cavity mirror transmission coefficient was determined experimentally. The photodiode amplifier transimpedance gain was $R_{gain} = 91\,\mathrm{k}\Omega$.

Inserting the fitted $b(\nu)$ and α_0 from Figs. 9.7 and 9.6 as well as the measured $I_0(\nu)$ from Fig. 9.8 into Eq. (9.34) we thus finally retrieve the desired result $g(\nu)/I_S$ shown in Fig. 9.8. This scaled velocity parameter carries the pure Lamb dip signature. Fitting it with the function 9.35 yields the saturation intensity of the transition, $I_S = 9.5\,\mathrm{kW/cm^2}$ at the homogeneous full width at half maximum of 418 kHz, which equally follows from the fit. With the average one-way light intensity from Fig. 9.8, this implies a saturation parameter $G = 2.4 \cdot 10^{-2}$ outside the dip for this measurement. A slight tilt of the experimental data points in Fig. 9.9 is due to an increase of pressure and therefore homogeneous linewidth during the scan. Future precision measurements might necessitate taking this effect into account. Alternatively, one may minimize it by further increasing measurement speed and decreasing outgassing. Comparing the noise on the baseline section to the inverse dip amplitude yields a potential dip signal-to-noise ratio of 115 for the present measurement.

Finally, let us consider the above results in view of the possibility of concentration-independent transition dipole moments by saturated-absorption CRDS. We have seen that a plot like in Fig. 9.9 yields experimental values both for I_S and γ. Equation (9.36) then implies an empirical value for the transition dipole moment. In the present case, one finds $\mu = 7.3{\cdot}10^{-34}$ Cm with the above values. Translating this dipole moment to an Einstein A coefficient for the inverse natural lifetime of the transition [253], one finds $A = 7.25$ mHz. This is in very good agreement with the value $A_{HITRAN} = 7.31$ mHz in the HITRAN 2012 database [212].

Clearly, this concentration-independent determination of μ for the 30013←00001 P18 transition of CO_2 cannot be considered an unbiased measurement, as very rough estimations were made in the parameters ξ and η. Nevertheless, it is a proof-of-principle

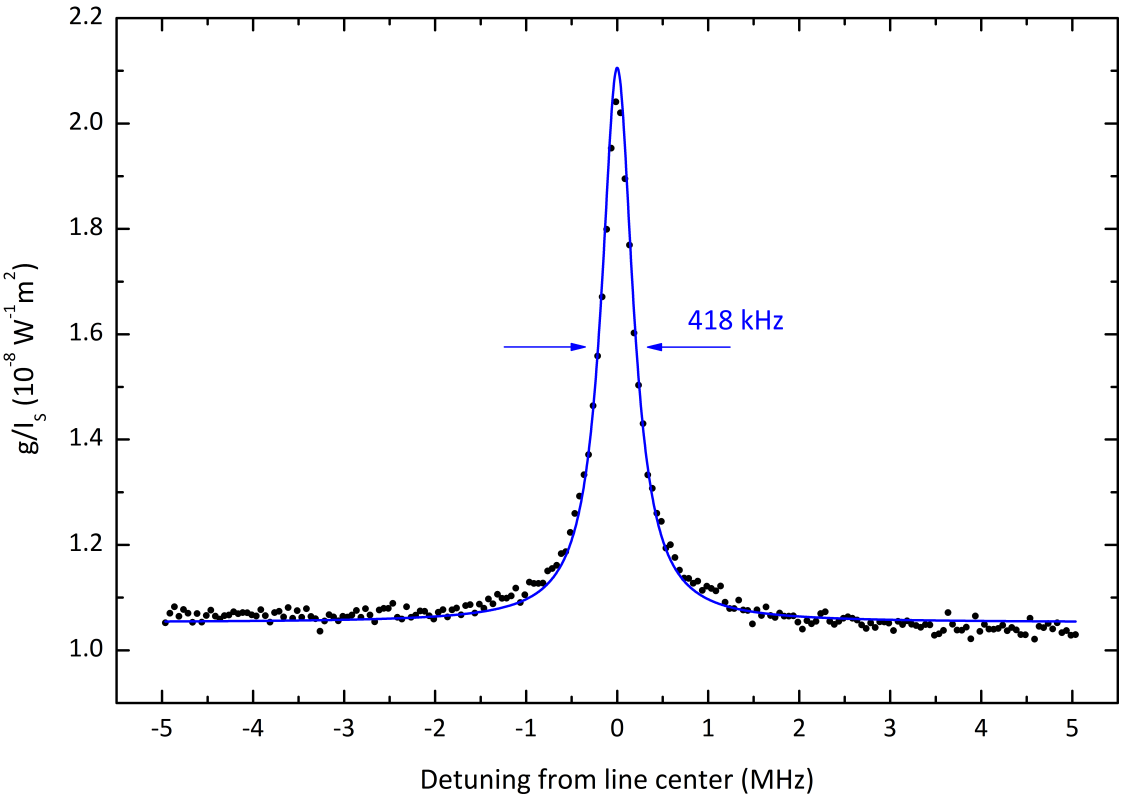

Figure 9.9 Velocity parameter g over saturation intensity I_S at the top of the CO_2 line at 6212.795 cm^{-1} obtained from the fitted $b(\nu)$ in Fig. 9.7 (black circles). Fit curve according to Eq. (9.35) (blue line).

experiment demonstrating the enormous potential of the method, provided that the constants η, ξ and T and their potential frequency dependences will be determined very precisely in future quantitative studies.

Importantly, the theory and measurements reported here clearly show how unsaturated absorption and saturation effects including Lamb dips emerge as two independent characteristics of a ring-down signal. Figures 9.6 and 9.9 illustrate how the two effects can be separated by fitting with the analytic formula for weakly saturated ring-downs. This approach opens the door to unbiased absorption coefficient measurements by CRDS in spite of saturation.

9.4 Comb-assisted Lamb-dip spectroscopy of CO_2

In this section, we shall discuss frequency-comb-assisted OFFS-CRDS measurement of saturated-absorption Lamb dips on twelve weak absorption lines of $^{12}C^{16}O_2$ near 1.6 µm with accuracies at the few kHz level. This outstanding performance is based on the high intracavity light intensity as well as extreme resolution and sensitivity offered by OFFS-CRDS, and relies on the absolute frequency supplied by an optical frequency comb referenced to the SI second through a GPS-disciplined Rubidium clock. Like the studies in Chapter 4, this work was carried out in collaboration with the group of Prof. Marco Marangoni from Politecnico di Milano.

Let us begin with the article [254] these results were originally reported in. Right after the article, the key spectroscopic results of this study are provided as a linelist in Table 9.1. Then, the signal correction, fitting procedure and error analysis methods, which are con-

cisely discussed in the article, are treated in bigger detail. Finally, the incorporation of the new kHz-accuracy transition frequencies into the carbon dioxide spectroscopic databank CDSD [255] will be discussed.

9.4.1 Article 6 - Communication: Saturated CO_2 absorption near 1.6 μm for kilohertz-accuracy transition frequencies

At the beginning of this article [254], previous CO_2 transition frequency measurements and their link to progress in frequency metrology, as well as prior saturated-absorption CRDS studies are discussed in a concise literature survey. Then, the experimental setup is described, with a main focus on the absolute frequency measurement based on a beat note between the frequency comb and the optical feedback frequency stabilized laser. The precision and averaging behavior of this frequency measurement is characterized in terms of an Allan plot before turning to the experimental Lamb dip spectra. The resulting experimental $^{12}C^{16}O_2$ transition frequencies are then compared to relevant reference data and subsequently used for an optimized spectroscopic constant fit for the upper vibrational state.

Communication: Saturated CO_2 absorption near 1.6 μm for kilohertz-accuracy transition frequencies

Johannes Burkart,[1,2,a)] Tommaso Sala,[3] Daniele Romanini,[1,2] Marco Marangoni,[3] Alain Campargue,[1,2] and Samir Kassi[1,2,b)]
[1]*Univ. Grenoble Alpes, LIPhy, F-38000 Grenoble, France*
[2]*CNRS, LIPhy, F-38000 Grenoble, France*
[3]*Physics Department of Politecnico di Milano and IFN-CNR, Piazza Leonardo da Vinci 32, 20133 Milano, Italy*

(Received 13 April 2015; accepted 12 May 2015; published online 21 May 2015; publisher error corrected 15 July 2015)

Doppler-free saturated-absorption Lamb dips were measured on weak rovibrational lines of $^{12}C^{16}O_2$ between 6189 and 6215 cm^{-1} at sub-Pa pressures using optical feedback frequency stabilized cavity ring-down spectroscopy. By referencing the laser source to an optical frequency comb, transition frequencies for ten lines of the 30013 ← 00001 band P-branch and two lines of the 31113 ← 01101 hot band R-branch were determined with an accuracy of a few parts in 10^{11}. Involving rotational quantum numbers up to 42, the data were used for improving the upper level spectroscopic constants. These results provide a highly accurate reference frequency grid over the spectral interval from 1599 to 1616 nm. © *2015 AIP Publishing LLC.* [http://dx.doi.org/10.1063/1.4921557]

The linear geometry of the carbon dioxide molecule as well as its internuclear distances was unveiled in the first half of the 20th century by means of rotational Raman spectroscopy[1] and infrared absorption spectroscopy.[2] Ever since, spectroscopic techniques with growing resolution and sensitivity have been used for scrutinizing the rovibrational energy structure of the CO_2 molecule. In recent years, the advent of self-referenced optical frequency combs (OFCs) has greatly facilitated the absolute measurement of optical frequencies[3] and has boosted metrological research, also on CO_2 transition frequencies.[4,5] The Gaussian broadening of spectral lines by the Doppler effect due to thermal motion, amounting to several hundred MHz at room temperature, is generally a critical limitation to the attainable precision. By repeatedly recording seven Doppler-broadened absorption lines from the R-branch of the 30013 ← 00001 band of $^{12}C^{16}O_2$ (see Ref. 6 for the vibrational nomenclature) at 1.6 μm with a high signal-to-noise ratio, Long *et al.*[7] nevertheless retrieved transition frequencies with an accuracy on the order of a few tens of kHz. For reducing uncertainties further, saturation spectroscopy is a powerful tool to circumvent the Doppler limit.[8] By overproportionally depopulating the ground state of molecules at rest with respect to two counter-propagating beams, it leads to an absorption decrease at the line center, commonly called Lamb dip.[9] This feature can be several orders of magnitude narrower than the inhomogeneously Doppler-broadened line. It is insensitive to the asymmetry that Doppler-broadened absorption profiles exhibit due to the speed-dependent impact of intermolecular collisions at non-zero pressure,[10] a potential source of systematic errors in Doppler-limited measurements. Consequently, saturation spectroscopy studies in the mid-infrared using frequency referencing to an OFC yielded CO_2 transition frequencies with unprecedented accuracies at the kHz-level[4] or better.[5] Optical-cavity-based techniques such as cavity ring-down spectroscopy (CRDS) are fundamentally well-suited for saturation spectroscopy. Their resonator modes are composed of two perfectly superposed counterpropagating beams with equal intensity, and their passive intracavity power amplification proportional to the cavity finesse increases with cavity mirror reflectivity. Lamb dips by CRDS could be observed on NO_2 lines near 0.8 μm,[11] for instance, and were used for resolving blended water lines near 1.4 μm[12] and the hyperfine structure of $^{17}O^{12}C^{16}O$ at natural abundance near 2.3 μm.[13] Due to the difficulty of coherently injecting laser light into a resonator with a mode width on the order of a few kHz, high-finesse CRDS techniques generally suffer from low intracavity intensity levels, impairing their capability of saturating weak rovibrational overtone transitions.

Here, we demonstrate that this limitation can be overcome by tightly locking a CRD spectrometer with a finesse of 4.5 × 10^5 to a sub-kHz linewidth laser, thereby achieving intracavity intensities on the order of 1 kW/cm^2 at an input power of 100 μW. Harnessing the combination of absorption sensitivity, frequency resolution, and light intensity offered by this optical feedback frequency-stabilized cavity ring-down spectrometer (OFFS-CRDS),[14] we measured Doppler-free Lamb dips on CO_2 lines with line strengths down to 5 × 10^{-25} cm/molecule, among the weakest ever studied by saturation spectroscopy. By referencing the spectrometer to an optical frequency comb, we used these narrow saturated-absorption features to determine absolute transition frequencies with an accuracy of a few kHz.

The experimental setup schematically depicted in Fig. 1 is based on the recently developed OFFS-CRD spectrometer described in detail in Refs. 14 and 15. Its distributed-feedback (DFB) diode laser is stabilized to a sub-kHz level by means of optical feedback from a highly stable V-shaped reference cavity made from ultra-low expansion (ULE) glass and Super Invar. Coarse frequency tuning between 1608 nm and 1616 nm is accomplished by locking to different longitudinal

a)Electronic mail: johannes.burkart@ujf-grenoble.fr
b)Electronic mail: samir.kassi@ujf-grenoble.fr

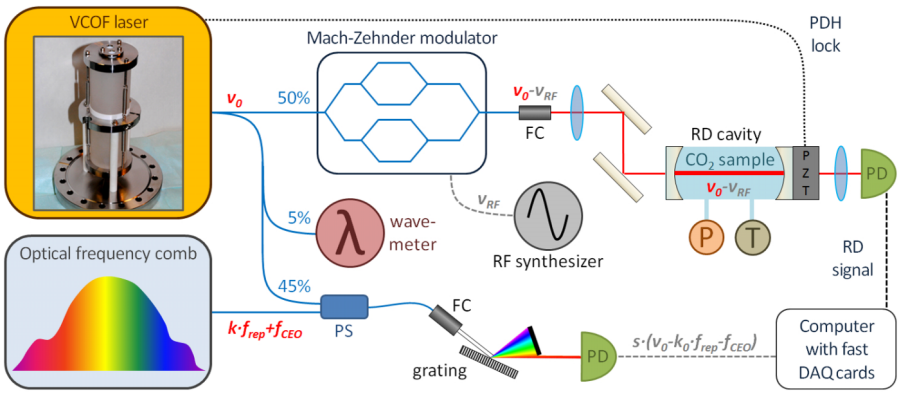

FIG. 1. Schematic of the experimental setup with optical fiber paths (curved lines), free-space laser beams (straight lines), electrical signals (dashed lines) as well as optical and radio frequencies (in italics). FC: fiber outcoupling, DAQ: data acquisition, RF: radio frequency, PD: photodiode, PS: 50% power splitter, PZT: piezoelectric actuator, PDH: Pound-Drever-Hall, P: pressure, T: temperature.

modes of the reference cavity. Arbitrarily fine tunability for high-resolution molecular spectroscopy is achieved by single-sideband modulation using an integrated dual-parallel Mach-Zehnder modulator (MZM).[16] The length of the massive, rugged ring-down (RD) cavity is tightly locked to this VCOF (V-cavity-based optical feedback) source by means of a Pound-Drever-Hall (PDH) locking scheme using a fiber-optic circulator. This guarantees an unbroken stability transfer chain from the V-shaped reference cavity to the spectral x axis as well as a near-optimal resonant intra-cavity intensity buildup. While this approach confers state-of-the-art stability and linearity to the spectrometer frequency axis, absolute frequency measurements at the sub-MHz level call for a self-referenced OFC. Representing its femtosecond pulses in frequency space, the comb consists of equidistant teeth $\nu_k = k f_{rep} + f_{CEO}$. For frequency metrology purposes, the radio frequencies f_{rep} and f_{CEO} are actively controlled and referenced to the SI second, typically by means of a global positioning system (GPS) disciplined rubidium clock. Consequently, the tooth number k establishes a direct link between the radio and the optical frequency domains. In OFFS-CRDS, frequency fine-tuning and laser-off events for RD measurements are carried out by the MZM. Its optical input signal, the unshifted VCOF laser locked to a reference cavity mode at frequency ν_0, is highly stable and never switched off. Therefore, this signal is ideally suited for continuously measuring the absolute frequency of the system by monitoring its beat frequency f_{BN} with the closest tooth k_0 of the frequency comb. With an approximate value $\tilde{\nu}_0$ known to better than $f_{rep}/2$ and the beat note sign s, which is 1 for $\nu_0 > \nu_{k_0}$ and -1 otherwise, ν_0 can be unambiguously determined

$$\nu_0 = \text{Round}\left(\frac{\tilde{\nu}_0 - f_{CEO} - s f_{BN}}{f_{rep}}\right) f_{rep} + f_{CEO} + s f_{BN}. \quad (1)$$

In the present setup, $\tilde{\nu}_0$ was measured by monitoring a fraction of the VCOF carrier on a Fourier-type wavemeter (Burleigh WA-1650) with a specified accuracy of ±20 MHz. To generate its beat note with the optical frequency comb (Toptica FFS model, f_{rep} = 100 MHz) on a fast photodiode, we used two fibered 50-50 splitters to superpose the stable laser light with a fiber-coupled, grating-filtered portion of the optical frequency comb. After low-pass filtering at 50 MHz, this beating signal was acquired at a sampling rate of 200 MHz in groups of 10 000 samples by a fast analog-to-digital converter card (GAGE model CS1622). Fourier transform of the successive beat note time series yielded 1000 frequency measurements per second with a resolution of 20 kHz, an order of magnitude below the 200 kHz short-term OFC-linewidth. While suboptimal in terms of averaging performance due to abundant dead times, this acquisition-card-based beat frequency measurement scheme constitutes a straightforward and efficient solution when the uncertainty budget is not limited by the optical frequency measurement itself, as is the case here.

The precision and averaging behavior of the beat note frequency measurement was characterized in terms of the Allan deviation plot shown in Fig. 2. From the comb-linewidth-limited single-measurement noise of about 200 kHz root-mean-square (RMS), the Allan deviation averages down to a minimum of 1.4 kHz at 30 s averaging time. For longer averaging the VCOF drift, amounting to 28 Hz/s here, dominates. When correcting for this drift by a linear trend removal, the Allan deviation drops below the 1 kHz mark at 46 s averaging. As a typical Lamb dip measurement takes less than 2 min, we therefore chose to fit the observed beat note frequencies with a linear model for each dip. The f_{BN} given by this fit were then inserted into Eq. (1) to correct the frequency of each individual data point of the spectrum. As the GPS-Rb-referenced OFC frequency stability is superior to the beat note measurement precision given by Fig. 2, we have taken the latter as the systematic error in the absolute frequency measurement for each recorded Lamb dip.

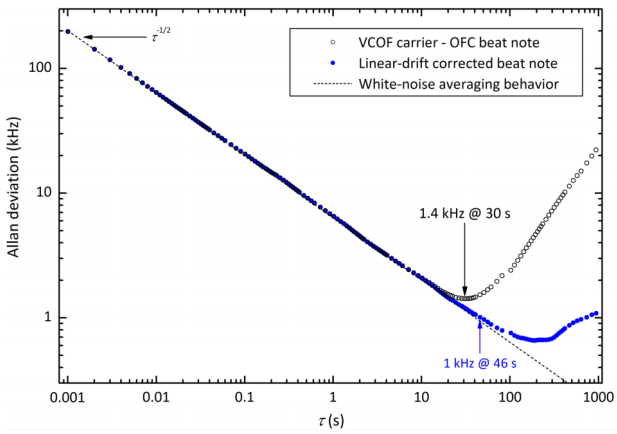

FIG. 2. Discrete Allan deviation of the beat note frequency of the optical-feedback-stabilized laser with one tooth of the optical frequency comb. On the x axis, the number of averaged individual beat note frequency values has been converted to averaging time τ.

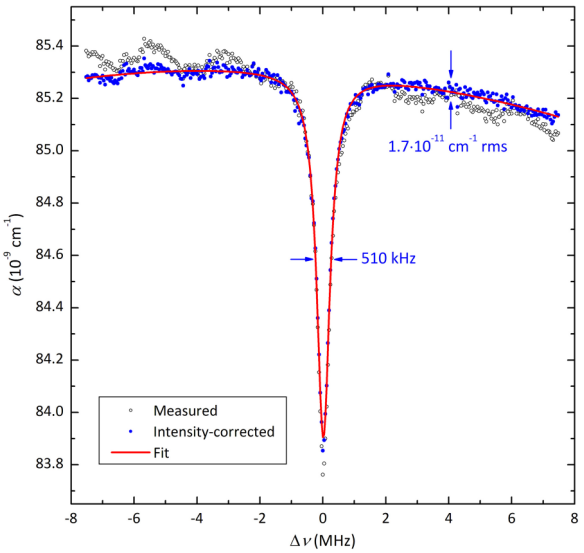

FIG. 3. Lamb dip at the center of the Doppler-broadened 30013 ← 00001 P16 absorption line in 0.27 Pa of CO_2.

Figure 3 shows a Lamb dip in the absorption coefficient α measured at the center of the 30013 ← 00001 P16 line in 0.27 Pa of CO_2 over a span of 15 MHz at frequency steps of 40 kHz. For the sake of simplicity, each RD signal was fitted with a pure exponential in spite of its slightly non-exponential shape in the saturated regime. The resulting relative imperfections of the exponential fit residuals were at the 10^{-3} level. This effect is negligible for the present study, as its objective was to determine highly accurate transition frequencies rather than the exact shape or surface of the Doppler-free absorption feature. The signal-to-noise ratio of the Lamb dip shown in Fig. 3 is close to 90, and its depth $\Delta\alpha$ implies a saturation parameter $S = 3.5 \times 10^{-2}$ in the present weakly saturated, inhomogeneously broadened regime.[17] Its Lorentzian full-width of 510 kHz due to collisional and transit-time-related broadening is almost three orders of magnitude smaller than the 345 MHz Gaussian width of the Doppler-broadened line at room temperature. The measured absorption coefficients exhibit a small oscillation with a period of roughly 2.4 MHz. It is caused by few-percent light intensity variations, probably due to uneven MZM single-sideband modulation depth, which are evidenced by the measured CRDS transmission photodiode signal. Using this signal and the empirical saturation parameter S, the slight changes in the absorption coefficient with light intensity could be unambiguously corrected for without any adjustable parameters. The remaining asymmetry of the intensity-fluctuation-corrected Lamb dip shown in Fig. 3 is attributed to a 1.4 μPa/s partial pressure increase of CO_2 due to outgassing from the cavity walls during the 6-min-long measurement. The fit curve takes this effect into account by a Lorentzian with a linearly varying amplitude factor on a baseline with a constant and a quadratic component. The latter two contributions correspond to the dip-free maximum of the Doppler-broadened absorption line.

Doppler-free Lamb dips were measured for ten lines from the 30013 ← 00001 band and two lines from the 31113 ← 01101 hot band of $^{12}C^{16}O_2$ at partial pressure ranging from 0.27 Pa to 4.5 Pa while continuously monitoring the beat note of the VCOF carrier with the OFC. To optimize measurement time allocation, the corresponding spectra were recorded at 30 or 40 kHz frequency steps over spans of 3 or 4 MHz. For each of the ten transitions, between 9 and 50 individual Lamb dip measurements were carried out, lasting around 1.5 min each. The observed line center frequencies obtained by means of the above-mentioned fitting procedure are red-shifted by collisions among CO_2 molecules and with other residual gas molecules. This pressure shift needs to be corrected for in order to retrieve the unperturbed rovibrational energy levels of the CO_2 molecule. The shift is proportional to pressure, and precise coefficient values based on extensive Fourier-transform spectroscopy exist in the literature for both self-shifts[18] and air-shifts.[19] Using the RD cell pressure reading, we therefore corrected the observed Lamb dip center frequencies by the expected pressure shifts, which amounted to less than 15 kHz. Table I lists the resulting absolute transition frequencies with their respective statistical and systematic uncertainties. The statistical error was estimated by weighting the spread in successive line center frequency measurements for each transition with Student's t-distribution in order to obtain a 1-σ uncertainty interval. Besides the sub-kHz systematic uncertainty due to the OFC-beat-note frequency measurement discussed above, several further effects contribute to the uncertainty budget of the present transition frequency measurement. First and foremost, there are systematic uncertainties related to several aspects of the Lamb dip fitting procedure. On the one hand, the uncertainty due to a slight asymmetry of the measurement window was quantified using the broad-span Lamb dip in Fig. 3 as a model, by retrieving the apparent line center shift which arises when fitting it on an equivalently smaller and asymmetric spectral interval. On the other hand, the uncertainties due to the intensity-correction and the fitted CO_2 partial pressure increase were cautiously estimated by propagating a 15% error in the respective parameters to dip center frequency errors. The combined 1-σ uncertainty due to the Lamb dip fitting procedure ranges from 1.5 to 14 kHz. Second, the pressure shift correction of observed transition

TABLE I. Measured $^{12}C^{16}O_2$ transition frequencies ν with combined statistical (σ_A) and systematic (σ_B) uncertainties.

Transition	ν (kHz)	σ_A (kHz)	σ_B (kHz)
30013 ← 00001			
P16e	186 308 650 586.8 (3.6)	0.5	3.6
P18e	186 254 902 894.2 (4.1)	0.7	4.1
P20e	186 200 304 286.2 (6.4)	1.0	6.3
P22e	186 144 851 639.3 (4.5)	0.7	4.5
P24e	186 088 541 462.1 (3.5)	0.8	3.4
P26e	186 031 369 904.4 (9.9)	1.9	9.7
P28e	185 973 332 755.6 (15.0)	3.0	14.7
P38e	185 669 994 726.4 (7.0)	1.9	6.7
P40e	185 606 659 086.7 (8.0)	2.6	7.6
P42e	185 542 420 573.5 (5.6)	2.8	4.8
31113 ← 01101			
R22f	186 247 597 864.1 (5.2)	2.9	4.3
R23e	186 251 719 634.6 (11.4)	2.9	11.0

frequencies relies on both accurate pressure readings and shift coefficient values. The RD cavity pressure measurement was limited at an uncertainty of 1 Pa by the zero-pressure calibration of the capacitive gauge. The error due to the uncertainty in intracavity gas composition was estimated by considering the difference between air- and self-broadened shifts. A 10% uncertainty for literature shift coefficients was assumed in view of the significant disagreement between four air-broadened pressure shift studies for J values between 16 and 42 displayed in Fig. 7 of Ref. 19. In spite of these conservative estimation, the uncertainty in the pressure-shift correction never exceeds 5.5 kHz. Third, the expected quadratic AC Stark shift term $\Delta E = -1/4\tilde{\alpha}E_0^2$ in the molecular Hamiltonian[20] due to the intense intracavity laser field with amplitude E_0 was estimated by taking an approximate value for the molecular polarizability $\tilde{\alpha}$ from the CO_2 refractive index $n = 1 + 4.38 \times 10^{-4}$ at 1610 nm and 1 atm.[21] A typical peak intracavity field E_0 = 60 kV/m yields $\Delta E/h = -420$ Hz, with the Planck constant h. The corresponding AC Stark shift of rovibrational transition frequencies is due to small differences in $\tilde{\alpha}$ for the involved upper and lower states. This effect should be much smaller than $\Delta E/h$ and is therefore negligible in the systematic error budget.

Figure 4 shows the measured 30013 ← 00001 band P-branch transition frequencies relative to the most recent version of the carbon dioxide spectroscopic databank (CDSD).[22] The measured and calculated R-branch frequencies of the same band given by Long *et al.*[7] based on Doppler-broadened line center measurements are equally shown. The agreement between the two studies within a few 100 kHz confirms a frequency error in the HITRAN 2012 database,[23] which increases with J, amounts to over 6 MHz for $J = 42$, and exceeds the HITRAN error bar of 10^{-4} cm^{-1} for $J \geq 28$. Line positions in CDSD are based on an exhaustive global effective Hamiltonian fit of empirical CO_2 transition frequencies. The center frequencies and uncertainties by Long *et al.* were used as input data for the 2014 version of CDSD. As indicated in Fig. 4, three pairs of lines from the present P-branch study and the R-branch measurements by Long *et al.* allow establishing combination differences corresponding to rotational level spacings of the vibrational ground state of $^{12}C^{16}O_2$. They should coincide with the ground state levels given by Long *et al.*[7] We checked that the latter agree with the CDSD ground state within 10 kHz for $J \leq 42$, as indicated qualitatively by the apparent symmetry of the Long *et al.* model curve in Fig. 4. For the P20 and R18 lines, the observed combination difference exhibits an insignificant (−28 ± 34) kHz offset from the ground state model level spacing. For P18 with R16 and P28 with R26, however, the differences between measured and calculated spacings amount to (−221 ± 32) kHz (6.9σ) and (−132 ± 23) kHz (5.7σ), respectively. This significant disagreement is incompatible with both the high accuracy of our Lamb-dip measurements and the well-established ground state model. Therefore, the R16 and R26 frequencies were excluded from the weighted fit of the Long *et al.* R-branch measurements with the P-branch frequencies from this study. The refined spectroscopic constants up to L_v for the 30013 state determined in this manner are reported in Table II. The experimental transition frequencies exhibit a RMS scatter of 24 kHz about this model, for which a detailed line list is provided as the supplementary material.[24] For the new, dip-based measurements, the spread is only 6.6 kHz, in good agreement with our error bars. This constitutes an order of magnitude improvement over the 62 kHz fit RMS reported for the Doppler-limited measurements by Long *et al.*[7]

In conclusion, highly accurate near-infrared CO_2 transition frequency measurements by saturation spectroscopy necessitate a combination of ultra-high frequency resolution, absorption sensitivity, and light intensity. In the present study, we demonstrated that comb-assisted OFFS-CRDS unites all

TABLE II. Improved spectroscopic constants for the 30013 state of $^{12}C^{16}O_2$ ($J_{max} = 42$).

G_v	186.708 240 752(22)	THz
B_v	11.593 307 06(15)	GHz
D_v	−5.143 40(32)	kHz
H_v	29.61(26)	mHz
L_v	0.31(7)	μHz

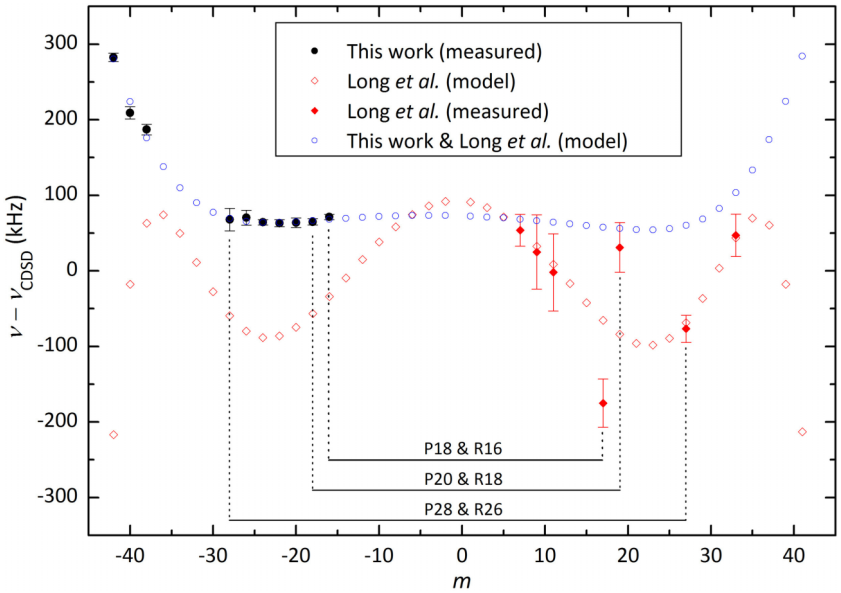

FIG. 4. Measured transition frequencies and calculated models from this study and Long *et al.*[7] relative to the corresponding values from the carbon dioxide spectroscopic databank CDSD 2014.[22] With the rotational quantum number J of the lower state, m is defined as $-J$ for P-branch transitions and $J+1$ for R-branch transitions, respectively.

these assets by reporting Doppler-free Lamb-dips on 12 $^{12}C^{16}O_2$ lines near 1.6 μm, among the weakest ever studied by saturation spectroscopy. The resulting experimental transition frequencies with 12 significant digits were used for refining the spectroscopic constants for the 30013 ← 00001 band of $^{12}C^{16}O_2$. This provides 42 reference frequencies with kHz-level accuracy spanning the spectral interval from 1599 to 1616 nm. They complement the well-known acetylene frequency standard by Madej *et al.*[25] between 1511 and 1545 nm. The accuracy of the $^{12}C^{16}O_2$ references from this study is comparable to that of the $^{12}C_2H_2$ frequencies,[25] although the latter are derived from transitions two to three orders of magnitude stronger. The new 1.6 μm CO_2 reference frequency grid may be beneficial for sub-MHz-accuracy frequency-calibrated spectroscopy, for further refining state-of-the-art databases, and for validating future generations of *ab initio* calculations for the CO_2 molecule. Beyond that, the performance of the experimental apparatus presented here should stimulate further fundamental research and frequency metrology by extensive frequency-comb-assisted saturated molecular absorption cavity ring-down spectroscopy.

This work was supported by Université Joseph Fourier (UJF) Pôle SMINGUE, LabexOSUG@2020 (ANR10 LABX56), Réseau FEMTO, and the Italian Ministry of Research and Education (ELI project—ESFRI Roadmap). We are grateful to S. A. Tashkun and V. I. Perevalov (IAO Tomsk) for providing CDSD line positions with 8 decimal places.

[1]W. Houston and C. Lewis, Proc. Natl. Acad. Sci. U. S. A. **17**, 229 (1931).
[2]P. E. Martin and E. F. Barker, Phys. Rev. **41**, 291 (1932).
[3]T. Udem, R. Holzwarth, and T. W. Hänsch, Nature **416**, 233 (2002).
[4]I. Galli, S. Bartalini, P. Cancio Pastor, F. Cappelli, G. Giusfredi, D. Mazzotti, N. Akikusa, M. Yamanishi, and P. De Natale, Mol. Phys. **111**, 2041 (2013).
[5]A. Amy-Klein, H. Vigué, and C. Chardonnet, J. Mol. Spectrosc. **228**, 206 (2004).
[6]L. S. Rothman and L. D. Young, J. Quant. Spectrosc. Radiat. Transfer **25**, 505 (1981).
[7]D. Long, G.-W. Truong, J. Hodges, and C. Miller, J. Quant. Spectrosc. Radiat. Transfer **130**, 112 (2013).
[8]T. Hänsch, I. Shahin, and A. Schawlow, Nature **235**, 63 (1972).
[9]R. A. McFarlane, W. R. Bennett, and W. E. Lamb, Appl. Phys. Lett. **2**, 189 (1963).
[10]J.-M. Hartmann, H. Tran, N. H. Ngo, X. Landsheere, P. Chelin, Y. Lu, A.-W. Liu, S.-M. Hu, L. Gianfrani, G. Casa, A. Castrillo, M. Lepère, Q. Delière, M. Dhyne, and L. Fissiaux, Phys. Rev. A **87**, 013403 (2013).
[11]D. Romanini, P. Dupré, and R. Jost, Vib. Spectrosc. **19**, 93 (1999).
[12]D. Lisak and J. T. Hodges, Appl. Phys. B **88**, 317 (2007).
[13]G. Giusfredi, S. Bartalini, S. Borri, P. Cancio, I. Galli, D. Mazzotti, and P. De Natale, Phys. Rev. Lett. **104**, 110801 (2010).
[14]J. Burkart, D. Romanini, and S. Kassi, Opt. Lett. **39**, 4695 (2014).
[15]J. Burkart and S. Kassi, Appl. Phys. B **119**(1), 97 (2015).
[16]J. Burkart, D. Romanini, and S. Kassi, Opt. Lett. **38**, 2062 (2013).
[17]V. Letokhov, *High-Resolution Laser Spectroscopy*, Topics in Applied Physics (Springer, Berlin, Heidelberg, 1976), Vol. 13, pp. 95–171.
[18]R. Toth, L. Brown, C. Miller, V. M. Devi, and D. C. Benner, J. Mol. Spectrosc. **239**, 243 (2006).
[19]A. Predoi-Cross, A. McKellar, D. C. Benner, V. M. Devi, R. Gamache, C. Miller, R. Toth, and L. Brown, Can. J. Phys. **87**, 517 (2009).
[20]L. A. Rahn, R. L. Farrow, M. Koszykowski, and P. Mattern, Phys. Rev. Lett. **45**, 620 (1980).
[21]J. Old, K. Gentili, and E. Peck, J. Opt. Soc. Am. **61**, 89 (1971).
[22]S. Tashkun, V. Perevalov, R. Gamache, and J. Lamouroux, J. Quant. Spectrosc. Radiat. Transfer **152**, 45 (2015).
[23]L. Rothman, I. Gordon, Y. Babikov, A. Barbe, D. C. Benner, P. Bernath, M. Birk, L. Bizzocchi, V. Boudon, L. Brown, A. Campargue, K. Chance, E. Cohen, L. Coudert, V. Devi, B. Drouin, A. Fayt, J.-M. Flaud, R. Gamache, J. Harrison, J.-M. Hartmann, C. Hill, J. Hodges, D. Jacquemart, A. Jolly, J. Lamouroux, R. L. Roy, G. Li, D. Long, O. Lyulin, C. Mackie, S. Massie, S. Mikhailenko, H. Müller, O. Naumenko, A. Nikitin, J. Orphal, V. Perevalov, A. Perrin, E. Polovtseva, C. Richard, M. Smith, E. Starikova, K. Sung, S. Tashkun, J. Tennyson, G. Toon, V. Tyuterev, and G. Wagner, J. Quant. Spectrosc. Radiat. Transfer **130**, 4 (2013).
[24]See supplementary material at http://dx.doi.org/10.1063/1.4921557 for the calculated line list.
[25]A. A. Madej, A. J. Alcock, A. Czajkowski, J. E. Bernard, and S. Chepurov, J. Opt. Soc. Am. B **23**, 2200 (2006).

Table 9.1 Line list of 30013←00001 transitions of $^{12}C^{16}O_2$. The calculated frequencies were obtained by fitting the measured P-branch transitions from this work with R-branch transitions and ground state constants from Long *et al.* [194]. $\tilde{\nu}_{calc}$: calculated transition wavenumber, S: line intensity from the HITRAN 2012 database [212], ν_{calc}: calculated transition frequency, ν_D: measured transition frequency from this work, σ_{ν_D}: 1-σ uncertainty in ν_D, ν_L: measured transition frequency by Long *et al.* [194], σ_{ν_L}: : 1-σ uncertainty in ν_L, $\nu_{obs} - \nu_{calc}$: Observed frequency minus calculated frequency.

Trans.	$\tilde{\nu}_{calc}$ (cm^{-1})	S (cm/molec.)	ν_{calc} (Hz)	ν_D (Hz)	σ_{ν_D} (Hz)	ν_L (Hz)	σ_{ν_L} (Hz)	$\nu_{obs} - \nu_{calc}$ (Hz)
P42e	6189.028963874	2.376×10^{-24}	185542420571291	185542420573500	5599			2209
P40e	6191.171730601	3.086×10^{-24}	185606659101702	185606659086738	8004			-14964
P38e	6193.284379271	3.938×10^{-24}	185669994715473	185669994726448	6954			10975
P36e	6195.367110811	4.938×10^{-24}	185732433436252					
P34e	6197.420119921	6.081×10^{-24}	185793981100967					
P32e	6199.443594144	7.354×10^{-24}	185854643332074					
P30e	6201.437713008	8.728×10^{-24}	185914425511648					
P28e	6203.402647216	1.016×10^{-23}	185973332757260	185973332755630	15000			-1630
P26e	6205.338557903	1.159×10^{-23}	186031369899601	186031369904425	9889			4824
P24e	6207.245595944	1.295×10^{-23}	186088541461784	186088541462055	3533			271
P22e	6209.123901319	1.416×10^{-23}	186144851640294	186144851639255	4539			-1039
P20e	6210.973602530	1.513×10^{-23}	186200304287547	186200304286176	6350			-1371
P18e	6212.794816072	1.577×10^{-23}	186254902896000	186254902894164	4113			-1836
P16e	6214.587645958	1.599×10^{-23}	186308650583804	186308650586755	3622			2951
P14e	6216.352183281	1.572×10^{-23}	186361550081941					
P12e	6218.088505843	1.492×10^{-23}	186413603722834					
P10e	6219.796677820	1.357×10^{-23}	186464813430399					
P8e	6221.476749475	1.167×10^{-23}	186515180711511					
P6e	6223.128756924	9.264×10^{-24}	186564706648869					
P4e	6224.752721940	6.444×10^{-24}	186613391895249					
P2e	6226.348651810	3.312×10^{-24}	186661236669114					
R0e	6228.689960744	1.678×10^{-24}	186731427345146					
R2e	6230.215738773	4.985×10^{-24}	186777169019710					

Table 9.1 (continued)

Trans.	$\tilde{\nu}_{calc}$ (cm^{-1})	S (cm/molec.)	ν_{calc} (Hz)	ν_D (Hz)	σ_{ν_D} (Hz)	ν_L (Hz)	σ_{ν_L} (Hz)	$\nu_{obs} - \nu_{calc}$ (Hz)
R4e	6231.713392026	8.107×10^{-24}	186822067534703					
R6e	6233.182862000	1.091×10^{-23}	186866121136238			186866121130000	21000	-6238
R8e	6234.624075705	1.328×10^{-23}	186909327636169			186909327580000	49000	-56169
R10e	6236.036945816	1.515×10^{-23}	186951684416499			186951684360000	51000	-56499
R12e	6237.421370859	1.646×10^{-23}	186993188435142					
R14e	6238.777235453	1.720×10^{-23}	187033836233085					
R16e	6240.104410596	1.739×10^{-23}	187073623942931			*187073623720000*	*32000*	*-222931*
R18e	6241.402753997	1.709×10^{-23}	187112547298874			187112547270000	33000	-28874
R20e	6242.672110454	1.636×10^{-23}	187150601648105					
R22e	6243.912312287	1.529×10^{-23}	187187781963692					
R24e	6245.123179815	1.397×10^{-23}	187224082858950					
R26e	6246.304521888	1.250×10^{-23}	187259498603346			*187259498470000*	*18000*	*-133346*
R28e	6247.456136470	1.096×10^{-23}	187294023139962					
R30e	6248.577811272	9.416×10^{-24}	187327650104564					
R32e	6249.669324447	7.940×10^{-24}	187360372846314			187360372790000	28000	-56314
R34e	6250.730445333	6.572×10^{-24}	187392184450172					
R36e	6251.760935261	5.342×10^{-24}	187423077761035					
R38e	6252.760548421	4.266×10^{-24}	187453045409662					
R40e	6253.729032785	3.347×10^{-24}	187482079840450					

The two transition frequencies marked *in italics* were not included in the fit.

9.4.2 Lamb dip fitting procedure and transition frequency uncertainty budget

In this section, we shall provide some additional details on the Lamb dip fitting procedure and the error analyis used for the CO_2 transition frequency measurements reported in Article 6 above.

To begin with, the absorption coefficients α were determined by subtracting the previously determined spectrometer baseline $1/(c\tau_0)$ from $1/(c\tau)$ according to the basis equation of CRDS, Eq. (5.1). As mentioned in the article and discussed in Section 9.3, the observed absorption coefficients had to be corrected for minute changes in the probe laser intensity prior to fitting in order to avoid deformations of the Lamb dip profile. This correction could be carried out in the weak saturation regime on the basis of Eq. (9.17), which states that the saturation parameter is approximately equal to twice the depth $\Delta\alpha$ of the Lamb dip normalized to the dip-free absorption coefficient $\alpha_1(\nu_0)$. To determine these quantities empirically, a preliminary Lorentzian fit of the Lamb dip was carried out. It eventually yields an empirical saturation parameter, which amounted to $G_{emp} = 0.035$ outside the Lamb dip in the measurement shown in Fig. 3 of Article 6, for instance. By combining Eqs. (9.17), (9.29), (9.33), (9.30) and (9.34), one can show that saturation fluctuations $\delta\alpha/\alpha$ in the absorption coefficient are related to the measured small CRDS transmission signal fluctuations $\delta S_{PD}/S_{PD}$ through

$$\frac{\delta\alpha}{\alpha} \approx -\frac{gG_{eff}}{2} \cdot \frac{\delta S_{PD}}{S_{PD}} \tag{9.37}$$

in the weak saturation regime. Using the nomenclature from Section 9.2, $1 \leq g \leq 2$ is the velocity parameter carrying the Lamb dip signature. After a first preliminary fitting run for G_{eff} and $g(\nu)$, Eq. (9.37) thus allows an empiric intensity-fluctuation correction of the measured absorption coefficients without any freely adjustable parameter. In Fig. 3 of Article 6 the intensity-corrected data points are shown as blue full circles, whereas the uncorrected α values are reported as black empty circles. The latter data points exhibit excess noise and a fringe-like oscillatory structure. The fact that they are not present on the blue curve reveals that these effects are actually real and simply due to intracavity intensity variations.

Let us now turn to the impact of slow variations of intracavity CO_2 partial pressure due to adsorption and desorption from the cavity walls. To take them into account, one may exploit the proportionality of the absorption coefficient to the number density of absorbers (cf. Eq.(4.4)). Thus taking $\alpha \sim N/V$, the ideal gas law implies $\alpha \sim P_p$ with the CO_2 partial pressure P_p. Further assuming a constant frequency scanning speed $\frac{\mathrm{d}\nu}{\mathrm{d}t}$ and pressure increase rate, which are given here to very good approximation, one may thus fit the intensity-corrected absorption signal with a function of the form

$$\alpha(\nu) = (1 + s(\nu - \nu_0)) \cdot \left(\alpha_0 - \Delta\alpha \frac{\gamma^2/4}{(\nu - \nu_0)^2 + \gamma^2/4}\right) \tag{9.38}$$

with peak absorption α_0, dip amplitude $\Delta\alpha$, Lorentzian full-width γ and center ν_0 as well as a linear slope factor s representing the speed of CO_2 partial pressure increase. Having eliminated the main sources for drift, tilt and distortion of the Lamb dip profile during and due to the measurement, the line center frequency ν_0 can be determined with a high degree of precision and confidence.

In order to obtain a conservative estimate of the uncertainty due to the intensity correction according to Eq. (9.37) and the fitted pressure increase rate parameter s, both

Table 9.2 Uncertainty budget of the transition frequency measurement for the 30013←00001 P16 line of CO_2.

	Correction (Hz)	Uncertainty (Hz)
Systematic		3592
Absolute frequency		971
Fit model		2388
I-correction		884
P-increase		947
Asymmetry		557
Pressure shift	9894	2536
Gas composition		301
Shift coefficients		487
Pressure gauge zeroing		1748
AC Stark shift	0	$\ll 420$
Statistical		463
Total	9894	3622

the best fit value for s and the empirical estimate for the laser intensity fluctuation effect $\delta\alpha$ were changed by 15%. The resulting apparent line center shift was taken to be the systematic uncertainty due to the two effects.

To complete the systematic error budget, details on the estimation of the uncertainty due to pressure shift coefficient literature values, intracavity gas composition, pressure gauge zeroing, the frequency-comb-beat-note-based absolute frequency measurement or an eventual asymmetry of the measurement window around the Lamb dip are discussed in the body of Article 6. A concise argument why the AC Stark shift is expected to be negligible in the present study is equally given therein.

All the systematic uncertainties following from the above considerations are reported in the global uncertainty budget shown in Table 9.2, on the example of the 30013←00001 P16 CO_2 line. Let us now turn to the estimation of the statistical uncertainty reported in Table 9.2. An upper bound for this error was estimated by computing the standard deviation $\tilde{\sigma}_{stat}$ of the N observed transition frequencies around their unweighted arithmetic mean. Then, the corresponding two-sided 70-percent confidence interval σ_{stat} was determined using Student's t-distribution:

$$\sigma_{stat} = t_\phi \cdot \frac{\tilde{\sigma}_{stat}}{\sqrt{N}} \tag{9.39}$$

The t values for this 1-σ confidence interval as a function of the number $\phi = N - 1$ of statistical degrees of freedom are tabulated in the literature. For $N = 5$, for instance, $t_4 = 1.19$. In the case of the 30013←00001 P16 CO_2 line, however, $N = 45$ averages correspond to $t_{44} = 1.048$, very close to the limiting case of the normal distribution $N \to \infty$ with $t_\infty = 1.036$. This value close to unity justifies the commonly used term 1-σ confidence interval for a two-sided 70-percent confidence interval.

Having set up a detailed uncertainty budget comprising both statistical and systematic uncertainties, as the one in Table 9.2, one can combine the statistical error σ_{stat} and the systematic error σ_{syst_i} for each individual dip measurement, which are statistically independent by definition. This yields the total uncertainty σ_i for each measurement:

$$\sigma_i = \sqrt{\sigma_{syst_i}^2 + \sigma_{stat}^2} \tag{9.40}$$

To combine the individual transition frequencies from N measurements with their respective σ_i-values to a final experimental transition frequency $\overline{\nu}$ with a well-defined uncertainty, we chose to follow a maximum-likelihood approach. It consists in maximizing the probability for measuring the very transition frequencies which were indeed measured. From basic statistics [202], it follows that this condition is met by a weighted average of the N frequencies according to

$$\overline{\nu} = \left(\sum_{i=1}^{N} \frac{1}{\sigma_i^2} \right)^{-1} \cdot \sum_{i=1}^{N} \frac{\nu_i}{\sigma_i^2} \tag{9.41}$$

The statistical and systematic uncertainties in the final value $\overline{\nu}$ are then obtained from elementary error propagation [202]

$$\overline{\sigma_{stat}} = \left(\sum_{i=1}^{N} \frac{1}{\sigma_i^2} \right)^{-1} \cdot \sqrt{\sum_{i=1}^{N} \frac{1}{\sigma_i^4}} \cdot \sigma_{stat} \tag{9.42}$$

$$\overline{\sigma_{syst}} = \left(\sum_{i=1}^{N} \frac{1}{\sigma_i^2} \right)^{-1} \cdot \sum_{i=1}^{N} \frac{\sigma_{syst_i}}{\sigma_i^2} \tag{9.43}$$

Again, the combined statistical and systematic uncertainty is retrieved as the quadratic sum of both values as in Eq. (9.40). The experimental CO_2 transition frequencies and uncertainties reported in Table 1 of Article 6 were determined using this procedure.

9.4.3 Integration of the results into the CO_2 spectroscopic databank CDSD

As discussed in Article 6, the line positions of the carbon dioxide spectroscopic databank CDSD are based on a broad survey of experimental data used for an exhaustive global fit of parameters in an effective Hamiltonian for the CO_2 molecule. The emergence of new, highly accurate experimental data thereby promises an improvement in the effective Hamiltonian parameters.

Consequently, the Lamb-dip-based experimental frequencies reported here and in Article 6 were incorporated into a new global CDSD fit for $^{12}C^{16}O_2$ by Sergey Tashkun from the V.E. Zuev Institute of Atmospheric Optics (IAO) in Tomsk, Russia. This fit also included the 30013 ← 00001 R-branch frequencies from Long *et al.* [194] and the 30012 ← 00001-band measurements around 1575 nm from a recent study by the same authors [256], both originating from a Doppler-broadened regime. The results are shown in Table 9.3 in terms of the residuals of this new fit. The agreement of the new CDSD fit with the Lamb-dip-based transition frequencies is consistent with the fact that the data could be very well described in terms of the polynomial rotational energy levels of Eq. (8.5), as can be seen in Fig. 4 of Article 6. The significant deviation of around 7 σ for the R16 and R26 lines by Long *et al.* [194] confirms the issue with these two experimental frequencies, which was pointed out and discussed in Article 6.

In conclusion, the excellent agreement of the CDSD fit model and the Lamb-dip-based data is a further confirmation of its high quality. Constituting the most accurate measurement of CO_2 30013 ← 00001 and 31113 ← 01101 band transition frequencies, its integration into the data pool for the effective global Hamiltonian fit can further improve the precision of the CO_2 databank CDSD.

Table 9.3 Comparison of measured transition frequencies ν to a new global fit of $^{12}C^{16}O_2$ effective Hamiltonian parameters for the CO_2 spectroscopic databank CDSD taking the new experimental data into account. Fit residuals ρ (observed-calculated) are reported both in absolute values and normalized to the uncertainties σ. The deviations are marked in italics wherever they exceed 3 σ.

Transition	ν (kHz)	σ (kHz)	ρ (kHz)	σ/ρ
Burkart *et al.* [254]:				
30013 ← 00001				
P16e	186308650586.8	3.6	2.4	0.67
P18e	186254902894.2	4.1	-0.1	-0.05
P20e	186200304286.2	6.4	1.7	0.26
P22e	186144851639.3	4.5	2.5	0.55
P24e	186088541462.1	3.5	3.1	0.89
P26e	186031369904.4	9.9	5.9	0.60
P28e	185973332755.6	15.0	-3.0	-0.20
P38e	185669994726.4	7.0	5.7	0.82
P40e	185606659086.7	8.0	-16.6	-2.07
P42e	185542420573.5	5.6	2.7	0.47
31113 ← 01101				
R22f	186247597864.1	5.2	-0.5	-0.09
R23e	186251719634.6	11.4	1.1	0.10
Long *et al.* [194]:				
30013 ← 00001				
R16e	187073623720.0	32	*-222*	*-6.94*
R32e	187360372790.0	28	-60	-2.15
R10e	186951684360.0	51	-64	-1.25
R8e	186909327580.0	49	-66	-1.35
R6e	186866121130.0	21	-19	-0.90
R18e	187112547270.0	33	-26	-0.80
R26e	187259498470.0	18	*-134*	*-7.42*

Chapter 10

Conclusion and perspectives

At the origin of this thesis work stood the idea of developing a new type of cavity ring-down spectrometer based on a highly coherent laser source stabilized to a separate reference cavity via optical feedback. This next-generation instrument was to be designed for tackling today's and tomorrow's most demanding metrological applications in molecular absorption spectroscopy, which necessitate a combination of supreme frequency stability and absorption sensitivity.

In this spirit, we devised the new spectroscopic technique put forth in this thesis, which we called optical feedback frequency stabilized cavity ring-down spectroscopy (OFFS-CRDS). It is based on a near-infrared distributed-feedback diode laser which is tightly locked to an ultrastable V-shaped reference Cavity by Optical Feedback (VCOF) and can be fine-tuned using optical single-sideband modulation.

In the framework of this thesis, we have carried out an exhaustive characterization of the VCOF laser, including a measurement of its frequency noise spectrum with a home-made etalon frequency discriminator and long-term drift measurements using both molecular transitions and an optical frequency comb as absolute frequency references. We found that the linewidth of the VCOF laser was smaller than 530 Hz and that its long term drifts did not exceed a few 10 Hz/s, thereby confirming its adequacy for OFFS-CRDS.

In order to transfer the spectral quality of the VCOF source to noisier lasers, we collaborated with our partners from Politecnico di Milano and set up a straightforward phase-coherence transfer scheme based on a single-sideband modulator acting as a fast frequency and phase actuator in a feed-forward configuration. This approach consists in measuring the phase error of the slave laser with respect to the reference and applying it as a high-bandwidth, real-time correction to the noisy laser field. We demonstrated cloning of the VCOF laser phase on a standard DFB laser with a residual phase error as low as 133 mrad. Importantly, we showed that this technique can be generalized by using an optical frequency comb as a transfer oscillator and reported sub-radian coherence transfer over a 12 THz spectral gap. This opens the door to extensive spectroscopy with VCOF-grade frequency resolution and stability over broad spectral ranges in the near infrared.

The new OFFS-CRD spectrometer developed on the basis of the VCOF laser involves several methodological advances. It dissolves the distinction between reference and probe laser by an unbroken stability transfer chain from the V-shaped reference cavity to the CRDS frequency axis. This is made possible by a tight Pound-Drever-Hall lock of ring-down cavity resonance to the probe laser frequency, in spite of the extreme cavity finesse of around 450,000. A decisive step towards this unprecedented accomplishment was the design and construction of a massive ring-down cavity that is mechanically and thermally stable, and that provides an intrinsic alignment of the two cavity mirrors, while

nevertheless allowing for fine adjustment of their orientation. Finally, the application of single-sideband modulation to laser tuning provides great versatility and ease of use for high-resolution spectroscopy.

OFFS-CRDS currently reaches a shot-noise limited absorption detectivity down to $2{\cdot}10^{-13}\,\mathrm{cm}^{-1}/\sqrt{\mathrm{Hz}}$ and features a tunability over 1 THz with kHz-resolution, using a single VCOF laser. In this thesis, we have provided a detailed characterization of the performance and limitations of the spectrometer, notably including the impact of photo-electron shot noise and parasitic interference fringes. By averaging the spectra from repeated OFFS-CRDS scans on a narrow 10-MHz spectral interval at frequency steps of 50 kHz over one day, we found a detection limit of $8.4 \cdot 10^{-14}\,\mathrm{cm}^{-1}$, which is the lowest ever reached in absorption spectroscopy to the best of our knowledge.

With the aim of better understanding the limitations of CRDS and of contributing to its metrological use, we have carried out an in-depth analysis of systematic errors and bias sources in CRDS. To cite a few examples, we have provided a quantitative criterion for the bandwidth requirements of the ring-down acquisition system and discussed the impact of the transverse mode structure of the ring-down cavity as well as a strategy for optimizing it. Furthermore, we have analyzed the role of polarization effects and reported the first observation of polarization mode beating in CRDS to our knowledge, in good agreement with our theoretical considerations.

First applications of OFFS-CRDS to the rovibrational spectrum of CO_2 near 1.6 µm have shown very promising results, such as a high-resolution broadband spectrum with a dynamic range approaching $8 \cdot 10^5$ and an isolated line-shape measurement with adaptive frequency stepping and a signal-to-noise ratio of $8 \cdot 10^4$.

A major focus was placed on applications in saturated absorption spectroscopy, as OFFS-CRDS is ideally suited for detecting and measuring sub-Doppler absorption features even on weak lines in the near infrared. This capability is founded on its unique combination of resonant kW/cm^2-level intracavity light intensity, high sensitivity and kHz-resolution. Consequently, OFFS-CRDS was used for recording Lamb dip spectra with single-scan signal-to-noise ratios better than 100 at sub-Pa pressures, on CO_2 transitions involving four vibrational quanta. In collaboration with our partners from Politecnico di Milano, we set up a comb-assisted OFFS-CRDS experiment to exploit the extreme intrinsic frequency precision offered by these narrow sub-Doppler features. We thus measured twelve transition frequencies of $^{12}C^{16}O_2$ near 1.6 µm with an accuracy of a few parts in 10^{11}, that is at the kHz level. These results were used for obtaining improved spectroscopic constants for a vibrationally excited level of $^{12}C^{16}O_2$ and provide the most accurate reference frequency grid near 1.6 µm at present.

In a detailed theoretical analysis on saturated-absorption effects in CRDS, we have notably derived an analytic formula for ring-down signals in the weakly saturated regime and established a link between the observed photodiode signal and the effective intracavity light intensity. By fitting saturated OFFS-CRDS ring-down signals with the analytic signal shape function, we demonstrated that it yields flat fit residuals also in saturated regimes where a simple exponential cannot reproduce the experimental signal. Importantly, the weak-saturation fit decouples the saturation parameter from the unsaturated absorption coefficient, so that both crucial quantities can be simultaneously retrieved. This enables unbiased CRDS absorption measurements also in saturated regimes and opens the door to concentration-independent measurements of molecular transition dipole moments.

Before turning to an outlook on upcoming developments and applications of OFFS-CRDS in the near future, let us take a rapid glance at preliminary results of a first proof-of-principle experiment towards CO_2 isotopic ratio measurements by OFFS-CRDS. For

details on basic concepts of laser-based isotopic ratio measurements, the reader is referred to the literature references in the introduction of this thesis. For the brief, preview-like account which is presented here, as many technical details as possible shall be omitted, and no real isotopic ratios involving a two-sample approach with a reference sample for traceability to an isotope standard were considered. Instead, relative changes in the ratio of integrated absorption of two lines have been measured, which are essentially isotopic ratios with an arbitrary reference. This approach allows us to assess the precision, stability and reliability of the measurement by OFFS-CRDS for upcoming applications.

In this experiment, we have recorded OFFS-CRDS spectra like the one shown in Fig. 10.1 on a promising spectral interval near 6197 cm^{-1} over one day.

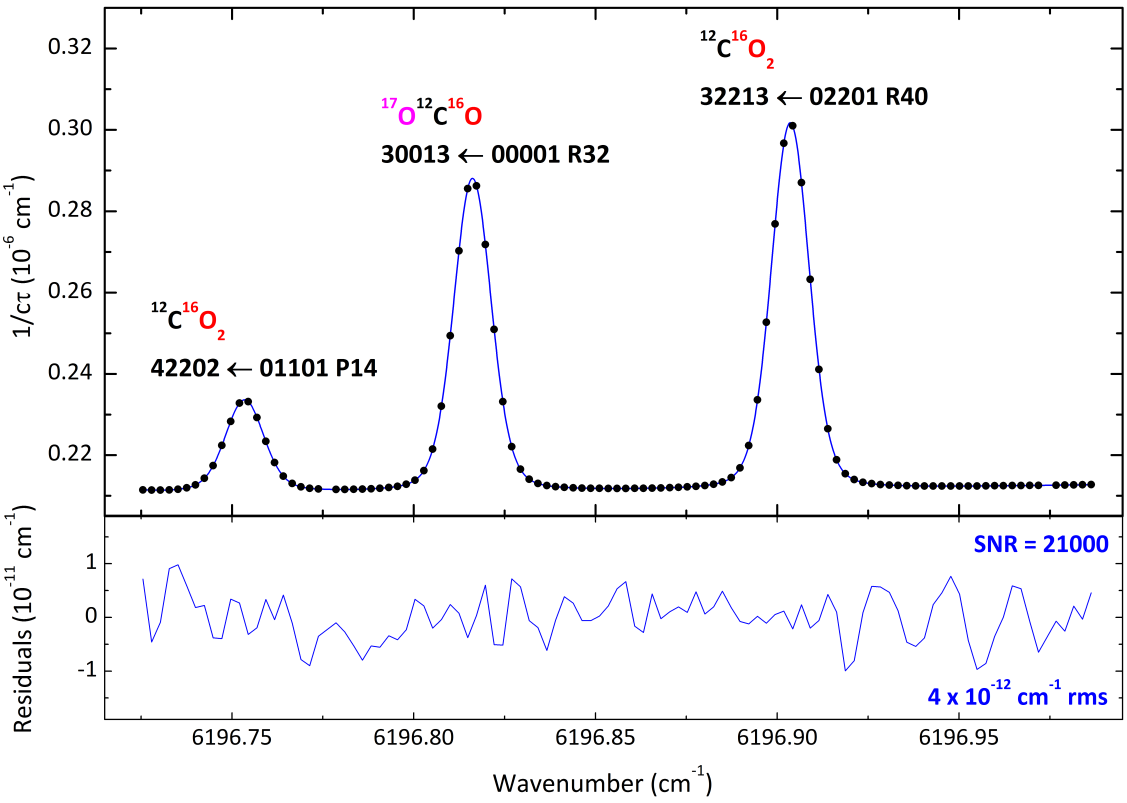

Figure 10.1 OFFS-CRDS spectrum of 1265 Pa of CO_2 at 19.85 °C recorded in 4 min at frequency steps of 43.5 MHz. The respective isotopologue and assignment is noted above each line. The integrated-absorption ratios of the $^{17}O^{12}C^{16}O$ line to the $^{12}C^{16}O_2$ lines provide a precise optical isotopic ratio measurement, whereas the ratio of the two $^{12}C^{16}O_2$ lines can be used for confirming the measured ring-down cavity temperature evolution.

For each of the 4-min scans, the three lines were fitted with a Hartmann-Tran-profile. Surrounding lines from the HITRAN database were also taken into account, so that merely a linear mirror baseline was needed for reproducing the spectra. The changes in the integrated absorption ratio between each pair of lines deduced from this measurement was corrected for the line-strength temperature dependence due to Boltzmann statistics [257] using the mK-precision ring-down cavity temperature reading. The result is equivalent to three isotopic ratios over time with respect to an arbitrary reference, and shown on the left of Fig. 10.2.

A first important result is that the ratio change between the two $^{12}C^{16}O_2$ lines is consistent with zero over the whole one-day measurement interval. As both lines measure the concentration of the same isotopologue, this is an important consistency check. It is complemented by the fact that the two ratios involving the $^{17}O^{12}C^{16}O$ line are also

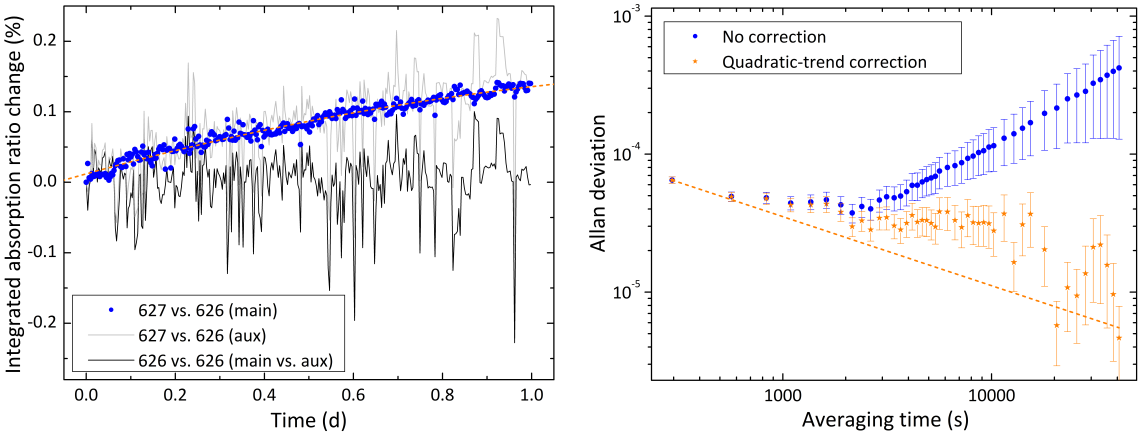

Figure 10.2 Left: Temperature-corrected integrated absorption ratios between the CO_2 lines in Fig. 10.1 over time. 627: $^{17}O^{12}C^{16}O$, 626: $^{12}C^{16}O_2$, main: stronger line, aux: weaker line. Dashed line: quadratic trend for the ratio between 627 and 626 (main). Right: Allan plot for the ratio between 627 and 626 (main), before and after removal of the quadratic trend. White-noise averaging behavior (dotted line) is indicated for comparison.

in excellent agreement, thus validating the line-strength correction scheme based on the ring-down cavity temperature reading. In the light of these results, a measurement of the smaller $^{12}C^{16}O_2$ line may be omitted in future studies as its weakness leads to excess noise.

By contrast, an isotopic ratio measurement based on the $^{17}O^{12}C^{16}O$ line and the stronger $^{12}C^{16}O_2$ line appears highly promising in view of its 65-ppm (parts-per-million) single-shot precision evidenced by the Allan plot shown on the right of Fig. 10.2. The detrended isotopic ratio averages down to the 10-ppm level during the one-day measurement. Precision levels improved by at least a factor of two are expected after an optimization of spectrometer baseline noise in view of the single-scan signal-to-noise ratio of $8 \cdot 10^4$ demonstrated in this thesis. Independently of the experimental technique, it is remarkable that variations of $^{17}O^{12}C^{16}O$ concentration can be measured with this degree of precision, given the natural abundance of the ^{17}O nucleus in nature, which is inferior to 0.04%.

The quadratic trend in the observed $^{17}O^{12}C^{16}O$ isotopic ratio, which changed by more than 1.4 permil over one day, seems to represent a real change in the isotopic composition of the sample. To confirm this beyond the mere encouraging agreement between the two $^{12}C^{16}O_2$ lines, we carried out experimental tests showing that pressure changes during the one-day measurement period cannot be held accountable for the effect. The origin of the observed $^{17}O^{12}C^{16}O$ ratio change therefore remains to be elucidated. Isotopic exchange of CO_2 molecules with water adsorbed on the cavity walls may be one potential subject for further investigations.

Beyond this promising proof-of-principle experiment, considerable efforts are currently devoted to the development of dedicated OFFS-CRDS instruments for isotopic ratio measurements for water and carbon dioxide. Both projects are carried out in close collaboration with Laboratoire des Sciences du Climat et de l'Environnement (LSCE) in Gif-sur-Yvette, France, where the operational instruments will be deployed for applications in atmospheric physics and geosciences after the initial development phase at LIPhy. Two PhD fellows are working on these joint projects at present. Tim Stoltmann is setting up an OFFS-CRDS spectrometer near 1.6 µm dedicated to the optical measurement of CO_2 isotopic ratios in the framework of the ANR (Agence Nationale de la Recherche) project LITOS directed by Mathieu Daëron, with a particular focus on the measurement of ^{17}O

anomalies [258, 259] on the one hand, and the multiply substituted, so-called clumped isotopologue $^{18}O^{13}C^{16}O$ [33, 260] on the other hand. Mathieu Casado is working on a 1.4 µm version of OFFS-CRDS for measuring the isotopic composition of water vapor in ambient air at very low humidity levels in the framework of the ERC (European Research Council) project COMBINISO led by Amaëlle Landais. It targets both fundamental studies on processes involved in isotopic fractionation of stable water isotopes [261] and field applications in environments with extremely low humidity levels, such as Antarctica, in particular. The considerable interest of these measurements to environmental and climate science contrasts with the fact that commercial optical isotopic ratio analyzers reach their sensitivity limits at air humidity levels on the order of 200 ppm [262]. Consequently, developing a dedicated ultra-sensitive OFFS-CRD spectrometer with high accuracy even at still lower humidity levels is a promising endeavor.

These projects also involve developments towards several further improvements to the experimental setup for OFFS-CRDS. Importantly, a new generation of VCOF sources is nearing completion. It is expected to yield a further stability enhancement by two orders of magnitude, thereby relaxing the environmental requirements for stable operation. In this context, let us underscore that OFFS-CRDS has a long-term potential for integration in compact, rugged instruments for field applications. Furthermore, this improvement in stability also broadens the scope of potential applications in fundamental physics or metrology. Refinements to the CRDS vacuum system and optimized automated solutions to sample handling and gas inlet are also currently being devised, and will allow both for static measurements on small sample sizes and for continuous-flow measurements for very long-term averaging under constant experimental conditions. Finally, a longer ring-down cavity with optimized transverse mode structure for further reducing OFFS-CRDS detection limits, which will be put into operation shortly, is another example for upcoming technical and experimental improvements.

To sketch out some directions for the near future, let us underscore that a stringent validation of the accuracy of Doppler thermometry by OFFS-CRDS is urgent in view of the enormous potential at hand, now that saturation effects have been mastered. Such a validation should be carried out in terms of a long-term comparison of the spectroscopic temperature reading with a calibrated temperature probe. In the expected case of a positive outcome, an attempt at measuring the Boltzmann constant by OFFS-CRDS before the Kelvin redefinition in 2018 should be made, with the appropriate equipment, infrastructure and know-how for extreme temperature stabilization and thermometry.

Broadband rovibrational spectroscopy is another highly promising application of OFFS-CRDS. In the short term, dedicated V-shaped reference cavities can be used for covering the spectral range corresponding to each respective molecular target. As soon as this approach becomes restricting, feed-forward coherence transfer through a frequency comb, which is now available at LIPhy, may be used for accessing essentially all spectral ranges where single-sideband modulators are available. Taking advantage of automated OFFS-CRDS routines, a particular application emphasis should be placed on measurements of isolated lines over whole absorption bands and with high signal-to-noise-ratios for subsequent multispectrum fitting, providing physical line parameters and putting most advanced lineshape models to the test.

Exploiting the unique combination of advantages of OFFS-CRDS for saturated absorption spectroscopy, extensive line center frequency measurements with kHz-accuracy by comb-assisted sub-Doppler Lamb dip spectroscopy should be carried out on various molecular species with weak transitions in the near infrared. This would provide a wealth of new absolute frequency information and thus contribute to establishing a complete near-

infrared reference frequency grid, with a catalytic effect for precision spectroscopy in the long-term. A particularly exciting and challenging quest is the saturation of simple molecular systems, for which more and more sophisticated theoretical predictions based on first principles exist. Confronting such calculations with experimental data with unprecedented accuracy provides a stringent test for quantum electrodynamics and thereby contributes to the search for fifth forces beyond the Standard Model. Finally, let us point out that a traceable measurement of intracavity light intensity will be the crucial step towards absolute, concentration-independent molecular transition dipole moment measurements by saturated-absorption OFFS-CRDS for a broad range of lines in the near infrared.

Already at the onset of this project, many fascinating application perspectives existed for an instrument with the characteristics and the performance of OFFS-CRDS. In parallel to the realization of the spectrometer and the other work accomplished in the framework of this thesis, the number and scope of these perspectives have continuously grown, and many promising developments are well underway. This leads us to hope that the brightest days of OFFS-CRDS are yet to come.

Appendix

C source code for fast exponential fitting with weights

```
// Based on an algorithm by Marco Prevedelli, Università di Bologna
case 3:      // New case for maximum likelihood least squares fit
{            //using Newton's method

for (j = 0; j<MAXIT; j++)   //main loop for f(p) and f'(p)
{

for (i = 1, s2 = w[0] * y[0], s3 = 0, c1 = w[0], c2 = w[0], c3 = 0, c4 = 0,
    m = 1; i<ndat; i++) // Weights and additional initializations for c1..c4.
{
q = w[i] * y[i] * m;     // Avoid recalculation
s2 += q*p;
s3 += q*i;
sumbuff = w[i] * i*m;    // Avoid recalculation
c3 += sumbuff;           // Iterative sum instead of analytic formula
c4 += sumbuff*m*p;       // Iterative sum instead of analytic formula
m *= p;
sumbuff = w[i] * m;      // Avoid recalculation
c1 += sumbuff;           // Iterative sum instead of analytic formula
c2 += sumbuff*m;         // Iterative sum instead of analytic formula
}

mp = 1 - p;
if (mp<1E-6 || p<1e-4)
{
errCode = 10;
goto error;
}

//p2=p*p;                                       //  Analytic formulae
//mp2=1-p2;                                     //  for geometric sums...
//pn=pow(p,ndat);                               //  ... sadly
//p2n=pn*pn;                                    //  no
//c1=(1-pn)/mp;                                 //  longer
//c2=(1-p2n)/mp2;                               //  possible,
//c4=(p+p2n*(p*(ndat-1)-ndat/p))/mp2/mp2;       //  therefore
//c3=(1+pn*((ndat-1)-ndat/p))/mp/mp;            //  unnecessary!

//f(p)
f = s1*(c2*c3-c1*c4) + s2*(c4*ndat-c1*c3) + s3*(c1*c1-c2*ndat); // c0=ndat

//converged ?
if (fabs(f)<EPS)     // convergence criterium unchanged with c0=ndat
break;

if ((fabs(fo)<fabs(f)) || (fabs(1 - fo / f)<TOL))
{
p = 0.5*(ppos + pneg);  //bisection step
```

```
}
else
{
//calculate f'(p)
for (i = 2, s4 = 0, c5 = 0, c6 = w[1], m = 1; i<ndat; i++)
{
sumbuff = w[i] * i*(i - 1)*m;        // Avoid recalculation
s4 += y[i] * sumbuff;
c5 += sumbuff;                  // Iterative sum instead of analytic formula
c6 += (2 * sumbuff + i*w[i] * m)*m; // Faster than c6+=w[i]*i*(2*i-1)*m*m
m *= p;
}

//c5=(2*p2-pn*(ndat*(ndat-1)+(ndat-2)*(ndat*(p2-p-p)-p2))    // Analytic
//       (p2*mp*mp*mp);                                      // formulae
//c6=-(ndat*(2*ndat-1)*p2n+p2*                               // no longer
//       (-1-3*p2+p2n*(1+(2*ndat-3)*(p2*(ndat-1)-2*ndat)))   // possible,
//       (p2*mp2*mp2*mp2);                                   // obsolete!
//

//f'(p)
fd = s1*(c4*c3 + c2*c5 - c1*c6) + s2*(c6*ndat - c3*c3 - c1*c5) + s3*(c3*c1 -
     c4*ndat) + s4*(c1*c1 - c2*ndat);    // c0=ndat
// Newton step
p -= f / fd;
}

//next
fo = f;
if (f>0.) ppos = p;
else          pneg = p;
}

if (j == MAXIT)
{
errCode = 40;
goto error;
}

m = c1*c1 - ndat*c2;     // c0=ndat
if (m == 0)
{
errCode = 39;
goto error;
}
break;
}                    // end new case 3 with weights

default:{break; }    // default

}                    // end switch

*exp_a = A = (s1*c1 - s2*ndat) / m;    // will be corrected in case 3

switch (*method)
{
case 0:
{*bsln = B = (c1*s2 - c2*s1) / m; break; }
case 1: {*bsln = B; break; }
case 2: {*bsln = B; break; }
case 3: {*bsln = B = (c1*s2-c2*s1)/m; *exp_a=A=(s1*c1-s2*ndat)/m; break; }
default: {*bsln = B; break; }
```

Bibliography

[1] O. W. Greenberg. Particles with small violations of Fermi or Bose statistics. *Phys. Rev. D*, 43(12):4111–4120, 1991. DOI: 10.1103/PhysRevD.43.4111.

[2] D. Mazzotti, P. Cancio, G. Giusfredi, M. Inguscio, and P. De Natale. Search for exchange-antisymmetric states for spin-0 particles at the 10^{-11} level. *Phys. Rev. Lett.* 86(10):1919, 2001. DOI: 10.1103/PhysRevLett.86.1919.

[3] L. Santamaria, V. Di Sarno, I. Ricciardi, S. Mosca, M. De Rosa, G. Santambrogio, P. Maddaloni, and P. De Natale. Assessing the time constancy of the proton-to-electron mass ratio by precision ro-vibrational spectroscopy of a cold molecular beam. *J. Mol. Spectrosc.* 300:116–123, 2014. DOI: 10.1016/j.jms.2014.03.013.

[4] E. Reinhold, R. Buning, U. Hollenstein, A. Ivanchik, P. Petitjean, and W. Ubachs. Indication of a cosmological variation of the proton-electron mass ratio based on laboratory measurement and reanalysis of H_2 spectra. *Phys. Rev. Lett.* 96(15):151101, 2006. DOI: 10.1103/PhysRevLett.96.151101.

[5] J. K. Webb, M. Murphy, V. Flambaum, V. Dzuba, J. Barrow, C. Churchill, J. Prochaska, and A. Wolfe. Further evidence for cosmological evolution of the fine structure constant. *Phys. Rev. Lett.* 87(9):091301, 2001. DOI: 10.1103/PhysRevLett.87.091301u.

[6] T. Udem, R. Holzwarth, and T. W. Hänsch. Optical frequency metrology. *Nature*, 416(6877):233–237, 2002. DOI: 10.1038/416233a.

[7] A. Amy-Klein, H. Vigué, and C. Chardonnet. Absolute frequency measurement of $^{12}C^{16}O_2$ laser lines with a femtosecond laser comb and new determination of the $^{12}C^{16}O_2$ molecular constants and frequency grid. *J. Mol. Spectrosc.* 228(1):206–212, 2004. DOI: 10.1016/j.jms.2004.07.005.

[8] I. Galli, S. Bartalini, P. Cancio Pastor, F. Cappelli, G. Giusfredi, D. Mazzotti, N. Akikusa, M. Yamanishi, and P. De Natale. Absolute frequency measurements of CO_2 transitions at 4.3 μm with a comb-referenced quantum cascade laser. *Mol. Phys.* 111(14-15):2041–2045, 2013. DOI: 10.1080/00268976.2013.782436.

[9] A. A. Madej, A. J. Alcock, A. Czajkowski, J. E. Bernard, and S. Chepurov. Accurate absolute reference frequencies from 1511 to 1545 nm of the $\nu_1+\nu_3$ band of $^{12}C_2H_2$ determined with laser frequency comb interval measurements. *J. Opt. Soc. Am. B*, 23(10):2200–2208, 2006. DOI: 10.1364/JOSAB.23.002200.

[10] O. L. Polyansky, A. G. Császár, S. V. Shirin, N. F. Zobov, P. Barletta, J. Tennyson, D. W. Schwenke, and P. J. Knowles. High-accuracy ab initio rotation-vibration transitions for water. *Science*, 299(5606):539–542, 2003. DOI: 10.1126/science.1079558.

[11] G. D. Dickenson, M. L. Niu, E. J. Salumbides, J. Komasa, K. S. E. Eikema, K. Pachucki, and W. Ubachs. Fundamental vibration of molecular hydrogen. *Phys. Rev. Lett.* 110(19):193601, 2013. DOI: 10.1103/PhysRevLett.110.193601.

[12] A. Campargue, S. Kassi, K. Pachucki, and J. Komasa. The absorption spectrum of H_2: CRDS measurements of the (2-0) band, review of the literature data and accurate ab initio line list up to 35 000 cm^{-1}. *Phys. Chem. Chem. Phys.* 14(2):802–815, 2012. DOI: 10.1039/C1CP22912E.

[13] E. J. Salumbides, J. C. J. Koelemeij, J. Komasa, K. Pachucki, K. S. E. Eikema, and W. Ubachs. Bounds on fifth forces from precision measurements on molecules. *Phys. Rev. D*, 87(11):112008, 2013. DOI: 10.1103/PhysRevD.87.112008.

[14] V. Letokhov. On difference of energy levels of left and right molecules due to weak interactions. *Phys. Lett. A*, 53(4):275–276, 1975. DOI: 10.1016/0375-9601(75)90064-X.

[15] M. Quack. How important is parity violation for molecular and biomolecular chirality? *Angew. Chem. Int. Ed.* 41(24):4618–4630, 2002. DOI: 10.1002/anie.200290005.

[16] C. Daussy, T. Marrel, A. Amy-Klein, C. Nguyen, C. J. Bordé, and C. Chardonnet. Limit on the parity nonconserving energy difference between the enantiomers of a chiral molecule by laser spectroscopy. *Phys. Rev. Lett.* 83(8):1554, 1999. DOI: 10.1103/PhysRevLett.83.1554.

[17] B. Darquié, C. Stoeffler, A. Shelkovnikov, C. Daussy, A. Amy-Klein, C. Chardonnet, S. Zrig, L. Guy, J. Crassous, P. Soulard, P. Asselin, T. R. Huet, P. Schwerdtfeger, R. Bast, and T. Saue. Progress toward the first observation of parity violation in chiral molecules by high-resolution laser spectroscopy. *Chirality*, 22(10):870–884, 2010. DOI: 10.1002/chir.20911.

[18] C. J. Bordé. Base units of the SI, fundamental constants and modern quantum physics. *Phil. Trans. R. Soc. A*, 363(1834):pp. 2177–2201, 2005. DOI: 10.1098/rsta.2005.1635.

[19] M. J. Milton, R. Davis, and N. Fletcher. Towards a new SI: a review of progress made since 2011. *Metrologia*, 51(3):R21, 2014. DOI: 10.1088/0026-1394/51/3/R21.

[20] P. J. Mohr, B. N. Taylor, and D. B. Newell. CODATA recommended values of the fundamental physical constants: 2010. *J. Phys. Chem. Ref. Data*, 41(4):043109, 2012. DOI: 10.1063/1.4724320.

[21] C. Daussy, M. Guinet, A. Amy-Klein, K. Djerroud, Y. Hermier, S. Briaudeau, C. Bordé, and C. Chardonnet. Direct determination of the Boltzmann constant by an optical method. *Phys. Rev. Lett.* 98(25):250801, 2007. DOI: 10.1103/PhysRevLett.98.250801.

[22] C. Lemarchand, K. Djerroud, B. Darquié, O. Lopez, A. Amy-Klein, C. Chardonnet, C. Bordé, S. Briaudeau, and C. Daussy. Determination of the Boltzmann constant by laser spectroscopy as a basis for future measurements of the thermodynamic temperature. *Int. J. Thermophys.* 31(7):1347–1359, 2010. DOI: 10.1007/s10765-010-0755-3.

[23] L. Moretti, A. Castrillo, E. Fasci, M. D. De Vizia, G. Casa, G. Galzerano, A. Merlone, P. Laporta, and L. Gianfrani. Determination of the Boltzmann constant by means of precision measurements of $H_2^{18}O$ line shapes at 1.39 μm. *Phys. Rev. Lett.* 111(6):060803, 2013. DOI: 10.1103/PhysRevLett.111.060803.

[24] M. R. Moldover, J. M. Trusler, T. Edwards, J. B. Mehl, and R. S. Davis. Measurement of the universal gas constant R using a spherical acoustic resonator. *Phys. Rev. Lett.* 60(4):249–252, 1988. DOI: http://dx.doi.org/10.1103/PhysRevLett.60.249.

[25] L. Pitre, F. Sparasci, D. Truong, A. Guillou, L. Risegari, and M. E. Himbert. Measurement of the Boltzmann constant k_B using a quasi-spherical acoustic resonator. *Int. J. Thermophys.* 32(9):1825–1886, 2011. DOI: 10.1007/s10765-011-1023-x.

[26] M. de Podesta, R. Underwood, G. Sutton, P. Morantz, P. Harris, D. F. Mark, F. M. Stuart, G. Vargha, and G. Machin. A low-uncertainty measurement of the Boltzmann constant. *Metrologia*, 50(4):354–376, 2013. DOI: 10.1088/0026-1394/50/4/354.

[27] N. Ngo, D. Lisak, H. Tran, and J.-M. Hartmann. An isolated line-shape model to go beyond the Voigt profile in spectroscopic databases and radiative transfer codes. *J. Quant. Spectrosc. Radiat. Transfer*, 129:89–100, 2013. DOI: 10.1016/j.jqsrt.2013.05.034k.

[28] P. Wcisło, H. Tran, S. Kassi, A. Campargue, F. Thibault, and R. Ciuryło. Velocity-changing collisions in pure H_2 and H_2 − Ar mixture. *J. Chem. Phys.* 141(7):074301, 2014. DOI: 10.1063/1.4892414.

[29] E. Kerstel and L. Gianfrani. Advances in laser-based isotope ratio measurements: selected applications. *Appl. Phys. B*, 92(3):439–449, 2008. DOI: 10.1007/s00340-008-3128-x.

[30] J. Jouzel. Calibrating the isotopic paleothermometer. *Science*, 286(5441):910–911, 1999. DOI: 10.1126/science.286.5441.910.

[31] P. Pearson and M. Palmer. Atmospheric carbon dioxide concentrations over the past 60 million years. *Nature*, 406(6797):695–699, 2000. DOI: 10.1038/35021000.

[32] V. Masson-Delmotte, G. Dreyfus, P. Braconnot, S. Johnsen, J. Jouzel, M. Kageyama, A. Landais, M.-F. Loutre, J. Nouet, F. Parrenin, D. Raynaud, B. Stenni, and E. Tuenter. Past temperature reconstructions from deep ice cores: relevance for future climate change. *Climate Past Discuss.* 2(4):399–448, 2006. DOI: 10.5194/cp-2-145-2006.

[33] J. M. Eiler. Paleoclimate reconstruction using carbonate clumped isotope thermometry. *Quat. Sci. Rev.* 30(25):3575–3588, 2011. DOI: 10.1016/j.quascirev.2011.09.001.

[34] L. Gianfrani, G. Gagliardi, M. Van Burgel, and E. Kerstel. Isotope analysis of water by means of near infrared dual-wavelength diode laser spectroscopy. *Opt. Express*, 11(13):1566–1576, 2003. DOI: 10.1364/OE.11.001566.

[35] J. Landsberg, D. Romanini, and E. Kerstel. Very high finesse optical-feedback cavity-enhanced absorption spectrometer for low concentration water vapor isotope analyses. *Opt. Lett.* 39(7):1795–1798, 2014. DOI: 10.1364/OL.39.001795.

[36] R. Wehr, S. Kassi, D. Romanini, and L. Gianfrani. Optical feedback cavity-enhanced absorption spectroscopy for in situ measurements of the ratio $^{13}C/^{12}C$ in CO_2. *Appl. Phys. B*, 92(3):459–465, 2008. DOI: 10.1007/s00340-008-3086-3.

[37] D. Long, M. Okumura, C. Miller, and J. Hodges. Frequency-stabilized cavity ring-down spectroscopy measurements of carbon dioxide isotopic ratios. *Appl. Phys. B*, 105(2):471–477, 2011. DOI: 10.1007/s00340-011-4518-z.

[38] Y. Chen, K. K. Lehmann, J. Kessler, B. S. Lollar, G. L. Couloume, and T. C. Onstott. Measurement of the $^{13}C/^{12}C$ of atmospheric CH_4 using near-infrared (NIR) cavity ring-down spectroscopy. *Anal. Chem.* 85(23):11250–11257, 2013. DOI: 10.1021/ac401605s.

[39] E. Steig, V. Gkinis, A. Schauer, S. Schoenemann, K. Samek, J. Hoffnagle, K. Dennis, and S. Tan. Calibrated high-precision ^{17}O-excess measurements using laser-current tuned cavity ring-down spectroscopy. *Atmos. Meas. Tech. Discuss*, 6:10191–10229, 2013. DOI: 10.5194/amtd-6-10191-2013.

[40] B. Tuzson, J. Mohn, M. Zeeman, R. Werner, W. Eugster, M. Zahniser, D. Nelson, J. McManus, and L. Emmenegger. High precision and continuous field measurements of δ^{13}C and δ^{18}O in carbon dioxide with a cryogen-free QCLAS. *Appl. Phys. B*, 92(3):451–458, 2008. DOI: 10.1007/s00340-008-3085-4.

[41] D. Romanini, A. Kachanov, N. Sadeghi, and F. Stoeckel. CW cavity ring down spectroscopy. *Chem. Phys. Lett.* 264(3):316–322, 1997. DOI: 10.1016/S0009-2614(96)01351-6.

[42] J. Morville, S. Kassi, M. Chenevier, and D. Romanini. Fast, low-noise, mode-by-mode, cavity-enhanced absorption spectroscopy by diode-laser self-locking. *Appl. Phys. B*, 80(8):1027–1038, 2005. DOI: 10.1007/s00340-005-1828-z.

[43] T. Gherman and D. Romanini. Modelocked cavity–enhanced absorption spectroscopy. *Opt. Express*, 10(19):1033–1042, 2002. DOI: 10.1364/OE.10.001033.

[44] S. Kassi and A. Campargue. Cavity ring-down spectroscopy with 5×10^{-13} cm^{-1} sensitivity. *J. Chem. Phys.* 137(23):234201, 2012. DOI: 10.1063/1.4769974.

[45] S. Kassi, O. Leshchishina, I. E. Gordon, S. Yu, and A. Campargue. Hyperfine structure of the transitions of ^{16}O^{17}O, ^{17}O^{18}O and ^{17}O$_2$ by CRDS at 80 K. *Chem. Phys. Lett.* 502(1-3):37–41, 2011. DOI: 10.1016/j.cplett.2010.12.017.

[46] A. Campargue, O. Leshchishina, L. Wang, D. Mondelain, and S. Kassi. The WKLMC empirical line lists (5852-7919 cm^{-1}) for methane between 80 K and 296 K: "Final" lists for atmospheric and planetary applications. *J. Mol. Spectrosc.* 291:16–22, 2013. DOI: 10.1016/j.jms.2013.03.001.

[47] S. Mikhailenko, D. Mondelain, S. Kassi, and A. Campargue. An accurate and complete empirical line list for water vapor between 5850 and 7920 cm^{-1}. *J. Quant. Spectrosc. Radiat. Transfer*, 140:48–57, 2014. DOI: 10.1016/j.jqsrt.2014.02.006.

[48] E. Lellouch, B. Sicardy, C. De Bergh, H.-U. Käufl, S. Kassi, and A. Campargue. Pluto's lower atmosphere structure and methane abundance from high-resolution spectroscopy and stellar occultations. *Astron. Astrophys.* 495(3):L17–L21, 2009. DOI: 10.1051/0004-6361/200911633.

[49] A. Campargue, L. Wang, D. Mondelain, S. Kassi, B. Bézard, E. Lellouch, A. Coustenis, C. de Bergh, M. Hirtzig, and P. Drossart. An empirical line list for methane in the 1.26-1.71 μm region for planetary investigations (T=80-300K). Application to Titan. *Icarus*, 219(1):110–128, 2012. DOI: 10.1016/j.icarus.2012.02.015.

[50] E. Kerstel, R. Iannone, M. Chenevier, S. Kassi, H. Jost, and D. Romanini. A water isotope (^{2}H, ^{17}O, and ^{18}O) spectrometer based on optical feedback cavity-enhanced absorption for in situ airborne applications. *Appl. Phys. B*, 85(2):397–406, 2006. DOI: 10.1007/s00340-006-2356-1.

[51] D. Romanini, M. Chenevier, S. Kassi, M. Schmidt, C. Valant, M. Ramonet, J. Lopez, and H.-J. Jost. Optical–feedback cavity–enhanced absorption: A compact spectrometer for real–time measurement of atmospheric methane. *Appl. Phys. B*, 83(4):659–667, 2006. DOI: 10.1007/s00340-006-2177-2.

[52] S. Kassi, M. Chenevier, L. Gianfrani, A. Salhi, Y. Rouillard, A. Ouvrard, and D. Romanini. Looking into the volcano with a mid-IR DFB diode laser and cavity enhanced absorption spectroscopy. *Opt. Express*, 14(23):11442–11452, 2006. DOI: 10.1364/OE.14.011442.

[53] I. Courtillot, J. Morville, V. Motto-Ros, and D. Romanini. Sub-ppb NO_2 detection by optical feedback cavity-enhanced absorption spectroscopy with a blue diode laser. *Appl. Phys. B*, 85(2-3):407–412, 2006. DOI: 10.1007/s00340-006-2354-3.

[54] P. Gorrotxategi-Carbajo, E. Fasci, I. Ventrillard, M. Carras, G. Maisons, and D. Romanini. Optical-feedback cavity-enhanced absorption spectroscopy with a quantum-cascade laser yields the lowest formaldehyde detection limit. *Appl. Phys. B*, 110(3):309–314, 2013. DOI: 10.1007/s00340-013-5340-6.

[55] I. Ventrillard-Courtillot, T. Gonthiez, C. Clerici, and D. Romanini. Multispecies breath analysis faster than a single respiratory cycle by optical-feedback cavity-enhanced absorption spectroscopy. *J. Biomed. Opt.* 14(6):064026, 2009. DOI: 10.1117/1.3269677.

[56] R. Grilli, G. Méjean, S. Kassi, I. Ventrillard, C. Abd-Alrahman, E. Fasci, and D. Romanini. Trace measurement of BrO at the ppt level by a transportable mode-locked frequency-doubled cavity-enhanced spectrometer. *Appl. Phys. B*, 107(1):205–212, 2012. DOI: 10.1007/s00340-011-4812-9.

[57] R. Grilli, M. Legrand, A. Kukui, G. Méjean, S. Preunkert, and D. Romanini. First investigations of IO, BrO, and NO_2 summer atmospheric levels at a coastal East Antarctic site using mode-locked cavity enhanced absorption spectroscopy. *Geophys. Res. Lett.* 40(4):791–796, 2013. DOI: 10.1002/grl.50154.

[58] J. Burkart. Diploma thesis. Technische Universität München, 2012.

[59] A. Einstein. Zur Quantentheorie der Strahlung. *Phys. Z.* 18:121–128, 1917.

[60] N. Basov and A. Prokhorov. Application of molecular beams for the radiospectroscopic study of rotational molecular spectra. *J. Exp. Theoret. Phys. (U.S.S.R.)* 27:431–438, 1954.

[61] J. P. Gordon, H. J. Zeiger, and C. H. Townes. The maser — new type of microwave amplifier, frequency standard, and spectrometer. *Phys. Rev.* 99(4):1264–1274, 1955. DOI: 10.1103/PhysRev.99.1264.

[62] T. Maiman. Stimulated optical radiation in ruby. *Nature*, 187:493–494, 1960. DOI: 10.1038/187493a0.

[63] J. L. Hall. Nobel Lecture: Defining and measuring optical frequencies. *Rev. Mod. Phys.* 78(4):1279–1295, 2006. DOI: 10.1103/RevModPhys.78.1279.

[64] R. E. Beehler, R. C. Mockler, and J. M. Richardson. Cesium beam atomic time and frequency standards. *Metrologia*, 1(3):114–131, 1965. DOI: 10.1088/0026-1394/1/3/004.

[65] C. G. Parthey, A. Matveev, J. Alnis, R. Pohl, T. Udem, U. D. Jentschura, N. Kolachevsky, and T. W. Hänsch. Precision measurement of the hydrogen-deuterium $1S - 2S$ isotope shift. *Phys. Rev. Lett.* 104(23):233001, 2010. DOI: 10.1103/PhysRevLett.104.233001.

[66] D. Jennings, R. Drullinger, K. Evenson, C. Pollock, and J. Wells. The continuity of the meter: the redefinition of the meter and the speed of visible light. *J. Res. Natl. Bur. Stand.* 92(1):11–16, 1987.

[67] G. Sagnac. L'éther lumineux démontré par l'effet du vent relatif d'éther dans un interféromètre en rotation uniforme. *C. R. Acad. Sci.* 157:708–710, 1913.

[68] T. Kessler, C. Hagemann, C. Grebing, T. Legero, U. Sterr, F. Riehle, M. Martin, L. Chen, and J. Ye. A sub-40-mHz-linewidth laser based on a silicon single-crystal optical cavity. *Nature Photon.* 6(10):687–692, 2012. DOI: 10.1038/nphoton.2012.217.

[69] J. Fourier. *Théorie analytique de la chaleur*. Chez Firmin Didot, père et fils, 1822.

[70] N. Wiener. Generalized harmonic analysis. *Acta Math.* 55(1):117–258, 1930. DOI: 10.1007/BF02546511.

[71] A. Khintchine. Korrelationstheorie der stationären stochastischen Prozesse. *Math. Ann.* 109(1):604–615, 1934. DOI: 10.1007/BF01449156.

[72] P. Maddaloni, M. Bellini, and P. De Natale. *Laser-based measurements for time and frequency domain applications: A handbook*. CRC Press, 2013.

[73] J. L. Hall and M. Zhu. An introduction to phase-stable optical sources. In: *Proceedings of the International School of Physics Enrico Fermi*. Ed. by E. Arimondo, W. Phillips, and F. Strumia. North Holland, Amsterdam, 1992, pp. 671–702.

[74] D. Elliott, R. Roy, and S. Smith. Extracavity laser band-shape and bandwidth modification. *Phys. Rev. A*, 26(1):12–18, 1982. DOI: http://dx.doi.org/10.1103/PhysRevA.26.12.

[75] G. Di Domenico, S. Schilt, and P. Thomann. Simple approach to the relation between laser frequency noise and laser line shape. *Appl. Opt.* 49(25):4801–4807, 2010. DOI: 10.1364/AO.49.004801.

[76] N. Bucalovic, V. Dolgovskiy, C. Schori, P. Thomann, G. Di Domenico, and S. Schilt. Experimental validation of a simple approximation to determine the linewidth of a laser from its frequency noise spectrum. *Appl. Opt.* 51(20):4582–4588, 2012. DOI: 10.1364/AO.51.004582.

[77] D. W. Allan. Statistics of atomic frequency standards. *Proc. IEEE*, 54(2):221–230, 1966. DOI: 10.1109/PROC.1966.4634.

[78] J. Von Neumann, R. Kent, H. Bellinson, and B. Hart. The mean square successive difference. *Ann. Math. Stat.* 12(2):153–162, 1941.

[79] B. Bloom, T. Nicholson, J. Williams, S. Campbell, M. Bishof, X. Zhang, W. Zhang, S. Bromley, and J. Ye. An optical lattice clock with accuracy and stability at the 10^{-18} level. *Nature*, 506(7486):71–75, 2014. DOI: 10.1038/nature12941.

[80] P. Werle, R. Mücke, and F. Slemr. The limits of signal averaging in atmospheric trace-gas monitoring by tunable diode-laser absorption spectroscopy (TDLAS). *Appl. Phys. B*, 57(2):131–139, 1993. DOI: 10.1007/BF00425997.

[81] P. Werle. Accuracy and precision of laser spectrometers for trace gas sensing in the presence of optical fringes and atmospheric turbulence. *Appl. Phys. B*, 102(2):313–329, 2011. DOI: 10.1007/s00340-010-4165-9.

[82] S. Schilt, N. Bucalovic, L. Tombez, V. Dolgovskiy, C. Schori, G. Di Domenico, M. Zaffalon, and P. Thomann. Frequency discriminators for the characterization of narrow-spectrum heterodyne beat signals: Application to the measurement of a sub-hertz carrier-envelope-offset beat in an optical frequency comb. *Rev. Sci. Instrum.* 82(12):123116, 2011. DOI: 10.1063/1.3670357.

[83] W. F. Egan. *Phase-lock basics*. John Wiley & Sons, 2007.

[84] M. Kourogi, C.-H. Shin, and M. Ohtsu. A 134 MHz bandwidth homodyne optical phase-locked-loop of semiconductor laser diodes. *IEEE Photon. Technol. Lett.* 3(3):270–272, 1991. DOI: 10.1109/68.79777.

[85] U. Gliese, T. Nielsen, M. Bruun, E. Lintz Christensen, K. Stubkjaer, S. Lindgren, and B. Broberg. A wideband heterodyne optical phase-locked loop for generation of 3-18 GHz microwave carriers. *IEEE Photon. Technol. Lett.* 4(8):936–938, 1992. DOI: 10.1109/68.149915.

[86] M. Prevedelli, T. Freegarde, and T. Hänsch. Phase locking of grating-tuned diode lasers. *Appl. Phys. B*, 60(2-3):S241–S248, 1995.

[87] S. Bartalini, S. Borri, P. Cancio, A. Castrillo, I. Galli, G. Giusfredi, D. Mazzotti, L. Gianfrani, and P. De Natale. Observing the intrinsic linewidth of a quantum-cascade laser: beyond the Schawlow-Townes limit. *Phys. Rev. Lett.* 104(8):083904, 2010. DOI: 10.1103/PhysRevLett.104.083904.

[88] H. Ludvigsen, M. Tossavainen, and M. Kaivola. Laser linewidth measurements using self-homodyne detection with short delay. *Opt. Commun.* 155(1):180–186, 1998. DOI: 10.1016/S0030-4018(98)00355-1.

[89] C. Henry. Theory of the linewidth of semiconductor lasers. *IEEE J. Quant. Electron.* 18(2):259–264, 1982. DOI: 10.1109/JQE.1982.1071522.

[90] B. Dahmani, L. Hollberg, and R. Drullinger. Frequency stabilization of semiconductor lasers by resonant optical feedback. *Opt. Lett.* 12(11):876–878, 1987. DOI: 10.1364/OL.12.000876.

[91] M. Bennett, M. F. Schatz, H. Rockwood, and K. Wiesenfeld. Huygens's clocks. *Proc. R. Soc. A*:563–579, 2002. DOI: 10.1098/rspa.2001.0888.

[92] P. Laurent, A. Clairon, and C. Breant. Frequency noise analysis of optically self-locked diode lasers. *IEEE J. Quant. Electron.* 25(6):1131–1142, 1989. DOI: 10.1109/3.29238.

[93] T. Sala, D. Gatti, A. Gambetta, N. Coluccelli, G. Galzerano, P. Laporta, and M. Marangoni. Wide-bandwidth phase lock between a CW laser and a frequency comb based on a feed-forward configuration. *Opt. Lett.* 37(13):2592–2594, 2012. DOI: 10.1364/OL.37.002592.

[94] T. Kawanishi, T. Sakamoto, T. Miyazaki, M. Izutsu, T. Fujita, S. Mori, K. Higuma, and J. Ichikawa. High-speed optical DQPSK and FSK modulation using integrated Mach-Zehnder interferometers. *Opt. Express*, 14(10):4469–4478, 2006. DOI: 10.1364/OE.14.004469.

[95] M. Daikoku, I. Morita, H. Taga, H. Tanaka, T. Kawanishi, T. Sakamoto, T. Miyazaki, and T. Fujita. 100-Gb/s DQPSK transmission experiment without OTDM for 100G ethernet transport. *J. Lightwave Technol.* 25(1):139–145, 2007. DOI: 10.1109/JLT.2006.888162.

[96] R. Griffin and A. Carter. Optical differential quadrature phase-shift key (oDQPSK) for high capacity optical transmission. In: *Optical Fiber Communication Conference and Exhibit (OFC 2002)*. 2002, pp. 367–368. DOI: 10.1109/OFC.2002.1036420.

[97] M. Izutsu, S. Shikama, and T. Sueta. Integrated optical SSB modulator/frequency shifter. *IEEE J. Quant. Electron.* 17(11):2225–2227, 1981. DOI: 10.1109/JQE.1981.1070678.

[98] S. Diddams, J. Bergquist, S. Jefferts, and C. Oates. Standards of time and frequency at the outset of the 21st century. *Science*, 306(5700):1318–1324, 2004. DOI: 10.1126/science.1102330.

[99] M. Takamoto, F.-L. Hong, R. Higashi, and H. Katori. An optical lattice clock. *Nature*, 435(7040):321–324, 2005. DOI: 10.1038/nature03541.

[100] C. Chou, D. Hume, J. Koelemeij, D. Wineland, and T. Rosenband. Frequency comparison of two high-accuracy Al^+ optical clocks. *Phys. Rev. Lett.* 104(7):070802, 2010. DOI: 10.1103/PhysRevLett.104.070802.

[101] N. Huntemann, M. Okhapkin, B. Lipphardt, S. Weyers, C. Tamm, and E. Peik. High-accuracy optical clock based on the octupole transition in $^{171}Yb^+$. *Phys. Rev. Lett.* 108(9):090801, 2012. DOI: 10.1103/PhysRevLett.108.090801.

[102] T. Nicholson, M. Martin, J. Williams, B. Bloom, M. Bishof, M. Swallows, S. Campbell, and J. Ye. Comparison of two independent Sr optical clocks with 1×10^{-17} stability at 10^3 s. *Phys. Rev. Lett.* 109(23):230801, 2012. DOI: 10.1103/PhysRevLett.109.230801.

[103] Y. Jiang, A. Ludlow, N. Lemke, R. Fox, J. Sherman, L.-S. Ma, and C. Oates. Making optical atomic clocks more stable with 10^{-16}-level laser stabilization. *Nature Photon.* 5(3):158–161, 2011. DOI: 10.1038/nphoton.2010.313.

[104] N. Kolachevsky, A. Matveev, J. Alnis, C. G. Parthey, S. G. Karshenboim, and T. W. Hänsch. Measurement of the 2S hyperfine interval in atomic hydrogen. *Phys. Rev. Lett.* 102(21):213002, 2009. DOI: 10.1103/PhysRevLett.102.213002.

[105] C. Fabry and A. Pérot. Théorie et applications d'une nouvelle méthode de spectroscopie interférentielle. *Ann. Chim. Phys*, 16(7):115–144, 1899.

[106] D. Romanini. Modelling the excitation field of an optical resonator. *Appl. Phys. B*, 115(4):517–531, 2014. DOI: 10.1007/s00340-013-5632-x.

[107] H. Kogelnik and T. Li. Laser beams and resonators. *Appl. Opt.* 5(10):1550–1567, 1966. DOI: 10.1364/AO.5.001550.

[108] A. E. Siegman. *Lasers*. University Science Books Mill Valley, CA, 1986.

[109] U. W. Hochstrasser. Orthogonal polynomials. In: *Handbook of mathematical functions with formulas, graphs, and mathematical tables*. Ed. by M. Abramowitz and I. Stegun. United States National Bureau of Standards, 1972. Chap. 22, p. 775.

[110] P. Milonni and J. Eberly. Laser resonators and Gaussian beams. In: *Laser Physics*. John Wiley & Sons, 2010. Chap. 7, pp. 269–330.

[111] L. Gouy. Optique : sur une propriété nouvelle des ondes lumineuses. *C. R. Acad. Sci.* 110:1251, 1890.

[112] S. Feng and H. G. Winful. Physical origin of the Gouy phase shift. *Opt. Lett.* 26(8):485–487, 2001. DOI: 10.1364/OL.26.000485.

[113] C. Fabre, R. G. DeVoe, and R. G. Brewer. Ultrahigh-finesse optical cavities. *Opt. Lett.* 11(6):365–367, 1986. DOI: 10.1364/OL.11.000365.

[114] M. Zeppenfeld and P. W. Pinkse. Calculating the fine structure of a Fabry-Perot resonator using spheroidal wave functions. *Opt. Express*, 18(9):9580–9591, 2010. DOI: 10.1088/1367-2630/17/1/013053.

[115] M. Uphoff, M. Brekenfeld, G. Rempe, and S. Ritter. Frequency splitting of polarization eigenmodes in microscopic Fabry-Perot cavities. *New J. Phys.* 17(1):013053, 2015. DOI: 10.1088/1367-2630/17/1/013053.

[116] P. Milonni and J. Eberly. The Fabry-Pérot etalon. In: *Laser Physics*. John Wiley & Sons, 2010, pp. 223–226.

[117] C. Salomon, D. Hils, and J. L. Hall. Laser stabilization at the millihertz level. *J. Opt. Soc. Am. B*, 5(8):1576–1587, 1988. DOI: 10.1364/JOSAB.5.001576.

[118] Corning Inc. *ULE Corning Code 7972 Ultra Low Expansion Glass*. 2006.

[119] Schott AG. *ZERODUR — Zero Expansion Glass Ceramic*. 2011.

[120] J. Alnis, A. Matveev, N. Kolachevsky, T. Udem, and T. W. Hänsch. Subhertz linewidth diode lasers by stabilization to vibrationally and thermally compensated ultralow-expansion glass Fabry-Pérot cavities. *Phys. Rev. A*, 77(5):053809, 2008. DOI: 10.1103/PhysRevA.77.053809.

[121] M. Notcutt, L.-S. Ma, J. Ye, and J. L. Hall. Simple and compact 1-Hz laser system via an improved mounting configuration of a reference cavity. *Opt. Lett.* 30(14):1815–1817, 2005. DOI: 10.1364/OL.30.001815.

[122] A. D. Ludlow, X. Huang, M. Notcutt, T. Zanon-Willette, S. M. Foreman, M. M. Boyd, S. Blatt, and J. Ye. Compact, thermal-noise-limited optical cavity for diode laser stabilization at 1×10^{-15}. *Opt. Lett.* 32(6):641–643, 2007. DOI: 10.1364/OL.32.000641.

[123] S. Webster, M. Oxborrow, S. Pugla, J. Millo, and P. Gill. Thermal-noise-limited optical cavity. *Phys. Rev. A*, 77(3):033847, 2008. DOI: 10.1103/PhysRevA.77.033847.

[124] K. Numata, A. Kemery, and J. Camp. Thermal-noise limit in the frequency stabilization of lasers with rigid cavities. *Phys. Rev. Lett.* 93(25):250602, 2004. DOI: 10.1103/PhysRevLett.93.250602.

[125] D. A. Shaddock, M. B. Gray, and D. E. McClelland. Frequency locking a laser to an optical cavity by use of spatial mode interference. *Opt. Lett.* 24(21):1499–1501, 1999. DOI: 10.1364/OL.24.001499.

[126] T. Hänsch and B. Couillaud. Laser frequency stabilization by polarization spectroscopy of a reflecting reference cavity. *Opt. Commun.* 35(3):441–444, 1980. DOI: 10.1016/0030-4018(80)90069-3.

[127] M. Kourogi and M. Ohtsu. Novel optical frequency discriminator for FM noise reduction of semiconductor lasers. *Opt. Commun.* 81(3):204–208, 1991. DOI: 10.1016/0030-4018(91)90639-U.

[128] R. V. Pound. Electronic frequency stabilization of microwave oscillators. *Rev. Sci. Instrum.* 17(11):490–505, 1946. DOI: 10.1063/1.1770414.

[129] R. W. P. Drever, J. L. Hall, F. V. Kowalski, J. Hough, G. M. Ford, A. J. Munley, and H. Ward. Laser phase and frequency stabilization using an optical resonator. *Appl. Phys. B*, 31(2):97–105, 1983. DOI: 10.1007/BF00702605.

[130] J. Morville, D. Romanini, M. Chenevier, and A. Kachanov. Effects of laser phase noise on the injection of a high-finesse cavity. *Appl. Opt.* 41(33):6980–6990, 2002. DOI: 10.1364/AO.41.006980.

[131] U. Keller. Recent developments in compact ultrafast lasers. *Nature*, 424(6950):831–838, 2003. DOI: 10.1038/nature01938.

[132] F. Krausz. From femtochemistry to attophysics. *Phys. World*, 14:41–46, 2001.

[133] G. Méjean, S. Kassi, and D. Romanini. Measurement of reactive atmospheric species by ultraviolet cavity-enhanced spectroscopy with a mode-locked femtosecond laser. *Opt. Lett.* 33(11):1231–1233, 2008. DOI: 10.1364/OL.33.001231.

[134] I. Coddington, W. Swann, and N. Newbury. Coherent dual-comb spectroscopy at high signal-to-noise ratio. *Phys. Rev. A*, 82(4):043817, 2010. DOI: 10.1103/PhysRevA.82.043817.

[135] S. A. Diddams, D. J. Jones, J. Ye, S. T. Cundiff, J. L. Hall, J. K. Ranka, R. S. Windeler, R. Holzwarth, T. Udem, and T. W. Hänsch. Direct link between microwave and optical frequencies with a 300 THz femtosecond laser comb. *Phys. Rev. Lett.* 84(22):5102–5105, 2000. DOI: 10.1103/PhysRevLett.84.5102.

[136] R. Holzwarth, T. Udem, T. W. Hänsch, J. Knight, W. Wadsworth, and P. S. J. Russell. Optical frequency synthesizer for precision spectroscopy. *Phys. Rev. Lett.* 85(11):2264–2267, 2000. DOI: 10.1103/PhysRevLett.85.2264.

[137] T. W. Hänsch. Nobel Lecture: Passion for precision. *Rev. Mod. Phys*, 78(4):1297–1309, 2006. DOI: 10.1103/RevModPhys.78.1297.

[138] M. Bellini and T. W. Hänsch. Phase-locked white-light continuum pulses: toward a universal optical frequency-comb synthesizer. *Opt. Lett.* 25(14):1049–1051, 2000. DOI: 10.1364/OL.25.001049.

[139] D. J. Jones, S. A. Diddams, J. K. Ranka, A. Stentz, R. S. Windeler, J. L. Hall, and S. T. Cundiff. Carrier-envelope phase control of femtosecond mode-locked lasers and direct optical frequency synthesis. *Science*, 288(5466):635–639, 2000. DOI: 10.1126/science.288.5466.635.

[140] J. T. Hodges, H. P. Layer, W. W. Miller, and G. E. Scace. Frequency-stabilized single-mode cavity ring-down apparatus for high-resolution absorption spectroscopy. *Rev. Sci. Instrum.* 75(4):849–863, 2004. DOI: 10.1063/1.1666984.

[141] D. J. Robichaud, J. T. Hodges, P. Masłowski, L. Y. Yeung, M. Okumura, C. E. Miller, and L. R. Brown. High-accuracy transition frequencies for the O_2 A-band. *J. Mol. Spectrosc.* 251(1):27–37, 2008. DOI: 10.1016/j.jms.2007.12.008.

[142] A. Wallard. Frequency stabilization of the helium-neon laser by saturated absorption in iodine vapour. *J. Phys. E*, 5(9):926–930, 1972. DOI: 10.1088/0022-3735/5/9/025.

[143] G. R. Hanes, K. M. Baird, and J. DeRemigis. Stability, reproducibility, and absolute wavelength of a 633-nm He-Ne laser stabilized to an iodine hyperfine component. *Appl. Opt.* 12(7):1600–1605, 1973. DOI: 10.1364/AO.12.001600.

[144] B. P. J. van Oorschot and C. J. van der Hoeven. A recently developed iodine-stabilised laser. *J. Phys. E*, 12(1):51–55, 1979. DOI: 10.1088/0022-3735/12/1/015.

[145] J. Burkart, D. Romanini, and S. Kassi. Optical feedback stabilized laser tuned by single-sideband modulation. *Opt. Lett.* 38(12):2062–2064, 2013. DOI: 10.1364/OL.38.002062.

[146] G. Galzerano, E. Fasci, A. Castrillo, N. Coluccelli, L. Gianfrani, and P. Laporta. Absolute frequency stabilization of an extended-cavity diode laser against Doppler-free $H_2^{17}O$ absorption lines at 1.384 μm. *Opt. Lett.* 34(20):3107–3109, 2009. DOI: 10.1364/OL.34.003107.

[147] S. F. Jacobs, S. C. Johnston, and D. E. Schwab. Dimensional instability of Invars. *Appl. Opt.* 23(20):3500–3502, 1984. DOI: 10.1364/AO.23.3500_1.

[148] H. Huang and K. K. Lehmann. Effects of linear birefringence and polarization-dependent loss of supermirrors in cavity ring-down spectroscopy. *Appl. Opt.* 47(21):3817–3827, 2008. DOI: 10.1364/AO.47.003817.

[149] A. Predoi-Cross, A. McKellar, D. C. Benner, V. M. Devi, R. Gamache, C. Miller, R. Toth, and L. Brown. Temperature dependences for air-broadened Lorentz half-width and pressure shift coefficients in the 30013-00001 and 30012-00001 bands of CO_2 near 1600 nm. *Can. J. Phys.* 87(5):517–535, 2009. DOI: 10.1139/P08-137.

[150] P. E. Ciddor. Refractive index of air: new equations for the visible and near infrared. *Appl. Opt.* 35(9):1566–1573, 1996. DOI: 10.1364/AO.35.001566.

[151] S. Borri, S. Bartalini, I. Galli, P. Cancio, G. Giusfredi, D. Mazzotti, A. Castrillo, L. Gianfrani, and P. De Natale. Lamb-dip-locked quantum cascade laser for comb-referenced IR absolute frequency measurements. *Opt. Express*, 16(15):11637–11646, 2008. DOI: 10.1364/OE.16.011637.

[152] R. Engelbrecht, B. Lins, P. Zinn, R. Buchtal, and B. Schmauss. Line shapes of near-infrared DFB and VCSEL diode lasers under the influence of system back reflections. *Appl. Phys. B*, 109(3):441–452, 2012. DOI: 10.1007/s00340-012-5097-3.

[153] D. Gatti, T. Sala, A. Gambetta, N. Coluccelli, G. N. Conti, G. Galzerano, P. Laporta, and M. Marangoni. Analysis of the feed-forward method for the referencing of a CW laser to a frequency comb. *Opt. Express*, 20(22):24880–24885, 2012. DOI: 10.1364/OE.20.024880.

[154] S. Koke, C. Grebing, H. Frei, A. Anderson, A. Assion, and G. Steinmeyer. Direct frequency comb synthesis with arbitrary offset and shot-noise-limited phase noise. *Nature Photon.* 4(7):462–465, 2010. DOI: 10.1038/nphoton.2010.91.

[155] R. Griffin and K. Kitayama. Optical millimetre-wave generation with high spectral purity using feed-forward optical field modulation. *Electron. Lett.* 34(8):795–796, 1998. DOI: 10.1049/el:19980577.

[156] J. Burkart, T. Sala, S. Kassi, D. Romanini, and M. Marangoni. Optical phase cloning by an integrated dual-parallel Mach–Zehnder modulator. *Opt. Lett.* 40(5):816–819, 2015. DOI: 10.1364/OL.40.000816.

[157] T. Sala, S. Kassi, J. Burkart, M. Marangoni, and D. Romanini. Comb-assisted coherence transfer between laser fields, 2014. arXiv: 1412.1102 [physics.optics].

[158] P. Bouguer. *Essai d'optique sur la gradation de la lumière*. Chez Claude Jombert, Paris, 1729.

[159] J. Lambert. *Photometria sive de mensura et gradibus luminis, colorum et umbrae*. Eberhardt Klett, Augsburg, 1760.

[160] A. Beer. Bestimmung der Absorption des rothen Lichts in farbigen Flüssigkeiten. *Ann. Phys. Chem*, 86(2):78–90, 1852.

[161] G. Herzberg. *Molekülspektren und Molekülstruktur I. — Zweiatomige Moleküle*. Verlag Theodor Steinkopff, Dresden, 1939.

[162] D. Z. Anderson, J. C. Frisch, and C. S. Masser. Mirror reflectometer based on optical cavity decay time. *Appl. Opt.* 23(8):1238–1245, 1984. DOI: 10.1364/AO.23.001238.

[163] A. O'Keefe and D. A. G. Deacon. Cavity ring-down optical spectrometer for absorption measurements using pulsed laser sources. *Rev. Sci. Instrum.* 59(12):2544–2551, 1988. DOI: 10.1063/1.1139895.

[164] K. K. Lehmann and D. Romanini. The superposition principle and cavity ring-down spectroscopy. *J. Chem. Phys*, 105(23):10263–10277, 1996. DOI: 10.1063/1.472955.

[165] J. D. Jackson. In: *Classical Electrodynamics*. 3rd ed. Wiley-VCH, 1999, p. 298.

[166] S. Kassi, D. Romanini, A. Campargue, and B. Bussery-Honvault. Very high sensitivity CW cavity ring-down spectroscopy: Application to the O_2 band near 1.58 μm. *Chem. Phys. Lett.* 409(4):281–287, 2005. DOI: 10.1016/j.cplett.2005.05.033.

[167] S. Kassi, A. Campargue, K. Pachucki, and J. Komasa. The absorption spectrum of D_2: Ultrasensitive cavity ring down spectroscopy of the (2–0) band near 1.7 μm and accurate ab initio line list up to 24 000 cm^{-1}. *J. Chem. Phys*, 136(18):184309, 2012. DOI: 10.1063/1.4707708.

[168] H. Huang and K. K. Lehmann. Long-term stability in continuous wave cavity ring-down spectroscopy experiments. *Appl. Opt.* 49(8):1378–1387, 2010. DOI: 10.1364/AO.49.001378.

[169] J. T. Hodges and R. Ciuryło. Automated high-resolution frequency-stabilized cavity ring-down absorption spectrometer. *Rev. Sci. Instrum.* 76(2):023112, 2005. DOI: 10.1063/1.1850633.

[170] A. White. Frequency stabilization of gas lasers. *IEEE J. Quant. Electron.* 1(8):349–357, 1965. DOI: 10.1109/JQE.1965.1072246.

[171] D. Lisak, J. T. Hodges, and R. Ciuryło. Comparison of semiclassical line-shape models to rovibrational H_2O spectra measured by frequency-stabilized cavity ring-down spectroscopy. *Phys. Rev. A*, 73(1):012507, 2006. DOI: 10.1103/PhysRevA.73.012507.

[172] D. Long, A. Cygan, R. van Zee, M. Okumura, C. Miller, D. Lisak, and J. Hodges. Frequency-stabilized cavity ring-down spectroscopy. *Chem. Phys. Lett.* 536:1–8, 2012. DOI: 10.1016/j.cplett.2012.03.035.

[173] D. Long, D. Havey, M. Okumura, H. Pickett, C. Miller, and J. Hodges. Laboratory measurements and theoretical calculations of O_2 A band electric quadrupole transitions. *Phys. Rev. A*, 80(4):042513, 2009. DOI: 10.1103/PhysRevA.80.042513.

[174] B. A. Paldus, C. C. Harb, T. G. Spence, B. Wilke, J. Xie, J. S. Harris, and R. N. Zare. Cavity-locked ring-down spectroscopy. *J. Appl. Phys.* 83(8):3991–3997, 1998. DOI: 10.1063/1.367155.

[175] T. G. Spence, C. C. Harb, B. A. Paldus, R. N. Zare, B. Willke, and R. L. Byer. A laser-locked cavity ring-down spectrometer employing an analog detection scheme. *Rev. Sci. Instrum.* 71(2):347–353, 2000. DOI: 10.1063/1.1150206.

[176] R. Martínez, M. Metsälä, O. Vaittinen, T. Lantta, and L. Halonen. Laser-locked, high-repetition-rate cavity ringdown spectrometer. *J. Opt. Soc. Am. B*, 23(4):727–740, 2006. DOI: 10.1364/JOSAB.23.000727.

[177] A. Cygan, D. Lisak, P. Masłowski, K. Bielska, S. Wójtewicz, J. Domysławska, R. S. Trawiński, R. Ciuryło, H. Abe, and J. T. Hodges. Pound-Drever-Hall-locked, frequency-stabilized cavity ring-down spectrometer. *Rev. Sci. Instrum.* 82(6):063107, 2011. DOI: 10.1063/1.3595680.

[178] A. Cygan, D. Lisak, S. Wójtewicz, J. Domysławska, J. Hodges, R. Trawiński, and R. Ciuryło. High-signal-to-noise-ratio laser technique for accurate measurements of spectral line parameters. *Phys. Rev. A*, 85(2):022508, 2012. DOI: 10.1103/PhysRevA.85.022508.

[179] A. Cygan, S. Wójtewicz, J. Domysławska, P. Masłowski, K. Bielska, M. Piwiński, K. Stec, R. Trawiński, F. Ozimek, C. Radzewicz, H. Abe, T. Ido, J. Hodges, D. Lisak, and R. Ciuryło. Spectral line-shapes investigation with Pound-Drever-Hall-locked frequency-stabilized cavity ring-down spectroscopy. *Eur. Phys. J. Spec. Top.* 222(9):2119–2142, 2013. DOI: 10.1140/epjst/e2013-01990-0.

[180] J. Domysławska, S. Wójtewicz, P. Masłowski, A. Cygan, K. Bielska, R. S. Trawiński, R. Ciuryło, and D. Lisak. Spectral line shapes and frequencies of the molecular oxygen B-band R-branch transitions. *J. Quant. Spectrosc. Radiat. Transfer*, 155:22–31, 2015. DOI: 10.1016/j.jqsrt.2014.12.015.

[181] P. R. Griffiths and J. A. De Haseth. *Fourier transform infrared spectrometry*. John Wiley & Sons, 2007.

[182] H. Huang and K. Lehmann. Noise in cavity ring-down spectroscopy caused by transverse mode coupling. *Opt. Express*, 15(14):8745–8759, 2007. DOI: 10.1364/OE.15.008745.

[183] G.-W. Truong, K. Douglass, S. Maxwell, R. van Zee, D. Plusquellic, J. Hodges, and D. Long. Frequency-agile, rapid scanning spectroscopy. *Nature Photon.* 2013. DOI: 10.1038/nphoton.2013.98.

[184] D. A. Long, G.-W. Truong, R. D. van Zee, D. F. Plusquellic, and J. T. Hodges. Frequency-agile, rapid scanning spectroscopy: absorption sensitivity of 2×10^{-12} cm^{-1}Hz$^{-1/2}$ with a tunable diode laser. *Appl. Phys. B*, 114(4):489–495, 2014. DOI: 10.1007/s00340-013-5548-5.

[185] S. Kassi and A. Campargue. Electric quadrupole transitions and collision-induced absorption in the region of the first overtone band of H_2 near 1.25 μm. *J. Mol. Spectrosc.* 300:55–59, 2014. DOI: 10.1016/j.jms.2014.03.022.

[186] A. Watanabe, J. L. Hunt, and H. L. Welsh. Structure of the pressure-induced infrared spectrum of hydrogen in the first overtone region. *Can. J. Phys.* 49(7):860–863, 1971. DOI: 10.1139/p71-102.

[187] A. Campargue, E. Karlovets, and S. Kassi. The 4-0 band of carbon monoxide by high sensitivity cavity ring down spectroscopy near 8200 cm^{-1}. *J. Quant. Spectrosc. Radiat. Transfer*, 154:113–119, 2015. DOI: 10.1016/j.jqsrt.2014.12.011.

[188] R. de L. Kronig. On the theory of dispersion of X-rays. *J. Opt. Soc. Am.* 12(6):547–556, 1926. DOI: 10.1364/JOSA.12.000547.

[189] H. Kramers. La diffusion de la lumière par les atomes. *Atti Cong. Intern. Fisica, (Transactions of Volta Centenary Congress) Como*, 2:545–557, 1927.

[190] K. G. Libbrecht and M. W. Libbrecht. Interferometric measurement of the resonant absorption and refractive index in rubidium gas. *Am. J. Phys.* 74(12):1055–1060, 2006. DOI: 10.1119/1.2335476.

[191] A. Cygan, D. Lisak, P. Morzyński, M. Bober, M. Zawada, E. Pazderski, and R. Ciuryło. Cavity mode-width spectroscopy with widely tunable ultra narrow laser. *Opt. Express*, 21(24):29744–29754, 2013. DOI: 10.1364/OE.21.029744.

[192] A. Cygan, P. Wcisło, S. Wójtewicz, P. Masłowski, J. T. Hodges, R. Ciuryło, and D. Lisak. One-dimensional frequency-based spectroscopy. *Opt. Express*, 23(11):14472–14486, 2015. DOI: 10.1364/OE.23.014472.

[193] G.-W. Truong, D. A. Long, A. Cygan, D. Lisak, R. D. van Zee, and J. T. Hodges. Comb-linked, cavity ring-down spectroscopy for measurements of molecular transition frequencies at the kHz-level. *J. Chem. Phys*, 138(9):094201, 2013. DOI: 10.1063/1.4792372.

[194] D. Long, G.-W. Truong, J. Hodges, and C. Miller. Absolute $^{12}C^{16}O_2$ transition frequencies at the kHz-level from 1.6 to 7.8 μm. *J. Quant. Spectrosc. Radiat. Transfer*, 130:112–115, 2013. DOI: 10.1016/j.jqsrt.2013.07.001.

[195] D. Mondelain, T. Sala, S. Kassi, D. Romanini, M. Marangoni, and A. Campargue. Broadband and highly sensitive comb-assisted cavity ring down spectroscopy of CO near 1.57 μm with sub-MHz frequency accuracy. *J. Quant. Spectrosc. Radiat. Transfer*, 154:35–43, 2015. DOI: 10.1016/j.jqsrt.2014.11.021.

[196] D. Gatti, T. Sala, R. Gotti, L. Cocola, L. Poletto, M. Prevedelli, P. Laporta, and M. Marangoni. Comb-locked cavity ring-down spectrometer. *J. Chem. Phys*, 142(7):074201, 2015. DOI: 10.1063/1.4907939.

[197] P. B. Tarsa, P. Rabinowitz, and K. K. Lehmann. Evanescent field absorption in a passive optical fiber resonator using continuous-wave cavity ring-down spectroscopy. *Chem. Phys. Lett.* 383(3):297–303, 2004. DOI: 10.1016/j.cplett.2003.11.043.

[198] F. Ye, C. Zhou, B. Qi, and L. Qian. Continuous-wave cavity ring-down evanescent-field sensing with a broadband source based on frequency-shifted interferometry. *Sens. Actuator B-Chem.* 184:150–155, 2013. DOI: 10.1016/j.snb.2013.04.058.

[199] H. Tian, C. Zhou, D. Fan, Y. Ou, and D. Yin. Continuous-wave fiber cavity ring-down magnetic field sensing method based on frequency-shifted interferometry. *Chin. Opt. Lett.* 12(12):120604–120604, 2014. DOI: 10.3788/COL201412.120604.

[200] J. Burkart, D. Romanini, and S. Kassi. Optical feedback frequency stabilized cavity ring-down spectroscopy. *Opt. Lett.* 39(16):4695–4698, 2014. DOI: 10.1364/OL.39.004695.

[201] K. Zapfe. *Leak Detection*. Deutsches Elektronen-Synchrotron DESY Hamburg, 2007.

[202] J. R. Taylor. In: *An introduction to error analysis: The study of uncertainties in physical measurements*. University Science Books Mill Valley (CA), 1982, pp. 130–133.

[203] D. Benner, C. P. Rinsland, V. Devi, M. A. H. Smith, and D. Atkins. A multispectrum nonlinear least squares fitting technique. *J. Quant. Spectrosc. Radiat. Transfer*, 53(6):705–721, 1995. DOI: 10.1016/0022-4073(95)00015-D.

[204] V. M. Devi, D. C. Benner, L. Brown, C. Miller, and R. Toth. Line mixing and speed dependence in CO_2 at 6227.9 cm^{-1}: constrained multispectrum analysis of intensities and line shapes in the 30013←00001 band. *J. Mol. Spectrosc.* 245(1):52–80, 2007. DOI: 10.1016/j.jms.2007.05.015.

[205] J. Old, K. Gentili, and E. Peck. Dispersion of carbon dioxide. *J. Opt. Soc. Am.* 61(1):89–90, 1971. DOI: 10.1364/JOSA.61.000089.

[206] S. Wójtewicz, D. Lisak, A. Cygan, J. Domysławska, R. S. Trawiński, and R. Ciuryło. Line-shape study of self-broadened O_2 transitions measured by Pound-Drever-Hall-locked frequency-stabilized cavity ring-down spectroscopy. *Phys. Rev. A*, 84(3):032511, 2011. DOI: 10.1103/PhysRevA.84.032511.

[207] H. Huang and K. Lehmann. Noise caused by a finite extinction ratio of the light modulator in CW cavity ring-down spectroscopy. *Appl. Phys. B*, 94(2):355–366, 2009. DOI: 10.1007/s00340-008-3293-y.

[208] J. C. Stover. *Optical scattering: measurement and analysis*. Vol. 2. SPIE optical engineering press Bellingham, WA, 1995.

[209] T. Klaassen, J. de Jong, M. van Exter, and J. P. Woerdman. Transverse mode coupling in an optical resonator. *Opt. Lett.* 30(15):1959–1961, 2005. DOI: 10.1364/OL.30.001959.

[210] I. Silander, T. Hausmaninger, W. Ma, P. Ehlers, and O. Axner. Doppler-broadened noise-immune cavity-enhanced optical heterodyne molecular spectrometry down to $4\times10^{-13}\,cm^{-1}Hz^{-1/2}$: implementation of a 50,000 finesse cavity. *Opt. Lett.* 40(9):2004–2007, 2015. DOI: 10.1364/OL.40.002004.

[211] R. C. Jones. A new calculus for the treatment of optical systems. *J. Opt. Soc. Am.* 31(7):488–493, 1941. DOI: 10.1364/JOSA.31.000488.

[212] L. Rothman, I. Gordon, Y. Babikov, A. Barbe, D. C. Benner, P. Bernath, M. Birk, L. Bizzocchi, V. Boudon, L. Brown, A. Campargue, K. Chance, E. Cohen, L. Coudert, V. Devi, B. Drouin, A. Fayt, J.-M. Flaud, R. Gamache, J. Harrison, J.-M. Hartmann, C. Hill, J. Hodges, D. Jacquemart, A. Jolly, J. Lamouroux, R. L. Roy, G. Li, D. Long, O. Lyulin, C. Mackie, S. Massie, S. Mikhailenko, H. Müller, O. Naumenko, A. Nikitin, J. Orphal, V. Perevalov, A. Perrin, E. Polovtseva, C. Richard, M. Smith, E. Starikova, K. Sung, S. Tashkun, J. Tennyson, G. Toon, V. Tyuterev, and G. Wagner. The HITRAN2012 molecular spectroscopic database. *J. Quant. Spectrosc. Radiat. Transfer*, 130:4–50, 2013. DOI: 10.1016/j.jqsrt.2013.07.002.

[213] G. Herzberg. *Molecular spectra and molecular structure. Vol. 2: Infrared and Raman spectra of polyatomic molecules*. New York: Van Nostrand, Reinhold, 1945.

[214] J. M. Hollas. *Modern spectroscopy*. John Wiley & Sons, 2004.

[215] M. Born and R. Oppenheimer. Zur Quantentheorie der Molekeln. *Ann. Phys. (Berlin)*, 389(20):457–484, 1927. DOI: 10.1002/andp.19273892002.

[216] M. Somoza. *Graphical depiction of the Morse potential with a harmonic potential for comparison*. 2006.

[217] D. J. Griffiths. *Introduction to quantum mechanics*. Pearson Education India, 2005.

[218] L. S. Rothman and L. D. Young. Infrared energy levels and intensities of carbon dioxide — II. *J. Quant. Spectrosc. Radiat. Transfer*, 25(6):505–524, 1981. DOI: 10.1016/0022-4073(81)90026-1.

[219] W. Voigt. *Das Gesetz der Intensitätsverteilung innerhalb der Linien eines Gasspektrums*. Verlag d. K. B. Akad. d. Wiss., 1912.

[220] R. H. Dicke. The effect of collisions upon the Doppler width of spectral lines. *Phys. Rev.* 89(2):472–473, 1953. DOI: 10.1103/PhysRev.89.472.

[221] M. Nelkin and A. Ghatak. Simple binary collision model for van Hove's $G_s(r,t)$. *Phys. Rev.* 135(1A):A4–A9, 1964. DOI: 10.1103/PhysRev.135.A4.

[222] L. Galatry. Simultaneous effect of Doppler and foreign gas broadening on spectral lines. *Phys. Rev.* 122(4):1218–1223, 1961. DOI: 10.1103/PhysRev.122.1218.

[223] P. L. Varghese and R. K. Hanson. Collisional narrowing effects on spectral line shapes measured at high resolution. *Appl. Opt.* 23(14):2376–2385, 1984. DOI: 10.1364/AO.23.002376.

[224] S. G. Rautian and I. I. Sobel'man. The effect of collisions on the Doppler broadening of spectral lines. *Phys. Usp.* 9(5):701–716, 1967. DOI: 10.1070/PU1967v009n05ABEH003212.

[225] P. R. Berman. Speed-dependent collisional width and shift parameters in spectral profiles. *J. Quant. Spectrosc. Radiat. Transfer*, 12(9):1331–1342, 1972. DOI: 10.1016/0022-4073(72)90189-6.

[226] M. D. De Vizia, A. Castrillo, E. Fasci, P. Amodio, L. Moretti, and L. Gianfrani. Experimental test of the quadratic approximation in the partially correlated speed-dependent hard-collision profile. *Phys. Rev. A*, 90(2):022503, 2014. DOI: 10.1103/PhysRevA.90.022503.

[227] B. Lance, G. Blanquet, J. Walrand, and J.-P. Bouanich. On the speed-dependent hard collision lineshape models: application to C_2H_2 perturbed by Xe. *J. Mol. Spectrosc.* 185(2):262–271, 1997. DOI: 10.1006/jmsp.1997.7385.

[228] R. Ciuryło, R. Jaworski, J. Jurkowski, A. S. Pine, and J. Szudy. Spectral line shapes modeled by a quadratic speed-dependent Galatry profile. *Phys. Rev. A*, 63(3):032507, 2001. DOI: 10.1103/PhysRevA.63.032507.

[229] H. Tran, N. Ngo, and J.-M. Hartmann. Efficient computation of some speed-dependent isolated line profiles. *J. Quant. Spectrosc. Radiat. Transfer*, 129:199–203, 2013. DOI: 10.1016/j.jqsrt.2013.06.015.

[230] J. Humlíček. An efficient method for evaluation of the complex probability function: the Voigt function and its derivatives. *J. Quant. Spectrosc. Radiat. Transfer*, 21(4):309–313, 1979. DOI: 10.1016/0022-4073(79)90062-1.

[231] J. Tennyson, P. F. Bernath, A. Campargue, A. G. Császár, L. Daumont, R. R. Gamache, J. T. Hodges, D. Lisak, O. V. Naumenko, L. S. Rothman, H. Tran, N. F. Zobov, J. Buldyreva, C. D. Boone, D. De Vizia, L. Gianfrani, J.-M. Hartmann, R. McPheat, D. Weidmann, J. Murray, N. H. Ngo, and O. L. Polyansky. Recommended isolated-line profile for representing high-resolution spectroscopic transitions (IUPAC Technical Report). *Pure Appl. Chem.* 86(12):1931–1943, 2014. DOI: 10.1515/pac-2014-0208.

[232] M. Schneider, F. Hase, J.-F. Blavier, G. Toon, and T. Leblanc. An empirical study on the importance of a speed-dependent Voigt line shape model for tropospheric water vapor profile remote sensing. *J. Quant. Spectrosc. Radiat. Transfer*, 112(3):465–474, 2011. DOI: 10.1016/j.jqsrt.2010.09.008.

[233] J. Burkart and S. Kassi. Absorption line metrology by optical feedback frequency-stabilized cavity ring-down spectroscopy. *Appl. Phys. B*, 119(1):97–109, 2015. DOI: 10.1007/s00340-014-5999-3.

[234] R. Tipping and Q. Ma. Theory of the water vapor continuum and validations. *Atmos. Res.* 36(1):69–94, 1995. DOI: 10.1016/0169-8095(94)00028-C.

[235] J. G. Cormier, R. Ciurylo, and J. R. Drummond. Cavity ringdown spectroscopy measurements of the infrared water vapor continuum. *J. Chem. Phys*, 116(3):1030–1034, 2002. DOI: 10.1063/1.1425825.

[236] D. Mondelain, A. Aradj, S. Kassi, and A. Campargue. The water vapour self-continuum by CRDS at room temperature in the 1.6 μm transparency window. *J. Quant. Spectrosc. Radiat. Transfer*, 130:381–391, 2013. DOI: 10.1016/j.jqsrt.2013.07.006.

[237] D. Romanini, P. Dupré, and R. Jost. Non-linear effects by continuous wave cavity ringdown spectroscopy in jet-cooled NO_2. *Vib. Spectrosc.* 19(1):93–106, 1999. DOI: 10.1016/S0924-2031(99)00018-1.

[238] C. R. Bucher, K. K. Lehmann, D. F. Plusquellic, and G. T. Fraser. Doppler-free nonlinear absorption in ethylene by use of continuous-wave cavity ringdown spectroscopy. *Appl. Opt.* 39(18):3154–3164, 2000. DOI: 10.1364/AO.39.003154.

[239] D. Lisak and J. T. Hodges. High-resolution cavity ring-down spectroscopy measurements of blended H_2O transitions. *Appl. Phys. B*, 88(2):317–325, 2007. DOI: 10.1007/s00340-007-2691-x.

[240] G. Giusfredi, S. Bartalini, S. Borri, P. Cancio, I. Galli, D. Mazzotti, and P. De Natale. Saturated-absorption cavity ring-down spectroscopy. *Phys. Rev. Lett.* 104(11):110801, 2010. DOI: 10.1103/PhysRevLett.104.110801.

[241] K. K. Lehmann. Theoretical detection limit of saturated absorption cavity ring-down spectroscopy (SCAR) and two-photon absorption cavity ring-down spectroscopy. *Appl. Phys. B*, 116(1):147–155, 2014. DOI: 10.1007/s00340-013-5663-3.

[242] I. Galli, S. Bartalini, S. Borri, P. Cancio, D. Mazzotti, P. De Natale, and G. Giusfredi. Molecular gas sensing below parts per trillion: radiocarbon-dioxide optical detection. *Phys. Rev. Lett.* 107(27):270802, 2011. DOI: 10.1103/PhysRevLett.107.270802.

[243] V. Letokhov. Saturation spectroscopy. In: *High-Resolution Laser Spectroscopy*. Ed. by K. Shimoda. Vol. 13. Topics in Applied Physics. Springer-Verlag Berlin Heidelberg, 1976, pp. 95–171. DOI: 10.1007/3540077197_20.

[244] W. Demtröder. *Laser spectroscopy*. 3rd ed. Springer-Verlag Berlin Heidelberg, 2003.

[245] S. Haroche and F. Hartmann. Theory of saturated-absorption line shapes. *Phys. Rev. A*, 6(4):1280–1300, 1972. DOI: 10.1103/PhysRevA.6.1280.

[246] C. J. Bordé, J. L. Hall, C. V. Kunasz, and D. G. Hummer. Saturated absorption line shape: Calculation of the transit-time broadening by a perturbation approach. *Phys. Rev. A*, 14(1):236–263, 1976. DOI: 10.1103/PhysRevA.14.236.

[247] L. Mandel and E. Wolf. Interaction between light and a two-level atom. In: *Optical coherence and quantum optics*. Cambridge University Press, 1995. Chap. 15, pp. 741–804.

[248] M. O. Scully and M. S. Zubairy. In: *Optical coherence and quantum optics*. Cambridge University Press, 1997, pp. 145–219.

[249] D. Walls and G. Milburn. In: *Quantum Optics*. Springer-Verlag Berlin Heidelberg, 1994, pp. 197–228.

[250] R. A. McFarlane, W. R. Bennett, and W. E. Lamb. Single mode tuning dip in the power output of an He-Ne optical maser. *Appl. Phys. Lett.* 2(10):189–190, 1963. DOI: 10.1063/1.1753727.

[251] W. E. Lamb. Theory of an optical maser. *Phys. Rev.* 134(6A):A1429–A1450, 1964. DOI: 10.1103/PhysRev.134.A1429.

[252] W. Zhang, M. J. Martin, C. Benko, J. L. Hall, J. Ye, C. Hagemann, T. Legero, U. Sterr, F. Riehle, G. D. Cole, and M. Aspelmeyer. Reduction of residual amplitude modulation to 1×10^{-6} for frequency modulation and laser stabilization. *Opt. Lett.* 39(7):1980–1983, 2014. DOI: 10.1364/OL.39.001980.

[253] M. Šimečková, D. Jacquemart, L. S. Rothman, R. R. Gamache, and A. Goldman. Einstein *A*-coefficients and statistical weights for molecular absorption transitions in the HITRAN database. *J. Quant. Spectrosc. Radiat. Transfer*, 98(1):130–155, 2006.

[254] J. Burkart, T. Sala, D. Romanini, M. Marangoni, A. Campargue, and S. Kassi. Communication: Saturated CO_2 absorption near 1.6 μm for kilohertz-accuracy transition frequencies. *J. Chem. Phys*, 142(19):191103, 2015. DOI: 10.1063/1.4921557.

[255] S. Tashkun, V. Perevalov, R. Gamache, and J. Lamouroux. CDSD-296, high resolution carbon dioxide spectroscopic databank: version for atmospheric applications. *J. Quant. Spectrosc. Radiat. Transfer*, 152:45–73, 2015. DOI: 10.1016/j.jqsrt.2014.10.017.

[256] D. Long, S. Wójtewicz, C. Miller, and J. Hodges. Frequency-agile, rapid scanning cavity ring-down spectroscopy (FARS-CRDS) measurements of the (30012)←(00001) near-infrared carbon dioxide band. *J. Quant. Spectrosc. Radiat. Transfer*, 161:35–40, 2015. DOI: 10.1016/j.jqsrt.2015.03.031.

[257] P. Bergamaschi, M. Schupp, and G. W. Harris. High-precision direct measurements of $^{13}CH_4/^{12}CH_4$ and $^{12}CH_3D/^{12}CH_4$ ratios in atmospheric methane sources by means of a long-path tunable diode laser absorption spectrometer. *Appl. Opt.* 33(33):7704–7716, 1994. DOI: 10.1364/AO.33.007704.

[258] M. H. Thiemens, T. Jackson, E. C. Zipf, P. W. Erdman, and C. van Egmond. Carbon dioxide and oxygen isotope anomalies in the mesosphere and stratosphere. *Science*, 270(5238):969–972, 1995. DOI: 10.1126/science.270.5238.969.

[259] H. Yurimoto and K. Kuramoto. Molecular cloud origin for the oxygen isotope heterogeneity in the solar system. *Science*, 305(5691):1763–1766, 2004. DOI: 10.1126/science.1100989.

[260] J. M. Eiler. "Clumped-isotope" geochemistry — The study of naturally-occurring, multiply-substituted isotopologues. *Earth Planet. Sci. Lett.* 262(3):309–327, 2007. DOI: 10.1016/j.epsl.2007.08.020.

[261] M. Casado, A. Cauquoin, A. Landais, J. Landsberg, E. Kerstel, and J.-F. Doussin. Experimental determination for kinetic fractionation during solid condensation at low temperature and theoretical framework. In: *EGU General Assembly Conference Abstracts*. Vol. 16. 2014, p. 14673.

[262] P. Gupta, D. Noone, J. Galewsky, C. Sweeney, and B. H. Vaughn. Demonstration of high-precision continuous measurements of water vapor isotopologues in laboratory and remote field deployments using wavelength-scanned cavity ring-down spectroscopy (WS-CRDS) technology. *Rapid Commun. Mass Spectrom.* 23(16):2534–2542, 2009. DOI: 10.1002/rcm.4100.

Abstract

High-precision molecular absorption spectroscopy is a powerful tool for fundamental physics and metrology, as well as for a broad range of applications in fields such as environmental sciences, planetology and astrophysics. In recent years, spectroscopic techniques based on the enhanced interaction of laser light with molecular samples in high-finesse optical cavities have provided outstanding detection sensitivities on the absorption axis, while the spectrometer frequency axis rarely met as high precision standards.

In this thesis, we addressed this challenge by the development of Optical Feedback Frequency-Stabilized Cavity Ring-Down Spectroscopy (OFFS-CRDS). This novel technique features a unique combination of sub-kHz frequency resolution and stability, kW/cm^2-level intracavity light intensity, a shot-noise limited absorption detectivity down to $2 \cdot 10^{-13}\,\mathrm{cm}^{-1}/\sqrt{\mathrm{Hz}}$, as well as a detection limit of $8.4 \cdot 10^{-14}\,\mathrm{cm}^{-1}$ on a narrow spectral interval. This unprecedented performance is based on the tight Pound-Drever-Hall lock of the ring-down cavity to a single-sideband-tuned distributed-feedback diode laser which is optical-feedback-stabilized to a highly stable V-shaped reference cavity. To transfer the coherence of this sub-kHz laser source to noisier lasers in other spectral regions through an optical frequency comb, we have explored a novel high-bandwidth feed-forward phase cloning scheme and demonstrated a residual phase error as low as 113 mrad. Applying OFFS-CRDS to the spectroscopy of CO_2 near 1.6 µm, we obtained a broadband spectrum with a dynamic range of $8 \cdot 10^5$ and retrieved twelve absolute transition frequencies with kHz-accuracy by measuring sub-Doppler saturated absorption Lamb dips with a comb-assisted setup. Furthermore, we have performed a comprehensive analysis of systematic error sources in CRDS and derived an analytic formula for the non-exponential ring-down signal in a weakly saturated regime, which may contribute towards future concentration-independent transition dipole moment measurements. Our results open up promising perspectives for metrological applications of OFFS-CRDS, such as advanced absorption lineshape studies, isotopic ratio measurements and extensive saturated absorption spectroscopy in the near infrared.

Résumé

La spectroscopie d'absorption moléculaire est un outil incontournable non seulement pour la physique fondamentale et la métrolgie mais aussi pour des domaines aussi divers que les sciences environnementales, la planétologie ou l'astrophysique. Ces dernières années, des techniques spectroscopiques qui exploitent l'amplification résonnante d'interaction entre lumière laser et molécules dans une cavité optique ont fourni des détectivités exceptionnelles sur l'axe d'absorption, tandis que l'axe de fréquence des spectromètres n'atteignait généralement pas le même niveau de précision.

Dans cette thèse, nous avons répondu à ce défi en développant la spectroscopie en cavité par temps de déclin stabilisée en fréquence par rétroaction optique (OFFS-CRDS en anglais). Cette nouvelle technique présente une combinaison unique de stabilité et résolution fréquentielles sub-kHz, d'un niveau d'intensité lumineuse intra-cavité de l'ordre du kW/cm^2, d'une detectivite de $2 \cdot 10^{-13}\,\mathrm{cm}^{-1}/\sqrt{\mathrm{Hz}}$ limitée par le bruit de photons, et d'une limite de détection de $8.4 \cdot 10^{-14}\,\mathrm{cm}^{-1}$ sur une plage spectrale étroite. Ces performances inédites sont dues à l'asservissement de la cavité spectroscopique à un laser balayé en fréquence par modulation à bande latérale unique et stabilisé par rétroaction optique avec une cavité en V de réference ultrastable. Pour transférer la cohérence de ce laser sub-kHz à des lasers plus bruiteux dans d'autres gammes spectrales à travers un peigne de fréquence optique, nous avons exploré une nouvelle méthode de clonage de phase par une correction anticipative à large bande passante et démontré une erreur résiduelle de phase de 113 mrad. En appliquant l'OFFS-CRDS à la spectroscopie du CO_2 à 1.6 µm, nous avons obtenu un spectre large bande avec une dynamique de $8 \cdot 10^5$, et nous avons déterminé douze fréquences de transition absolues avec une exactitude de l'ordre du kHz en mesurant des Lamb dips sub-Doppler en absorption saturée avec un dispositif équipé d'un peigne de fréquence. Par ailleurs, nous avons procédé à une analyse détaillée des sources d'erreurs systematiques en CRDS et nous avons déduit une formule analytique pour le déclin de cavité non-exponentiel dans un régime faiblement saturé qui est susceptible de contribuer à de futures mesures de moments de transition dipolaire indépendantes de la concentration. Nos résultats ouvrent des perspectives prometteuses pour des applications métrologiques de l'OFFS-CRDS, comme par exemple l'étude de profils de raie poussés, la mesures de rapports isotopiques et la spectroscopie d'absorption saturée extensive dans le proche infrarouge.